

Electronic Thesis and Dissertation Repository

7-24-2017 12:00 AM

Flow Characterization Under Idealized Stenosis Geometry and Performance Assessment of the Hemodynamic Flow Facility

Marin Vratonjic
The University of Western Ontario

Supervisor
Professor Eric Savory
The University of Western Ontario

Graduate Program in Mechanical and Materials Engineering
A thesis submitted in partial fulfillment of the requirements for the degree in Doctor of Philosophy
© Marin Vratonjic 2017

Follow this and additional works at: <https://ir.lib.uwo.ca/etd>



Part of the [Biomechanical Engineering Commons](#)

Recommended Citation

Vratonjic, Marin, "Flow Characterization Under Idealized Stenosis Geometry and Performance Assessment of the Hemodynamic Flow Facility" (2017). *Electronic Thesis and Dissertation Repository*. 4885.

<https://ir.lib.uwo.ca/etd/4885>

This Dissertation/Thesis is brought to you for free and open access by Scholarship@Western. It has been accepted for inclusion in Electronic Thesis and Dissertation Repository by an authorized administrator of Scholarship@Western. For more information, please contact wlsadmin@uwo.ca.

ABSTRACT

It is well known that regions inside the human arterial network susceptible to atherosclerosis experience a complex flow environment. Endothelial Cells (ECs) lining the inner wall of arteries are sensors to spatially and temporally varying shear stress (i.e. wall shear stress gradients). This complex force-loading can disrupt local cell-to-cell attachment regions triggering a cascade of biological events leading to the formation of atherosclerotic lesions. Consequently, researchers predominantly use a Parallel Plate Flow Chamber (PPFC) to study the hemodynamic-cell cycle relationship due to its simplicity and ability to achieve a two-dimensional fully-developed steady laminar flow across the cell monolayer. Researchers also resort to a PPFC with a vertical step to disrupt the incoming steady and/or pulsatile flow and, thus, generate a complex force-loading on the live ECs.

The present study is focused on the development and validation (by means of quantifying all elements of the design, performance and experimental uncertainty) of a hemodynamic flow facility allowing two-component (u, v) Laser Doppler Velocimetry (LDV) measurements as close as $40\ \mu\text{m}$ from the cell monolayer inside the PPFC. The study uses a backward-facing step (BFS) with 50% area reduction to model an idealized stenosis and, hence, disturb the incoming steady and pulsatile laminar flow. To provide insight not only into the fluid dynamic comparison but also on how the BFS models wall shear stress (WSS) and its spatial and temporal gradient (along with the oscillatory shear index, OSI) in a stenosed tube representing an artery, a detailed quantitative comparison with more realistic models of stenosis is provided (i.e. carotid artery phantom). To the best of the author's knowledge such a quantitative comparison is not available in the literature. In addition, the present study provides mean flow and turbulence statistics downstream of the BFS, thereby adding knowledge to stenosed cases (away from the wall in the developing shear layer) allowing Computational Fluid Dynamics (CFD) modelers to reference experimental data when simulating intermittent turbulent flows.

The results indicate that despite the simplicity of the chosen geometry, the measured flow downstream of the BFS under steady and pulsatile flow exhibits a number of features that are documented in previous work with more realistic configurations of stenoses (i.e. asymmetric tube stenosis). The author believes this simple geometry will set the stage for more advanced studies in the PPFC with more realistic geometrical configurations of stenoses. Lastly, additional work with live ECs cultured inside the PPFC can be undertaken under disturbed flow conditions reported in the present investigation.

Keywords: Endothelial cells (ECs), time-varying shear stress, Laser Doppler Velocimetry (LDV), parallel-plate flow chamber (PPFC), pulsatile flow, intermittent turbulence, backward-facing step (BFS), separated flow region, and asymmetric stenosis.

DEDICATION

This thesis is dedicated to my advisor Professor Eric Savory for his direction, insight and patience during the various stages of my experimental research. Without his support and flexibility, it would not have been possible to complete this work.

I would also like to acknowledge my parents and sister for their on-going financial and emotional support. My family has always stood by my side and for that I will always be grateful. Working full-time and taking care of my three beautiful dogs while completing this work presented challenges that seemed, at times, insurmountable. As the work neared completion, I realized how much I had grown intellectually and as an individual by forcing myself to persevere in the face of numerous obstacles. There is value in struggle if we are willing and able to endure it.

To say that this thesis has not been easy would be a gross understatement and its completion is profoundly gratifying. I sincerely hope that my contribution to the rich body of research that has inspired and directed me since the outset of this project will be meaningful.

ACKNOWLEDGMENTS

My supervisor, Eric Savory, has been instrumental towards this project in helping me reach feasibility and useable flow measurements at the working section inside the parallel-plate flow chamber.

I would also like to acknowledge the University Machine Services (UMS) for their valuable input and hard work in manufacturing the hemodynamic flow facility. Doug Phillips, Clayton Cook, Dan Sweiger, and Kevin Lee have all been instrumental in the success of this project.

I would like to thank TSI Inc. (Dr. Joseph Shakal, Dr. Tyson Strand, and Dr. Dan Troolin), and LSM Tech. (Brad Bobbitt) since they offered me tremendous support towards understanding LDV fundamentals and constructing the hemodynamic probe (i.e. near-wall configured LDV system). I would also like to acknowledge my colleagues in the Advanced Fluids Mechanics (AFM) research group for their support throughout my Ph.D. studies.

Finally, the financial support was provided by Ontario Innovation Trust (OIT), Canada Foundation of Innovation, National Science and Engineering Research Council of Canada (NSERC), and CIHR Strategic Training Program in Vascular Research, University of Western Ontario.

TABLE OF CONTENTS

ABSTRACT.....	ii
DEDICATION.....	iii
ACKNOWLEDGMENTS.....	iv
TABLE OF CONTENTS.....	v
LIST OF FIGURES.....	xi
LIST OF TABLES.....	xxi
LIST OF APPENDICES.....	xxii
LIST OF ABBREVIATIONS.....	xxiii
NOMENCLATURE.....	xxv
CHAPTER ONE	INTRODUCTION TO HEMODYNAMICS AND ENDOTHELIAL CELLS: MOTIVATION, METHODS OF RESEARCH, AND PRESENT SCOPE.....
	1
1	Introduction.....
	1
1.1	The relationship between Hemodynamics and Endothelial Cells.....
	1
1.2	A Concise Overview of Previous Methods of Investigation.....
	6
1.2.1	Deficiencies in the Technical Literature.....
	11
1.2.2	Present Work Contribution.....
	11
1.2.2.1	Original Contribution of the Flow Facility Performance Assessment: An Extension to the Work of Avari et al (2016).....
	12
1.2.2.2	Present Work Limitations.....
	14
1.3	Research Scope: The General Concept.....
	15
1.3.1	Detailed Research Objectives.....
	16
1.3.1.1	Development and Validation of the Hemodynamic Flow Facility.....
	17
1.3.1.2	LDV Performance and Experimental Uncertainty.....
	20

1.3.1.3 Two-Component Velocity Measurements over a BFS (Steady and Pulsatile Flow Investigation).....	21
1.4 Thesis Outline.....	22
1.4.1 Chapter Two: Literature Review.....	22
1.4.2 Chapter Three: Experimental Apparatus and Methods.....	23
1.4.3 Chapter Four: Experimental Uncertainty.....	23
1.4.4 Chapter Five: Two Component Velocity Measurements Downstream of a BFS under Steady and Pulsatile Flow.....	24
1.4.5 Chapter Six: Conclusions and Future Work.....	25
1.4.6 Appendices.....	25
1.5 Chapter One Summary.....	26
 CHAPTER TWO LITERATURE REVIEW.....	 27
2 Introduction.....	27
2.1 Endothelial Cell Response to Flow.....	28
2.2 Parallel-Plate Flow Chamber (PPFC) Classification for Biomedical Applications.....	34
2.2.1 Investigation of Steady and Pulsatile Flow inside a PPFC over ECs.....	36
2.2.2 Analytical and Experimental Methods for Quantifying Wall Shear Stress.....	39
2.2.2.1 Analytical Solution for Pulsatile Flow (Laminar Regime) inside a PPFC.....	41
2.3 BFS Flow Inside Rectangular Flow Channels under Steady Laminar Flow...46	
2.3.1 Paths to Flow Instability.....	51
2.3.1.1 Vortex Shedding Mechanisms in Internal Flows.....	54

2.3.2 The Effect of Expansion Ratio (ER) on the Flow Physics Downstream of a BFS.....	57
2.3.3 Shortfalls in the Literature Surrounding BFS Flows under Steady Laminar Flow.....	60
2.4 Idealized Stenosis Flow Inside Rectangular Flow Channels under Steady and Pulsatile Laminar Flow.....	61
2.4.1 General Motivation.....	61
2.4.2 The Asymmetric and Axi-Symmetric Stenosis Models.....	63
2.4.3 Shortfalls in the Literature Surrounding Idealized Stenosis Flows Under Steady and Pulsatile Laminar Flow: Two-Dimensional Flow Channel.....	68
2.5 Steady and Pulsatile Laminar Flow in a Straight Section of Tube Under the Influence of a Stenosis.....	69
2.5.1 General Motivation.....	69
2.5.2 The Axi-Symmetric Stenosis Models.....	71
2.5.3 Previous Studies Pertaining to Asymmetric and Axi-Symmetric Stenosis Models Under Steady and Pulsatile Laminar Flow.....	72
2.5.3.1 Paths to Flow Instability.....	78
2.6 Chapter Two Summary.....	81
 CHAPTER THREE EXPERIMENTAL APPARATUS AND METHODS.....	 84
3 Introduction.....	84
3.1 An Overview of the Hemodynamic Flow Facility.....	85
3.1.1 Latest Revision of the PPFC.....	89
3.1.2 Pulsatile Flow Pump.....	93

3.1.3 An In-House Developed LDV System for Near-Wall Flow Measurements.....	95
3.1.3.1 Custom Near-Wall Micro-Probe Contribution.....	98
3.2 Vertical Profiles of the Streamwise Mean Velocity under a Steady Laminar Flow: Analytical Predictions.....	99
3.3 The Working Section Geometry and Characteristic Length Scales: Backward-Facing Step Flow Cases.....	114
3.4 Relative Surface Roughness at the Working Section inside the PPFC.....	116
3.5 Fluid Specifications.....	117
3.6 Computer-Controlled Application Interface.....	117
3.7 Chapter Three Summary.....	119
CHAPTER FOUR EXPERIMENTAL UNCERTAINTY.....	122
4 Introduction.....	122
4.1 Mean Flow and Turbulence Statistics Uncertainties.....	123
4.2 Estimation of the Micro-Transpose Uncertainty (Motorized Laboratory Jack).....	127
4.3 Wall Datum Identification Methods: Origin Uncertainty Analysis.....	130
4.3.1 Spatial Uncertainty of Measurement Volume Position along the Streamwise and Spanwise Directions (x and z, respectively).....	134
4.4 Derivation of Wall Shear Stress from Near-Wall LDV Data and its Uncertainty.....	139
4.5 Hemodynamic Pulsatile Pump Performance Evaluation.....	145
4.5.1 Normal Carotid Waveform Repeatability and Damping.....	150
4.5.1.1 Normal Carotid Waveform Energy Loss.....	151
4.6 Sample Size and the Selection Criteria for the Bin Size for Steady and Pulsatile Flow over a Backward-Facing Step.....	160

4.7 In-Situ Measurement of the Step Height and Expansion Ratio.....	165
4.8 Chapter Four Summary.....	166
CHAPTER FIVE TWO-COMPONENT VELOCITY MEASUREMENTS DOWNSTREAM OF A BACKWARD-FACING STEP UNDER STEADY AND PULSATILE FLOW	169
5 Introduction.....	169
5.1 Steady Laminar Flow over a Backward-Facing Step.....	170
5.1.1 Problem Definition.....	170
5.1.2 Creating the Stenosis Models.....	171
5.1.3 Scope of Measurements and Data Processing.....	175
5.1.4 Results and Discussion.....	178
5.2 Pulsatile Laminar Flow over a Backward-Facing Step.....	203
5.2.1 Problem Definition.....	203
5.2.2 Creating the Stenosis Models.....	204
5.2.3 Scope of Measurements and Data Processing.....	205
5.2.4 Results and Discussion.....	208
5.3 Chapter Five Summary.....	230
CHAPTER SIX CONCLUSION AND FUTURE WORK.....	235
6.1 A Review on the Purpose of the Thesis Work.....	235
6.2 A Summary of the Objectives and the Corresponding Results.....	235
6.3 Possible Future Work.....	239
REFERENCES.....	241
APPENDIX 1.....	259
APPENDIX 2.....	305

APPENDIX 3.....363

APPENDIX 4.....365

CURRICULUM VITAE.....370

LIST OF FIGURES

Fig. 1.1	Arterial locations exhibiting disturbed flow pattern (from Chiu & Chien, 2011). 1, Aortic sinus; 2, ascending aorta; 3, inner (lesser) curvature of aortic arch; 4, outer (greater) curvature of aortic arch; 5, innominate artery; 6, right common carotid artery; 7, left common carotid artery; 8, left subclavian artery; 9, thoracic aorta; 10, renal artery; 11, abdominal aorta; 12, iliac artery.....	3
Fig. 1.2	Hemodynamic loading on ECs (From: Chiu & Chen, 2009).....	4
Fig. 1.3	Mechanical representation of the hemodynamic-cell loading cycle.....	6
Fig. 1.4	An example of a Parallel-Plate Flow Chamber (PPFC) used for EC research under steady laminar and disturbed flow (i.e. flow subjected to step) conditions. From: Chiu & Chen (2009).....	9
Fig. 1.5	Illustration showing an EC with mechanosensors. Modified from Givens & Tzima (2016). The diagram is not to scale.....	15
Fig. 1.6	Illustration demonstrating design challenges associated with penetrating both blue and green beams inside a small 1.8 mm channel.....	18
Fig. 2.1	Hemodynamic loading on the ECs (Ohashi & Sato 2005).....	33
Fig. 2.2	Fluorescent images of actin filaments (Ohashi and Sato, 2005).....	34
Fig. 2.3	Common <i>in-vitro</i> devices to study EC response to flow under steady laminar, pulsatile laminar and disturbed flow conditions. PPFC (A), Cone and Plate Apparatus (B), Parallel Disk Viscometer (C), Orbital Shaker (D) and Capillary Tube (E). Image taken and modified from Avari (2015)....	35
Fig. 2.4	Schematic of a BFS to disturb the oncoming steady and pulsatile laminar flow. Illustration from Chien (2008).....	37
Fig. 2.5	From Loudon & Tordesillas (1998): velocity profiles as a function of the Wormersley number.....	42
Fig. 2.6	Geometry for flow between parallel plates.....	44
Fig. 2.7	Typical geometry of a BFS test problem for analysis. This Figure defines the various length scales at the working section. The normalized reattachment length of the primary recirculation region is denoted by variable $x_1 = x/S$. Furthermore, x_4 and x_5 denote the start and the end of the upper wall recirculation region ('roof eddy'), respectively. Illustration taken from Biswas et al (2004).....	47

Fig. 2.8	Measurements of the separation and reattachment locations as a function of the Reynolds number. Plot taken from the work of Armaly et al (1983).....	49
Fig. 2.9	Results from Williams & Baker (1997) showing penetration of side-wall separation regions out to the main stream flow. The case simulated was for $Re_S = 800$	56
Fig. 2.10	Results from Williams & Baker (1997) showing oil flow streak lines for $Re_S = 800$. Flow near the floor (a) and near the roof (b).....	56
Fig. 2.11	Results from Thangam & Knight (1989) showing reattachment length as a function of the Reynolds number for various expansion ratios. Note that the reattachment length (primary on the lower wall) was normalized with the hydraulic diameter at the step ($D_h = 2h$) and not the step height (S). Another note is that variable E in the Figure represents ER , however, defined as $E = S/H$	59
Fig. 2.12	Results from Nie & Armaly (2002) showing the effect of step height on the reattachment line. It should be noted that z and L are, respectively, the spanwise direction and the channel half-width.....	59
Fig. 2.13	From Griffith (2009): Test section geometry under investigation which includes a semi-circular stenosis. The variable D and r , are, respectively, the channel height (distance between the unblocked walls) and radius of the semi-circular stenosis. The blockage is defined as $b = r/D$	63
Fig. 2.14	From Griffith (2009): Recirculation lengths as a function of the Re value for various constriction ratios. The reattachment length (L_r) normalized with (a) channel height and (b) the blockage radius.....	64
Fig. 2.15	Test-section geometry for an idealized semi-circular stenosis. From Mittal et al (2003) showing an asymmetric semi-circular blockage (a) and from Beratlis et al (2005) showing an axi-symmetric blockage (b). For Mittal et al (2003), it should be noted that x_1 , x_2 and x_3 indicate the streamwise, wall-normal and spanwise directions, respectively. For further reference, the working section for Beratlis et al (2005) is $146H \times 12H \times 1H$; length, width, height, respectively).....	67
Fig. 2.16	From Griffith (2009): Axi-symmetric stenosis model inside a straight section of tubing.....	71
Fig. 2.17	Axi-symmetric stenosis model inside a straight section of tube (Illustration taken from Varghese et al. 2007a). It should be noted that D , L , x , z and y are, respectively, the diameter of the non-stenosed tube, length of the stenosis ($L = 2D$), the streamwise and cross-stream coordinates, respectively. For reference purposes, the dashed lines in the illustration indicate an eccentric model.....	71

- Fig. 2.18 Axi-symmetric stenosis model inside a straight section of tube (Illustration taken from Long et al. 2001). It should be noted that in the work of Long et al (2001), the diameter (D) upstream of the constriction is 8 mm. In addition, all the dimensions in the illustration are in mm.....72
- Fig. 2.19 Flow visualization photographs with hydrogen bubbles from the work of Ahmed & Giddens (1983). 50% stenosis at $Re = 500$ (a), 50% stenosis at $Re = 750$ (b) and 50% stenosis at $Re = 1000$ (c).....74
- Fig. 2.20 Flow visualization photographs with hydrogen bubbles from the work of Ahmed & Giddens (1984). The 50% stenosis at $Wo = 7.5$ (a), 50% stenosis at $Wo = 15$ (b) and 75% stenosis at $Wo = 7.5$ (c). The illustrations are pertaining to the deceleration phase of the pulse cycle.....76
- Fig. 2.21 From Long et al (2001): Downstream recirculation regions for the 50% asymmetrical stenosis during the deceleration phase of the pulse cycle...77
- Fig. 3.1 Hemodynamic Flow Facility consisting of the LDV probe, a PPFC, a commercial LDV receiver and the pulsatile flow pump. The pump connects to the PPFC with bio-compatible tubing with an inner diameter of 6.35 mm. The tubing was procured from Cole-Palmer, Canada. The pulsatile pump is mounted on a mobile pushcart to minimize the length of the tubing between the pump and the channel. Depending on the flow case considered, the pump was elevated above the PPFC accordingly to purge air bubbles at the working section inside the PPFC.....86
- Fig. 3.2 Hemodynamic flow facility showing flow measurements being captured with the LDV receiver oriented off-axis. The off-axis configuration was used to minimize reflections associated with the input and output beams.....87
- Fig. 3.3 Hemodynamic flow facility showing the PPFC mounted on a motorized laboratory jack and $x - z$ cross-slide milling table. The milling table was used to adjust the position of the channel in relation to the LDV probe and receiver. It was also used to traverse in the streamwise and spanwise directions to capture vertical flow profiles, $\bar{u}(y)$ downstream of a BFS.....88
- Fig. 3.4 The PPFC mounted to a computer controlled laboratory jack and $x - z$ milling table. The lab jack allows for both manual and PC-controlled height adjustment. It connects to the computer via USB cable and was specifically important (i.e. as a result of its superior spatial resolution) for locating the datum associated with the wall position (i.e. the closest velocity measurement point at the wall).....91
- Fig. 3.5 PPFC showing the upstream, downstream, and the working section. The length of the upstream and downstream sections is 251 mm and 94 mm,

	respectively. The working section extends for 82.55 mm. Once the channel was assembled with the bottom and top cavities and the glass canopy, the internal channel formed was 1.8 mm in height and 17.5 mm in width.....	92
Fig. 3.6	Working Section showing microscopy slide and the step used in the study. The distance between the step edge and the centre of the slide is 25 mm. The step protrudes into the channel $\approx 50\%$ of the original channel height (1.8 mm).....	93
Fig. 3.7	Positive displacement pulsatile pump used with the flow measurement experiments.....	95
Fig. 3.8	LDV Probe for near wall flow measurements mounted on a precision cross-slide milling table. There was no requirement to traverse the probe/receiver in the y –direction since the velocity gradient was resolved by traversing the channel alone.....	97
Fig. 3.9	Schematic representation of the working section inside the PPFC. A) The diagram is sectioned through the plane $z = 0$. The streamwise velocity is in the direction of the x –axis. B) Top view of the working section and section through plane $x - z$. The schematics outlined in a) and b) are not to scale.....	109
Fig. 3.10	Streamwise mean velocity $\bar{u}(y, z = 0.0w)$ normalized against the maximum streamwise velocity for an infinitely wide plate solution.....	110
Fig. 3.11	Streamwise channel velocity $\bar{u}(y, z = 0.45w)$ normalized against the maximum streamwise velocity for an infinitely wide plate solution.....	110
Fig. 3.12	Streamwise channel velocity $\bar{u}(y, z = 0.49w)$ normalized against the maximum streamwise velocity for an infinitely wide plate solution.....	111
Fig. 3.13	Streamwise channel velocity $\bar{u}(y = 900 \mu\text{m}, z)$ normalized against the maximum streamwise velocity for an infinitely wide plate solution. The laminar flow theory was not plotted in this figure since it assumes no boundary layer developing at the side walls.....	111
Fig. 3.14	Isometric view of the working section of the final revision PPFC. The blue colour indicates the symmetry plane (x - y).....	115
Fig. 3.15	Schematic illustration of the working section with the backward-facing step. The drawing is not to scale. The figure defines the various length scales at the working section. The normalized reattachment length of the primary recirculation region is denoted by variable $x_1^* = x_1/S$. Furthermore, x_4^* and x_5^* denote the start and the end of the upper wall recirculation region ('roof eddy'), respectively. Finally, x_2^* and x_3^*	

- represent the start and the end of the second recirculation zone on the lower wall, respectively.....115
- Fig. 4.1 Streamwise mean velocity $\bar{u}(y)$ plotted versus y -position at the working section ($2z/w = 0$). Theoretical data points were also plotted for the range, $100 < y \leq 900 \mu\text{m}$, to compare with the measured values. With the latter, the data points were not plotted near the wall for clarity purposes. The error bars were calculated from Eq. (6-2). The maximum absolute error (in the wall region, $20 \mu\text{m} \leq y \leq 100 \mu\text{m}$) was $\pm 0.008 \text{ m/s}$ (or 3.2% of \bar{u}_{max}). It should be noted that the velocity data near the wall were captured in $10 \mu\text{m}$ increments to obtain more accuracy in the wall shear stress determination.....125
- Fig. 4.2 Motorized laboratory jack validation of precision and accuracy. Shown in the figure are the traversing platform, the digital dial indicator and the gauge blocks used to calibrate the indicator and, thus, confirm the accuracy of $\pm 0.001 \text{ mm}$ ($\pm 1 \mu\text{m}$).....127
- Fig. 4.3 Accuracy and precision validation plot for the computer-controlled motorized laboratory jack. a) $10 \mu\text{m}$ increments over a range of $100 \mu\text{m}$, b) $50 \mu\text{m}$ increments over a range of $500 \mu\text{m}$. The difference is between the averaged and the theoretical data.....129
- Fig. 4.4 Measurement volume being traversed into the wall at the working section of the PPFC for determination of the measuring position (i.e. absolute location of the measurement volume). The near-wall beam configuration did not require tilting of the probe to capture the velocity gradient near the wall.....130
- Fig. 4.5 An outline of the initial set-up procedure to determine the measurement volume location in reference to the wall. All units in the figure are in μm . The nearest measurement point to the wall was $\approx 20 \mu\text{m}$ and $\approx 40 \mu\text{m}$ for the $F = 120 \text{ mm}$ and $F = 261 \text{ mm}$ lenses, respectively.....132
- Fig. 4.6 Streamwise mean velocity $\bar{u}(y)$ plotted against position readings of the motorized laboratory jack to demonstrate abrupt slope change. Points 1 and 2 refer to the positions on the microscopy slide (at $2z/w = 0$), left and right edges being $\approx \pm 11 \text{ mm}$ from the centre of the slide. Experiment was performed using $Q = 7.50 \pm 0.075 \text{ mL/s}$. The uncertainty error bars are only shown for the velocity data points related to measurements with the $F = 261 \text{ mm}$ lens (point 2).....133
- Fig. 4.7 Spanwise profile of the streamwise mean velocity $\bar{u}(z)$ plotted against the z -axis at the working section at $y/h = 0.5$. The simulated flow rate was $3.90 \pm 0.039 \text{ mL/s}$ ($Re_m = 600$).....136
- Fig. 4.8 Fixture for positioning the measurement volume on the step edge ($x/l = 0$) at the working section to establish a starting position for the

	downstream measurements of the $\bar{u}(y)$ and $\bar{v}(y)$ velocity profiles. The fixture was also used without the obstacle for steady and turbulent flow measurements at the working section. The other end of the fiber was connected to a power meter to measure the power (i.e. mW) to ensure optimal alignment between the measurement volume and the ferrule core diameter.....	139
Fig. 4.9	Percent Shear Rate Error for linear regression (theoretical data points) using $N_p = 3,4,5$ and 6 points (including the zero velocity data point at the wall). The points $y_1 = 20, 30, 40, 50, 60$ and $70 \mu\text{m}$ indicate distances from the wall (first measurement point considered). The general expression for the linear (straight-line) regression can be expressed as $u = by + b_0$, where b is the slope and b_0 is the intercept (Hutchins & Choi, 2002)...	140
Fig. 4.10	Percent Shear Rate Error for 2nd order polynomial regression (theoretical data points) using $N_p = 3,4,5$ and 6 points. The points $y_1 = 20, 30, 40, 50, 60$ and $70 \mu\text{m}$ indicate starting points from the wall. It should be noted that using this approximation yields an exact solution of the shear rate and the reported error in the y-axis is a result of rounding errors associated with Eq. 3-7. These results are in agreement with the findings from Fatemi & Rittgers (1994).....	142
Fig. 4.11	Percent Shear Rate Error for 2nd order polynomial regression (LDV data points) using $N_p = 3,4,5$ and 6. The points $y_1 = 20, 30, 40, 50, 60$ and $70 \mu\text{m}$ indicate starting points from the wall.....	144
Fig. 4.12	Transit-time ultrasonic flow meter mounted in-line between the pump outlet and reservoir. The flow meter was connected to the PC using a USB cable. The software allowed direct monitoring of the flow rate.....	146
Fig. 4.13	Measurement of linearity and accuracy of the steady flow produced by the pump for programmed $Q = 1, 5, 10$ and 15 mL/s . The trend line in the figure represent linear regression (averaged data points). The difference refers to the linear regression values subtracted by the programmed values.....	147
Fig. 4.14	Bias error of the programmed flow rates.....	148
Fig. 4.15	Set-up demonstrating the use of air-release valves to remove the air inside the cylinder prior to steady flow operation.....	150
Fig. 4.16	Measured normal carotid waveforms under $f = 1.08 \text{ Hz}$ at the working section.....	151
Fig. 4.17	Critical dimensions of the closed flow circuit.....	153
Fig. 4.18	Waveform damping analysis: (a) attenuation of a sinusoidally fluctuating component (P) of the pressure wave, (b) mechanical model of the PPFC	

	flow and, (c) flow response to oscillatory pressure gradient inside the PFFC.....	156
Fig. 4.19	Geometry of the working section under steady and pulsatile laminar flow over a backward-facing step (BFS). Illustration showing point for statistical convergence analysis ($x/S = 21.12$ and $y/h = 0.5$).....	161
Fig. 4.20	r.m.s. velocity plotted against the number of velocity realizations captured by the LDV system (and the number of pulsatile cycles): (a) r.m.s. v' (b) r.m.s. u' . The downstream station (from BFS) and the time instant of the cycle reflected in the plot is $x/S = 21.12$ and $t/T = 0.35$, respectively.....	162
Fig. 4.21	Skewness plotted against the number of velocity realizations captured by the LDV system: (a) $S_{v'}$ (b) $S_{u'}$. The downstream station and the time instant of the cycle reflected in the plot is $x/S = 21.12$ and $t/T = 0.35$, respectively.....	162
Fig. 4.22	Excess kurtosis plotted against the number of velocity realizations captured by the LDV system: (a) $K_{v'}$ (b) $K_{u'}$. The downstream station and the time instant of the cycle reflected in the plot is $x/S = 21.12$ and $t/T = 0.35$, respectively.....	163
Fig. 4.23	Reynolds Shear Stress ($-\overline{u'v'}$) convergence plot. The downstream station and the time instant of the cycle reflected in the plot is $x/S = 21.12$ and $t/T = 0.35$, respectively.....	164
Fig. 4.24	In-situ measurement of the actual step height, S	166
Fig. 5.1	Stenosis models: (a) BFS model referencing present work, the work of Armaly et al (1983) and Erturk (2008), (b) semi-circle model (2-D channel flow) referencing the work of Griffith (2009), (c) axi-symmetric tube model referencing the work of Griffith (2009), (d) <i>in-vitro</i> CA model from the work of Buchmann & Jermy (2007) and (e) <i>in-vitro</i> stenosed CA model from Buchmann et al (2008).....	173
Fig. 5.2	Schematic of the present BFS test-section showing measurement stations and other critical dimensions (Modified from Adams & Johnston, 1988).....	177
Fig. 5.3	An illustration of the expected flow field downstream of the flow blockage: (a) present BFS model (modified from Juste et al (2016)) and (b) axi-symmetric stenosis model inside a straight section of tube.....	179
Fig. 5.4	An illustration of the flow field inside the common carotid artery (CCA) phantom. Modified from the work of Buchmann & Jermy (2007).....	179
Fig. 5.5	Measured and normalized streamwise mean velocity profile $\bar{u}(y)$ at the inlet channel at $2z/w = 0$ and $x/S = -1.18$. The y -axis is normalized	

- against the channel height at the blockage ($h - S$). The maximum absolute error (in the wall region, $0.5 \leq y/h \leq 0.7$ is ± 0.01 m/s (or 1.25 % of \bar{u}_{\max}).....180
- Fig. 5.6 Normalized streamwise mean velocity at various downstream stations: (a) present BFS model in comparison with the work of Armaly et al (1983) and Erturk (2008), (b) present BFS model in comparison with the semi-circle model whereby the streamwise distance is normalized with the blockage height (S) and, (c) present BFS model in comparison with the semi-circle model whereby the streamwise distance is normalized with the reattachment length (x_1). (d) present BFS model in comparison with the axi-symmetric model (work of Griffith, 2009) whereby the wall-normal distance is normalized with channel/tube height and (e) present BFS model in comparison with the axi-symmetric model, whereby the wall-normal distance is normalized with the blockage height (S). (f) present BFS model in comparison with the axi-symmetric model (work of Griffith, 2009) whereby the streamwise distance is normalized with the reattachment length (g) present BFS model in comparison with the axi-symmetric model, whereby the streamwise distance is normalized with the reattachment length and only showing for $y^* \leq 0.2$. For the present study, the normalized typical uncertainty at $y/h = 0.5$ (mid-plane in reference to the height) is $\epsilon_{\bar{u}}/|\bar{u}| = \pm 2.50\%$182
- Fig. 5.7 Turbulence statistics: (a) normalized streamwise and wall-normal r.m.s. velocity profiles downstream of the BFS covering the range, $12.07 \leq x/S \leq 30.17$. The normalized typical uncertainties at $y/h = 0.5$ are $\epsilon_{r.m.s. u'}/r.m.s. u' = 5.65\%$ and $\epsilon_{r.m.s. v'}/r.m.s. v' = 5.65\%$, (b) $E_{u'u'}$ of u' at $y/h = 0.5$ at various downstream stations, (c) $E_{v'v'}$ of v' at $y/h = 0.5$ at various downstream stations, (d) $E_{u'u'}$ of u' at $y/h = 0.4$ at various downstream stations.....188
- Fig. 5.8 Measured Reynolds shear stress profiles at various x/S positions downstream of the step. No measurement of the wall-normal component (v) was possible for $y/h > 0.6$ as a result of the beam geometry (i.e. beams' half-angle) and finite channel height (i.e. 1.8 mm). The normalized typical uncertainty at $y/h = 0.5$ is $\epsilon_{\overline{u'v'}}/|\overline{u'v'}| = \pm 8.00\%$189
- Fig. 5.9 (a) Streamwise distribution of the local skin friction coefficient downstream of the blockage comparing the various stenosis models depicted in Fig. 7.1.(b) streamwise distribution of the skin friction spatial gradient.....200
- Fig. 5.10 Stenosis models: (a) BFS geometry referencing present work, (b) axi-symmetric channel model, Beratlis et al (2005) and (c) asymmetric tube model, Long et al (2001).....204

Fig. 5.11 Phase-averaged velocity profiles prior to flow separation: (a) present study temporal profile (U/\bar{U}) at $x/S = -1.18$ plotted against the normalized cycle time (averaged over 60 cycles), (b) temporal profiles inclusive of the work of Long et al (2001) and Beratlis et al (2005) whereby the cycle time is normalized with the systole rise time (SRT) and, (c) present study spatial profiles at $x/S = -1.18$ whereby the y -positions are normalized with the channel height. It should be noted that the temporal profiles of the other authors is given upstream of the blockage. The normalized typical uncertainty at $y/h = 0.75$ (midplane in reference to the height) is $\epsilon_{\langle u \rangle} / |\langle u \rangle| = \pm 2.50\%$209

Fig. 5.12 Phase-averaged velocity profiles at $x/S = -1.18$ for the present BFS model and upstream of the blockage for the axi-symmetric channel model (work of Beratlis et al. 2005). The streamwise velocity is normalized with the bulk velocity (U) corresponding to $t^* = 0.5, 1.0$ and 1.5 . It should be noted that the velocity profile associated with the channel model is not provided for $t^* = 1.5$. The normalized typical uncertainty at $y/h = 0.75$ (midplane in reference to the height) is $\epsilon_{\langle u \rangle} / |\langle u \rangle| = \pm 2.50\%$211

Fig. 5.13 Phase-averaged streamwise velocity profiles downstream of the blockage (comparing the present BFS model with the axi-symmetric channel model) at various measurement stations (x/S) and time instants (t^*). The normalized typical uncertainty at $y/h = 0.50$ (midplane in reference to the height) is $\epsilon_{\langle u \rangle} / |\langle u \rangle| = \pm 2.50\%$. The streamwise phase-averaged velocity is normalized with the mean bulk velocity (\bar{U}) upstream of the blockage.....213

Fig. 5.14 Phase-averaged streamwise velocity profiles downstream of the blockage (comparing the present BFS model with the axi-symmetric channel model) at various measurement stations (x/x_1) and time instants (t^*). The normalized typical uncertainty at $y/h = 0.50$ (midplane in reference to the height) is $\epsilon_{\langle u \rangle} / |\langle u \rangle| = \pm 2.50\%$. The streamwise phase-averaged velocity is normalized with the mean bulk velocity (\bar{U}) upstream of the blockage.....214

Fig. 5.15 Normalized streamwise and wall-normal r.m.s. velocity profiles (comparing the present BFS model with the axi-symmetric channel model) at various measurement stations (x/x_1) and time instants (t^*). The normalized typical uncertainty at $y/h = 0.50$ (midplane in reference to the height) for both velocity components is $\epsilon_{r.m.s \langle u' \rangle} / r.m.s \langle u' \rangle = 5.65\%$. The $\langle v' \rangle$ profile only shown for $t^* = 1.5$ since during other time instants of the pulse cycle yield $\langle v' \rangle \approx 0$ (whereby the scatter is within the experimental uncertainty).....217

Fig. 5.16 Energy spectra ($E_{u'u'}$) of the streamwise velocity fluctuation (u') for $x/S = 12.07, 15.08, 18.10$ and 21.12 measurement positions downstream of the step at the channel centreline ($y/h = 0.5$).....220

- Fig. 5.17 Phase-averaged streamwise velocity profiles downstream of the blockage (comparing the present BFS model with the asymmetric tube model) at various measurement stations (x/S) and time instants (t^*). The normalized typical uncertainty at $y/h = 0.50$ (midplane in reference to the height) is $\epsilon_{\langle u \rangle} / |\langle u \rangle| = \pm 2.50\%$. The streamwise phase-averaged velocity is normalized with the mean bulk velocity (\bar{U}) upstream of the blockage..221
- Fig. 5.18 Phase-averaged streamwise velocity profiles downstream of the blockage (comparing the present BFS model with the asymmetric tube model) at various measurement stations (x/x_1) and time instants (t^*). The normalized typical uncertainty at $y/h = 0.50$ (midplane in reference to the height) is $\epsilon_{\langle u \rangle} / |\langle u \rangle| = \pm 2.50\%$. The streamwise phase-averaged velocity is normalized with the mean bulk velocity (\bar{U}) upstream of the blockage.....222
- Fig. 5.19 (a) Distribution plot of the local skin friction coefficient (c_f) in the streamwise direction downstream of the blockage (i.e. $2z/w = 0$) comparing the present BFS model to the asymmetric tube model given by Long et al (2001). The average uncertainty of the skin friction is $\pm 5.2\%$. (b) streamwise distribution of the skin friction spatial gradient at $t^* = 1.0$ (peak flow), (c) streamwise distribution of the skin friction spatial gradient at $t^* = 1.5$ (deceleration phase).....229
- Fig. 5.20 (a) Temporal profile of the local skin friction coefficient at $x/x_1 = 0.75$ and (b) temporal profile of c_{f_t}' at $x/x_1 = 0.75$. The average uncertainty of the skin friction is $\pm 5.2\%$230

LIST OF TABLES

Table 2.1	A summary of the flow studies over ECs inside the PPFC.....	38
Table 2.2	Separation and reattachment locations: a comparison between experimental and numerical results for $Re_S = 800$	51
Table 3.1	Comparison of wall shear stress (at the working section, $x = 0, z = 0, y = 0$) computed from channel flow theory and a solution for an infinitely wide plate.....	113
Table 4.1	Individual uncertainties contributing to ϵ_y^2 . The uncertainty associated with ϵ_{canopy} was calculated via the standard deviation (95% confidence) from multiple height measurements (i.e > 10) along the length and width of the canopy. The latter was measured using a dial indicator (Varta indicator: 36.5 mm contact point length, 0-0.5 mm range) in relation to a surface plate (datum location with uncertainty better than $\pm 1 \mu\text{m}$).....	124
Table 4.2	Normalized errors in statistical quantities. Equations given by Casarsa & Giannattasio (2007). As review, $t_1 = 1.96$ (95% confidence interval). It should be noted for the pulsatile flow over a BFS, the mean flow statistic (time averaged), \bar{u} , should be replaced with $\langle u \rangle$ (phase-averaged)...	126
Table 5.1	A comparison of the geometry and flow specifications (under steady laminar flow at the blockage) between the present BFS model and other models of stenosis.....	174
Table 5.2	Measurement stations at the working section downstream of the step. Measurements are taken at the mid-plane of the working section, $2z/w = 0$. The normalized error of the measurement volume position downstream of the step is $\epsilon_x/S = \pm 0.06$. For reference, it should be noted that the distance between the step edge and the centre of the microscopy slide is 25 mm.....	177
Table 5.3	A comparison of the geometry and flow specifications between the present BFS model and other models of stenosis.....	205
Table 5.4	Normalized measurement stations at the working section of the PPFC. Pulsatile flow measurements are captured at the mid-plane of the working section, $2z/w = 0$. The normalized error of the measurement volume position downstream of the step is $\epsilon_x/S = \pm 0.06$	207

LIST OF APPENDICES

Appendix 1: Timeline Development of the Hemodynamic Flow Facility

Appendix 2: Near-Wall LDV System: Design, Performance, and Uncertainty

Appendix 3: Mathematical Definition of Skewness, Kurtosis and Standard Error

Appendix 4: Scaling Selection Criteria for Comparison of PPFC and Circular Pipe Type Stenoses

LIST OF ABBREVIATIONS

AFM	Atomic Force Microscopy
BFS	Backward-Facing Step
CA	Carotid Artery
CFD	Computational Fluid Dynamics
DAQ	Data Acquisition
DNS	Direct Numerical Simulation
EC	Endothelial Cell
ECA	External Carotid Artery
ER	Expansion Ratio
FBS	Fetal Bovine Serum
FFT	Fast Fourier Transform
HUVEC	Human Umbilical Vein Endothelial Cells
ICA	Internal Carotid Artery
LDL	Low Density Lipoproteins
LDV	Laser Doppler Velocimetry
LES	Large Eddy-Simulation
MEMS	Micro-Electro-Mechanical Systems
mm	Millimeter
nm	Nanometer
OSI	Oscillatory Shear Index
PAEC	Porcine Aortic Endothelial Cells
PDM	Photo-Detector Multiplier
PFP	Pulsatile Flow Pump

PI	Pulsatility Index
PID	Proportional-Integral-Derivative
PIV	Particle Image Velocimetry
PMT	Photomultiplier Tube
PPFC	Parallel-Plate Flow Chamber
rms	Root-Mean-Square
RAEC	Rat Aortic Endothelial Cells
RANS	Reynolds-Averaged Navier-Stokes
RSS	Reynolds Shear Stress
SI	Shape Index
SNR	Signal-to-Noise Ratio
SRT	Systolic Rise Time
TR-PIV	Time-Resolved Particle Image Velocimetry
WSS	Wall Shear Stress
μ LDV	Micro-Laser Doppler Velocimetry
μ m	Micrometer
μ PIV	Micro-Particle Image Velocimetry

NOMENCLATURE

A	Cross-sectional area of the PPFC at the working section [mm ²]
b	Blockage ratio [-]
c_f	Local skin friction coefficient [-]
c_f'	Local skin friction spatial gradient [-]
c_{f_t}'	Local skin friction temporal gradient [-]
c	Pressure wave speed [m/s]
d_a	Aerodynamic diameter of a tracer particle [μm]
d_p	Mean tracer particle diameter [μm]
d_e	Laser beam waist (at the measurement volume crossing) [μm]
d_m	Theoretical measurement volume diameter [μm]
d_{ma}	Actual measurement volume diameter [μm]
D_e	Upstream laser beam diameter (prior to focus by LDV probe) [μm]
D_h	Hydraulic diameter at the working section [mm]
D	Tube diameter [mm]
E	Young's modulus of elasticity [N/m ²]
ER	Expansion ratio [-]
f	fundamental frequency of the pulse [Hz]
f_D	Doppler frequency [Hz]
F	Focal length of the probe lens [mm]
h	Channel height at the working section [mm]
h_a	Allowable green-beams' traverse height at the working section [mm]
k	Distance from the pump outlet to the working section of the PPFC [-]
K_u, K_v	Kurtosis statistic (fourth-order; non-dimensional quantity) of u' and v' [-]

l	Working section length inside the PPFC [mm]
l_e	Hydrodynamic entrance length [mm]
l_s	Length of the backward-facing step [mm]
L_m	Length of the measurement volume [mm]
n	Refractive index of a medium [-]
\tilde{N}	Tracer particle concentration [particles/m ³]
N	LDV sample size (captured data) [-]
\dot{N}	LDV data rate [Hz]
N_{fr}	Number of fringes inside the measurement volume [-]
$P(t)$	Time-varying pressure [mmHg]
P_o	Pressure amplitude [mmHg]
P_w	Wetted perimeter [mm]
Q	Volumetric flow rate [m ³ /s]
Re_m	Reynolds number based on the bulk velocity and hydraulic diameter [-]
Re_c	Reynolds number based on the maximum velocity at the centre of the channel [-]
Re_τ	Frictional Reynolds number [-]
S_t	Strouhal Number [-]
S	Backward-facing step height [mm]
St_λ	Stoke's number (based on integral time-scale) [-]
St_o	Unsteady pulsatile flow Stoke's number [-]
S_u, S_v	Skewness statistic (third-order; non-dimensional quantity) of u' and v' [-]
t	time [s]
t_{SRT}	Systole rise time [s]
t_t	Wall thickness of the tube [mm]
T	Pulsatile cycle period [s]

u, v	Instantaneous streamwise and wall normal velocity (x and y directions, respectively) [m/s]
\bar{u}, \bar{v}	Streamwise and wall-normal mean velocity [m/s]
\bar{u}_{\max}	Maximum streamwise velocity (averaged quantity) [m/s]
$\langle u \rangle$	Phase-averaged streamwise velocity [m/s]
$\langle u \rangle^*$	Normalized phase-averaged streamwise velocity [-]
$\langle u' \rangle$	Normalized phase-averaged streamwise r.m.s.
u', v'	Streamwise and wall-normal velocity fluctuations [m/s]
u^+	Non-dimensional streamwise velocity [-]
u_τ	Friction velocity [m/s]
$\sqrt{u'^2}, \sqrt{v'^2}$	r.m.s. of the streamwise and wall-normal velocity fluctuations [m/s]
u'^*, v'^*	r.m.s. of the streamwise and wall-normal velocity fluctuations (normalized with the bulk velocity) [-]
u'^+, v'^+	r.m.s. of the streamwise and wall-normal velocity fluctuations normalized with the friction velocity [-]
$-\overline{u'v'}$	Reynolds shear stress [m ² /s ²]
$-\overline{(u'v')^+}$	Reynolds shear stress normalized with the friction velocity [-]
U	Bulk velocity [m/s]
\bar{U}	Average bulk velocity [m/s]
$\langle v' \rangle$	Normalized phase-averaged wall-normal r.m.s.
V_m	Measurement volume [μm^3]
w	Channel width at the working section [mm]
Wo	Wormersley Number [-]
x, y, z	Streamwise, wall-normal and spanwise directions at the working section of PPFC [-]
x_1	Dimensional reattachment length associated with the primary recirculation region [mm]
x_i^*	Normalized separation and reattachment length [-]

x^*	Non-dimensional x-axis (streamwise distance) [-]
y^+	Non-dimensional y-axis (wall-normal distance) [-]
y^*	Non-dimensional y-axis (wall-normal distance) [-]
y_r	Measurement volume reference position from the wall [μm]
α	Aspect ratio of the PPFC at the working section [-]
α_S	Aspect ratio of the inlet flow channel (at the step) [-]
ϵ_s	Surface roughness at the working section [μm]
ϵ_s^+	Non-dimensional surface roughness at the working section [-]
$\epsilon_{\text{traverse}}$	Micro-traverse uncertainty in the y-direction [μm]
ϵ_{datum}	Uncertainty of datum location (lower wall, side wall and step edge) [μm]
ϵ_{canopy}	Uncertainty of the optical glass (canopy) height [μm]
$\epsilon_x, \epsilon_y, \epsilon_z$	Total spatial uncertainty of the measurement volume in x, y and z directions [μm]
$\epsilon_{\bar{u}}$	Uncertainty in the streamwise mean velocity [m/s]
$\epsilon_{\text{r.m.s.}u'}$	Uncertainty in the streamwise turbulence intensity [m/s]
$\epsilon_{\bar{u}\text{total}}$	Total uncertainty in the streamwise mean velocity including the spatial uncertainty of the measurement volume [m/s]
ϵ_c	Circumferential strain inside the tube [-]
ϵ_l	Longitudinal strain inside the tube [-]
ρ	Fluid density [kg/m^3]
ρ_p	Tracer particle density [kg/m^3]
τ_w	Wall shear stress [dyne/cm^2]
τ_p	Response time of a tracer particle [s]
τ_Λ	Integral time-scale [s]
τ_η	Kolmogorov time-scale [s]
μ	Dynamic fluid viscosity [cP]

ν	Kinematic fluid viscosity [m^2/s]
ν	Poisson's ratio [-]
ω	Natural frequency of the pulse [rad/s]
$\dot{\gamma}$	Shear rate [$1/\text{s}$]
γ	Ratio between the particle and fluid densities [-]
δ_v	Viscous length scale [mm]
λ	Laser beam wavelength [nm]
θ	Laser beams' half-angle [deg]
δ	Fringe spacing [μm]
σ_c, σ_l	Circumferential and longitudinal stress inside the tube [Pa]
ϕ	Phase-angle [deg]
Λ	Integral length-scale [mm]

CHAPTER ONE

INTRODUCTION TO HEMODYNAMICS AND ENDOTHELIAL CELLS: MOTIVATION, METHODS OF RESEARCH AND PRESENT SCOPE

1 Introduction

This first section of this Chapter introduces the relationship between hemodynamics (blood flow mechanics) and endothelial cells (ECs). Work dating back to the 1960s lays the groundwork for demonstrating the effect of flow on development of atherosclerotic lesions in regions of disturbed flow. A mechanical description of the hemodynamic-cell cycle relationship is presented to streamline the understanding between flow-induced shear stress and cell response. The subsequent section provides a brief overview of the various experimental and numerical techniques that have been used to study the effect of flow on ECs under laminar and disturbed conditions, thereby outlining current shortfalls on the subject. An experimental facility is presented identifying the use of a custom near-wall configured Laser Doppler Velocimetry (LDV) system and a Parallel-Plate Flow Chamber (PPFC) to study cell response to flow (laminar and disturbed conditions under steady and pulsatile flow). The present investigation allowed for capture of near-surface steady and intermittently turbulent pulsatile flow. The final sections of this Chapter focus on identifying the objectives of this thesis work covering the areas of development and validation of the flow facility, experimental uncertainty and two-component velocity measurements (u, v) inside the PPFC over a backward-facing step (BFS - a simple step model to represent stenosis geometry). The Chapter is then concluded by providing a summary of the work presented in each of the thesis Chapters.

1.1 The Relationship Between Hemodynamics and Endothelial Cells

Build-up of plaque on the inside walls of the arteries (which is mainly composed of low density lipoproteins (LDL), smooth muscle cells, macrophages, platelets and other substances) has the potential to restrict blood flow and lead to strokes and heart attacks in humans. This process of plaque build-up known as atherosclerosis is well correlated with endothelial cell dysfunction. This is because blood flow imposed forces alter the

endothelial morphology, gene expression, and finally endothelial integrity bringing forward the onset of disease.

It is well known that spatially and temporally varying hemodynamic shear stresses play a vital role in the endothelial cell behaviour and, hence, in the onset and development of heart disease (including narrowing of the arteries) and strokes. The direct link between arterial blood flow dynamics and the cell cycle has not yet been established. The relationship between hemodynamics and endothelial cell structural and functional changes can be addressed through the use of a hemodynamic flow facility presented in this thesis. The next few paragraphs start by briefly describing the link between blood flow induced shear stress and endothelial cell response (this discussion is continued in Chapter Two).

Investigation between hemodynamics and arterial disease dates back to the early 1960s whereby McDonald (1960) and Fox & Hugh (1966) suggested that atherosclerosis is closely associated with areas of flow separation whereby sites of curvature and branching exist in the vasculature. Several locations of a disturbed flow pattern at arterial branches and curvatures are shown in Fig. 1.1. A review by Chiu & Chien (2011) associates these regions with a flow pattern that includes changes in direction with space and time (i.e. recirculation eddies). As a result, ECs do not align parallel to the artery axis and exhibit a less polarized shape (i.e. cobblestone morphology, Abe et al. 2014). Abe et al (2014) also explains that the altered topology (cells change shape) of the ECs (in the disturbed flow regions) exposes them to greater shear stress gradients across their length increasing the risk of plaque development.

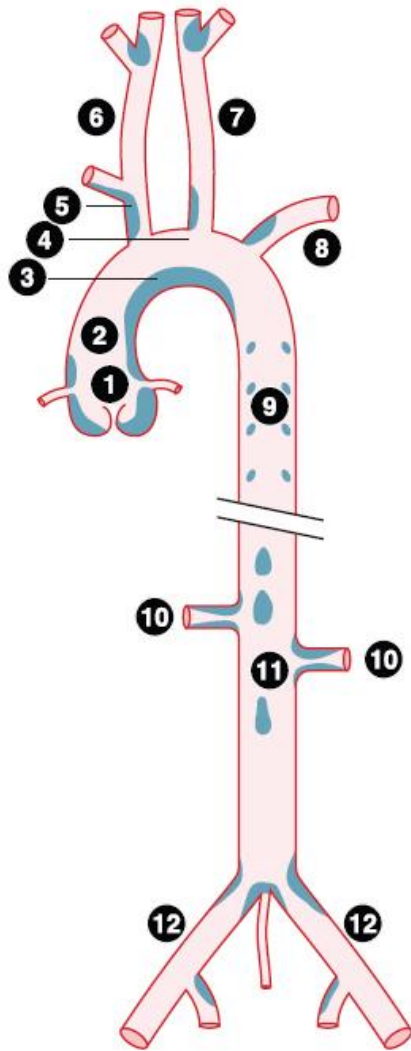


Fig. 1.1 Arterial locations exhibiting disturbed flow pattern (from Chiu & Chien, 2011). 1, Aortic sinus; 2, ascending aorta; 3, inner (lesser) curvature of aortic arch; 4, outer (greater) curvature of aortic arch; 5, innominate artery; 6, right common carotid artery; 7, left common carotid artery; 8, left subclavian artery; 9, thoracic aorta; 10, renal artery; 11, abdominal aorta; 12, iliac artery.

From that pioneering work to date, there have been numerous research studies performed with the goal of better understanding the hemodynamic-cell cycle relationship. A better understanding of this relationship has provided and will continue to provide more insight into the formation of vascular diseases, such as atherosclerosis. To understand the complex behaviour of ECs upon subjection to blood-flow induced shear stress requires a basic overview of the cardiovascular physiology pertaining to vascular health. Tarbell et al (2014) explains the cardiovascular system as an efficient piping network composed of pipes (analogue to arterial network) in which the flow is driven by a pump system (analogue to the heart), providing a small quantity of power to the recirculating fluid (blood volume). The inner wall surface of an individual pipe is continuously subjected to frictional

loading (shear stress), normal loading (pressure) and hoop stress (circumferential) as the fluid passes through the pipe. In terms of the arterial wall structure, the inner wall surface layer consists of ECs which are in direct contact with the blood flow and experience magnitude of shear stress which range from 1-70 dyne/cm² (Chiu & Chen, 2011). The hoop stress acting on the ECs is generated due to the cyclic strain driven by the pressure pulse (Tarbell et al 2014). The main focus in the literature in the last few decades has been surrounding the effect of wall shear stress (WSS) on cell behaviour. Tarbell et al (2014) further describe the wall structure of the artery as having three main layers. The first layer is covered by ECs (tightly packed together with junctions) whereas the second and the third consist of smooth muscle and fibroblast cells, respectively. This introduction to vascular anatomy will strictly focus on the first layer, ECs.

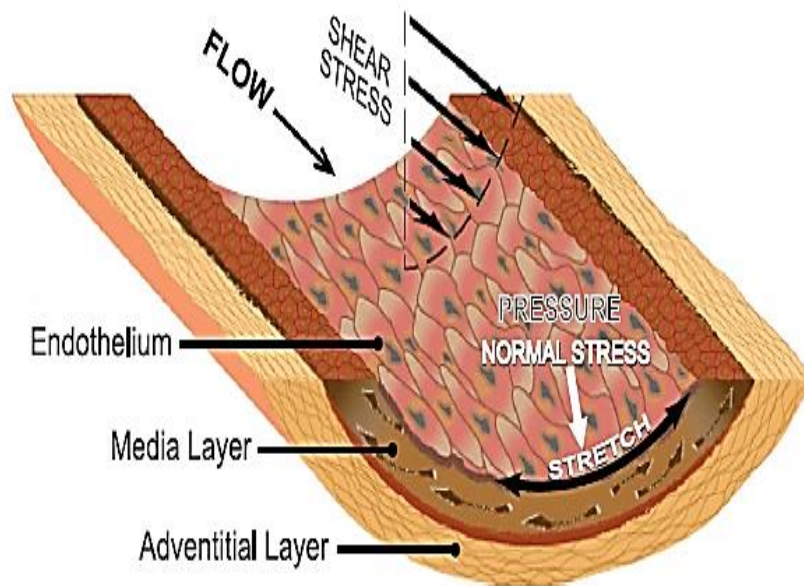


Fig. 1.2 Hemodynamic loading on ECs (From: Chiu & Chen, 2009)

The hemodynamic-cell loading relationship is explained by Gimbrone (1999) from a mechanical perspective. Gimbrone (1999) notes that ECs may be perceived as individual circus tents grouped together subjected to wind forces shearing the surface of the roof. This

concept is illustrated in Fig.1.3 whereby the rope securing an individual tent is perceived as the cell structure and the anchoring stake as the cell-matrix adhesion receptors. The transmission of the fluctuating wind load down the ropes (analogous to cytoskeletal stress fibers) generates a movement of the stakes (analogous to focal adhesion complexes) in the ground. Gimbrone (1999) explains that this movement of the stakes represents biochemical changes in the adhesion receptors along the cell base. Hence, the receptors can be thought as biomechanical-biochemical sensors located away from the loading source that regulate shape, orientation, and cell movement. From a biological point of view, the sensing of the mechanical load (arising from blood dynamics) is typically referred to as mechanotransduction, whereby the conversion between mechanical and chemical energies occurs under various type of mechanisms (Chien, 2007). Based on the review from Abe et al (2014), possible mechano-sensing macromolecules (and a variety of sensor cell structures) includes: (1) endothelial cell-cell junction, (2) focal adhesions and integrins, (3) glycocalyx, (4) ion channels, (5) actin cytoskeleton, (6) intermediate filaments, (7) caveolae, (8) primary cilium and, (9) heterotrimeric G-proteins. A basic overview of the molecular mechanism of flow-induced mechanotransduction (cells respond to a host of chemical and morphological changes) is given in Chapter Two.

The preceding few paragraphs presented the motivation behind studying the effect of blood flow on arterial cell response, whereas the subsequent paragraphs will discuss the previous research efforts undertaken to gain more insight into this relationship.

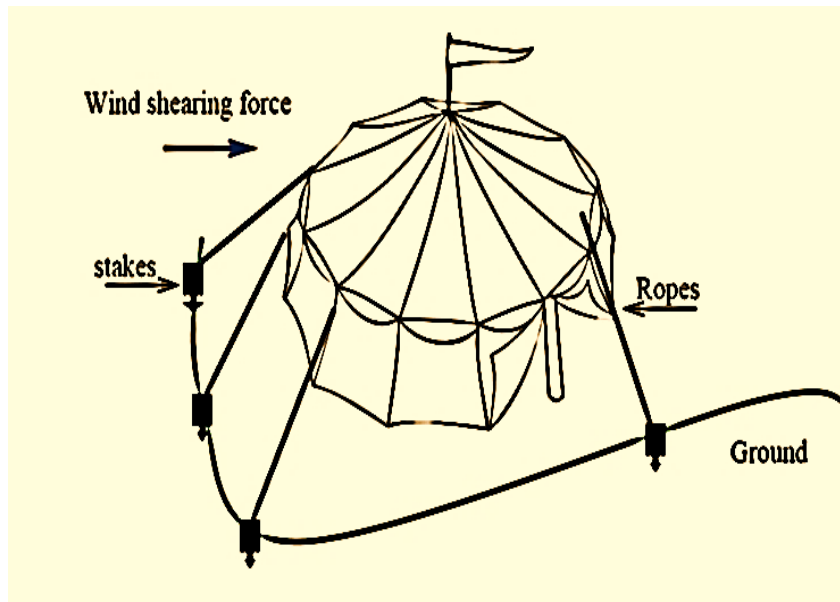


Fig. 1.3 Mechanical representation of the hemodynamic-cell loading cycle

1.2 A Concise Overview of Previous Methods of Investigation

Some of the pioneering work by Fry (1969) pointed to high shear stress regions (around arterial branches and bifurcations) as the main culprit leading to localized endothelial dysfunction and, hence, disease. This work demonstrated that increased shear stress changed the morphology, orientation, and transendothelial protein transport of ECs. In fact, shear stress values above 380 dyne/cm^2 demonstrated endothelial damage and the presence of fat and fibrin in the cells. Studies by Caro et al (1969, 1971) contradicted earlier studies by Fry (1969) and showed that fatty plaques correlated with regions of low shear values. This work showed that early lesions around the arterial branches (in human cadavers) in the abdominal aorta occurred upstream of the flow dividers where WSS was expected to be relative low. Since then, there has been increasing evidence (LoGerfo et al. 1981; Friedman et al. 1981; Zamirs et al. 1983; Ku et al. 1985; Giddens & Ku, 1987) that concurred with the work of Caro et al (1969, 1971), demonstrating that plaque formation tends to localize around regions of low and fluctuating WSS. All of this work has, as well, reported that atherosclerosis is more likely to occur in regions of the artery experiencing complex flow dynamics and stress distributions. A review from Davies (2009) summarized that the current thinking in the field is that regions of low and oscillating shear are the main

factors in the formation of atherosclerosis. Regardless, early work by Fry (1969) and Caro (1969, 1971) brought forward important observations that there is a strong correlation between blood flow mechanics and arterial disease. For a detailed review of specific effects of blood flow on EC morphology, cytoskeletal structure, proliferation and migration the reader should refer to work by Avari et al (2016), and reviews by Dolan et al (2012) and Chiu & Chien (2011). Although it is not the scope of this thesis to study EC response to flow (and, hence, shear stress), Chapter Two (literature review) does briefly summarize the present state of knowledge surrounding the hemodynamic-cell cycle relationship.

Although there has been abundant work (experimental and numerical methods) reported that studied the effects of mechanical loading (shear stress specifically) on ECs, accurate quantification of the fluid mechanics (specifically near the surface) over ECs (and on a single cell basis) remains elusive. Previous methods used to study the hemodynamic-cell cycle interaction that are reported in the literature include *in-vitro* (physical systems), *in-vivo* (inside the body), and numerical methods (specifically on the fluid mechanics). *In-vivo* experimental models have been reported which mostly focused on either the creation of arteriovenous fistula using carotid or femoral arteries, carotid artery ligation as a means of increasing flow and shear, and transposition of a vein graft into an artery to increase shear and pressure (Chiu & Chen, 2011). A common approach to generating a disruption to the local blood flow for *in-vivo* studies is through the introduction of a local stenosis into a section of a large artery in larger animals (baboons, sheep and dogs). An example is work done by Hutchison (1991) that used such a strategy and measured the low-velocity recirculation (downstream of the stenosis throat) using transcutaneous pulsed Doppler velocimetry to study cell response to local flow. The challenges associated with *in-vivo* studies generally result from a lack of models which are able to generate controlled flow shear patterns and defining molecular and cellular responses (Chiu & Chen, 2011). *In-vivo* studies tend to examine the bulk response of the arterial wall as opposed to individual cell response (Chung et al 2003). In addition, the complexity of the blood vessels and the limitations of the measurement resolution continue to present challenges (Helmlinger et al 1991; Chung et al 2003) when using an *in-vivo* approach. Another limitation of *in-vivo* or *ex-vivo* approaches to studying cell response to flow is the recovery of far less cellular material for analysis than methods utilizing *in-vitro* devices (Chung et al 2003).

Helmlinger et al (1991) note that the difficulty associated with quantifying detailed characteristics representing the hemodynamic environment is one of the main reasons researchers have resorted to development of *in-vitro* systems. With *in-vitro* devices, well-defined flow conditions and accurate control of shear stress allowed researchers to test specific hypothesis in relation to arterial cell response.

In general, the parallel-plate flow chamber (PPFC) is the most common *in-vitro* device used that is reported in the literature (Chiu & Chien, 2011). A typical PPFC is illustrated in Fig. 1.4. The simplicity of its design along with the ability to achieve a two-dimensional fully-developed steady laminar flow across the cell monolayer has made this device attractive to many researchers. Although some work reported (Dol et al, 2010; Avari et al, 2016) has implemented micro-Particle Image Velocimetry (μ PIV) and Laser Doppler Velocimetry (LDV) to measure the velocity field over the ECs, the majority of the work has relied on analytical solutions and computational fluid dynamics (CFD) to solve the flow field above the ECs. Though the analytical solutions have provided means of quantifying steady and pulsatile laminar shear stress above ECs inside various *in-vitro* channels (Koslow et al, 1986; Ruel et al, 1995; Bacabac et al, 2005; Dol et al, 2010), these solutions are invalid in circumstances where the velocity field is highly complex and the shear stress varies in space and time (e.g. intermittent turbulence under a pulsatile flow).

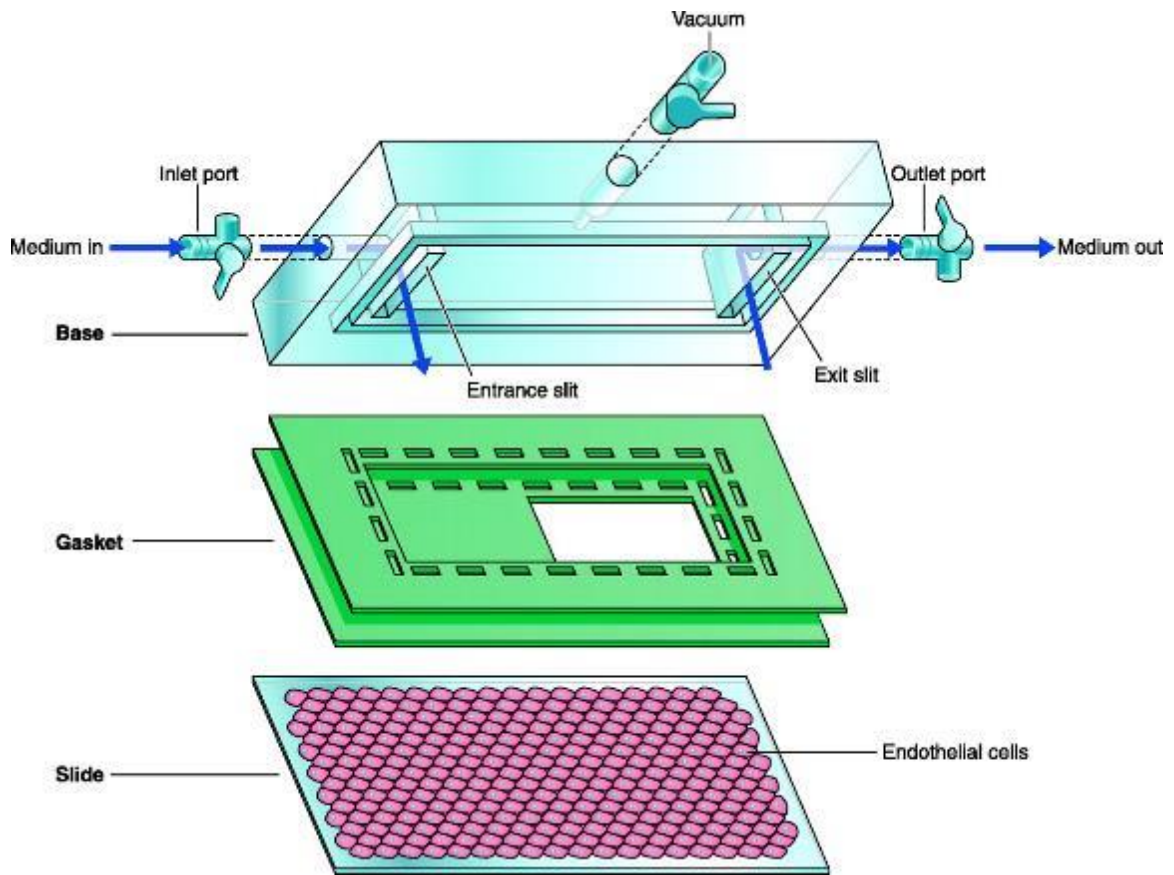


Fig. 1.4 An Example of a Parallel-Plate Flow Chamber (PPFC) used for EC research under steady laminar and disturbed flow (i.e. flow subjected to step) conditions. From: Chiu & Chen, 2009.

Previous methods for studying cell response to flow using CFD includes modeling idealized cell surfaces (Dewey & DePaola, 1989) and using atomic force microscopy (AFM) to map actual cell surfaces (Yamaguchi et al, 2000; Fukushima et al, 2001) thereby having realistic cell geometries that could be imported to Computational Fluid Dynamics (CFD). Both of these techniques of modeling ECs provide insight into flow behaviour near the surface, however, they fall short in studying actual flow over ECs and quantifying cell response to the complex flow behaviour. Mittal et al (2003) explains that most computations to date have focused on simulating laminar flow regimes due to the fact that pulsatile turbulent flows continue to present challenges in the transitional and turbulent regimes. The use of Direct Numerical Simulation (DNS) provides accurate solutions for spatial and temporal scales of turbulence at high enough Reynolds numbers, however, it is

extremely taxing on computing resources and the pulsatile nature of the flow (at relatively low Reynolds numbers) yields flows that are far from fully-developed and turbulent (Mittal et al. 2003). Therefore, turbulence models such as Reynolds-averaged Navier-Stokes (RANS) are not well suited for pulsatile flows since these models have been developed to simulate developed and high-Reynolds-number turbulent flows (Mittal et al. 2003). Work by Scotti & Piomelli (2001) supports this statement and demonstrates limitations of the RANS models when simulating pulsatile flows. Other numerical methods such as Large Eddy-Simulation (LES) have been used by several researchers to study pulsatile flow through constricted arteries (Mittal et al. 2001; Mittal et al. 2003). Mittal et al (2003) noted that the advantage of LES over DNS is that the smallest scales of turbulence do not need to be resolved and, hence, the requirement for spatial and temporal resolution is much lower. On the other hand, the disadvantage of LES is recognized by the computational expense of simulating relatively complex geometries and of increasing the Reynolds number (Piomelli, 1999). In general, much of the research to date on cell response to flow has failed to consider the complex flow environment on a subcellular level (and on a single cell basis) and, instead, has applied CFD methodologies without measuring the actual flows over cells (Voorhees et al. 2007).

To measure flows on a subcellular level requires advanced technologies such as μ PIV and μ LDV. Even though the conventional PIV technique is not well suited for high frequency flows, other methods such as the time resolved-PIV (TR-PIV) and μ PIV (Dol et al. 2010) could be used. However, the cost associated with such technology is much greater (Avari et al. 2016). Furthermore, Castrejon et al (2006) measured (both with LDV and PIV) the velocity as a function of the wall distance in a laminar oscillatory viscous boundary layer and found that LDV measurements were in better agreement with the theoretical results than those from PIV. They found that the LDV results were within $\pm 1\%$ of the theory whereas the PIV measurements were within $\pm 3\%$. In addition, Castrejon et al (2006) noted that LDV results were obtained as close as 14 μm from the wall and with PIV it was 55 μm . It is common with the LDV technique to sink the measurement volume (crossing region of the beams) into the wall to obtain a measurement closer to that surface. Even with the measurement volume embedded in the wall, it is still possible to obtain reliable velocity measurements since there is a portion of the measurement volume that is still exposed to

the tracer particles in the flow (Castrejon et al. 2006; Avari et al. 2016). Additional work comparing LDV and PIV velocity measurements inside a rectangular channel with flow was reported by Marx et al (2010). The first advantage reported in relation to LDV was the ability to capture time-resolved measurements and, hence, have more data to perform reliable averaging and r.m.s.. statistics. The second advantage was in relation to the closest measurement point from the wall; that is, with LDV a measurement was captured as close as 250 μm from the wall, whereas PIV presented difficulty in determining the exact location of the wall thereby generating a wall offset of 1 mm.

1.2.1 Deficiencies in the Technical Literature

In general, there has been a vast amount of work over the past few decades reported on arterial cell response to flow under both steady and pulsatile flow (laminar and disturbed conditions). However, there is still a requirement to measure actual physiological flow close to the surface (i.e. order of microns) of the cells with sufficient fidelity to determine accurate shear stresses, mean flow behaviour and turbulence statistics. Furthermore, there appears to be a lack of literature which quantifies pulsatile flow (with a physiological waveform shape such as the normal carotid waveform) inside a two-dimensional channel (i.e. with phase-averaged mean and turbulence statistics near the cell surface) with an idealized stenosis model (i.e. backward-facing step) and as well compares the results to more realistic models of stenosis (i.e. asymmetric stenosis model inside a straight section of tube) to determine whether a PPFC with a simple step can emulate an *in-vivo* environment (in relation to obstructed artery conditions) and, hence, be used for insightful EC research.

1.2.2 Present Work Contribution

To provide researchers with reliable mean flow and turbulence statistics (under steady and pulsatile flow) near and away from the wall (in the shear layer) above the cell microscopy slide (placeholder for ECs), a hemodynamic flow facility was developed and validated. The LDV resolved intermittent turbulence under a pulsatile flow (i.e. normal carotid

waveform) downstream of the step at multiple stations will provide researchers with comprehensive data for CFD modeling (and, thus, code validation) and further cell response studies. It will also provide the necessary data to make a useful comparison with more realistic stenosis geometries to evaluate how well the PPFC with simple step geometry can model these types of flows. This is important since placing a microscopy slide (with cultured ECs) inside tubular geometry (i.e. curved surface) along with LDV measurements bring forward many additional challenges not found with the PPFC geometry (i.e. refraction at the circular interface).

For this reason, the present author presents a small-scale PPFC (designed from several iterations of earlier versions – refer to Appendix 1) with optical access to allow two-component LDV velocity measurements and microscopy access for live cell imaging. To capture regions of low and oscillatory shear stress at the working section and in the vicinity of the microscopy slide, a backward-facing step (BFS) was used to disturb the oncoming steady and pulsatile laminar flow, thereby allowing the mean flow and turbulence statistics to be captured with a two-component (u, v) LDV system. The LDV system was developed to capture near-wall velocity measurements (u, v , coincident mode) with a spatial resolution (better than $45 \mu\text{m}$) thereby allowing accurate quantification of WSS. The design of the PPFC together with the superior spatial resolution of the near-wall configured LDV system allowed u and v velocity components to be simultaneously captured within $\approx 40 \mu\text{m}$ from the wall at several stations downstream of the step. The detailed objectives of the present research work are described in the subsequent sections.

1.2.2.1 Original Contribution of the Flow Facility Performance Assessment: An Extension to the Work of Avari et al (2016)

The earlier work of Avari et al (2016) which provide both a low-Re turbulent and pulsatile laminar flow velocity measurements at the working section of the present PPFC (reported in Chapter Three) is excellent groundwork to better understand the performance of the flow facility. The present study complements this work by providing a comprehensive review of the experimental uncertainty associated with all remaining elements necessitating quantification prior to the capture of two-component velocity measurements

downstream of the backward-facing step (BFS). This additional analysis includes the following:

(1) Spatial positioning uncertainty of the measurement volume with respect to the wall and the step datums (using a different method than that of Avari et al. 2016), together with the uncertainty of the micro-traverse units.

(2) Uncertainty of the critical dimensions at the working section including the step height (important to understand the actual expansion ratio).

(3) Statistical convergence of r.m.s. and higher order statistics (i.e. skewness, kurtosis, Reynolds Shear Stress).

(4) Accuracy and precision of the pulsatile flow pump including the carotid waveform repeatability and damping across the flow circuitry. It should be noted that the present author considers the damping analysis a major contribution with regards to the performance assessment of the flow facility given the importance of waveform shape on the downstream flow physics. The present author mathematically models and quantifies both, the attenuation of a sinusoidally fluctuating component of the pressure wave (along straight section of tube and PPFC) and the effects of viscous resistance and inertance on flow response to the periodic driving pressure gradient.

In addition, given that the work of Avari et al (2016) uses a commercial Laser Doppler Velocimetry (LDV) probe, a comprehensive performance assessment of the probe is not required. For the present study, a custom near-wall configured LDV system is used (built based on extracting the optical fibers from a commercial TSI Inc. TR-360 probe) and, hence, additional analysis is required to ensure validity of the two-component velocity measurements. This analysis includes: (1) design and performance of the LDV system considering two lenses of different focal lengths to study spatial resolution implications on wall shear stress accuracy, (2) quantification of both the bias and the precision errors, (3) flow tracers and the required seeding concentration and, (4) the effect of the forward-scatter commercial receiver orientation on the velocity measurements (data rate, signal quality,

signal-to-noise ratio). It should be noted that a comprehensive overview of the LDV design, performance, and uncertainty is given in Appendix 2.

1.2.2.2 Present Work Limitations

The limitations (and their potential implications on accuracy of the present findings) of the present hemodynamic flow facility (together with the measurement technique) are as follows:

(1) The closest velocity measurement (of u and v velocity components) from the wall (cell surface) is $40 \pm 10 \mu\text{m}$. The implication of this could be inaccurate representation of the shear loading on the ECs. As example, the glycocalyx (a luminal mechano-sensor molecule) protrudes approximately 500 nm (Givens & Tzima, 2016) into the flow thereby having the probability of sensing different flow conditions than that of the reported values (via extrapolation technique to determine WSS). This is demonstrated in Fig. 1.5. Another important point about the glycocalyx molecule is that it dampens the force of shear stress acting on the ECs and, hence, the cells do not experience appreciable shear forces at their plasma membranes (Givens & Terzi, 2016).

(2) The surface whereby the extra-cellular matrix attaches to (at the working section) is rigid inside the present PPFC (deflection is negligible). Arterial walls inside the human body are elastic and, hence, basal mechano-sensors such as integrins (which sense substrate stiffness) could give different signaling pathway responses given the rigid wall in the present study (Givens & Tzima, 2016). However, according to Givens & Tzima (2016), evidence that integrins are direct shear stress sensors is limited. It should be noted that the

type of EC matrix (as opposed to vessel elasticity) and its effect on EC response has been the focus of researchers (Givens & Terzi, 2016).

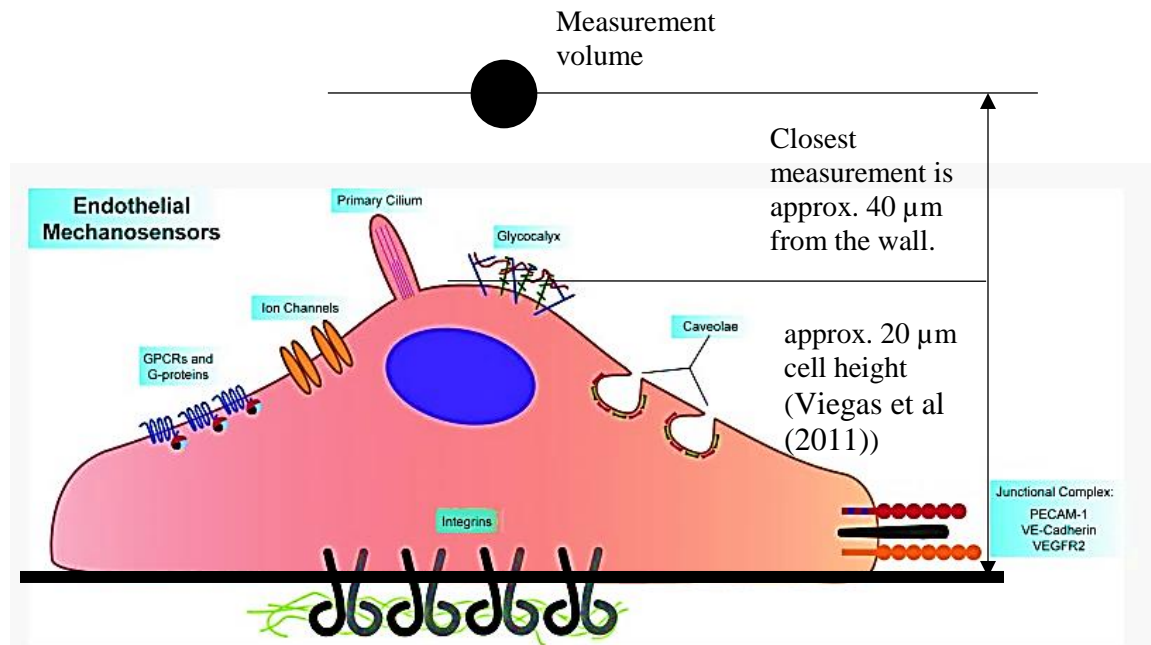


Fig. 1.5 Illustration showing an EC with mechanosensors. Modified from Givens & Tzima (2016). The diagram is not to scale.

1.3 Research Scope: The General Concept

The fundamental objective of this work was to design, construct and validate (through velocity measurements and uncertainty analysis) a hemodynamic flow facility with the main component being the PPFC (with an aspect ratio of $\alpha = w/h = 9.72$; whereby w and h are the width and height of the flow channel at the working section, respectively) and the near-wall configured LDV system. With the facility validated, the aim was then to compare the flow physics downstream of the step to that of more realistic models of stenosis (i.e. asymmetric stenosis flow inside a tube) to gain insight on how well the facility emulates realistic *in-vivo* conditions. To the best of the author's knowledge such a quantitative comparison is not available in the literature.

The flow facility would thus include a PPFC to simulate idealistic post-stenotic flows (i.e. BFS representing an idealized constriction of an artery) such as found in the arteries consisting of plaque (i.e. arterial narrowing or sometimes referred to as a stenosis). The

facility would as well have to include a pulsatile flow pump (PFP) to supply realistic flow (i.e. normal carotid waveforms with a frequency of approximately 1 Hz) to the PPFC and a near-wall Laser Doppler Velocimetry (LDV) system to capture the velocity data (mean and turbulence statistics) near the wall where ECs would be cultured. The spatial resolution of the measurement volume (formed by the LDV system where the blue and green beams cross) would ideally be less than 50 μm or better to ensure accurate determination of wall shear stress (i.e. by extrapolation of the polynomial curve to the wall where the velocity is zero). It is important to, as well, note that the LDV system needed to have the capability to spatially move along the x, y and z directions to capture the velocity data in the streamwise, wall-normal and spanwise direction, respectively. In terms of the latter, the wall-normal spatial positioning of the LDV measurement volume was considered to be the most important given that the wall shear stress (WSS) is determined from the velocity gradient, $\frac{\partial \bar{u}}{\partial y}$ (i.e. whereby \bar{u} is the streamwise mean velocity in the x-direction and y represents the wall-normal direction).

The integration of the entire system noted presented a significant challenge to the present author and is explained in greater detail in the subsequent sections. In addition, it should be noted that while measurement of ECs biological response is not included in this work, the thesis does discuss the implications of the facility design on cell vitality and successful *in-situ* imaging of live ECs. Work by Avari et al (2016) showed that with the current design of the facility (latest revision) it was possible to monitor the cell survival and time-sensitive structural changes for at least 10-12 hours using real-time microscopy.

1.3.1 Detailed Research Objectives

The research scope is divided into three main sections which include: (1) the development and testing of the flow facility, (2) the near-wall LDV system performance and experimental uncertainty and, (3) two-component velocity measurements (u, v) inside a PPFC with the major contribution being the measurement of steady and pulsatile flow over a backward-facing step (BFS) with an expansion ratio (ER) of ≈ 2 (i.e. 50% narrowing of the artery).

1.3.1.1 Development and Validation of the Hemodynamic Flow Facility

The objective was to advance, further develop and validate an initial concept of the hemodynamic flow facility which was presented to the author at the beginning of the thesis work. From an assessment of the limitations and drawbacks of various experimental facilities (numerous refined concepts which are reported by the present author in Appendix 1) and measurement techniques, the present author reports a final revision of the flow facility and quantifies the performance of the main components that constitute the entire facility (i.e. custom LDV system, pulsatile pump). It should be noted that the limitations and drawbacks were determined through velocity measurements where possible (i.e. depending on the revision of the flow facility) and these results are presented in Appendix 1 of this thesis. For example, a limitation could be the inability to measure the v component of the velocity vector as a result of the channel geometry. Another example would be measuring waveforms at the working section that are not realistic (i.e. damped/attenuated waveforms).

The development of the PPFC was critical to ensuring successful capture of the velocity data at the working section and it was designed to achieve the following: (1) for the oncoming flow to fully develop prior to reaching the working section, (2) to allow optical access for both the blue (u) and green (v) beams to penetrate into the working section to measure the instantaneous velocity simultaneously and in coherence mode with an acceptable data rate (i.e. 100-1000 Hz; refer to Fig. 1.6 for further clarity), (3) to ensure the flow at the working section of the PPFC is two-dimensional (i.e. $\frac{\partial \bar{u}}{\partial z} = 0$) covering at least 60% of the microscopy slide (i.e. width of the channel since the microscopy slide extended across the entire width of the channel) and, (4) to be able to collect the scattered light from the measurement volume with a commercial forward-scatter receiver. The latter presented great challenges as a result of the small height of the channel (i.e. 1.8 mm) and reflections which could cause additional noise to be collected by the receiver.

It should be noted that there is a trade-off between two-dimensionality of the flow (i.e. by having a much larger width than height of the channel) and waveform damping and, thus, considering both of these factors has led to the current choice for the aspect ratio (w/h) of

9.72. The details of the final revision of the PPFC are presented in Chapter Three of this thesis (experimental methods). Other important factors that were incorporated into the design of the final revision of the PPFC were the appropriate material (i.e. ULTEM bio-plastic) to withstand several autoclave cycles (i.e. create a sterile environment for the cells), a gradual entrance curvature to minimize incoming flow disruption and bottom-top imaging for the cells.

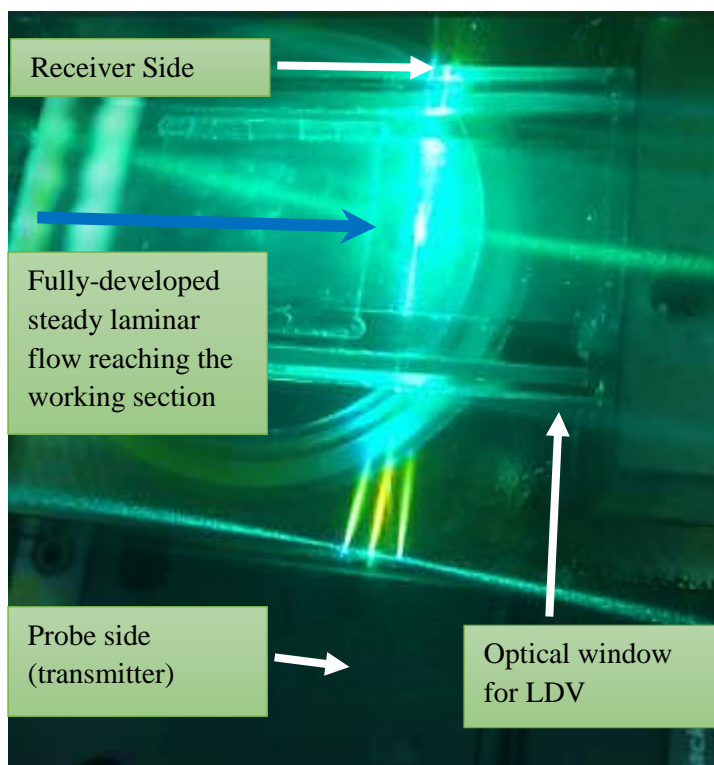


Fig. 1.6 Illustration demonstrating design challenges associated with penetrating both blue and green beams inside a small 1.8 mm channel.

For clarity purposes, the bottom-top imaging refers to access for the microscope objective lens below the microscopy slide to image the cells in real-time (i.e. objective lens aperture to be positioned a few microns away from the slide). It should as well be noted that the final revision of the PPFC was not designed by the present author. Rather it was designed by Avari et al (2016) which based the design decisions on earlier revisions reported by the present author (Appendix 1).

Furthermore, to allow precise measurement of the streamwise and wall-normal velocities close to the surface that contains the ECs and, thereby, provide a quantification of the time-varying shear stresses the present author developed a custom and open-configuration near-wall LDV system with a measurement volume diameter and length of 42.2 and 203.3 μm , respectively. The open-configuration design allows for better control (i.e. installation of beam expansion modules) of the incoming laser beam diameter (i.e. for the present study was 1.8 mm) and steering of the four laser beams (i.e. 2 blue and 2 green). Various lenses with different focal lengths can be installed to control the measurement volume diameter and length depending on the accuracy required and the application. In fact, for the present study, two lenses were used one with a focal length of 120 mm and the other with a focal length of 261 mm. This is explained in more detail in Appendix 2 of the thesis covering the LDV design, performance, and uncertainty. For this application which includes a very small channel height of 1.8 mm, the key advantage of the near-wall LDV system (over other commercial systems) is the ability to quantitatively measure the shear stresses and turbulence in the flow very close to the surface over the ECs, thereby allowing measurement of intermittently turbulent flow regimes and the examination of the fluid dynamics during any phase of the cardiac cycle. It was found that by using the lens with a focal length of 120 mm, velocity measurements were possible as close as 20 μm from the wall.

The final objective of the development phase was to integrate a set of micro-traverses with the facility to allow for movement of the measurement volume in the x, y and z direction. Spatial resolution and accuracy was very important for the movement of the PPFC in the y-direction and so the PPFC was mounted on a very accurate and precise PC-controlled motorized laboratory jack. The details of the controls, accuracy and precision are discussed in Chapter Four (experimental uncertainty). In addition, to traverse in the x and z direction the PPFC was as well mounted on top of a cross-slide milling table. The latter allowed two-component velocity measurements to be captured at several stations downstream of the step. The LDV probe and receiver were as well mounted on the cross-slide tables to allow for accurate initial alignment of the measurement volume inside the working section of the PPFC.

1.3.1.2 LDV Performance and Experimental Uncertainty

The performance of the custom near-wall LDV system together with the uncertainty of all other components (and measurement techniques) of the flow facility was considered very important and, thus, it was quantified to ensure the implications it may have on the flow measurements were clearly understood.

In terms of the pumping unit, the main objectives were as follows (1) to quantify the uncertainty of the pump under steady flow operation using an ultrasonic flow meter for the range, $1 \text{ mL/s} \leq Q \leq 15 \text{ mL/s}$, (2) to quantify the carotid waveform accuracy and repeatability and, (3) to quantify waveform damping of the carotid waveform throughout the flow circuitry. In terms of objective (1), this was considered important since there have been numerous modifications completed on the pumping unit, thereby making the manufacturer's certificate of calibration invalid. Moving forward, objective (2) was completed to quantify the cycle-to-cycle and stroke-to-stroke variability of the waveforms which allowed identification of the spurious r.m.s. values (which do not contribute to turbulence) within the individual bins when the pulsatile flow was analyzed. Finally, the attenuation of the pulsatile flow profiles from that specified at the pump compared to that in the PPFC (at the working section) were also evaluated by estimating the effects of capacitance; that is, the instantaneous storage capacity of the tubing due to expansion under pressure as the pressure pulse develops (the latter was computed based on hoop stress straining the tubing wall and, thus, increasing the interior volume). The effect of viscous energy losses was also considered when evaluating waveform damping.

With respect to the near-wall LDV system performance, the first objective was to measure the r.m.s. u' and v' under a steady laminar flow to identify the spurious r.m.s. values representing the noise of the system. These experiments were carried out inside the present PPFC (final revision channel at the working section) and with an additional long and narrow channel (to ensure no disruption to the flow further downstream of the entrance) made out of acrylic (i.e. plexi-glass with channel geometry of 600 mm x 17.5 mm x 2 mm representing length, width and height, respectively). The second objective was to assess the particle selection (i.e. TiO_2 for the present study) and how well the particles follow the flow for the cases presented in Chapter Five (backward-facing step flow cases). The latter

is particularly important with turbulent flows since a larger particle will cease to be able to follow the small scale (high frequencies) turbulent fluctuations in the flow and, hence, here the author discusses Stokes' principles of drag on small spheres including Stokes regime and frequency response. The third objective was to validate the probe's spatial resolution (and its implication on WSS accuracy) via capturing vertical profiles of the streamwise mean velocity $\bar{u}(y)$ under a steady laminar flow (inside the final revision PPFC) at the working section (near the surface) for $Re_m = 100, 600, 900$ and 1240 (considering the bulk velocity and twice the channel height as characteristic length scale) to quantify wall shear stress (WSS) using both the $F = 120$ and 261 mm lenses. The final objective was to measure a low- Re turbulence flow case (transitional regime given the flow rate limitation) to validate the LDV probe in its ability to measure u and v velocity components simultaneously and in coherence mode. The flow measurements (at the working section of the PPFC) were compared to published literature on low- Re turbulence flows inside PPFCs (refer to Appendix 2 for details).

In addition to the above objectives, other performance metrics were assessed and discussed. These included developing a methodology for finding the proper position of the measurement volume inside the PPFC (at the working section) with respect to the bottom wall (cell surface), the step edge (for step flow cases) and the side walls (to determine the location of the mid-plane of the channel). In addition, other objectives consisted of evaluating the uncertainty of the channel geometry (including step height (S), channel width (w) and height (h)) and calculating the uncertainty of the mean and turbulence quantities reported in Chapter Five (two -component velocity measurements).

1.3.1.3 Two-component Velocity Measurements over a BFS (Steady and Pulsatile Flow Investigation)

To investigate how well the flow facility compares (in terms of the flow physics downstream of a blockage) to other *in-vitro* facilities (i.e. flow in a tube with asymmetric and axi-symmetric stenosis) and to contribute useful mean flow and turbulence statistics, two flow cases were investigated: (1) steady laminar flow over a BFS ($Re_m = 1240$; considering the hydraulic diameter and the bulk velocity upstream of the step) and (2)

pulsatile laminar flow over a BFS ($Re_m = 775$). It is important to note that laminar regime refers to the inlet conditions for the BFS cases (verified by r.m.s. statistics).

For both steady and pulsatile laminar flow cases, averaged statistics of mean and turbulence quantities (streamwise and wall-normal turbulence intensity profiles, Reynolds shear stress profiles, energy spectra) were evaluated at the midplane of the channel (at the working section; near and away from the lower wall surface) at several stations downstream of the step until the point of relaminarization. The primary recirculation region on the lower wall was also measured together with the reattachment length and the skin friction spatial (in the streamwise direction) and temporal distribution. Specifically for the pulsatile laminar flow case, phase-averaged statistics are given downstream of the step at four time instants of the carotid waveform pulsatile cycle. Both flow cases were analyzed in great depth downstream of the step with a large emphasis on comparing the flow physics to more realistic stenosis geometries (i.e. semi-circular stenosis) inside channels and tubes (whereby the flow was reported either using experimental methods and/or numerical methods such as DNS and LES). The various models of stenosis to which the present study is compared with, together with two-component velocity measurements, is reported in Chapter Five.

1.4 Thesis Outline

1.4.1 Chapter Two: Literature Review

This chapter provides a background on studies pertaining to disturbed and undisturbed flows over endothelial cells (ECs). It then provides an overview of the various *in-vitro* flow facilities and methods used to study cell response to flow, with emphasis on wall shear stress (WSS) quantification. An analytical solution to pulsatile laminar flow inside a PPFC is provided together with an overview of some of the more advanced methods to quantify WSS including the LDV technique. With respect to the latter, challenges associated with the LDV technique in terms of WSS accuracy are also reviewed (i.e. wall datum identification). The literature survey shifts its focus on the many studies which aim to describe the complex behaviour of flow (and the variation of the wall shear stress) downstream of a stenosis in a more classic fluid mechanics approach. In terms of the latter, studies pertaining to steady and pulsatile laminar flow in blocked geometries including the

backward-facing step (BFS) together with a wide sample of different geometries is reviewed (i.e. flow in a tube with an axi-symmetric stenosis). The literature review aims at describing the key states of knowledge associated with post-stenotic flows, thereby highlighting the contribution of the present work.

1.4.2 Chapter Three: Experimental Apparatus and Methods

This Chapter presents the final revision of the hemodynamic flow facility including all the components that made up the entire facility. These components included: (1) a custom near-wall LDV system, (2) a steady and pulsatile pump covering a range of flow rates, $25 \text{ mL/s} \geq Q \geq 1 \text{ mL/s}$, (3) A PPFC with a rectangular cross-section ($h = 1.8 \text{ mm}$, $w = 17.5 \text{ mm}$) that included optical access for both LDV and *in-situ* cell imaging (microscopy), and (4) micro-traverse platforms to allow capture of the streamwise (u) and wall-normal (v) velocities at various stations downstream of the BFS and away from the bottom wall.

Furthermore, the streamwise velocity profiles $\bar{u}(y, z)$ at the working section of the PPFC are presented which were computed based on existing analytical solutions for channel flow under steady laminar conditions. Results are compared with the analytical solution for the infinitely-wide plate (i.e. flow between two parallel plates with $w \gg h$) case. In addition, WSS is reported using both the channel flow and the infinitely-wide plate analytical solutions ($Q = 3.90$ and 7.50 mL/s). Fluid selection used in the present study was also reviewed and the fluid constituents, along with the density and the viscosity, were reported at 37°C . Finally, the relative roughness (ϵ_s/D_h) at the working section (bottom wall) of the PPFC is reviewed with emphasis on all sources contributing to the surface roughness.

The final section of the Chapter gives the working section geometry for the flow cases in Chapter Five under the influence of the backward-facing step (BFS). The working section provides an overview of all the critical length scales.

1.4.3 Chapter Four: Experimental Uncertainty

This Chapter begins with an overview of the uncertainty of the mean and turbulence quantities which are reported in Chapter Five. A wall datum identification method was presented and the uncertainty associated with the closest measurement point in relation to the lower wall was quantified for both the $F = 120 \text{ mm}$ and 261 mm lenses. In addition,

the spatial uncertainty of the measurement volume along the streamwise (x-) and spanwise direction (z-) was quantified and reported together with the uncertainty of both, the PC-controlled motorized laboratory jack and the cross-sliding milling tables.

This Chapter continues by discussing the shear rate derivation and curve fitting approximation errors for steady laminar flow. Additional subjects are presented and discussed including: (1) statistical converge of both the mean (1st order statistic) and higher-order statistics (i.e. r.m.s., skewness, kurtosis, Reynolds Shear Stress) and (2) criteria used for bin size selection for pulsatile flow.

The final section of the Chapter focuses on the uncertainty analysis of the pulsatile flow pump under steady and pulsatile flow operation. For the steady flow case, an ultrasonic flow meter was used to determine the actual flow rates together with the limits of uncertainty. For the pulsatile flow, cycle-to-cycle and stroke-to-stroke waveform repeatability was quantified. The final component of the pump analysis included studying waveform damping across the closed-loop flow circuitry.

1.4.4 Chapter Five: Two-Component Velocity Measurements Downstream of a BFS under Steady and Pulsatile flow

The first case in this Chapter is a steady laminar flow (prescribed at the inlet via the pump unit) over a backward-facing step (BFS). The streamwise mean velocity profiles (normalized with the inlet bulk velocity) across the channel height at various measurement stations downstream of the step are reported. The vertical profiles of the streamwise mean velocity are reported (at the midplane of the channel) over a sufficiently large length (downstream of the step) to cover the primary (lower wall) and secondary (upper wall) recirculation regions to the point of relaminarization ($\frac{\partial \tau}{\partial x} \approx 0$). In addition, the reattachment length downstream of the step (in reference to the primary recirculation region) is reported together with the skin friction (normalized wall shear stress) distribution along the streamwise direction. Finally, the streamwise and wall-normal r.m.s. profiles together with the Reynolds Shear Stress (RSS) profiles are reported at various measurement stations downstream of the step. The mean flow and turbulence statistics together with other flow characteristics are compared with the pioneering work of Armaly

et al. (1983) and other more realistic phantoms of stenosis under steady laminar flow in both channels and tubes.

Since the steady flow case represents a limiting case of physiological flow whereby the amplitude of pulsation is zero, a pulsatile laminar flow was prescribed at the inlet of the step (i.e. carotid pulse) and the flow was characterized downstream. Similarly as with the steady case, phase-averaged mean flow and turbulence statistics (at four instants of the carotid pulse cycle) downstream of the step are presented, discussed and compared to other channel step flows and *in-vitro* phantoms of stenosis (i.e flow in a tube) which includes both asymmetric and axi-symmetric constrictions (i.e. arterial narrowing). Finally, energy spectra are plotted at the centreline (with respect to the height of the channel) of the channel at various measurement stations downstream of the step to gain more insight of the flow behaviour upstream and downstream of the reattachment point at the lower wall (i.e. shear layer instability).

1.4.5 Chapter Six: Conclusions and Future Work

This Chapter provides a summary of the thesis objectives together with the corresponding results (with quantified evidence) related to both, the performance of the flow facility and the two-component velocity measurements downstream of the BFS (i.e. flow physics at the midplane of the channel). The Chapter also outlines possible future work related to both improving the flow facility and advancing the field forward related to post-stenotic flows over live ECs.

1.4.6 Appendices

These appendices contain valuable information in regards to the development of the hemodynamic flow facility (i.e. timeline development), LDV performance and uncertainty (together with wall shear stress measurement and low-Re turbulence flow case), uncertainty of the third and fourth order statistics (i.e. skewness, kurtosis) and scaling for the comparison of PPFC and circular pipe type stenoses.

1.5 Chapter One Summary

This Chapter introduced the relationship between hemodynamics and endothelial cell response to provide a brief overview on the effect of flow on the development of atherosclerotic lesions. Furthermore, a concise review of the various *in-vivo* (inside the body), *in-vitro* (experimental and outside the body) and numerical methods that have been used to study the flow-cell cycle was presented, thereby outlining some of the current short-falls on the subject. A hemodynamic facility was briefly presented with a detailed breakdown of the objectives of the present work which consisted of development and validation of the flow facility, LDV performance and experimental uncertainty and detailed two-component velocity measurements over a backward-facing step (BFS) under steady and pulsating laminar flow. Finally, a brief overview of the content in each thesis Chapter was presented.

The next Chapter gives a detailed overview of the technical literature surrounding idealized (i.e. simple step geometry) and more realistic stenotic flows (cosine function stenosis silhouette) inside channels and straight sections of tubing. The chapter reviews flow physics (downstream of the various stenosis models), methods of flow measurement, scope of measurements and processing of data. The chapter also provides a more in-depth review of the hemodynamic-cell cycle relationship, together with quantification methods for wall shear stress (WSS).

CHAPTER TWO

LITERATURE REVIEW

2 Introduction

This Chapter continues with an overview of the motivations that have driven so many researchers to study endothelial cell response to fluid flow. It first includes some of the recent work which used *in-vitro* devices (experimental flow facilities) to investigate effects of flow (and, hence, wall shear stress) on endothelial cell response (i.e. dysfunction of ECs by measurement of morphological changes, proliferation, apoptosis, migration, permeability and structural remodeling). Second, the various *in-vitro* devices that have been used in the literature to study endothelial cell response and fluid mechanics are reviewed (with emphasis on the parallel-plate flow chamber (PPFC)) together with the analytical solution for the pulsatile laminar flow inside a two-dimensional channel. Furthermore, a survey of the various measurement techniques and numerical methods reported in the literature as means of characterizing the flow downstream of idealized stenosis models is presented. Since the present work uses a Laser Doppler Velocimetry (LDV) technique to measure the flow downstream of a backward-facing step (BFS), the author reviews the various challenges associated with this technique with an emphasis on locating the measurement volume with respect to the lower wall (to accurately determine the wall shear stress).

Following an overview of the relationship between flow and cell dysfunction, the literature survey shifts its focus to the many studies which aim to describe the complex behaviour of flow (and the variation of the wall shear stress) downstream of a stenosis in a more classic fluid mechanics approach. This section of the literature review is categorized by the type of geometry, whereby steady and pulsatile flow in both the rectangular channel and tube (obstructed geometry) are reviewed. Conversely, Chapter Five (two-component velocity measurements downstream of the BFS) addresses the gaps in the literature by bringing together (through a comparison of the flow physics) the various geometries and comparing the simple step stenosis model (in the present work) to more realistic models of stenosis inside both channels and tubes.

2.1 Endothelial Cell Response to Flow

Hemodynamic loading on the endothelial cell (EC) wall is hypothesized to be partially responsible for the localization of atherosclerotic plaques (narrowing of the artery). It is typical for atherosclerotic lesions to develop near branch points and in the vicinity of complex curvature in arteries. An example would be the common carotid artery that splits into the internal and external artery. These regions experience complex flow phenomena such as boundary layer separation, secondary flows with flow reversal, dynamic stagnation points, and spatial and temporal shear stress gradients (Gimbrone, 1999).

There have been numerous studies conducted to quantify the effect of flow on ECs and to demonstrate that this relationship is a significant factor in the onset of arterial diseases (i.e. atherosclerosis). In fact, clinical studies reported that the location of atherosclerosis (inside the arterial network) is linked to a dysfunctional endothelium layer and non-laminar flow behaviour (Heo et al. 2011). This section reviews some of the key findings associated with the hemodynamic-cell cycle relationship (biological responses that have induced endothelial dysfunction and have motivated fluid mechanics research into cardiovascular flows) that have been reported over the last few decades, all of which demonstrate the importance of further studies on the subject.

From a review of the literature, it appears that the most important mechanical characteristic of arterial flows is wall shear stress (WSS). In fact, it is often the key focus in studies of biological flows (Strony et al. 1993; Hodgson & Tarbell 2002; Avari et al. 2016) since it is directly felt as a force on the ECs (in contrast to the fluid pressure). For further clarity, an illustration of WSS acting on the EC layer is given in Fig. 2.1. It should be noted that ECs have very sophisticated mechano-sensing abilities to detect flow magnitude, direction and the amplitude and frequency of the pulsatile flow (Baeyens et al. 2017).

The WSS accurate calculation, measurement and prediction has, as well, gained a lot of attention in the literature (Reese & Thompson, 1998; Deplano & Siouffi, 1999; Avari et al. 2016). Some of the earlier work reported endothelial shape and orientation changes as being very sensitive to different fluid shear stress levels (Dewey et al. 1981). The latter built upon the much earlier observations which showed changes in the ECs as a result of

increased blood flow rates (Fry, 1969; Caro et al. 1971). The field was even further advanced when Davies et al (1986) reported that endothelial cells respond very differently depending on the flow conditions (laminar or turbulent flow), whereby the cells aligned themselves uniquely for each flow case (refer to Fig. 2.2 for further clarity). Furthermore, Levesque et al (1989) noted that the cell elongation and orientation significantly depends on the exposure of time and the magnitude of the fluid shear stress. Kataoka, Ujita & Sato (1998) found that the flow direction plays a critical role on morphological responses of bovine ECs. In fact, the ECs aligned with the direction of a one-directional flow whereas under a reciprocating flow condition they did not (Kataoka, Ujita & Sato 1998). As a result of this finding, Kataoka, Ujita & Sato (1998) concluded that the ECs recognize the flow direction and change their shape and structure accordingly. According to Zhou et al (2012), in the arterial region downstream of a stenosis (arterial narrowing) the ECs had rounded shapes and higher levels of proliferation (i.e. cell production). Zhou et al (2012) also noted that in the stenosis throat (narrowed region), the ECs had more polarized shapes. According to Heo et al (2011, a, b), the absence of the polarized shape leads to a higher exposure of shear stress gradients and makes the ECs more accessible to atherosclerosis lesions.

In addition, a large number of studies recognized a large variety of cell response phenomena when influenced by fluid flow including gene expression (effect attributed to a particular gene), cytoskeletal rearrangement (morphological changes), ionic response and proliferation (Nerem et al. 1994; Davies, 1995; Gooch & Tennant, 1997). Several key findings have indicated that ECs have multiple flow-induced functional changes. Haselton and Heimark (1997) showed that the distribution of endothelial cadherin (molecule that forms adherence junction) was reorganized under fluid shear. Another study by Nagel et al (1994) demonstrated that the intracellular adhesion molecule-1 was increased by fluid shear, whereas the expression of E-selectin and vascular adhesion molecule-1 was not. All of the above findings show that many physiological functions can change as a result of fluid shear stress. For example, expression of EC genes was distinguished between regions of laminar and disturbed flows as follows: (1) in the laminar regime, expression of transcription factor KLF2 associated with the cell survival was increased together with upregulation of the VE-cadherin (a component of the adherens junctions suggesting increased barrier function) whereas, (2) in the disturbed flow regime (post-stenotic region),

the expression of both the KLF2 and VE-cadherin was reduced and the marker of cell proliferation (SMAD1/5) was activated (Wang et al. 2006b; Miao et al. 2005).

There has as well been a vast amount of work which reported pulsatile flow over ECs (under both laminar and turbulent regimes). Some of the earlier work by Frangos et al (1985) reported that ECs subjected to a pulsatile shear stress generated an increase in the rate of platelet aggregation inhibitors when compared to steady laminar and stationary fluid conditions. The latter work was paramount as it established groundwork for further studies in the field by studying pulsatile flow (more realistic flows) over ECs. Some of this work included Helmlinger et al (1991) who studied pulsatile shear stress and the effect it has on the morphology of endothelial cells and White et al (2001) who investigated the effect of different velocity profiles on the endothelial cell response. With respect to the latter, White et al (2001) found that there is a stronger dependence of cell proliferation on the temporal gradients of shear stress in comparison to spatial gradients. Some of the more recent research included work by Chien (2007) who demonstrated that ECs that are exposed to a disturbed flow significantly differ in their response than the cells that are exposed to steady shear stresses. Chien (2007) found that the mechanotransduction process (shear stimulation of the sensors) depends on the mode of shearing. The mechanotransduction process (conversion of mechanical forces to intracellular biochemical responses) differs significantly for the ECs that are subjected to a disturbed flow from that of a steady laminar flow (Chien, 2007). In addition, Chien (2007) showed that cell proliferation is prevalent under a disturbed flow whereas cells that are exposed to steady shear express low proliferation rates. Furthermore, Chien (2007) demonstrated that cytoskeletal remodeling is not observed under a disturbed flow and that the cytoskeletal fibers are randomly oriented. This is presumably because the frequency and the magnitude of the forces are highly variable. It has been theorized that cytoskeletal fibers which are exposed to laminar steady flows help ECs to withstand hemodynamic loading since the stress fibers have a clear orientation (Wong et al. 1983). This is in contrast to ECs that are exposed to low and unsteady shear stress and, thus, experience a loss of fiber orientation (Chien, 2007).

In a more recent study, Avari et al (2016) investigated the effect of steady and pulsatile flow on porcine aortic endothelial cells (PAECs) morphology and cytoskeletal structure. The author specifically focused on EC area, perimeter, shape index (S.I; can be considered as a flow-sensitive morphometric parameter), angle of orientation, F-actin bundle remodeling and PECAM-1 re-distribution. In fact, the author simulated non-zero mean sinusoidal and carotid waveforms using the PFFC which is used in the present study (reported in Chapter Three – experimental methods). Avari (2015) reported that the S.I. decreased for both steady and pulsatile flow conditions and concluded that the S.I. changes correlated with the reversing/uni-directional nature of the flow together with the mean and peak amplitude of the pulse for the pulsatile flow conditions. These findings substantiate previous research which demonstrates that EC response is dependent on the type of flow.

In terms of the activation signaling pathways induced by fluid shear stress, extensive work has been carried out over the last few decades to better understand the signaling mechanisms involved in the formation of plaque in arteries. In fact, one of the more recent avenues of research surrounds the importance of the identity of the extra-cellular matrix (Givens & Tzima, 2016). According to Givens & Tzima (2016), the current view is that the extra-cellular matrix (the integrins binding to it) serve as a “check-point” that determine which intra-cellular signaling responses are going to be activated and/or inhibited. An example is the activation of JNK for cells plated on fibronectin and activation of p38 MAP kinase when cells are plated on collagen (Givens & Terzi, 2016). In addition, according to Givens & Terzi (2016), another important set of signaling molecules which are highly sensitive to spatial and temporal shear stress gradients are the members of the Rho family of GTPases.

Furthermore, according to Baeyens et al (2017), a coherent model for EC flow sensing is still lacking in the literature. The authors note that the best studied mechanotransducer is a complex of endothelial-specific molecules (proteins) localized at their junctions, consisting of PECAM-1, VE-Cadherin, and two VEGF receptors. However, it is known that low and oscillatory shear stresses activate many inflammatory events including increased

permeability, ROS generation, NF- κ B activity and receptor expression which recruit leukocytes (Baeyens et al. 2017).

It is, thus, critical to simulate physiological flows over live ECs to closely mimic realistic *in-vivo* conditions. According to Chistiakov et al (2016), links between mechanical forces and endothelial response (epigenetics – modification of gene expression) should be further studied to gain more insight into epigenetical regulator points and their changes when exposed to different flow conditions (laminar and disturbed). The present flow facility allows for further studies of EC response exposed to laminar and turbulent flow conditions through stenosis modeling using a simple backward-facing step.

In general, all these studies demonstrate the importance of measuring a two-dimensional velocity field over live ECs together with surface shear stress distribution over the individual cells close to the surface. The latter is further supported by the work of Dol et al (2010) which demonstrated (using μ PIV) inside a micro-chamber ($h = 127 \mu\text{m}$; where h is the chamber height) that with the introduction of ECs into the chamber the local shear stress variation was large and the velocity profiles were no longer uniform. In fact, Dol et al (2010) showed that as a result of the velocity distribution between peaks and valleys (as a result of the ECs), the wall shear stress ranged between 47-164% of the nominal values. This study demonstrated the importance of studying the sub-cellular force acting on the ECs and that the non-uniform shear stress should not be neglected (specifically in small vessels and channels).

The present work intends to help address some of these deficient areas in the literature by two-component velocity measurements (as close as $40 \mu\text{m}$ in reference to the cell surface) downstream of an idealized stenosis model (thereby disturbing the oncoming pulsatile laminar flow and subjecting the ECs to spatial and temporal wall shear stress gradients) and in addition, present a flow facility whereby direct quantification of the response of the cells (in order of milliseconds) is possible. Furthermore, through a comparison of flow physics in relation to more realistic models of stenosis (i.e. axi-symmetric stenosis model inside a tube) the present investigation aims to demonstrate how well a simple step geometry (used by several researchers to study ECs response to flow) can model the actual *in-vivo* environment associated with a diseased artery.

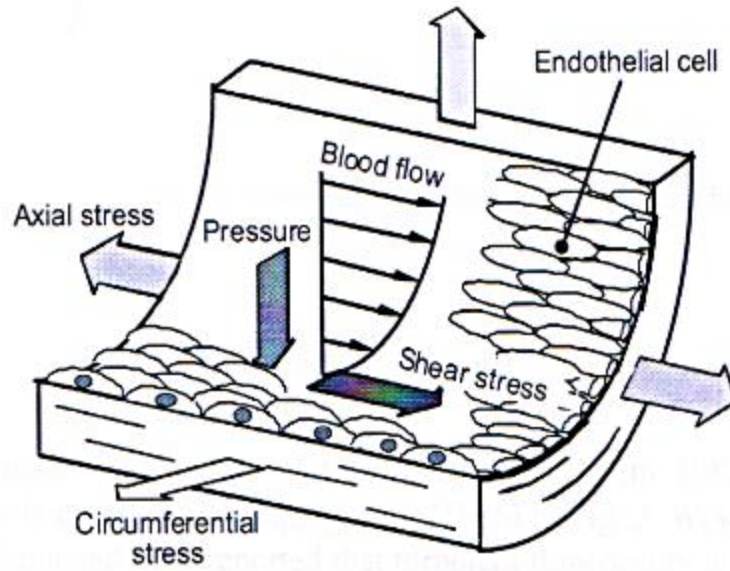


Fig. 2.1 Hemodynamic loading on the ECs (Ohashi & Sato 2005)

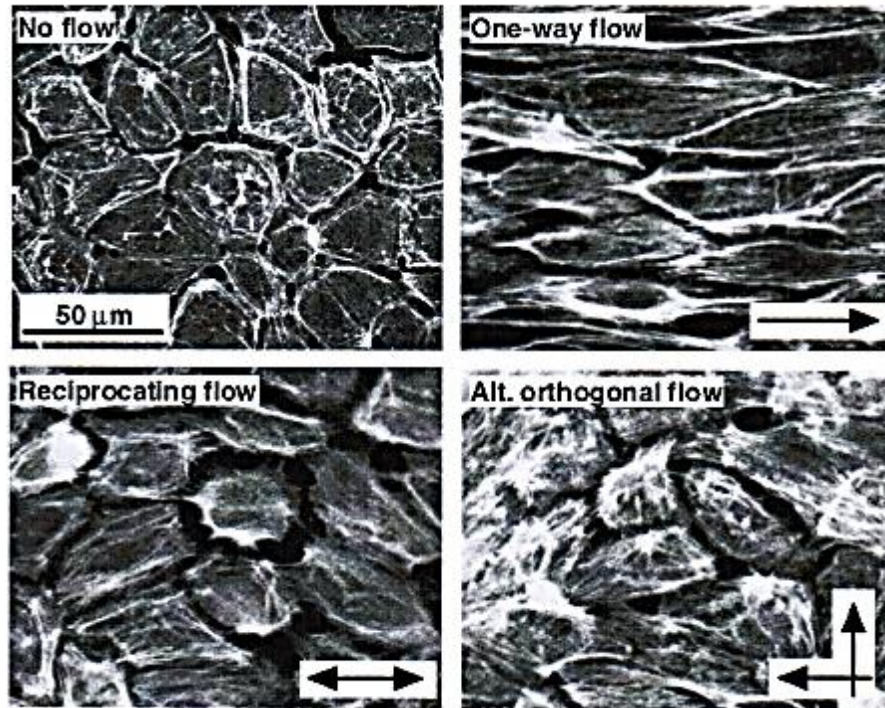


Fig. 2.2 Fluorescent images of actin filaments (Ohashi and Sato, 2005).

2.2 Parallel-Plate Flow Chamber (PPFC) Classification for Biomedical Applications

According to Kandlikar et al (2014), a PPFC can be classified based on its hydraulic diameter, D_h , as follows: (1) mini-channels having a hydraulic diameter in the range, $3 \text{ mm} \geq D_h > 200 \text{ } \mu\text{m}$, (2) micro-channels having a hydraulic diameter in the range, $200 \text{ } \mu\text{m} \geq D_h > 10 \text{ } \mu\text{m}$ and (3) conventional and compact channels for cases whereby $D_h > 3 \text{ mm}$. The latter category is pertinent to the present study whereby $D_h = 3.6 \text{ mm}$ based on the definition $D_h = 2h$, where h is the channel height at the working section (the mathematical definition is based on a two-dimensional flow channel). The two most common types of channels reported in the literature are the radial flow (Kuo & Lauffenburger, 1993; Goldstein & DiMilla, 1998) and the parallel-plate flow chambers. These systems have found a widespread use with the predominant focus on measurement of biological response of a cell layer to long-term exposure of both steady and pulsatile shear stress (i.e. time-varying). In this Chapter, the majority of the literature survey only

discusses the PPFC as it relates to the present study, however, a brief review of other *in-vitro* devices is provided in the subsequent paragraph and illustrated in Fig. 2.3 for general knowledge.

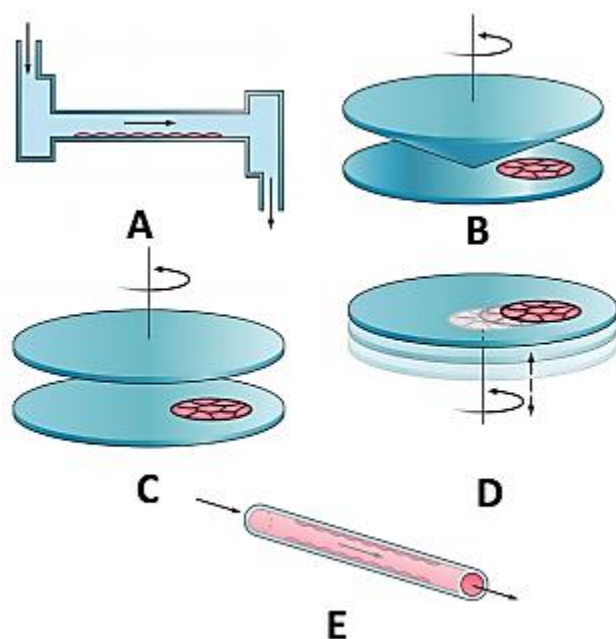


Fig. 2.3 Common *in-vitro* devices to study EC response to flow under steady laminar, pulsatile laminar and disturbed flow conditions. PPFC (A), Cone and Plate Apparatus (B), Parallel Disk Viscometer (C), Orbital Shaker (D) and Capillary Tube (E). Image taken from Avari (2015).

The radial flow chamber (i.e. cone-and-plate) is less frequently used as an *in-vitro* device to study flow over ECs. It has, however, been used by researchers (Blackman et al. 2002; Buschmann et al. 2005; Chung et al. 2005) and, thus, a brief review is provided. The device consists of a fixed plate and a rotating cone. The distance between the cone axis and the plate surfaces increase linearly from the cone axis. The relative velocity as well increases linearly with the distance from the axis and, thus, constant shear stress is achieved irrespective of position (Ohashi & Sato, 2005). Furthermore, the shear stress can be varied by changing the angular velocity and the taper of the cone (Ohashi & Sato, 2005). According to Chung et al (2005), the disadvantage of this device is the introduction of a secondary flow through an increase of the rotational speed, while the Reynolds number is the prevailing parameter of secondary flow since it represents the relative value of centrifugal force to viscous force. This apparatus has been used in the past to formulate an unsteady problem using a Weissenberg rheogoniometer whereby the cone oscillates with

respect to the plate to subject the ECs to an unsteady flow (Drasler et al. 1987). Furthermore, Blackman et al (2000) reported a cone-and-plate apparatus (viscometer device) to study the dynamic response of ECs in a controlled hemodynamic environment under a pulsatile flow. However, velocity field measurements continue to present a challenge with such a device and, thus, heavily rely on analytical and numerical solutions to solve the flow field (Avari et al. 2016).

Other less frequently reported *in-vitro* devices used to study endothelial cell response to flow include a parallel-disk viscometer (Laplaca & Thibault, 1997), an orbital shaker (Dardik et al. 2005) and capillary tube (Chiu & Chien, 2011). The first two devices cannot achieve a uniform shear stress over the entire cell monolayer and the capillary tube does not yield a sufficient amount of ECs for bioassay analysis (Avari et al. 2016). For these reasons, researchers continue to use the PPFC as an *in-vitro* device together with the advantages of being able to load the ECs with uniform shear stress, the ease of equipment installation (assembly/disassembly which relates to cell media exchange) and, ability to view the live cells and measure the velocity field at the working section through an optical window installation (Avari et al. 2016).

2.2.1 Investigation of Steady and Pulsatile Flow inside a PPFC over ECs

Numerous works have focused on studying endothelial cell response inside the PPFC under steady and pulsatile flow (laminar and disturbed conditions characterized by recirculation regions and high oscillatory shear). For the reader's general knowledge, table 2.1 (page 36) summarizes some of the research (applicable to the present study for a comparison of flow conditions, channel size, method of calculating shear stress) throughout the last few decades which studied cell response to flow inside a PPFC under both steady and disturbed flow conditions. The table shows various simulated flow conditions and the corresponding EC responses investigated together with the size of the channels and the methods used to quantify the wall shear stress.

Disturbed flow over ECs has as well been studied inside a PPFC under the influence of a step (Nagel et al. 1999; DePaola et al. 1999; Phelps & DePaola, 2000) to generate spatial

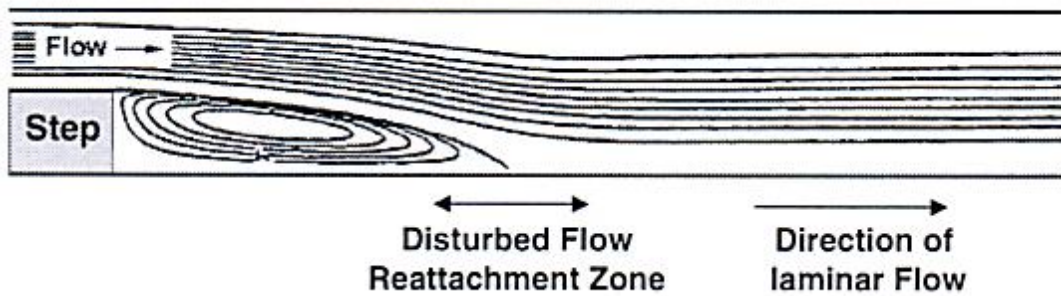


Fig. 2.4 Schematic of a BFS to disturb the oncoming steady and pulsatile laminar flow. Illustration from Chien (2007).

and temporal shear stress gradients. The typical configuration which uses a BFS (also known as the vertical-step flow channel) is shown in Fig. 2.4. However, most of these studies strictly focused on endothelial cell response and, at most, reported the wall shear stress profile along the streamwise direction (i.e. using Computational Fluid Dynamics) and did not provide detailed mean flow and turbulence statistics. Given the established link between cell response to flow (a clear association between WSS and cell response), many studies strictly focus the research efforts on describing the behaviour of the flow (and the variation of the wall shear stress) downstream of a stenosis in a more classic fluid mechanics approach (i.e. detailed velocity field investigation and no EC studies). This is actually the intention of the present study; that is, to evaluate the flow field downstream (using detailed two-component LDV measurements) of a BFS (under steady and pulsatile laminar flow) and provide useful data which can then be used to study EC response (i.e. by having quantified wall shear stress values (within a clearly defined degree of uncertainty) for given Q values (specified at the pump) and flow conditions).

Although the BFS inside a PPFC does not represent the geometry of an artery found in the body, it does provide a starting point to better understanding occluded and separated flows. In fact, it will be seen further in the thesis (Chapter Five – two-component velocity measurements downstream of BFS) that the channel geometry (with the step) shares some similar flow behaviour with that of more realistic geometries such as a section of straight tubing with an asymmetric stenosis.

Table 2.1 A summary of the flow studies over ECs inside the PPFC

Author	Flow Conditions	Channel height (μm)	Velocity Field Solution	ECs Investigation	Shear Stress (dyne/cm^2)
Avari et al (2016)	Steady and pulsatile laminar	1800	LDV	F-actin and PECAM-1 (ECs)	1-12
Wang et al (2012)	Steady laminar	500	Numerical methods (OpenFOAM)	Actin remodeling and morphological changes	12
Fry et al (2011)	Steady laminar	254	CFD and μPIV	Methicillin resistant Staphylococcus aureus adhesion to endothelial cells	0-12
Dol et al (2010)	Steady laminar	127	Fluent and μPIV	Local wall shear stress variation over re-constructed endothelial cell surfaces	2 and 10
Voorhees et al (2007)	Steady laminar	1000	μPIV	Biochemical response of ECs – cell shape and alignment	5 and 10
DePaola et al (1999)	Disturbed flow using a BFS	1000	CFD	Gap junction protein – connexin43 (Cx43) and intracellular communications	13.5 (downstream of the disturbance) Absolute value within the recirculation region was 0-8.5
Helminger et al (1991)	Pulsatile and oscillatory flow (1 Hz), laminar regime	250	Analytical solution	Influence of pulsatile flow on cell shape and orientation together with actin microfilament localization in bovine aortic endothelial cells	Non-reversing sinusoidal shear stress of 40 ± 20 dyne/cm^2
Lawrence et al (1987)	Steady laminar	250	Laminar flow theory	Adhesion of polymorphonuclear leukocytes to vascular endothelium	0.98, 1.96, 3.01 and 3.92
Frangos et al (1985)	Steady laminar	220	Laminar flow theory	Production of prostacyclin	Up to 24
Koslow et al (1986)	Steady laminar	160-690	Electrochemical, LDV and flow visualization techniques	Morphological response of ECs	4-12

2.2.2 Analytical and Experimental Methods for Quantifying Wall Shear Stress

In addition to the computational methods used for quantifying WSS (briefly reviewed in section 1.2), analytical methods have also been used as means of quantifying steady and pulsatile laminar shear stresses above the ECs in the PPFCs (Ruel et al. 1995; Truskey, Barber & Rinker 2002; Bacabac et al. 2005; Shen et al. 2006; Avari et al. 2016). For steady laminar flow, the shear stress was calculated as follows:

$$\tau_w = \frac{6\mu Q}{wh^2} \quad (2-1)$$

where μ is the dynamic viscosity, Q is the volumetric flow rate, w is the width of the chamber, and h is the total height. It should be noted that the analytical solutions cannot be used for steady and pulsating flow over a BFS, given the complexity of the flow regime downstream of the step (i.e. intermittent turbulence for pulsatile flow together with the unsteady recirculation region). To measure WSS under complex flow regimes requires advanced methods such as μ PIV and μ LDV to directly measure the flow near the endothelial cell surface.

Experimental studies of flow inside channels and tubes cover a wide range of measurement techniques to deduce wall shear stress (WSS). Due to the small-scale size and confined geometry of these type of flows, invasive methods such as the hot-wire anemometry technique are not optimal (Teuffl et al. 1992). In addition, MEMS-based sensors are not ideal for these sort of velocity measurements because they are invasive and introduce additional complexity into the experimental set-up (Antony et al. 2014). There are advanced methods that are suited for measuring high-frequency flows near the surface such as time-resolved-PIV (TR-PIV). However, they are more expensive than traditional techniques such as LDV. Much of the work studying channel flows (where $h < 60$ mm and represents the channel height) covering steady laminar, pulsatile laminar and turbulent regimes have resorted to the LDV technique due to its spatial accuracy and high-frequency response (So et al. 2002; Verhelst et al. 2004; Appel et al. 2005; Castrejon et al. 2006;

Arbeiter et al. 2007; Marx et al. 2010; Avari et al. 2016). However, the LDV technique presents several challenges for boundary-layer measurements, with the major obstacle being the difficulty associated with locating the measurement volume in reference to the wall. Inaccurate determination of the absolute and relative wall positions can lead to incorrect values of the near-wall mean and turbulence quantities. It can also lead to an incorrect friction velocity (u_τ) and wall shear stress (τ_w) as a result of fitting the data in the viscous sublayer region (Orlu et al. 2010). The latter is as a result of the velocity measurements not being assigned to the correct spatial reference.

There have been several direct methods described in the literature to determine the location of the first measurement point (using the LDV technique) at the wall for both steady laminar and turbulent boundary layers. Among these methods, Durst et al (1995) proposed traversing the measurement volume into the wall and monitoring the output signal of the photodetector until the maximum signal is obtained. The maximum signal corresponds to the zero location of the measurement volume with respect to the wall. By this approach, the author stated that the small seeding particles attached to the wall would cause the signal to be generated from the photodiode. Another study by Radomsky & Thole (2002) used a two-step process to determine the measurement volume location on a turbine stator vane: (1) lowering the power of the individual beams and visually observing the measurement volume as it traversed into the wall and, (2) monitoring the output of the photodetector using an oscilloscope as the beams' crossing was traversed into the wall. Using both of these techniques and repeating the process several times, the authors were able to locate the measurement volume (with respect to the wall) to within $\pm 20 \mu\text{m}$ (i.e. $y^+ \approx 2$). Furthermore, Ching et al (1995) studied low-Reynolds-number effects in a turbulent boundary layer and determined the wall location by monitoring the analogue signal as the measurement volume was traversed into the wall. This was followed by linearly fitting at least four data points in the wall region (i.e. $y^+ < 12$) and extrapolating this line to $u(y = 0) = 0$ for a comparison. The two techniques were always within $\pm 0.075 \text{ mm}$. In some of the more recent work, Avari et al (2016) determined the measurement volume location by tilting the probe ($\approx 4.5^\circ$) and traversing the measurement volume into the wall whilst monitoring the voltage output of the photo-detector module (PDM). The author then assigned the centre of the measurement volume to the maximum voltage reported on the

oscilloscope. A post-processing method was also applied to compare to the direct method by fitting a 2nd order polynomial curve across the channel half-height to find the distance from the peak (centre-line velocity) to the wall. The author reported the positional uncertainty to be within $\pm 27 \mu\text{m}$.

In the present study, a method suggested by Durst et al (1988) was used and is explained in Chapter Four of this thesis (experimental uncertainty Chapter). As a brief overview, the method is based on monitoring and capturing the streamwise velocity as the measurement volume is embedded into the wall to detect an abrupt slope change in the streamwise velocity profile. This is then supplemented by extrapolating the velocity data points using linear regression prior to the abrupt slope change to find the zero velocity point (which can be considered to be the wall location). For the present study, this method was used to find the location of both the lower wall (to then traverse in the y-direction and deduce wall shear stress) and the side wall (to then traverse in the z-direction to the mid-plane of the channel span).

2.2.2.1 Analytical Solution for Pulsatile Flow (Laminar Regime) inside PFC

For a plane channel flow with a pulsatile pressure gradient, Langlois & Deville (2014) provide a review of the analytical solution which is explained in-depth in the following paragraphs. However, before proceeding to the mathematical derivation of the pulsatile flow, a brief review of this type of flow is provided to assist the reader with the basic principles. A pulsatile flow is characterized as a unsteady flow and it consists of a steady component (mean flow) and a time-varying component (Gundogdu & Carpinlioglu 1999). The time-varying component is the superimposed oscillation (Carpinlioglu & Gundogdu 2001). A distinct type of pulsatile flow is the oscillatory flow which consists only of the time-varying component, as the net-flow over each cycle is zero (Zamir, 2000). The latter is indicative of a zero steady flow component. An example of oscillatory flow is a simple sine wave which is solely governed by an oscillation which, in turn, only moves the fluid back and forth producing zero net-flow (Zamir, 2000).

One of the most critical parameters of a pulsatile flow is the Womersley number (Wo), which explains the behaviour of a pulsating flow (Oates, 2001). For a two-dimensional pulsatile flow in a PPFC, the Womersley number can be expressed as $Wo = h \sqrt{2\pi\rho/T\mu}$, where T, μ, ρ are, respectively, the period of the pulse cycle, the dynamic viscosity of the fluid and the fluid density (Shen et al. 2006). Wo is the ratio between the unsteady inertial forces and the viscous forces (Shen et al. 2006). Moreover, the Wo definition shows its dependence on the fundamental frequency of the cycle (i.e. $f = 1/T$) and the vessel size (in this case, channel height). The fundamental frequency represents the frequency of a cyclic complex waveform (Oates, 2001). Throughout the cardiovascular system the Wo parameter varies whereby in the larger arteries (near the heart) it is in the range, $15 \leq Wo \leq 25$, and further downstream in the arterioles and capillaries it is $Wo < 10$ (Griffith, 2009).

The magnitude of Wo significantly influences flow response to pressure gradient changes (Oates, 2001). If the change occurs rapidly (i.e. $Wo \gg 1$) the flow fails to instantly respond from its acquired inertia and as a result the flow lags behind the driving pressure (Zamir, 2000). It can be seen from Fig. 2.5 how Wo influences the development time of the boundary layer (determined by the fluid viscosity relative to the pulse period length); that is, at $Wo \gg 1$ the unsteady forces dominate the flow and the velocity profiles are flatter

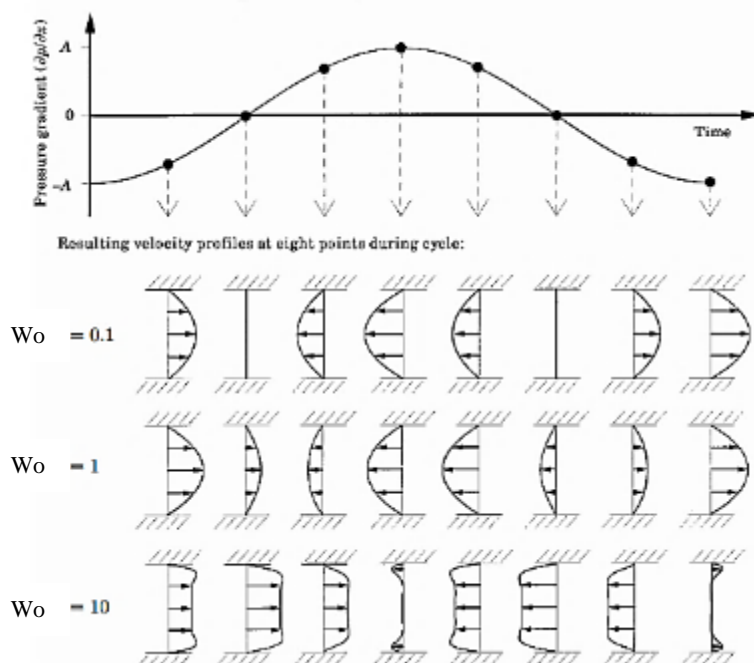


Fig 2.5 From Loudon & Tordesillas (1998): velocity profiles as a function of the Womersley Number.

(boundary layer extends a short distance from the wall) whereas, at $Wo < 1$ the velocity profiles exhibit the profile shape of the Poiseuille solution (Griffith, 2009). A relevant note based on a review by Oates (2001) states that it is the boundary layer which affects the shape of the streamwise velocity profiles inside channels and tubes and it is the frequency of the pulse which affects the boundary layer (i.e. based on the time available for the boundary layer to develop). Oates (2001), as well, notes that it is the diameter of the vessel (or in the present case, the channel height) which determines how thick the boundary layer must grow to affect all of the fluid. Both of these factors are incorporated into the Wo parameter which ultimately affects the shape of the velocity profiles.

Furthermore, at $Wo \gg 1$ the amplitude of the flow during a cycle will be restricted (Zamir, 2000). In fact, the amplitude is to some extent less than it is for Poiseuille flow under a constant driving pressure gradient equal to the peak of the oscillatory pressure (Zamir, 2000). The reason for the loss in amplitude is insufficient acceleration time, which is necessary to bring the fluid up to full velocity (Oates, 2001). Hence, the larger the value of Wo , the more considerable is the loss in flow amplitude during a cycle. In contrast, gradual pressure changes during the cycle ($Wo \ll 1$) result in no lag between flow and pressure and the Poiseuille relation between pressure and flow is satisfied at any instant of the cycle (Zamir, 2000).

According to Langlois & Deville (2014), the standard Poiseuille flow (with a steady constant pressure gradient) together with a oscillatory pressure gradient can be mathematically expressed as follows (Fig 2.6 shows geometry for reference):

$$-\frac{1}{\rho} \frac{\partial p(t)}{\partial x} = -G - C \cos(\omega t) \quad (2-2)$$

where C is a constant from experimental data and G is the constant pressure gradient. In addition, ω is the natural frequency of the pulsation and ρ is the density of the fluid. Using Fourier representation, equation (2-2) can be re-written as follows:

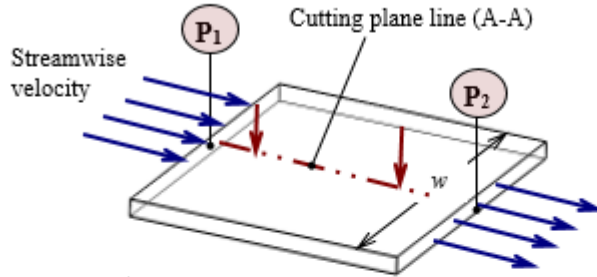
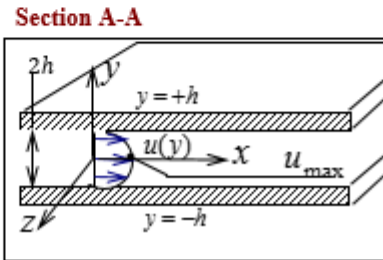


Fig 2.6 Geometry for flow between parallel plates



$$-\frac{1}{\rho} \frac{\partial p(t)}{\partial x} = -G - \Re(Ce^{i\omega t}) \quad (2-3)$$

where \Re represents the real part. It should be noted that variable x represents the streamwise direction of the flow and variable y represents the wall-normal direction (see Fig 2.6 for reference).

Furthermore, the solution can be written as a complex function (since a steady-state solution is required for the velocity field) as follows:

$$u = u_p + \Re(u(\omega, y)e^{i\omega t}) \quad (2-4)$$

where u_p represents the Poiseuille solution defined as $u_p = \left(\frac{Gh^2}{2\mu}\right)\left(1 - \frac{y^2}{h^2}\right)$, where h represents the channel half-height and μ the dynamic viscosity of the fluid.

Furthermore, the Navier-Stokes equations lead to the relation:

$$\frac{\partial u}{\partial t} = -\frac{1}{\rho} \frac{\partial p}{\partial x} + \nu \frac{\partial^2 u}{\partial y^2} \quad (2-5)$$

With Eqs. (2-3) and (2-4), Eq. (2-5) gives the following mathematical relation:

$$i\omega u = -C + \nu \frac{\partial^2 u}{\partial y^2} \quad (2-6)$$

Langlois & Deville (2014) note the following boundary conditions:

$$u(h) = 0, \frac{\partial u}{\partial y}(0) = 0 \quad (2-7)$$

The solution of Eq. (2-6) yields the following relation:

$$u = \Re \left[\frac{iC}{\omega} \left(1 - \frac{\cosh \sqrt{\frac{i\omega}{\nu}} y}{\cosh \sqrt{\frac{i\omega}{\nu}} h} \right) \right] \quad (2-8)$$

Langlois & Deville (2014) further note that $i^{1/2} = (1 + i)/\sqrt{2}$ can be taken into account to yield the final form (real part) of the velocity field:

$$u = u_p - \frac{C}{\omega} \left[\left(1 - \frac{f_1(\omega, y)}{f_3(kh)} \right) \sin \omega t - \frac{f_2(\omega, y)}{f_3(kh)} \cos \omega t \right] \quad (2-9)$$

where $k = \sqrt{\omega/2\nu}$ and other notations defined as follows (Langlois & Deville, 2014):

$$cc(x) = \cos x \cosh(x)$$

$$ss(x) = \sin(x) \sinh(x)$$

$$f_1(\omega, y) = cc(ky)cc(kh) + ss(ky)ss(kh) \quad (2-10)$$

$$f_2(\omega, y) = cc(ky)ss(kh) - ss(ky)cc(kh)$$

$$f_3 = cc^2(\omega) + ss^2(\omega)$$

Langlois & Deville (2014), as well, note that for the low frequency flow the solution (approaching steady flow) can be obtained by taking the limit of Eq. (2-9), whereby $k \rightarrow 0$. Furthermore, since $cc(x) \rightarrow 1$ and $ss(x)$ is asymptotic to x^2 (for $x \rightarrow 0$), the flow solution can be reduced to the following mathematical expression:

$$u = u_p + \frac{Ch^2}{2\nu} \cos(\omega t) \left(1 - \left(\frac{y}{h}\right)^2\right) \quad (2-11)$$

Finally, the authors note that for a high-frequency case (or equivalently inviscid fluid), the flow solution can be deduced by considering $hk \gg 1$ and given that $cc(x)$ and $ss(x)$ are asymptotic to $1/2e^x \cos x$ and $1/2e^x \sin x$, respectively, for $x \rightarrow 0$. The limit solution can thus be expressed as:

$$u = u_p - \frac{C}{\omega} (\sin \omega t - \sin \omega t - \eta) e^{-\eta} \quad (2-12)$$

The new variable η measures the distance from the upper wall and can be defined as follows (Langlois & Deville, 2014):

$$\eta = k(h - y) = \frac{h-y}{\sqrt{2\nu/\omega}} \quad (2-13)$$

2.3 BFS Flow Inside Rectangular Flow Channels under Steady Laminar Flow

The backward-facing step (BFS) inside a two-dimensional flow channel is a recognized test-section geometry that a vast number of researchers have studied both experimentally (by means of measurement of flow) and by numerical methods. The sudden expansion creates a separating shear layer originating from the step edge thereby forming a recirculation region in the vicinity of the step (Armaly et al. 1983). This type of flow has a wide number of engineering applications including biomedical and is considered an important benchmark test problem for CFD (Gartling, 1990). For biomedical applications (specifically studying cell response to flow), the step inside the channel is typically modeled as either a right-angle (i.e. sharp edge) or semi-circle and is placed either on the bottom or the top of the channel wall to represent narrowing of the artery (Dvinski & Ojha, 1994; Mittal et al. 2003; Griffith et al. 2009). An illustration of the BFS geometry is given in Fig. 2.7 for further clarity.

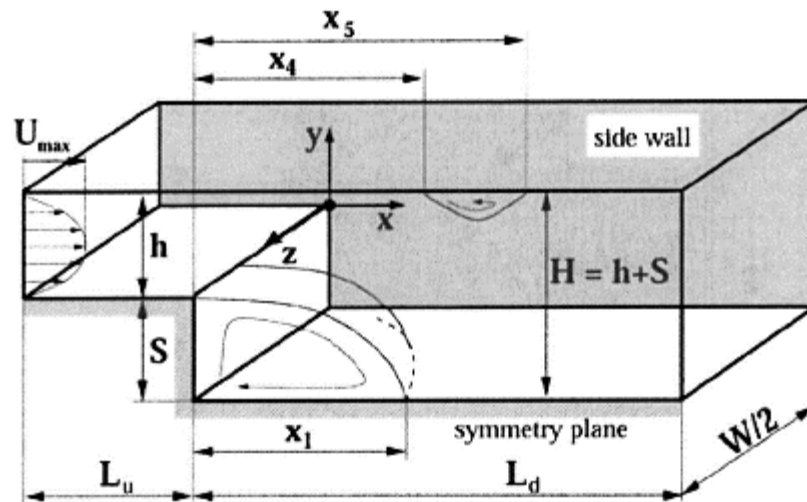


Fig. 2.7 Typical geometry of a BFS test problem for analysis. This Figure defines the various length scales at the working section. The normalized reattachment length of the primary recirculation region is denoted by variable $x_1 = x/S$. Furthermore, x_4 and x_5 denote the start and the end of the upper wall recirculation region ('roof eddy'), respectively. Illustration taken from Biswas et al (2004).

In fact, most researchers have resorted to tubular geometry to study flow downstream of the stenosis by modeling the arterial narrowing as an asymmetric or axi-symmetric constriction (Cassanova & Giddens, 1978; Ahmed & Giddens, 1984; Dvinsky & Ojha, 1994). The tubular geometry is less technically challenging for the fluid dynamicist as the flow in a section of straight tubing is much easier to model than the flow inside a two-dimensional channel (Griffith, 2009). In addition, according to Griffith (2009) the flow inside a two-dimensional channel with the infinitely wide channel dimension can be rather difficult to model with the isolation of the side wall effects. All of this work is explained in the subsequent sections with the starting point of the BFS (i.e. right angle geometry). It should be noted that this literature review does not cover turbulent boundary layers (as the inlet flow condition) since the present work deals with steady and pulsatile laminar flow.

The work of Armaly et al (1983) provides a detailed review of the fluid mechanics downstream of a BFS ($ER = H/h = 1.94$, where it represents the expansion ratio; see Fig. 2.7) which includes LDV measurements (u velocity component representing the streamwise flow) inside a PPFC with an aspect ratio of $W/h = 36$ (where W is the width of the channel). Armaly et al (1983) report a $Re_S = U(2h)/\nu$ range (70 to 8000; where subscript “S” represents the step conditions, U is the bulk velocity and $D_h = 2h$ is the hydraulic diameter) which extends through laminar, transitional and turbulent regimes. The study conducted by Armaly et al (1983) continues to be the leading reference for various CFD modelers as means of comparing results and validating the accuracy of the numerical predictions (Erturk, 2007; Hossain et al. 2013). In fact, the present study relies on the work of Armaly et al (1983) to compare the normalized streamwise mean velocity profiles (vertical profiles) and the reattachment length downstream of the step for the BFS flow case (under steady laminar flow inlet conditions). The latter is presented in more detail and discussed in Chapter Five (two-component velocity measurements downstream of the BFS). The details of the findings Armaly et al (1983) report is discussed in Chapter Five in more detail (specifically making a comparison with the present work), however, a few relevant notes from their study are briefly presented here. The relationship between the Reynolds number and the primary recirculation region (on the lower wall adjacent to the step) is defined as follows: (1) in the laminar regime ($Re_S < 1200$), the reattachment length increases non-linearly with Re_S , (2) in the transitional regime ($1200 < Re_S < 6600$), the reattachment length rapidly decreases followed by a gradual decrease and, (3) in the turbulent regime (characterized by $Re_S > 6600$), the reattachment length experiences a gradual increase to a constant level. It should be noted that Armaly et al (1983) report the primary reattachment length to be the greatest at $Re_S \approx 1200$, followed by a sharp decrease. The latter is explained by the action of the Reynolds stresses, which according to Biswas et al (2004) must be present for even slightly lower Reynolds numbers. For further clarity, Armaly et al (1983) show measurements of the reattachment length ($x_1 = x/S$) as a function of the Reynolds number to demonstrate a clear indication of the different flow

regimes (laminar, transitional and turbulent). This plot from the work of Armaly et al (1983) is given in Fig. 2.8.

This criterion for characterizing the flow regime downstream of the BFS has been widely accepted in the literature and is as well considered in the present study. The upper wall recirculation region (whereby the separation and reattachment points are denoted by x_4 and x_5 , respectively in Fig. 2.8) is also reported by Armaly et al (1983). The author notes that this secondary recirculation region (“roof eddy”) forms (as a result of the adverse pressure gradient) during the laminar regime ($Re_S > 400$) and remains in existence throughout the transitional regime. The secondary recirculation region is noted by Armaly et al (1983) to be expansion ratio (ER) dependant and is further discussed in Chapter Five. It should be noted that Armaly et al (1983) also reports a third recirculation region between x_2 and x_3 on the lower wall (see Fig. 2.8) for parts of laminar and transitional flow regimes. Work by Lima et al (2008) which considers identical flow and geometry conditions (with the

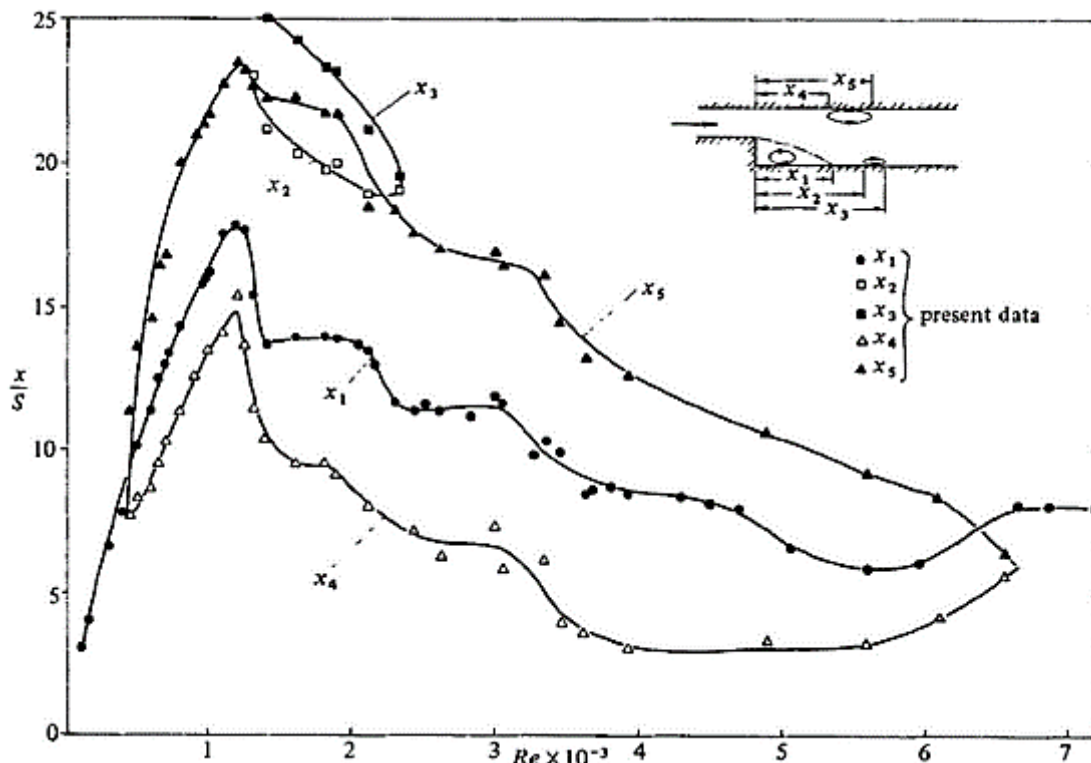


Fig. 2.8 Measurements of the separation and reattachment locations as a function of the Reynolds number. Plot taken from the work of Armaly et al (1983).

exception of using two-dimensional numerical simulations; finite element and volume methods) as Armaly et al (1983), only reports this third recirculation region in the range, $2500 \geq Re_S \geq 1800$ (transitional regime). The third recirculation region on the lower wall was not captured in the present work and, hence it is not further discussed.

Table 2.2 shows a summary of the separation and reattachment points at the lower and upper walls for $Re_S = 800$ based on pertinent studies (similar ER and Re_S values) in relation to the present work. The $ER = H/h$ values are all 1.94 unless otherwise specified in the table and both experimental and numerical work (two-dimensional) is included. It is important to note that both the experimental work of Armaly et al (1983) and Lee & Mateescu (1998) report maximum values of x_1 at $Re_S \approx 1200$ (transitional flow regime). In fact, in reference to table 2.2 (at $Re_S = 800$) their experimental results (reattachment and separation values for both recirculations) are fairly similar (a maximum difference of $\approx 10\%$) given the differences in the ER values. However, the two-dimensional numerical work of Armaly et al (1983) does not agree with their experimental results for $Re_S > 400$ (encapsulates laminar, transitional and turbulent regimes). This is also evident from table 4.2 whereby the two-dimensional numerical x_1 values are smaller than the experimental values for all work listed. According to Lima et al (2008) and Erturk (2008), the discrepancy between the experimental and numerical work (in terms of the x_1 values) is attributed to the three-dimensional behaviour of the flow and unsteadiness features of laminar-turbulent transition at relatively larger Re_S values (i.e. flow not captured by the steady/unsteady laminar two-dimensional numerical solution). It should be noted that the work of Kitoh et al (2007) is in better agreement with the experimental work (listed in table 2.2) in reference to the x_1 values, given that the author used three-dimensional Direct Numerical Simulations (DNS). Kitoh et al (2007) reports (considering $ER = 2.0$ and aspect ratio of $W/h = 36.0$) excellent agreement with the work of Armaly et al (1983) across the laminar and transitional flow regimes, further substantiating the three-dimensionality of the flow which Armaly et al (1983) report for $Re_S > 400$.

In terms of the x_4 values listed in table 2.2 (separation point on the upper wall), similarly the experimental work shows relative larger values (farther starting point of the secondary recirculation region from the step edge) than the two-dimensional numerical work at Re_S

= 800. The reattachment length (i.e. x_5) for the upper wall recirculation region seems to be more consistent between the numerical work and the experiments (with the exception of the work by Armaly et al (1983)). However, according to Lima et al (2008) this only holds true in the range of $648 \leq Re_S \leq 1000$.

Table 2.2 Separation and reattachment locations: a comparison between experimental and numerical results for $Re_S = 800$.

	Numerical Work					Experimental Work	
	Armaly et al (1983)	Gartling (1990)*	Lee & Mateescu (1998)*	Lima et al (2008)	Erturk (2008)	Armaly et al (1983)	Lee & Mateescu (1998)*
x_1	7.47	12.00	12.00	11.97	11.98	14.00	12.94
x_4	5.32	10.00	9.60	9.51	--	11.11	10.60
x_5	11.28	21.00	20.60	20.04	--	19.33	20.56
*ER = 2.0							

2.3.1 Paths to Flow Instability

Armaly et al (1983) first observed flow becoming three-dimensional (downstream of the reattachment point) for $Re_S > 400$ and contended that this three-dimensionality was a result of an inherent instability mechanism associated with the secondary recirculation region on the upper wall (discrepancy was as well reported between experimental and two-dimensional numerical predictions reported by Armaly et al (1983)). Since then, this hypothesis has been challenged and tested by several researchers using computational methods which are discussed in the subsequent paragraph.

The paths to instability for a BFS test problem have received a lot of attention over the last few decades, starting with Ghia et al (1989) who suggested that the flow instability was associated with the secondary recirculation region on the upper wall. Ghia et al (1989) postulated that the secondary recirculation region subjected the mainstream flow to a

concave curvature thereby activating the centrifugal Taylor-Görtler instability. Furthermore, the work of Kaiktsis et al (1991, 1996) set the groundwork and motivation for much of the later BFS studies by reporting a convectively unstable flow (response is convected away and does not expand from the impulse point) for Reynolds number in the range, $700 < Re_S < 2500$, which was in contrast to the findings reported by Armaly et al (1983) given that Kaiktsis et al (1991, 1996) found a higher Re_S value associated with the three-dimensionality. Some of the more recent work reported by Barkley et al (2002) who numerically studied (steady two-dimensional solutions using time-dependent simulations and/or Newton method) the instability of a two-dimensional steady flow as well reported a much larger Reynolds number (that of the work by Armaly et al. 1983) whereby the flow would naturally transition to unsteady state (i.e. three-dimensional flow). In their work, they performed a stability analysis up to $Re_S = 1500$ and reported that the flow remains linearly stable to two-dimensional perturbations. Their results showed no evidence of any two-dimensional bifurcation up to $Re_S = 1500$ (absolute instability). The work of Barkley et al (2002) also disregarded the initial hypothesis made by Ghia et al (1989) with respect to the secondary recirculation region (upper wall) being responsible for the mainstream flow instability. Barkley et al (2002) showed that the two dimensional flow remained linearly stable following the formation of the secondary recirculation region ($Re_S \approx 400$). Barkley et al (2002) also noted that when the instability was activated it did not take the form of streamwise vortices within the main flow as one would expect from this type of mechanism (centrifugal Taylor-Görtler instability). A similar result was reported by Fortin et al (1997) who studied the stability of a two-dimensional flow over a BFS up to a Reynolds number of 1600. The authors mentioned that by considering the boundary conditions and the mesh used in their numerical simulations, there was no evidence of a pair of eigenvalues (resulting from the discretization of the incompressible Navier-Stokes equations) which crossed the imaginary axes, thereby concluding that the flow was stable up to $Re_S = 1600$. Both of the numerical studies mentioned above used a BFS with $ER = 2.0$ (thus comparable with the work of Armaly et al (1983)). It should be noted however that the threshold Reynolds number values reported by both of the numerical studies should be considered with caution (when comparing with experiments) since numerical calculations can suffer from discretization errors which are able to sustain perturbations

and, thus, obscure potential intrinsic instabilities (Kaiktsis et al. 1996). Equally, with experiments, the strong influence of external perturbations can make it challenging to achieve reproducible results when compared to numerical methods. The external perturbations can lead to an earlier inception of the transitional flow regime (Tihon et al. 2012).

According to Tihon et al (2012), there are two sources of three-dimensionality for internal flows with a BFS: (1) the influence of channel geometry (side walls) and, (2) the intrinsic flow instability (i.e. action of hydrodynamics). The mechanisms of the shear layer instability together with vortex-shedding is discussed in the next section. With regards to the side wall effects on the three-dimensionality of the flow (downstream of the BFS), the work of Williams & Baker (1997) shed light on the importance of channel aspect ratio (i.e. W/h). The authors compared their three-dimensional simulation to both two dimensional simulations and experiments (whereby the flow conditions and channel geometry was equivalent to the work of Armaly et al. 1983: $\alpha_S = 35$, $ER = 1.94$, $Re_S = 800$). Their investigation reported an interaction between the main fluid flow (mid-plane flow structure in reference to the span width) and a wall jet (located at the step plane near the side wall), with increasing penetration of the three-dimensional flow structures into a two-dimensional flow region with an increasing Reynolds number (i.e. $100 < Re_S < 800$; refer to Fig. 2.9 and Fig. 2.10 for an illustration). Williams & Baker (1997) reported that the vortex enters the primary recirculating flow (entrained by the primary two-dimensional motion) and exits into the mainstream flow. The authors further concluded that the three-dimensionality reported by Armaly et al (1983) in the laminar regime ($Re_S < 1200$) was a result of the predetermined aspect ratio (i.e. side wall effect) and not an instability inherent to the two-dimensional flow. Their findings were further validated by the work of Chiang & Sheu (1998) who demonstrated that the interaction of the side wall induced flow and the two-dimensional flow (mid-plane region) is dependent on Re_S and the aspect ratio of the channel and, concluded that the side wall effects can only be ignored for an inlet aspect ratio greater than 50 (i.e. $\alpha_S = W/h > 50$). Furthermore, Chiang & Sheu (1998) reported that when $\alpha_S = 100$, the flow structure at the channel midplane for the two-dimensional and three-dimensional numerical solutions were identical. The work of Williams & Baker (1997) was, as well, corroborated with a further investigation by Tylli et al (2002), which

reported penetration of a side wall separation region into the two-dimensional streamwise flow for $Re_S > 400$. The work of Williams & Baker (1997) and Chiang & Sheu (1998) is discussed in Chapter Five in the context of comparison with the present work.

2.3.1.1 Vortex Shedding Mechanisms in Internal Flows

The vortex shedding phenomenon has been observed in many experimental and numerical research papers concerning stenosed vessels and, hence, it is reviewed. According to Boghosian & Cassel (2010), an understanding of this phenomenon is important since the breakdown of the vortices plays a key role in the transition to turbulence. Furthermore, according to Boghosian & Cassel (2010) there are several mechanisms which induce vortex shedding, one of them being a classic inviscid Kelvin-Helmholtz instability in a free shear layer. In terms of the Kelvin-Helmholtz instability, the shear layer rolls up into a sequence of vortices that subsequently detach from the shear layer. The Kelvin-Helmholtz instability is reported by several authors studying axi-symmetric stenosis flows inside a straight section of tube and is the primary reason for the generated turbulence downstream of the reattachment point (Varghese et al. 2007 a,b). In fact, there is a distinct frequency range (i.e. shear layer oscillation) attributed to this type of instability that facilitates identification of these types of flows (non-dimensional frequency of $S_t \cong \sigma(10^{-1})$ corresponds to start-up structures originating in the shear layer as a result of a Kelvin-Helmholtz instability).

Another mechanism responsible for vortex shedding is explained by Obabko & Cassel (2002). The authors note that for a sufficiently large Re value and adverse pressure gradient, the shedding process is started via periodic ejections of near-wall secondary vorticity taking a “spike-like” character. According to Obabko & Cassel (2002), the boundary layer ejects the fluid (away from the wall) and divides the primary recirculation region into discrete co-rotating vortices. Following this process, the vortices are shed downstream with the flow. Other mechanisms of vortex shedding (pertinent to two-dimensional internal flows) summarized by Boghosian & Cassel (2010) are as follows: (1) convective instability (Kelvin-Helmholtz-like) which propagates in the shear layer, (2) an absolute instability situated in the vicinity of the recirculation region and (3) an absolute instability whereby bisection of the main vortex occurs as a result of a secondary recirculation region. In the present work, an energy spectrum was computed at several

stations downstream of the step (in the shear layer at various positions in relation to the height of the channel) to detect the presence of vortex shedding. This is further explained in Chapter Five of this thesis.

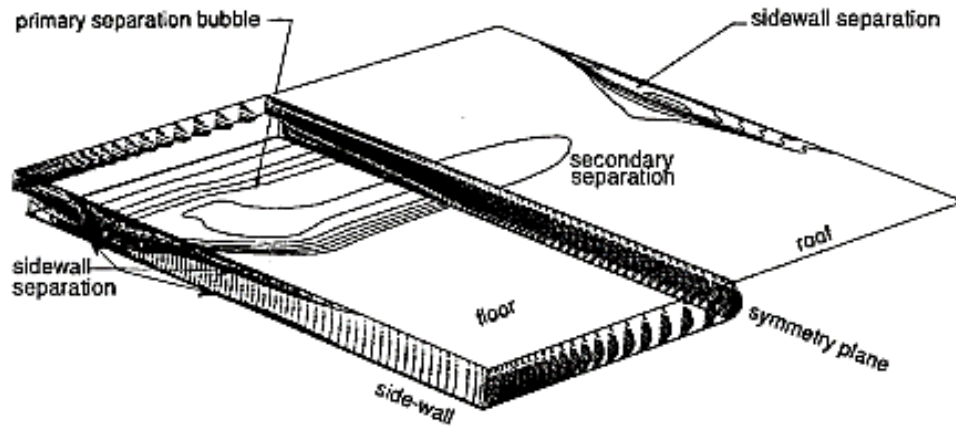


Fig. 2.9 Results from Williams & Baker (1997) showing penetration of side-wall separation regions out to the main stream flow. The case simulated was for $Re_S = 800$

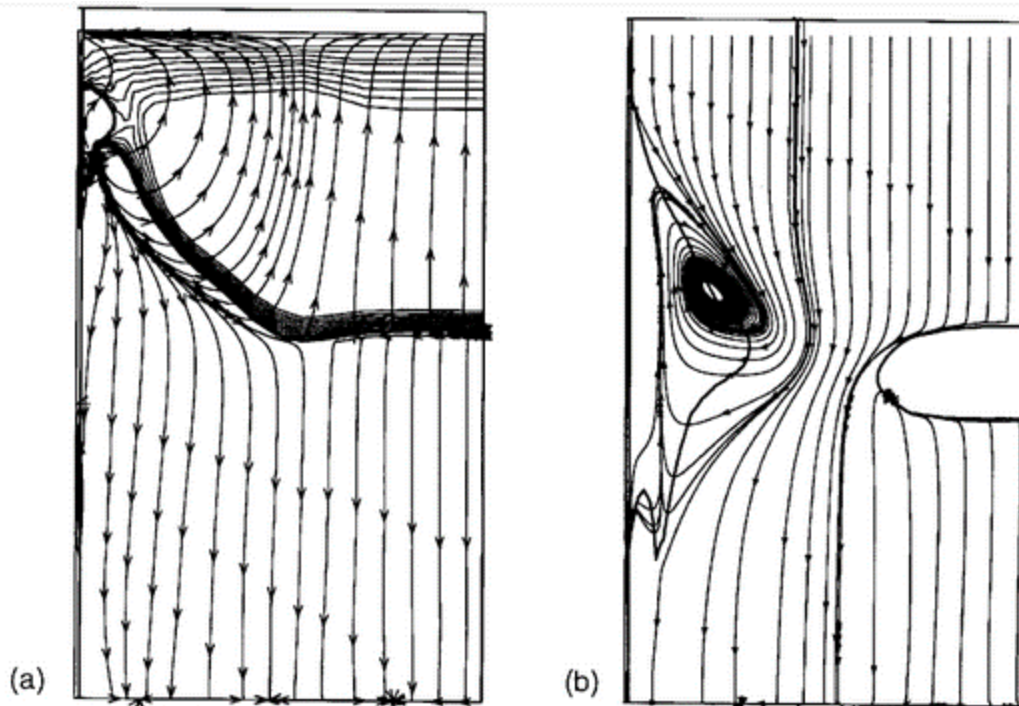


Fig. 2.10 Results from Williams & Baker (1997) showing oil flow streak lines for $Re_S = 800$. Flow near the floor (a) and near the roof (b).

2.3.2 The Effect of Expansion Ratio (ER) on the Flow Physics Downstream of a BFS

The effect of expansion ratio (ER) on BFS flows has as well received a lot of attention in the literature (Thangam & Knight, 1989; Nie & Armaly, 2002; Biswas et al. 2004). The work of Thangam & Knight (1989) investigated (2-D numerical simulations finite volume scheme of laminar flow in the range, $50 \leq Re_S \leq 900$) a wide range of ER values and the effects on the downstream flow. Their findings showed a strong dependence of reattachment length (primary recirculation region on the lower wall) on the step height as per Fig. 2.11; that is, at relatively larger E (increased step height) values there is an increased value in the reattachment length (as a result of increased velocity at the step). Thangam & Knight (1989) also included in Fig. 2.11 results from Armaly et al (1983) for $ER = H/h = 1.94$ (or $E = S/H \approx 0.5$) which favorably compared to their work up to $Re_S \approx 300$. Thangam & Knight (1989) concluded that for a specified E value the increase in the reattachment length (x_1/D_h) with Re_S exhibited a moderately non-linear trend (more noticeable at larger E values), which they attributed to increased inertial effects as a result of the increase in Re_S . They also attributed this non-linear behaviour to flow retardation (flow decelerates on the upper wall which caused downward displacement of the streamlines and, thus, hindered the growth of the primary recirculation region) downstream of the step as a result of the pressure increase inside the channel at relatively larger E values.

Further to that, the work of Nie & Armaly (2002) (three-dimensional simulations: laminar steady Navier-Stokes equations under $Re_H = UH/\nu = 343$ and $\alpha = W/H = 4$; whereby U is the average velocity at the step and α is the aspect ratio downstream of the step) investigated an expansion ratio range, $1.67 < ER < 2.50$, and the effects on the three-dimensional flow downstream of the step. Nie & Armaly (2002) report that the increase in the ER value increases both the reattachment length (validating the work of Thangam & Knight (1989)) and three-dimensionality features of the flow downstream of the step (i.e. penetration of the side wall induced three-dimensional effects). Their findings are also shown in Fig. 2.12 for further clarity. Fig. 2.12 shows the lines of reattachment varying with the step height and the distance from the side wall to the symmetry plane (midplane of the channel). It can also be seen from Fig. 2.12 that for relative larger ER values, the

penetration of three-dimensional effects caused by the side walls increases. An interesting observation made by Griffith (2009) is that Nie & Armaly (2002) kept the Reynolds number constant across the various step heights by changing the inlet velocity profile, however, the mass flow rate over the step was not kept constant and hence Griffith (2009) noted that the full range of blockage effects were not adequately explored. An interesting note is that the findings from Kitoh et al (2007) contradicted both of the studies noted above. Kitoh et al (2007) studied ER effects on the downstream flow for $ER = 1.5, 2.0$ and 3.0 using DNS (finite difference method) in a rectangular channel with an aspect ratio of 36.0 . In their study, the Reynolds number varied from 300 to 1000 and was calculated based on the step height and the mean inlet velocity. Kitoh et al (2007) reported that the reattachment length (of the primary recirculation region) on the centre-line of the channel (midplane) increased with a decrease of ER. The reason for such a discrepancy was not addressed by Kitoh et al (2007). However, Kitoh et al (2007) did report that the reattachment length decreased (at a fixed ER value) at relatively larger Reynolds numbers (corresponding to transition to turbulence) as a result of the unsteady nature of the flow. This finding does agree well with the literature whereby the actions of the Reynolds stresses retard the growth of the reattachment length (Biswas et al. 2004).

Furthermore, Biswas et al (2004) also investigated the effect of ER ($1.94 \leq ER \leq 3$) on the downstream flow at low and moderate Reynolds numbers (i.e. $Re_S < 800$). The authors used two-dimensional numerical predictions to solve the flow field downstream of the step and showed that for $Re_S < 400$ the flow was predominantly two-dimensional and the reattachment lengths increased with ER (substantiating with the work of Thangam & Knight (1989) and Nie & Armaly (2002)). Biswas et al (2004) also reported that for $ER = 1.94$ the flow remained two-dimensional over the entire Reynolds number range tested ($Re_S \leq 800$) whereas, for $ER = 3.0$ the unsteadiness was observed at $Re_S = 500$ (i.e. low frequency oscillation was reported in the flow field).

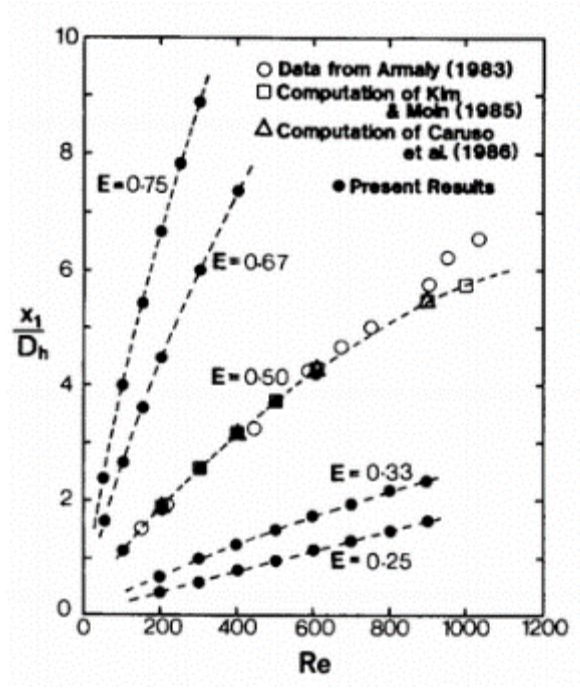


Fig. 2.11 Results from Thangam & Knight (1989) showing reattachment length as a function of the Reynolds number for various expansion ratios. Note that the reattachment length (primary on the lower wall) was normalized with the hydraulic diameter at the step ($D_h = 2h$) and not the step height (S). Another note is that variable E in the Figure represents ER, however, defined as $E = S/H$.



Fig. 2.12 Results from Nie & Armaly (2002) showing the effect of step height on the reattachment line. It should be noted that z and L are, respectively, the spanwise direction and the channel half-width.

2.3.3 Shortfalls in the Literature Surrounding BFS Flows under Steady Laminar Flow

In general, there is very little work which reports wall shear stress (WSS) and/or skin friction data downstream of the step under steady laminar flow. WSS data are very useful for the present study to better understand the streamwise and spanwise shear stress distribution and magnitude and, thus, provide researchers with data to correlate with EC response. There is also an absence of detailed mean flow and turbulence statistics (Reynolds Shear Stress, streamwise and wall-normal r.m.s. profiles and energy spectra) downstream of the step (at various stations), whereby turbulence arises from either side-wall effects and/or an inherent instability (i.e. Kelvin-Helmholtz instability). Finally, researchers typically study steady laminar flow over a BFS with an aspect ratio range, $10 \geq \alpha_S \geq 25$. This is to ensure that the flow is two-dimensional at the test section (i.e. no perturbation of flow from the side walls) and in the case of smaller aspect ratios, to deliberately study the side wall influence on the downstream flow field (i.e. mid-plane flow structure, reattachment length distribution along the span of the channel). Since, in the present study, the inlet aspect ratio (α_S) of the channel is 18.26, this work will add to the body of previous work which has investigated the effect of side-walls on the midplane flow structure (via understanding whether turbulence originates from the side walls and/or an inherent instability in the shear layer).

It should be noted that to the best of the present author's knowledge, detailed two-component velocity measurements (u, v ; at the inlet and downstream of the step) under steady laminar flow over a BFS remain unreported. The present author hopes to address this gap and provide insightful mean flow and turbulence statistics (together with the flow quantity uncertainty) to both EC researchers and CFD modelers who can benefit from detailed average statistics near and away from the wall in the shear layer. The present author also provides detailed skin friction data (in the streamwise direction) downstream of the step at the mid-plane of the channel by capturing the streamwise velocity data as close as $40 \mu\text{m}$ from the wall.

2.4 Idealized Stenosis Flow Inside Rectangular Flow Channels under Steady and Pulsatile Laminar Flow

This section deals with steady and pulsatile laminar flow inside rectangular channels considering the backward-facing step (BFS) and other more realistic stenosis geometries. Various stenosis models are given and defined (in terms of length scales and flow conditions at the working section) to which the present work is compared in Chapter Five for both the steady and pulsatile flow over the BFS. Conversely, section 2.5 reviews the literature for steady and pulsatile laminar flow in a straight section of tube under the influence of a stenosis. Section 2.5 also presents models of stenosis to which the present work is compared and presented in Chapter Five.

2.4.1 General Motivation

Pulsatile laminar flow inside two-dimensional flow channels (over a BFS) has not received adequate attention over the last few decades and is one of the main contributions of the present work. Some of the shortfalls in the literature surrounding stenosis flows inside two-dimensional flow channels (under pulsatile laminar flow) is reviewed in the subsequent section 2.4.3, thereby continuing to highlight the contribution of the present work. Pulsatile laminar flow over a BFS is an important *in-vitro* model to study the effects of rapid changes in surface geometry and perturbations which are key factors influencing cell-attachment and physiological properties of cells (Salek et al. 2009).

Some of the earlier work studying pulsatile flow inside a two-dimensional flow channel is the experimental and numerical investigation by Sobey (1985). The focus in this work was on the presence of vortex waves in the oscillatory flow with a variety of symmetric and asymmetric geometries (for $Re = 80$ and $St = 0.003$). Following this work, Sobey & Drazin (1986) studied steady flow bifurcations in a symmetric channel expansion. They reported a Coanda wall attachment whereby the flow jet arising from the expansion deflected to one side of the channel. The work of Tutty (1992) which studied pulsatile flow (sinusoidal waveform with Wo parameter between 3 to 7.5 and $Re = 750$) through a channel with an asymmetrical semi-circular blockage (50% area reduction), demonstrated that for pulsatile flow the maximum wall shear stress (WSS) was much larger than for the steady flow

conditions. Much of this early work on pulsatile flow inside a two-dimensional flow channel has spurred further work on the subject given the reported differences between steady and pulsatile flow physics downstream of the stenosis. Some of this work included the efforts of Valencia (1997) who studied the influence of pulsating inlet flow conditions (laminar regime), the height of the step and the Reynolds number on the reattachment length. Valencia (1997) reported pulsatile laminar flow over a backward-facing step (with numerical methods) inside a planar channel considering $ER = 2.0$, $Re_s = 100$ and $St = f(2h)/U_{avg} = 1.0$ (whereby f and U_{avg} are, respectively, the fundamental frequency of the pulsatile cycle and the average bulk velocity upstream of the step). Significant differences of flow physics downstream of the step in comparison to steady flow were reported. Substantiating the work of Tutty (1992), Valencia (1997) reported significantly larger skin friction coefficient (c_f) on the lower channel wall (in the primary recirculation region) for the pulsatile flow case ($c_f = 0.28$) in comparison to steady flow case ($c_f = 0.05$ at the same $Re_s = 100$). The author also reported an increased reattachment length (primary recirculation region) during the deceleration phase of the pulse cycle as a result of an increased adverse pressure gradient throughout the channel. This finding is in agreement with much of the work presented in the subsequent paragraphs.

Unfortunately, much of the early work on pulsatile flow inside two-dimensional flow channels does not provide detailed phase-averaged mean and turbulence statistics for a quantitative comparison with the present work. However, it did lay the groundwork for further work on the subject which included the work of Dol et al (2014). Dol et al (2014) focused on the effect of pulsation on the mean flow field and vortex formation downstream of a BFS inside a planar flow channel ($ER = 2.0$). The authors used PIV technique to quantify the flow field downstream of the step for the mean $Re = U_{avg}(2h)/\nu = 100$ and Strouhal number range, $0.035 \leq St \leq 2.19$ ($St = f(2h)/U_{avg}$). Dol et al (2014) reported that the pulsation does affect the flow downstream in comparison to the steady flow field, specifically, the coherent structures and the vortex shedding phenomenon. In addition, at very small inlet frequency ($St = 0.035$) stronger vortices were generated which the authors associated with the larger formation time. They did, however, mention that the slow formation process caused the developing vortices to decay prior to shedding. On the other

hand, for $St > 2.19$, they reported the primary vortex to be fairly weak with the absence of a second vortex formation. Very similar results were found for the $Re = 100$ and 200 flow cases.

2.4.2 The Asymmetric and Axi-Symmetric Stenosis Models

The test section geometry given in Fig. 2.13 is from the work of Griffith (2009), which reports steady laminar flow over a semi-circular stenosis inside a two-dimensional flow channel. Since the geometry Griffith (2009) considers has a lot in common with the backward-facing step it is compared to the present work in Chapter Five. Using two-

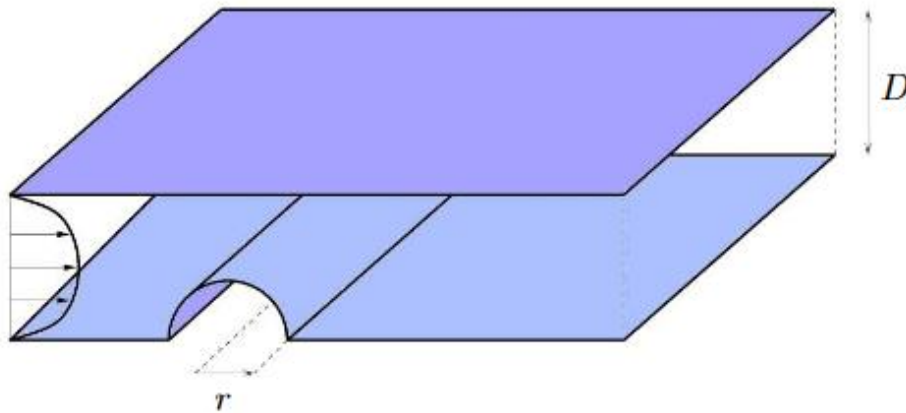


Fig. 2.13 From Griffith (2009): Test section geometry under investigation which includes a semi-circular stenosis. The variables D and r , are, respectively, the channel height (distance between the unblocked walls) and radius of the semi-circular stenosis. The blockage is defined as $b = r/D$.

dimensional numerical simulations, Griffith (2009) presents streamwise mean velocity profiles and streamlines (together with skin friction data) for $Re = 2UD/\nu = 1000$ and $b = 0.5$ downstream of the semi-circular blockage and reported a recirculation region on lower and upper walls. Interestingly, the author also reported that the mean streamwise velocity profile at the inlet of the stenosis (midpoint of the blockage) was skewed to one side given the absence of the Poiseuille profile upstream of the constriction (in the immediate vicinity of the blockage). It should be noted that details of the work presented by Griffith (2009) are given and discussed in Chapter Five. However, a concise overview of the author's findings is provided in this section. The normalized flow recirculation

length (L_r/D and L_r/r) as a function of Re across various blockage ratios, is shown in Fig. 2.14.

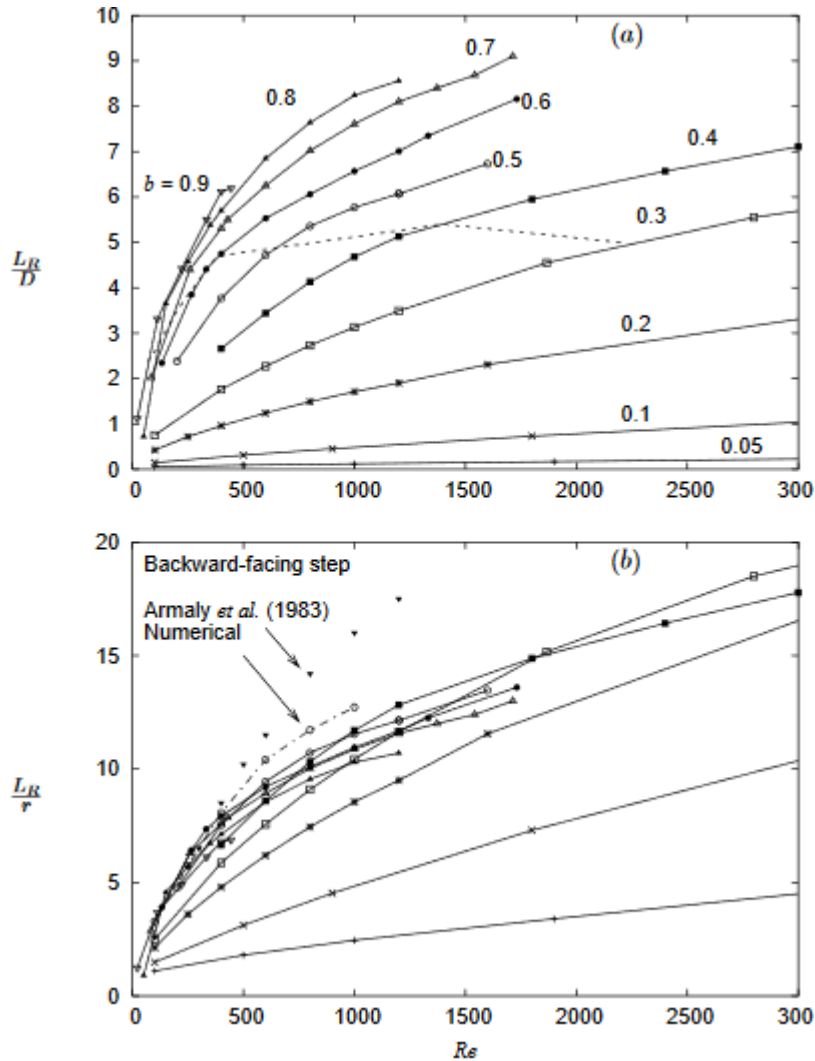


Fig. 2.14 From Griffith (2009): Recirculation lengths as a function of the Re value for various constriction ratios. The reattachment length (L_r) normalized with (a) channel height and (b) the blockage radius.

Referencing the plots in Fig. 2.14, Griffith (2009) notes that across the blockage range considered, L_r increases linearly at lower Reynolds numbers but not for moderate to high Reynolds values. The author attributes the non-linearity to the possible appearance of the secondary recirculation region on the upper wall (dotted line in Fig. 2.14a represents the linear behaviour boundary). It is interesting to compare Fig. 2.14b with the work of Armaly et al (1983), which is reviewed in the earlier sections of this Chapter. Griffith (2009) notes that for $Re > 400$ the agreement between the numerical results of their work (at $b = 0.5$)

and the work of Armaly et al (1983) is poor. As reviewed in the previous sections of this Chapter (2.3.1 Paths to Flow Instability), Griffith (2009) also considers this discrepancy to be the result of the three-dimensionality for $Re > 400$ in the work of Armaly et al (1983). It is interesting to note (and will be further discussed in Chapter Five) that the flow separation point for the semi-circular blockage is not defined by the step edge as with the BFS flow. Rather, according to Griffith (2009) it is defined by the adverse pressure gradient and the Reynolds number whereby the separation point moves upstream with an increase in Re . Hence, it would be expected that the reattachment length (of the primary recirculation region and considering $x = 0$ at the inception of flow expansion) would be different given the delayed separation point for the semi-circular stenosis (in comparison to the BFS). In fact, Ratha & Sarkar (2015) reports that the reattachment length of the primary recirculation region differs for the BFS with rounded edges in comparison to the vertical step. Using two-dimensional simulations (i.e. FLUENT) inside a two-dimensional flow channel at $Re_S = 1000$ and $ER = 1.94$, Ratha & Sarkar (2015) report a smaller value of the reattachment length for the BFS with rounded edges. Notwithstanding the location of the $x = 0$ point, the stenosis geometry (i.e. angle) influence on the flow physics (midplane flow structure) is further considered in Chapter Five to explain the differences between the present work and other models of stenosis in terms of the reattachment length (i.e. considering $x = 0$ at point of flow expansion for various models of stenosis).

Other flow features that Griffith (2009) reports include: (1) multiple downstream recirculation regions at relatively higher Re values ($Re_C > 794$; where Re_C is the critical Reynolds number for transition to three-dimensionality at $b = 0.5$) together with vortex shedding (convective in nature), (2) at $b \geq 0.3$ and sufficiently high Re values, a secondary recirculation region is found on the upper wall, (3) at $b \geq 0.6$ and sufficiently high Re values a third recirculation region is found on the lower wall and (4) at $Re \geq 1800$ and for $b = 0.5$ and 0.6 the flow starts to shed vortices from the blockage region. It is interesting to note that the critical Reynolds number (Re_C) Griffith (2009) reports is larger than that reported by Armaly et al (1983). As review, Armaly et al (1983) reports three-dimensionality of the flow at $Re_S > 400$ (whereby $Re_S \approx Re$ for this comparison). This discrepancy is most likely attributable to the aspect ratio of the channel and, hence, side

wall influences on the mid-plane flow structure as described by Williams and Baker (1997). Another interesting observation is that Griffith (2009) reports a third recirculation region (downstream of the primary recirculation region for the approximate range, $1300 \leq Re \leq 1800$) which concurs with the work of Armaly et al (1983) whereby the authors report a third recirculation region (lower wall) in the range, $1200 \leq Re_S \leq 2300$. Hence, it is clear that there is an abundance of similarities (in terms of flow physics) between the semi-circular and the right-edge step geometries.

Furthermore, the work of Mittal et al (2003) and Beratlis et al (2005) provides excellent mean flow and turbulence statistics data downstream of an idealized stenosis (under pulsatile flow conditions) via Direct Numerical Simulation (DNS) and detailed single-component Laser Doppler Velocimetry (LDV) measurements, respectively. In fact, the work of Beratlis et al (2005) is compared to the present work (for the pulsatile flow case) in Chapter Five. Geometry models for both the work of Mittal et al (2003) and Beratlis et al (2005) are presented in Fig. 2.15. Mittal et al (2003) simulates pulsatile flow (non-zero mean sinusoidal waveform with $St = Hf/U_{\max} = 0.024$ and $Wo = (\pi Re St / 2)^{1/2} = 5.3 - 8.6$; where S_t, Wo, f, U_{\max} are, respectively, the Strouhal number, Wormersley number, pulse frequency and the peak inflow velocity) inside a planar channel with one-sided (upper wall) semi-circular stenosis model (50% reduction in area). Furthermore, Mittal et al (2003) simulate a Reynolds number range, $750 < Re < 2000$ (whereby $Re = U_{\max} H / \nu$), whereas Beratlis et al (2005) reports $Re = 0.5 U_b H / \nu = 570$ and $Wo = 0.5 H (2\pi f / \nu)^{0.5} = 8.25$ (where U_b is the mean bulk velocity). The other distinction between the two studies is that Beratlis et al (2005) simulates an axi-symmetric (semi-circle on both sides of the channel with a blockage ratio of 50%) stenosis model.

A complete quantitative analysis together with a comparison in relation to the present work is given in Chapter Five (which includes phase-averaged statistics of mean flow and turbulence). However, a brief overview of the findings from Mittal et al (2003) and Beratlis et al (2005) is given as review. To begin with, both Mittal et al (2003) and Beratlis et al (2005) present phased-averaged mean flow and turbulence statistics downstream of the

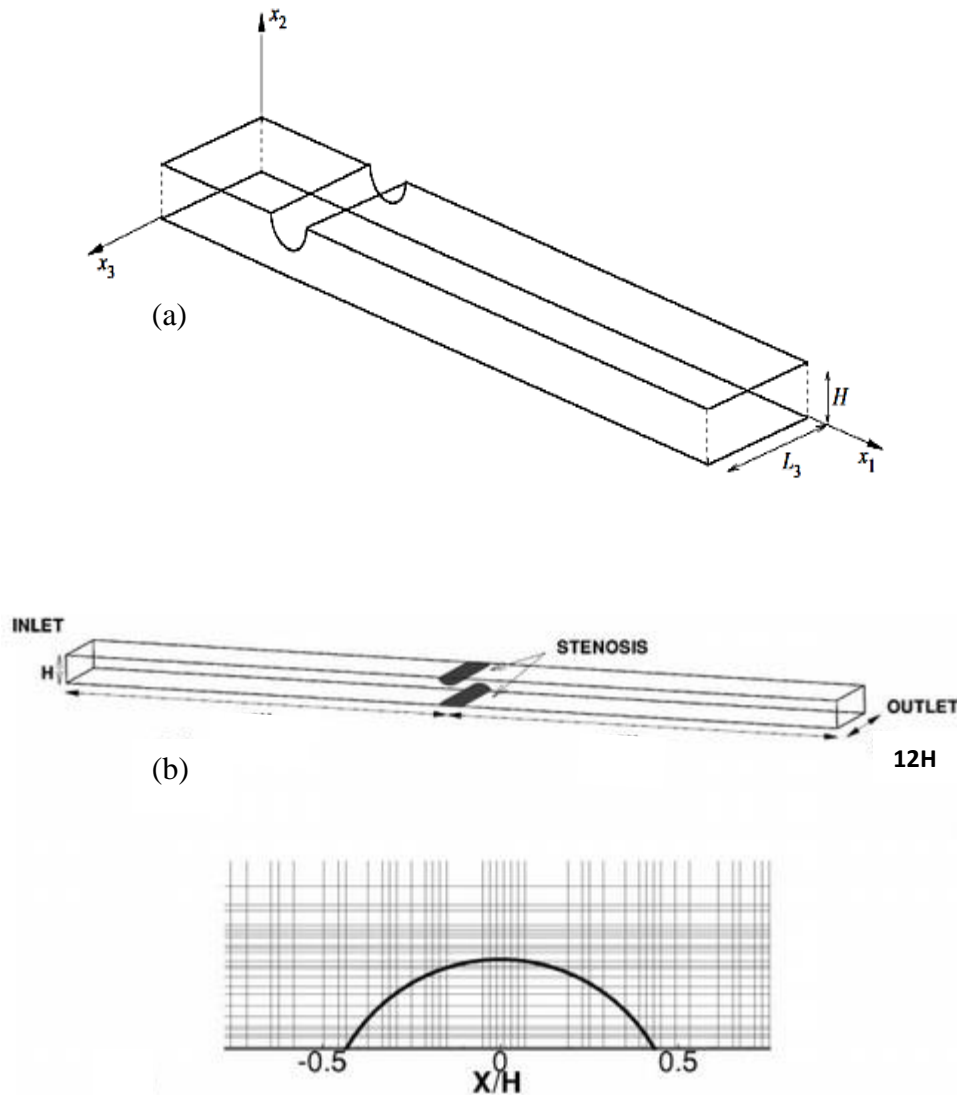


Fig. 2.15 Test-section geometry for an idealized semi-circular stenosis. From Mittal et al (2003) showing an asymmetric semi-circular blockage (a) and from Beratlis et al (2005) showing an axi-symmetric blockage (b). For Mittal et al (2003), it should be noted that x_1 , x_2 and x_3 indicate the streamwise, wall-normal and spanwise directions, respectively. For further reference, the working section for Beratlis et al (2005) is $146H \times 12H \times 1H$; length, width, height, respectively).

stenosis (at several measurement stations) and conclude similar flow behaviour as reported by several authors for tube flows (discussed in the subsequent section). The aim of both of these studies is to better understand the dynamics of flow downstream of the stenosis by simulation of flow conditions close to those of an *in-vivo* environment. Furthermore, Mittal et al (2003) report that for $Re > 1000$, a series of Kelvin-Helmholtz type vortices are created

in the shear layer which separates from the lip of the constriction. Furthermore, according to Mittal et al (2003) these vortices become more energetic with an increase in the Reynolds number (leading to an increase in the turbulent kinetic energy). Another interesting finding by Mittal et al (2003) is that the increase in the turbulent kinetic energy also results in an increase in dissipation; that is, at 10H downstream of the constriction the turbulent kinetic energy is similar for all flow cases suggesting an increase in dissipation at higher-Reynolds-number cases. Mittal et al (2003) further reports that there exists a relatively large mean recirculation region (downstream of the constriction) which reduces in size with an increase in the Reynolds number. The author also notes that in the recirculation region, the skin friction values are relative low. Furthermore, Mittal et al (2003) reports a secondary recirculation region on the lower wall as a result of the boundary layer separation. Similarly as with the upper wall recirculation region, the secondary recirculation region (lower wall) moves closer to the constriction with an increase in the Reynolds number.

Beratlis et al (2005) report very similar flow behaviour downstream of the axi-symmetric stenosis; that is, the confined jet becomes unstable and forces a roll-up and subsequent breakdown of the shear layer. Beratlis et al (2005) also report that the large-scale structures (originating from the shear layer) disturb the near flow and as a result create packets of near-wall hairpin vortices. Furthermore, both authors report intermittent turbulence during the pulsatile cycle whereby turbulence originates near the peak flow of the pulsatile cycle and extends throughout the deceleration phase.

2.4.3 Shortfalls in the Literature Surrounding Idealized Stenosis Flows under Steady and Pulsatile Laminar Flow: Two-Dimensional Flow Channel

Pulsatile flow inside a two-dimensional flow channel geometry remains poorly explored both experimentally and numerically. The literature would benefit from detailed phase-averaged statistics (mean flow and turbulence) downstream of the step to better understand the flow physics. The effects of pulsation amplitude, frequency, ER and aspect ratio on the pulsatile mean flow field should be further explored for a better understanding of transition to turbulence downstream of the step (i.e. initiation of turbulence whereby individual contributions of the side wall effects and shear layer instability are considered and

quantified). In addition, a comparison of simple step geometry (right angle, rounded edges, semi-circle) to more realistic models of stenosis would be very useful to understand how well the two-dimensional flow channel models *in-vivo* flows in occluded arteries. The present work aims to address some of these shortfalls by providing phase-averaged statistics (mean flow and turbulence) downstream of the step (at the midplane) at various stations and through a comparison with both an asymmetric and axi-symmetric models of stenosis inside straight section of tubing and channel, respectively. Various flow physics are discussed and compared to highlight the similarities and differences between channel and tube flows under the influence of a stenosis.

2.5 Steady and Pulsatile Laminar Flow in a Straight Section of Tube under the Influence of a Stenosis

2.5.1 General Motivation

Since, in the present work, it was important to compare the flow behaviour (downstream of the step at the midplane) between the channel flow and other phantoms of stenosis (i.e. flow in a section of straight tube with a smooth axi-symmetrical constriction), a comprehensive literature survey was carried out on these types of post-stenotic flows. Although the flow in arteries is considered to be laminar in nature, the presence of a stenosis increases the local Reynolds number (as a result of the constriction) and introduces an inflection point into the velocity profile downstream of the stenosis (Sherwin & Blackburn, 2005). Due to the latter, the laminar flow can transition to turbulence downstream of the constriction.

Winter & Nerem (1984) provided a classification for pulsatile flows inside tubes (under a stenosis influence) as follows: (1) laminar flow, without any disturbances throughout the pulse cycle, (2) phase-dependent generation of turbulence (i.e. intermittent turbulence), which occurs when the high frequency velocity fluctuations appear during the decelerating phase of the cycle, followed by a decrease in intensity as the mean flow velocity decreases and dissipates as the flow relaminarizes at the start of the subsequent acceleration phase and (3) fully turbulent flow occurring throughout the entire cycle. With respect to (2), He & Jackson (2000) provided a detailed review of turbulence in transient tube flows and observed that turbulence decreases in accelerating flows and increases in decelerating

flows. He & Jackson (2000) reported that the increase of turbulence during deceleration is a result of delayed production of turbulence including the delay associated with turbulent energy redistribution between its three components. Relevant to this subject of discussion, it will be shown in Chapter Five (two-component velocity measurements downstream of the BFS) that for the present work similar patterns of turbulence are observed; that is, an increase in high-frequency velocity fluctuations during the deceleration phase of the pulse cycle. Although there has been work which studied flow inside tubing with more complex derived geometries of stenosis (Stroud et al. 2002), the focus in this review will be on the idealized stenosis models given the difficulty in reproducing these anatomically derived geometries.

The earliest studies found in the literature on steady flows inside tubular geometry using more realistic stenosis models (i.e. smooth asymmetrical and axi-symmetrical stenosis) was performed by Clark (1976a). The author measured the pressure drop across various nozzle designs which represented various stenosis shapes. The pressure at the centre of a tube was measured and the author did not provide any additional information on the details of the flow. As reviewed by Griffith (2009), the majority of the work on steady flow in tubular geometry over a stenosis centred around finding methods to detect plaque in arteries (i.e. atherosclerosis) for clinical applications. The rationale for carrying out these investigations is that stenosis geometry would induce flow disruption and instabilities exhibiting particular frequencies which could then be measured and identified.

Furthermore, the work of Tobin & Chang (1976) investigated wall pressure spectra (at various x/D positions; where D is the tube diameter) for 75% axi-symmetric stenosis (i.e. area reduction) to identify distinct frequencies in the flow to better characterize and identify stenosis flows. The authors did mention that the flow consisted of a turbulent shear layer (downstream of the stenosis) but did not report a critical Reynolds number or discuss the flow transition in any depth. Tobin & Chang (1976) did, however, demonstrate that the spectra associated with the location of maximum root-mean square (r.m.s.) wall pressure can be correlated to the degree of stenosis and other flow variables.

2.5.2 The Axi-Symmetric Stenosis Models

Shown in Fig. 2.16 is typical geometry used by researchers to model an axi-symmetric stenosis inside straight section of tubing. For the steady flow investigation in the present study, the BFS flow is compared to the axi-symmetric flow inside a tube and, hence, it is important to illustrate and define the characteristic length scales associated with this model. Other axi-symmetric models have been proposed, such as that shown in Figs. 2.17 and 2.18 given by Varghese et al (2007a) and Long et al (2001), respectively.

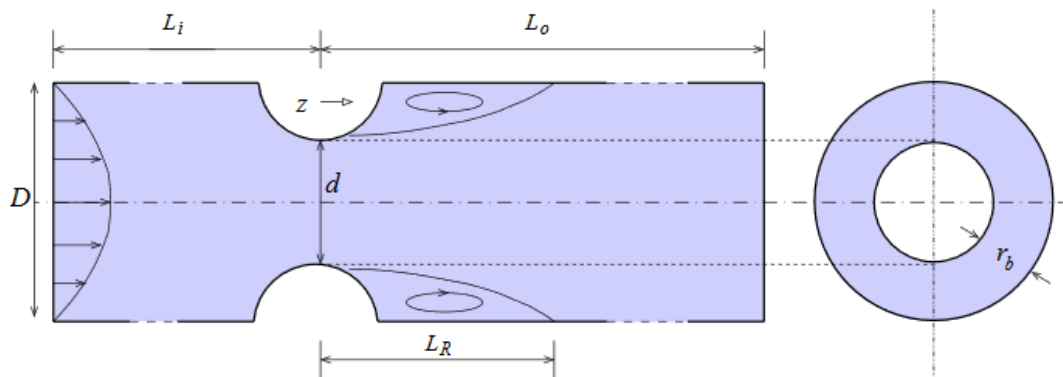


Fig. 2.16 From Griffith (2009): Axi-symmetric stenosis model inside a straight section of tubing.

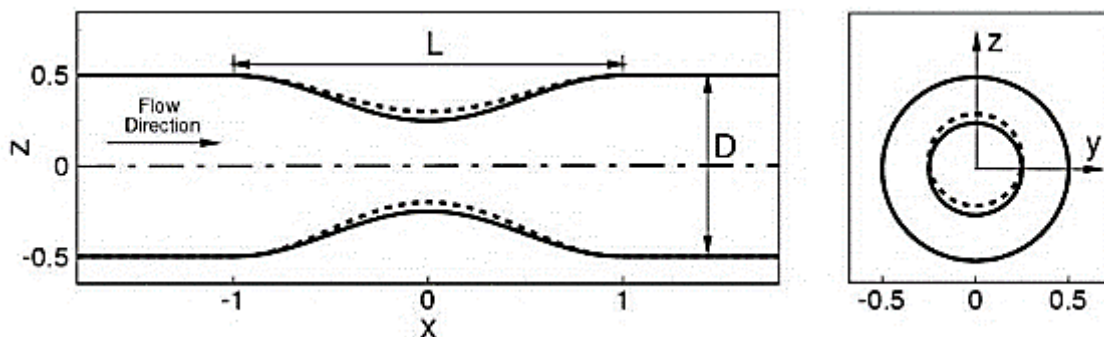


Fig. 2.17 Axi-symmetric stenosis model inside a straight section of tube (Illustration taken from Varghese et al. 2007a). It should be noted that D , L , x , z and y are, respectively, the diameter of the non-stenosed tube, length of the stenosis ($L = 2D$), the streamwise and cross-stream coordinates, respectively. For reference purposes, the dashed lines in the illustration indicate an eccentric model.

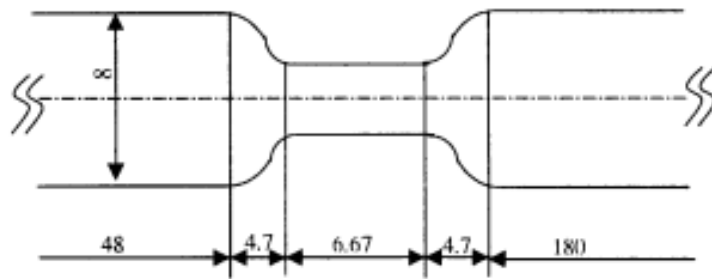


Fig. 2.18 Axi-symmetric stenosis model inside a straight section of tube (Illustration taken from Long et al. 2001). It should be noted that in the work of Long et al (2001), the diameter (D) upstream of the constriction is 8 mm. In addition, all the dimensions in the illustration are in mm.

The main difference between these various models presented in the preceding Figures is the silhouette of the stenosis; that is, in Fig. 2.16 the stenosis is modeled as a semi-circle whereas in Figs 2.17 and 2.18 it is modeled by a cosine function and by a long straight segment with two integrated Gaussian functions at the corresponding ends, respectively.

2.5.3 Previous Studies Pertaining to Asymmetric and Axi-Symmetric Stenosis Models under Steady and Pulsatile Laminar Flow

The early work of Cassanova & Giddens (1978) focused on steady laminar flow (upstream of the stenosis) inside a rigid tube over a smooth stenosis (50% and 75% area reduction via plexiglass models of axi-symmetrical stenosis) using a commercial Laser Doppler Velocimetry (LDV) system and provided a detailed discussion on the instability of the downstream flow. The authors did not report a critical Reynolds number associated with the onset of the transition to turbulence (i.e. instability). However, their study did show that unsteadiness occurs at $x \approx 4D$ downstream of the stenosis (where x represents the streamwise direction of the flow). Furthermore, using a dye-visualization technique the authors showed that the instability was associated with the Kelvin-Helmholtz shear layer oscillation. The other finding reported by Cassanova & Giddens (1978) was that a stenosis of approximately 50% severity (by area) was required to generate noticeable disturbances in the flow for the Reynolds number range, $318 < Re < 2540$ (Reynolds number calculated based on the mean velocity and unblocked tube diameter). This is in contrast with their pulsatile flow case whereby a mild stenosis (i.e. 25% area reduction) generated

disturbances during the deceleration phase of the cycle (i.e. pulsatility effects destabilize the flow). The other critical finding from Cassanova & Giddens (1978) was that a sharp-edged stenosis created much greater flow disturbance (at a given Re and downstream of stenosis) than the smooth configuration. In fact, this is further explored in the present study (Chapter Five) to evaluate the effect of various models of stenosis (i.e. geometry) on the downstream flow behaviour (mean flow and turbulence).

Further work on the subject was reported by Ahmed & Giddens (1983a); the authors used the LDV technique and reported the streamwise mean velocity profiles downstream of various smooth axi-symmetric stenosis models (i.e. 25%, 50% and 75% area reduction). The steady laminar flow experiments were performed ranging from $Re = 500$ to 2000 . The flow visualization (using hydrogen bubbles) results are illustrated in Fig. 2.19 for the 50% stenosis at different Re values. In reference to Fig. 2.19, Ahmed & Giddens (1983a) reported the generation of vortex ring systems in the shear layer at $Re = 1000$ without transition to turbulence. For $Re = 2000$ (not shown in the Figure), the disruption to a turbulent flow field occurred at 3-4D downstream of the stenosis throat (reattachment point occurred at $x > 3D$ and $x \approx 2D$ for the $Re = 1000$ and 2000 , respectively). For the 75% stenosis case, Ahmed & Giddens (1983a) reported a laminar flow at $Re = 250$, periodic oscillations in the shear layer at $Re = 500$ (reattachment point occurred at $x \approx 4D$) and turbulence for $Re = 1000$ and 2000 (reattachment point occurred at $x \approx 5D - 6D$). Similar results were reported by Griffith (2009), who studied (numerically and using PIV) steady laminar flow under the influence of a stenosis (depicted in Fig. 2.16) for various blockage ratios ($b = 1 - (d/D)^2 = 0.50, 0.75$ and 0.90) and Reynolds number values ($Re = UD/\nu = 100$ to 2500 ; where U is the average velocity in the channel). Griffith (2009) noted for the 75% stenosis cases (at $Re \approx 500$) that the instability consisted of a convectively amplified perturbation in the shear layer generating breakdown of the flow at $x \approx 4D$ downstream of the stenosis throat. On the other hand, the reattachment length reported by Griffith (2009) for $Re \approx 500$ and $b = 0.75$ was significantly larger (i.e. $x \approx 11D$) than the value reported by Ahmed & Giddens (1983a).

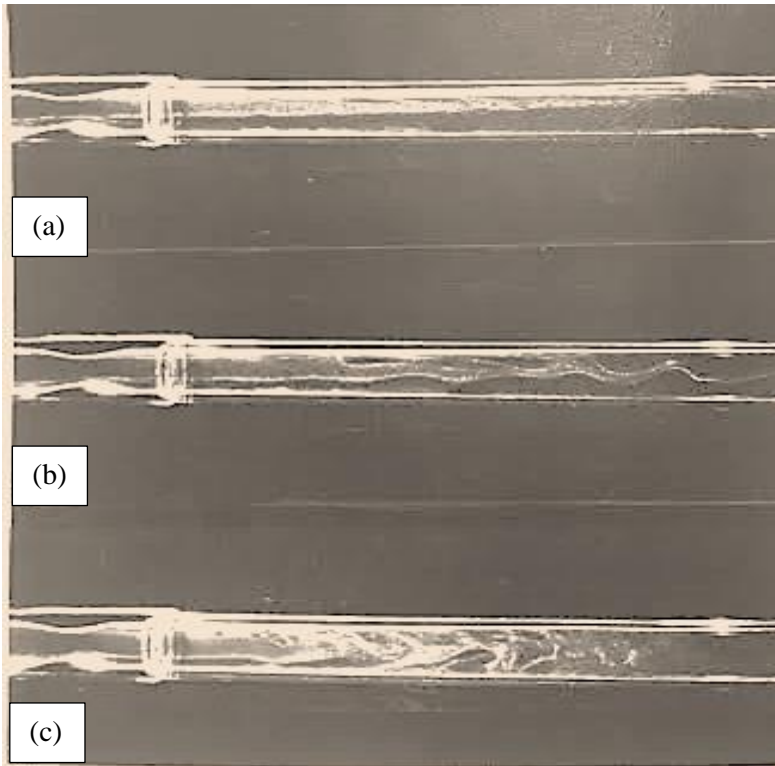


Fig. 2.19 Flow visualization photographs with hydrogen bubbles from the work of Ahmed & Giddens (1983). 50% stenosis at $Re = 500$ (a), 50% stenosis at $Re = 750$ (b) and 50% stenosis at $Re = 1000$ (c).

Griffith (2009) credited the variability of the reattachment lengths ($\Delta x \approx 7D$) to a difference in measurement method. The author contended that predicting the reattachment length from the velocity profiles (as in the work of Ahmed & Giddens (1983a)) can be very challenging, requiring high spatial resolution near the wall. Griffith (2009) further argued that his method of using coloured dye visualization more accurately deduced the reattachment length given the contrast between the main stream flow and the recirculation region. Nevertheless, both Griffith (2009) and Ahmed & Giddens (1983a) reported the reattachment length of $x \approx 4D$ for the 50% stenosis and $Re = 1000$.

Pulsatile flow studies inside a straight section of tube with an axi-symmetric stenosis (25%, 50% and 75%) continued with the work of Ahmed & Giddens (1984) using the LDV technique. This work was considered as an extension to that of Ahmed & Giddens (1983a). Their focus was on pulsatile flow with a sinusoidal waveform (superimposed on the mean flow) with a mean $Re = 600$ (based on the mean inlet centreline velocity and tube diameter) and $Wo = 7.5$ (whereby $Wo = D/2 (\omega/\nu)^{0.5}$ and ω and ν are the fundamental frequency

of the pulse and kinematic viscosity of the fluid, respectively). Ahmed & Giddens (1984) also studied the flow field at $Wo = 15$ to better understand the effect of the Womersley number on the flow field downstream of the stenosis. Their findings using the hydrogen bubble technique are illustrated in Fig. 2.20. Ahmed & Giddens (1984) reported a predominantly laminar flow for the 50% stenosis at $Wo = 7.5$ (with periodic oscillations during limited time of the cycle). An increase in Wo to 15 resulted in increased vortex structures which extended for several wavelengths of the cycle. Finally, for the 75% stenosis case, the flow transitioned to broadband turbulence (i.e. whereby discrete oscillations disrupted into random fluctuations in the far field, $x > 6D$) during the deceleration phase of the pulse cycle. As a result of their findings, Ahmed & Giddens (1984) characterized the downstream flow into four regions: (1) the stable jet region whereby three Kelvin-Helmholtz type vortex roll-ups were detected, (2) the transitional region whereby the roll-ups lost their symmetry, (3) the turbulent region which showed a breakdown of these structures and which extended over the entire diameter of the pipe and for a length of $3D$ (three diameters in the streamwise direction) and (4) relaminarization which occurred after approximately $x = 8D$ downstream of the stenosis.

The work of Ahmed & Giddens (1984) agreed well with the later work of Ojha et al (1989), which also studied pulsatile flow in axi-symmetric stenosis ($Wo = 7.5$; mean $Re = 575$). For a stenosis with an area reduction of $< 50\%$ and using a photochromic tracer method, Ojha et al (1989) reported isolated regions of vertical structures in the vicinity of the reattachment point (i.e. during the deceleration phase). However, for moderate stenosis models (50% – 80%), transition to turbulence was initiated prior to peak flow in the cycle and extended throughout the deceleration phase via breakdown of the streamwise vortices which were shed in the upstream shear layer. The work of Varghese et al (2007b) accorded well with the work of Ahmed & Giddens (1984) immediately downstream of the stenosis. The main difference was that the simulations predicted a laminar flow downstream of the stenosis, whereas Ahmed & Giddens (1984) reported evidence of disturbed flow using the same flow parameters and geometry. Varghese et al (2007b) used Direct Numerical Simulation (DNS) with pulsatile inlet flow under the influence of 75% stenosis (by area) with $Re = 600$, $A = 0.667$ (amplitude) and $Wo = 7.5$ (equal definition of parameters as per Ahmed & Giddens (1984)). The other difference was associated with the

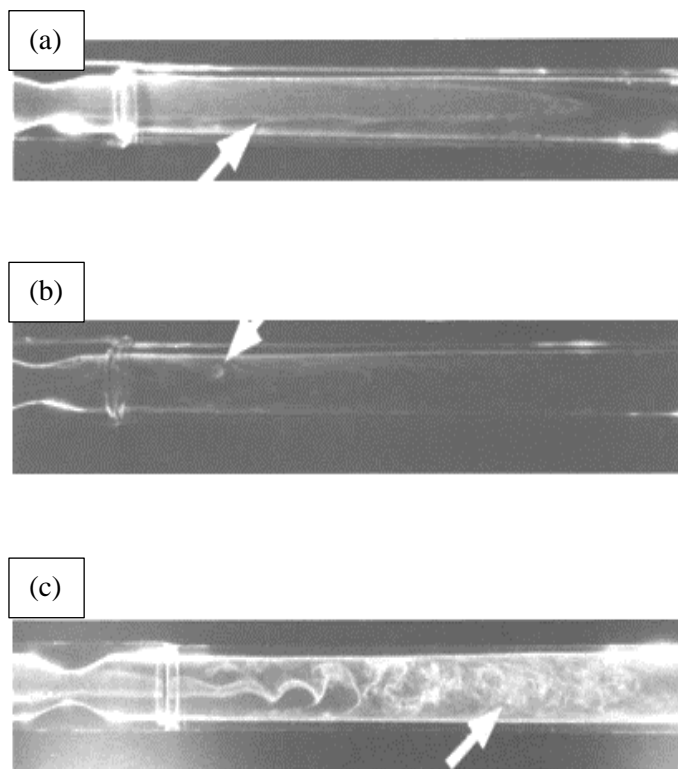


Fig. 2.20 Flow visualization photographs with hydrogen bubbles from the work of Ahmed & Giddens (1984). The 50% stenosis at $Wo = 7.5$ (a), 50% stenosis at $Wo = 15$ (b) and 75% stenosis at $Wo = 7.5$ (c).

The illustrations are pertaining to the deceleration phase of the pulse cycle.

reattachment length; that is, Ahmed & Giddens (1984) reported reattachment occurring between $x = 5D$ and $6D$ whereas Varghese et al (2007b) predicted a value between $x = 7D$ and $8D$ (at 75% stenosis). Using geometric eccentricity (see Fig. 2.16 – dashed line stenosis geometry) tripping mechanism for instability and turbulence, Varghese et al (2007b) reported the reattachment occurring at the exact region as in the experiments of Ahmed & Giddens (1984). The authors noted that the closer reattachment length was a result of transition to turbulence which was triggered by the eccentricity. It is interesting to note that both authors (Varghese et al. 2007b; Ahmed & Giddens, 1984) reported an absence of the recirculation region during the early acceleration phase with the forward flow occurring across the entire vessel. The work of Varghese et al (2007b) is, as well, in good agreement with that of Khalifa & Giddens (1981), Cassanova & Giddens (1978) and Ojha et al (1989). All of these authors reported similar flow behaviour downstream of the stenosis; that is, the jet flow extending for $x \approx 3D$ and stable, followed by a transitional state throughout the cycle (i.e. $x = 3D$ and $4.5D$) and maximum turbulence intensity in the vicinity of the reattachment point (i.e. $x = 5D$ and $6D$).

The results from Varghese et al (2007b) were also in agreement with Long et al (2001) which reported (three-dimensional numerical methods) pulsatile flow in a straight tube stenosis model (i.e. axi-symmetrical stenosis by 75% area reduction – see Fig. 2.18) with a prescribed carotid waveform (peak flow of ≈ 16 mL/s) corresponding to a mean Reynolds number of 300 (calculated based on $D = 8$ mm upstream of a straight segment with rounded edges stenosis model) and $Wo = 5.31$ (based on the definition of $Wo = D/2 (\omega/\nu)^{0.5}$). Long et al (2001) reported a ‘plug’ type jet flow immediately downstream of the stenosis (throughout the pulse cycle) and showed that the primary recirculation extended for $x \approx 7D$ and $x \approx 6D$ during the peak systole velocity and the deceleration phase, respectively. Interestingly, Long et al (2001) reported different flow behaviour for the asymmetrical stenosis model (75% by area) whereby the primary reattachment length was $x \approx 5D$ and $x \approx 4D$ during the peak systole velocity and the deceleration phase, respectively. Long et al (2001) also noted that the recirculation regions for the axi-symmetrical flow case resembled cylindrical shells (i.e. ring shape) whereas for the asymmetrical case, the recirculation regions were not circumferentially uniform which occurred on the lower and

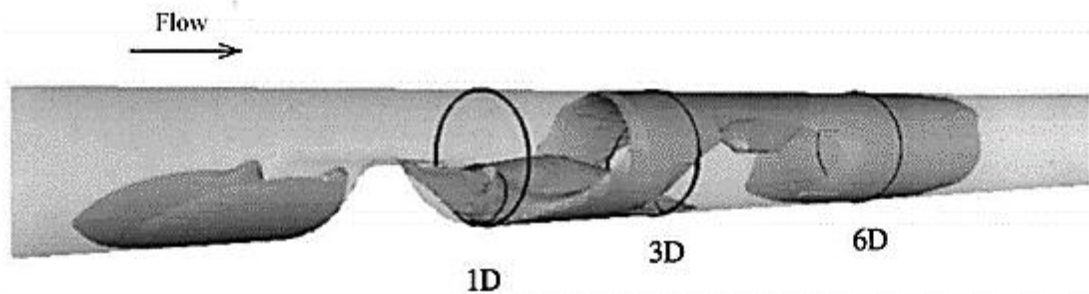


Fig. 2.21 From Long et al (2001): Downstream recirculation regions for the 50% asymmetrical stenosis during the deceleration phase of the pulse cycle.

upper walls. For further clarity to the reader, the 3D-surface plot for the 50% asymmetrical stenosis from the work of Long et al (2001) is shown in Fig. 2.21. Long et al (2001) noted that at $x = 3D$ the primary recirculation region (lower wall) separates into two fragments and those two recirculation regions eventually merge circumferentially at $x \approx 6D$.

In terms of the wall shear stress (WSS), Varghese et al (2007b) reported that, in the vicinity of the reattachment point and the turbulence region the wall shear stress is between four

and twelve times the upstream values. Similarly, Ojha et al (1989) reported three times higher values in the vicinity of the reattachment point. The experimental work of Ahmed & Giddens (1984) did not report the same shear stress levels. Ahmed & Giddens (1984) reported wall shear stress values close to that of the upstream magnitudes. The main difference is the work of Ojha et al (1989) used the photochromic measurements and Ahmed & Giddens (1984) used the LDV technique. Varghese et al (2007b) noted that the discrepancy could be as a result of the LDV technique; that is, the challenges and difficulties associated with the spatial position of the measurement volume in reference to the wall, which could lead to inaccurate estimation of WSS.

2.5.3.1 Paths to Flow Instability

Other work on steady flow in a section of straight tube with a smooth axi-symmetric 75% stenosis was undertaken by Sherwin & Blackburn (2005). This study investigated the flow field using both linear stability and numerical methods with an attempt to better understand the nature of the observed instability in stenosis flows (i.e. three-dimensional instabilities and transition to turbulence of steady laminar flow). The authors reported an instability at $Re = 750$ which was consistent with the experimental findings of Cassanova & Giddens (1978) and Ahmed & Giddens (1983a). Although the LDV-experimental work (mentioned in the latter) did not report a critical Reynolds number, it did outline discrete frequency oscillations associated with vortex shedding between $Re = 500$ and $Re = 1000$ (at $x = 2.5D$). It should be noted that the non-dimensional frequency of $S_t \cong \sigma(10^{-1})$ corresponds to start-up structures (originating in the shear layer as a result of a Kelvin-Helmholtz instability) and is typical for backward-facing step and other types of flows (laminar and transitional flows) associated with stenosis geometry (Tihon et al. 2012). For example, the work of Varghese et al (2007a) reports a high energy peak at $S_t \approx 0.39$ (the frequency is scaled with U_{max}/d_S , where d_S is the reduced diameter at the throat of the stenosis) prior to the reattachment at $x = 3D$. Similarly, Mittal et al (2003) detected vortex shedding at $S_t \approx 0.45$.

The cause of the instabilities between the LDV-experimental work of Ahmed & Giddens (1983a) and the numerical work of Sherwin & Blackburn (2005) appear to be dissimilar. In the LDV-experimental work by Ahmed & Giddens (1983a), the instability appeared to

be convective and highly dependent on experimental noise. In the numerical work of Sherwin & Blackburn (2005), the initial bifurcation to instability was absolute. It is interesting to note that similar flow behaviour was noted by Griffith (2009). Using linear stability analysis, Griffith (2009) reported a critical Reynolds number of 2350 for the 50% stenosis case (corresponding to an absolute instability). For the 75% stenosis case, the critical Reynolds value reported by Griffith (2009) was 770 which compared well with the value of 722 reported by Sherwin & Blackburn (2005). Furthermore, Griffith (2009) reported that the presence of noise (for PIV experiments) induced small waves developing in the shear layer (i.e. Kelvin-Helmholtz instability) downstream of the blockage indicating a strong convective instability and, thus, corroborating the experimental work of Ahmed & Giddens (1983a). Griffith (2009) further noted that the absolute instability modes were not detected in the PIV experiments and that the instability of the shear layer was the dominant factor in the transition of the flow from a steady state.

Since the LDV-experimental work of Ahmed & Giddens (1983a) had shown evidence of shear-layer oscillations (which is a typical form of convective instability), Blackburn & Sherwin (2007) continued their work and studied the response of the steady flow to periodic forcing. The authors plotted the vorticity for $Re = 700$ subject to periodic forcing and reported roll-up of the shear layer into discrete vortices, which is more consistent with the findings realized by both Cassanova & Giddens (1978) and Ahmed & Giddens (1983a). The work of Varghese et al (2007a) continued to demonstrate the effects of external perturbations on flow whereby the authors used Direct Numerical Simulations (DNS) to simulate steady inlet flow for $Re = 500$ and 1000 (based on upstream tube diameter and mean inlet velocity) over a smooth axi-symmetric stenosis (i.e. 75% area reduction). Their initial findings reported the flow downstream of the stenosis to be completely stable at both $Re = 500$ and 1000 , thereby contradicting the work of Ahmed & Giddens (1983a). Furthermore, Varghese et al (2007a) introduced a 5% eccentricity to the stenosis geometry and, as a result, generated a perturbation resulting in transition of the flow to turbulence. The latter was only observed (via turbulence statistics and energy spectra) for the $Re = 1000$ case and not at $Re = 500$. The authors noted that the 5% eccentricity resulted in a very similar flow downstream of the stenosis compared to the work of Ahmed & Giddens (1983a) at the same Reynolds number.

Furthermore, Sherwin & Blackburn (2005) started to provide a better understanding of the critical Reynolds number for instability in stenosis flows. In their work, a Floquet stability analysis was used to determine the critical Reynolds number associated with pulsatile flow inside tubing with a smooth cosine stenosis (similar to the work of Ahmed & Giddens, 1984). Identification of a linear instability was reported in the flow (for much of the pulse cycle relevant to physiological flows) as a period-doubling vortex-tilting (i.e. corresponding to azimuthal wavenumber; $m = 1$). Furthermore, an introduction of a small flow perturbation revealed a breakdown of the vortex rings occurring at $x = 4D$ downstream of the stenosis, which was in good agreement with the work of Ohja et al (1989). Blackburn & Sherwin (2007) presented a study of flows with a wider range of pulse periods than the work reported in Sherwin & Blackburn (2005). Blackburn & Sherwin (2007) identified different linear instability modes for shorter pulse period flows for the higher end of the range of the Wo parameters (i.e. relevant to physiological flow). The modes of azimuthal wavenumber ($m = 3$ and 4) which were dominant at higher Wo parameters were reported as Windnall instability modes and displayed as waves growing on each of the vortex rings. The authors, as well, investigated convective instability in the pulsating flow over a smooth cosine stenosis. They simulated a high-frequency and low amplitude oscillation ($a_1 = 0.001$; $a_1 =$ amplitude) which was added to the inlet velocity and presented contours of instantaneous azimuthal vorticity for $Re = 700$ and $U_{red} = 0.3$ (whereby $U_{red} = tU/D$ is the reduced velocity which can be thought of as non-dimensional pulse period). The authors found that the flow was significantly less stable to linear instability modes (i.e. using Floquet stability analysis) for the case of periodically-forced flow (specifically for longer pulse periods). The authors, as well, reported that this type of perturbation excited the separated shear layer downstream of the stenosis which led to a shear-layer roll-up (at $x/D = 2.5$). In fact, they reported that the shear layer susceptibility commenced at even lower Re values (i.e. $Re = 133$). A possible interaction between the convective shear layer instability and the linear Floquet instability was, as well, suggested. The exact role of linear instability modes in experimental stenosis flows still remains a subject for further investigation since noise is not present in the numerical simulations.

2.6 Chapter Two Summary

This Chapter provides an introduction to the motivation behind studying endothelial cell response to flow inside the PPFC, which includes some of the previous work, all which demonstrates evidence of cell remodeling induced by various flow regimes (i.e. laminar, disturbed). Furthermore, the Chapter provides a table which lists various work performed in the last few decades which used the PPFC to study cell response to both, steady and unsteady flows. An analytical solution for pulsatile laminar flow inside a two-dimensional channel is given to provide the reader with an understanding of the main differences between steady and pulsatile flow. This Chapter also provides a general review of experimental measurement techniques which have been used in channel flows to measure the velocity field and accurately quantify wall shear stress (WSS). Additional focus is placed on the challenges associated with the LDV technique, specifically, the difficulties associated with locating the wall datum.

In addition, the Chapter focuses on reviewing some of the earliest and most recent studies inside flow channels with a BFS and other stenosis models (i.e. semi-circle) as means of modeling a stenosis (i.e. arterial narrowing). Both steady and pulsatile laminar flows are reviewed with emphasis on providing an overview of the behaviour of the flow downstream of the constriction. Since it is the intent of this study to better understand how the PPFC (in the present work) models post-stenotic (steady and pulsatile) flow in a tube (i.e. with more realistic stenosis geometries), the literature survey provides an overview of such studies (i.e. tube flow).

In summary, the current state of knowledge on steady and pulsatile laminar flows over simple step and other more realistic stenosis geometries (for internal wall-bounded flows) is very limited to particular geometries (and the resulting downstream flow physics) and does not expand to understand the differences (with quantifiable evidence) between these types of flows. EC research is typically undertaken inside PPFCs with a simple step (given the complexity of culturing ECs inside tubular geometry) to disturb the incoming flow without a clear understanding of whether these types of flows actually emulate *in-vivo* conditions (or at least more realistic flow conditions) in relation to diseased arteries.

There is also an absence of quantifiable flow physics data (specifically for pulsatile flow) downstream of the simple step geometry taking into account detailed mean flow, turbulence statistics and wall shear stress distribution. Hence, it is the intent of the present study to provide such data and quantify the differences in the flow physics between a simple step and more realistic models of stenosis.

Some of the outstanding questions from the review of the literature that the present study intends to address are as follows:

- (1) How well does a simple step model in the present study emulate an asymmetric tube stenosis under pulsatile flow conditions in reference to the wall shear stress and its spatial and temporal gradient together with the oscillatory shear index (OSI)?
- (2) Does a simple step model replicate steady flow inside a healthy and stenosed *in-vitro* carotid artery model in terms of WSS and its spatial gradient?
- (3) What influence does the pulsatile waveform shape (i.e. du/dt) have on the flow physics downstream of the BFS?
- (4) What are the similarities and differences between the steady and pulsatile flow downstream of the BFS under similar Reynolds numbers?
- (5) What is the implication of the near-wall LDV spatial resolution on WSS accuracy under steady laminar flow at the working section?
- (6) How does the aspect ratio of the present PPFC ($\alpha_S = 18.26$) influence the mid-plane flow structure and how well does the flow compare to that found inside a PPFC with a relatively larger aspect ratio (i.e. $\alpha_S = 36.0$)?
- (7) Do the steady and pulsatile laminar flows in the present work experience an inherent shear layer instability upstream of flow reattachment and, hence, induce turbulence in the vicinity of flow reattachment?

The next Chapter provides a detailed overview of the final revision flow facility (including the final revision PPFC and the LDV system – designed based on the work outlined in Appendix 1). It further provides a review of the essential components that make up the entire facility together with an overview of the flow physics inside the PPFC (under steady laminar flow) considering both laminar flow theory and the channel flow analytical solution. In addition, the Chapter provides a review of the relative surface roughness at the working section (together with EC effect on the flow) and gives a breakdown of the cell fluid constituents, together with the physical properties of the fluid. Lastly, the geometry, together with the characteristic length scales, are presented for the backward-facing step flow cases reported in Chapter Five.

CHAPTER THREE

EXPERIMENTAL APPARATUS AND METHODS

3 Introduction

This Chapter provides an overview of the final revision of a hemodynamic flow facility which was used to validate the LDV probe (custom near-wall configured) under steady laminar and low-Re turbulent flow (transitional regime) reported in Appendix 2. The facility is also used to measure steady and pulsatile flow over a backward-facing step (BFS) inside the PPFC at the working section, which is reported in Chapter Five. A review of the essential components that make up the entire facility is also presented. These components included a pulsatile flow pump, a custom near-wall LDV system (highlighting its contribution), an in-line 600 W heater and temperature controller and the latest revision of a PPFC (with an aspect ratio, $\alpha = 9.72$). Additional auxiliary components, including a motorized micro-scale laboratory jack (to traverse the channel in the y – direction) and three precision cross-slide milling tables (used to adjust the x – z position of the LDV probe, the receiver and the flow channel), are also described.

Streamwise mean vertical flow profiles, $\bar{u}(y, z)$, are presented; these were computed at the working section of the channel for a steady laminar flow ($Q = 3.90 \pm 0.039$, and 7.50 ± 0.075 mL/s). Both laminar flow theory and the channel flow analytical solution are presented and compared. In terms of the channel flow analytical solution, both an exact and an estimated (based on empirical constants) solution is presented and compared. Wall shear stress (at the working section) is reported using both laminar flow theory and the channel flow solution. Following this analysis, the working section geometry together with the characteristic length scales and the coordinate system used with the backward-facing step flow cases are given. Last of all, the relative surface roughness (ϵ_s/D_h) together with the criterion used for evaluating whether the walls are hydraulically smooth at the working section (and, hence, whether ECs disturb the flow) is discussed considering both the protrusions as a result of ECs and the wall roughness as a result of machining. A breakdown of the cell fluid constituents, together with the physical properties of the fluid, are also provided.

3.1 An Overview of the Hemodynamic Flow Facility

The hemodynamic flow facility is shown in Fig. 3.1, 3.2 and 3.3. The flow facility consists of three major assemblies: a computer-controlled pulsatile pump (CompuFlow 1000 MR), the latest revision of a PPFC (Avari et al. 2016) and a custom near-wall LDV system. The pulsatile pump was designed and manufactured by Shelley Medical Imaging Technologies. The pump was selected to provide accurate and repeatable flow waveforms (i.e. normal carotid waveform) to the PPFC. The manufacturer reported that the flow waveforms hold an accuracy of $\pm 1\%$ over the flow range, 1 - 35 ml/s. The pump's accuracy and precision assessment is reported in Chapter Four of this thesis (uncertainty Chapter) and it significantly deviated from the original manufacturer's specification of $\pm 1\%$. The verification of the pulse accuracy and repeatability was an important element of the velocity measurements, since there have been modifications made to the pump over several years that have changed its performance. Modifications carried out on the pump included the change of the pump cylinder (together with plunger components and accessories), installation of a new bio-compatible solenoid valve (Avari, 2015), the installation of an in-line heater (to maintain the fluid at 37°C) and the addition of a proximity switch (purchased from Omron Basic, USA).

The pump and the PPFC were connected in a closed-loop configuration to provide a continuous flow and to prevent disruption to the operation during flow measurements. The tubing and the fittings used to connect the two devices were purchased from Cole-Palmer (Canada) to ensure bio-compatibility. The inner diameter of the tubing was 6.35 mm and the upstream and downstream lengths (from pump to channel distance) were 610 mm and 300 mm, respectively. The effect of tubing length (distance the fluid travels prior to entering the working section of the flow channel) on waveform damping and distortion (as a result of tubing capacitance and the pulse pressure) is discussed in Chapter Four.

The LDV system consists of a two-component LDV probe (transmitter) and a forward-scatter LDV receiver (purchased from TSI, USA). The LDV system was used to measure

u and v velocity components at the working section of the PPFC. Both of these units are discussed in the subsequent sections of this Chapter

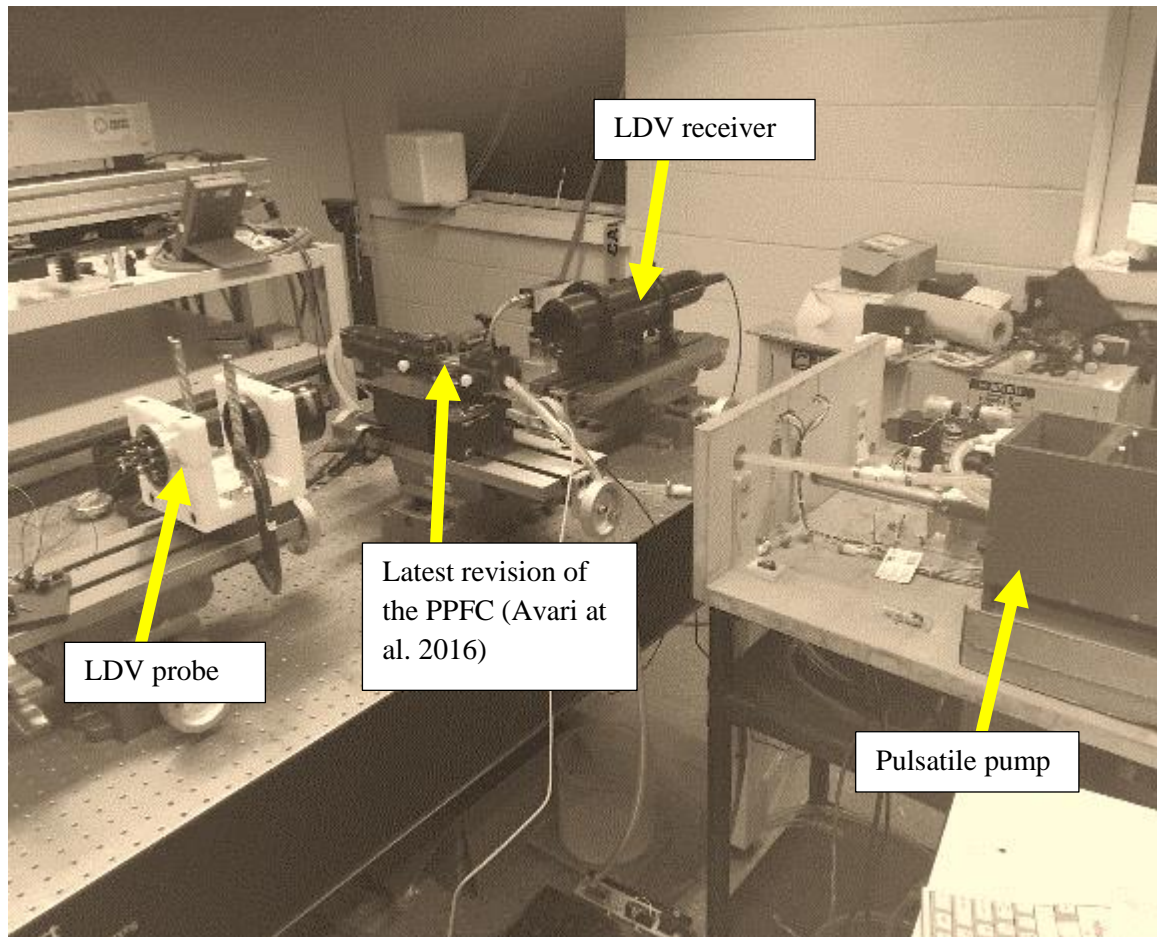


Fig. 3.1. Hemodynamic Flow Facility consisting of the LDV probe, a PPFC, a commercial LDV receiver and the pulsatile flow pump. The pump connects to the PPFC with bio-compatible tubing with an inner diameter of 6.35 mm. The tubing was procured from Cole-Palmer, Canada. The pulsatile pump is mounted on a mobile pushcart to minimize the length of the tubing between the pump and the channel. Depending on the flow case considered, the pump was elevated above the PPFC accordingly to purge air bubbles at the working section inside the PPFC.

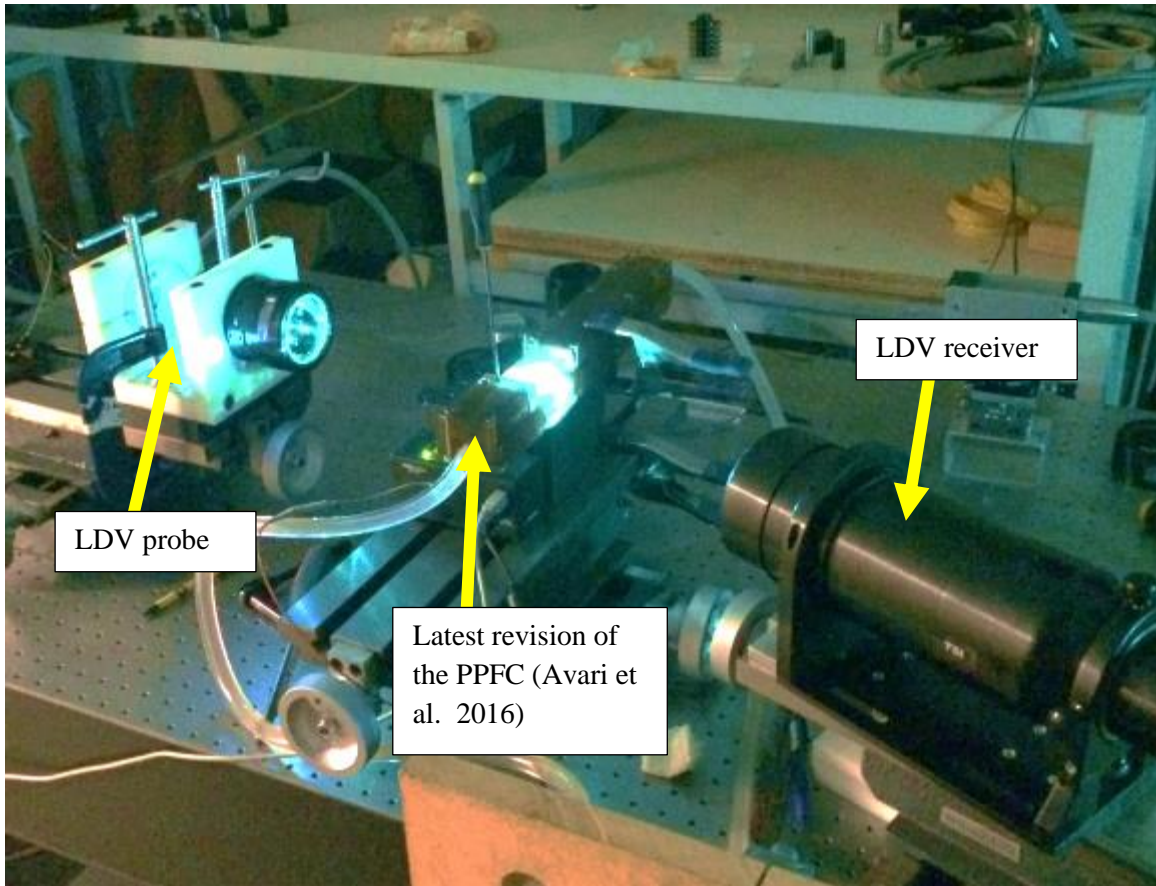


Fig. 3.2 Hemodynamic flow facility showing flow measurements being captured with the LDV receiver oriented off-axis. The off-axis configuration was used to minimize reflections associated with the input and output beams.

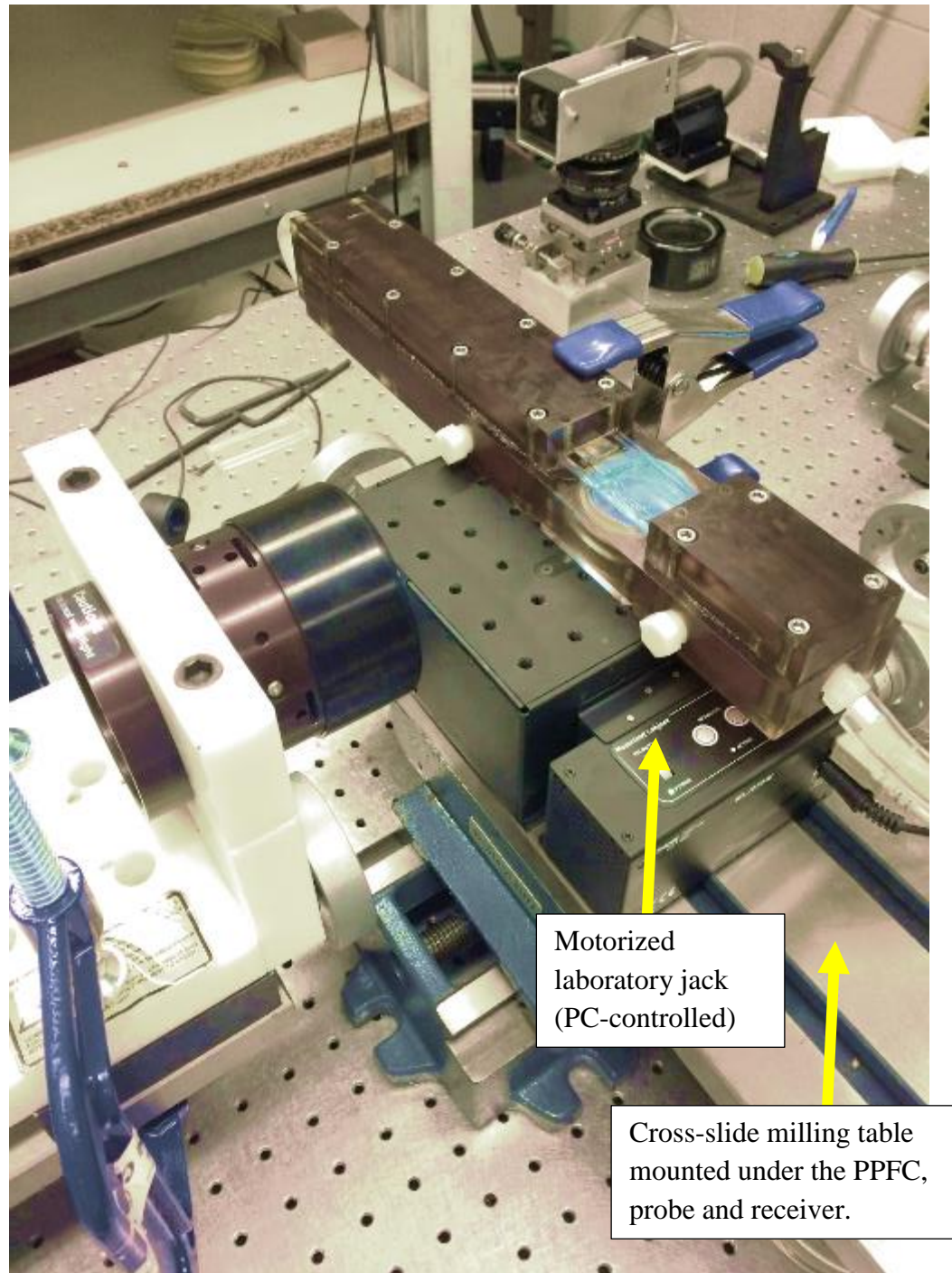


Fig. 3.3. Hemodynamic flow facility showing the PPFC mounted on a motorized laboratory jack and $x - z$ cross-slide milling table. The milling table was used to adjust the position of the channel in relation to the LDV probe and receiver. It was also used to traverse in the streamwise and spanwise directions to capture vertical flow profiles, $\bar{u}(y)$ downstream of a BFS.

3.1.1 Latest Revision of the PPFC

The latest revision of the PPFC (inspired by the commercial PPFC reviewed in Appendix 1) shown in Fig. 3.4, 3.5, and 3.6 was manufactured by University Machine Services (UMS), at Western University. The purpose of the channel is to simulate realistic waveforms (i.e. normal carotid waveform, $f = 1.08$ Hz) at the working section (above live ECs) and to observe changes in cell behaviour (in-situ) as a result of the time-varying shear loading. This is facilitated by providing LDV access to simultaneously measure the velocity near the wall (u, v , in coherence mode).

In recent work by Avari et al (2016), Porcine Aortic Endothelial Cells (PAECs) were monitored in-situ with an infinity optics microscope in a bottom-top configuration (objective lens positioned below the microscopy slide). To allow for such imaging, the channel bottom cavity was designed with access for the microscope objective lens to image the cells, which were flush mounted on a microscopy slide.

The channel is composed of two cavities (top and bottom) manufactured from ULTEM 1000 resin (biocompatible) plastic and an optical (glass) window at the working section of the channel. The ULTEM plastic comes from a family of polyetherimide-unfilled PEI and is typically used in many biomedical related applications due to its ability to withstand autoclaving temperatures of 170°C and its resistance to chemical solutions, Avari et al (2016). According to Avari (2015), the tensile strength and density of the ULTEM plastic is 91.9-101 MPa and 1280 kg/m^3 , respectively. The precision optical glass (grade B270) had a thickness of 6 mm and its external dimensional size was 81.3 mm x 30.0 mm x 5.0 mm in terms of length, width, and height, respectively. The optical window was manufactured by Angstrom Precision Optics Inc., USA.

Furthermore, the PPFC has an upstream section (situated before the working section) and a downstream section of approximately 251 mm and 94 mm, respectively. The working section of the channel has a rectangular cross-section (1.8 mm height and 17.5 mm width) and the section extends for 82.55 mm. There is a microscopy slide (22 mm x 22 mm) that is flush mounted in a square recess (0.22 mm in depth) in the lower cavity of the channel (refer to Fig. 3.5 and Fig. 3.6). At the onset of the working section, a backward-facing step

was mounted to reduce the rectangular cross section height by $\approx 50\%$ for selected flow cases, which represented arterial narrowing.

The flow channel is mounted on a computer-controlled motorized laboratory jack and the jack is mounted on a precision milling table to ensure perpendicularity to the incoming laser beams (2 blue and 2 green). The channel is mounted on both of those traverse stages to allow for micro spatial positioning in all three axes (with a resolution better than $\pm 1 \mu\text{m}$ for the lab jack and $\pm 10 \mu\text{m}$ for the cross-slide milling table). Such a set-up allows for capture of the velocity gradient at the wall in the working section. The other advantage of using this configuration is that the LDV probe and receiver do not have to be moved once the initial alignment is complete (the four beams are positioned to penetrate into the channel and near the wall), thus allowing the measurement volume region to stay in focus. The precision cross-slide milling table is used to position the PPFC in the other two directions (x, z) to evaluate the streamwise velocity along the span of the PPFC and to measure the flow at various locations downstream of a backward-facing step.

It should be noted that the uncertainty of the spatial positioning of both the laboratory jack and the cross-slide milling table is reported in Chapter Four (experimental uncertainty).

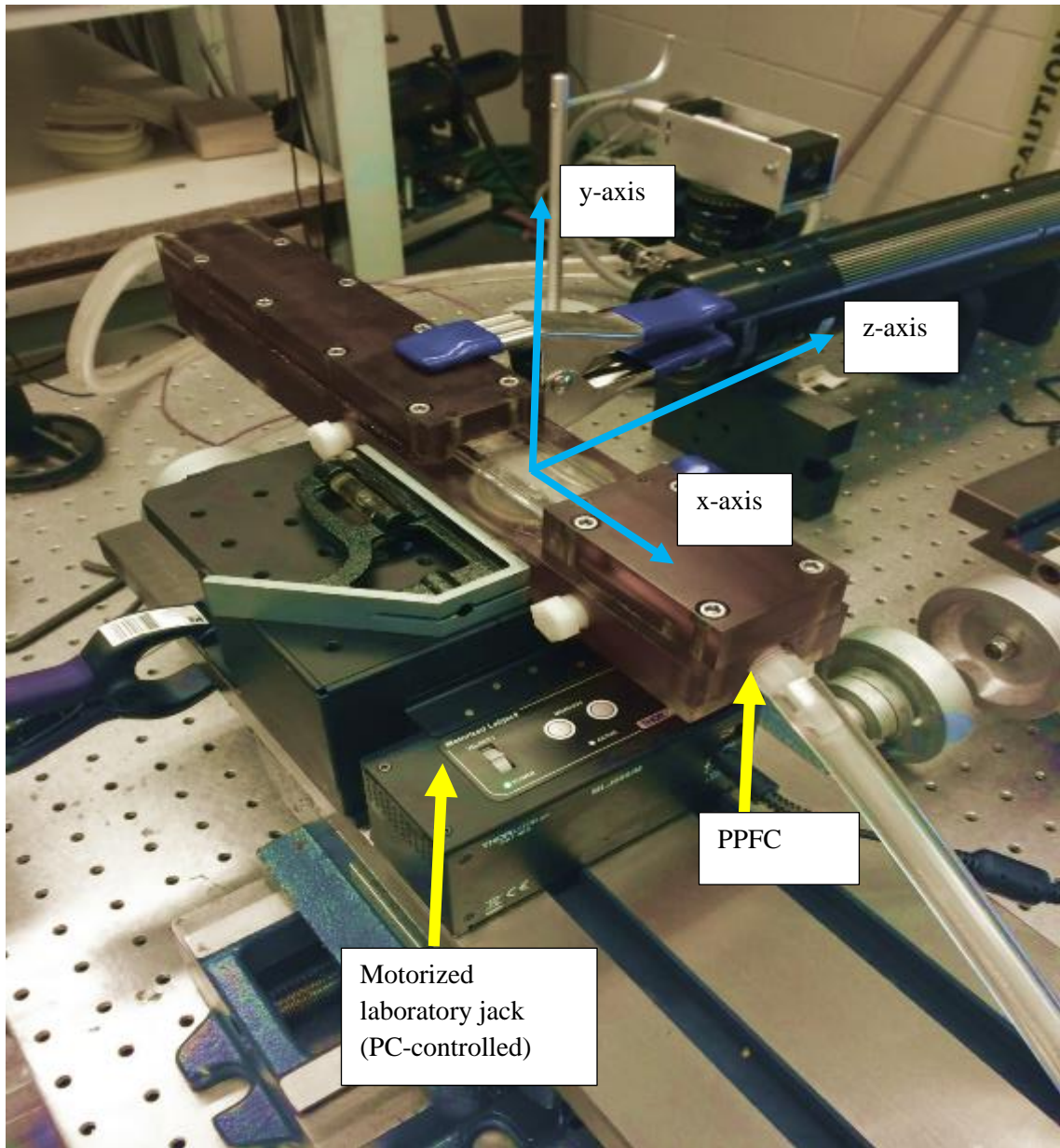


Fig. 3.4 The PPFC mounted to a computer controlled laboratory jack and x – z milling table. The lab jack allows for both manual and PC-controlled height adjustment. It connects to the computer via USB cable and was especially important (i.e. as a result of its superior spatial resolution) for locating the datum associated with the wall position (i.e. the closest velocity measurement point at the wall).

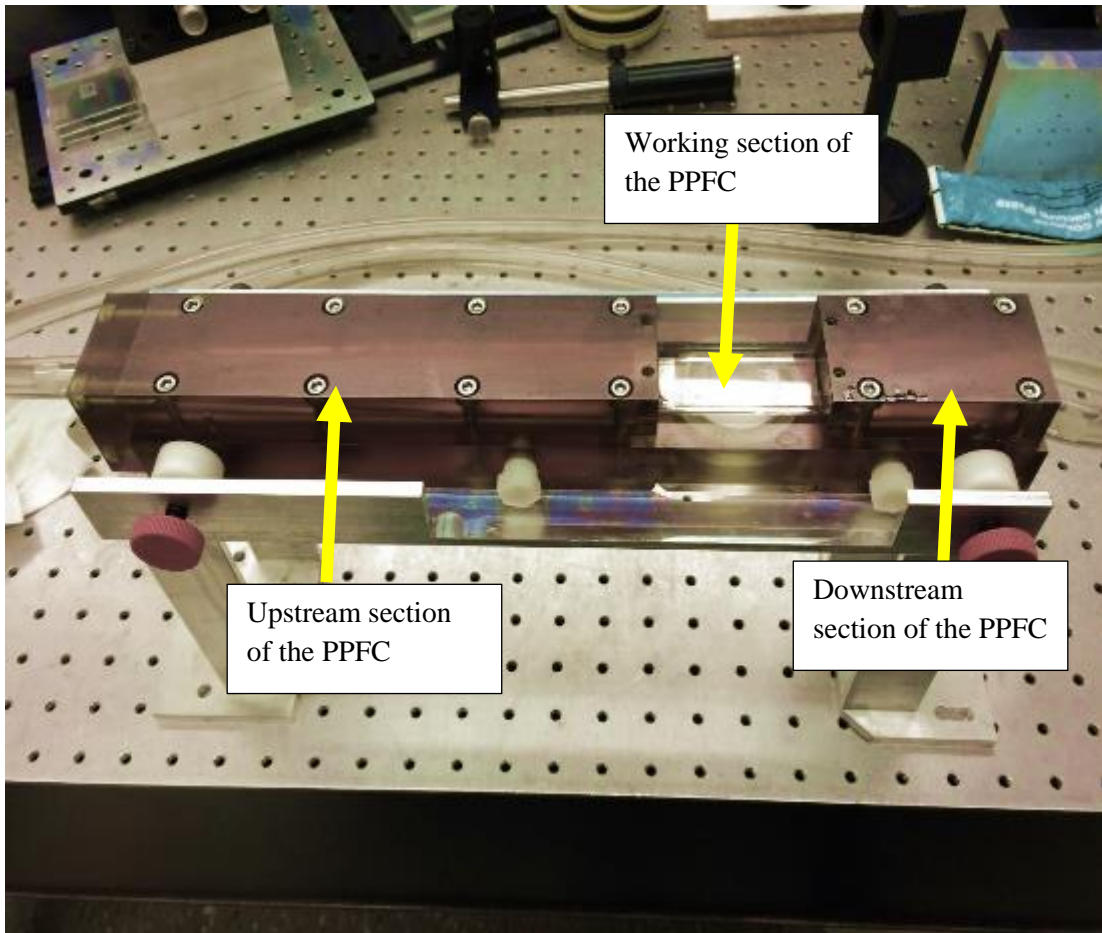


Fig. 3.5. PPFC showing the upstream, downstream, and the working section. The length of the upstream and downstream sections is 251 mm and 94 mm, respectively. The working section extends for 82.55 mm. Once the channel was assembled with the bottom and top cavities and the glass canopy, the internal channel formed was 1.8 mm in height and 17.5 mm in width.

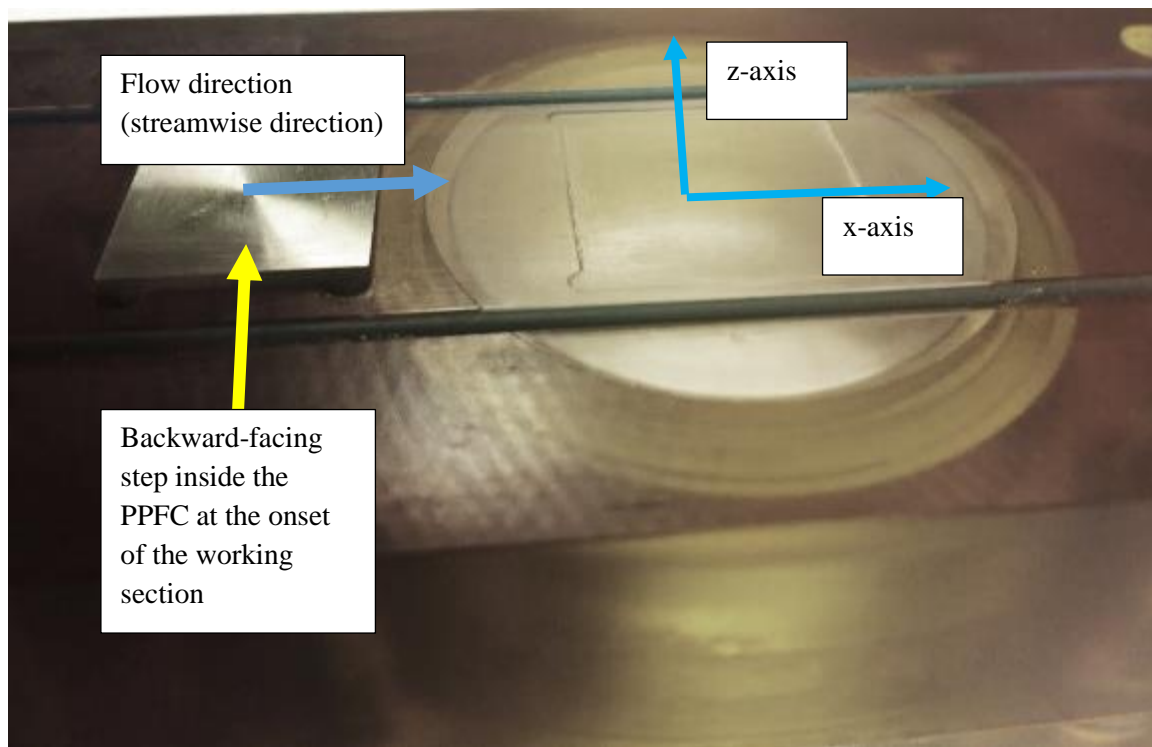


Fig. 3.6. Working Section showing microscopy slide and the step used in the study. The distance between the step edge and the centre of the slide is 25 mm. The step protrudes into the channel \approx 50% of the original channel height (1.8 mm).

3.1.2 Pulsatile Flow Pump

The pulsatile pump assembly (see Fig. 3.7) consists of a computer-controlled positive displacement piston, solenoid valve (to ensure unidirectional flow over different strokes), a 4L fluid reservoir (to hold the cell fluid), a sterile Mellipak filtering unit (0.45 μm pore size, Sigma Aldrich, USA) and a proportional-integral-derivative (PID) heater controller (Zesta, USA) with a 600 W cylindrical inline heater (Zesta Engineering, USA). In addition, two 0.64 mm T type thermocouples (Zesta, USA) were used to monitor the temperature of the flow in the closed loop flow circuitry. The first thermocouple was mounted on the inlet tubing (where the tubing connects to the PPFC) and the second inside the reservoir of the pump. The pump was selected to produce pulsatile flow waveforms over a wide-range of flow rates, which is critical for effective study of vascular hemodynamics. It is capable of producing steady flows (from 0.1 to 25 mL/s). The pump is also programmable, to deliver

a normal carotid waveform (with $f = 1.08$ Hz; $T = 0.92$ s where f is the frequency of the pulse and T is the cycle period) to the working section of the PPFC with peak flows (waveform magnitude) between 5 mL/s and 20 mL/s). It is important for the cycle-to-cycle variability to be small since examination of pulsatile flows requires measurements to be taken over several cycles (i.e. > 200 cycles near the wall in the present work). The number of pulsatile cycles for each measurement location was selected to ensure that statistical moments were independent of the bin size and that the number of bins used were adequate to resolve the waveform. Typical coincident data rates (\dot{N}) associated with measuring the waveform were 500 Hz at $y/h > 0.11$ and approximately 100 Hz at $y/h < 0.11$ (refer to coordinate system in Fig. 3.9). Bin size determination and statistical convergence of higher-order statistics are discussed in Chapter Four of this thesis (experimental uncertainty).

The functionality of the pump includes a double-acting piston which is horizontally driven. One side of the piston delivers fluid against the system pressure whilst the other side receives the fluid. The suction side of the piston receiving the fluid has a lower pressure (partial vacuum) and, thus, the fluid was brought in from the reservoir. To prevent backflow at stroke-end, a directional-control solenoid valve was used. The solenoid valve is a modified version of the original valve that was installed by the manufacturer. Avari et al (2016) reported that the new 4-way double solenoid valve was made out of ULTEM plastic to allow for several autoclave cycles and prevent sticking (which resulted due to residue build-up on the valve mechanism). At the end of each stroke the valve interchanges the outlet and the inlet flow paths. The pump generates a disruption to the continuous flow at the end of each stroke (approximately 40 ms in duration) and this was filtered out to allow accurate phase averaging of the flow measurements.

Furthermore, in support of pulsatile flow measurements, marking the beginning of each cycle was critical to effectively phase average (ensemble average). To mark the start of each cycle the output signal (pulse from 0-5 Vdc) from the pump computer was fed into a sync-pulse input port in the FSA multi-bit digital processor (TSI commercial processor).

At the cycle start, the computer provided a pulse to the FSA processor and, thus, the captured data (from individual cycles) was superimposed.

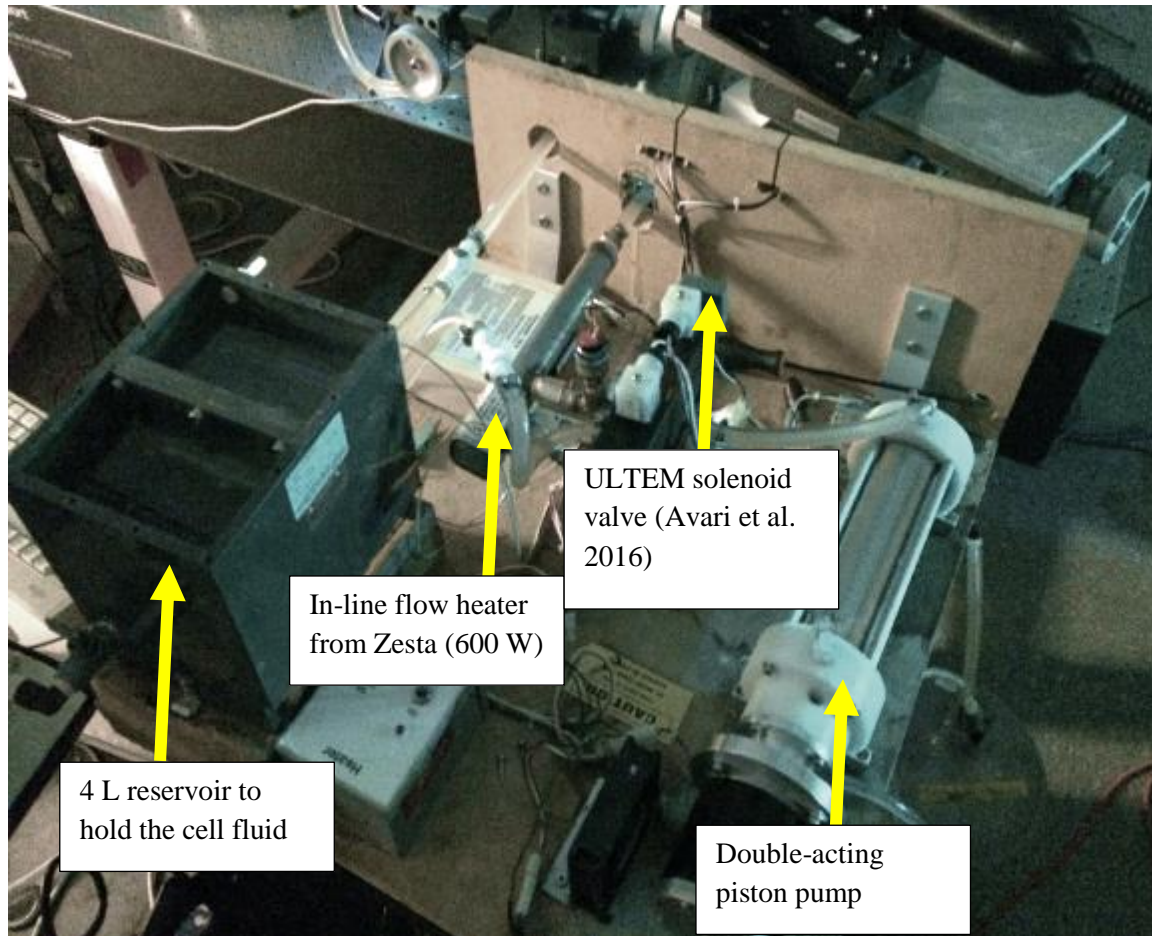


Fig. 3.7 Positive displacement pulsatile pump used with the flow measurement experiments.

3.1.3 An In-House Developed LDV System for Near-Wall Flow Measurements

A complete overview of the custom LDV system is provided in Appendix 2 of this thesis (a comprehensive design and performance assessment). However, a brief overview is provided to remind the reader of the basic workings of the probe/receiver together with a presentation of a few minor changes that were undertaken with respect to

mounting/traversing the probe (refer to Appendix 1 to understand the various design iterations).

A two-component LDV probe was built to allow for direct, non-invasive and simultaneous flow measurements at the working section of the PPFC. The probe transmitted 2 blue (488 nm) and 2 green (514 nm) beams which measured u and v velocity components simultaneously near the wall (closest measurement of $\approx 20 \mu\text{m}$ and $\approx 40 \mu\text{m}$ for the $F = 120 \text{ mm}$ and 261 mm lens, respectively) at the working section. The fiber terminations were extracted from a commercial TSI probe (TR-360 with 1.8 mm beam diameter) and mounted on the rear of the probe to allow for near-wall flow measurements. This was achieved by configuring one of the green beams to transmit through the centre of the optical focusing lens. Both a 120 mm and 261 mm focal length lens were used for the flow measurements. The choice of one versus the other was solely based on the beams' half angle to ensure that the upper green beam transmitted into the flow and measured the v -component of the velocity vector. The spacing of the two green beams (prior to focus), the beams' half-angle and the channel height were the deciding factors in the success of measuring the v -component over a specific vertical distance in relation to the wall. It was found that the v -component could only be measured up to $\approx 900 \mu\text{m}$ ($y/h \approx 0.5$) from the wall by using a 261 mm focal length lens. Details corresponding to the latter are presented in Appendix 2.

Since the scattered light from the measurement volume was collected with a TSI commercial forward-scatter receiver, the probe and receiver were mounted on precision cross-slide milling tables to ensure alignment was successful. Once alignment and focus on the two units was achieved, the remainder of the spatial movement (during flow measurements) was completed with a computer-controlled motorized laboratory jack that traversed the PPFC in the vertical direction ($50 \mu\text{m}$ or less intervals). This allowed the streamwise and wall-normal velocity to be captured at various locations across the channel height. The LDV probe is shown in Fig. 3.8 for further clarity.

The remaining components of the LDV system were standard commercial parts; these included the laser source, a colour separator and two processors for signal manipulation. The laser source was a Coherent 5 W water-cooled argon-ion laser. TSI couplings were

mounted on the colour separator to launch the four laser beams into the fiber-optic light guides (fibers). A Bragg cell provided a 40 MHz frequency shift (default set by the manufacturer) which could be adjusted inside FlowSizer (TSI software) to permit measurement of reversed flows (i.e. relevant for flow cases including the backward-facing step).

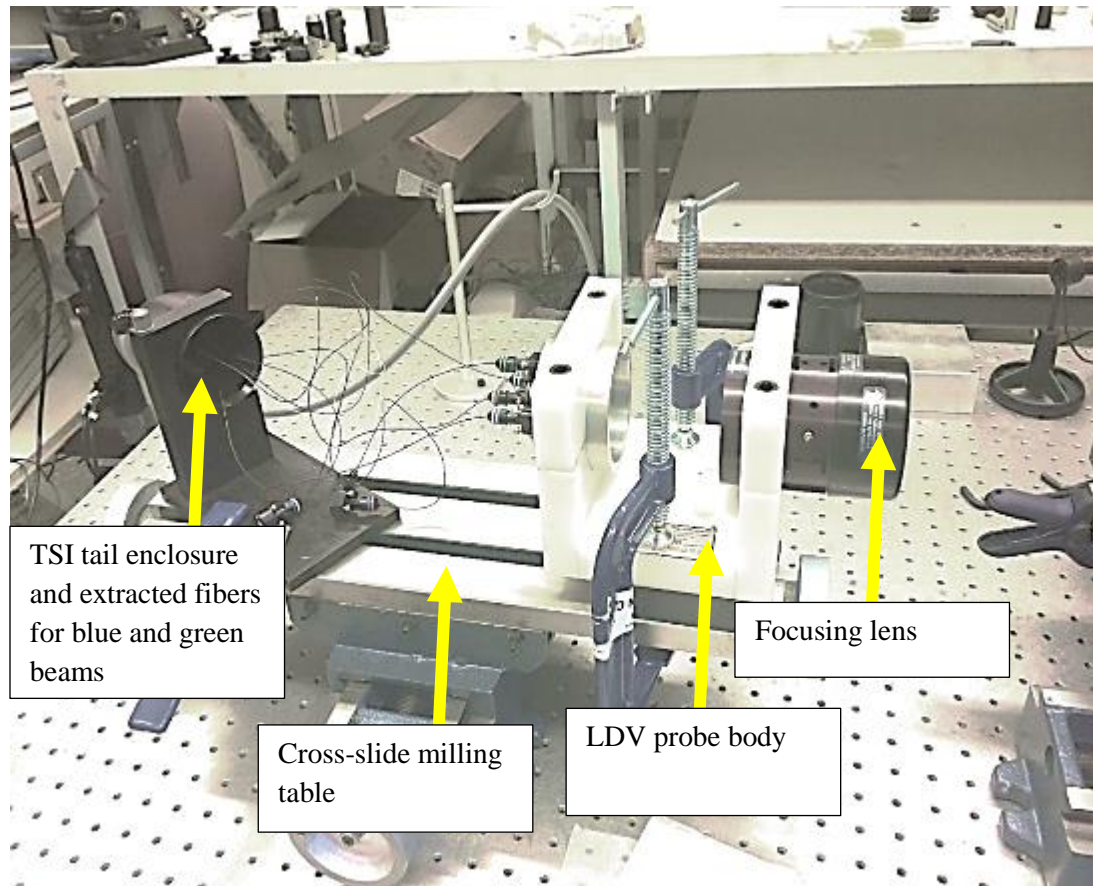


Fig. 3.8. LDV Probe for near wall flow measurements mounted on a precision cross-slide milling table. There was no requirement to traverse the probe/receiver in the y –direction since the velocity gradient was resolved by traversing the channel alone.

3.1.3.1 Custom Near-Wall Micro-Probe Contribution

Standard commercial probes available on the market today (i.e. TSI Inc: TR-360 or TR 110 (Avari et al. 2016)) do not have the flexibility to be reliable for micro and/or mini-channel velocity measurements (i.e. small scale PPFCs). This is specifically the case for capturing velocity measurements close to the cell surface (i.e. sub-cellular scale) to obtain accurate wall shear stress data. It is for this reason that the present author designed and built a custom near-wall configured micro-probe (Fig. 3.8). The features which make the custom probe (reported in the former section) ideal for these sorts of measurements are outlined below:

(1) Open-configuration design to allow installation of beam expander and polarization optics. It is reviewed in Appendix 2 (LDV design, performance and uncertainty) that the upstream beam diameter (prior to lens focusing, Eq. 2A-4) is one of the critical variables which controls the measurement volume size (i.e. beam waist). Hence, with the open configuration design it is possible to install beam expansion optics which increase the laser beam diameter prior to focusing. The latter would result in a reduced measurement volume size. Similarly, polarization optics (i.e. wave plates) can be installed upstream of the focusing lens to rotate the polarity axis and, hence, ensure viability of the velocity measurements. This is especially important in cases where the researcher must resort to using additional optics (i.e. 45 degree reflecting mirrors as example) downstream of the focusing lens to re-direct the laser beams (i.e. polarization changes with reflection, refraction). An example of the latter could be taking measurements in difficult-to-access locations inside the PPFC. In the present study, this would refer to velocity measurements at the backward-facing step (BFS). An additional advantage of the open-configuration design relates to the beam spacing (distance between the parallel beams prior to the focusing of light). For velocity measurements inside micro and mini channels, it is very important that the beam spacing is reduced as much as possible to reduce the beams' half-angle. The latter would potentially allow penetration of all four beams inside the PPFC (i.e. for small height channels). Reducing the beam spacing is especially important when lenses are used with a relatively smaller focal length. This is because a lens with a smaller focal length will tend to increase the beams' half angle. Hence, the collimation assemblies

mounted at the tail of the custom probe (see Fig. 3.8) can be re-positioned (moved closer to the centre axis) to obtain the desired beams' half angle. This is not possible with standard commercial probes on the market.

(2) Smaller weight of the custom LDV probe (excludes the heavy aluminum housing and other optical components such as prisms) allows mounting to micro-traverses with a weight limitation. Traverses with micro-accuracy and repeatability tend to have a weight restriction as a result of the delicate mechanisms used to actuate the load (i.e. an example is the MAX 311 traverse from Thorlabs with a weight restriction of 1 kg). Since it is important to reduce the spatial uncertainty of the measurement volume near the cell surface, the custom near-wall probe is ideal given its low weight.

(3) An additional advantage of the custom probe in the present study is in its configuration for a near-wall velocity measurement; that is, tilting of the probe to measure the v -component of the velocity vector is not required (one of the green beams transmits through the centre of the focusing lens). With commercial probes such as the one reported by Avari et al (2016), tilting of the probe axis is required, which results in additional measurement errors. The near-wall configuration also allows easier and more accurate determination of the wall datum as per the outlined method in Chapter Four (experimental uncertainty).

3.2 Vertical Profiles of the Streamwise Mean Velocity under a Steady Laminar Flow: Analytical Predictions

The purpose of this section is twofold: first, to present computations of the streamwise mean velocity profiles, $\bar{u}(y, z)$, at the working section using existing analytical solutions for a steady laminar channel flow and, second, to determine the wall shear stress (τ_w) and the required entrance length (upstream length of the channel and prior to the working section) to ensure the flow was fully developed. The streamwise mean velocity $\bar{u}(y)$ was computed to determine a range of velocities (at programmed $Q = 5$ mL/s and $Q = 10$ mL/s) across the height of the channel (wall-normal direction), whereas the spanwise profile of the streamwise velocity, $\bar{u}(z)$, was computed to report the limits of flow uniformity. It should be noted that $Q = 5$ and 10 mL/s were prescribed flow rates in the pump software

and not the actual flow rate values. The uncertainty analysis in Chapter Four shows that the actual flow rates are significantly smaller and were $Q = 3.90 \pm 0.039$ and 7.50 ± 0.075 mL/s for the prescribed $Q = 5$ and 10 mL/s, respectively. For this reason, only the actual flow rates will be reported from here onward. The importance of obtaining a two-dimensional flow ($\frac{\partial u}{\partial x} \approx 0$; $\frac{\partial u}{\partial z} \approx 0$) at the working section was to ensure that the ECs would be exposed to equal shear loading along both the streamwise and spanwise directions. In this study, the microscopy slide (where ECs will be cultured) extends along the entire width of the channel and, thus, one can expect a region (near the vertical lateral walls) where the shear stress varies. This variation in shear stress would expose ECs to different loading from that of the uniform velocity core near the centre of the channel.

In fact, Chung et al (2003) noted that even if a group of cells (located near the lateral walls and subjected to flow) are exempt from post-processing analysis or have not substantially affected the data, cell-to-cell communication can influence the response of other neighboring cells located away from the lateral walls (uniform core region). Chung et al (2003) also reported that cell-to-cell communication occurs through cell gap junctions and it is well known that gap junction regulation is influenced by shear stress (DePaola et al. 1999). Hence, understanding the effect of the lateral walls on the uniform velocity core is critical and was carefully evaluated using existing channel flow solutions.

As mentioned above, $\bar{u}(y)$ was computed by an analytical equation to obtain a range of velocities present at the working section. These data provided insight into the applicable range of Doppler frequencies associated with the flow and allowed a selection of the correct bandpass filter range (inside LDV software: FlowSizer) to obtain an optimal sampling rate and an increase in the signal-to-noise (SNR) value. This relationship between velocity and Doppler frequency is reviewed in Appendix 2 (LDV development). The analytical data were also used as a comparison with the experimental data to validate the custom LDV system in terms of its measurement accuracy and, thus, the uncertainty of the wall shear stress. This is reported and discussed in Appendix 2.

For each steady laminar flow case investigated ($Q = 3.90 \pm 0.039$ and 7.50 ± 0.075 mL/s), the Reynolds number (Re_m) was calculated in order to verify that flow at the working

section was laminar. The effect of aspect ratio on the transitional Reynolds number (Re_{trans}) was given by Xing et al (2013) as a polynomial correlation:

$$Re_{\text{trans}} = 2691(1 - 1.6805\beta + 1.6956\beta^2 - 0.5639\beta^3 - 0.0452\beta^4) \quad (3-1)$$

where $\beta = \frac{h}{w} = 0.10$ for the present study. Alternatively, $\beta = 1/\alpha$ where $\alpha = w/h$ (defined as the aspect ratio in this thesis, $\alpha = 9.72$). Xing et al (2013) obtained the polynomial expression by fitting the results of the energy gradient method (using the least square method, $r^2 = 0.99995$) which was given by Dou (2006). The equation above demonstrates that increasing β decreases Re_{trans} . For $\beta = 1.0$ (square duct) the transitional Reynolds number is 1127 and as $\beta \rightarrow 0$ the rectangular channel flow approaches the flow for an infinitely wide plate (Chang et al. 2012). According to Eq. (3-1), Re_{trans} at $\beta = 0$ is approximately 2689. The energy gradient mechanism was proposed by Dou (2006), Dou & Khoo (2010) and Dou et al (2010). The authors considered the entire flow field as an energy field and demonstrated that the total energy gradient in the wall-normal direction of the main flow increases the disturbance. They also found that the total energy from viscous friction (in the streamwise direction) resists and absorbs the disturbance, maintaining the laminar flow state. The conclusions of the authors was that the relative magnitudes of the two effects mentioned above govern the laminar-to-turbulent transition.

For this work and based on $\beta = 0.1$, $Re_{\text{trans}} \approx 2282$. The latter is under the assumption that the present PPFC is free of any entrance/exit effects (i.e. very long channel). To ensure $Re_m < Re_{\text{trans}}$, the following equation was used to calculate the Reynolds number inside the PPFC at the working section (Viegas et al. 2011):

$$Re_m = \frac{UD_h}{\nu} \quad (3-2)$$

where the hydraulic diameter is defined as (Patel & Head, 1969) $D_h = 4(wh)/2(w + h)$, $\nu = \mu/\rho$ is the kinematic viscosity of the cell fluid, and $U = 2/3 u_{\text{max}}$ is the bulk velocity for an infinitely wide plate. (Alternatively, the streamwise bulk velocity U can be determined by $U = 1/h \int_0^h \bar{u}(y)dy$ where \bar{u} is the time-average of the streamwise velocity sampled at various locations across the channel height). It should be noted that using the

definition, $D_h = 2h$ (used for an infinitely wide plate where $w \gg h$), yields a $\approx 12\%$ difference in the hydraulic diameter (i.e. in comparison to $D_h = 4(wh)/2(w + h)$). In the present study, the hydraulic diameter was equal to 3.2 mm. The Re_m for $Q = 3.90 \pm 0.039$ and 7.50 ± 0.075 mL/s was 600 and 1240, respectively. It should be noted that other definitions of the channel Re are reported in the literature such as $Re = U(2\delta)/\nu$, where U is the bulk velocity and $\delta = h/2$ is defined as the channel half height (Avari et al. 2016).

Furthermore, since the Reynolds numbers were smaller than $Re_{trans} \approx 2282$, the flow in the channel was considered to be laminar (also verified in Appendix 2 by measuring r. m. s. u' for a wide-range of flow rates). The polynomial equation given by Xing et al (2013) is in good agreement with pioneering work by Patel & Head (1969) to determine Re_{trans} in two-dimensional channel flows. Patel & Head (1969) investigated the velocity field inside a two-dimensional fully developed channel flow. According to their work, for $Re_m < 1350$ the flow was laminar, whereas in the range, $1380 < Re_m < 1800$, there was evidence of intermittent turbulence. For $Re_m > 1800$ the flow was considered to be fully turbulent. The observation here is that Patel & Head (1969) defined Re_m using h as the gap distance between the upper and lower channel walls (not $D_h = 2h$). For this reason, the values computed from Eq. (3-1) yield larger values of Re_{trans} compared to reported values from Patel & Head (1969).

For pulsatile flow inside rectangular channels, Loudon & Tordesillas (1998) noted that Re_{trans} may be different from that of steady flow and is influenced by both Re and Wo , specifically for $Wo > 8$. They also noted that the flow may become intermittently turbulent (corresponding to larger velocities during the cycle) and return back to laminar during smaller velocities in the cycle. In this study, results on the measured intermittent turbulence during the pulsatile cycle of a normal carotid waveform and a comparison to the available literature is thoroughly discussed in Chapter Five of this thesis (i.e. backward-facing step flow case).

In terms of dynamic and dimensional similarity between the present study and general *in-vivo* conditions, the computed Re_m values correspond to a physiological range of 200-6000 (Barber et al. 1998). The hydraulic diameter is 3.2 mm and is also in the range of

physiological arterial sizes. As an example, the coronary artery has a diameter of ≈ 3.7 mm (Dodge et al. 1992). The other parameter that is relevant in achieving dynamic similarity that of *in-vivo* conditions is Wo . The implications of Wo on the pulsatile flow inside a rectangular channel is demonstrated in Chapter Five (two-component velocity measurements).

In terms of the hydrodynamic entrance length required to achieve a fully developed flow at the working section (steady flow), Ruel et al (1995) suggested using $l_e = ahRe$, where $a = 0.04$ is an empirical constant related to the hydrodynamic entrance length and h is the distance between two parallel plates (or the channel height). Other authors such as Kandlikar & Campbell (2002) defined the hydrodynamic entry length as $l_e = aD_h Re_m$, which uses the hydraulic diameter instead of the distance between two parallel plates. The solution presented by Ruel et al (1995) should only be used for an infinitely wide plate and, hence, for this study given that $\alpha = 9.72$, the hydraulic diameter was used instead of the distance between two plates, h . Although $a = 0.04$ was proposed by Schlichting (1934), different values have been proposed by other authors (Frangos et al. 1988; Truskey & Pirone, 1990). The effect of the entrance condition (i.e. smooth or abrupt) and the aspect ratio on the constant a (and, hence, on the magnitude of the entrance length) has been studied by Hartnett et al (1962). The authors showed that for $\alpha = 10$ the constant of $a = 0.033$ did not change with the type of entrance configuration (abrupt/smooth) for $Re_m < 2000$. For $\alpha = 5$, the constant of $a = 0.046$ was reported by the authors, which demonstrates that there is a significant dependence of the entrance length on the aspect ratio.

In this study, $l_e = 0.033D_h Re_m$ was used to compute the entrance length for $Re_m = 1240$ which yielded a value of $l_e = 131$ mm. Since the upstream length of the PFFC used in the present study extended for ≈ 251 mm, it was concluded that the entrance length was sufficient to generate a fully-developed flow at the working section. The latter was also verified by measuring the streamwise mean velocity at the working section (across the channel height) at three distinct locations (streamwise direction). The results show the flow was fully-developed (at the working section) and this is further discussed in Appendix 2.

Furthermore, referring to the working section geometry and coordinate system defined in Fig. 3.9, the velocity profile $\bar{u}(y, z)$ of a rectangular channel can be computed by the following expression (Truskey et al. 2010):

$$\bar{u}(y, z) = \frac{3Q}{2wh} \left(1 - \frac{4y^2}{h^2}\right) - \frac{3Q}{2wh} \sum_{n=0}^{\infty} \frac{32 (-1)^n \cosh((2n+1) \pi z/h) \cos((2n+1) \pi y/h)}{(2n+1)^3 \pi^3 \cosh((2n+1) \pi w/2h)} \quad (3-3)$$

The first term (RHS) in the equation represents the solution for one-dimensional flow (infinitely wide plate) whereas the second term (RHS) takes into account the effect of the channel width on the streamwise velocity profile and the wall shear stress (Truskey et al. 2010). The theoretical velocity profiles $\bar{u}(y, z)$ plotted using this equation are in reference to the coordinate system defined in Fig. 3.9. Eq. (3-3) was solved using Mathlab R 2015a to obtain the streamwise velocity profile $\bar{u}(y)$ and the spanwise profile of the streamwise velocity $\bar{u}(z)$. In addition, Purday (1949) and Natarajan and Lakshmanan (1972) provided an alternative and approximate solution (referencing the same coordinate system as Eq. 5-3) to solve the velocity profiles (under steady laminar flow) inside rectangular flow channels as follows:

$$\bar{u}(y, z) = \frac{Q}{wh} \left(\frac{m+1}{m}\right) \left(\frac{n+1}{n}\right) \left[1 - \left(\frac{2z}{w}\right)^m\right] \left[1 - \left(\frac{2y}{h}\right)^n\right] \quad (3-4)$$

$$\text{where } m = 1.7 + 0.5\beta^{-1.4} \text{ and } n = \begin{cases} 2 & \text{for } \beta \leq 1/3 \\ 2 + 0.3 \left(\beta - \frac{1}{3}\right) & \text{for } \beta \geq 1/3 \end{cases}$$

Since in this study $\beta = 0.10$, the values for m and n were 13.774 and 2, respectively. To compare and to provide quantitative evidence of the errors arising from the use of the parallel plate approach (laminar flow theory where $w \gg h$ under a fully developed steady flow) in contrast to a rectangular channel flow, the following equation was used (Truskey et al. 2010):

$$\bar{u}(y) = \frac{3Q}{2wh} \left(1 - \frac{4y^2}{h^2}\right) \quad (3-5)$$

Fig's 3.10 to 3.13 show the streamwise mean velocity, $\bar{u}(y, z)$, profiles at the working section normalized against the maximum velocity (\bar{u}_{\max}) for an infinitely wide plate solution (laminar flow theory). Both the exact solution given by Truskey et al (2010) and the approximate solution given by Natarajan and Lakshmanan (1972) are presented and compared to an infinitely wide plate solution. Fig. 3.10 shows the normalized streamwise channel flow velocity (\bar{u}/\bar{u}_{\max}) at $z/w = 0$ for all three flow solutions. The y-axis in the plot was normalized against the channel half height, $h/2$. Given that the flow inside a rectangular channel (for a two-dimensional steady laminar flow) is statistically symmetric (Pope, 2010) about the mid-plane ($x - z$), velocity profiles were only presented for half of the channel height. Fig. 3.10 shows the exact channel solution (Truskey et al. 2010) for the \bar{u}/\bar{u}_{\max} profile in excellent agreement with the infinitely wide plate \bar{u}/\bar{u}_{\max} profile at $z/w = 0$. It can also be seen from Fig's 3.11 and 3.12, that the exact channel solution starts to deviate away from the infinitely wide plate solution as the lateral walls of the channel are approached (i.e. $z/w = 0.45, 0.49$). In Fig. 3.11, at $z/w = 0.45$, $(\bar{u}/\bar{u}_{\max})_{\text{exact}} = 0.78(\bar{u}/\bar{u}_{\max})_{\text{laminar}}$ for $2y/h = 1$. Furthermore, from Fig. 3.12 it is evident that the deviation is even larger between the two profiles (at $z/w = 0.49$) where $(\bar{u}/\bar{u}_{\max})_{\text{exact}} = 0.25(\bar{u}/\bar{u}_{\max})_{\text{laminar}}$ for $2y/h = 1$. At $z/w = 0.45$, the start of the deviation between the exact and the infinitely wide plate solution starts to become apparent at $2y/h \approx 1.9$ and increases as $2y/h \rightarrow 1$. In terms of the latter, an equal observation can be made at $z/w = 0.49$, with an exception being the start of the deviation at $2y/h \approx 2$. Comparing profile \bar{u}/\bar{u}_{\max} for the approximated and the infinitely wide plate solution at $z/w = 0$ shows deviation beginning at $2y/h \approx 1.9$ and reaching a maximum at $2y/h = 1$, corresponding to a difference of approximately 10%. Thus, the approximate solution given by Natarajan and Lakshmanan (1972) slightly overestimates the velocity at $2y/h = 1$ in comparison to both the exact and an infinitely wide plate solution. However, it can be seen from Figs 3.11 and 3.12 that the approximate channel solution is in good agreement with the exact channel solution closer to the side walls. In fact, at $z/w = 0.49$, the two solutions are nearly identical.

To evaluate the spanwise uniformity, $\bar{u}(z)$, both the exact and the approximated channel solutions for \bar{u}/\bar{u}_{\max} profiles were plotted along the z -direction (at $2y/h = 1$, $x = 0$). For both of these solutions, the effect from the lateral walls is evident at $z/w \approx 0.325$ (refer to Fig. 3.13). The results from Fig. 3.13 were used to determine the uniformity region of the velocity at the working section. It was found that approximately 65% of the channel width is exposed to uniform flow ($-0.65 < 2z/w < 0.65$). The criterion used to define uniform flow was an absence of deviation in the streamwise velocity over the range reported. The actual velocity variation (measured by commercial LDV under steady laminar flow) across this range ($0.65 < 2z/w < 0.65$) reported by Avari et al (2016) is discussed in Chapter Five. Using commercial LDV, Avari et al (2016) measured the lateral profiles of the streamwise velocity for $Re_m = 100$ and $Re_m = 900$ and found the maximum average deviation of the experimental data (at 3 distinct locations along the x -direction) from the analytical solution (using Truskey et al. 2010) to be 3.6% and 4.4%, respectively. These results are also in good agreement with the work performed by Holmes and Vermeulen (1968) which captured photographs of the flow pattern inside a central plane of a transparent duct ($\beta \approx 0.1$, same as this study). The method was based on diluting the fluid with a fine phosphorescent powder and exposing it to a collimated electronic photo-flash lamp to capture the velocity profiles. Holmes and Vermeulen (1968) fitted the lateral profiles of the streamwise velocity to the equation given by Natarajan and Lakshmanan (1972). They then calculated the m and n exponents (presented in Eq. 3-4) by both measuring the gradient at the wall and the surface areas under the curves. The maximum deviation reported between their experimental values of the exponents to those calculated (Purday, 1949) was 10%. The measured velocity profiles in the present study for $Q = 3.90 \pm 0.039$ and 7.50 ± 0.075 mL/s (under steady laminar flow) are compared to the analytically computed velocity profiles (presented in this section) in Appendix 2.

Other factors which influence the uniformity of flow over ECs are the variations associated with the channel height and surface roughness. In addition, if the microscopy slide where ECs are cultured is not adequately supported inside the working section, this can lead to deflections from the pressure pulse. According to McCann et al (2005), even small machining (i.e. microns) tolerances (when manufacturing the PPFC) can cause non-

negligible channel height and shear stress variations. Using μ PIV, McCann et al (2005) quantified the local flow velocity variation (under a laminar steady flow) inside a PPFC (at the working section with a height of 330 μm and width of 38.1 mm) together with rat aortic endothelial cells (RAEC) response variation. The authors found that the wall shear stress values across the channel working section deviated as much as 11% from the average shear stress (given that the shear stress is inversely proportional to the channel height). Similarly, the authors found that the gene expression was not uniform over the channel working section as one would assume using laminar flow theory. The authors attributed the non-uniform flow behaviour to the machining tolerances and assembly protocol for typical PPFCs. In the present study, the variation in the height of the channel at the working section was dictated by the machining tolerances of the bottom cavity and the glass canopy (which forms the upper channel wall inside the working section when assembled). The manufacturer (University Machine Services at Western University) reported a machining tolerance of ± 0.02 mm on the bottom cavity wall and the glass canopy height uncertainty of ± 11.42 μm . Both of these values were evaluated with a dial indicator and it was confirmed that the values mentioned above were correct. The same glass canopy was used with all velocity measurements reported in Chapter Five.

The effect of the channel height variation on the wall shear stress was evaluated using an analytical equation (see Eq. (3-7)) and was within the experimental uncertainty (the uncertainty associated with curve fitting the velocity data at the wall produced an error orders of magnitude larger).

McCann et al (2005) also studied the effect of the channel pressure on the microscopy slide deflection and quantified the deflection to evaluate whether it had any effect on the channel height. The authors numerically solved a two-dimensional plate deflection equation for the fixed boundary condition on all four sides of the microscopy slide under a linearly varying load of 4000 dynes/cm^2 (in addition, a uniformly distributed load was superimposed on the linearly varying load of 500 dyne/cm^2). The reported deflection was 2.3 μm based on the assumed Young's modulus of 65 GPa for the microscopy slide. In the present work, the deflection of the square microscopy slide was calculated based on the maximum hydrostatic pressure (mmHg) of the carotid waveform reported by Avari et al (2016) using

the same PPFC. Avari et al (2016) reported a maximum pressure of ≈ 60 mmHg (phase-averaged which represented peak systole hydrostatic pressure) inside the channel approximately 80 mm upstream of the working section. As a reference, the hydrostatic pressure inside the human body under normal conditions approximately varies between 2 to 140 mmHg (Vozzi et al. 2014). To determine the maximum deflection of the microscopy slide which was all around simply supported (all four edges), Ragab & Bayoumi (1988) suggested using $w = ((4qL^4)/\pi^6)(12(1 - \nu^2))/(Et^3)$, where q, L, ν, E, t for this study were, respectively, the uniformly distributed pressure over the entire slide surface (60 mmHg), the length of the square sides (22.0 ± 0.03 mm), Poisson's ratio (0.2; manufacturer reported), Young's Modulus (≈ 69 GPa; manufacturer reported) and the thickness of the microscopy slide (0.220 ± 0.002 mm). Using the equation above, the maximum deflection (centre of the coverslip) was calculated to be ≈ 0.015 mm (≈ 15 μ m). This deflection is one-half smaller than that of the variations in the channel height as a result of machining tolerances and five times smaller than that of the flatness of the optical window. As a result, the effect of pressure on the channel height variation was considered negligible and is not further discussed.

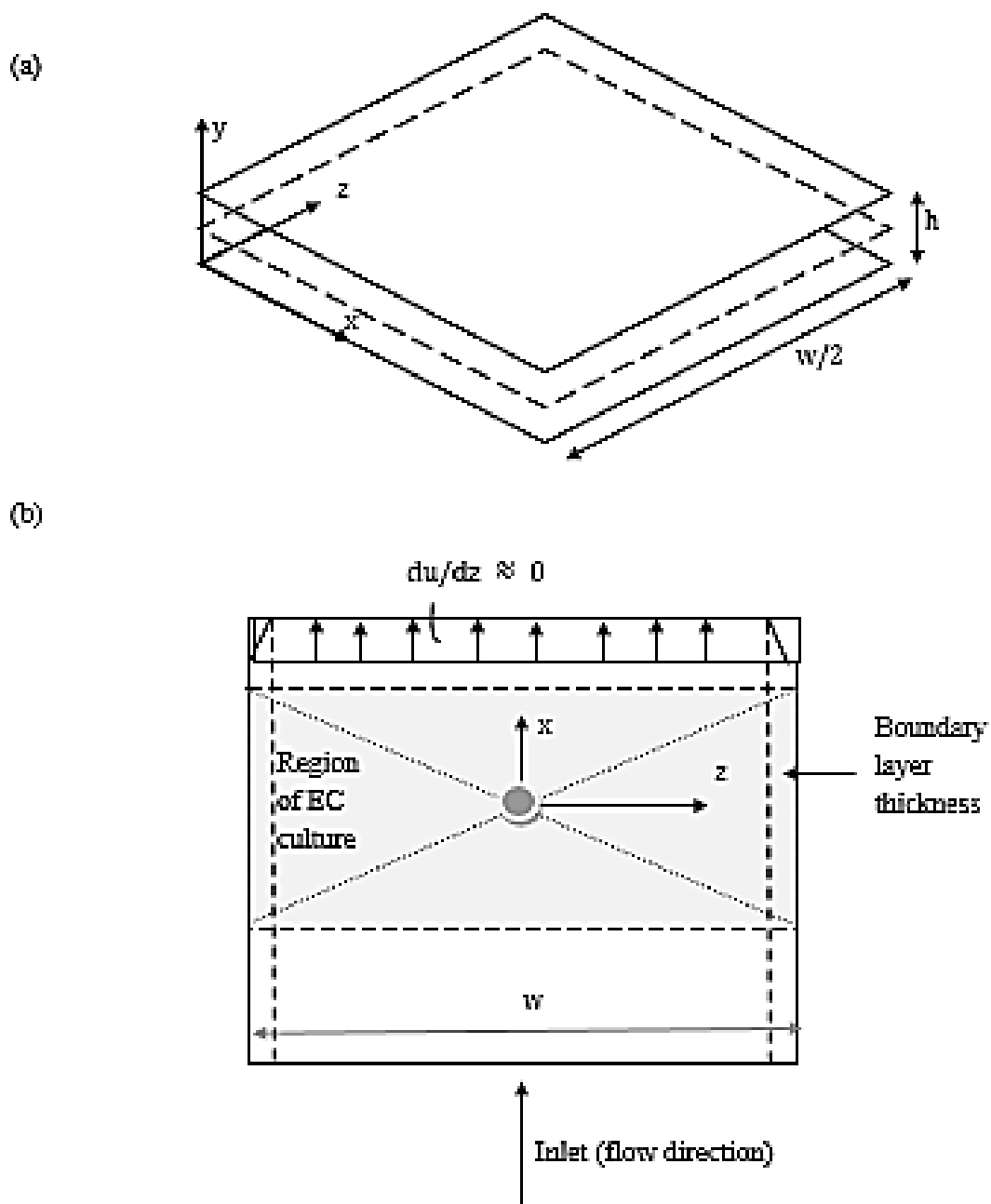


Fig. 3.9 Schematic representation of the working section inside the PPFC. a) The diagram is sectioned through the plane $z = 0$. The streamwise velocity is in the direction of the x -axis. b) Top view of the working section and section through plane $x - z$. The schematics outlined in a) and b) are not to scale.

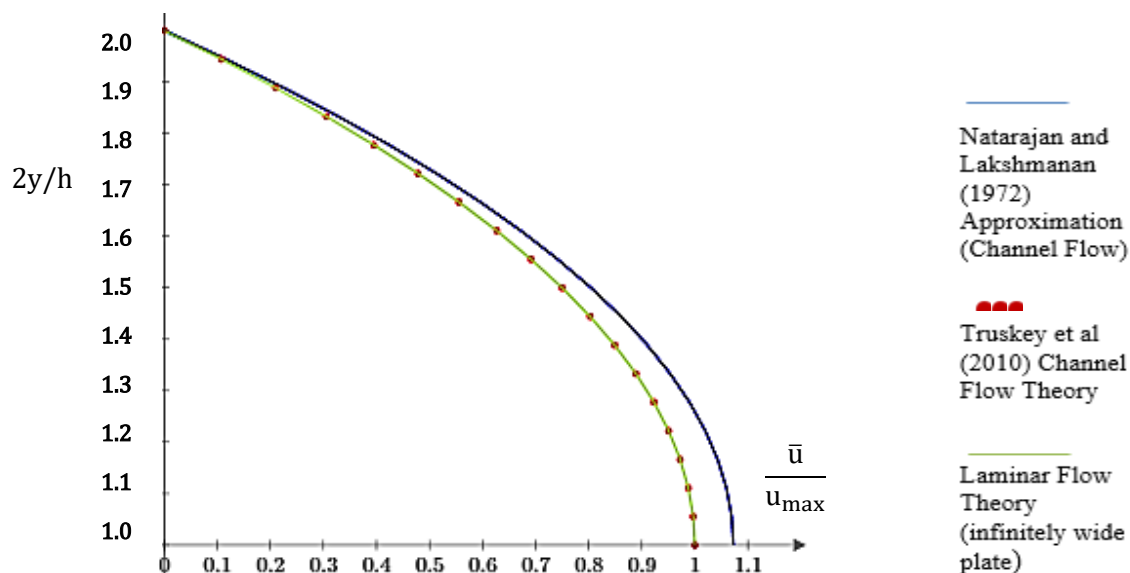


Fig 3.10 Streamwise mean velocity $\bar{u}(y, z = 0.0w)$ normalized against the maximum streamwise velocity for an infinitely wide plate solution.

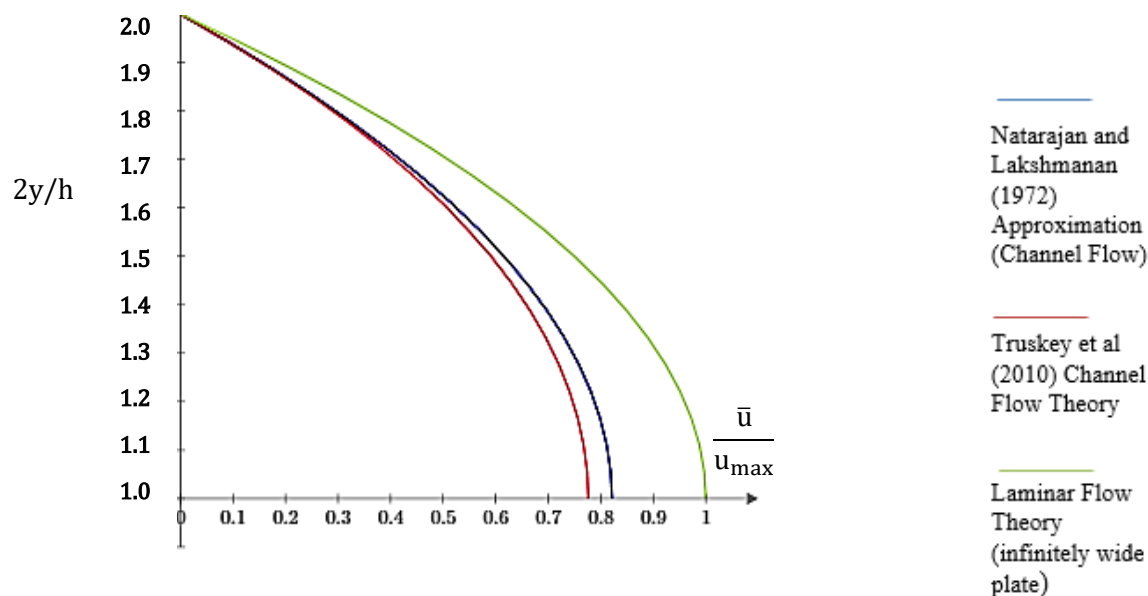


Fig 3.11 Streamwise channel velocity $\bar{u}(y, z = 0.45w)$ normalized against the maximum streamwise velocity for an infinitely wide plate solution.

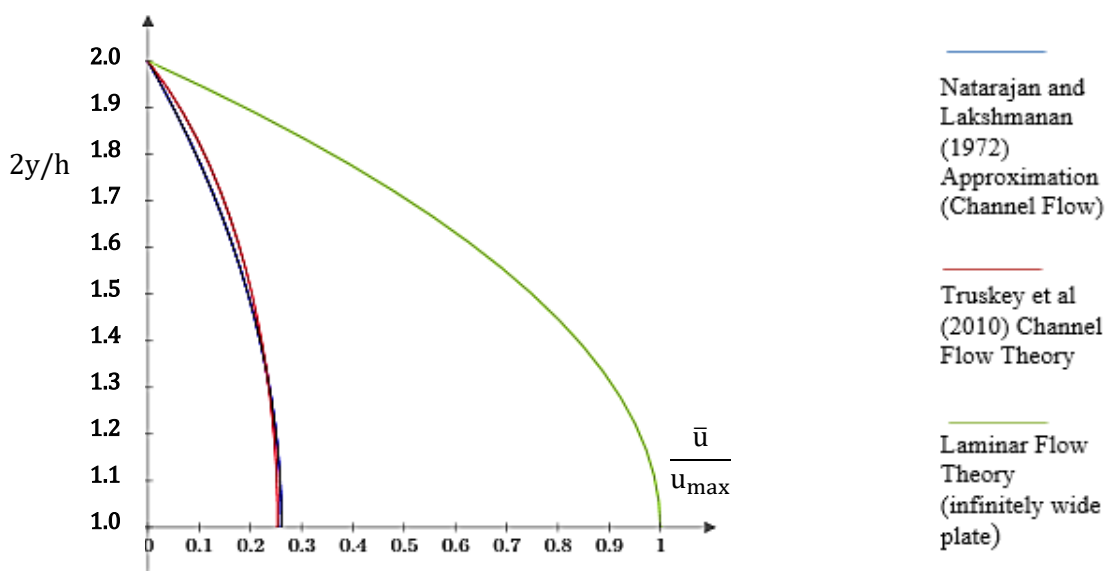


Fig 3.12 Streamwise channel velocity $\bar{u}(y, z = 0.49w)$ normalized against the maximum streamwise velocity for an infinitely wide plate solution.

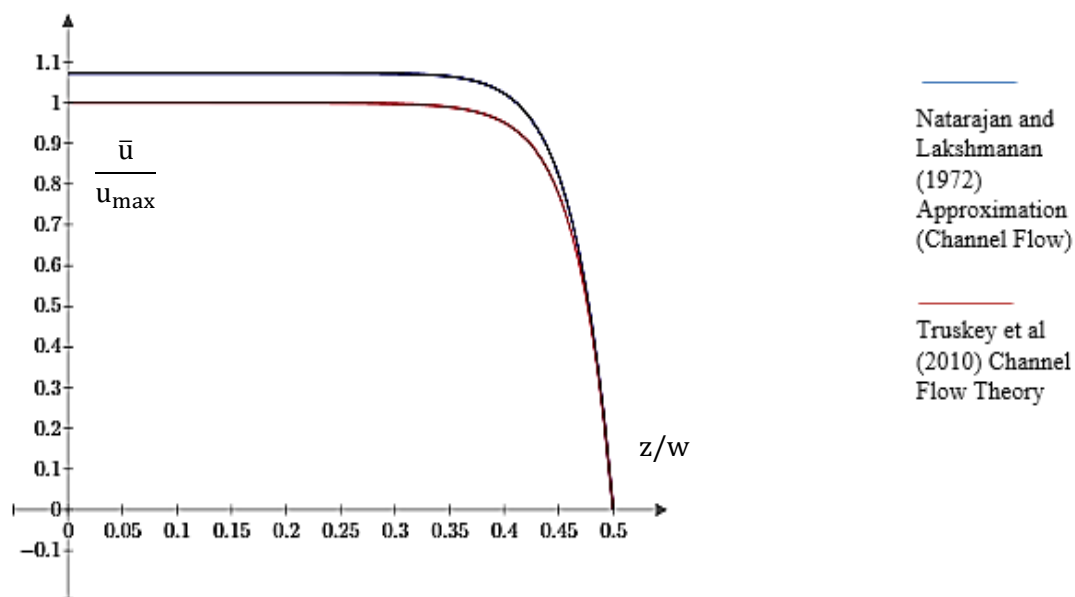


Fig. 3.13. Streamwise channel velocity $\bar{u}(y = 900 \mu\text{m}, z)$ normalized against the maximum streamwise velocity for an infinitely wide plate solution. The laminar flow theory was not plotted in this figure since it assumes no boundary layer developing at the side walls.

To compute the wall shear stress ($y = \pm h/2$), Truskey et al (2010) suggested differentiating the velocity field (Eq. 3-3) in the y –direction and integrating in the z –direction. Hence, the average shear stress on the surface ($y = \pm h/2$) can be represented as follows:

$$\tau_w = \frac{\mu}{w} \int_{\frac{w}{2}}^{\frac{w}{2}} \left(\frac{\partial u}{\partial y} \Big|_{y=-\frac{h}{2}} \right) dz = \frac{6\mu Q}{wh^2 \left(1 - 16 \left(\frac{h}{w} \right) \sum_{n=0}^{\infty} \frac{(-1)^n \tanh\left(\frac{(2n+1)\pi w}{2h}\right)}{(2n+1)^3 \pi^3} \right)} \quad (3-6)$$

Alternatively, the approximated channel flow solution can be used by differentiating Eq. (3-4) in the y –direction and multiplying the velocity gradient by the dynamic viscosity, μ . The wall shear stress can be computed as follows:

$$\tau_w = \frac{2\mu Q}{wh^2} \left(\frac{m+1}{m} \right) (n+1) \quad (3-7)$$

$$\text{where } m = 1.7 + 0.5\beta^{-1.4} \text{ and } n = \begin{cases} 2 & \text{for } \beta \leq 1/3 \\ 2 + 0.3 \left(\beta - \frac{1}{3} \right) & \text{for } \beta \geq 1/3 \end{cases}$$

Since in the present study $\beta = 0.10$, the values for m and n were 13.774 and 2, respectively, such that Eq. (3-7) yields:

$$\tau_w = \frac{6\mu Q}{wh^2} \left(\frac{m+1}{m} \right) = 1.073 \frac{6\mu Q}{wh^2} \quad (3-8)$$

Eq. (3-8) demonstrates that using the Natarajan and Lakshmanan (1972) approximation yields a shear stress that is approximately 7-8% larger than the solution based on infinitely wide plates ($\tau_w = 6\mu Q/(wh^2)$). In fact, Lightstone (2014) plotted $(\tau_w)_{\text{laminar}}/(\tau_w)_{\text{approximation}}$ against a wide range of channel widths for various channel heights. Given the design constraints presented by Purday (1949) of using Eq. (3-4) only for a valid range, $0.1 < \beta < 0.5$, Lightstone (2014) showed a maximum of 30% deviation in wall shear stress to that of τ_w for the infinitely wide plate solution at $\beta \approx 0.5$. Since the Purday (1949)

and Natarajan and Lakshmanan (1972) approximation accounts for lateral wall effects, it provides a better overall estimation of the wall shear stress than that of laminar flow theory.

Table 3.1 compares wall shear stress at $Q = 3.90 \pm 0.039$ and 7.50 ± 0.075 mL/s calculated from Eq. (3-6), Eq. (3-8) and laminar flow theory. The difference between $(\tau_w)_{\text{exact}}$ and $(\tau_w)_{\text{laminar}}$ for $Q = 3.90 \pm 0.039$ and 7.50 ± 0.075 mL/s was 5.26 and 5.13%, respectively. In general, the wall shear stress values in this study are in the range of earlier *in-vitro* work (Anderson et al. 2006; Dol et al. 2010; Avari et al. 2016) which simulated shear stress in the range between 0-10 dyne/cm². The shear stress values are also in the range of that found (1 to 6 dyne/cm²) inside the human venous system (Chiu & Chien, 2011). In general, the shear stress inside the arteries of the human body ranges from 10 to 70 dyne/cm² (Chiu & Chien, 2011). In the present study, to reach these values of shear stress inside the PPFC at the working section, the pulsatile pump can be adjusted to deliver larger flow rates.

Table 3.1 Comparison of wall shear stress (at the working section, $x = 0, z = 0, y = 0$) computed from channel flow theory and a solution for an infinitely wide plate.

Re_m	Q mL/s	$(\tau_w)_{\text{exact}}$ dyne/cm ²	$(\tau_w)_{\text{approximation}}$ dyne/cm ²	$(\tau_w)_{\text{laminar}}$ dyne/cm ²	$ (\tau_{\text{exact}} - \tau_{\text{laminar}}) / (\tau_{\text{laminar}}) \times 100\%$
600	3.90	2.88	3.96	3.04	5.26%
1240	7.50	5.54	6.27	5.84	5.13%

3.3 The Working Section Geometry and Characteristic Length Scales: Backward-Facing Step Flow Cases

The working section geometry together with the characteristic length scales and the coordinate system used with the backward-facing step flow cases (in Chapter Five) are presented in Figures 3.14 and 3.15. The zero locations for the x, y, z coordinate system are prescribed as $x = 0$ at the step edge, $y = 0$ at the bottom wall and $z = 0$ at the symmetry plane of the working section (shaded with blue colour in Fig. 3.14).

According to Lee & Mateescu (1998), the expansion ratio (ER) can be defined as $ER = h/(h - S)$. In Fig. 3.15, h and S represent the channel height upstream and/or downstream of the step and the step height, respectively (whereby the term $h - S$ represents the inlet channel height). The ER in the present study is 1.88 ($\approx 50\%$ reduction of channel height and area) and the aspect ratio of the working section (downstream of the backward-facing step) is defined as $\alpha = w/h = 9.72$, whereas the aspect ratio of the smaller channel (inlet channel at the step) is $\alpha_s = w/(h - S) = 18.26$. The length of the working section (downstream of the step edge) is denoted by l and is 82.55 ± 0.02 mm (i.e. ≈ 98 step heights).

According to Demuren et al (1994), an increase in l/S beyond 7 does not have any effect on the numerical solutions of the flow downstream of the step. Furthermore, Kaiktais et al (1999) show (via numerical methods) that the flow downstream of the step does not significantly change for $Re > 100$ for any value of l/S as long as a parabolic velocity profile is prescribed at the inlet (steady laminar flow). In addition, the step length (l_s) in the present study is 17.5 mm (i.e. $l_s \approx 21S$), which according to Biswas et al (2004) is sufficiently long to have a negligible effect on the mean velocity and turbulence statistics downstream of the step (i.e. criteria is $l_s \geq 5S$). Hence, for this study both the step and the downstream lengths are assumed not to influence the flow downstream of the step under steady laminar flow.

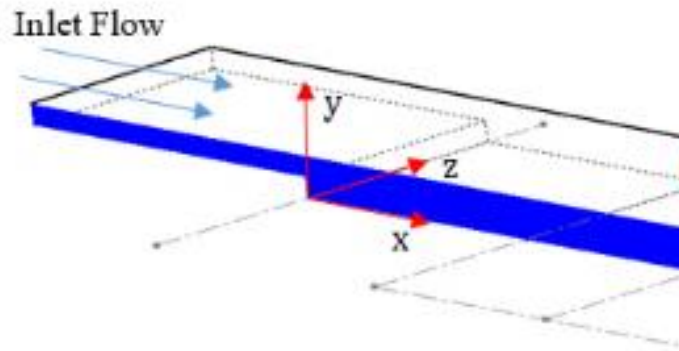


Fig. 3.14 Isometric view of the working section of the final revision PPFC. The grey colour indicates the symmetry plane (x-y).

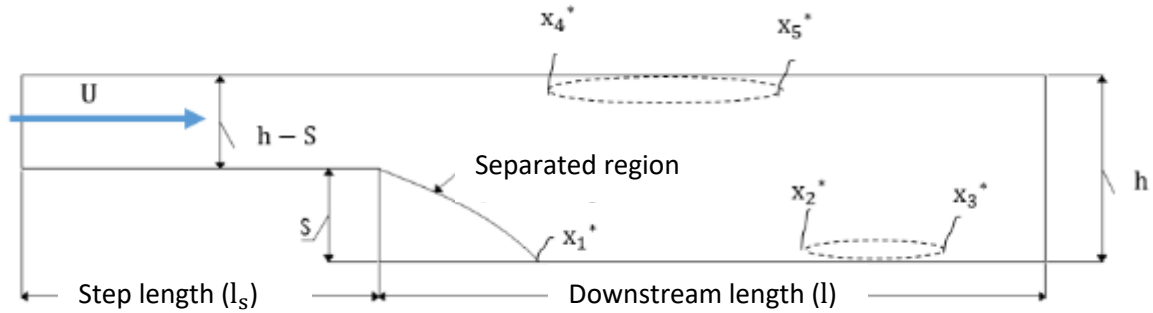


Fig. 3.15. Schematic illustration of the working section with the backward-facing step. The drawing is not to scale. The figure defines the various length scales at the working section. The normalized reattachment length of the primary recirculation region is denoted by variable $x_1^* = x_1/S$. Furthermore, x_4^* and x_5^* denote the start and the end of the upper wall recirculation region ('roof eddy'), respectively. Finally, x_2^* and x_3^* represent the start and the end of the second recirculation zone on the lower wall, respectively.

3.4 Relative Surface Roughness at the Working Section inside the PPFC

It was important to identify all sources contributing to surface roughness at the working section to evaluate appropriate length scales, K , pertaining to protrusions and/or indentations on the bottom wall. This study considered both the roughness due to the ECs cultured and flush mounted in the bottom cavity and as a result of finishing operations such as machining (milling specifically), on the surface of the cavity. A common method for determining wall roughness in mini and micro channels is to use a surface roughness profiler instrument such as a Dektak IIA (Li & Olsen, 2006). In the absence of such an instrument, the present author referred to a standard that tabulates roughness averages by various machining techniques (Mott, 2004, pp. 580). Since the base cavity was machined (UMS, Western University) by a milling operation, Mott (2004) suggested using a roughness average range, $6.3 \mu\text{m} > \epsilon_s > 0.80 \mu\text{m}$. To best of the author's knowledge, there were no secondary operations such as honing and lapping to improve the surface finish. Based on the worst-case scenario, a value of $\epsilon_s \approx 6.3 \mu\text{m}$ was used. According to Li & Olsen (2006), the relative roughness can be defined as ϵ_s/D_h , where ϵ_s is the surface roughness and D_h is the hydraulic diameter. In this study, this resulted in a relative roughness of $\epsilon_s/D_h \approx 0.0019$ based on $\epsilon_s \approx 6.3 \mu\text{m}$ and $D_h = 3.2 \text{ mm}$. In terms of the roughness as a result of EC projections into the channel, recent work by Avari et al (2016) suggests a cell height of approximately $5 \mu\text{m}$ (based on Porcine Aortic Endothelial Cells). Avari et al (2016) carried out cell response analysis using the same PPFC as reported in this Chapter. Other work by Viegas et al (2011) reported a cell height (including the height of the extracellular matrix) of $20.1 \pm 3.9 \mu\text{m}$ for human umbilical vein endothelial cells (HUVEC). According to Viegas et al (2011), this was a good model to use since it represents a realistic endothelial model and has been widely used in the literature. Since the PPFC in the present study was designed by Avari et al (2016) to study flow over various type and size of ECs, it was important to consider the worst case scenario to determine surface roughness effects on the flow. It should be noted that the present study did not use ECs during velocity measurements and, hence, wall roughness was only considered in the analysis as a source of flow disturbance. However, the present author did examine the cell height suggested by Viegas et al (2011) to provide insight for future work using the PPFC. Using a cell height of $20.1 \pm 3.9 \mu\text{m}$, the relative roughness of $\epsilon_s/D_h \approx 0.006$ was calculated.

To determine whether the ECs protruding into the working section have an effect on the flow (and, hence, the friction), the following smooth-surface criterion (Pope, 2000) was used, $\varepsilon_s^+ = \frac{\varepsilon_s u_\tau}{\nu} < 5$, where $u_\tau = (\tau_w/\rho)^{0.5}$ is the friction velocity, which was 0.040 ± 0.003 m/s (see Appendix 2 for evaluation). Based on $\varepsilon_s = 20.1 \pm 3.9 \mu\text{m}$, $\varepsilon_s^+ = \frac{\varepsilon_s u_\tau}{\nu} \approx 1 < 5$ and, hence, the walls of the working section were considered as hydraulically smooth (Avari 2015).

3.5 Fluid Specifications

Dulbecco's Modified Eagle Medium (DMEM) solution without phenol red containing 10% Fetal Bovine Serum (FBS), 1% penicillin and streptomycin and 10 mM/l (4-(2-hydroxyethyl)-1-piperazineethanesulfonic acid) [HEPES] was used. This media was not commercially available and, thus, was prepared in-house. Accordingly, characterization of the media, including its adaptability with cells, density and viscosity measurements, were carried out by Avari et al (2016). Viscosity was measured using an Ubbelohde viscometer in a 37 °C water bath. The density and viscosity were measured to be $997.96 \pm 0.12 \text{ kg/m}^3$ and $0.737 \pm 0.0012 \text{ mPa}\cdot\text{s}$ (cP), respectively (Avari et al. 2016).

3.6 Computer-Controlled Application Interface

As discussed in the earlier sections, the motorized laboratory jack and the pulsatile pump were both computer-controlled using manufacturer-developed software applications. For the motorized jack, a Thorlabs USA application platform was used to control the traverse increments in the vertical direction (y-axis). The software allowed for a specification of the travel distance (in this case it was 50 μm) and the residence time at each jog step. The residence time was selected accordingly in order to sample over enough cycles to ensure that sufficient data pairs (simultaneous u and v) were captured in each bin to perform reliable turbulence statistics. The home or the zero reference location was determined based on the beam pairs positioned as close as possible to the wall whilst still obtaining a good signal. Datum identification for determining the measurement volume location in relation to the wall is discussed in the next Chapter. The total travel length of the jack was 20 mm and this allowed for the vertical velocity profiles $\bar{u}(y)$ to be captured across the entire channel height. The lab jack was traversed to the home position each time a new velocity

profile was measured. This ensured that the same number of measurement points across the channel height were captured for each profile at the working section. The uncertainty of the lab jack in terms of travel accuracy and precision is discussed in the next Chapter .

Computer control of the pulsatile pump was managed using the SimufLOW III application (Shelley Medical Imaging Technologies). The interface allowed for adjustment of variables such as peak flow (for the pulsatile waveform) and the number of cycle and strokes the user elected to use for each experiment. The period of the pulse cycle was also adjustable to control the waveform frequency and, thus, the Womersley number, Wo . The ECG output (trigger signal sent to LDV processor) location of the waveform could also be specified. For example, the user could mark the beginning of each pulsatile cycle at any point during the pulse phase.

Finally, the LDV signal was monitored using the FlowSizer data acquisition and analysis software. Signal management was achieved using various control factors such as the photomultiplier tubes (PMT) voltage, burst threshold, signal-to-noise ratio (SNR), bandpass filter, and downmix frequency. The optimal PMT voltage suggested by the manufacturer (TSI, USA) was in the range between 300-600 V. In general, increasing this setting in the LDV control panel increases the gain of the PMT. Caution should be used when setting large values of the voltage since the gain increase of the PMT is proportional to the signal and the noise. In relative terms, smaller particles require a larger PMT voltage than larger particles. This is because smaller particles scatter less light (Tavoularis, 2005) and may need an increase in signal strength to be detected by the processors. In the present work, the PMT voltage was adjusted to 500 V, which was the default setting in the LDV control panel. Defined by the manufacturer (TSI Inc. PDPA/LDV Operations Manual, 2006), the burst threshold setting is defined as the analog voltage level that a signal must reach for the burst gate in the processor to become active. Based on a mean particle diameter of $0.36 \mu\text{m}$ (in this work using TiO_2), a setting of 30 mV or slightly higher was suggested as a guideline by TSI Inc. Measurements close to the wall (within $100 \mu\text{m}$ of the wall) required larger burst threshold values (i.e. $\geq 100 \text{ mV}$) due to significant background noise. Furthermore, SNR is essentially a burst validation technique; that is, if the “high” selection is used, only the highest quality bursts pass validation. SNR is an

important variable that needs to be maximized to obtain an accurate signal with a high enough data rate to obtain reliable velocity statistics.

The bandpass filter range was selected based on the range of frequencies that were in the flow associated with both the steady laminar and turbulent conditions. The range of frequencies was calculated in Appendix 2 and was obtained by dividing the fringe spacing by the particle velocity. Predicted velocity profiles $\bar{u}(y)$ derived from channel flow theory were used to calculate the expected frequencies. Furthermore, any downmix frequency value (increase of frequency shift) must be added to the Doppler signal in order to choose the correct bandpass filter range. The concept behind frequency shifting and downmixing was also presented in Appendix 2. The downmix function was used in order to capture negative velocities in the recirculation regions for the backward-facing step flow cases.

3.7 Chapter Three Summary

A hemodynamic flow facility capable of simulating pulsatile waveforms at the working section of a PPFC was reviewed. In this study, the pulsatile pump was programmed to provide a normal carotid waveform to the working section with a frequency of approximately 1 Hz and a maximum amplitude (peak flow rate) of 20 mL/s. The pump and the PPFC were connected in a closed-loop configuration to provide continuous operation and to minimize flow disruption at the working section. A PPFC with a rectangular cross-section (1.8 mm by height and 17.5 mm by width) encompassed an optical window and a viewport (base cavity) for two-component LDV (to measure the streamwise and wall-normal velocity components) and microscopy access at the working section, respectively. The PPFC was mounted on a computer-controlled micro-traversing platform with a resolution better than $\pm 1 \mu\text{m}$. This allowed initial positioning of the four LDV beams as close as possible to the channel wall (within $\approx 20 \mu\text{m}$ using the $F = 120$ mm lens) and, thereafter, allowing for $50 \mu\text{m}$ traversing across the channel height.

Furthermore, it was confirmed that the flow inside the PPFC was laminar and that the upstream length of the channel was sufficiently long to produce a fully developed flow at the working section. To determine the streamwise velocity profiles at the working section both laminar flow theory (based on an infinitely wide plate) and an exact solution for a

channel flow was presented. An alternative and approximate solution for a channel flow (based on empirical constants) was also presented and compared with the laminar flow theory and the exact channel solution. It was found that the approximate solution overestimated the maximum streamwise velocity (at the centre of the channel, $x = 0$, $2y/h = 1, z/w = 0$) by approximately 8% compared to the infinitely wide channel solution. The velocity profiles computed from the exact and the approximate solutions were in better agreement closer to the lateral walls of the channel and were within $\pm 5\%$ of each other at $z/w = 0.49$. It was also reported that approximately 65% of the channel width is exposed to uniform flow for $\alpha \approx 10$ (where α is the channel aspect ratio). The wall shear stress was calculated to be 2.88 and 5.54 dyne/cm² (using the exact channel flow theory) for $Q = 3.90 \pm 0.039$ and 7.50 ± 0.075 mL/s, respectively. These values were $\pm 5.5\%$ smaller than the solution based on laminar flow theory. The shear stresses reported were within both the physiological range and the range of previous work reported in the literature.

The relative roughness $\varepsilon_s/D_h \approx 0.006$ was reported at the working section based on a cell height of $\varepsilon_s = 20.1 \pm 3.9$ μm . Considering the smooth-surface criterion ($\varepsilon_s^+ = \frac{\varepsilon_s u_\tau}{\nu} < 5$) together with $\varepsilon_s = 20.1 \pm 3.9$ μm and $u_\tau = 0.040 \pm 0.003$ m/s, the walls of the working section were considered as hydraulically smooth ($\varepsilon_s^+ = \frac{\varepsilon_s u_\tau}{\nu} \approx 1 < 5$). Furthermore, the recirculating cell fluid used was a modified DMEM mixture maintained at 37 °C with a density and viscosity of 997.96 ± 0.12 kg/m³ and 0.737 ± 0.0012 mPa·s (cP), respectively. TiO₂ was used to seed the cell fluid with a mean particle diameter of 0.36 μm and a density of 4.0 g/cm³.

Finally, both the step length (based on the criterion $l_s \geq 5S$) and the downstream length (based on the criterion $l > 7S$) were sufficiently long (whereby $l_s \approx 21S$ and $l \approx 98S$ for the present study) to not influence the flow downstream of the step under steady laminar flow. It should be noted that for both steady and pulsatile flow over the BFS (reported in Chapter Five), the flow at the inlet (at the step) is laminar.

The next Chapter provides a comprehensive review of the experimental uncertainty associated with all remaining elements necessitating quantification prior to proceeding with BFS flow cases in Chapter Five. The analysis in Chapter Four includes the following:

(1) statistical sampling error for mean and turbulence quantities for the BFS flow cases, (2) spatial positioning uncertainty of the measurement volume with respect to the wall and the step datums, together with the uncertainty of the micro-traverse units, (3) the uncertainty of the critical dimensions at the working section including the step height, (4) curve-fitting approximation errors together with statistical converge of r.m.s. and higher-order statistics and (5) the accuracy and precision of the pulsatile flow pump including carotid waveform repeatability and damping across the flow circuitry.

CHAPTER FOUR

EXPERIMENTAL UNCERTAINTY

4 Introduction

This Chapter begins with a review of the equations presented in Appendix 2 (LDV Design, Performance and Uncertainty) related to statistical sampling error (i.e. uncertainty of the acquired data) of the first and second moment statistics. Considering the latter, together with the uncertainty of the measurement volume position (in the y-direction, which adds to the uncertainty in the velocity), the total uncertainties in the mean flow and turbulence statistics are reported. To determine the relative position of the measurement volume at the working section, together with its uncertainty, a two-step process is reviewed considering both an experimental technique and post-processing of the acquired data. The latter is presented for determining the measurement volume position relative to the lower wall, vertical side-wall and the step edge to determine the datum for all three directions (x, y and z). In addition, an experimental evaluation to determine the uncertainty of the motorized laboratory jack and the cross-slide milling table is reported.

Furthermore, curve-fitting approximation errors and their implications on the wall shear stress uncertainty is discussed. The analysis associated with the latter is reported considering both the $F = 120$ and the $F = 261$ mm lens. In addition, to demonstrate the adequacy of the sample size (number of velocity realizations captured for all flow cases reported in Chapter Five) an analysis is presented to demonstrate that the second-order and higher moments converge (i.e. Reynolds shear Stress, r.m.s., skewness and kurtosis). Additional work is presented on the selection criteria for the bin size considering pulsatile flow. The final section of the Chapter focuses on experimental evaluation of the pulsatile flow pump (using an ultrasonic flow meter) considering the accuracy and precision of the steady flow supplied to the PPFC. In terms of the pulsatile flow supplied by the pump, waveform accuracy and repeatability is quantified together with an in-depth analysis of the main contributors leading to waveform damping. The latter analysis would help in reducing energy loss of the waveforms inside the flow circuitry in future work.

4.1 Mean Flow and Turbulence Statistics Uncertainties

Considering Eq's (2A-5), (2A-18) and (2A-19), the total uncertainty associated with the first-order and second-order statistics can be evaluated using the following mathematical expressions, respectively:

$$\varepsilon_{\bar{u}} = \pm \sqrt{B^2 + \left(t_1 \frac{\text{r.m.s.}u'}{\sqrt{N}} \right)^2} \quad (4-1a)$$

$$\varepsilon_{\text{r.m.s.}u'} = \pm \sqrt{B^2 + \left(t_1 \frac{\text{r.m.s.}u'}{\sqrt{2N}} \right)^2} \quad (4-1b)$$

It should be noted that Eq's (4-1a) and (4-1b) consider the LDV biases to be negligible (whereby the term B is zero). The latter is discussed in Appendix 2. As a review, N represents the sample size and $t_1 = 1.96$ for 95% confidence interval. However, it should be noted that the spatial uncertainty of the measurement volume position (along the y-direction) adds to the uncertainty in the mean velocity and turbulence intensity and, thus, the total error in the mean velocity can be defined as follows (Iyer & Woodmansee, 2005):

$$\varepsilon_{\bar{u}\text{total}}^2 = \varepsilon_{\bar{u}}^2 + \left(\frac{\partial \bar{u}}{\partial y} \right)^2 \varepsilon_y^2 \quad (4-2)$$

The first term, $\varepsilon_{\bar{u}}^2$, is the uncertainty associated with the statistical sampling error, whereas the second term, $\left(\frac{\partial \bar{u}}{\partial y} \right)^2 \varepsilon_y^2$, relates to the uncertainty of the spatial position, where $\varepsilon_y^2 = \varepsilon_{\text{traverse}}^2 + \varepsilon_{\text{datum}}^2 + \varepsilon_{\text{canopy}}^2$. The terms $\varepsilon_{\text{traverse}}$, $\varepsilon_{\text{datum}}$ and $\varepsilon_{\text{canopy}}$ represent the uncertainties arising from the traverse system (motorized laboratory jack), the wall determination method and the optical window, respectively. These uncertainties are shown in the below table 4-1.

Table 4.1 Individual uncertainties contributing to ϵ_y^2 . The uncertainty associated with ϵ_{canopy} was calculated via the standard deviation (95% confidence) from multiple height measurements (i.e > 10) along the length and width of the canopy. The latter was measured using a dial indicator (Varta indicator: 36.5 mm contact point length, 0-0.5 mm range) in relation to a surface plate (datum location with uncertainty better than $\pm 1 \mu\text{m}$).

Spatial uncertainty contributors (y-direction)	Absolute uncertainty values
$\epsilon_{\text{traverse}}$	$\pm 6 \mu\text{m}$ for 0-100 μm range at 10 μm increments and $\pm 12 \mu\text{m}$ for 0-500 μm range at 50 μm increments.
ϵ_{datum}	$\pm 10 \mu\text{m}$
ϵ_{canopy}	$\pm 11.42 \mu\text{m}$
ϵ_y^2	For near-wall measurement ($20 \leq y \leq 100 \mu\text{m}$), $\epsilon_y = \pm 16.3 \mu\text{m}$. For outer region of the velocity gradient ($100 < y \leq 900 \mu\text{m}$), $\epsilon_y = \pm 19.3 \mu\text{m}$

To determine the overall uncertainty in the streamwise mean velocity (\bar{u}) for steady laminar flow, term $\left(\frac{\partial \bar{u}}{\partial y}\right)^2 \epsilon_y^2$ was evaluated across the channel half-height. The velocity data were fitted ($20 \mu\text{m} \leq y \leq 900 \mu\text{m}$) using a 2nd order polynomial regression (correlation coefficient, $r^2 = 0.998$). Fig. 4.1 shows the streamwise mean velocity plotted

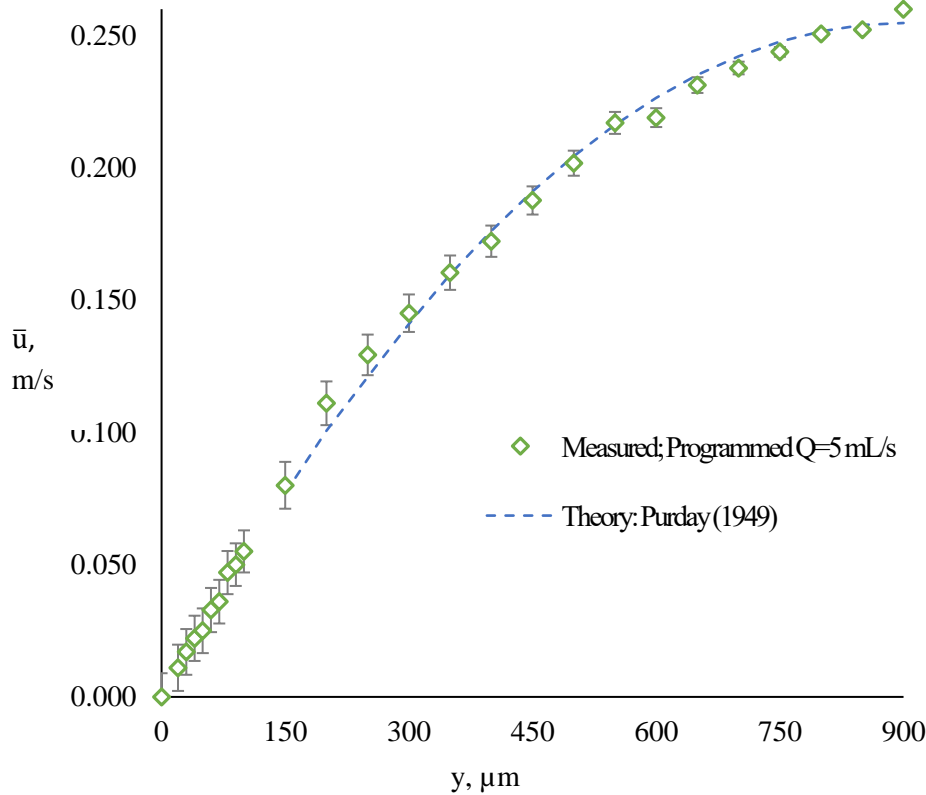


Fig 4.1 Streamwise mean velocity $\bar{u}(y)$ plotted versus y -position at the working section ($2z/w = 0$). Theoretical data points were also plotted for the range, $100 < y \leq 900 \mu\text{m}$, to compare with the measured values. With the latter, the data points were not plotted near the wall for clarity purposes. The error bars were calculated from Eq. (4-2). The maximum absolute error (in the wall region, $20 \mu\text{m} \leq y \leq 100 \mu\text{m}$) was $\pm 0.008 \text{ m/s}$ (or 3.2% of \bar{u}_{max}). It should be noted that the velocity data near the wall were captured in $10 \mu\text{m}$ increments to obtain more accuracy in the wall shear stress determination.

against the y -position at the working section ($2z/w = 0$) together with the error bars deduced from Eq. (4-2). The flow rate was set to $3.90 \pm 0.039 \text{ mL/s}$ (programmed $Q = 5 \text{ mL/s}$) which corresponds to $Re_m = 600$ (based on Eq. 3-2). The error in the streamwise velocity is at the maximum value of $\pm 0.008 \text{ m/s}$ (3.2% of \bar{u}_{max}) for the range, $20 \mu\text{m} \leq y \leq 100 \mu\text{m}$. In the range, $20 \mu\text{m} < y \leq 900 \mu\text{m}$, the error reduces linearly along the positive y -direction, with its smallest values of $\pm 0.004 \text{ m/s}$ at $y = 900 \mu\text{m}$ ($y/h = 0.5$). These results show that the uncertainties in the streamwise mean velocity (for steady laminar flow) are dominated by the uncertainties of the measurement volume position in the high velocity gradient region ($20 \mu\text{m} \leq y \leq 200 \mu\text{m}$).

For all flow cases considered in the present study, a summary of the uncertainty analysis for the LDV measurements, including mean flow and turbulence statistics (for a sample size of $N = 1500$), is shown in table 4.2. The sample size of $N = 1500$ was sufficient to obtain statistical convergence for both the first-order (mean) and higher-order statistics such as r.m.s. velocity, skewness and kurtosis. The analysis associated with the latter is demonstrated in section 4.4 and, as a review, the sample size was selected considering both the run-time and convergence of higher-order statistics. In the present work, as a result of large variations of turbulence activity in the flow (across the channel height and downstream-of-step positions), the statistical sampling error is a strong function of position at the working section. The typical uncertainties at $y/h = 0.5$ (midplane in reference to the height) are shown in table 4.2 whilst keeping in mind that the normalized errors (i.e. presented as a percentage of their local value) are generally higher near the wall. However, in the centre of the channel the uncertainties are a fairly constant percentage of their local value.

Table 4.2 Normalized errors in statistical quantities. Equations given by Casarsa & Giannattasio (2007). As review, $t_1 = 1.96$ (95% confidence interval). It should be noted for the pulsatile flow over a backward-facing step, the mean flow statistic (time averaged), \bar{u} , should be replaced with $\langle u \rangle$ (phase-averaged).

Statistical Quantity	Normalized Error	Equation Used
$\varepsilon_{\bar{u}}/ \bar{u} $	$\pm 2.50\%$	$t_1 \frac{\text{r. m. s. } u'}{\sqrt{N}} \frac{1}{ \bar{u} }$
$\varepsilon_{\text{r.m.s.}u'}/\text{r. m. s. } u'$	$\pm 5.65\%$	$\frac{t_1}{\sqrt{2N}}$
$\varepsilon_{\text{r.m.s.}v'}/\text{r. m. s. } v'$	$\pm 5.65\%$	$\frac{t_1}{\sqrt{2N}}$
$\varepsilon_{\overline{u'v'}}/ \overline{u'v'} $	$\pm 8.00\%$	$\frac{t_1}{\sqrt{N}}$

4.2 Estimation of the Micro-Transpose Uncertainty (Motorized Laboratory Jack)

The accuracy and precision of the motorized laboratory jack (micro-translation system in the y-direction) was evaluated using a digital dial indicator (Varta indicator: 36.5 mm contact point length, 0-0.5 mm range) over a range of 100 μm in 10 μm increments and over a 500 μm range in 50 μm increments. These two tests were performed by traversing the motorized stage in pre-determined steps (as noted above) whilst taking discrete readings on the dial indicator to validate the prescribed traversed distances along the y-direction. It was not possible to validate the traverse over the entire 1.8 mm range (channel height) since the indicator's range was limited to 500 μm . The range and step selection was selected to emulate the traverse operation during the velocity measurements at the working section. For example, the 10 μm traverse increments were used very close to the wall to accurately determine the friction velocity (u_{τ}) and the wall shear stress (τ_w). The 50 μm traverse increments were used away from the wall ($0.011 \leq y/h < 1$) to capture the mean flow and turbulence quantities across the channel height. The traverse-indicator set-up is shown in Fig. 4.2.

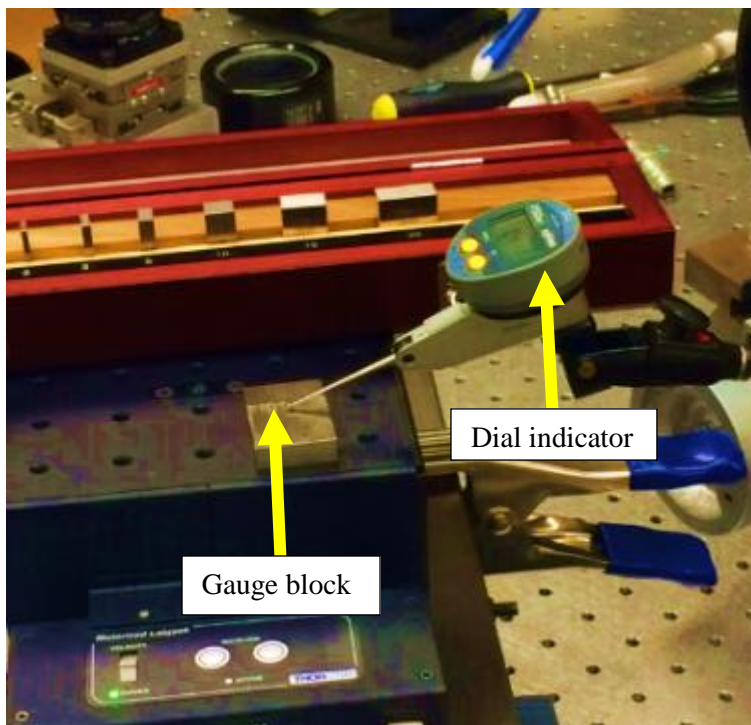


Fig. 4.2

Motorized laboratory jack validation of precision and accuracy. Shown in the figure are the traversing platform, the digital dial indicator and the gauge blocks used to calibrate the indicator and, thus, confirm the accuracy of ± 0.001 mm (± 1 μm).

Fig 4.3a shows a plot of the indicator readout (measured) against the traverse readings (theoretical or prescribed) for a range between 0-100 μm at every 10 μm step in the positive y-direction. Five separate trials were conducted to obtain the standard deviation and, hence, the precision of the traversing stage. Phase-averaged data (by averaging indicator readout values measured at the same traverse position over the five trials) across the simulated 100 μm range is also plotted and subtracted from the theoretical values at every 10 μm step to obtain the accuracy of the traversing stage. The precision uncertainty at 95% confidence interval on the mean over the five data points (N) at each 10 μm step was estimated using $P_{\text{traverse}} = t_{\alpha/2} S/\sqrt{N}$, where $t_{\alpha/2}$ and S are, respectively, a statistic referred to as the Student's t and the standard deviation for the five data points at every 10 μm traverse step. Given that the sample size was less than 30, using the t-distribution table at 95% confidence interval yielded $t_{\alpha/2} = 2.776$ (Wheeler & Ganji, 2004). It should be noted that the term (subscript) $\alpha/2 = 0.025$ for a 95% confidence level and is referred to as the level of significance (Wheeler & Ganji, 2004). It was found that the maximum precision error across the 100 μm interval was approximately $\pm 5 \mu\text{m}$. The bias error distribution (accuracy uncertainty corresponding to the difference between the theoretical and phase-averaged data) across the 100 μm interval is plotted in Fig. 4.3a (secondary y-axis) and it shows the maximum error of $\pm 3 \mu\text{m}$. The accuracy of the dial indicator was better than $\pm 1 \mu\text{m}$ (manufacturer reported) and, hence, its uncertainty was considered negligible in this study (as well it was verified with a gauge block). The total uncertainty was computed by $\epsilon_{\text{traverse}} = \pm\sqrt{3^2 + 5^2} = \pm 6 \mu\text{m}$, which represents the sum of the squares pertinent to the accuracy and the precision quantified above.

Similarly, Fig. 4.3b shows a plot of the indicator readout against different traverse readings (theoretical) for a range between 0-500 μm at every 50 μm step in the positive y-direction. Using the same mathematical formulation as described above, the total uncertainty, $\epsilon_{\text{traverse}}$, was found to be $\pm 12 \mu\text{m}$.

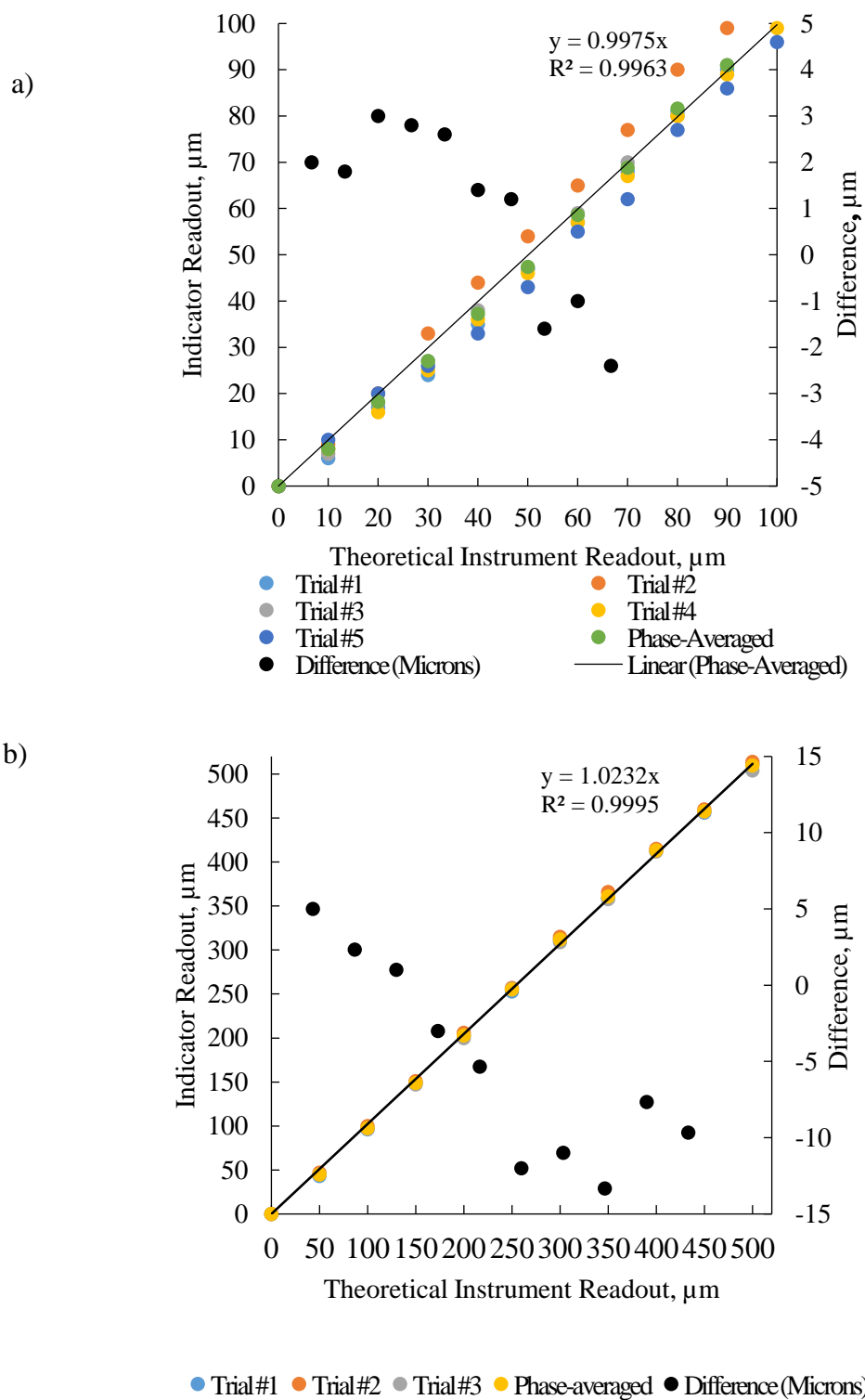


Fig 4.3 Accuracy and precision validation plot for the computer-controlled motorized laboratory jack. a) 10 μm increments over a range of 100 μm , b) 50 μm increments over a range of 500 μm . The difference is between the averaged and the theoretical data.

4.3 Wall Datum Identification Methods: Origin Uncertainty Analysis

The first step to determine the measurement volume location in reference to the lower wall was to shut-off the upper green beam (non-centre beam) at the colour separator. This allowed for better clarity in the visual observation of the three other beams (2 blue and the centre green beam) in the vicinity of the lower wall. This concept is illustrated in Fig. 4.4. In addition, the individual beam power was reduced to approximately 10 mW (typical value during an experiment was ≈ 25 mW). Reducing the laser beam power diminished the intensity of light at the wall for a clearer observation and positioning of the measurement volume. Reducing the power of the beams also generated a sharper image (less reflections) of the measurement volume whilst observing via the viewport of the forward-scatter receiver.

The second step was to implement a technique that was reported by Durst et al (1988) which involved positioning the measurement volume away from the wall at a reference position y_r (in this case $y_r \approx 100 \mu\text{m}$). This was followed by traversing the measurement volume in pre-defined increments (along the negative y -direction) using the motorized laboratory jack. For both the lens with $F = 120$ mm ($d_{\text{ma}} = 42.0 \mu\text{m}$) and $F = 261$ mm ($d_{\text{ma}} = 80.3 \mu\text{m}$), the measurement volume was traversed in $10 \mu\text{m}$ increments followed by $5 \mu\text{m}$ when the approximate distance from the wall to the theoretical centre of

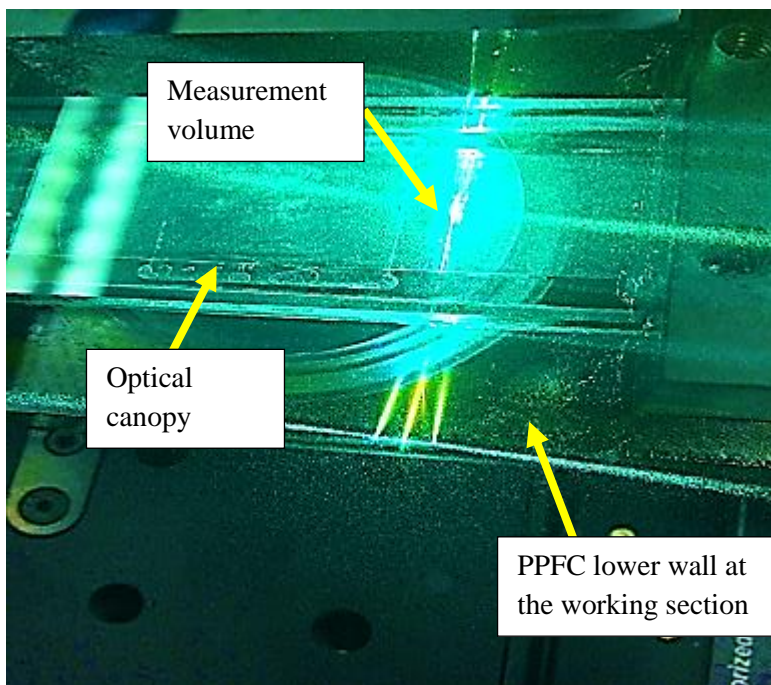


Fig. 4.4

Measurement volume being traversed into the wall at the working section of the PPFC for determination of the measuring position (i.e. absolute location of the measurement volume). The near-wall beam configuration did not require tilting of the probe to capture the velocity gradient near the wall.

the measurement volume was less than $\frac{1}{2} d_{ma}$. As a review from Appendix 2, d_{ma} refers to the actual measurement volume at the working section and not the theoretical (d_m). The number of $5 \mu\text{m}$ steps recorded was solely a function of being able to capture velocity data since the data rates of 10-100 Hz, together with an increase in noise, is not uncommon as the measurement volume starts to sink into the wall (Durst et al. 1996). Furthermore, the changeover from 10 to $5 \mu\text{m}$ steps was calculated based on the reference position y_r and the size of the measurement volume diameter. As an example, for the $F = 120 \text{ mm}$ lens it was expected that the measurement volume would start to embed into the wall after approximately eight individual $10 \mu\text{m}$ steps since $y_r - (d_{ma}/2) = 80 \mu\text{m}$. The intent of using smaller traversing steps (i.e. $5 \mu\text{m}$ at the wall) was to capture as many velocity data points (as the measurement volume started to sink into the wall) as possible to clearly distinguish a departure in the mean velocity (slope change of the streamwise mean velocity) during post-processing of the data. The assumed reference location of the measurement volume was established using the receiver viewport (imaging of the beams' crossing) by viewing the beams' crossing until it was fully embedded into the wall (inability to detect the beams' crossing via the viewport). This was followed by traversing in the positive y -direction by the amount that is equal to $\frac{1}{2}d_{ma}$ (centre of the measurement volume positioned at the wall). Once this approximate position was established, the measurement volume was traversed $100 \mu\text{m}$ in the positive y -direction. This process is defined in Fig. 4.5 for further clarity. Fig. 4.6. shows the post-processing result from the process outlined above. The streamwise mean velocity was plotted on the y -axis and the micro-traverse readings (assumed y -position) on the x -axis. For both lenses under consideration, the results indicate that as the measurement volume starts to embed into the lower wall there is an evident increase in the measured streamwise velocity (i.e. abrupt slope change) in comparison to the steady approach towards zero velocity which the no-slip condition implies. This departure in the mean velocity is evident at $y \approx 20$ and $y \approx 40 \mu\text{m}$ for the $F = 120$ and $F = 261 \text{ mm}$ lenses, respectively. According to Durst et al (1988), this abrupt increase in velocity is attributed to the resultant mean velocity being located at the actual centre of the measurement volume which is covered by the fluid (not the embedded portion). Since it is general practice to assign the resultant mean velocity to the centre of the theoretical volume, larger velocities were measured. Furthermore, according to Durst

et al (1988), the measurement point where the profile of the measured mean velocity changes abruptly is taken as the first measurement point. In addition, this first measurement point has an approximate distance from the wall of $\frac{1}{2}d_{ma}$ (Durst et al. 1988). A second technique suggested by Durst et al (1988) was to extrapolate the velocity data points (using linear regression) prior to the abrupt slope change to find the zero velocity point which can be considered to be the wall location. Using 2nd order regression (i.e. a polynomial fit) for all four data sets in Fig 4.6 indicates an approximate intercept in the region $y \approx -8 \mu\text{m}$. This result shows that the measurement volume was initially positioned ($y_r \approx 100 \mu\text{m}$) $\approx 10 \mu\text{m}$ too close to the wall as it is clearly short of the origin. However, as noted by Hutchins & Choi (2002), the accuracy of this method is limited, as the best-fit line (as shown in Fig. 4.6) is itself fraught with error. Both of the techniques validated the manual positioning of the measurement volume with respect to the wall to within $\pm 10 \mu\text{m}$.

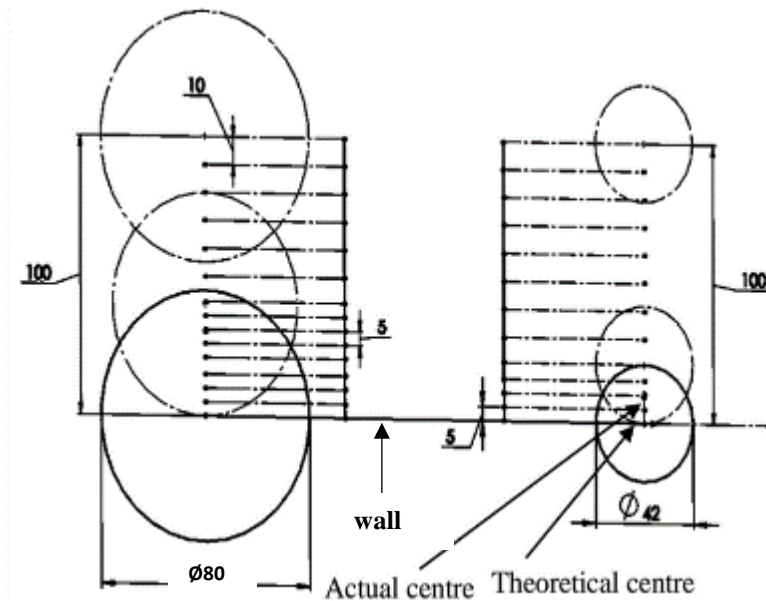


Fig. 4.5

An outline of the initial set-up procedure to determine the measurement volume location in reference to the wall. All units in the figure are in μm . The nearest measurement point to the wall was $\approx 20 \mu\text{m}$ and $\approx 40 \mu\text{m}$ for the $F = 120 \text{ mm}$ and $F = 261 \text{ mm}$ lenses, respectively.

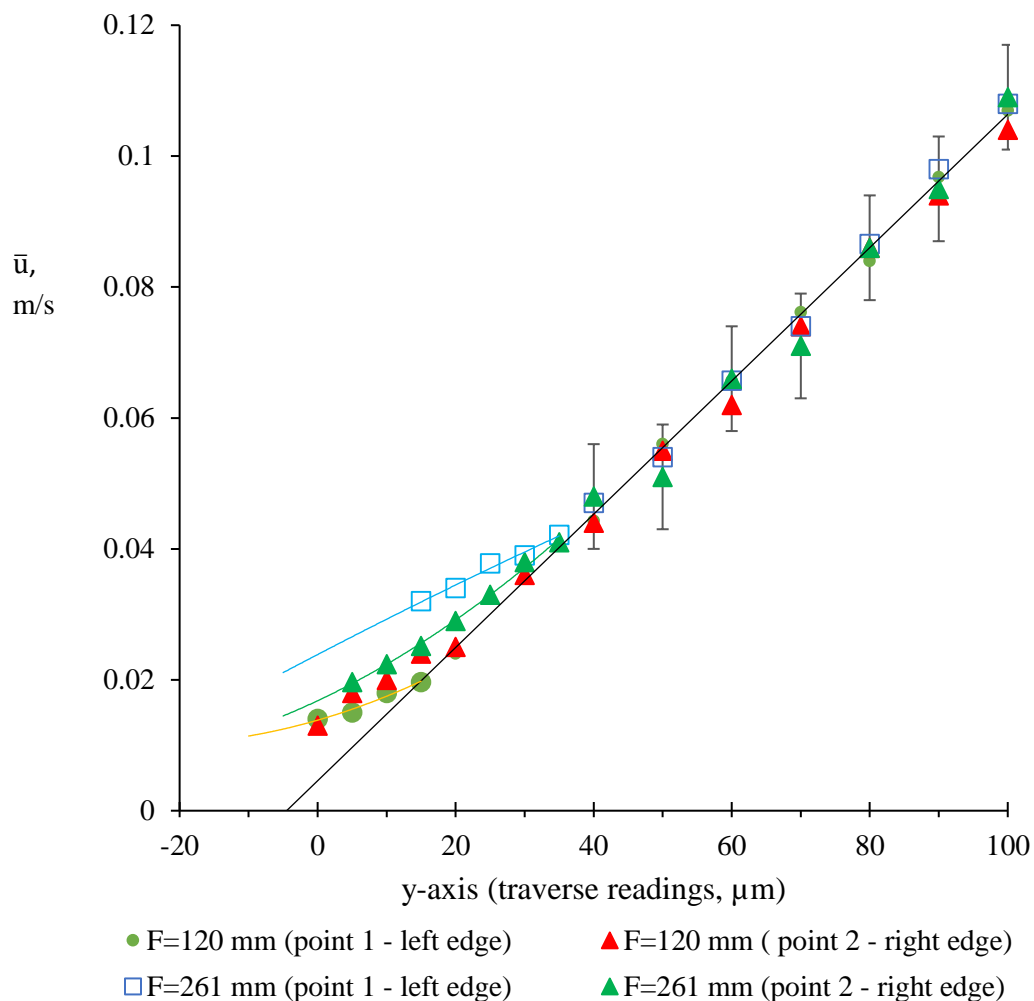


Fig 4.6 Streamwise mean velocity $\bar{u}(y)$ plotted against position readings of the motorized laboratory jack to demonstrate abrupt slope change. Points 1 and 2 refer to the positions on the microscopy slide (at $2z/w = 0$), left and right edges being $\approx \pm 11$ mm from the centre of the slide. Experiment was performed using $Q = 7.50 \pm 0.075$ mL/s. The uncertainty error bars are only shown for the velocity data points related to measurements with the $F = 261$ mm lens (point 2).

4.3.1 Spatial Uncertainty of Measurement Volume Position along the Streamwise and Spanwise Directions (x and z, respectively).

To determine the measurement volume spatial uncertainty in the streamwise (x-) and spanwise (z-) directions, both the estimated datum location and the cross-slide milling table uncertainties were considered. For the fully-developed steady laminar and low-Re turbulent (transitional regime) flows reported in Appendix 2, the measurement volume spatial uncertainty in those two directions is less significant. This is because the change in the streamwise and wall-normal mean velocity (\bar{u} and \bar{v} , respectively) in those directions is prevalent by the uncertainty in the velocity readings (sampling error only since $\partial\bar{u}/\partial x \approx 0$). However, for the backward-facing step flow cases (steady and pulsatile inlet flow) the analysis presented in this section should be considered since the measurement volume spatial uncertainty adds to the uncertainty in the mean velocity ($\partial\bar{u}/\partial x \neq 0$ prior to relaminarization) as per Iyer & Woodmansee (2005). Hence, the addition of the term $\left(\frac{\partial\bar{u}}{\partial x}\right)^2 \epsilon_x^2$ was added to Eq. (4-2) to determine the overall error in the mean velocity.

All of the flow measurements reported in Chapter Five were captured at the midplane of the working section (i.e. $2z/w = 0$;) and, hence, it was important to estimate the spatial uncertainty of the measurement volume associated with this position. To position the measurement volume at $2z/w = 0$, a datum associated with the vertical side wall (closest to the probe end) was located. This was then followed by traversing the measurement volume in the amount of $w/2 = 8.75$ mm. To determine the z-position of the measurement volume in reference to the vertical side wall, the probe lens ($F = 120$ mm) was initially positioned 120 mm away from the glass canopy wall (using a Vernier indicator: Starrett electronic caliper with a range of 150 ± 0.02 mm). Following this, the measurement volume was traversed in $10 \mu\text{m}$ (i.e. 0.01 mm) increments (along the z-direction using the cross-slide milling table) until the measurement volume appeared inside the flow channel (which illuminated when exposed to the recirculating fluid). The latter was also verified by visually observing the beams' crossing through the receiver viewport and monitoring the data rate (\dot{N}) in FlowSizer. Starting at the assumed reference position ($z_r = 20 \mu\text{m}$) from the wall (centre of the volume to the wall distance corresponds to $\approx \frac{1}{2}d_{ma}$), $\bar{u}(z)$ velocity measurements were captured over a range, 20-200 μm (i.e. $-0.99 \leq 2z/w \leq -0.97$). The

measurement of the velocity was repeated four times and each time the set-up was restarted to capture the positioning error of the technique. The flow rate for the velocity measurements was set to $Q = 3.70 \pm 0.039$ which corresponded to $Re_m = 600$. These results are shown in Fig. 4.7. In addition, the velocity data at each z -position was ensemble averaged (over the four trials) and curve fitted with a 2nd order polynomial. The first polynomial regression curve shown in Fig. 4.7. was extrapolated to find the zero velocity point which can be considered to be the side wall location (Durst et al. 1988). The second polynomial was corrected by forcing the curve to the no slip condition at the wall ($\bar{u} = 0$ for $2z/w = -1$). Fig. 4.7 shows that the uncertainty associated with the initial $z_r = 20 \mu\text{m}$ measurement volume position was $\pm 25 \mu\text{m}$. This process was repeated for the $F = 261 \text{ mm}$ lens and the results were consistent. It should be noted that with the latter the considered value for the initial estimate was $z_r \approx 40 \mu\text{m}$ given the larger measurement volume (i.e. $d_{ma} = 80.3 \mu\text{m}$).

Furthermore, other uncertainties associated with the z -position of the measurement volume were $\epsilon_{\text{width}} = \pm 20 \mu\text{m}$ (channel width obtained via digital vernier caliper), $\epsilon_{\text{cross-slide}} = \pm 10 \mu\text{m}$ (cross-slide milling table manufacturer reported uncertainty). The sum of all squares was thus calculated to be $\epsilon_z^2 = \epsilon_{\text{cross-slide}}^2 + \epsilon_{\text{width}}^2 + \epsilon_{\text{side_datum}}^2 = \pm 37.7 \mu\text{m}$. It should be noted that traversing in the z -direction with the cross-slide milling table is related linearly to the measurement volume movement (in the same direction) but not of equal amount. As an example, if the cross-slide table was moved by a certain amount in the z -direction it would not displace the measurement volume of equal amount in that direction. In the present study, it was decided to traverse in $10 \mu\text{m}$ increments (i.e. minimum dial graduations) to capture a sufficient number of velocity data points near the side wall as illustrated in Fig. 4.7. To define the relationship between the cross-slide milling table and the measurement volume displacement, Snell's law was used which is defined as $n_1 \sin(\theta_1) = n_2 \sin(\theta_2)$, where n, θ were, respectively, the refractive index of each medium and the angle that the incident beam makes with the normal of the boundary (Gu et al. 2008). Using Snell's law and a ray analysis (using a CAD interface, CATIA VR5) it was possible to plot the relationship between the cross-slide table and the measurement volume spatial positions. The data were fitted with a linear regression model

($r^2 = 1$) which showed that the measurement volume and the cross-slide z-direction spatial position relate as $z_{m.v.} = 0.35z_{cross-slide}$. Thus, moving the cross-slide table by 10 μm in the z-direction moves the measurement volume by 3.5 μm inside the working section (i.e. $F = 261$ mm lens). This analysis was complete for both lenses (different beams' half angle) to ensure that the reported z-positions were correct. It should be noted that for this analysis the refractive index for air, the cell fluid (DMEM mixture) and the optical window were 1.00, 1.34 and 1.52, respectively (Avari, 2015).

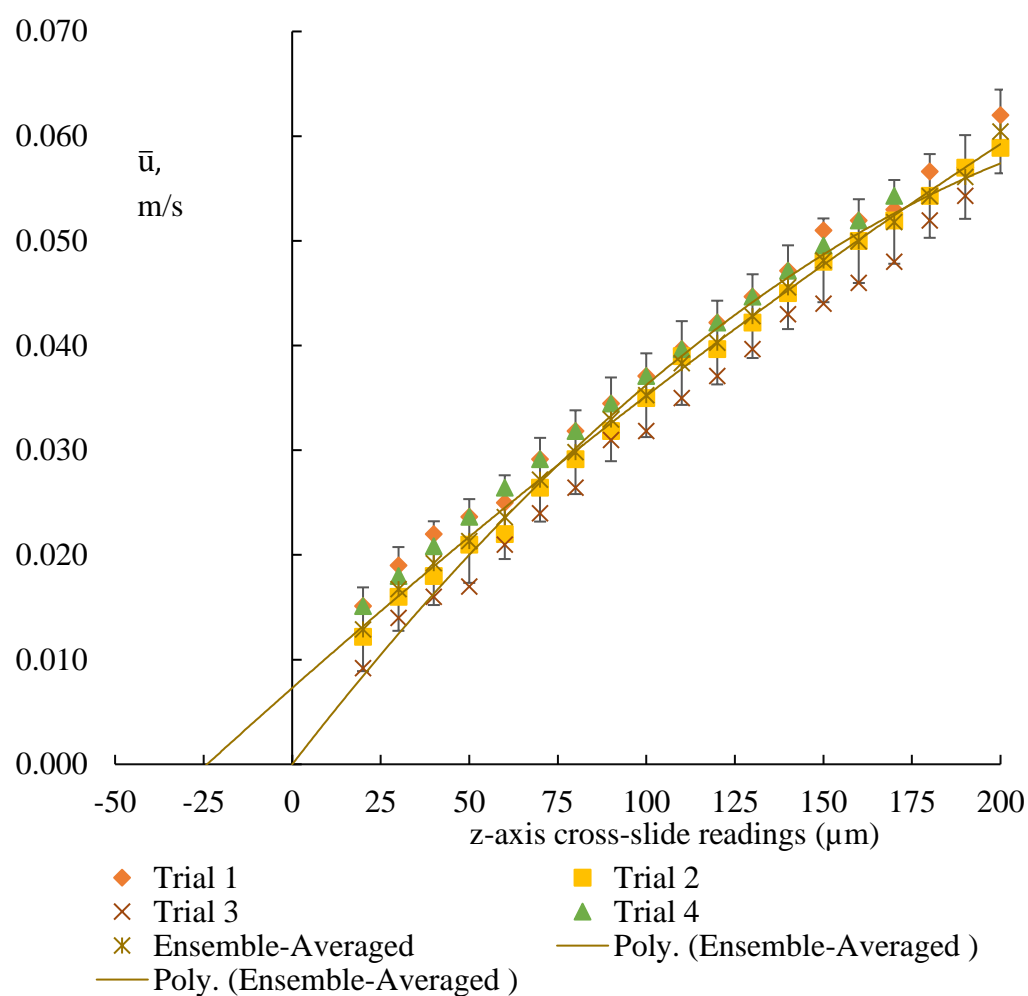


Fig. 4.7 Spanwise profile of the streamwise mean velocity $\bar{u}(z)$ plotted against the z-axis at the working section at $y/h = 0.5$. The simulated flow rate was 3.90 ± 0.039 mL/s ($Re_m = 600$).

To locate the measurement volume at the step edge (for the backward-facing step flow case, see Fig. 3.15 for geometry of the working section) with reduced spatial uncertainty in reference to the x-direction, a fixture was designed and built as per Fig. 4.8. This procedure consisted of launching the measurement volume (blue beams) for the $F = 261$ mm lens (used with the backward-facing step velocity measurements to simultaneously capture u and v velocity components) into a 105 μm core multimode fiber ($\text{\O}105 \mu\text{m}$, 0.22 NA, SMA-SMA fiber patch cable from Thorlabs) whilst monitoring the power output (i.e. mW) using a power-meter (PM100D from Thorlabs). As per Fig. 4.8, the fiber ferrule was centred and mounted inside a kinematic mount (SM1-threaded kinematic mount for thin $\text{\O}25.4$ mm optics from Thorlabs) for fine-adjustment of the y-position (i.e. better than $\pm 5 \mu\text{m}$). In addition, the kinematic mount assembly was mounted on a x – y – z traverse (MAX312 from Thorlabs with accuracy better than $\pm 1 \mu\text{m}$) for even finer adjustment of the y-position. These traverse units were only used to fine-tune the position of the ferrule centre in the y-direction and not to deviate away from the pre-determined x-distance between the datum plate (precision ground aluminum plate with a thickness uncertainty of $\pm 50 \mu\text{m}$) and the ferrule centre axis. This pre-determined distance was equal to the distance between the channel datum (flow entry position of the channel) and the step edge. To launch the measurement volume (i.e. each beam at 25 mW) inside the core of the multi-mode fiber both the LDV cross-slide milling table (in the x-direction) and the micro-traverse (fiber assembly) were used. The power output from the other end of the multi-mode fiber (mounted to the power meter with a SMA connection) was monitored whilst positioning the measurement volume into the core. Once the y-axis position was optimally set (i.e. reaching maximum power value), the LDV cross-slide milling table was used to fine-tune the position in the x-direction to maximize the power output. Given that the core diameter of the multi-mode fiber was $105 \pm 2.1 \mu\text{m}$ (manufacturer reported) and the measurement volume was $80.3 \pm 10.7 \mu\text{m}$, there was a region inside the ferrule core (x-direction) of approximately $\pm 12.3 \mu\text{m}$ for which the power output remained approximately constant. The uncertainty of the measurement volume position at the step edge as a result of the multi-mode fiber alignment process was, therefore, $\pm 12.3 \mu\text{m}$. The additional uncertainty as a result of this process was the predetermined distance between the aluminum datum plate and the centre axis of the multi-mode fiber (kinematic assembly).

This distance was measured with a digital Vernier caliper three times and the average value was 217.50 ± 0.05 mm. This was accomplished by setting the vernier centre-gauge-locators (as per Fig 4.8) to predetermined positional holes (i.e. $\approx \emptyset 0.1$ mm) for accurate distance determination. Hence, the total spatial uncertainty of the measurement volume at the step edge was $\epsilon_{\text{datum}_x} = \sqrt{12.3^2 + 50^2} = \pm 51.4$ μm . In addition, the uncertainty of the working section length (i.e. length of the glass canopy corresponding to the working section, $l = 82.55$ mm) was measured with a digital vernier caliper to be ± 25 μm . It should be noted that $l = 82.55$ mm is the downstream length (from the step edge) of the working section which extends across the entire length of the glass canopy (i.e. measurable region). Hence, the total spatial uncertainty of the measurement volume in the x-direction was $\epsilon_x^2 = \epsilon_{\text{cross-slide}}^2 + \epsilon_{l_d}^2 + \epsilon_{\text{datum}_x}^2 = \pm 58$ μm , where $\epsilon_{\text{datum}_x}$ is the value related to the multi-mode fiber alignment of the measurement volume described above. Following the initial alignment of the measurement volume and the step edge, the flow channel was mated (flush-mounted) with the aluminum block datum and clamped into position. This ensured that the measurement volume was positioned at the step edge ($x = 0.0 \pm 51.4$ μm) inside the working section. It should be noted that the ± 51.4 μm corresponds to the uncertainty of only the initial measurement volume location at the step edge. The total uncertainty (ϵ_x) of the measurement volume position in the x-direction includes other uncertainties listed above, all of which influence the uncertainty of the measurement volume position along the x-direction. The latter uncertainty is relevant for the backward-facing step flow cases where streamwise and wall-normal velocity profiles were measured across the channel height at various downstream locations from the step edge.

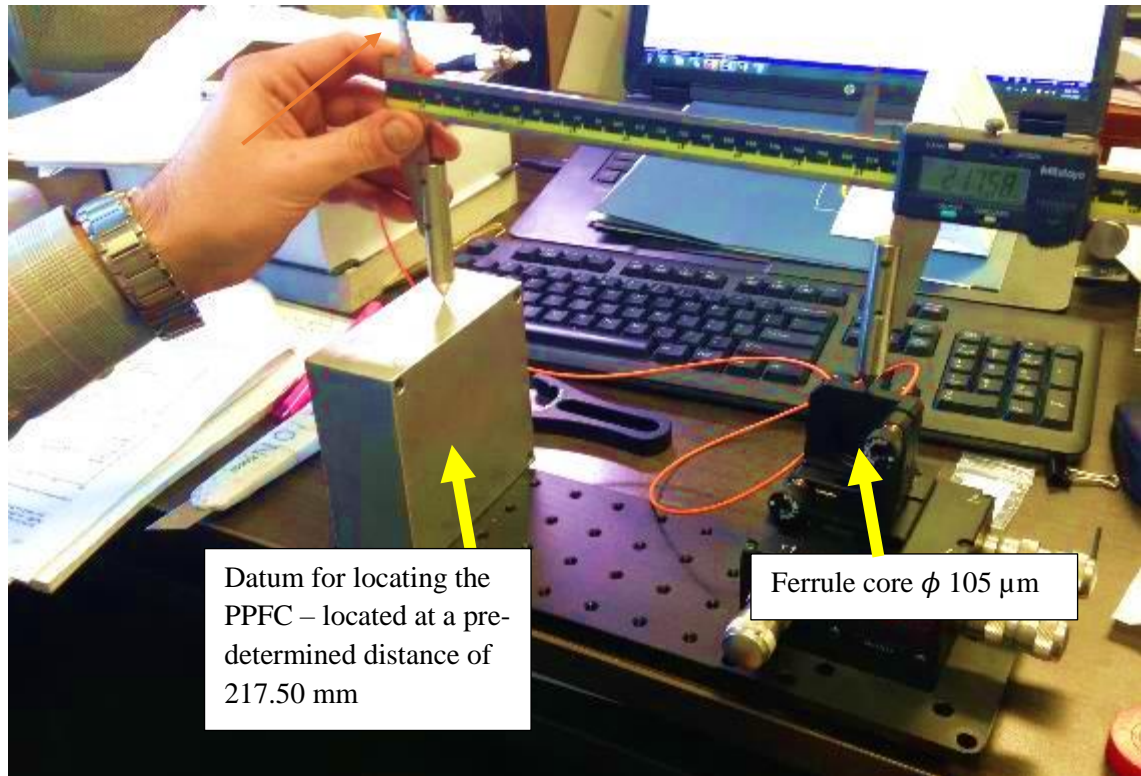


Fig. 4.8 Fixture for positioning the measurement volume on the step edge ($x/l = 0$) at the working section to establish a starting position for the downstream measurements of the $\bar{u}(y)$ and $\bar{v}(y)$ velocity profiles. The fixture was also used without the obstacle for steady and turbulent flow measurements at the working section. The other end of the fiber was connected to a power meter to measure the power (i.e. mW) to ensure optimal alignment between the measurement volume and the ferrule core diameter.

4.4 Derivation of Wall Shear Stress from Near-Wall LDV Data and its Uncertainty

The wall shear rate ($\dot{\gamma}$) and stress (τ_w) uncertainty (under steady laminar flow) is predominantly a result of velocity measurement and curve fitting approximation errors (Fatemi & Rittgers, 1994). As explained in section 4.1, the total error associated with the velocity data results from the LDV instrument (precision error) and the positioning system together with the uncertainty of the measurement volume position in reference to the wall. This section demonstrates how the accuracy of the wall shear rate $\dot{\gamma} := \left(\frac{d\bar{u}(y)}{dy} \Big|_{y=0} \right)$ via curve fitting was evaluated for steady laminar flow. In addition, determination of the wall shear

stress $\left(\mu \frac{d\bar{u}(y)}{dy}\right)_{y=0}$ uncertainty was also discussed and the results were presented in Appendix 2 as part of probe validation. Factors affecting the curve fitting approximation error include: (1) wall offset (location of the closest velocity measurement point captured near the wall), (2) the number of data points captured in the wall-region and the spacing between each subsequent point (in the y-direction) and (3) the order of the curve fitting (Fatemi & Rittgers, 1994). To select the correct regression model (i.e. linear or higher order curve fitting) for the present study, the relative error was estimated based on $\left|(\dot{\gamma}_{\text{est}} - \dot{\gamma}_{\text{theory}})/\dot{\gamma}_{\text{theory}}\right| \times 100\%$, where $\dot{\gamma}_{\text{est}}$ refers to either experimental or theoretical (no experimental error, based on Eq. 3-4) velocity data at the wall. In addition, $\dot{\gamma}_{\text{theory}}$ refers to the theoretical shear rate at the wall calculated using Eq. 3-7 (hence, no curve fitting errors). The latter is an acceptable approach to determine the shear rate error and was also considered by both Avari (2015) and Lou et al (1993).

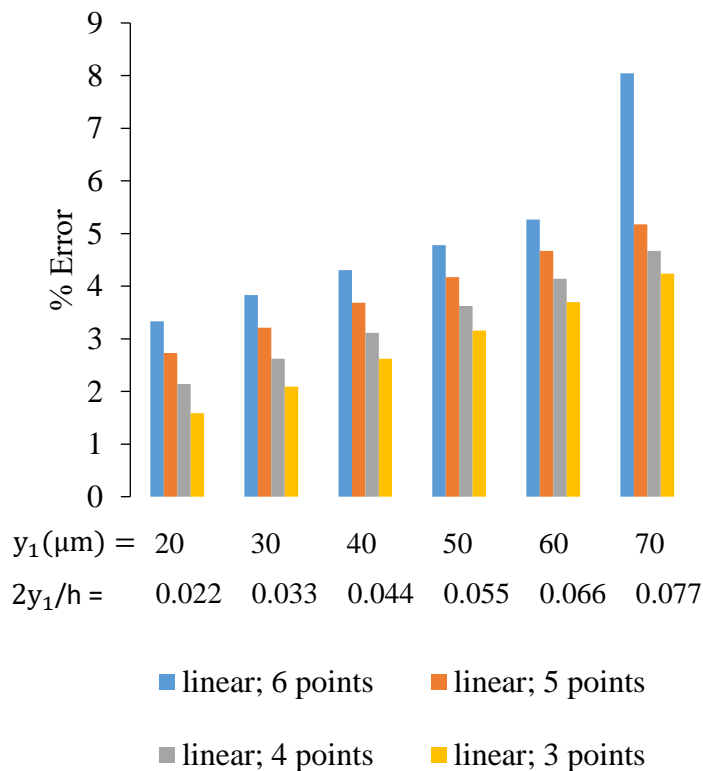


Fig 4.9 Percent Shear Rate Error for linear regression (theoretical data points) using $N_p = 3, 4, 5$ and 6 points (including the zero velocity data point at the wall). The points $y_1 = 20, 30, 40, 50, 60$ and $70 \mu\text{m}$ indicate distances from the wall (first measurement point considered). The general expression for the linear (straight-line) regression can be expressed as $u = by + b_0$, where b is the slope and b_0 is the intercept (Hutchins & Choi, 2002).

To evaluate the accuracy of the curve-fitting approximation technique both the linear and 2nd order polynomial regression are used on the estimated velocity data points (measured and based on the analytical equation) close to the wall which can be expressed as a polynomial power series (Fatemi & Rittgers, 1994):

$$u(y) = a_0 + a_1y + a_2y^2 + a_3y^2 + \dots + a_ny^n \quad (4-3)$$

$$\text{for } 1 \leq n \leq 8; n \leq N_p - 1$$

where n, N_p were, respectively, the degree of the polynomial and the number of velocity data points fitted near the wall. For steady laminar flow, both the theoretical and experimental data were evaluated for $Q = 3.90 \pm 0.039$ mL/s ($Re_m = 600$). It should be noted that there have been reported studies in the literature that have applied higher-order polynomial regression (i.e. up to 5th order) to the full cross-sectional velocity profiles (Bell et al. 1989; Shu & Hwang, 1991). However, the most common approach reported to determine the wall shear stress has been to either use a linear or even a 2nd order polynomial to fit 1 to 3 velocity data points captured at the wall together with the zero-velocity point at the wall (Fatemi & Rittgers, 1994).

Furthermore, Fig. 4.9 shows a linear fit analysis on the theoretical velocity data points at the wall with $N_p = 3, 4, 5$ and 6 (including the zero velocity point at the wall) for various $y_1 = 20, 30, 40, 50, 60$ and 70 μm starting positions from the wall (referring to $2y/h = 0.022, 0.033, 0.044, 0.055, 0.066$ and 0.077 ; where y is taken as zero at the wall). It is evident from Fig. 4.9 that the linear fit error is associated to y_1 , with the largest and smallest errors occurring when $N_p = 6$ and 3 , respectively. The largest error observed from Fig. 4.9 is $\approx 8\%$ at $y_1 = 70$ μm and considering $N_p = 6$. In general, linear regression using $N_p = 3$ was consistently more accurate for all starting positions from the wall. In addition, the wall shear rate deduced from the linear regression model is consistently underestimated in comparison to the theoretical values (i.e. using Eq. 3-7).

Moreover, using a 2nd order polynomial curve to fit the theoretical data points for various starting positions (i.e. $y_1 = 20, 30, 40, 50, 60$ and $70 \mu\text{m}$) and number of points ($N_p = 3, 4, 5$ and 6) results in a significantly smaller relative error (i.e. $< 1\%$) in comparison to the linear fit. In fact, these results were expected given the parabolic nature of the velocity profile and no experimental error as a result of the LDV system.

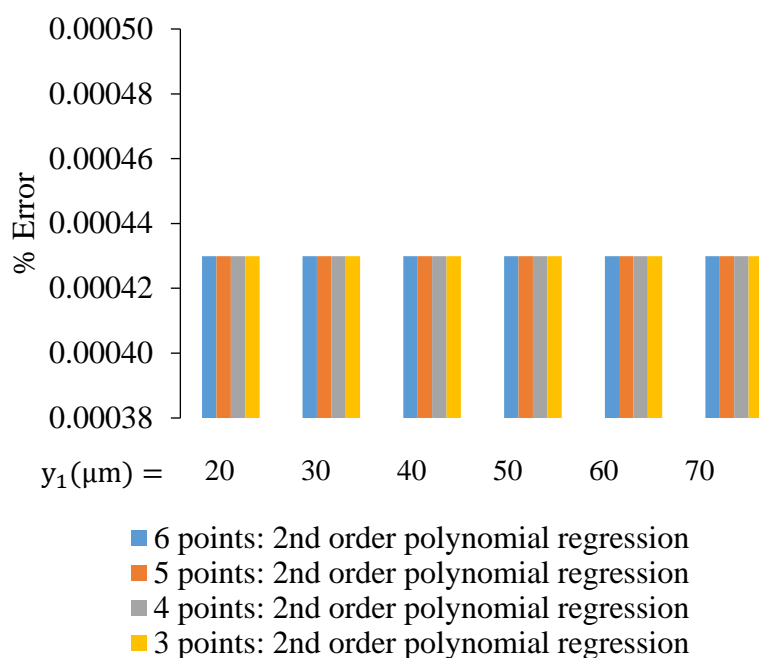


Fig 4.10 Percent Shear Rate Error for 2nd order polynomial regression (theoretical data points) using $N_p = 3, 4, 5$ and 6 points. The points $y_1 = 20, 30, 40, 50, 60$ and $70 \mu\text{m}$ indicate starting points from the wall. It should be noted that using this approximation yields an exact solution of the shear rate and the reported error in the y-axis is a result of rounding errors associated with Eq. 3-7. These results are in agreement with the findings from Fatemi & Rittgers (1994).

Given that the 2nd order curve fitting produced an exact fit on the theoretical data points (refer to Fig. 4.10), it was used to perform a similar analysis on the experimental data points captured at the wall with LDV. Fig. 4.11 shows the results of this analysis and it can be seen that amongst the different regression curves with a different number of experimental data points, $N_p = 6$ has the overall smallest error which is $< 5\%$ at $2y/h = 0.022$ and 0.033 . A polynomial regression trend line in Fig. 4.11 shows a slight increase in error for $N_p = 6$

as $2y/h = 0.055$ is approached followed by a gradual decrease in error thereafter with $< 5\%$ at $2y/h = 0.077$. Similar observations are seen for $N_p = 5$ across the various measurement start positions. It is worth noting that up to $y \leq 100 \mu\text{m}$ (or $2y/h \leq 0.11$) velocity measurements were recorded every $10 \mu\text{m}$ whereas, for $y > 100 \mu\text{m}$ (or $2y/h > 0.11$) it was every $50 \mu\text{m}$. The latter also affected the shear rate error when the number of points considered extended into the $y > 100 \mu\text{m}$ (or $2y/h > 0.11$) region. However, given that the smallest error is shown for $N_p = 6$ and a starting point of $2y/h = 0.022$, this was not relevant. It should be noted that error trends were fairly consistent based on the streamwise velocity profiles near the wall obtained for $Re_m = 100, 600, 900$ and 1240 for both the $F = 120$ and 261 mm lenses, with the main difference being the error amount of 11% for the $F = 261$ mm lens as a result of a larger wall offset (i.e. no measurement was possible at $2y/h = 0.022$ and 0.033 with the $F = 261$ mm lens given the wall offset condition explained in the preceding sections).

Another important aspect of this analysis to note is that all velocity data at the wall were repeated several times (i.e. 3-5 times) to take the ensemble average and smooth out the data. The latter is a result of errors in the velocity and position via traverse uncertainty and other near-wall influences such as background noise and wall reflections (Fatemi & Rittgers, 1994). The maximum difference between the individual velocity data points (for each data run) and the ensemble average (all the runs averaged) was within the experimental uncertainty. Hence, for the steady laminar flow in the present study a 2nd order polynomial curve fit was used considering $N_p = 6$ and $y_1 = 20 \mu\text{m}$ to deduce the wall shear stress. Again, for the $F = 261$ mm lens, the shear stresses were reported based on the 2nd order curve fit using $N_p = 6$ and $y_1 = 40 \mu\text{m}$.

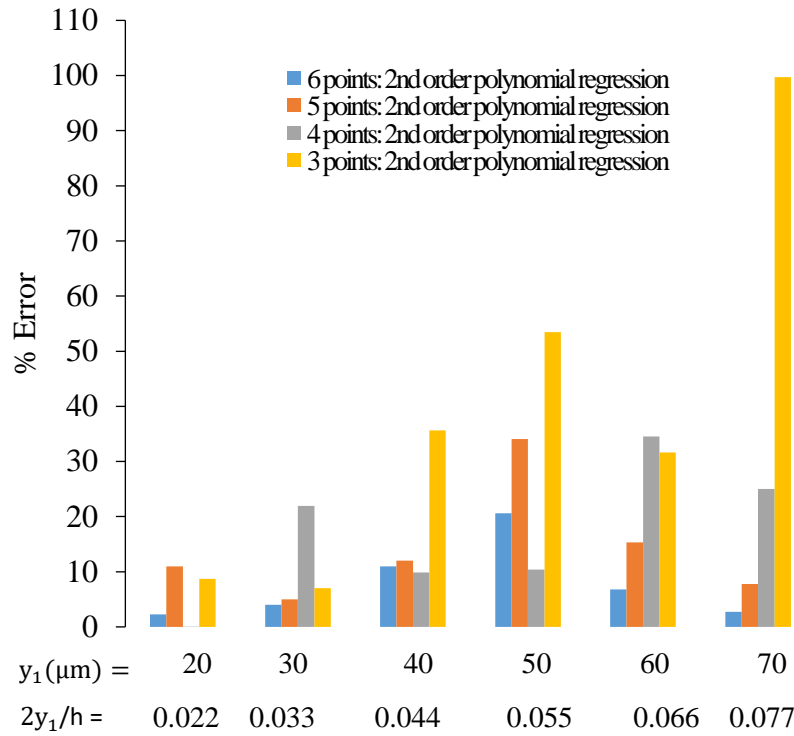


Fig 4.11

Percent Shear Rate Error for 2nd order polynomial regression (LDV data points) using $N_p = 3, 4, 5$ and 6. The points $y_1 = 20, 30, 40, 50, 60$ and $70 \mu\text{m}$ indicate starting points from the wall.

Furthermore, the uncertainty in the wall shear stress, τ_w , can be defined as follows (Avari, 2015):

$$\varepsilon_{\tau_w} = \sqrt{\sum_{i=1}^n \left[\frac{\partial \tau_w}{\partial x_i} \varepsilon_{x_i} \right]^2} \quad (4-4)$$

$$\varepsilon_{\tau_w}^2 = \left(\frac{\partial \tau_w}{\partial \dot{\gamma}} \right)^2 \varepsilon_{\dot{\gamma}}^2 + \left(\frac{\partial \tau_w}{\partial \mu} \right)^2 \varepsilon_{\mu}^2$$

$$\varepsilon_{\tau_w}^2 = \mu^2 (\varepsilon_{\dot{\gamma}}^2) + \dot{\gamma}^2 (\varepsilon_{\mu}^2)$$

where $\frac{\partial \tau_w}{\partial x_i}$ and ε_{x_i} are the partial derivative of τ_w with respect to the individual variables contributing to the shear stress value and the uncertainty of the individual variables involved in the calculation of τ_w , respectively. The absolute uncertainty associated with the dynamic viscosity (ε_{μ}) of the fluid was ± 0.0012 cP and for $\varepsilon_{\dot{\gamma}}$ the relative uncertainties were approximately ± 2.3 and ± 11.0 % ($F = 120$ and 261 mm lenses, respectively) across the range of Re . The τ_w values, together with the uncertainties for $Re_m = 100, 600, 900$ and 1240 , under steady laminar flow are reported in Appendix 2.

4.5 Hemodynamic Pulsatile Pump Performance Evaluation

As reviewed in Chapter Three, the pulsatile flow pump was used to supply the PPFC with a steady ($1 \text{ mL/s} \leq Q \leq 25 \text{ mL/s}$) and pulsatile flow (normal carotid waveform with $f = 1.08 \text{ Hz}$, $Q_{\text{max}} = 20 \text{ mL/s}$). The higher flow rate (i.e. programmed flow rate of $Q = 25 \text{ mL/s}$) was used for studying turbulent flow inside the PPFC and was described in Appendix 2. The manufacturer reported (Shelley Medical Imaging Technologies, Canada) accuracy of the pump is specified as $\pm 3\%$ over the flow rate range of 0.01 to 35 mL/s. However, since there have been numerous modifications (S83-93-MO Parker Stepper Motor replaced together with gearing and plunger) completed on the pump it was important to re-evaluate the accuracy and repeatability (precision) of the pump under both steady and pulsatile operation. Since the velocity data pairs (u, v) at the working section required capture (with the LDV system) over several strokes and cycles (to obtain a sufficient number of velocity data points, N) for both steady and pulsatile flow, the cycle-to-cycle (pulsatile flow) and stroke-to-stroke (steady and pulsatile flow) repeatability was evaluated. For review, the motor-to-home stroke refers to the distance traveled by the piston away from the motor and towards the home position that was registered by the pump using a limit switch.

This section also presents a modeling analysis of the effects of tubing length and compliance on the damping of the carotid waveform. This analysis helps in the understanding of where the maximum attenuation of the waveforms occurs along the closed-loop flow circuitry. Findings from this analysis will help with prospective work to minimize waveform attenuation via reconfiguring the pump together with selecting the ideal tubing (i.e. length, material, diameter) and/or re-programming the waveform (at the pump) to yield a desired shape at the working section of the channel.

To evaluate the performance of the pump under steady operation, a simple test system was used consisting of the pump, a 25 cm length of 6.35 mm diameter (inner dia.)

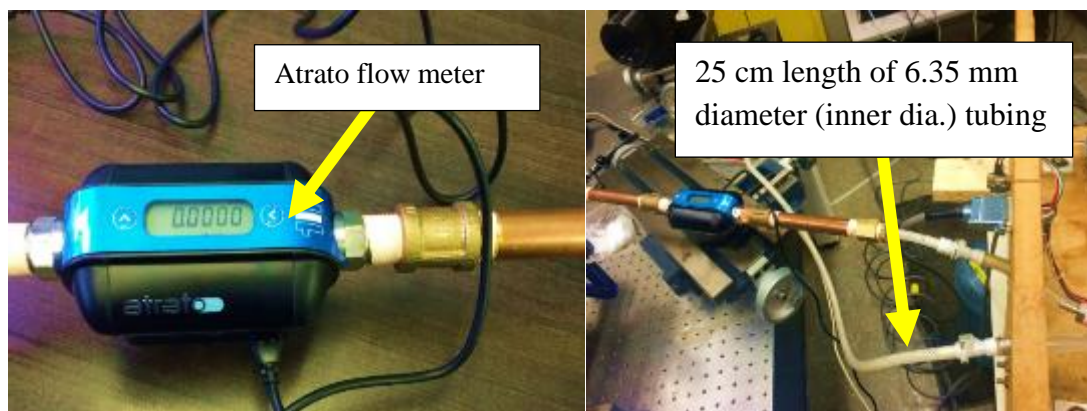


Fig. 4.12. Transit-time ultrasonic flow meter mounted in-line between the pump outlet and reservoir. The flow meter was connected to the PC using a USB cable. The software allowed direct monitoring of the flow rate.

tubing connected between the outlet and a 4L reservoir and an in-line transit-time ultrasonic flow meter (Atrato model 720-V-0-0-SD; manufactured by Titan Enterprises Ltd.) to measure the steady flow rate. The instrument was able to measure volumetric flow rate between 0.01-1.70 lpm (0.0026-0.450 gpm) with an accuracy and repeatability better than $\pm 1\%$ of a reading (over the flow range specified) and $\pm 0.1\%$ of full scale output (0.16-28.0 mL/s), respectively. The flow meter works on the principle of time-of-flight (in contrast to the Doppler shift measurement method) which measures the time for the sound to travel between the transmitter and the receiver (Tavoularis, 2005). The two transmitters send pulsating ultrasonic waves (in predefined frequency via PZT 5A transducers) to the receiver (mounted upstream and downstream of their mate transmitter) and the difference in frequency is proportional to the average fluid velocity (the frequencies of the two pairs differ since sound travels faster downstream than upstream). This method of measurement is insensitive to the fluid viscosity, temperature and density. In addition, this method of measurement does not require flow seeding which is required with the Doppler shift method to generate reflected signals (Tavoularis, 2005). For all the experiments, the DMEM mixture (as per section 3.4) was used as the recirculating fluid at 37°C. The experimental flow circuitry is shown in the Fig. 4.12 for reference to the reader.

Using the experimental configuration described above, programmed steady flow rates ranging from 1 to 15 mL/s were measured using the flow meter. The programmed flow rates under test were $Q = 1, 5, 10$ and 15 mL/s. Each flow rate was measured over 20

strokes consisting of 10 motor-to-home strokes and 10 home-to-motor strokes. The sampling frequency of the transit flow meter was ≈ 10 Hz (10 flow realizations per second) which allowed for a sufficient number of data points to obtain statistical convergence for both the mean and r.m.s. quantities (i.e. \bar{Q} , r.m.s. Q').

As an example, for the programmed $Q = 10$ mL/s over 20 strokes leads to a sampling time of approximately 20 minutes. This captured approximately 12,000 data points in total corresponding to approximately 6,000 data points for each stroke direction (motor-to-home and home-to-motor). The measured data points pertinent to a given stroke direction were time-averaged (i.e. to compute \bar{Q}) to make a comparison with the prescribed flow rate at the pump. The result can be seen in the Fig. 4.13. The 12,000 data points were also time-averaged to obtain the mean flow across a total of 20 strokes and that is also shown in the plot.

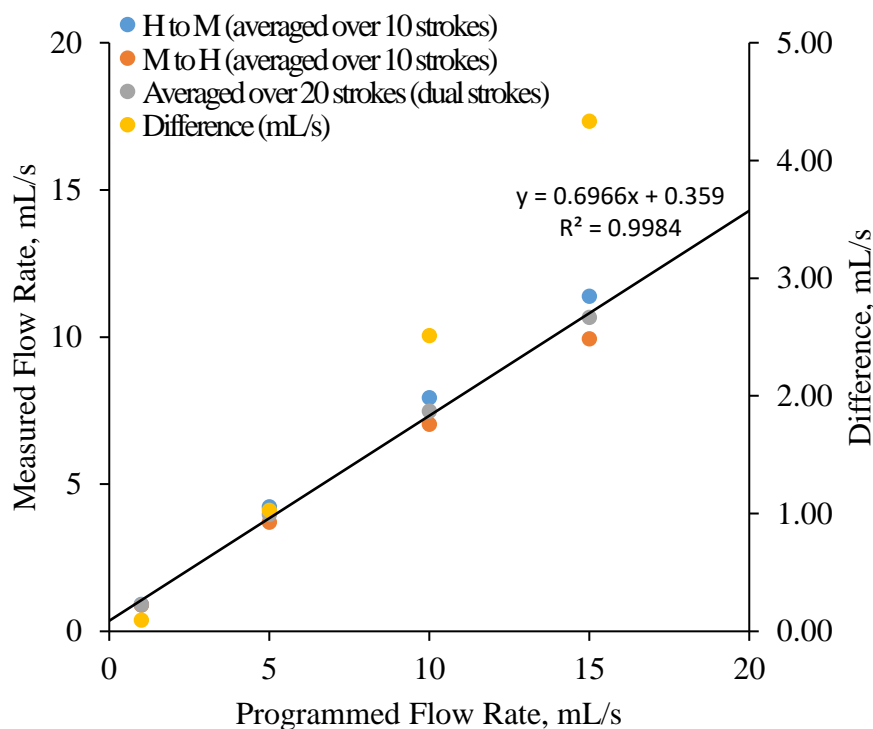


Fig. 4.13. Measurement of linearity and accuracy of the steady flow produced by the pump for programmed $Q = 1, 5, 10$ and 15 mL/s. The trend line in the figure represent linear regression (averaged data points). The difference refers to the linear regression values subtracted by the programmed values.

The linear regression (trend line in the plot) of the data (averaged over 20 strokes) has a slope of 0.69 and y-intercept of 0.35 mL/s. As suggested by Holdsworth et al (1991), the residual errors (bias error) was calculated by subtracting the linear regression flow rates by the programmed flow rates and is shown in Fig. 4.14. The plot also shows the subtracted error between the time-averaged flow rates (for individual stroke directions) and the programmed values. The latter was plotted to show the difference in accuracy between the motor-to-home and home-to-motor strokes. It is evident from Fig. 4.14 that there is an increase in error for an increase in flow rate and it is such that for the programmed $Q = 1$ and $Q = 15$ mL/s the error is 0.09 mL/s (or 90 μ L/s) and 4.33 mL/s (or 4330 μ L/s), respectively. With all flow cases, the measured flow rates are smaller than the programmed values. In addition, for all flow rates there is a larger error associated with the motor-to-home than the home-to-motor strokes. At $Q = 15$ mL/s, the maximum absolute error for the motor-to-home and the home-to-motor strokes is 5.05 and 3.60 mL/s, respectively.

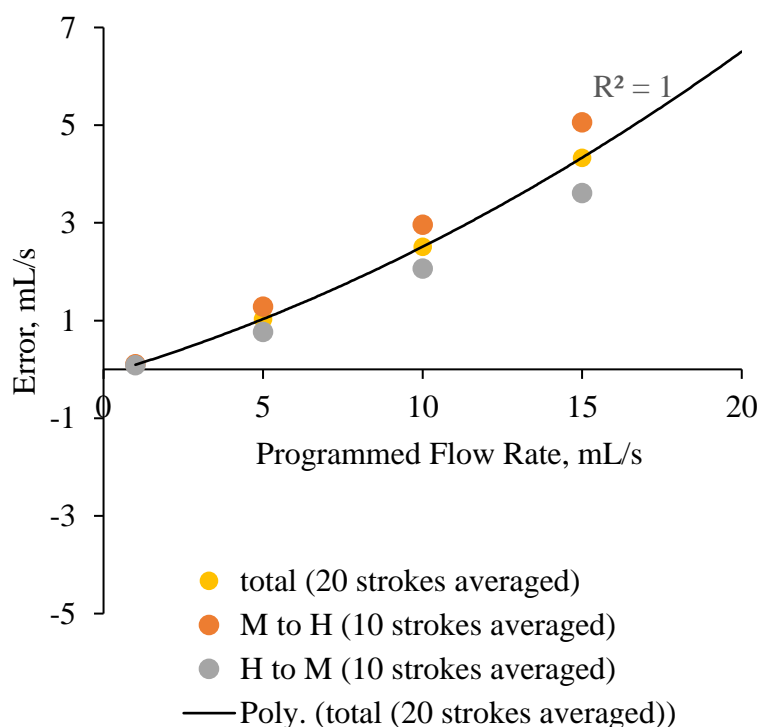


Fig. 4.14

Bias error of the programmed flow rates.

The errors bars of the measured flow rate in Fig 4.13 are smaller than the plotted points (therefore not apparent) and were calculated based on the sum of the squares associated with the accuracy (Atrato flow meter: $\pm 1\%$) and the repeatability (r.m.s. Q') of the signal (as a result of the pump unsteadiness and the flow meter repeatability of $\pm 0.1\%$ (from 25 to 100% of the range) and $\pm 0.5\%$ (from 0-25% of the range)). The total uncertainty for the measured flow rates was calculated by the expression, $\varepsilon_{\text{flow}} = \pm \sqrt{(B^2) + (t_1 * \text{r.m.s. } Q' / \sqrt{N})^2}$, where B and t_1 are the bias error of the flow measurements and $t_1 = 1.96$ represents a confidence level of 95%, respectively (Wheeler & Ganji, 2004). The r.m.s. Q' (fluctuating component) was 0.03, 0.05, 0.07 and 0.19 mL/s for the programmed $Q = 1, 5, 10$ and 15 mL/s, respectively (i.e. within the measured r.m.s. u' for steady flow with LDV at the working section). An increase in the r.m.s. values is, therefore, evident with an increase in the flow rate of the pump. At the programmed $Q = 1$ and 5 mL/s the r.m.s. is dominated by the repeatability of the flow meter whereas at higher programmed flow rates (i.e. $Q = 10$ and 15 mL/s) by the unsteadiness of the pump. The author presumes the unsteadiness of the pump is as a result of the motor controller dividing each shaft rotation into 25,000 discrete micro-steps. The actual flow rates together with the uncertainties were $Q = 0.90 \pm 0.09, 3.90 \pm 0.039, 7.50 \pm 0.075$ and 10.65 ± 0.10 mL/s for the programmed flow rates of $Q = 1, 5, 10,$ and 15 mL/s, respectively. The random error component of the total uncertainty ($t_1 * \text{r.m.s. } Q' / \sqrt{N}$) was a negligible as a result of the large sample size (i.e. 12,000).

It should be note that the large difference of 4.5 mL/s in 15 mL/s between the programmed (specified) flow rate and the measured value directly comes from air occupying a volume inside the pump cylinder. It was verified that the actual plunger does move the total length specified and in the time expected. Hence, the problem was not associated with the drive train or in the number steps made by the motor. In addition, there was no problem with the flow getting past the piston. The latter was verified by evaluating the pressure difference across the piston together with the gap required (between the piston and the wall) for excessive leakage to occur. At relatively larger specified flow rates (i.e. 15 mL/s under steady flow operation only) and during the stroke whereby the pump received the fluid, there was more air occupying the volume inside the pump cylinder. In pulsatile operation,

this effect was negligible; that is, the cylinder was completely filled with the cell fluid. Several attempts have been made to remove the air inside the cylinder at higher specified flow rates via air-release valves (as per Fig. 4.15) to maintain consistent flow. However, the end result was not positive.

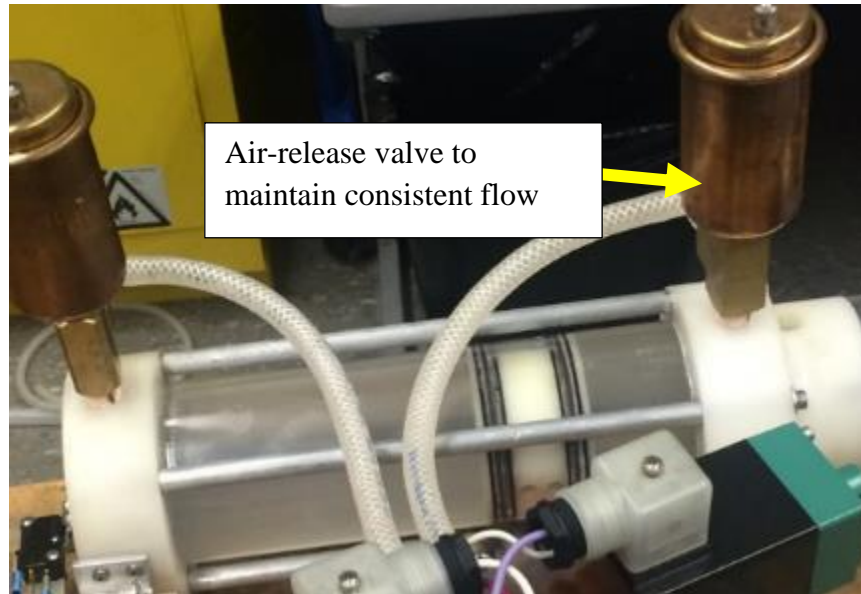


Fig. 4.15 Set-up demonstrating the use of air-release valves to remove the air inside the cylinder prior to steady flow operation.

4.5.1 Normal Carotid Waveform Repeatability and Damping

To evaluate the repeatability of the normal carotid waveform ($f = 1.08$ Hz, and $Q_{\max} = 20$ mL/s) at the working section of the PPFC, streamwise flow measurements were conducted at $y/h = 0.5$ (midplane in reference to the channel height) over 140 pulsatile cycles (70 cycles/stroke direction) under a pulsatile laminar flow. The waveform shown in Fig. 4.16 was resolved using 26 equally-sized bins (i.e. 35.3 ms wide) and the individual velocity realizations in each bin were phase-averaged (i.e. $\langle u \rangle$) over the 140 pulse cycles representing both stroke direction. The number of velocity realizations per bin was $N > 1000$ (statistical convergence was ensured for first and higher-order statistics) and the r.m.s. $u' \approx 0.0025$ m/s was detected which corresponds to the spurious r.m.s. velocity (review Appendix 2) under steady laminar flow. For this reason, the error associated with

the waveform repeatability was considered negligible (i.e. within the spurious r.m.s. quantity). In addition, the difference between the programmed mean flow rate (\bar{Q}) and the measured (i.e. $\bar{Q} = \bar{U}A$; where \bar{U} is the average bulk velocity and was spatially and temporally averaged at the working section) were within ± 0.14 mL/s (i.e. $\pm 2.3\%$).

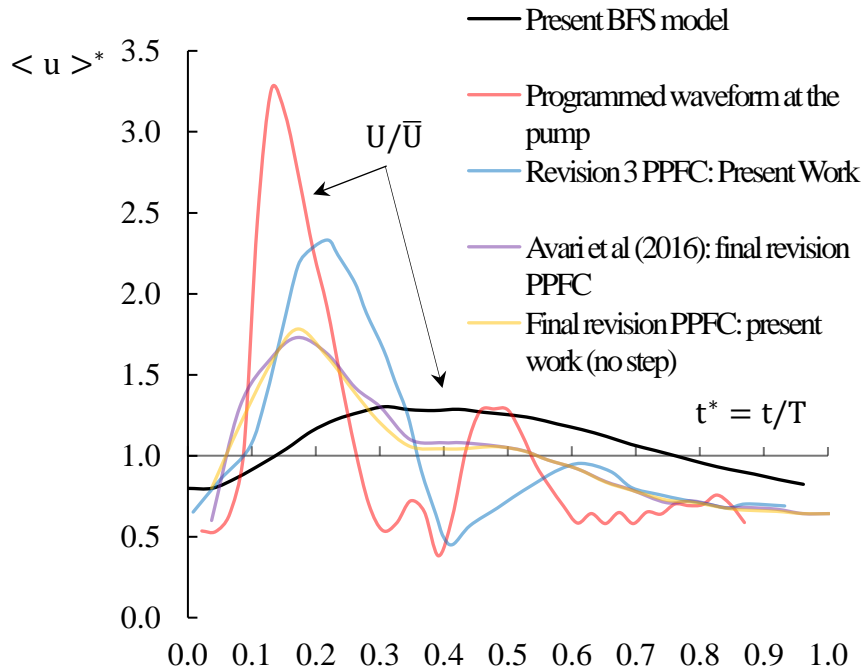


Fig. 4.16 Measured normal carotid waveforms under $f = 1.08$ Hz at the working section.

4.5.1.1 Normal Carotid Waveform Energy Loss

To start, the normal carotid waveforms reported in Fig. 4.16 measured by the present author and Avari et al (2016) are not physiological in shape and amplitude. There is a clear distinction between the programmed (i.e. prescribed at the pump software) and the measured waveforms. Therefore, it is expected that the time-varying shear loading on the ECs (at the working section of the PPFC) would not emulate *in-vivo* conditions. This section of the Chapter is focused on identifying the various sources (together with quantitative evidence) which contribute to both pressure and flow waveform energy loss across the closed-loop flow circuit in the present set-up.

To begin, the normal carotid waveform (depicted in Fig. 4.16) is a composite waveform (highly irregular in shape) and is therefore not easy to describe analytically. However, using Fourier analysis a composite waveform can be modeled as a sum of simple sine or cosine waves (different frequencies and phases) referred to as harmonics (Zamir, 2005). As an example, the basic fundamental frequency (i.e. $\omega = 2\pi f$) of the normal carotid waveform is $f \approx 1$ Hz (in the present study) and is considered as the first harmonic with the lowest frequency (Oates, 2001). The second and third harmonics would be at two times and three times the frequency of the first harmonic and so on for higher harmonics (Oates, 2001). According to Zamir (2005), in many cases the first 10 harmonics are adequate to model a composite pressure wave originating from the heart.

It should be noted that it is outside the present scope to model a composite carotid waveform given the complexity of the modeling. Rather, a simple sine waveform (with zero mean pressure over a single cycle – steady component) is used as a building block to model the pressure waveform attenuation (of the oscillatory component) across the rigid flow circuit (inclusive of tubing and PPFC). A simple sine wave is also used to model the ability of flow to respond to the driving pressure gradient at the working section of the PPFC (i.e. impedance – inclusive of viscous resistance and inertance). Both the attenuation of the pressure waveform across the rigid flow circuit together with the inability of the flow to respond to the driving pressure gradient (at the working section) is presumably accountable for damping of the flow waveform at the working section (i.e. amplitude and shape). It is important to understand that a simple sine wave model is not an adequate representation of the waveform damping in the present flow closed-loop circuit. This is because a composite waveform (which consists of higher frequency harmonics) attenuates and distorts with the distance traveled via dispersion (Zamir, 2005). The latter is the main reason for the change in shape of the pressure and flow waveforms inside the arterial network given that the higher harmonics attenuate more than the lower harmonics (Zamir, 2005). Hence, although the simple sine wave model (used in the present analysis) will highlight the governing factors which contribute to waveform damping (pressure and flow) it will not necessarily explain (with quantitative evidence) the differences highlighted in Fig. 4.16 between the various measured waveforms. To quantify the waveform differences between the various studies requires a comprehensive analysis

of the entire flow circuit (i.e. considering geometry changes, area changes, bends in the flow circuit, pump componentry: un lumped model to deduce the attenuation of the driving pressure gradient amplitude across each component, $P_0 e^{-k}$; where P_0 is the amplitude and k is the attenuation factor). For example, the flow waveform illustrated in Fig. 4.16 measured inside the revision 3 PPFC did not include an in-line heating unit (inside the pump system with a 90° change of flow direction) which would add to the attenuation of the pressure waveform via wave reflections (i.e. the opposition to pressure wave propagation, Zamir, 2005). Recommendations from the present author on the configuration of the pump system to minimize pressure waveform attenuation are given near the end of this section.

The closed-loop flow circuit under analysis is shown in Fig. 4.17. It consists of the pulsatile flow pump, tubing which connects the pump and the PPFC and the PPFC itself which returns the fluid back to the pump reservoir via additional tubing.

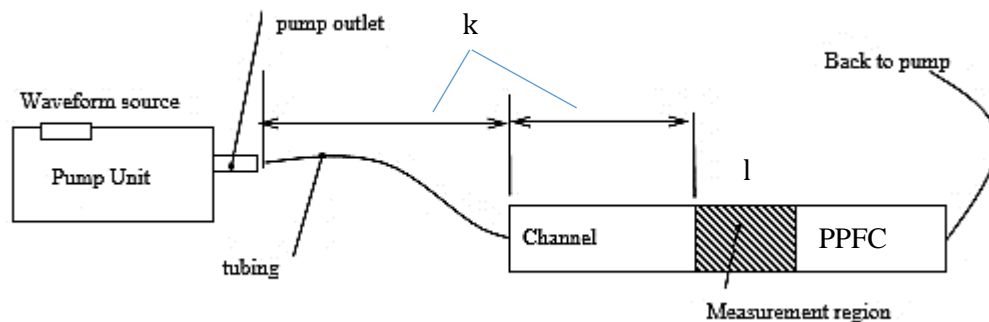


Fig. 4.17 Critical dimensions of the closed flow circuit.

Since vessel elasticity (in the present case the elastomer tubing connecting the pump and the PPFC) does affect both the pressure wave attenuation and impedance (flow response to time-varying pressure gradient, Zamir, 2005), the visco-elastic losses could contribute to waveform damping. To determine its significance, standard mechanics of materials theory can be used. According to Beer et al (2006), considering the basic stress and strain theory together with both circumferential ($\sigma_c = PD/2t_t$) and longitudinal stress ($\sigma_l = 0.5\sigma_c$)

inside a straight section of tubing, the circumferential strain may be expressed as $\epsilon_c = \left(\frac{PD}{4t_t E}\right)(2 - \nu) = \Delta D/D$. In the latter mathematical relation, P is the difference between internal and external pressure, D is the inner diameter of the tube, t_t is the wall thickness of the tube, E is the modulus of elasticity and ν is the Poisson's ratio. Considering the elastic modulus of $E = 1$ MPa and $\nu = 0.39$ (manufacturer reported, Cole-Palmer, Canada) together with a maximum pressure inside the tubing of ≈ 60 mmHg (Avari et al. 2016), the circumferential strain is $\epsilon_c = \Delta D/D = 6 \times 10^{-3}$ (whereby $D = 6.35$ mm) which yields a change in tubing diameter of $\Delta D = 0.04$ mm. Hence, the increase in diameter as a result of the pressure is $< 1\%$. According to Beer et al (2006), the longitudinal strain can also be calculated by the relation $\epsilon_l = 1/E(\sigma_1 - \nu\sigma_c) = \Delta L/L = 8 \times 10^{-4}$ (whereby $L \approx 1000$ mm and represents the tubing length) which demonstrates that the change in the tubing length is negligible ($< 0.1\%$). Hence, the effect of tube compliance (i.e. $C = \Delta V/\Delta P$; where $\Delta V = \pi\Delta D^2\Delta L/4$ is the change in volume of the tube) on waveform damping is presumably negligible and, hence, the elasticity effects on waveform amplitude and shape are not further discussed.

To evaluate the attenuation of a sinusoidally fluctuating component (P) of the pressure wave (prescribed at the pump) along straight section of tube and PPFC inside the present flow circuit, the following expression can be used (Caro et al. 2012):

$$P = P_o e^{-kx} \cos \left[\omega \left(t - \frac{x}{c} \right) - \phi \right] \quad (4-5)$$

where k , λ , c , P_o and ϕ are, respectively, the attenuation factor ($k = \ln \left(\frac{P}{P_o} \right) / \Delta x = 2\mu\omega^2/3\rho c^3$), wavelength ($\lambda = c/f$), the wave speed ($c = \sqrt{K/\rho}$), the pressure amplitude and the phase angle ($\pi/2$). It should be noted that K represents the bulk modulus of the fluid and for water (at 20 °C) is $K \approx 2.2 \times 10^9$ Pa (Kittel, 2005). Given the similarity in fluid density of water and the cell fluid ($< 0.3\%$), it is considered sensible to continue the analysis with this value of K . Given that the elastomer tube and the PPFC are considered rigid (i.e. $E \rightarrow \infty$), the pressure wave speed across a straight section of tube and channel is $c \approx 1485$ m/s. In addition, the wavelength of the pressure wave is $\lambda \approx 1485$ m (i.e. $f \approx 1$ Hz; fundamental frequency of the sine wave). It is thus evident from Eq. (4-5) that the

term $e^{-kx} \rightarrow 1.0$ given the relatively large wavelength (in comparison to the length of the flow circuit of ≈ 1 m) of the pressure wave. For this reason, it is concluded that there is no attenuation of the pressure amplitude (P_0) along the flow circuit (tube + PPFC) and that the local change of pressure occurs instantaneously at every point along the tube and the PPFC. The instantaneous pressure change can be further explained by understanding that there is an absence of time delay between the peak amplitude (of the time-varying pressure) between two points along the x-direction.

Fig. 4.18a shows the normalized oscillatory pressure ($P(t)/P_0$) plotted over a duration of $t = 1$ s (single oscillatory cycle for $f = 1$ Hz). Plotted also is the $P(t)/P_0$ function for the $f = 10$ Hz case, which is present in the composite carotid waveform (Oates, 2001). Both functions are solved considering $\mu = 0.000773$ Pa s and $\rho = 997$ kg/m³ (cell fluid properties reported in Chapter Three). It can be seen from Fig. 4.18a that both the fundamental frequency of 1 Hz (representing the first harmonic) and the 10 Hz (representing higher harmonics) remain unattenuated over the $x = 1.2$ m distance ($k/l \approx 15$; where k is the distance from the pump outlet to the working section of the PPFC – see Fig. 4.17). These results are expected given the relatively large wavelength of the pressure waveform. In addition, these results substantiate the work of Avari et al (2016), which reports constant $(P_{\max} - P_s)/P_0 = 0.7$ (difference within experimental uncertainty and P_s is the mean component of pressure waveform) across the present PPFC (i.e. normal carotid waveform for $f = 1.08$ Hz using pressure transducers). The remaining uncertainty surrounds the loss of the oscillatory pressure amplitude (i.e. $\Delta(P_{\max} - P_s)/P_0 = 0.3$) across the flow circuit. The latter is presumably attributed to additional pressure waveform attenuation across the various flow circuit components (including the components inside the pump assembly) as a result of waveform reflections due to characteristic impedance changes at boundaries (discontinuity in the properties of the present flow circuit, Rienstra & Hirschberg, 2004).

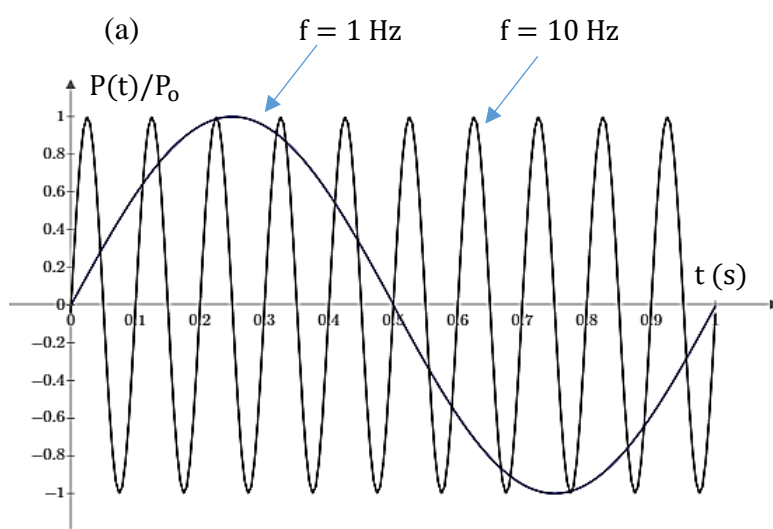
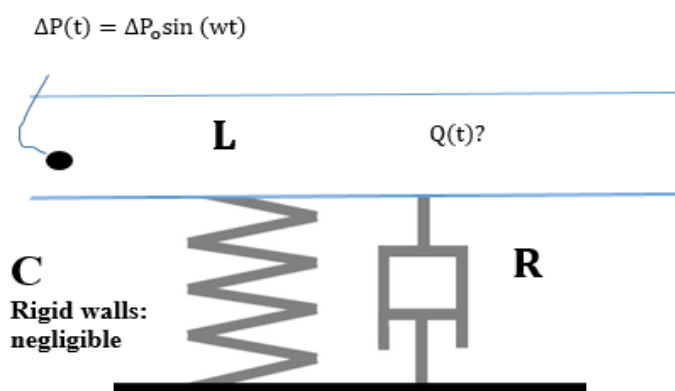
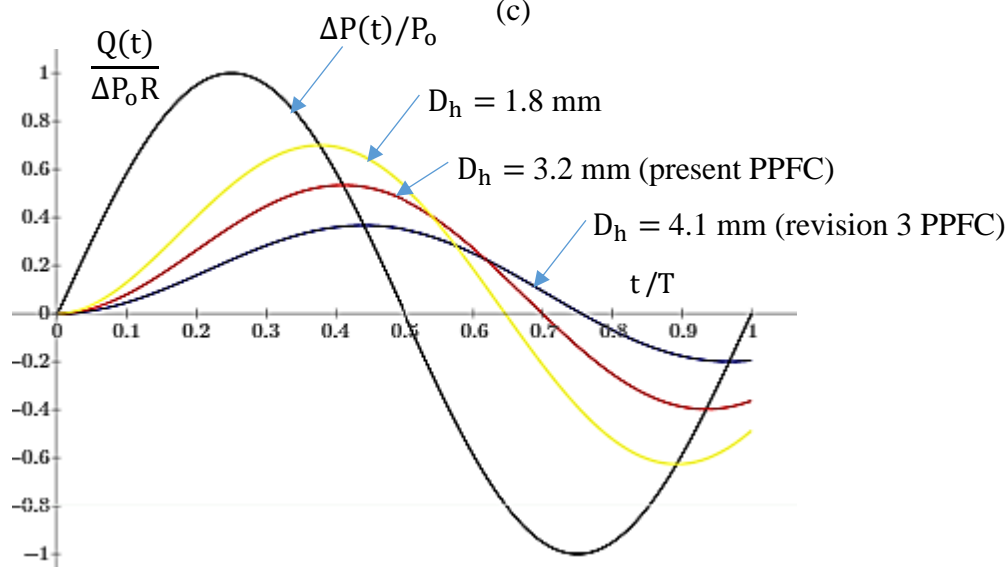


Fig. 4.18 Waveform damping analysis: (a) attenuation of a sinusoidally fluctuating component (P) of the pressure wave, (b) mechanical model of the PPFC flow and, (c) flow response to oscillatory pressure gradient inside the PPFC.

(b)



(c)



The other interesting observation from the work of Avari et al (2016) is that the measured (LDV) waveform amplitude (i.e. $(Q_{\max} - \bar{Q})/Q_0 = 0.4$; where \bar{Q} = steady component) and shape at the working section is different that of the pressure waveform reported. The observed difference between the pressure and flow waveforms in the work of Avari et al (2016) is presumably attributed to the inability of the flow to respond to the driving pressure gradient as a periodic function, $\Delta P(t) = \Delta P_0 \sin(\omega t)$.

To quantify the effect of inertance (an analogue to inductance in electrical engineering) using a simple sine wave flow inside the present PPFC and, hence, better understand the flow response to pressure, a basic model illustrated in Fig. 4.18b is used. The purpose of such an analysis is to bring insight on the relationship between the pulsatile pressure wave and the flow wave (i.e. loss of amplitude in flow). The total pressure gradient (ΔP) to drive the flow (capacitance neglected as per previous analysis) under oscillatory conditions is the sum of all pressure differences required to overcome fluid viscosity (resistance which is an analogue to the damper in a mass-spring-damper system) and fluid inertance (inductance: an analogue to inertia of a solid object).

According to Zamir (2005), the equation of motion representing such a system is given as follows (first-order ordinary differential equation):

$$L \frac{dQ}{dt} + RQ = \Delta P = P_2 - P_1 \quad (4-6)$$

where L is the inertial constant, R is the viscous resistance, Q is the net flow rate and ΔP is the total driving pressure difference. This equation generally represents an analytical model of an oscillatory flow in a rigid tube/channel as a single or lumped-system. Furthermore, L and R can be mathematically defined as $L = \left(\frac{\rho l_c}{wh}\right)$ and $R = \frac{\Delta P}{Q} = \left(\frac{2Po l_c \mu}{D_h^2}\right)$, respectively (Zamir, 2005). It should be noted that l_c and Po are, respectively, the length of the PPFC and the Poiseuille number. According to Shaw & London (1978), the Poiseuille number can be defined as $Po = f_c Re = (24)(1 - 1.3553\beta + 1.9467\beta^2 - 1.7012\beta^3 + 0.9564\beta^4 - 0.2537\beta^5)$, which demonstrates its dependence on the aspect ratio of the channel ($\beta = h/w$). In addition, the pressure loss per unit length (in the developed region of the steady

laminar flow inside the PPFC) can be expressed as $\Delta P/l_c = 2 f_c \rho U^2 / D_h$ (Kandlikar et al. 2007). Furthermore, Eq. (6-6) has a well-known solution which can be expressed as follows (Zamir, 2005):

$$Q(t) = \frac{e^{-t/(\frac{L}{R})}}{L} \int \Delta P e^{t/(\frac{L}{R})} dt \quad (4-7)$$

Assuming the driving pressure gradient as a periodic function, $\Delta P(t) = \Delta P_o \sin(\omega t)$ where $\omega = 2\pi f$ ($f = 1$ Hz and hence $\omega = 6.78$ rad/s), upon integration (by parts) Eq. (4-7) can be written as follows (Zamir, 2005):

$$Q(t) = \frac{\Delta P_o}{R^2 + \omega^2 L^2} (R \sin \omega t + \omega L \cos \omega t + \omega L e^{-\left(\frac{R}{L}\right)t}) \quad (4-8)$$

Eq. (4-8) can also be expressed in a non-dimensional form as follows (Zamir, 2005):

$$\frac{Q(t)}{\Delta P_o R} = \frac{1}{\sqrt{1 + \omega^2 t_L^2}} \left((\sin \omega t - \phi) + \frac{\omega t_L}{\sqrt{1 + \omega^2 t_L^2}} e^{-t/t_L} \right) \quad (4-9)$$

where t_L is the inertial time constant and is defined as $t_L = L/R$ and, ϕ is the phase angle defined as $\phi = \tan^{-1}(\omega t_L)$. Substituting the values of L and R into t_L generates a new expression of the inertial time constant, $t_L = \rho D_h^2 / 2 P_o \mu A$ (where $A = wh$). It should be noted that the units for the inertial time constant are seconds which represents the time required for the flow to reach steady state (Zamir, 2005).

Moreover, Fig. 4.18c gives sinusoidal flow waveforms for one oscillatory cycle ($f = 1$ Hz) corresponding to $D_h = 4.1$ mm (revision 3 PPFC), $D_h = 3.2$ mm (present PPFC) and $D_h = 1.8$ mm (arbitrarily selected PPFC). The arbitrarily-selected PPFC simply represents an additional study to demonstrate the effect of D_h on the flow waveform attenuation at the working section. The normalized cycle time, $t^* = t/T$, is plotted on the x-axis where T represents the cycle period. It is evident from Fig. 4.18c that all the flow waveforms exhibit much attenuated amplitudes of oscillation with a corresponding phase shift. For example,

the present PPFC shows $\frac{Q(t)}{\Delta P_{oR}} = 0.52$ (highest flow rate reached at the peak of each cycle) and a phase shift of $\Delta t^* = 0.17$ in comparison to the driving pressure waveform. In general, the larger the inertial time constant (t_L), the larger the amplitude attenuation and phase shift. Since the revision 3 PPFC has a relatively larger hydraulic diameter and $t_L \propto D_h^2$, the values of the normalized flow amplitude and phase shift are $\frac{Q(t)}{\Delta P_{oR}} = 0.36$ and $\Delta t^* = 0.20$, respectively. Similarly, A PPFC with $D_h = 1.8$ mm would result in less attenuation as reflected in Fig. 4.18c. This effect can also be explained by the Womersley parameter (Wo), such that a larger D_h would result in a larger Wo under a fixed fundamental frequency and viscosity of the fluid. As reviewed in section 2.2.2.1, for $Wo \gg 1$ the flow fails to instantly respond from its acquired inertia and, as a result, the flow lags behind the driving pressure.

Hence, if one considers the factors which influence flow waveform amplitude and shape at the working section of a PPFC, both the pressure amplitude attenuation (along the flow circuit) and the flow response to the driving pressure gradient should be taken into account. Both of these factors presumably explain the differences observed in Fig. 4.16. As an example, it would be expected that the revision 3 PPFC (see Appendix 1) would result in smaller amplitude attenuation of the pressure wave (as it travels inside the flow circuit) given the absence of the in-line heater at the pump unit (i.e. no waveform reflections). Similarly, one would expect larger pressure wave attenuation for the present study inclusive of the backward-facing step. Once again, the backward-facing step represents a obstruction whereby the characteristic impedance changes which leads to possible reflections of the pressure pulse.

To conclude, an ideal design of the flow circuit to minimize waveform damping would thus include: (1) a tube with a constant cross-sectional area which connects the plunger to the PPFC and, (2) a relatively small hydraulic diameter at the working section (i.e. 1 mm). It should be noted that the present configuration of the pump unit includes many boundaries between fluid elements (i.e. valve, heater, fittings) which contribute to changes in the characteristic impedance.

4.6 Sample Size and the Selection Criteria for the Bin Size for Steady and Pulsatile Flow over a Backward-Facing Step

The two flow case studies presented in Chapter Five are the steady and pulsatile (laminar flow at the inlet) over a backward-facing step (BFS). It is important that the sample size (number of velocity realizations captured), N , is chosen correctly (i.e. sufficient amount of data points) to ensure statistical convergence of the mean flow and turbulence statistics. There is generally a compromise between run-time (capture time of the data based on the coincidence data rate, \dot{N}) and the uncertainty of the flow statistics (i.e. since an increase in N results in relatively smaller uncertainties). The run-time in the present study is selected based on the coincidence data rate (i.e capture of u and v simultaneously and in coherence mode) which, in turn, prescribes the required number of pulse cycles (i.e. carotid waveform with $f = 1.08$ Hz) and/or strokes to reach statistical convergence (in a given bin size) of the first and higher-order statistics. The coincidence data rate for the steady and pulsatile flow over the BFS was $\dot{N} \approx 500$ Hz away from the wall (i.e. $y/h > 0.11$) and $\dot{N} \approx 100$ Hz in the vicinity of the wall (i.e. $y/h < 0.11$). This implies that under a pulsatile flow with $f = 1.08$ Hz ($T = 920$ ms), the number of velocity realizations (u and v) captured was $N \approx 500$ over a single pulsatile cycle (for $y/h > 0.11$). Based on 26 equally-sized bins and a cycle period of $T = 920$ ms, the corresponding bin width for the present study is 35.3 ms. The latter implies that over a single pulse cycle the number of u and v velocity realizations per bin is $N \approx 18$.

The statistics (for both u and v velocity components) under examination for convergence (r.m.s., skewness, kurtosis and Reynolds Shear Stress) are reported at $y/h = 0.5$ and $x/S = 21.12$ (downstream of the reattachment point), where S is step height (geometry details below in Fig. 4.19). In addition, the time instant of the cycle reflecting the analysis corresponds to the peak systole velocity. The convergence criteria under consideration for

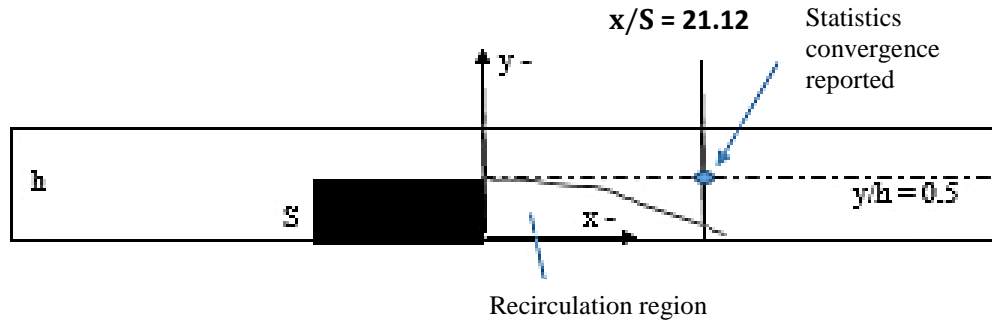


Fig. 4.19 Geometry of the working section under steady and pulsatile laminar flow over a backward-facing step (BFS). Illustration showing point for statistical convergence analysis ($x/S = 21.12$ and $y/h = 0.5$).

the first and higher-order statistics requires that the subsequent sample size (i.e. $N + 18$, whereby the statistics are recalculated by increasing the sample size by 18 which corresponds to approximate number of data points per bin over a single pulse cycle) yields a change in the value that is smaller than the uncertainty of the statistic under investigation. It can be seen from Fig. 4.20 that to obtain statistical convergence of the r.m.s. quantity (both u' and v'), the required number of pulsatile cycles is ≈ 30 . Since $N \approx 18$ per bin over a single pulsatile cycle, the total number of velocity realizations required to obtain statistical convergence is $N \approx 540$. The difference in the r.m.s. values for the subsequent sample size (i.e. $N + 18$) is within the uncertainty (calculated by Eq. (4-1b)) of $\epsilon_{r.m.s.u'} = \pm 0.002$ m/s. Furthermore, Fig. 4.21 shows the convergence of skewness (third moment of u' and v') statistic whereas, Fig. 4.22 shows the convergence of the excess kurtosis (fourth moment of u' and v') statistic. Both of these statistics are plotted against the number of velocity realizations (sample size) and the number of pulsatile cycles (secondary axis). The mathematical definition of both the skewness and kurtosis together with their standard error is given in Appendix 3.

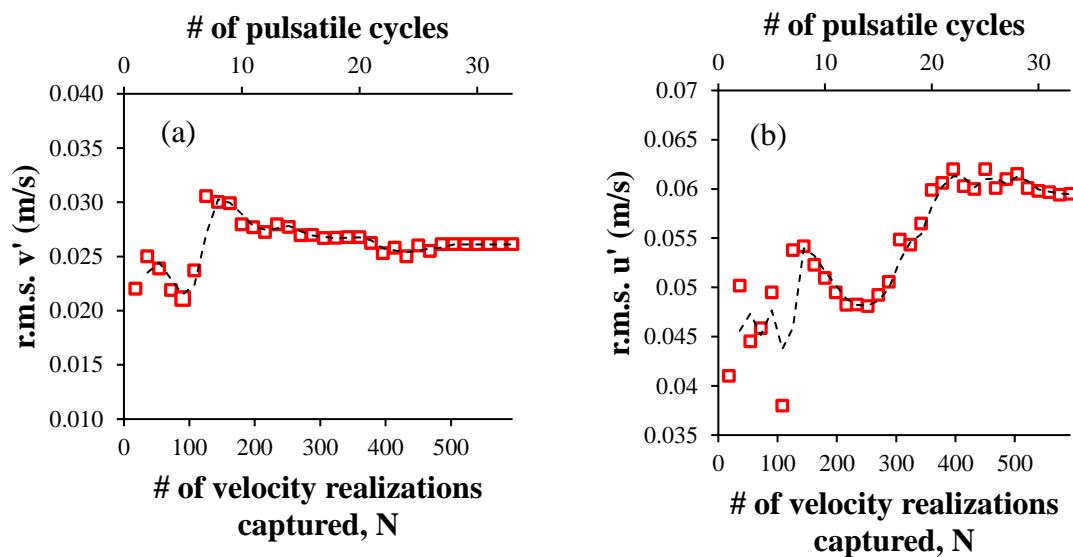


Fig. 4.20 r.m.s. velocity plotted against the number of velocity realizations captured by the LDV system (and the number of pulsatile cycles): (a) r.m.s. v' (b) r.m.s. u' . The downstream station (from BFS) and the time instant of the cycle reflected in the plot is $x/S = 21.12$ and $t/T = 0.35$, respectively.

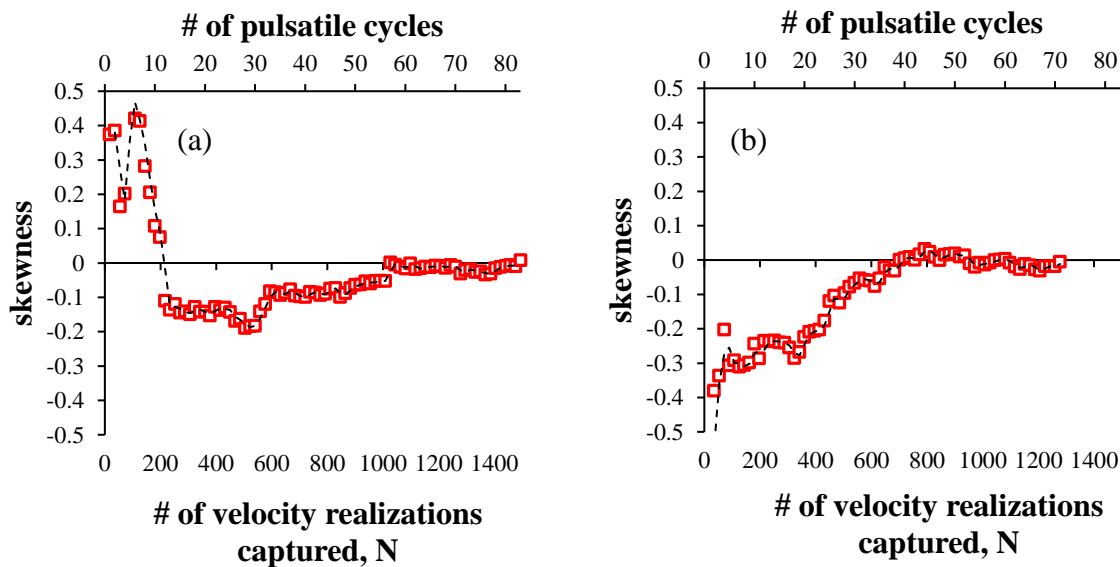


Fig. 4.21 Skewness plotted against the number of velocity realizations captured by the LDV system: (a) $S_{v'}$ (b) $S_{u'}$. The downstream station and the time instant of the cycle reflected in the plot is $x/S = 21.12$ and $t/T = 0.35$, respectively.

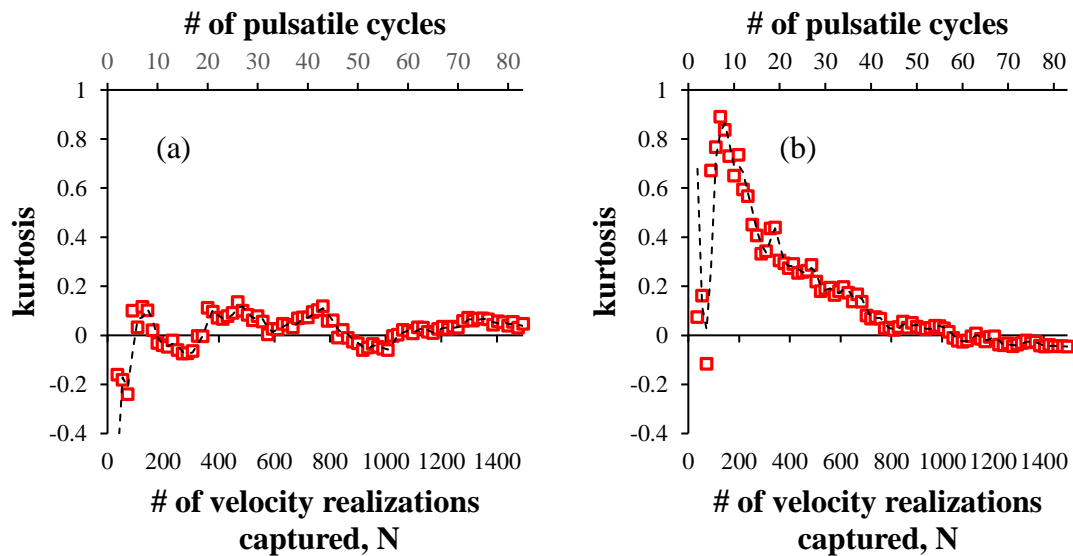


Fig. 4.22 Excess Kurtosis plotted against the number of velocity realizations captured by the LDV system: (a) K_v' (b) K_u' . The downstream station and the time instant of the cycle reflected in the plot is $x/S = 21.12$ and $t/T = 0.35$, respectively.

It can be seen from Figs. 4.21 and 4.22 that both the skewness and the kurtosis statistic for both velocity components converge close to zero (within the standard error of the statistic; that is, for skewness and kurtosis the standard error is ± 0.15 (Cramer, 1979), indicating a normal distribution (Iyer & Woodmansee, 2005). Furthermore, It can be seen from Figs. 4.21 and 4.22 that to obtain statistical convergence of the skewness and kurtosis statistic, the required number of pulsatile cycles is ≈ 60 (total number of velocity realizations required is $N \approx 1000$) and ≈ 70 (total number of velocity realizations required is $N \approx 1300$), respectively. The difference in the skewness and kurtosis values for the subsequent sample size (i.e. $N + 18$) is within the standard error (95% confidence) of the quantity.

It should be noted that similar results were obtained for various pulse cycle time instants, together with the downstream of the step measurement stations. It should also be noted that for u and v measurements near the wall (i.e. $y/h < 0.11$), the number of pulse cycles required to reach statistical convergence (for r.m.s., skewness and kurtosis statistics) was approximately 325 (corresponding to $N \approx 1300$) based on $\dot{N} \approx 100$ Hz and a bin width of 35.3 ms. For reference to the reader, 325 pulse cycles of the normal carotid waveform (peak

flow of 20 mL/s) is equal to approximately 5 pumping strokes with a run time of approximately 5 minutes.

Finally, the Reynolds Shear Stress ($-\overline{u'v'}$) convergence plot is shown in Fig. 4.23 plotted against the sample size (N) and the number of pulsatile cycles. The convergence is reached at $N \approx 800$ whereby the difference in the $-\overline{u'v'}$ values for the subsequent sample size (i.e. $N + 18$) is within the uncertainty of $\varepsilon_{\overline{u'v'}} = \pm 0.0001 \text{ m}^2/\text{s}^2$. Similar results are obtained for various time instants of the pulse cycle and at various spatial locations at the working section (downstream of the step and across the channel height).

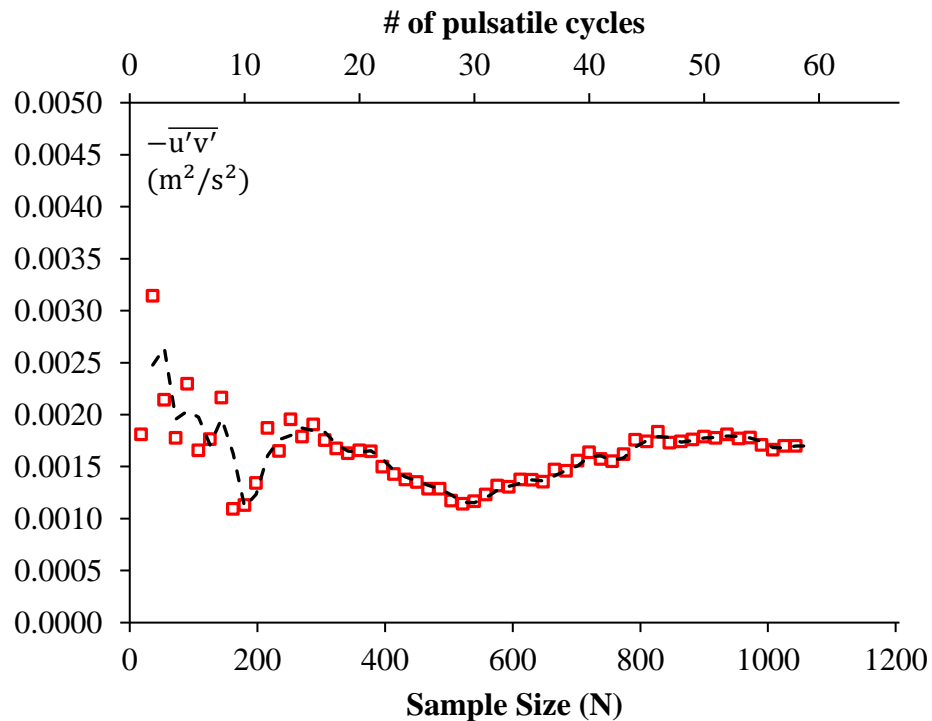


Fig. 4.23 Reynolds Shear Stress ($-\overline{u'v'}$) convergence plot. The downstream station and the time instant of the cycle reflected in the plot is $x/S = 21.12$ and $t/T = 0.35$, respectively.

As a result of the convergence analysis for the second and higher moment statistics, a sample size of $N = 1500$ was used for all backward-facing step flow cases reported in Chapter Five. A final note in this section is in regards to the bin size selection criteria. According to both Zhang et al (1997) and Kehoe (2001), bin selection criteria must

consider the temporal (phase) velocity gradient inside the bin as well. If the bin size is too large, it can lead to over-estimation of the r.m.s. velocity. The latter is specifically important for flows which exhibit a large temporal velocity (i.e. large intra-bin velocity variation, du/dt) and relatively small turbulence intensity. For the carotid waveform in the present work ($f = 1.08$ Hz, $Q_{\max} = 20$ mL/s), the r.m.s. u' quantity was not influenced by the bin size through approximately 30 to 60 ms (bin resolution) with a spurious r.m.s. of ≈ 0.0025 m/s which corresponds to the detected noise under laminar flow. The latter implies that the intra-bin velocity variation was within the spurious r.m.s. quantity and it is, thus, negligible. Smaller bin resolution was not considered, as a result of a significant increase in the required run-time in order to collect a sufficient amount of velocity data to obtain statistical convergence.

4.7 In-Situ Measurement of the Step Height and Expansion Ratio

Given that the next Chapter discusses velocity measurements downstream of a backward-facing step, it is important that the step height uncertainty is evaluated. Hence, a measurement of the actual step height, S , was performed in-situ (step mounted inside the channel) at the working section. This measurement was performed using a dial indicator (Varta indicator: 36.5 mm contact point length, 0 to 0.5 mm range) and a 1 mm precision gauge block (Mitutoyo Steel Metric). The flatness of the gauge block surface is better than ± 0.001 mm (± 1 μ m). The latter is reported in the certificate of accuracy from the manufacturer and is also traceable to NIST (National Institute of Standards and Technology). In addition, the accuracy of the dial indicator is better than ± 1 μ m (manufacturer reported). The measurement of the step height was performed whilst the step was secured to the lower cavity of the channel (at the working section) to account for the uncertainty associated with the depth of the cut-out where the step was inserted and secured. This procedure is shown in Fig. 4.24. The dial indicator was zeroed at the surface of the gauge block and gently moved along the block and the step. An average of three separate measurement trials yielded a difference of 158 ± 50 μ m. Notwithstanding this, the step height is given as 0.842 ± 0.05 mm (842 ± 50 μ m). The inlet channel height uncertainty is defined as $\varepsilon_{h-s}^2 = \sqrt{50^2 + 11^2} = \pm 51.1$ μ m (i.e. 11 μ m corresponding to inlet channel

uncertainty with no step present, which was also measured by a digital Vernier scale). Based on the above, the expansion ratio is given as $ER = 1.8 / (1.8 - 0.842) = 1.88$.

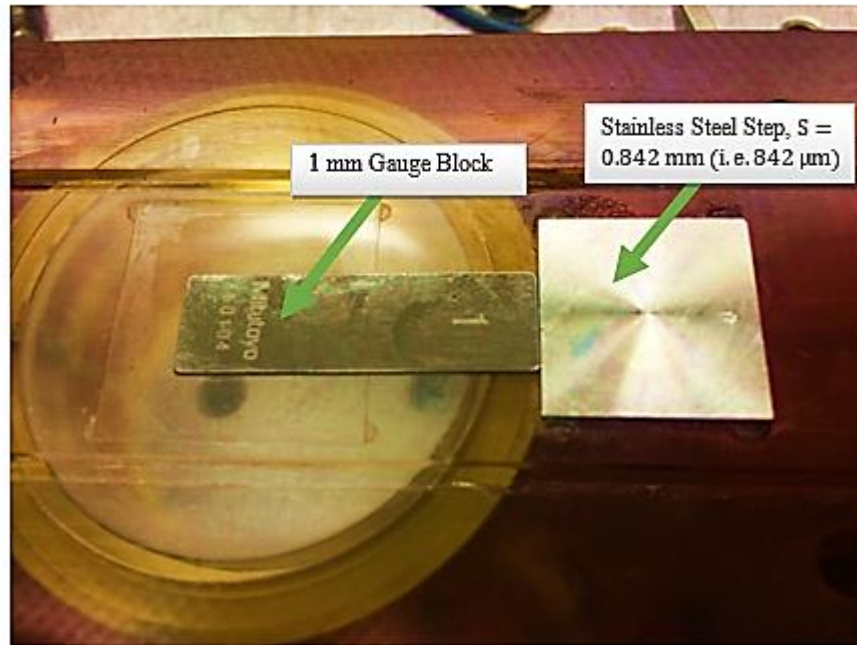


Fig. 4.24 In-situ measurement of the actual step height, S

4.8 Chapter Four Summary

This Chapter commenced with reporting the normalized errors in statistical flow quantities (reported in Chapter Five) with a value of $\varepsilon_{\bar{u}}/|\bar{u}| = \pm 2.50\%$ for the mean velocities, $\varepsilon_{r.m.s.u'}/r.m.s.u' = \pm 5.65\%$ for the r.m.s. velocities and $\varepsilon_{\overline{u'v'}}/|\overline{u'v'}| = \pm 8.00\%$ for the Reynolds shear stresses. The sample size of $N \approx 1500$ considered with the uncertainty analysis was deduced based on statistical convergence of the mean flow and higher-order statistics.

Furthermore, the accuracy and precision of the motorized laboratory jack were also experimentally evaluated showing a spatial uncertainty in the y-direction of $\varepsilon_{\text{traverse}} = \pm 6 \mu\text{m}$ in the range, $0 < y < 100 \mu\text{m}$, and $\varepsilon_{\text{traverse}} = \pm 12 \mu\text{m}$ in the range, $0 < y < 500 \mu\text{m}$. To determine the nearest measurement point in reference to the lower wall, a two-step process was demonstrated consisting of manual positioning of the measurement volume

(with an assumed initial position) and post-processing of those near-wall data. It was found that the closest measurement points to the wall were $20 \pm 10 \mu\text{m}$ and $40 \pm 10 \mu\text{m}$ for the $F = 120$ and 261 mm lenses, respectively. As a result, the errors in the shear rate at the wall were $\pm 2.3\%$ and $\pm 11.0\%$ for the $F = 120$ and 261 mm lenses, respectively. Furthermore, an experimental technique was presented to determine the location of the measurement volume at the step edge (for the backward-facing step flow cases in Chapter Five) to accurately report the downstream measurement positions of the streamwise (\bar{u}) and wall-normal velocity (\bar{v}) profiles. It was found that this technique was able to locate the step edge with an uncertainty better than $\pm 51.4 \mu\text{m}$. In addition, the step height uncertainty was evaluated using a dial indicator and 1 mm gauge block. The step height was measured at $842 \pm 50 \mu\text{m}$ which yielded an expansion ratio (ER) of 1.88 (i.e. ≈ 2.0).

Furthermore, the pulsatile flow pump under both steady and pulsatile flow was evaluated in terms of its accuracy and repeatability. For steady flow, it was found that the actual flow rates together with their uncertainties were $Q = 0.90 \pm 0.09$, 3.90 ± 0.039 , 7.50 ± 0.075 and 10.65 ± 0.10 mL/s for the programmed flow rates of $Q = 1$, 5 , 10 , and 15 mL/s, respectively. The steady volumetric flow rates were evaluated using a transit-time ultrasonic flow meter. For pulsatile flow, the repeatability and accuracy of the normal carotid waveform prescribed at the pump was evaluated at the working section of the PPFC using Laser Doppler Velocimetry (LDV). The results showed that the r.m.s. velocity inside the individual bins (i.e. 35.3 ms) was within the spurious value of r.m.s. $u' \approx 0.0025$ m/s over several pulse cycles (i.e. > 100). In addition, the difference between the programmed mean flow rate and the measured value was within ± 0.14 mL/s (i.e. $\pm 2.3\%$).

Finally, although the measured carotid waveform at the working section was in good agreement with the work of Avari et al (2016), both waveforms did not bear a resemblance to physiological conditions. Hence, the present author mathematically modeled and quantified both, the attenuation of a sinusoidally fluctuating component of the pressure wave (along straight section of tube and PPFC) and the effects of viscous resistance and inertance (i.e. impedance) on flow response to the periodic driving pressure gradient. The results showed that compliance of the tubing was negligible and that the pressure amplitude attenuation notwithstanding wave reflections was also negligible (for both $f = 1$ and 10

Hz fundamental frequency). However, the ability for the oscillating flow to respond to the driving pressure gradient did reveal significant flow attenuation at the working section of the PPFC (i.e. $\approx 50\%$).

The next Chapter is focused on quantifying both steady and pulsatile flow under the influence of a backward-facing step (BFS) to model an idealized stenosis flow. Both of these BFS flow cases are compared to more realistic stenosis geometries (i.e. pulsatile flow in a tube with an asymmetric stenosis) to evaluate how the present flow facility models such flows. Hence, the main contribution of the present work is presented in Chapter Five.

CHAPTER FIVE

TWO-COMPONENT VELOCITY MEASUREMENTS DOWNSTREAM OF A BACKWARD-FACING STEP UNDER STEADY AND PULSATILE FLOW

5 Introduction

This chapter presents two-dimensional velocity measurements (u, v) downstream of a backward-facing step (BFS) at multiple measurement stations (mid-plane, $2z/w = 0$) and compares the results to other models of stenosis to gain insight into how well a simple step can model *in-vivo* post-stenotic flows. The present flow investigation is divided into steady and pulsatile flow cases, thereby allowing a direct comparison between these types of flows. As part validation to ensure present velocity measurements are valid and to gain more insight into the effect of side-walls on the mid-plane flow structure, the present steady laminar flow case is compared to the pioneering experimental work of Armaly et al (1983) and 2-D numerical work of Erturk (2008) which both simulate a simple step geometry with a blockage ratio of 0.5. This is then followed by comparing the present results to more realistic stenosis models (including an axi-symmetric stenosis inside a straight section of tube) to gain insight into the similarities and differences of the flow physics downstream of the blockage. In addition, the spatial gradient of wall shear stress (computed in the present study) is compared with a physiologically accurate *in-vitro* carotid phantom model (for normal, disease-free and 63% stenosed internal carotid artery under steady flow) to gain insight on how well a simple step can model flows found in the human anatomy.

A similar analysis is provided with the pulsatile flow case with the added complexity of phase-dependent flow behaviour. The present pulsatile flow case is compared with both an asymmetric and axi-symmetric stenosis inside a straight section of tube and channel, respectively. Given the nature of the pulsatile flow, both temporal and spatial gradient of wall shear stress is computed and compared to more realistic models of stenosis. For both steady and pulsatile flow cases, vertical streamwise mean velocity profiles are given at the channel mid-plane (at the working section) for multiple measurement stations (downstream of the BFS) to the point of relaminarization. Turbulence statistics (including streamwise and wall-normal r.m.s. profiles, Reynolds shear stress and energy spectra) are also given.

5.1 Steady Laminar Flow over a Backward-Facing Step

The fundamental objective of this section is to quantify the mean flow and turbulence statistics at the mid-plane of the working section (i.e. $2z/w = 0$) downstream of the BFS at multiple measurement stations. The present results are compared (with quantitative evidence) to literature which report flow physics downstream of a simple step and for more realistic stenosis geometries. Such a quantitative analysis would bring insight into how well a simple step model in the present work emulates *in-vivo* conditions in post-stenotic flows. In addition, the steady laminar flow case would add to the knowledge of post-stenotic flow instability phenomenon whereby the flow can transition into broadband turbulence from an extrinsic (i.e. side wall influence) and/or an intrinsic (action of hydrodynamics) instability. Finally, a better understanding of endothelial cell (EC) response in disturbed flow regions (i.e. downstream of a stenosis) can be obtained whereby a direct correlation can be made with the quantified flow physics from the present work.

5.1.1 Problem Definition

To simulate a fully-developed steady laminar flow at the step (inlet channel – blocked region), a standard parabolic profile is prescribed via running the pump in steady operation at $Q = 7.50 \pm 0.075$ mL/s. This particular flow case is chosen to ensure transition to turbulence (from the state of knowledge in the literature, Armaly et al. 1983) downstream of the step and, hence, provide mean flow and turbulence statistics at the mid-plane of the channel.

According to Biswas et al (2004), it is common to define the Reynolds number at the step as $Re_S = \rho U S / \mu$, where S is the step height and U is the bulk velocity in the blocked region. Other definitions of Re_S in the literature include $Re_S = \rho U 2h / \mu$, where $2h$ corresponds to the hydraulic diameter of the inlet channel (Armaly et al 1983). Hereinafter, the same definition for the Reynolds number ($Re_m = U D_h / \nu$) based on the hydraulic diameter and the bulk velocity (upstream of the blockage) employed in the work of Griffith (2009) is used, to allow for an effective comparison with the literature (other models of stenosis referenced in Fig. 5.1). For the sake of simplicity in the notation, the subscript m is dropped in the rest of the thesis; that is, all of the references to the Reynolds number, Re (without the additional subscript) refer to Re_m . Furthermore, the hydraulic diameter is defined as

(Patel & Head, 1969) $D_h = 4(wh)/2(w + h)$ and $\nu = \mu/\rho$ is the kinematic viscosity of the cell fluid. The streamwise bulk velocity (U) is determined by $U = 1/h \int_0^h \bar{u}(y)dy$ (where \bar{u} is the time-average of the streamwise velocity sampled at various locations across the channel height). It should be noted that using the definition, $D_h = 2h$ (used for an infinitely wide plate assumption where $w \gg h$), yields a $\approx 12\%$ difference in the hydraulic diameter (i.e. in comparison to $D_h = 4(wh)/2(w + h)$). In the present study, the hydraulic diameter (upstream of the blockage) is equal to 3.2 mm and the Reynolds number is 1240 (transitional regime – laminar separation and turbulent reattachment – Armaly et al. 1983).

5.1.2 Creating the Stenosis Models

In order to provide a comparison between the present work and other published data for obstructed flows, Fig. 5.1a,b,c gives a schematic of the present geometry (BFS – idealized stenosis model), the asymmetric semi-circular stenosis (inside a channel with an infinitely wide plate geometry) model and the axi-symmetric stenosis model inside a straight section of tube. It should be noted that both the semi-circle and the axi-symmetric stenosis models reflect the work of Griffith (2009). It is anticipated that the 2-D channel models (Fig. 5.1a, b) have more similarity (in terms of the flow physics) in comparison to the axi-symmetric stenosis model. Nevertheless, given the physiological relevance of the axi-symmetric stenosis, it is important to provide such a comparison.

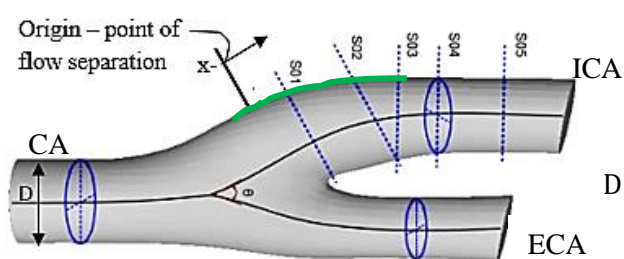
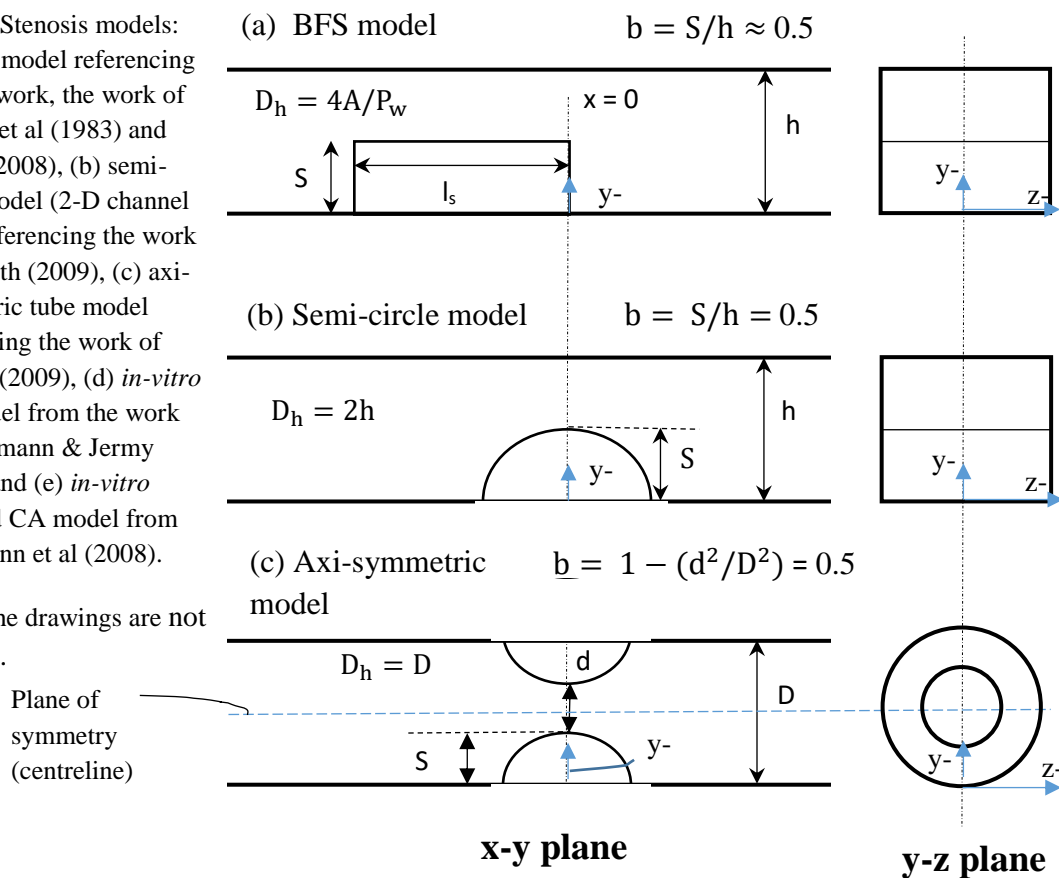
Furthermore, it should be noted that in Fig. 5.1 the blockage ratio (b) represents percent area reduction (stenosis severity). In addition, for the axi-symmetric model the blockage height is given by $S = (D - d)/2$ (refer to Fig. 5.1c). It should also be noted that for the axi-symmetric model, the diameter ratio (d/D) is not the same as the area ratio (d^2/D^2). This means that for a stenosis severity of 75% by area (i.e. $1 - d^2/D^2$) equals 50% by diameter ($1 - d/D$). The diagrams in Fig. 5.1 provide additional clarity how the blockage ratio is calculated between the various models of stenosis.

Also, given in Fig 5.1d and 5.1e are the geometries of the physiologically realistic *in-vitro* carotid models pertaining to healthy (disease-free) and stenosed cases, respectively. Fig. 5.1e is the geometry from the work of Buchmann et al (2008), an extension of the work from Buchmann & Jermy (2007) using the same ‘tuning fork’ shaped carotid artery. The main difference between the carotid models is that Buchmann et al (2008) includes a 63% concentric stenosis (by diameter) located on the outer and inner walls of the ICA. The present BFS model is compared (with sole emphasis on WSS and its spatial gradient) to both carotid models. Both models are considered since for a healthy and diseased internal carotid artery (ICA) atherosclerotic lesions tend to form along the outer and inner walls, respectively (Buchmann et al. 2008). The inner wall of the ICA is more susceptible to plaque formation (for cases where plaque has already formed) since that region experiences low WSS (Buchmann et al. 2008). Both, Fig. 5.1d and Fig. 5.1e highlight regions of where both studies report WSS. It should also be noted that the $x = 0$ location for both models corresponds to a point (along the streamwise direction) where the flow separates.

Lastly, for an effective comparison to be made between the different models given in Fig. 5.1, table 5.1 provides a summary of the geometry and flow specifications under consideration.

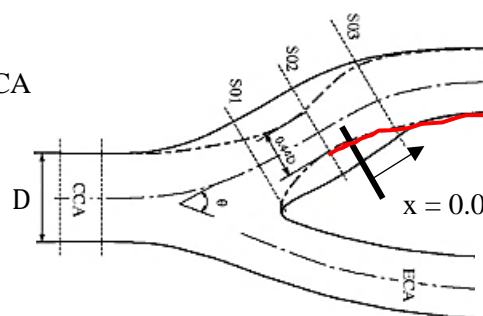
Fig. 5.1 Stenosis models: (a) BFS model referencing present work, the work of Armaly et al (1983) and Erturk (2008), (b) semi-circle model (2-D channel flow) referencing the work of Griffith (2009), (c) axi-symmetric tube model referencing the work of Griffith (2009), (d) *in-vitro* CA model from the work of Buchmann & Jermy (2007) and (e) *in-vitro* stenosed CA model from Buchmann et al (2008).

Note: The drawings are not to scale.



Note: S01-S05 are PIV planes of measurement

— Outer wall (ICA)
WSS reported



— Inner wall (ICA)
WSS reported

(d) *In-vitro* CA model

(e) *In-vitro* stenosed CA model

Table 5.1 A comparison of the geometry and flow specifications (under steady laminar flow at the blockage) between the present BFS model and other models of stenosis.

Model Type	Re	Aspect Ratio (α_s)	Geometry Type	Blockage Ratio (b)	Author(s)
Present BFS model	1240	18.26	PPFC type flow	≈ 0.5	Present author
Experimental BFS model	1290	36.00	PPFC type flow	≈ 0.5	Armaly et al (1983)
2-D Numerical BFS model	1290	Infinite wide plate assumption $w \gg h$	PPFC type flow	≈ 0.5	Erturk (2008)
Semi-circle model	1000	Infinite wide plate assumption $w \gg h$	PPFC type flow	0.5	Griffith (2009)
Axi-symmetric model	791	--	Tube flow	0.5	Griffith (2009)
<i>In-vitro</i> CA model*	700	--	Tube flow	--	Buchmann & Jermy (2007)
<i>In-vitro</i> CA model with a stenosis*	800	--	Tube flow	--	Buchmann et al (2008)

*Reynolds Number is calculated based on the CA diameter and bulk velocity

5.1.3 Scope of Measurements and Data Processing

To obtain $u(\bar{u}, u')$ and $v(\bar{v}, v')$ velocity data downstream of the BFS, the Laser Doppler Velocimetry (LDV) system is spatially fixed and the working section is traversed in pre-determined steps along the positive x- and y- directions. All velocity measurements are captured at $z = 0.00$ (i.e. $2z/w = 0$; symmetry mid-plane). For velocity measurements in the y-direction, the starting location of the measurement volume is determined in relation to the bottom wall as per section 4.3. For measurement stations along the x-direction, the BFS edge is used as reference ($x = 0$) as per section 4.3.1.

In addition, the u and v velocity components are captured simultaneously in coherence mode. In the wall region (i.e. $0.022 \leq y/h \leq 0.11$), velocity data are recorded every $10 \mu\text{m}$ along the positive y-direction, whereas away from the wall data they are recorded in the range, $0.11 \leq y/h \leq 0.94$, every $50 \mu\text{m}$. The higher data density in the wall region allows for more accurate computation of the WSS as per section 4.4. It is noted that the beams' half-angle for the wall-normal component, v, together with the relatively small channel height (i.e. $h = 1.8 \text{ mm}$) limits the number of measurement points captured along the positive y- direction. The v-component is not measurable past $y/h = 0.63 \pm 0.05$, which corresponds to the upper-half of the channel at the working section. The uncertainty associated with the value given in the latter is a result of both the uncertainty of the measurement volume position along the y-direction and optical imperfections (i.e. smudges, scratches and digs).

Furthermore, the reattachment length (associated with the separation at the BFS edge) is determined based on the streamwise component of shear stress (i.e. $\mu \left. \frac{\partial \bar{u}}{\partial y} \right|_{y=0} = 0$) being zero (Armaly et al 2003). A second technique which is used to determine the reattachment length in the present work is suggested by Kueny & Binder (1984). The technique consists of scanning the streamwise mean velocity at various parallel planes in reference to the lower wall (i.e. $0.027 < y/h < 0.11$). The locations in these planes where $\bar{u}/U = 0$ are extrapolated to the lower wall to determine the reattachment length, x_1^* (i.e. where $x_1^* = x_1/S$).

The energy spectra ($E_{u'u'}$, $E_{v'v'}$) of the temporal variation of u' and v' reported in section 5.1.4 (Results and Discussion) are computed to determine the frequency components as well as the energy contribution of the measured streamwise u' and wall-normal v' downstream of the BFS. The energy spectra are computed by using a Fast Fourier transform (FFT) on the streamwise and wall-normal velocity fluctuations (i.e. u'). The u' values are computed from the mathematical expression $u' = u - \bar{u}$ (Reynolds & Hussain, 1972) at various y/h and x/S measurement positions (the analysis is performed with Matlab and Visual Basic to deduce u' over $N \approx 2000$).

It should be noted that the energy spectra analysis is relatively more complex given that the data points captured with LDV are non-uniformly sampled. Hence, reconstruction of the time-series via linear interpolation of the velocity signal between the measured values is performed (Benedict et al. 2000). Essentially, the time series is resampled at equidistant time intervals using the same number of data points and range. The results from the FFT analysis (i.e. the spectra plots) are then integrated to ensure the corresponding $\frac{1}{2} \overline{u'u'}$ is obtained. Another verification which is performed in the present work to ensure accuracy of the spectra plots is using the Lomb-Scargle method (Kysela et al. 2013) which does not require resampling of the uneven data points. Essentially both methods provide similar results.

Finally, table 5.2 and Fig. 5.2 show the measurement stations downstream of the step at $2z/w = 0$ (mid-plane). The streamwise distance where the measurements are captured is normalized with the step height, hydraulic diameter (unblocked region) and reattachment length. It should be noted that linear interpolation is used where required (of the normalized streamwise velocity profiles) to coincide the measurement stations between the present and other work (referenced in Fig. 5.1).

Table 5.2 Measurement stations at the working section downstream of the step. Measurements are taken at the mid-plane of the working section, $2z/w = 0$. The normalized error of the measurement volume position downstream of the step is $\epsilon_x/S = \pm 0.06$. For reference, it should be noted that the distance between the step edge and the centre of the microscopy slide is 25 mm.

Measurement Stations	x/S (where $S = 842 \pm 50 \mu\text{m}$)	x/D_h (where $D_h = 3.2 \text{ mm}$ for unblocked channel)	x/x_1 (where $x_1 = 13.45 \text{ mm}$ and is the dimensional reattachment length)	Dimensional location of the measurement volume in reference to $x = 0$ at the step edge [mm]
Pt. 1	-1.18	-0.03	-0.06	-1
Pt. 2	3.02	0.79	0.19	2.54
Pt. 3	6.03	1.58	0.38	5.08
Pt. 4	9.05	2.38	0.57	5.62
Pt. 5	12.07	3.17	0.76	10.16
Pt. 6	15.08	3.96	0.94	12.70
Pt. 7	18.10	4.76	1.13	15.24
Pt. 8	21.12	5.55	1.32	17.78
Pt. 9	30.17	7.93	1.89	25.40

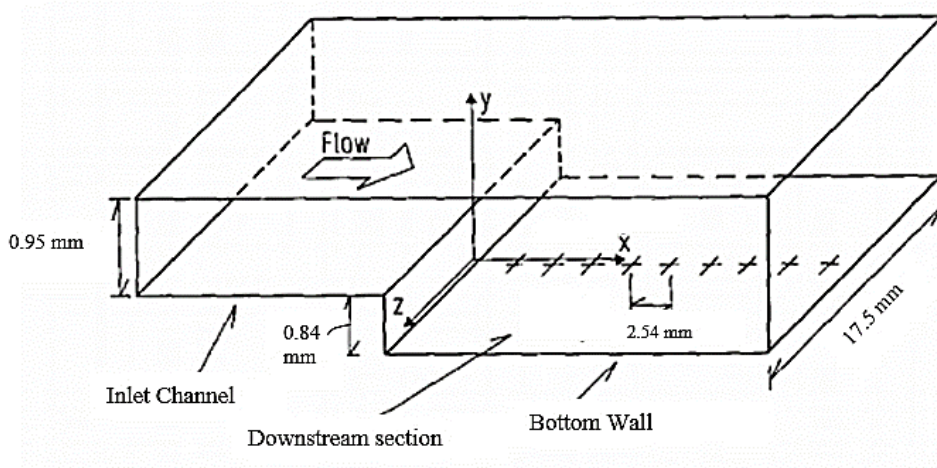


Fig. 5.2 Schematic of the present BFS test-section showing measurement stations and other critical dimensions (Modified from Adams & Johnston, 1988).

5.1.4 Results and Discussion

Before presenting the measured flow quantities downstream of the backward-facing step (BFS) at the midplane of the channel (and comparing the results to other models of stenosis), the present author highlights Fig. 5.3a. This Figure is an illustration of the expected flow field (based on the present state knowledge from the literature) for the present BFS model under steady laminar flow. It should be noted that, x_1^* , x_2^* , x_3^* , x_4^* and x_5^* represent non-dimensional distances (in reference to the step edge) associated with flow reattachment in reference to the primary recirculation region, separation and reattachment in reference to the tertiary recirculation region (on the lower wall) and, separation and reattachment in reference to the secondary upper wall recirculation region (“roof eddy”), respectively. It should also be noted that the tertiary recirculation region on the lower wall is not detected in the present study. Similarly, an illustration is also provided for the axi-symmetric stenosis model (semi-circle shape stenosis inside a tube) in Fig. 5.3b. The semi-circle asymmetric stenosis model inside a 2-D channel is not provided given the similarity to the BFS model (with the exception of the stenosis geometry and absence of the side-walls).

The flow field inside the healthy carotid artery (CA) phantom (captured by PIV) from the work of Buchmann & Jermy (2007) is also shown in Fig. 5.4. It should be noted that the CA phantom studies in the literature consider healthy and diseased (with a stenosis) arteries to better understand the correlation between WSS (and its spatial/temporal gradient) and EC response. For the healthy ICA flow, regions of low WSS are found on the outer wall (as a result of flow separation) whereas, for the diseased ICA flow, they are found on the inner wall downstream of the concentric stenosis. According to Buchmann et al (2008), the flow does not separate on the outer wall of the ICA downstream of the stenosis.

The present author believes that the illustrations of the flow field in Figures 5.3 and 5.4 will help the reader better understand the various flow structures (and the quantified data) discussed in the subsequent paragraphs. They will also help the reader to attain a general idea of the expected flow field associated with the various stenosis models.

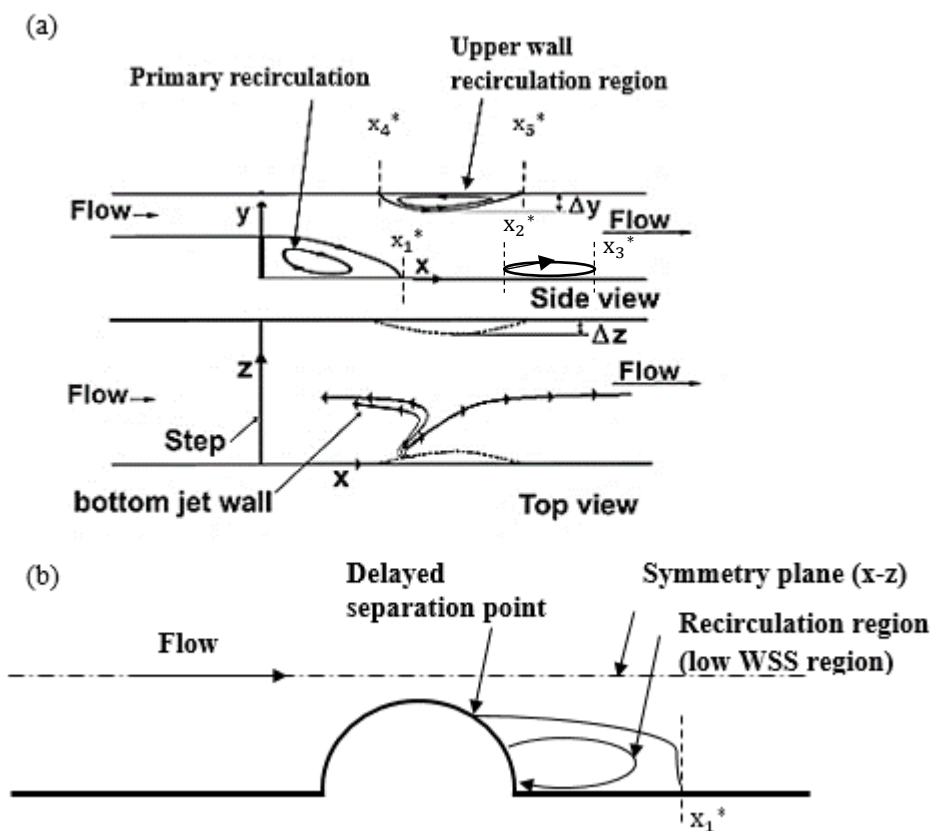


Fig. 5.3 An illustration of the expected flow field downstream of the flow blockage: (a) present BFS model (modified from Juste et al (2016)) and (b) axi-symmetric stenosis model inside a straight section of tube.

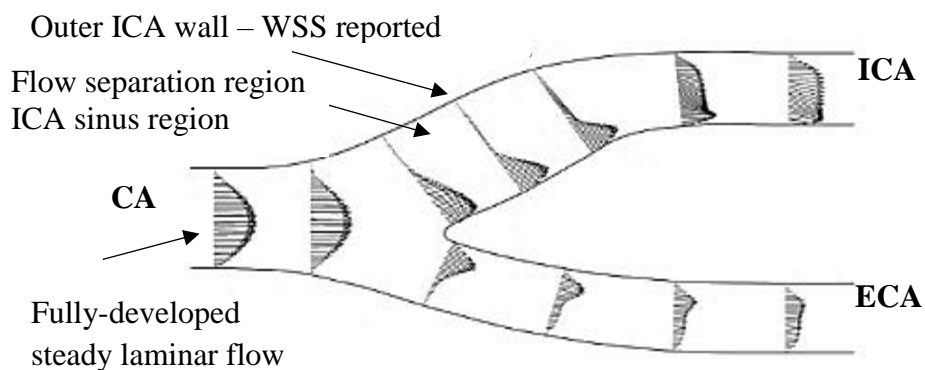


Fig. 5.4 An illustration of the flow field inside the carotid artery (CA) phantom. Modified from the work of Buchmann & Jermy (2007).

To begin with, in Fig. 5.5, the measured streamwise mean velocity (normalized with $\bar{u}_{\max} = 0.797 \pm 0.001$ m/s) profile and the empirical correlation analytical solution for channel flow are given at the step. Also given in Fig. 5.5 are the inlet streamwise mean velocity profiles measured by Armaly et al (1983) and Nie & Armaly (2004) for $Re = 1290$ and $Re = 3236$, respectively. Literature cited in the former and the latter report flow over a backward-facing step with aspect ratios of 36.0 and 8.0, respectively.

In general, there is excellent agreement between the measured (present work), empirical correlation and the profile of Armaly et al (1983). The average deviation of the experimental data points in the present work from the empirical correlation is $\pm 3.5\%$. It is interesting to note that the streamwise mean velocity profile given by Nie & Armaly (2004) deviates away from the fully-developed laminar flow at $Re = 3236$. The latter is in good agreement with Patel & Head (1969) who report a transition from laminar flow at $Re > 1350$ (based on h as the characteristic length scale and not $D_h = 2h$). Furthermore, the turbulence intensity of the inlet flow at the step is an important factor which influences the

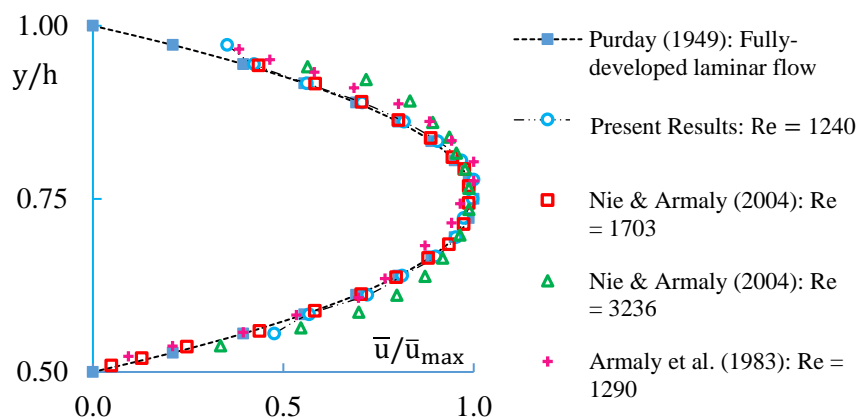


Fig. 5.5 Measured and normalized streamwise mean velocity profile $\bar{u}(y)$ at the inlet channel at $2z/w = 0$ and $x/S = -1.18$. The y-axis is normalized against the channel height at the blockage ($h - S$). The maximum absolute error (in the wall region, $0.5 \leq y/h \leq 0.7$ is ± 0.01 m/s (or 1.25 % of \bar{u}_{\max}).

downstream flow structure (Jongebloed, 2008). In the present work, the flow is considered laminar at the inlet channel since $\sqrt{u'^2} \approx 0.0025$ m/s (spurious r.m.s., LDV noise level) is detected across the channel height.

In addition, in the present study, the spanwise profile of the streamwise velocity $\bar{u}(z)$ is not measured and reported at the inlet of the channel to verify two-dimensionality of the flow. This is as a result of measurement difficulty at the step (i.e. probe rotation along the y-axis). Nevertheless, according to Avari et al (2016), the flow at the working section in reference to the present PFFC considering $\alpha = 9.72$ and a Reynolds number of 990 (considering the bulk velocity and h as the characteristic length scale) is approximately 65% uniform across the width (i.e. $-0.65 < 2z/w < 0.65$). Given the larger aspect ratio at the inlet channel (i.e. $\alpha_s = 18.26$), the flow is considered two-dimensional in the blocked region with negligible side-wall effects on the mid-plane flow structure. It should also be noted that the streamwise mean velocity does not vary (outside the experimental uncertainty) along the step (i.e. top of the block at $2z/w = 0$) in the x-direction between the step edge ($x/S \approx -1.18$) and $x/S = -2.37$ (the shear layer separating at the upstream corner of the step does not interfere with the downstream corner – disturbance generated from the leading edge dies out by the time it reaches the trailing edge).

Fig. 5.6a compares the normalized streamwise velocity profiles of the present BFS model to experimental (Armaly et al. 1983) and 2-D numerical (Erturk, 2008) BFS models (refer to table 5.1 for geometry and flow specifications). The first five measurement stations given in Fig. 5.6a ($x/S = 3.02, 6.03, 9.05, 12.07$ and 15.08) are in favorable agreement (average deviation of $\pm 7.5\%$) in terms of the \bar{u}/U profile (where U is the bulk velocity at the step) between the present, experimental and 2-D numerical BFS models. Furthermore, the present work maximum value of the \bar{u}/U profile agrees well with both BFS models being $\bar{u}/U \approx 1.5$ at $y/h \approx 0.7$ with a maximum deviation of $\pm 1.4\%$ (for the first four measurement stations). In the present work, the largest magnitude of the \bar{u}/U profile inside the primary recirculation region (lower wall) is $\bar{u}/U = -0.2$. This is in good agreement with the experimental and 2-D numerical BFS models which display a maximum value of $\bar{u}/U \approx -0.19$. At $x/S = 15.08$, the present work \bar{u}/U profile shows existence of a second

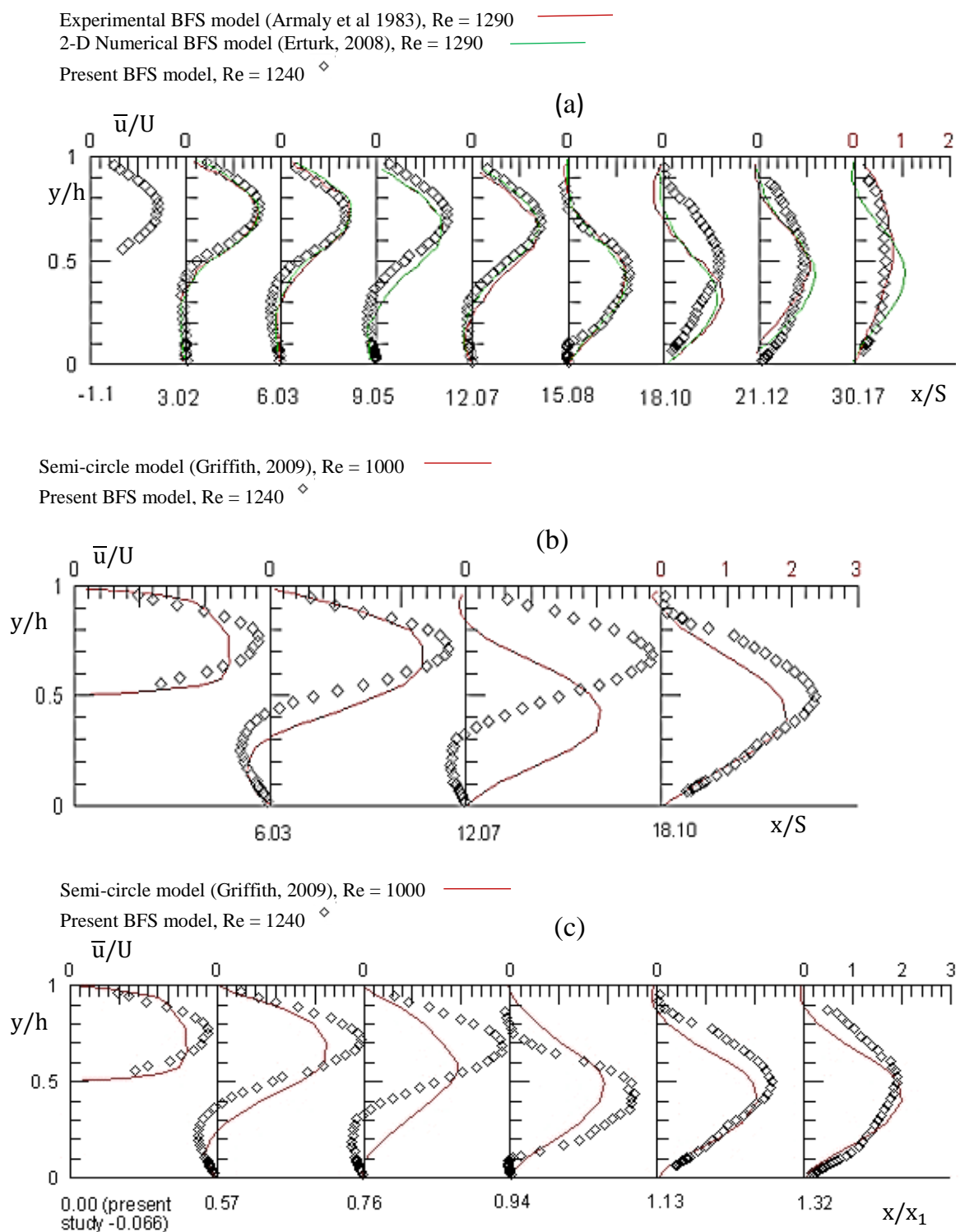


Fig. 5.6 Normalized streamwise mean velocity at various downstream stations: (a) present BFS model in comparison with the work of Armaly et al (1983) and Erturk (2008), (b) present BFS model in comparison with the semi-circle model whereby the streamwise distance is normalized with the blockage height (S) and, (c) present BFS model in comparison with the semi-circle model whereby the streamwise distance is normalized with the reattachment length (x_1).

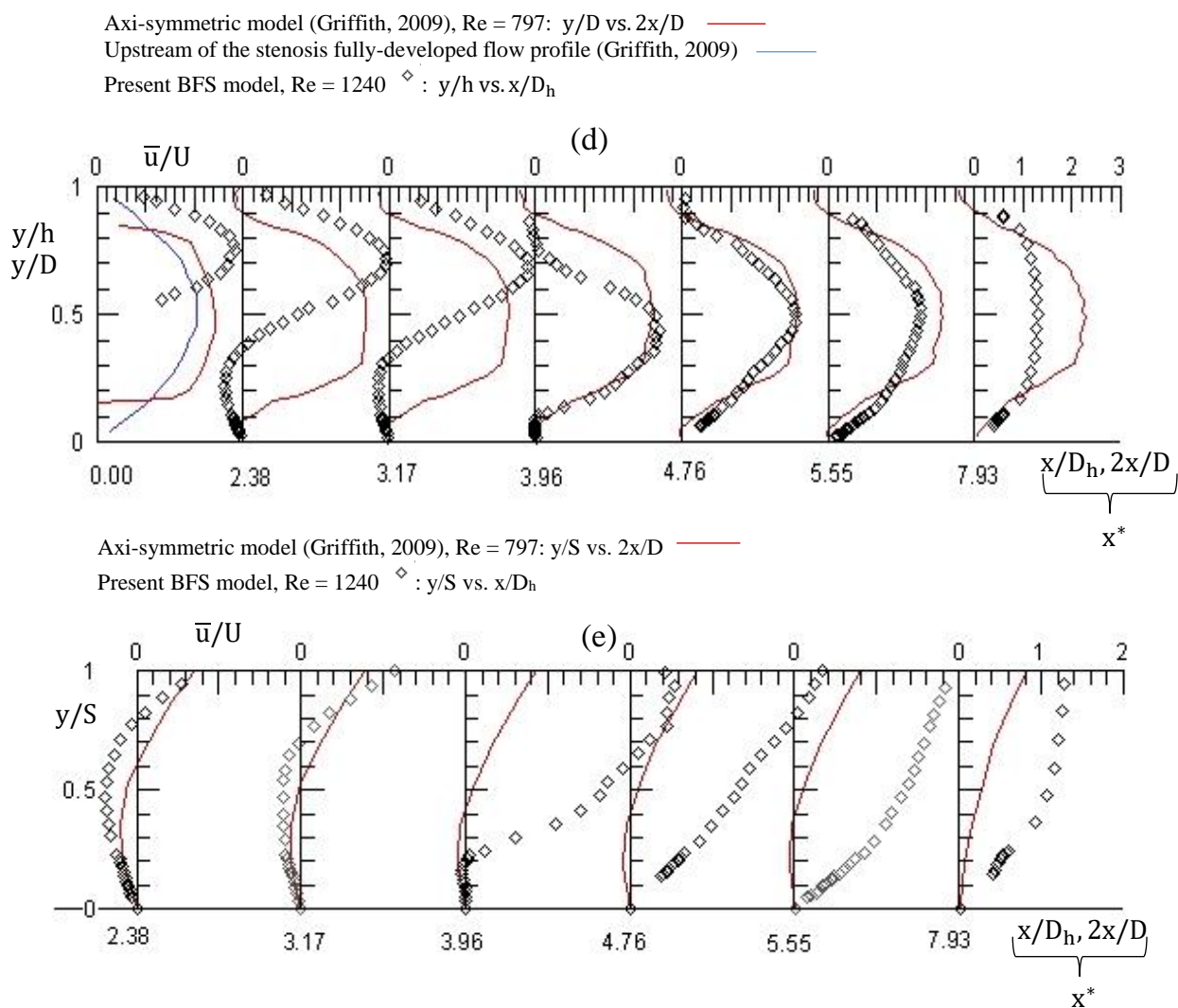


Fig. 5.6 Continued: Normalized streamwise mean velocity at various downstream stations: (d) present BFS model in comparison with the axi-symmetric model (work of Griffith, 2009) whereby the wall-normal distance is normalized with channel/tube height and (e) present BFS model in comparison with the axi-symmetric model, whereby the wall-normal distance is normalized with the blockage height (S).

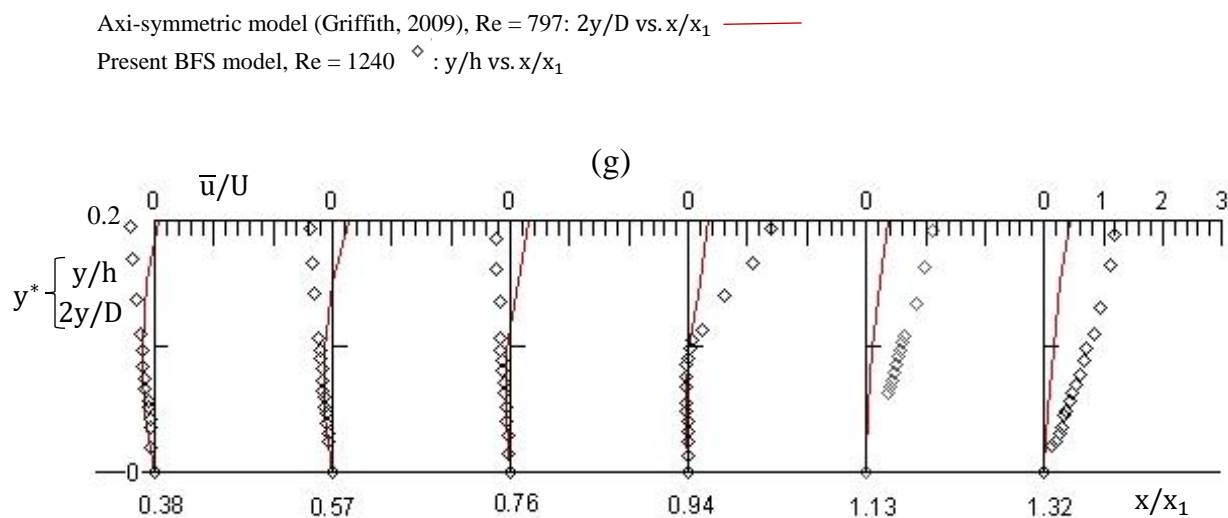
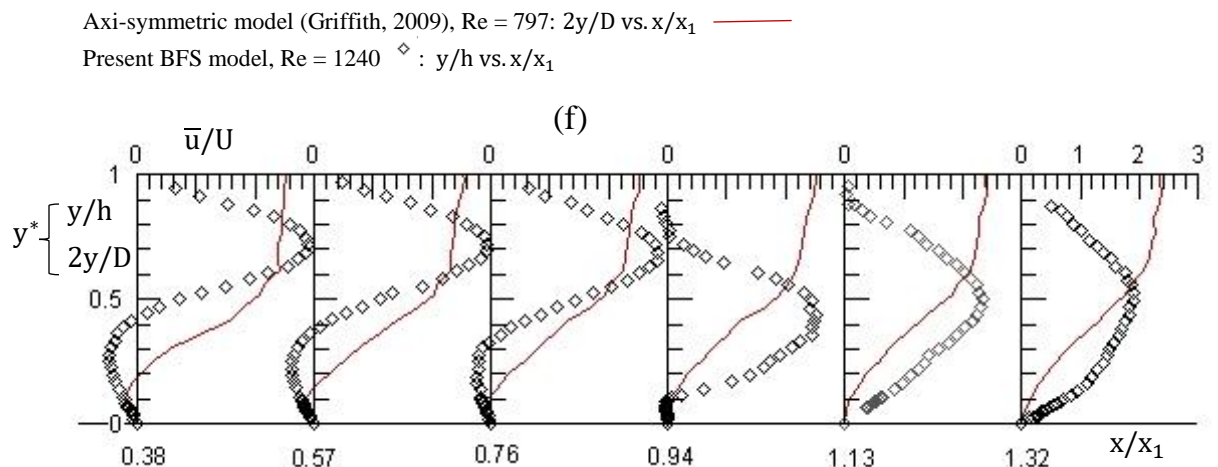


Fig. 5.6 Continued: Normalized streamwise mean velocity at various downstream stations: (f) present BFS model in comparison with the axi-symmetric model (work of Griffith, 2009) whereby the streamwise distance is normalized with the reattachment length (g) present BFS model in comparison with the axi-symmetric model, whereby the streamwise distance is normalized with the reattachment length and only showing for $y^* \leq 0.2$. For the present study, the normalized typical uncertainty at $y/h = 0.5$ (mid-plane in reference to the height) is $\epsilon_{\bar{u}}/|\bar{u}| = \pm 2.50\%$.

recirculation region on the upper wall (i.e. “roof eddy”). At this measurement station, the \bar{u}/U profile compares favorably with both the experimental and 2-D numerical BFS models, also reporting the presence of negative velocities in the region $y/h > 0.75$. The reattachment length (associated with the primary recirculation region) of the present BFS model based on both methods discussed in section 5.1.3 is $x_1^* = x_1/S = 15.9 \pm 0.1$, which is within $\pm 4.3\%$ of the value given by Armaly et al (1983) at $Re = 1290$.

The first major discrepancy of the \bar{u}/U profiles (in Fig. 5.6a) between the present and the other BFS models is realized at $x/S = 18.10$. At this measurement station, the \bar{u}/U profile displays a relatively small region of negative velocities at $y/h > 0.9$ ($\bar{u}/U \approx -0.01$) which is not in favorable agreement with the experimental and 2-D numerical BFS models. The upper wall recirculation depth extends for $\Delta y/h \approx 0.3$ with a maximum value of $\bar{u}/U \approx -0.18$ and -0.07 in reference to the experimental and 2-D numerical BFS models, respectively. Although the maximum value of the \bar{u}/U profile is comparable between all of the profiles at $x/S = 18.10$, the locations (in reference to y -) in which they occur are different. The position of the maximum value of $\bar{u}/U \approx 1.16$ differs in the amount of $\Delta y/h \approx 0.2$ (in comparison to the other work), presumably as a result of the relatively larger recirculation region (i.e. greater depth) realized (by the other two BFS models) on the upper wall shifting the maximum value downwards (i.e. negative y -direction).

Another interesting observation is that the experimental BFS model reports the upper wall recirculation region extending for $\Delta_{x_5^* - x_4^*} \approx 7.14$, whereas in the present work it extends for $\Delta_{x_5^* - x_4^*} \approx 3.02$. Equally interesting is that the 2-D numerical BFS model shows the upper wall recirculation extending for $\Delta_{x_5^* - x_4^*} \approx 11.22$ (evident up to $x/S = 30.17$). The present \bar{u}/U profile at $x/S = 30.17$ agrees favorable with the experimental BFS model whereby both profiles seem to have redeveloped (reached fully-developed state) with a maximum value of $\bar{u}/U \approx 0.7$. In contrast, both the present and experimental BFS \bar{u}/U profiles do not agree with the 2-D numerical BFS model at ($x/S = 30.17$) as a result of the extended upper wall recirculation region, whereby the maximum value of $\bar{u}/U \approx 1.06$ occurs at $y/h \approx 0.44$ (shifted downward in relation to the y -axis).

The present author postulates that the reason for the start of the discrepancy at $x/S = 18.10$ is as a result of the difference in the aspect ratio of the BFS models. This is supported by the work of Chiang & Sheu (1998), whereby the authors report that the secondary flow induced by the side-walls does affect the mid-plane flow structure and can only be ignored for $\alpha_S > 50$. Furthermore, Chiang & Sheu (1998) report that when $\alpha_S = 100$, the flow structure at the channel mid-plane for the 2-D and 3-D numerical solutions are identical. The authors further provide evidence of the upper wall recirculation region increasing in size (streamwise and spanwise length) with an increase in channel width. In fact, for $\alpha_S < 35$ Chiang & Sheu (1998) report no evidence of an upper wall recirculation at the mid-plane of the channel, which is very much supportive of the relatively smaller recirculation region found on the upper wall in the present work (i.e. $\Delta_{x_5^* - x_4^*} \approx 3.02$). It is also supportive of the much longer streamwise length of the recirculation region reported by the 2-D numerical simulations of Erturk (2008). It should be noted that the experimental BFS model studied by Armaly et al (1983) shows three-dimensional flow downstream of the flow reattachment (although the flow kept its symmetry to the mid-plane of the channel) and is detected in the range, $Re > 400$ and $Re < 6000$. The findings in the latter seem to be in agreement with the start of the \bar{u}/U profile deviation in the present work which appears to occur somewhere in the range, $15.08 < x/S \leq 18.10$. In addition, Armaly et al (1983) reports that the flow remains two-dimensional over the streamwise length of the primary recirculation region. The latter finding presumably explains the favourable agreement of the \bar{u}/U profile with the present work in the range, $3.02 < x/S < 15.08$. This agreement of the profiles is expected since according to Brederode & Bradshaw (1972), the influence of the side-walls on the mid-plane flow structure (in the primary separation region) can be ignored for $\alpha_S > 10$.

The mechanism involved whereby the side-walls influence the mid-plane flow structure is explained by Williams & Baker (1997). The authors analyze the flow field downstream of the BFS ($\alpha_S = 36$, $ER = 1.94$, $Re = 800$) using 3-D numerical methods and show a side-wall induced three-dimensional vortex penetrating towards the mid-plane of the channel and, thus, decreasing the extent of the two-dimensional flow region (i.e. formation of a side-wall jet at the channel lower wall). According to Williams & Baker (1997), the vortex

enters the primary recirculating flow (entrained by the primary 2-D motion) and exits into the mainstream flow. The findings from Williams & Baker (1997) are in agreement with the work of Chiang & Sheu (1998), which report that the continuous penetration of the side-wall flow to the mid-plane is highly dependent on both the Reynolds number and the aspect ratio of the channel. In the present study, it is expected that $\bar{u}(z)$ varies across the channel (at the working section in the vicinity of the reattachment point) since Chiang & Sheu (1998) only report a 2-D flow in the range, $-0.20 < 2z/w < 0.20$ at $Re = 1000$ for $\alpha_S = 36$. It should be noted that in both the work of Williams & Baker (1997) and Chiang & Sheu (1998), the flow remains steady laminar and, thus, the side-wall influence is likely not responsible for transition to turbulence (in the vicinity of flow reattachment) in the present study.

Turbulence statistics are also provided in the present study. It is expected for the flow to reveal laminar separation and turbulent reattachment (Von Terzi, 2016). This is because in the present work, $Re = 1240$ represents a transitional flow based on the characterization given by Armaly et al (1983). The laminar, transitional and turbulent regimes are characterized by Armaly et al (1983) based on the reattachment lengths in reference to the primary recirculation region. In the transitional regime (i.e. $6600 > Re > 1200$), Armaly et al (1983) notes a significant increase in the velocity fluctuations (in the vicinity of the reattachment point) corresponding to the onset of transition to turbulence. According to Von Terzi (2016), it is the vortex shedding phenomenon that explains the increase in the velocity fluctuations and the sudden drop in the reattachment length reported by Armaly et al (1983). It should also be noted that according to Biswas et al (2004), the limit of steady laminar flow for a 3-D BFS model is $Re \approx 1200$.

Furthermore, Fig. 5.7a gives the streamwise and wall-normal r.m.s. velocity profiles normalized with the bulk velocity at the step ($u'^* = \sqrt{u'^2}/U$, $v'^* = \sqrt{v'^2}/U$) in the range, $12.07 \leq x/S \leq 30.17$. Once the spurious r.m.s. velocities (i.e. inherent LDV noise) are subtracted from the data, the turbulence intensities in the range, $3.02 \leq x/S < 12.07$, are negligible indicating a steady laminar flow. It is clear from Fig. 5.7a that both u'^* and v'^* increase in magnitude as one moves away from the BFS. The peaks in the u'^* and v'^* profiles at $x/S = 15.08$ (onset of flow reattachment) are concentrated in the shear layer

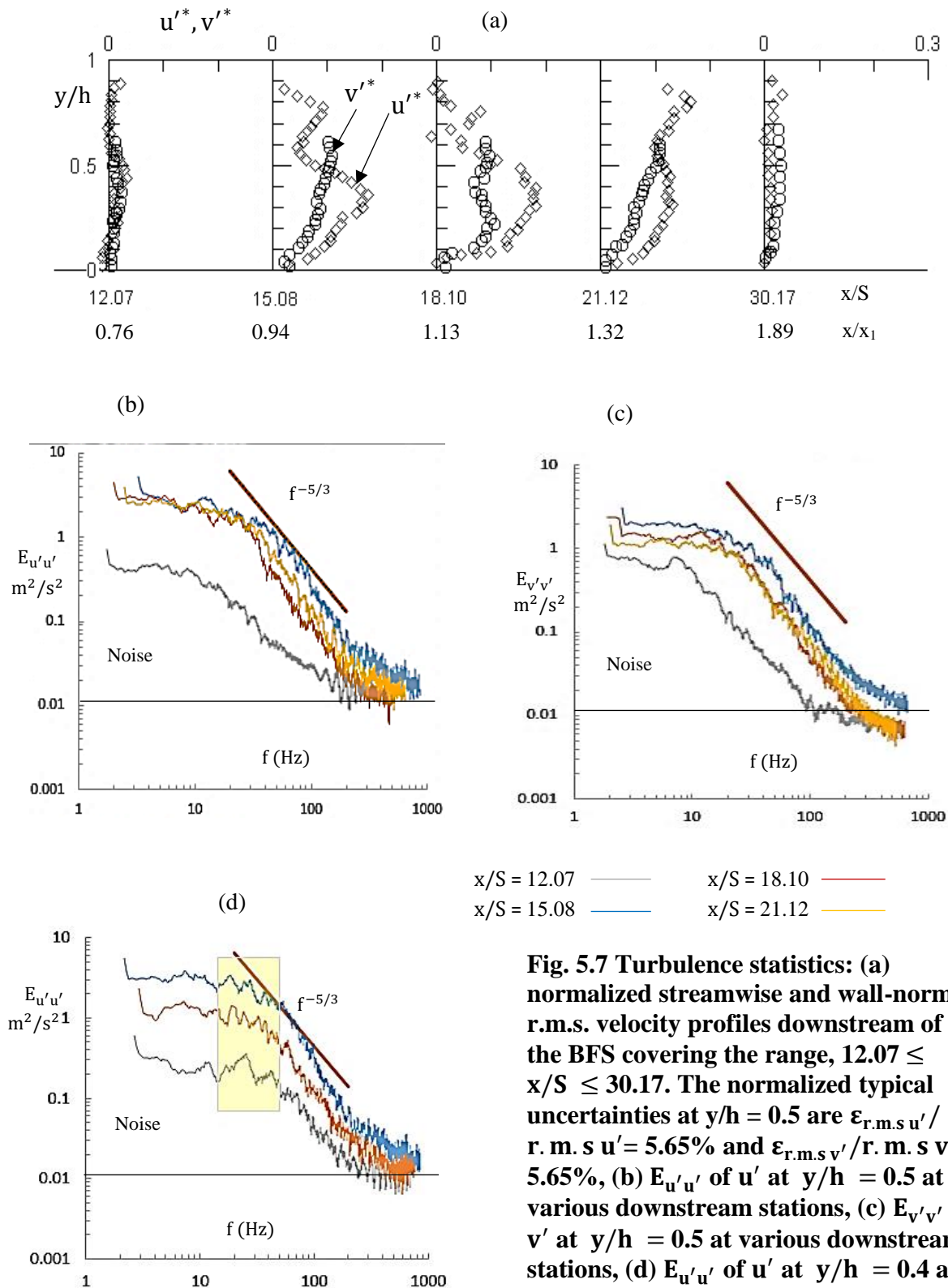


Fig. 5.7 Turbulence statistics: (a) normalized streamwise and wall-normal r.m.s. velocity profiles downstream of the BFS covering the range, $12.07 \leq x/S \leq 30.17$. The normalized typical uncertainties at $y/h = 0.5$ are $\varepsilon_{r.m.s. u'}/r.m.s. u' = 5.65\%$ and $\varepsilon_{r.m.s. v'}/r.m.s. v' = 5.65\%$, (b) $E_{u'u'}$ of u' at $y/h = 0.5$ at various downstream stations, (c) $E_{v'v'}$ of v' at $y/h = 0.5$ at various downstream stations, (d) $E_{u'u'}$ of u' at $y/h = 0.4$ at various downstream stations.

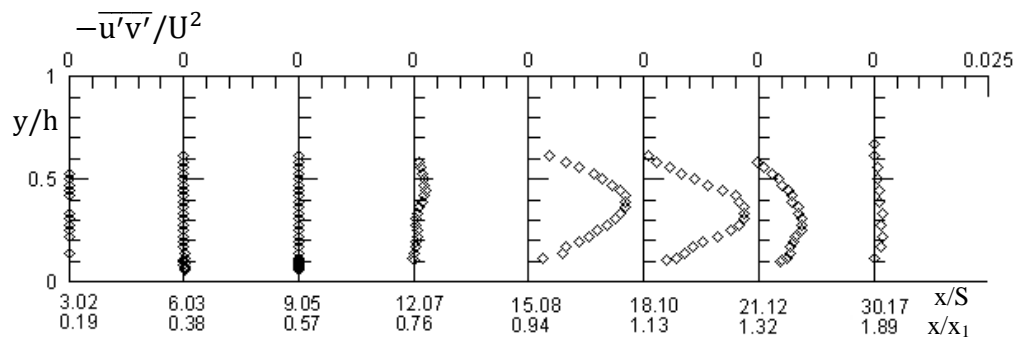


Fig. 5.8 Measured Reynolds shear stress profiles at various x/S and x/x_1 positions downstream of the step. No measurement of the wall-normal component (v) was possible for $y/h > 0.6$ as a result of the beam geometry (i.e. beams' half-angle) and finite channel height (i.e. 1.8 mm). The normalized typical uncertainty at $y/h = 0.5$ is $\varepsilon_{\overline{u'v'}}/|\overline{u'v'}| = \pm 8.00\%$

(i.e. $y/h \approx 0.4$) indicating that the instability occurs and propagates in the shear layer. At $x/S = 15.08$, the maximum values of u'^* and v'^* are 0.21 and 0.12, respectively. At $x/S = 18.10$ (downstream of flow reattachment), the maximum value of v'^* shifts downward (in reference to y -) and occurs at $y/h = 0.2$. Subsequently, for $x/S > 18.10$, the u'^* and v'^* profiles demonstrate more uniform shapes, presumably as a result of the turbulent jet breakdown and the disturbances rapidly diffusing over the entire channel cross-section. Lastly, at $x/S = 30.17$ the turbulence intensities decay to almost negligible levels of $u'^* \approx 0.01$ and $v'^* \approx 0.02$ indicative of flow relaminarization. In support of the r.m.s. profiles, the energy spectra ($E_{u'u'}$ $E_{v'v'}$) are given in Fig. 5.7b, 5.7c and 5.7d downstream of the BFS in the range, $12.07 \leq x/S \leq 21.12$. In Fig. 5.7b and 5.7c (corresponding to $y/h = 0.5$), it is rather difficult to distinguish peaks with high energy content within a narrow frequency range corresponding to shear layer oscillation and subsequent vortex shedding. However, in Fig. 5.7d (corresponding to $y/h = 0.4$) at $x/S = 12.07$ there is clearer evidence of concentrated energy within a narrow frequency band with a mild peak occurring at $f \approx 30$ Hz corresponding to a Strouhal number of $St = fS/U = 0.11$ (where U refers to bulk velocity upstream of the BFS). According to Tihon et al (2012), a non-dimensional frequency of $St \cong \mathcal{O}(10^{-1})$ corresponds to vortex shedding (originating in the shear layer as a result of a Kelvin-Helmholtz instability – caused by the interaction between the shear layer and the recirculating flow near the step wall; Rani et al. 2007) and is typical for BFS flows (transitional flow). From Fig. 5.7d, at $x/S = 15.08$ and 18.10, the intensity of the

spectral peaks reduces with multiple peaks seen in the range, $0.1 < St < 0.14$. It should be noted that the formation of multiple peaks could be as a result of coalescing of the vortices (Varghese et al. 2007a). Furthermore, the spectra do not indicate developed turbulence in the vicinity and farther downstream of flow reattachment (i.e. $x/S = 15.08, 18.10$ and 21.12). This is because developed turbulence would show a wide range of frequencies matching with a $-5/3$ slope. In the present results, only a narrow band is reflected by the $-5/3$ slope. Although the literature refers (Von Terzi, 2016) to this as turbulence (for BFS type flows), it is more likely that the present results are showing turbulent spots representing breakdown of structure and transition.

The expected turbulent integral time scale (large eddies) is $\tau_\Lambda = \Lambda / \text{r.m.s. } u' = 0.016 \text{ s}$ ($f \approx 60 \text{ Hz}$). It should be noted that in the above expression Λ is the integral length scale defined as $0.92(h/2)$ and $\text{r.m.s. } u' \approx 0.05 \text{ m/s}$ is the typical turbulence intensity of the flow (Avari, 2015). It is emphasized that this time scale should only be regarded as an estimate. To determine the Kolmogorov time scale (τ_η), the following mathematical expression is used, $\tau_\eta = [\nu \Lambda / (\text{r.m.s. } u')^3]^{1/2}$ (Pope, 2000). It should be noted that $[(\text{r.m.s. } u')^3 / \Lambda]$ represents the dissipation rate (ϵ). Following the substitution of the quantities in the above expression yields $\tau_\eta = 0.002 \text{ s}$ ($f \approx 500 \text{ Hz}$). Hence, the estimated time scales are in reasonable agreement with the frequency range shown in Fig. 5.7b, 5.7c and 5.7d.

The instability which occurs at $Re = 1240$ for the present work is lower than that of $Re = 2000$ (linearly unstable two-dimensionally) reported by Barkley et al (2002) for the BFS flow with $b = 0.5$ (using computational stability analysis). However, as noted by Haggmark et al (2000) and Tihon et al (2012), experimental verification of the critical Re value given by Barkley et al (2002) is not easy as a result of a strong influence of small external perturbations (i.e. such as mean flow variations, surface roughness, asymmetry, surface vibrations and freestream turbulence) found in experiments which could lead to earlier inception of an instability. Another note worth making is that according to Blackburn et al (2008), rapid variation in the channel geometry (i.e. BFS flow) is found to produce a local flow region which is highly receptive to inlet conditions, thereby developing a transient convective instability (i.e. spatially growing oscillations convecting with the flow) much below the onset of any absolute instability.

Furthermore, the Reynolds shear stress (i.e. $-\overline{u'v'}/U^2$) in the range, $3.02 \leq x/S \leq 30.17$, is given in Fig. 5.8. It is apparent that for $x/S = 3.02, 6.03$ and 9.05 , the Reynolds shear stress is zero for all locations along the channel height for $y/h < 0.6$ (limitation of v -component measurement). The scatter around the zero mark is within the given experimental uncertainty of $\varepsilon_{\overline{u'v'}}/|\overline{u'v'}| = \pm 8.00\%$. There is an increase in $-\overline{u'v'}/U^2$ at $x/S = 12.07$ associated with the increase of turbulence intensity in the shear layer at $y/h = 0.4$. At $x/S = 15.08$ and 18.10 , the $-\overline{u'v'}/U^2$ profiles significantly increase in magnitude showing a maximum value of ≈ 0.02 at $y/h \approx 0.35$. The largest magnitude in $-\overline{u'v'}/U^2$ near flow reattachment is as a result of impingement of the unsteady shear layer on the lower wall (Shih & Ho, 1994). Furthermore, there is a decrease of $-\overline{u'v'}/U^2$ at $x/S = 21.12$ with the maximum value of 0.01 . It is interesting to note that the value of $-\overline{u'v'}/U^2 \approx 0.02$ (for the present study) in the vicinity of the reattachment agrees well with the pioneering work of Bradshaw & Wong (1972), whereby the authors note measured values as high as 0.02 .

Since the main motivation of the present work is to compare the mean flow and turbulence statistics (together with the reattachment point and the skin friction coefficient) downstream of a simple 2-D step to more realistic stenosis models, a comparison is made with other geometry types (with similar blockage ratios; $b = 0.5$) as depicted in Fig. 5.1. It should be noted that both stenosis geometry studies given in Fig. 5.1b,c do not provide turbulence statistics downstream of the blockage and, hence, only the mean flow and other statistics (i.e. reattachment point) are compared to the present BFS model. Furthermore, Fig. 5.6b compares the normalized streamwise velocity profiles (\overline{u}/U ; where U is the bulk velocity upstream of the blockage) of the present BFS model to the semi-circle model (computed based on 2-D numerical work of Griffith, 2009). It should be noted that in Fig. 5.6b, the streamwise distance is normalized with the blockage height (S). The purpose of Fig. 5.6b is to demonstrate and discuss the difference in the normalized reattachment length ($x_1^* = x_1/S$) in reference to the primary recirculation region between the two models. In reference to the semi-circle model, the reattachment length is smaller with a difference of $\Delta x_1^* = 4.4$. This result is, to a certain degree, expected since it is known from the literature that steady laminar flow over rounded steps (i.e. quarter-circle) gives relatively smaller

x_1^* values in comparison to vertical steps with a defined edge (Ratha & Sarkar, 2015). According to Griffith (2009), it is the delayed flow separation induced by the semi-circle geometry that leads to a difference in the x_1^* values, whereby for the semi-circle geometry the separation point is dependent on the Reynolds number and the distribution of the adverse pressure gradient on the downstream half of the blockage (together with the shape of the streamwise velocity profile) along the surface (Griffith, 2009). This is in contrast to the BFS model whereby the separation point is fixed at the step edge given that the boundary layer is unable to follow the turn in the sharp corner (i.e. geometry-induced separation, Haggmark et al. 2000). To demonstrate the effect of the blockage geometry (i.e. semi-circle versus vertical step) on x_1^* , the work of Ratha & Sarkar (2015) is considered. The authors report (for $b = S/h \approx 0.5$; $Re = 1000$; using 2-D numerical methods – planar channel) a difference of $\Delta x_1^* \approx 1.0$ between the vertical and rounded step reattachment lengths (whereby a quarter-circle is used on the step edge to model a smooth transition). Hence, other factors may also contribute to the difference in the x_1^* values between the present BFS model and the semi-circle model. Both, the Reynolds number difference and the three-dimensionality of the flow (discussed in the preceding paragraphs when comparing to the work of Armaly et al 1983) contribute to the difference observed in the x_1^* value (Erturk, 2008). It is interesting to note that Armaly et al (1983) shows, at $Re = 1000$, that the difference in the normalized reattachment length is $\Delta x_1^* = 4.0$ (a difference of 9.5% with the present comparison of $\Delta x_1^* = 4.4$) between their experimental and 2-D numerical BFS models (whereby the numerical 2-D model yields a relatively smaller reattachment length). This difference in the reattachment length is related to the aspect ratio of the channel (α_S) and is well documented in the literature (Erturk, 2008). The upper wall recirculation (which initiates closer to the step edge with numerical 2-D models in the range, $400 < Re < 6000$, Armaly et al. 1983) subjects the streamwise flow to curvature and acts as a blockage which results in a smaller x_1^* value (Barkley et al. 2002). Another reason which extends the primary recirculation region for BFS models (with a finite aspect ratio; that is with the no slip condition imposed on the side-walls) is the existence of the upper wall recirculation near the side-walls which enhances the existing side-wall jets developing on the lower wall adjacent to the side-walls (Juste et al. 2016). It is important to note that for 2-D numerical BFS models (no side-wall effect), the upper wall

recirculation region extends across the entire span of the channel whereas, in 3-D numerical BFS models its spanwise reach (from the side-walls) depends on the aspect ratio of the channel and the Re value (Chiang & Sheu, 1998).

It is worth noting that in the present comparison (Fig. 5.6b), the semi-circle model shows the upper wall recirculation commencing at $x/S = 12.07$ (possibly even farther upstream). For the present BFS model, the upper wall recirculation region commences at $x/S \approx 15.08$. However, to a certain degree this is expected given the scaling of the streamwise distance (with the blockage height) and the delayed flow separation in reference to the semi-circle model (smaller primary recirculation region). A better comparison of the upper wall recirculation regions (separation/reattachment points between the models) is depicted in Fig. 5.6c, whereby the streamwise distance is scaled with the reattachment length (i. e. x/x_1). From Fig. 5.6c, both models show the upper wall recirculation approximately starting at the onset of flow reattachment associated with flow separation at the blockage ($x/x_1 = 0.94$). Nevertheless, the main difference is that the upper wall recirculation extends for $\Delta x_{x_5^* - x_4^*} \approx 0.19$ and 0.62 (possibly for longer) for the present BFS and semi-circle models, respectively. The latter agrees well with the 2-D numerical work of Erturk (2008) which shows an extended recirculation region (upper wall at $Re = 1000$) in the streamwise direction relative to the experimental BFS model of Armaly et al (1983).

Furthermore, the difference in the Re values between the present BFS model and the semi-circle model is negligible. This is because Armaly et al (1983) shows that the difference in the reattachment length (associated with the primary recirculation region) for $Re = 1000$ and 1290 is approximately $\Delta x_1^* \approx 0.5$ (whereby the streamwise distance is scaled with the blockage height). Similarly, with the semi-circle model, Griffith (2009) reports a difference of $\Delta x_1^* \approx 0.5$ for the Re values mentioned above. Hence, it is likely probable that a better agreement in x_1^* is expected (in the present comparison) with the absence of the side-wall influence on the mid-plane flow structure (i.e. $\alpha_S > 50$, Chiang & Sheu (1998)). This is also supported by the fact that Griffith (2009) reports excellent agreement in the x_1^* value for $Re < 400$ (absence of three-dimensionality) with the work of Armaly et al (1983).

In terms of the differences in the \bar{u}/U profiles between the present BFS model and the semi-circle model, the reader is referred to Fig. 5.6c. The first observed difference is at the blockage ($x/x_1 \approx 0$), whereby the semi-circle model shows an absence of a fully-developed Poiseuille flow and is skewed to one side. According to Griffith (2009), this is because of the rapid constriction (i.e. the streamwise length of the semi-circle blockage corresponds to $x = 2S$). In general, it is important to quantify the flow conditions at the blockage (prior to flow expansion) since the boundary layer state (laminar vs. turbulent) and the ratio of boundary layer thickness to step height (δ/S) does influence the downstream flow physics (Tihon et al. 2012). Although the boundary layers are laminar for both studies at separation, an attempt has not been made to study the influence from δ/S differences on the downstream flow field. Furthermore, at the blockage, the difference in the maximum value is $\Delta\bar{u}/U \approx 0.5$ (i.e. larger magnitude for present work) given that the flow is fully-developed (laminar regime) for the present BFS model. It is presumably one of the reasons why the maximum magnitude of \bar{u}/U for the semi-circle model continues to display relatively smaller values downstream of the blockage before flow reattachment at $x/x_1 = 1.00$.

The magnitudes of the \bar{u}/U profiles inside the primary recirculation region are relatively larger for the present BFS model with a maximum difference of $\Delta\bar{u}/U \approx 0.2$ at $x/x_1 = 0.57$. However, closer to the lower wall (i.e. $y/h < 0.1$) the magnitudes of \bar{u}/U for the two models are in better agreement with an average deviation of $\pm 3.5\%$. The depth of the primary recirculation region at $x/x_1 = 0.57$ between the two models shows a difference of $\Delta y/h \approx 0.2$ (smaller for the semi-circle model). This is presumably as a result of the delayed separation (of the streamwise velocity profile near the curved wall) in reference to the semi-circle geometry (Ratha & Sarkar, 2015). At the onset of flow reattachment (i.e. $x/x_1 = 0.94$), the present BFS model displays a relatively larger depth of the upper wall recirculation region with a difference of $\Delta y/h \approx 0.26$ between the models. Downstream of the reattachment point, the upper wall recirculation region for the present BFS model seems to cease at $x/x_1 = 1.13$ whereas, for the semi-circle model it continues to $x/x_1 = 1.32$. As the flow starts to redevelop downstream of the flow reattachment, the maximum difference in the normalized streamwise velocity profile is $\Delta\bar{u}/U \approx 0.6$ between the

models. It should be noted that the local skin friction streamwise distribution (and its spatial gradient) is discussed following a quantitative comparison (of the streamwise velocity profiles and the reattachment length) between the present BFS model and the axis-symmetric model.

Moving closer to more realistic stenosis geometry (i.e. tube geometry), Fig. 5.6d and 5.6e compare the normalized streamwise velocity profiles (normalized with the bulk velocity upstream of the blockage) between the present BFS model and the axis-symmetric model (refer to Fig. 5.1c for geometry details). It should be noted that (in both Figures) the streamwise distance is normalized with the hydraulic diameter for the BFS model and, for the axis-symmetric model with the half-section of the tube (i.e. $D/2$) whereby the upper wall boundary is the plane of symmetry. For the purpose of simplicity and since $x/D_h \equiv 2x/D$ (equal by definition and representing the normalized streamwise distance in Fig. 5.6d and 5.6e), a new non-dimensional variable x^* is used to represent the streamwise distance. The selection of scaling for the streamwise distance is described in Appendix 4. Generally, there is a very small amount of guidance from the literature on consistent scaling when comparing PPFC/tube type stenoses to better understand the contributing factors which lead to a difference in the reattachment length (associated with the primary recirculation region). It should also be noted that Fig. 5.6f compares the normalized streamwise velocity profiles (between the models) with the streamwise distance scaled with the reattachment length (x/x_1). This allows for a more effective comparison of the streamwise velocity profiles (upstream/downstream of flow reattachment) between the present BFS model and the axis-symmetric model.

As with the semi-circle model in the preceding section, the first observation from Fig. 5.6d is that the \bar{u}/U profile for the axis-symmetric model deforms (and is flatter) at $x^* = 0.00$ (at the blockage) in order to pass through the constriction. For comparison purposes, the fully-developed (steady laminar) streamwise velocity profile (in reference to the axis-symmetric model) upstream of the blockage is given in Fig. 5.6d, whereby $\bar{u}/U = 2$ (at $y/D = 0.5$). The streamwise length of the semi-circle blockage corresponds to $x = 2S$ (or $0.3D$; where D is the unblocked tube diameter). Several other authors who study steady and pulsatile (laminar regime) flow downstream of an axis-symmetric stenosis impose a length

of $x = 2D$ (Long et al. 2001; Mallinger & Drikakis, 2002) to ensure a fully-developed velocity profile prior to flow expansion. Nevertheless, the semi-circle blockage inside a tube provides a respectable comparison with the present BFS model to gain insight into the similarities and differences of the flow physics between PFFC/tube type of flows.

Fig. 5.6d is only provided to demonstrate general differences in the normalized streamwise velocity profiles (across the channel/tube height) between the present BFS and axisymmetric models. Conversely, Fig. 5.6e is provided to gain insight of the \bar{u}/U profile and reattachment length differences (between the models) considering the flow behaviour below the blockage (i.e. $y/S \leq 1$; whereby the wall-normal distance is scaled with the blockage height). For the present BFS model, the reattachment length (associated with the primary recirculation region) is $x_1^* = x_1/D_h = 4.20$ which is smaller by the amount of $\Delta x_1^* = 4.94$ (i.e. $x_1^* = 2x_1/D$ for axisymmetric model) in comparison to the axisymmetric model (at $Re = 1200$). It is important to note that the \bar{u}/U profiles of the axisymmetric model (in Fig. 5.6d,e) are given at $Re = 797$ (see table 5.1), whereas the reattachment length is compared with the present BFS model considering $Re = 1200$ for a more effective comparison. This is because Griffith (2009) does not provide streamwise velocity profiles (experimental-PIV and coloured-dye visualizations) at $Re = 1200$. The author does, however, provide a plot of reattachment length versus Re via 2-D numerical methods (spectral-element code) up to $Re = 2500$.

There are several possible reasons for the discrepancy in x_1^* between the models. First, the present BFS flow at $Re = 1240$ corresponds to a transitional flow regime (Armaly et al. 1983), whereby x_1^* experiences a rapid decrease due to action of the Reynolds stresses (Biswas et al. 2002 – refer to Fig. 4A-2). For the axisymmetric model, Griffith (2009) does not report transition to turbulence (near the reattachment point) at $Re = 1200$ since the convective instability in the shear layer is not accounted for in the numerical simulations (experimental data only provided for $Re < 1000$). For this reason, the reattachment length plot given by Griffith (2009) shows linear behaviour up to $Re = 2500$. The second reason for the difference in x_1^* , is presumably, as a result of the upper wall recirculation which is not present at the plane of symmetry for the axisymmetric model. This is supported by the work of Juste et al (2016), whereby the authors report $x_1^* = x/D_h$

≈ 13 (using commercial CFD-Fluent; 3-D simulation) for a BFS model ($\alpha_s = 8.0$ and $b = 0.5$ at $Re = 1000$) at the mid-plane of the channel. According to the authors, the extended primary recirculation (lower wall) is due to the absence of the upper wall recirculation at the mid-plane (hence, no blockage effect on the streamwise flow), together with stronger side-wall jets. The flow reattachment length reported by Juste et al (2016) extends for an additional $\Delta x_1^* = 3.86$ in comparison to the axi-symmetric model and is in favourable agreement with the scaling outlined in Appendix 4 (whereby the BFS model would produce a relatively larger x_1^* value given the geometrical difference). The work of Juste et al (2016) possibly demonstrates that smaller aspect ratio PPFCs model the axi-symmetric stenosis flows more effectively.

For a comparison of the streamwise velocity profiles between the present BFS model and the axi-symmetric model, the reader is referred to Fig. 5.6f and 5.6g. In both Figures, the wall-normal distance is scaled with the channel height (h) and with $D/2$ (half-section - plane of symmetry for axi-symmetric model). Once again, for simplicity and since $y/h \equiv 2y/D$ (equal by definition and representing the normalized wall-normal distance), a new non-dimensional variable y^* is used to represent the wall-normal distance. The main difference between the plots is such that Fig. 5.4g shows the \bar{u}/U profiles only for $y^* \leq 0.2$ as it is difficult to visualize the streamwise velocity data between the models near the bottom wall given the geometrical difference (ratio of blockage height to channel/tube height).

The first observation from Fig. 5.6f is that the maximum value of the \bar{u}/U profiles upstream of the reattachment is relatively smaller for the axi-symmetric model with a difference of $\Delta \bar{u}/U \approx 0.4$ across the four measurement stations. This is presumably as a result of the flow profile not being developed at the blockage for the axi-symmetric model. The other difference between the profiles is that the depth of the primary recirculation region is smaller for the axi-symmetric model as a result of both the delayed separation of the boundary layer and a smaller ratio of blockage height to tube half-diameter (i.e. $2S/D$ – considering half diameter). Scaling of the wall-normal distance with $D/2$ for the axi-symmetric model downstream of flow reattachment (i.e. $x/x_1 > 1.00$) is not ideal and, hence, results in the difference in the \bar{u}/U profiles. Scaling with D (considering the entire

cross-section) would provide a better comparison with the \bar{u}/U profiles of the BFS model. However, half-diameter scaling is selected to more clearly visualize the depth of the primary recirculation region upstream of flow reattachment. Nevertheless, the maximum values of the \bar{u}/U profiles at $x/x_1 = 1.13$ are very similar with a difference of $\Delta\bar{u}/U \approx 0.05$, with the exception that the maximum value occurs at the plane of symmetry for the axisymmetric model ($y^* = 1$). Furthermore, in Fig. 5.6g the \bar{u}/U profiles (prior to flow reattachment) in the region, $0.0 < y^* < 0.1$, demonstrate favorable agreement with an average deviation of $\pm 4.3\%$. The absolute maximum value of normalized streamwise profiles (for both models) at $y^* = 0.1$ for $x/x_1 = 0.38$ and 0.57 is $\bar{u}/U \approx 0.2$. The deviation of the \bar{u}/U profiles downstream of flow reattachment is, presumably, a result of wall-normal distance scaling (i.e. $2y/D$ and not y/D).

Possibly the most important quantity to compare between the various stenosis models depicted in Fig. 5.1 is the local skin friction ($c_f = \tau_w / (0.5\rho U^2)$, where U is the bulk velocity upstream of the blockage or in the case of the CA models upstream of the bifurcation inside the common carotid artery) and its spatial gradient ($c_f' = \left| \frac{\partial c_f}{\partial (x/x_1)} \right|$), downstream of the blockage. This is because both *in-vitro* and *in-vivo* studies report atherosclerosis susceptible regions where the wall shear stress is low with a large spatial and temporal shear stress gradient (Phelps & DePaola, 2000). It should be noted that the temporally-varying wall shear stress is discussed in the subsequent section (i.e. pulsatile flow). It should also be noted that the spatial gradient of c_f is given as an absolute value, since the emphasis here is on the magnitude and not its direction. For all stenosis models depicted in Fig. 5.1, the local skin friction and the spatial gradient streamwise distributions are given in Fig. 5.9a and Fig. 5.9b, respectively. Included with both plots are the *in-vitro* carotid artery (CA) models. In addition to the stenosed CA model (i.e. diseased artery, whereby WSS is reported on the inner wall of the ICA), the present analysis also includes the healthy CA model (i.e. no plaque, whereby WSS is reported on the outer wall of the ICA). The healthy CA model is included because in the vicinity of the carotid bifurcation plaque is likely to occur along the outer wall of the internal carotid artery (ICA), given that its geometry is likely to induce spatially and temporally varying shear stress (Wells et al. 1996). Hence, the comparison between the present BFS and the healthy CA

models brings insight into how well a simple step emulates regions (in terms of WSS) of the carotid artery that are susceptible to atherosclerosis. Both, the early initiation and subsequent formation (further downstream) of atherosclerosis is considered important in the literature.

Starting the comparison with the semi-circle model, the local skin friction is in favorable agreement inside the primary recirculation region. For the present BFS model, the maximum absolute value in the recirculation region is $c_f = 0.038$, with a difference of $\Delta c_f = 0.005$ in comparison with the semi-circle model (within the experimental uncertainty of the skin friction coefficient in the present study). It should be noted that more than one study (which use a BFS to study EC response) report that the relative large spatial gradient of WSS in the vicinity of flow reattachment induces a proatherosclerotic cell-proliferation-migration-loss cycle (Tardy et al. 1997; White et al. 1999). For the present BFS model, the maximum spatial gradient of c_f is found in the range, $0.94 \leq x/x_1 \leq 1.13$, with a magnitude of $c_f' \approx 0.50$. Similarly, the semi-circle model displays a maximum $c_f' \approx 0.50$ in the vicinity of flow reattachment, thereby demonstrating favorable agreement with the present BFS model. Furthermore, the effect of the upper wall recirculation on c_f can be seen from Fig. 5.9a, whereby both models demonstrate well-defined peaks with similar magnitudes (i.e. $c_f \approx 0.036$) at $x/x_1 \approx 1.13$. The peaks are a result of the reduced effective channel height (Mittal et al. 2003). The discrepancy in c_f between the models occurs immediately downstream of the peaks in the range, $1.13 < x/x_1 \leq 1.70$, given the rapid decrease in c_f for the present BFS model. This rapid decrease in c_f is presumably because of the absence of the upper wall recirculation region. For the semi-circle model, the gradual decrease in c_f (downstream of the peak) is reflected by the extended upper wall recirculation region. For the present study, the c_f value begins to revert back to a nominal channel flow at $x/x_1 \approx 1.32$. The difference between the measured c_f value at $x/x_1 = 1.89$ and that of a fully-developed steady laminar flow under $Q = 7.50 \pm 0.075$ is within $\pm 2.5\%$ (i.e. the shear stress magnitude recovers to 97.5% that of the fully developed downstream flow).

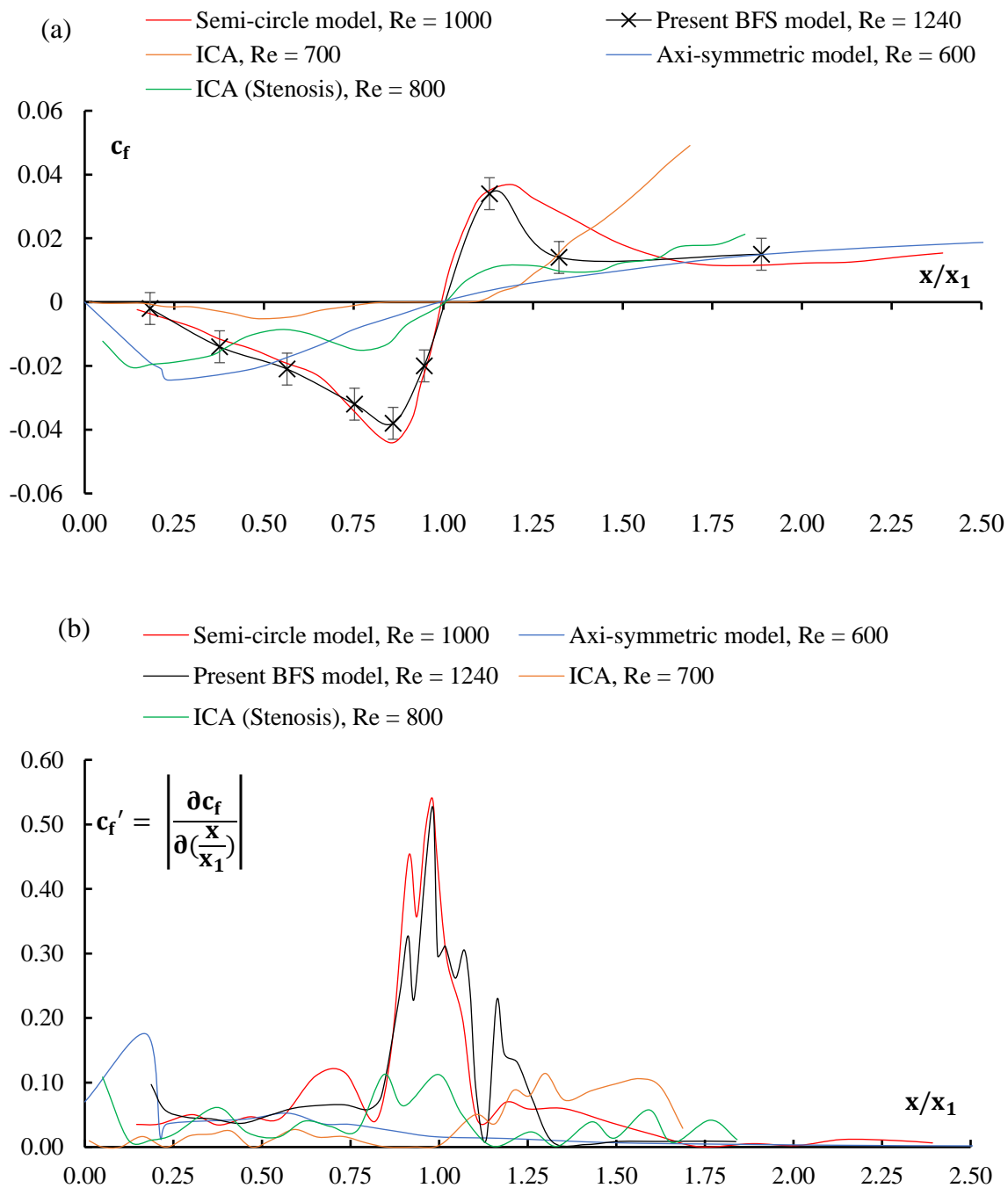


Fig. 5.9 (a) Streamwise distribution of the local skin friction coefficient downstream of the blockage comparing the various stenosis models depicted in Fig. 5.1. (b) streamwise distribution of the skin friction spatial gradient.

In reference to the axi-symmetric model, the absolute maximum value of $c_f \approx 0.024$ occurs at $x/x_1 \approx 0.23$ in the primary recirculation region. In contrast, for the BFS model the absolute maximum value of $c_f \approx 0.038$ occurs at $x/x_1 = 0.86$ (closer to the flow reattachment point). The difference in the absolute maximum c_f is due to a larger $\frac{\partial(\bar{u}/U)}{\partial y^*}$ (inside the recirculating region) and Re for the present BFS model. The axi-symmetric model displays a maximum $c_f' \approx 0.01$ in the vicinity of flow reattachment, thereby demonstrating poor agreement with the present BFS model (a difference of $\Delta c_f' \approx 0.45$). Given the absence of the upper wall recirculation for the axi-symmetric model (at the plane of symmetry), the skin friction coefficient does not display a rapid increase (in the vicinity of flow reattachment and, hence, a smaller c_f') as in the case of the present BFS model. For this reason, the maximum value of c_f occurs farther downstream of flow reattachment whereby the flow is still redeveloping at $x/x_1 \approx 2.50$. Better agreement in c_f between the models is found for $x/x_1 > 1.50$, with a difference of $\Delta c_f = 0.002$ at $x/x_1 = 1.89$. It should be noted that c_f' is in better agreement (between the models) inside the recirculating region in the range, $0.20 \leq x/x_1 \leq 0.80$, with an average deviation of $\Delta c_f' \approx 0.01$. The present author assumes that a double backward-facing step (axi-symmetric) together with a closer agreement in Re would yield a better collapse of shear data between the models. This is because a double backward-facing step would not display a recirculating region in the plane of symmetry (as in the tube model). The better agreement is also expected since the magnitude of the normalized streamwise velocity (inside the primary recirculation region) increases with Re (Armaly et al. 1983).

To finish, the present author compares the present BFS model to both the healthy and the stenosed *in-vitro* CA models (depicted in Figures 5.1d and 5.1e) in terms of c_f and c_f' . In reference to the healthy CA model, it can be seen from Fig. 5.9a that much smaller absolute values of c_f are found in the primary recirculation region in comparison to the present BFS model. The difference in the maximum absolute skin friction coefficient between the healthy CA and BFS models is $\Delta c_f \approx 0.03$. In terms of the spatial gradient of c_f inside the recirculation region ($x/x_1 < 1.0$), the healthy CA model shows smaller c_f' values with an average difference of $\Delta c_f' \approx 0.04$ in comparison to the present BFS model. This result is somewhat expected since the healthy CA model represents a non-stenosed case with only

mild arterial curvature inducing flow separation. Downstream of flow reattachment ($x/x_1 > 1.0$), the healthy CA model shows a sudden increase in c_f due to the decrease in cross-sectional area of the ICA. The increase in c_f' is also realized downstream of flow reattachment with a maximum value of $c_f' \approx 0.10$ (a difference of $\Delta c_f' \approx 0.40$ in comparison to the maximum value of the BFS model). In reference to the stenosed CA model, Fig. 5.9a shows better agreement (inside the recirculation region) with the present BFS model with a difference in the maximum absolute skin friction coefficient of $\Delta c_f \approx 0.02$. In terms of c_f' inside the recirculation region, the stenosed CA model shows smaller values with an average difference of $\Delta c_f' \approx 0.01$ in comparison to the present BFS model. In contrast to the healthy CA model, the stenosed CA model displays a maximum $c_f' \approx 0.10$ in the vicinity of flow reattachment which is consistent with the present BFS model. Nevertheless, the difference in the maximum c_f' (in the vicinity of flow reattachment) between the stenosed CA and BFS models is still significant (i.e. $\Delta c_f' \approx 0.4$). Downstream of flow reattachment at $x/x_1 = 2.32$, the skin friction coefficient shows better agreement between the models with a difference of $\Delta c_f \approx 0.004$. In general, both CA models show better agreement with the present BFS model in c_f' inside the primary recirculation region than in the vicinity of flow reattachment (smallest WSS region). It is thus appropriate to note that the present BFS model does not appear to emulate an ICA flow with or without the presence of a stenosis.

This next section of this Chapter focuses on pulsatile (unsteady) laminar flow considering a normal carotid waveform with a physiological fundamental frequency of $f = 1.08$ Hz. The present author believes that the steady laminar flow reported in the present section lays the groundwork necessary to better understand mean flow and turbulence behaviour downstream of a backward-facing step, whereby the amplitude of pulsation is zero. In terms of the wall shear data (under a pulsatile laminar flow), the skin friction streamwise distribution (at various time instants of the pulse cycle) together with the spatial and temporal gradient profiles are compared to shear data corresponding to an asymmetric stenosis inside a tube.

5.2 Pulsatile Laminar Flow over a Backward-Facing Step

This section presents a pulsatile laminar flow over a backward-facing step (BFS) with a blockage ratio of $b = 0.5$ (50% by area). Mean flow and turbulence statistics are presented downstream of the step at the mid-plane of the channel at various measurement stations. Results are compared to other models of stenosis inside both a parallel-plate flow chamber (PPFC) and straight section of tube. From the comparison of the flow physics downstream of the blockage, similarities and differences between these types of flows are discussed to better understand how a simple step (present work) can model more realistic models of stenosis.

5.2.1 Problem Definition

According to Dol et al (2014), the flow field downstream of the BFS under a pulsatile laminar flow depends on the following parameters: (1) the Reynolds number defined as $Re = \bar{U}D_h/\nu$ (where \bar{U} is the mean bulk velocity upstream of the step), (2) the pulsation Strouhal number defined as $S_t = fD_h/\bar{U}$ (non-dimensional frequency), (3) the blockage ratio (b) and, (4) the pulsation amplitude, $A_0 = U_{max}/\bar{U}$. It should be noted that the Womersley number given as $Wo = D_h/2\sqrt{\omega/\nu}$ (where $\omega = 2\pi f$) can also be calculated from, $Wo = \sqrt{2\pi Re S_t}$ (Rubenstein et al. 2015). It should also be noted, however, that the time derivative of the flow rate (i.e. dQ/dt) is also an important quantity when comparing flows of different waveform shapes. This is because the differences associated with the acceleration and deceleration phases influence the inertial fluid forces (Shu et al. 2009).

For the pulsatile laminar flow reported in the present section, a normal carotid waveform is prescribed at the pump. In the present study, the fundamental frequency of the waveform is $f = 1.08$ Hz (i.e. $T = 920$ ms) which gives $Wo = 4.7$. In addition, the mean Reynolds number upstream of the step is $Re = 775$. It should be noted that both the Re and Wo values are in the range of physiological importance (Tutty, 1992).

5.2.2 Creating the Stenosis Models

In order to provide a comparison between the present work and other published data for obstructed flows, Fig. 5.10 gives a schematic of the present geometry (BFS – idealized stenosis model), the axi-symmetric stenosis (i.e. semi-circle representation) inside a PPFC (Beratlis et al. 2005) and the asymmetric stenosis inside a tube (Long et al. 2001). For the asymmetric tube, Long et al (2001) models the stenosis silhouette as a long straight segment with two integrated Gaussian functions at the corresponding ends. For all models shown in Fig. 5.10, the x -origin (referencing the streamwise distance) is placed at the onset of flow expansion (i.e. for BFS at the edge). Similarly, the y -origin is placed on the lower wall for all stenosis models.

Table 5.3 compares the geometric and flow specifications between the present BFS model and the other models of stenosis depicted in Fig. 5.10.

Fig. 5.10 Stenosis models: (a) BFS geometry referencing present work, (b) axi-symmetric channel model, Beratlis et al (2005) and (c) asymmetric tube model, Long et al (2001).

Note: The drawing is not to scale.

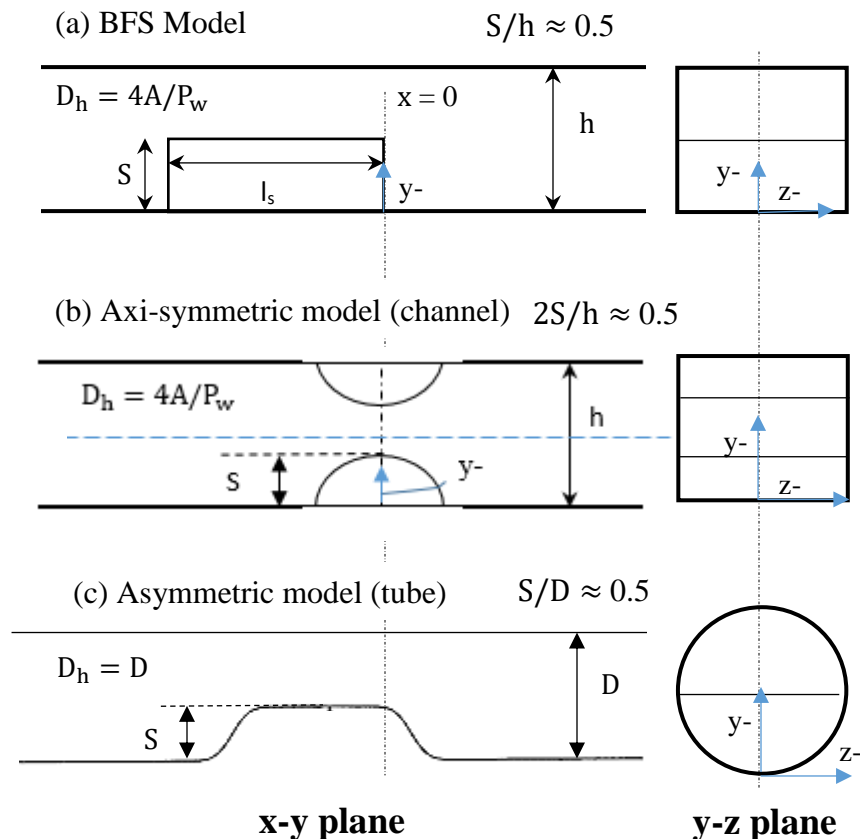


Table 5.3 A comparison of the geometry and flow specifications between the present BFS model and other models of stenosis.

Model Type	Re	Aspect Ratio (α)	Geometry/waveform type	Blockage Ratio (b)	Wo parameter	U_{\max}/\bar{U}	Author(s)
Present BFS model	775	9.72	PPFC/carotid	≈ 0.5	4.7	1.3	Present author
Axi-symmetric channel model – experimental LDV	2100	12.00	PPFC/sinusoidal	$= 0.5$	15.1	1.7	Beratlis et al (2005)
Asymmetric tube model - CFD	300	--	Tube/carotid	$= 0.5$	5.3	1.9	Long et al (2001)

5.2.3 Scope of Measurements and Data Processing

As with steady flow reported in section 5.1.3, $10\ \mu\text{m}$ traverse increments are used in the range, $0.022\ \mu\text{m} < y/h \leq 0.11\ \mu\text{m}$, to obtain accurate time-varying shear stress data. Further away from the wall ($y/h > 0.11$), the data are captured every $50\ \mu\text{m}$.

By way of review, for pulsatile laminar flow, the instantaneous streamwise velocity can be decomposed such that $\langle u \rangle = U + \tilde{u}$, where U is the time-averaged bulk velocity, \tilde{u} is the periodic bin-average velocity and $\langle u \rangle$ is the phase-averaged velocity (Kehoe, 2001). To account for perturbations in the flow downstream of the BFS, u' is added to the above mathematical expression such that $u = U + \tilde{u} + u'$. An equal instantaneous velocity decomposition can be applied for the wall-normal component, v .

To calculate the turbulence statistics in the present study, the randomness of the isolated turbulent fluctuations is verified by ensuring that $\overline{u'} = 0$ and $\overline{v'} = 0$ in each bin of the pulse cycle. The interpretation of the bin r.m.s. needs careful attention as the r.m.s. velocities can be overestimated by both the phase velocity gradient inside the bin and the inherent LDV noise. Both of these factors are discussed in Chapter Four and Appendix 2. It should be noted, as with the steady flow case, the inherent LDV noise is subtracted (i.e. quadrature subtraction) from the resulting r.m.s. velocities in every bin during the pulse cycle. This type of analysis is also conducted by Kehoe (2001) who uses a two-component LDV to

study the flow downstream of a mildly stenosed carotid bifurcation (i.e. physiologically life-size model phantom).

For the computation of the energy spectra ($E_{u'u'}$), the reader is referred to section 5.1.3 (steady flow section). The added complexity for pulsatile flow is in subtracting the running mean from the fluctuations. The u' values are computed from the mathematical expression $u' = u - \langle u \rangle$ (Reynolds & Hussain, 1972) for every measured pulse cycle (the analysis was performed with Matlab and Visual Basic to deduce u' over several cycles). As with steady flow, the $E_{u'u'}$ is computed by performing a fast Fourier transform (FFT) on the streamwise velocity fluctuations (i.e. u') and is presented as a log-log plot.

Lastly, Table 5.4 gives a summary of the downstream measurement stations (including the location at the step) at the mid-plane of the channel ($2z/w = 0$). The streamwise distance is normalized with the step height (S). As with steady flow, linear interpolation is used where required (of the normalized phase-averaged streamwise velocity profiles) to coincide the measurement stations of other work to the present study measurement stations depicted in Table 5.4. In reference to measurement stations scaled with the reattachment length (x/x_1 ; given the phase-dependent flow reattachment), the present streamwise velocity profiles (corresponding to different phases of the pulse cycle) are linearly interpolated to coincide with the normalized positions associated with the peak mass flow phase. This ensures consistent measurement stations when comparing flow at different phases during the pulse cycle.

Table 5.4 Normalized measurement stations at the working section of the PFC. Pulsatile flow measurements are captured at the mid-plane of the working section, $2z/w = 0$. The normalized error of the measurement volume position downstream of the step is $\epsilon_x/S = \pm 0.06$.

Measurement Points	x/S (where $S = 842 \pm 50 \mu\text{m}$)	Dimensional location of the measurement volume in reference to $x = 0$ at the step edge [mm]
Pt. 1	-1.18	-1
Pt. 2	3.02	2.54
Pt. 3	6.03	5.08
Pt. 4	9.05	7.62
Pt. 5	12.07	10.16
Pt. 6	15.08	12.70
Pt. 7	18.10	15.24
Pt. 8	21.12	17.78
Pt. 9	24.13	20.32
Pt. 10	33.18	27.94
Pt. 11	42.23	35.56

5.2.4 Results and Discussion

The streamwise velocity temporal profile (U/\bar{U} ; where \bar{U} is the mean bulk velocity at $x/S = -1.18$ – spatially and temporally averaged) of the normal carotid waveform (prescribed at the pump) is given in Fig. 5.11a. The measured waveform is significantly damped in comparison to the waveform prescribed at the pump (refer to section 4.5.1 for details of the programmed carotid waveform at the pump) and has an amplitude of $A_0 = 1.3$.

Shown in Fig. 5.11a on the secondary y-axis is the Re value plotted against the normalized cycle time. As per table 5.3, the mean Reynolds number is 775 with maximum and minimum values being 1010 and 540, respectively. As in the steady laminar flow case reported in the previous section, the pulsatile flow at the step is considered laminar since a spurious r.m.s. $u' \approx 0.0025$ m/s is detected in every bin (26 equally-sized bins with a 35.3 ms bin width - review Appendix 2). Furthermore, the spanwise profile of the phase-averaged streamwise velocity ($\langle u \rangle (z)$) is not measured at the step in the present study. This is because Avari et al (2016) reports approximately 60% of the channel width (i.e. $-0.6 < 2z/w < 0.6$) exposed to uniform flow (under carotid waveform with $f = 1.08$ Hz) at the working section at various time instants of the cycle (under laminar flow). It should be further noted that velocity measurements at the step are extremely difficult to capture given the geometry of the working section. In terms of the latter, rotation of the probe is required (around the y-axis) to position the measurement volume at the step which brings forward challenges associated with unequal beam refraction.

Fig. 5.11b compares U/\bar{U} temporal profiles between the present study and the other stenosis models depicted in Fig. 5.10. A difference in the shape of the U/\bar{U} profiles is evident between all of the studies, whereby the asymmetric tube model and the axi-symmetric channel model studies prescribe normal carotid and sinusoidal waveforms (upstream of the blockage), respectively. The amplitude of pulsation for the present study is smaller by the amount of $\Delta U/\bar{U} = 0.4$ and 0.6 in comparison to the axi-symmetric channel and asymmetric tube models, respectively. In addition, for the present study the temporal change (i.e. dU/dt) of the streamwise bulk velocity for the time periods between $t^* = 0.5$ and 1.0 and $t^* = 1.0$ and 1.5 is $\frac{\Delta U}{\bar{U}}/\Delta t^* = 0.6$ and 0.2 , respectively. For the axi-symmetric channel and

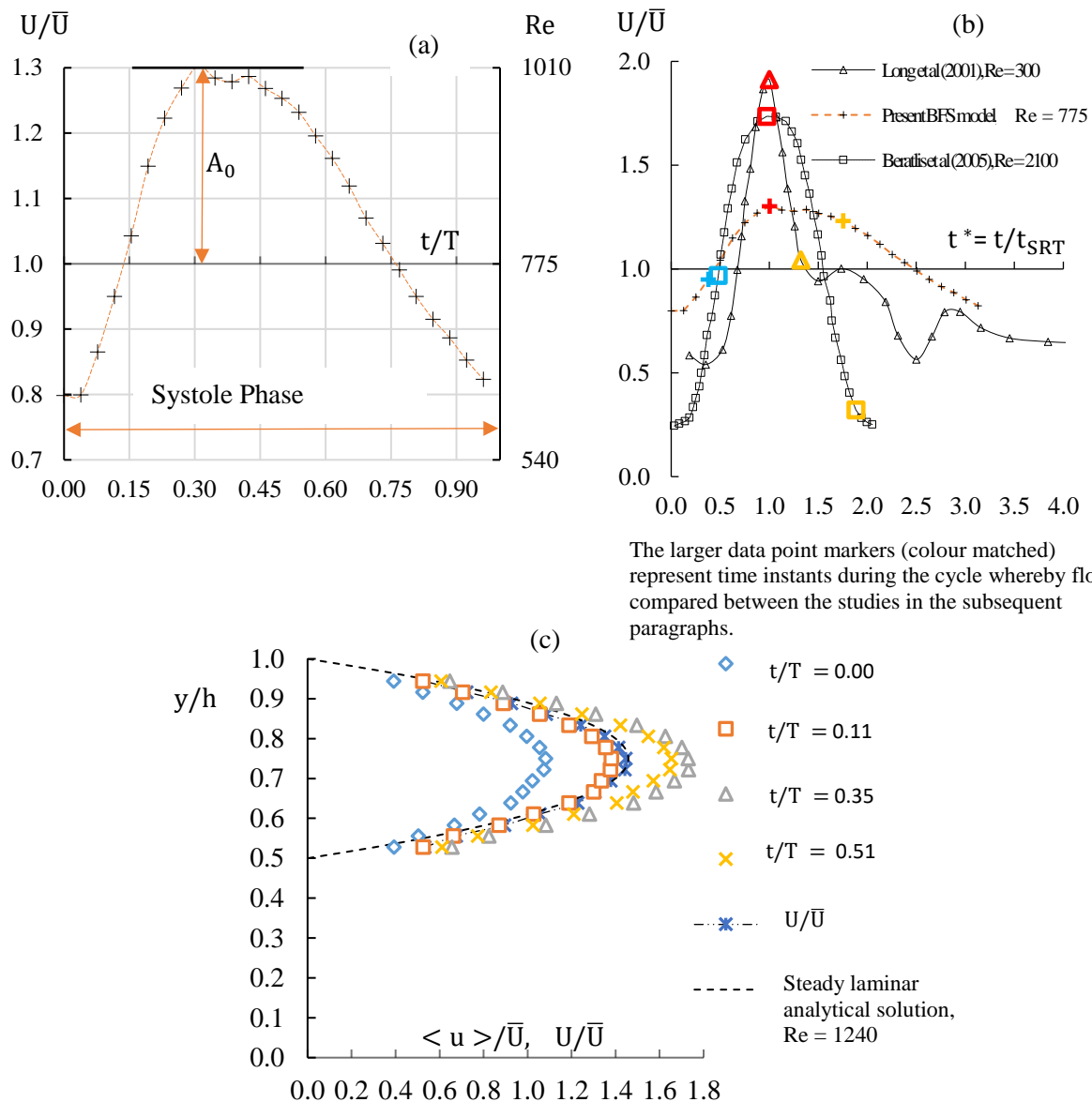


Fig. 5.11 Phase-averaged velocity profiles prior to flow separation: (a) present study temporal profile (U/\bar{U}) at $x/S = -1.18$ plotted against the normalized cycle time (averaged over 60 cycles), (b) temporal profiles inclusive of the work of Long et al (2001) and Beratis et al (2005) whereby the cycle time is normalized with the systole rise time (SRT) and, (c) present study spatial profiles at $x/S = -1.18$ whereby the y -positions are normalized with the channel height. It should be noted that the temporal profiles of the other authors is given upstream of the blockage. The normalized typical uncertainty at $y/h = 0.75$ (midplane in reference to the height) is $\varepsilon_{\langle u \rangle} / |\langle u \rangle| = \pm 2.50\%$.

asymmetric tube models the temporal change is $\frac{\Delta U}{\bar{U}}/\Delta t^* = 1.4$ and 1.8 , respectively (equal for acceleration and deceleration phases). It should be noted that in Fig. 5.11b, the cycle time is normalized with the systole rise time (SRT – onset of cycle to max value of U/\bar{U}) to more clearly demonstrate the waveform shape differences (in terms of acceleration/deceleration during the systole phase) and to compare the velocity/r.m.s. data (downstream of the blockage) at the same relative position within the cycle. This being said, the mean flow and turbulence statistics between the studies (presented in the subsequent sections) are compared at $t^* = t/t_{\text{SRT}} = 1.0 \pm 0.5$, whereby +/- signs indicate the amount of time after and prior from the peak mass flow, respectively. However, in order to facilitate an effective comparison during the mass flux deceleration phase, $t^* = 1.5 \pm 0.25$ is considered given the differences in the flow waveforms. It should also be noted that Long et al (2001), in reference to the asymmetric tube model, do not provide velocity data for the acceleration phase of the pulse cycle. Furthermore, Long et al (2001) provide velocity data downstream of the stenosis under the assumption of laminar flow (i.e. given the relatively small mean Re value of 300). This is in contrast to the work of Beratlis et al (2005), whereby the authors report a borderline turbulent flow upstream of the blockage (i.e. ten channel heights upstream for mean Re = 2100). Upstream of the blockage, the authors report an increase in the phase-averaged r.m.s. velocity (i.e. 7% of the mean bulk velocity) only during middle and late deceleration phases, with two distinct peaks closer to the walls. According to the authors, the flow does not transition to a fully developed turbulent flow upstream of the blockage.

Furthermore, Fig. 5.11c gives the normalized phase-averaged streamwise velocity profiles at the step (i.e. $x/S = -1.18$) corresponding to various time instants of the pulse cycle (i.e. agreeing with the start of the cycle, the mid-acceleration phase, the peak mass flow and the deceleration phase, respectively). Also, plotted in Fig. 5.11c are the measured bulk velocity (under pulsatile flow, U/\bar{U} whereby U is the temporally-averaged bulk velocity and \bar{U} is the mean bulk velocity at the step) and steady laminar flow (analytical solution at Re = 1240) streamwise velocity profile. The average deviation between the pulsatile bulk velocity and steady laminar streamwise profiles is $\pm 2.8\%$, thereby presenting evidence of a Poiseuille type flow (as opposed to a Wormersley flow with flatter flow profiles). The

latter is further explained by Straatman et al (2002) who note that the shape of the streamwise velocity profiles is dictated by the ratio of the diffusive time scale to the pulsation time scale. Furthermore, the authors note that at a larger ratio the flow is dominated by the viscous forces which allow the flow to respond to the pulsating pressure. For the pulsatile flow in the present study, there still appears to be an approximate balance between viscous and inertial forces and, hence, respectable agreement with the steady flow profile given at $Re = 1240$.

Finally, Fig. 5.12 shows the phased-averaged streamwise velocity profiles (normalized with the bulk velocity) corresponding to $t^* = 0.5, 1.0$ and 1.5 at $x/S = -1.18$ (at the step) and upstream of the blockage for the present BFS and axi-symmetric channel models, respectively. The plot is presented to show that the profiles between the two models are in favorable agreement, with a maximum value of $\langle u \rangle / U \approx 1.4$.

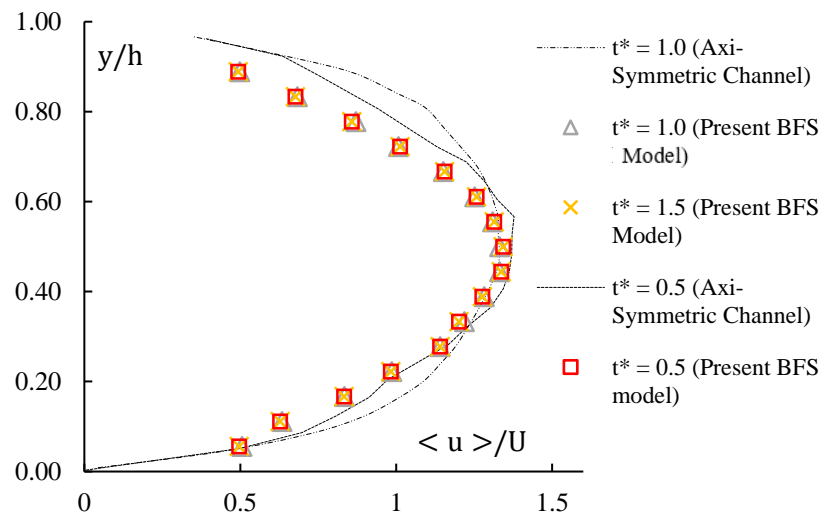


Fig. 5.12 Phase-averaged velocity profiles at $x/S = -1.18$ for the present BFS model and upstream of the blockage for the axi-symmetric channel model (work of Beratlis et al. 2005). The streamwise velocity is normalized with the bulk velocity (U) corresponding to $t^* = 0.5, 1.0$ and 1.5 . It should be noted that the velocity profile associated with the channel model is not provided for $t^* = 1.5$. The normalized typical uncertainty at $y/h = 0.75$ (midplane in reference to the height) is $\epsilon_{\langle u \rangle} / |\langle u \rangle| = \pm 2.50\%$.

Fig. 5.13 and 5.14 give the phase-averaged streamwise velocity profiles (normalized with the mean bulk velocity upstream of the blockage), whereby the streamwise distance is normalized with the blockage height (S) and the reattachment length (phase-dependent), respectively. Both Figures compare the present BFS model to the axi-symmetric channel model given by Beratlis et al (2005). In addition, Fig. 5.15 gives the streamwise and wall-normal r.m.s. profiles at various measurement stations (x/x_1 ; where x_1 is the phase-dependent reattachment length) for the mid-acceleration ($t^* = 0.5$), peak mass flow ($t^* = 1.0$) and deceleration ($t^* = 1.5$) time instants during the pulse cycle. The r.m.s. profiles are also compared to the work of Beratlis et al (2005). It should be noted that the phase-averaged velocity profiles portrayed in Fig. 5.13 are not given for comparison with the work of Beratlis et al (2005) at the various measurement stations (given the difference in x_1). Rather, they are given to show the difference in the reattachment lengths between the studies.

The present study starts with comparing the reattachment lengths (associated with the flow separation at the blockage) given that amongst the various quantities characterizing a BFS flow, the length of the separated region is frequently used in the literature as a meaningful quantity. Starting with the acceleration phase ($t^* = 0.5$), the reattachment length for the present BFS model extends for $\Delta x_1^* = \Delta x_1/S = 14.5 \pm 0.1$ (from $x = 0$; point of separation at the step edge). In contrast, the axi-symmetric channel model does not show a recirculation region (associated with the lower wall). It should be noted that a small region may exist, however, it is not possible to deduce the data with the phase-averaged streamwise velocity profiles given by Beratlis et al (2005). The absence of the recirculating region (with forward flow occurring across the entire vessel) during acceleration is noted by several other authors that study post-stenotic pulsatile flow (Ahmed & Giddens, 1984; Varghese et al. 2007b). This can be explained by the added inertial force or added mass force during the acceleration phase (i.e. $\rho \frac{\partial \langle u \rangle}{\partial t}$) that is proportional to the magnitude of the acceleration (that the opposing pressure must overcome to separate the flow) which is relatively smaller for the present work (Zamir, 2005). During the peak mass flow ($t^* = 1.0$), the reattachment length increases for both studies reaching values of $x_1^* = 14.8 \pm 0.1$ and 12.0 for the present BFS and the axi-symmetric channel models, respectively.

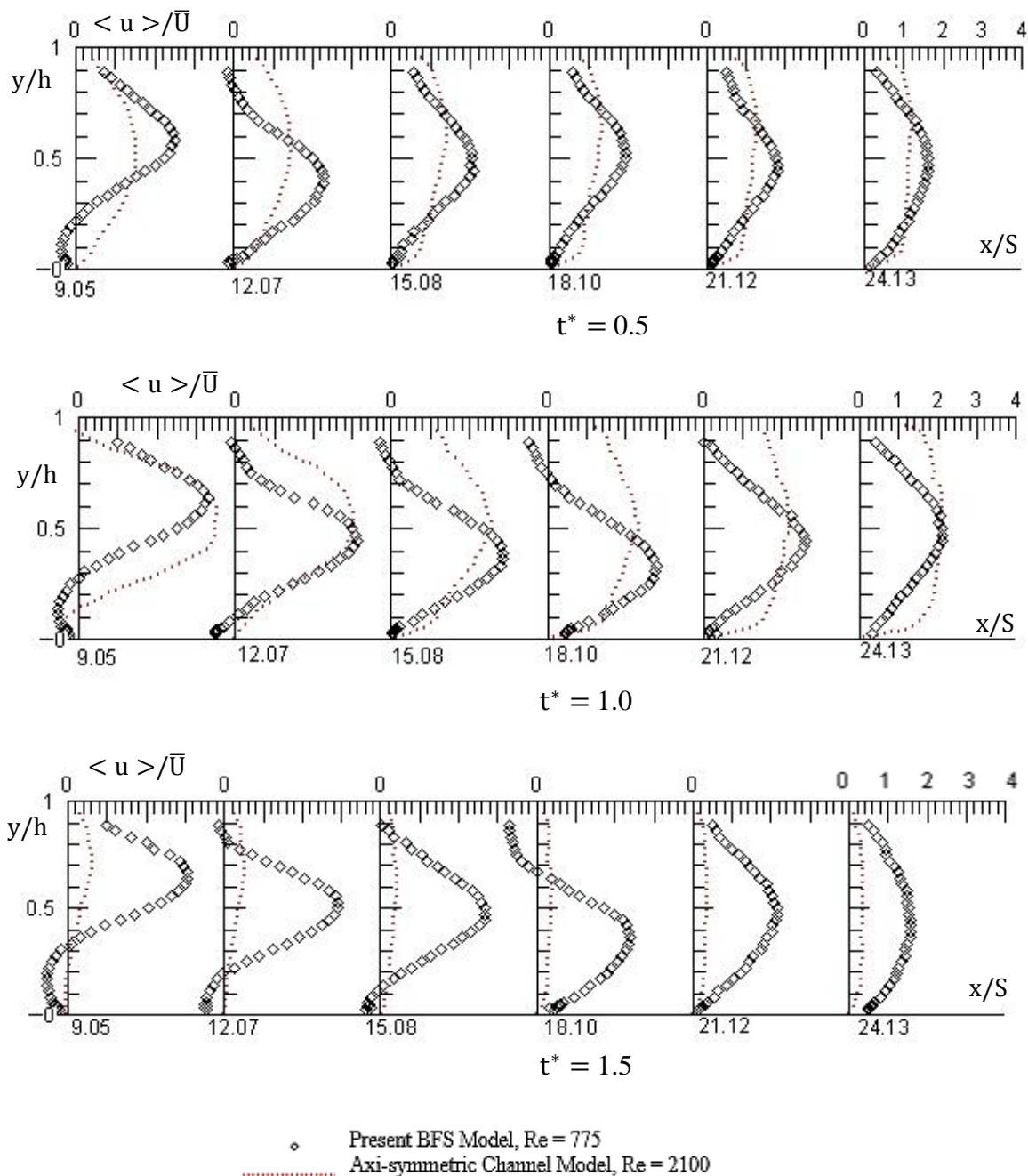


Fig. 5.13 Phase-averaged streamwise velocity profiles downstream of the blockage (comparing the present BFS model with the axi-symmetric channel model) at various measurement stations (x/S) and time instants (t^*). The normalized typical uncertainty at $y/h = 0.50$ (midplane in reference to the height) is $\epsilon_{\langle u \rangle} / |\langle u \rangle| = \pm 2.50\%$. The streamwise phase-averaged velocity is normalized with the mean bulk velocity (\bar{U}) upstream of the blockage.

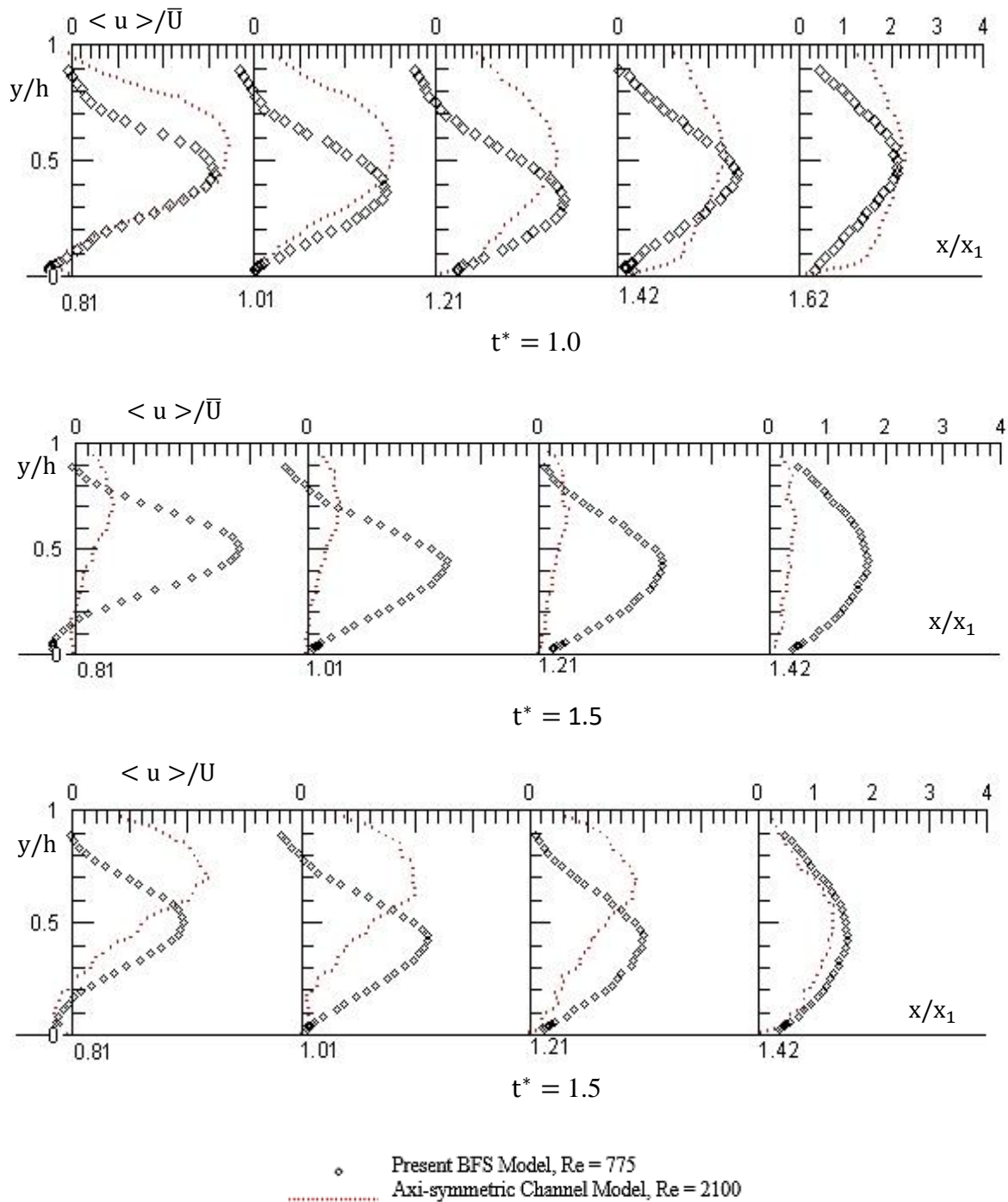


Fig. 5.14 Phase-averaged streamwise velocity profiles downstream of the blockage (comparing the present BFS model with the axi-symmetric channel model) at various measurement stations (x/x_1) and time instants (t^*). The normalized typical uncertainty at $y/h = 0.50$ (midplane in reference to the height) is $\epsilon_{\langle u \rangle} / |\langle u \rangle| = \pm 2.50\%$. The streamwise phase-averaged velocity is normalized with the mean bulk velocity (\bar{U}) upstream of the blockage.

The reattachment length of the axi-symmetric channel model (obtained through linear interpolation of the streamwise velocity profiles) is in reasonable agreement (given the blockage geometry differences) with the work of Armaly et al (1983) at a instantaneous $Re = 3570$ (calculated based on U_{max}), with a difference of 9.1%. The relatively smaller recirculating flow region (for the axi-symmetric channel model in comparison to the present BFS model) on the lower wall is presumably a result of the shear layer instability (which the authors report during the peak mass flow phase) occurring closer to the blockage given the larger Re value, thereby decreasing the extent of the recirculation region (Mittal et al. 2003).

For the deceleration phase ($t^* = 1.5$), the present BFS model shows an extended recirculating region by the amount of $\Delta x_1^* = 1.66$ (from the peak mass flow phase). The increase in x_1^* during the decrease in the mass flux can be attributed to an increase in the adverse pressure gradient (not geometrically induced adverse pressure gradient but the time-varying changes in the driving pressure) throughout the channel (Valencia, 1997). In contrast, the axi-symmetric channel model does not show an increase in x_1^* , presumably because at $t^* = 1.5$ the bulk flow is $U = 0.32\bar{U}$ and is very close to the start of the cycle (late in the deceleration phase). In fact, linear interpolation of the authors profiles shows $x_1^* = 10.8$ for $t^* = 1.5$. However, Beratlis et al (2005) does note an increase in x_1^* (that of the value corresponding to the peak mass flow) during mid-deceleration but does not provide streamwise profiles at that phase.

To compare the phase-averaged streamwise velocity profiles between the studies, the reader is referred to Fig. 5.14 whereby the streamwise distance is scaled with the reattachment length corresponding to the time instants under consideration. The streamwise velocity profiles are only compared at $t^* = 1.0$ and 1.5, since the primary recirculation region is not reported in the work of Beratlis et al (2005) associated with the acceleration phase. Starting with $t^* = 1.0$, upstream of flow reattachment (i.e. $x/x_1 = 0.81$) the maximum value of the $\langle u \rangle^* = \langle u \rangle / \bar{U}$ profiles are in the expected agreement with a difference of $\Delta \langle u \rangle^* = 0.4$. The relatively smaller value of $\langle u \rangle^*$ for the present BFS model is as a result of the differences in the pulsation amplitude. For the present BFS model, the flow is displaced downward (as a result of a recirculation region developing on

the upper wall) until $x/x_1 = 1.42$ and thereby resulting in an unfavorable collapse of velocity data between the studies. In addition, given the absence of the upper wall recirculating region for the channel model the flow starts to immediately redevelop downstream of flow reattachment causing additional differences in the streamwise velocity profiles between the studies.

To compare the $\langle u \rangle^*$ profiles between the studies during the deceleration phase of the pulse cycle at $t^* = 1.5$, two succeeding plots are provided in reference to the work of Beratlis et al (2005). In the first plot, the phase-averaged streamwise velocity is normalized with the mean bulk velocity upstream of the blockage (\bar{U}) and, for the second plot, it is normalized with the spatially-averaged bulk velocity (U) corresponding to $t^* = 1.5$. The second plot (whereby the streamwise velocity is normalized with the bulk velocity) is provided given the relatively lower U/\bar{U} magnitude at $t^* = 1.5$ (refer to Fig. 5.11b) for the axi-symmetric channel model (i.e. it is difficult to make an insightful comparison with the present work). With the exception of the favorable collapse of $\langle u \rangle/U$ data $x/x_1 = 1.42$ (average deviation of $\pm 7.2\%$), the phase-averaged velocity profiles do not demonstrate a respectable agreement. According to Beratlis et al (2005), at $t^* = 1.5$ the flow becomes asymmetric and the jet attaches to the upper side of the channel.

Fig. 5.15 gives the phase-averaged streamwise and wall-normal r.m.s. velocities, $\langle \sqrt{u'^2} \rangle / \bar{U}$ (denoted by $\langle u' \rangle$) and $\langle \sqrt{v'^2} \rangle / \bar{U}$ (denoted by $\langle v' \rangle$), normalized with the mean bulk velocity, respectively. Along with the work of Beratlis et al (2005), the r.m.s. profiles are plotted at $t^* = 0.5, 1.0$ and 1.5 at various x/x_1 measurement stations. It should be noted, for $t^* = 0.5$ the r.m.s. profiles are given with the streamwise distance scaled with the blockage height (S) since Beratlis et al (2005) do not report a recirculating region associated with the lower wall. Furthermore, at $t^* = 0.5$ it is less critical to compare the r.m.s. profiles (between the studies) since the turbulence intensity is negligible (negligible production of turbulence) throughout the channel (for both studies, whereby for the channel model the magnitude is below 2% of the mean bulk velocity). For the present BFS model, the $\langle u' \rangle$ profile data scatter around zero (within experimental uncertainty) across the channel height for all measurement stations with the exception at $x/S = 15.08$ (vicinity of reattachment)

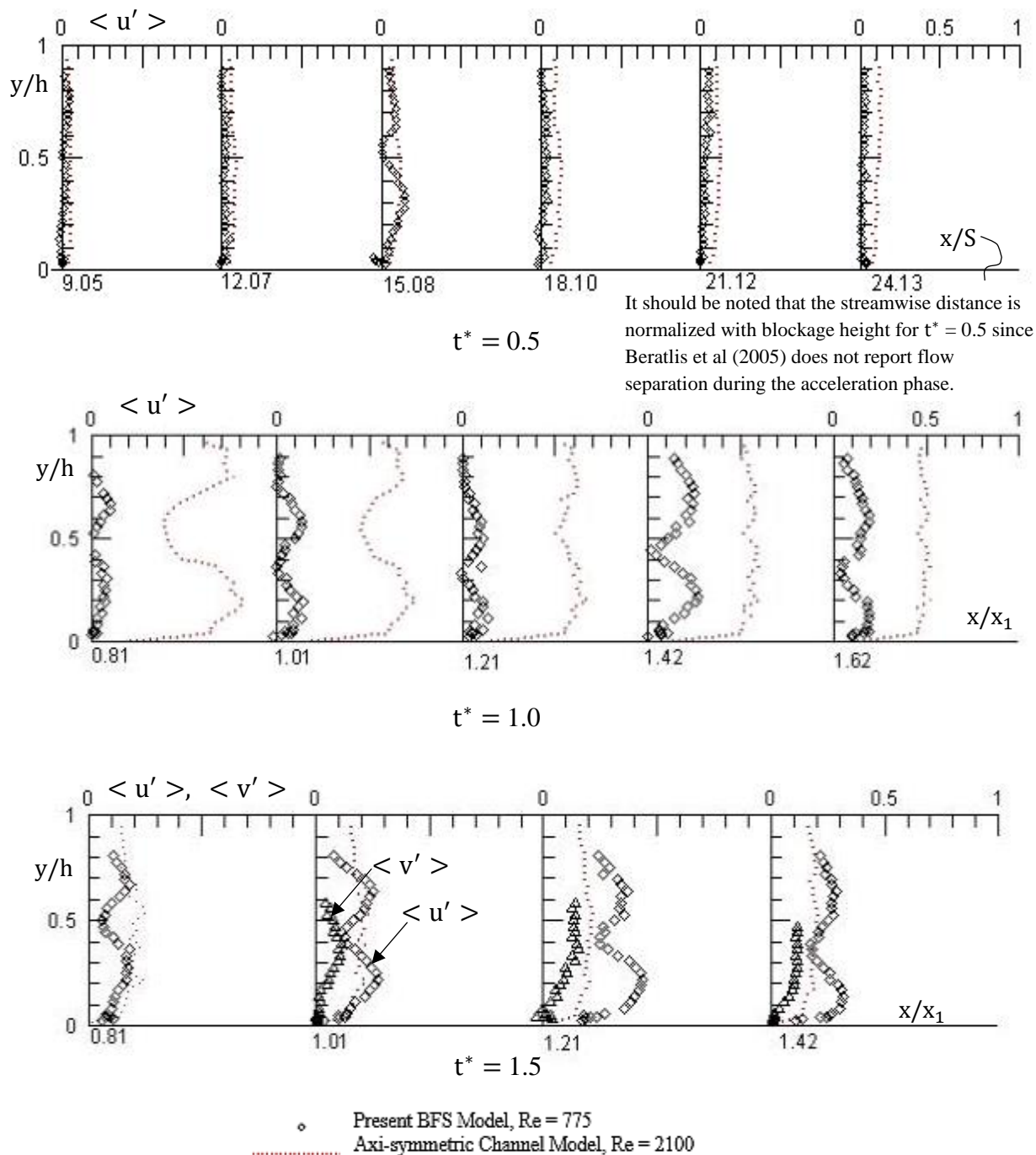


Fig. 5.15 Normalized streamwise and wall-normal r.m.s. velocity profiles (comparing the present BFS model with the axi-symmetric channel model) at various measurement stations (x/x_1) and time instants (t^*). The normalized typical uncertainty at $y/h = 0.50$ (midplane in reference to the height) for both velocity components is $\epsilon_{r.m.s.\langle u' \rangle} / r.m.s.\langle u' \rangle = 5.65\%$. The $\langle v' \rangle$ profile only shown for $t^* = 1.5$ since during other time instants of the pulse cycle yield $\langle v' \rangle \approx 0$ (whereby the scatter is within the experimental uncertainty).

whereby $\langle u' \rangle$ shows a slight increase in magnitude (i.e. $\langle u' \rangle \approx 0.1$). In contrast, during the peak mass flow ($t^* = 1.0$), both studies show increased turbulence levels with maximum values of $\langle u' \rangle \approx 0.25$ and 0.8 (occurring at $y/h \approx 0.2$) for the present BFS and axi-symmetric channel models, respectively. The increased levels of $\langle u' \rangle$ for the axi-symmetric channel model can be attributed to the larger Re value (Mittal et al. 2003). Both the present BFS model and the channel model display two distinct peaks in the $\langle u' \rangle$ profile as a result of the shear layer instability (i.e. shear layer that forms the edge of the jet becomes unstable and rolls up into vortices). Notwithstanding the magnitude differences in $\langle u' \rangle$ between the models, it appears that for the axi-symmetric channel model the shear layer instability occurs further upstream of flow reattachment (i.e. closer to the blockage which is accompanied with upstream advancement of high turbulence activity – Mittal et al. 2003). Immediately downstream of flow reattachment ($x/x_1 = 1.21$) there is evidence of initial jet breakdown and of the disturbances rapidly diffusing over the entire channel cross-section (i.e. spreading of the peaks). This is in contrast to the BFS model, whereby the maximum value in $\langle u' \rangle$ does not occur until $x/x_1 = 1.42$ with evidence of redistribution of turbulence at $x/x_1 = 1.62$. As the mass flux decelerates at $t^* = 1.5$, for the present BFS model the turbulence levels increase throughout the channel with a maximum value of $\langle u' \rangle = 0.45$ occurring downstream of flow reattachment at $x/x_1 = 1.21$. Higher levels of the streamwise r.m.s. velocity are also evident upstream of flow reattachment in the shear layer (a difference of $\langle u' \rangle \approx 0.1$ in compare to the peak mass flow phase). During deceleration, for the present BFS model there also appears to be an increase in the wall-normal r.m.s. velocity (not detected during the peak mass flow) with a maximum value of $\langle v' \rangle = 0.18$ at $x/x_1 = 1.21$. For the axi-symmetric channel model, the streamwise r.m.s. levels are relatively lower during the deceleration phase (maximum of $\langle u' \rangle \approx 0.2$) presumably as a result of significantly reduced mass flow rate. Although not shown, it should be noted that for the present BFS model the turbulence levels decay to negligible values (i.e. spurious r.m.s. velocities) at $x/x_1 \approx 2.5$ for both the peak mass flow and the deceleration phases. It should also be noted that the intermittent behaviour of turbulence over the pulse cycle observed in Fig. 5.15 (whereby the largest values of turbulence intensity are observed during the peak mass flow and deceleration phases of the

cycle) is also reported by several other authors who studied post-stenotic flows (Ahmed & Giddens, 1984; Lieber & Giddens, 1990, Kehoe, 2001, Mittal et al. 2003).

The energy spectra $E_{u'u'}$ of the temporal variation of u' (with the running mean subtracted) at $y/h = 0.5$ downstream of the blockage in the range, $12.07 \leq x/S \leq 21.12$ is given in Fig. 5.16. The energy spectra are computed to determine the frequency components as well as the energy contribution of the measured streamwise u' during the pulse cycle. In contrast to the steady laminar flow case (reported in the previous section), there is evidence of more pronounced concentration of energy within a narrow frequency band (multiple peaks) in the range, $70 \text{ Hz} \leq f \leq 130 \text{ Hz}$ corresponding to a Strouhal number range, $0.13 \leq St \leq 0.25$ (where $St = f(h - S)/U_{\max}$; where U_{\max} is the maximum bulk velocity during the pulse cycle at the step). The scaling of frequency by $U_{\max}/(h - S)$ is typically used in the literature (for pulsatile flow studies) given that it is the peak stenotic jet velocity which initiates transition to turbulence further downstream (Casanova & Giddens, 1978). Using equivalent non-dimensionalization of frequency, Mittal et al (2003) considering pulsatile flow inside a PPFC with a semi-circle stenosis report a non-dimensional vortex shedding frequency of $St = 0.45$. In addition, work of Lu et al (1983) which study steady flow in a pipe with an axi-symmetric stenosis report vortex shedding frequency ranging from $St \approx 0.5$ in the vicinity of the blockage to $St \approx 0.1$ further downstream. Hence, it is presumably the shear layer instability in the present study (upstream of flow reattachment at $x/S \approx 12.07$) which is responsible for the turbulence spots further downstream. Furthermore, according to Rosenfeld (1995), pulsatile flow over a BFS is more prone to vortex formation and shedding at a much lower Re value than steady flow.

As with the steady flow case, the turbulent spots in the vicinity and farther downstream of flow reattachment do not indicate developed turbulence given that the $-5/3$ slope only covers a very narrow band of frequencies. Once again, it is more likely that these turbulent spots represent breakdown of structure and transition.

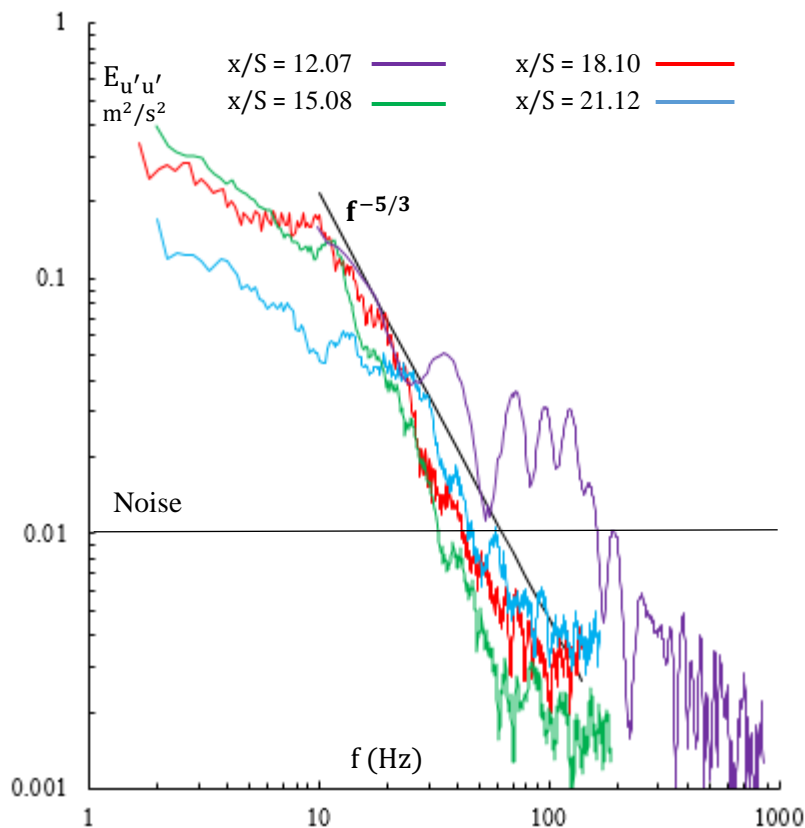


Fig. 5.16 Energy spectra ($E_{u'u'}$) of the streamwise velocity fluctuation (u') for $x/S = 12.07, 15.08, 18.10$ and 21.12 measurement positions downstream of the step at the channel centreline ($y/h = 0.5$).

Moving forward with a comparison with the asymmetric tube model depicted in Fig. 5.10c, Fig. 5.17 and 5.18 give the phase-averaged streamwise velocity profiles (normalized with the mean bulk velocity upstream of the blockage). In Fig. 5.17 and 5.18, the streamwise distance is normalized with the blockage height (S) and the reattachment length (phase-dependent), respectively. Both Figures compare the present BFS model to the asymmetric tube model given by Long et al (2001). As with the former comparison (i.e. work of Beratlis et al. 2005), normalization of the streamwise distance by the blockage height is only provided to show the difference in $x_1^* = x_1/S$ between the models and attempt to explain the factors which lead to a difference. At $t^* = 1.0$ (peak mass flow during the cycle), the present BFS model reattachment length associated with flow separation at the step edge is $x_1^* = 14.8 \pm 0.1$. The present BFS model reattachment length is larger by the amount of $\Delta x_1^* \approx 9.40$ that of the asymmetric tube model, presumably as a result of the larger Re value in the present study together with the rounded stenosis corners for the tube model. The latter and the former are supported by the fact that laminar flow over a curved surface experiences a delay in separation (Haggmark et al. 2000) and since x_1^* increases

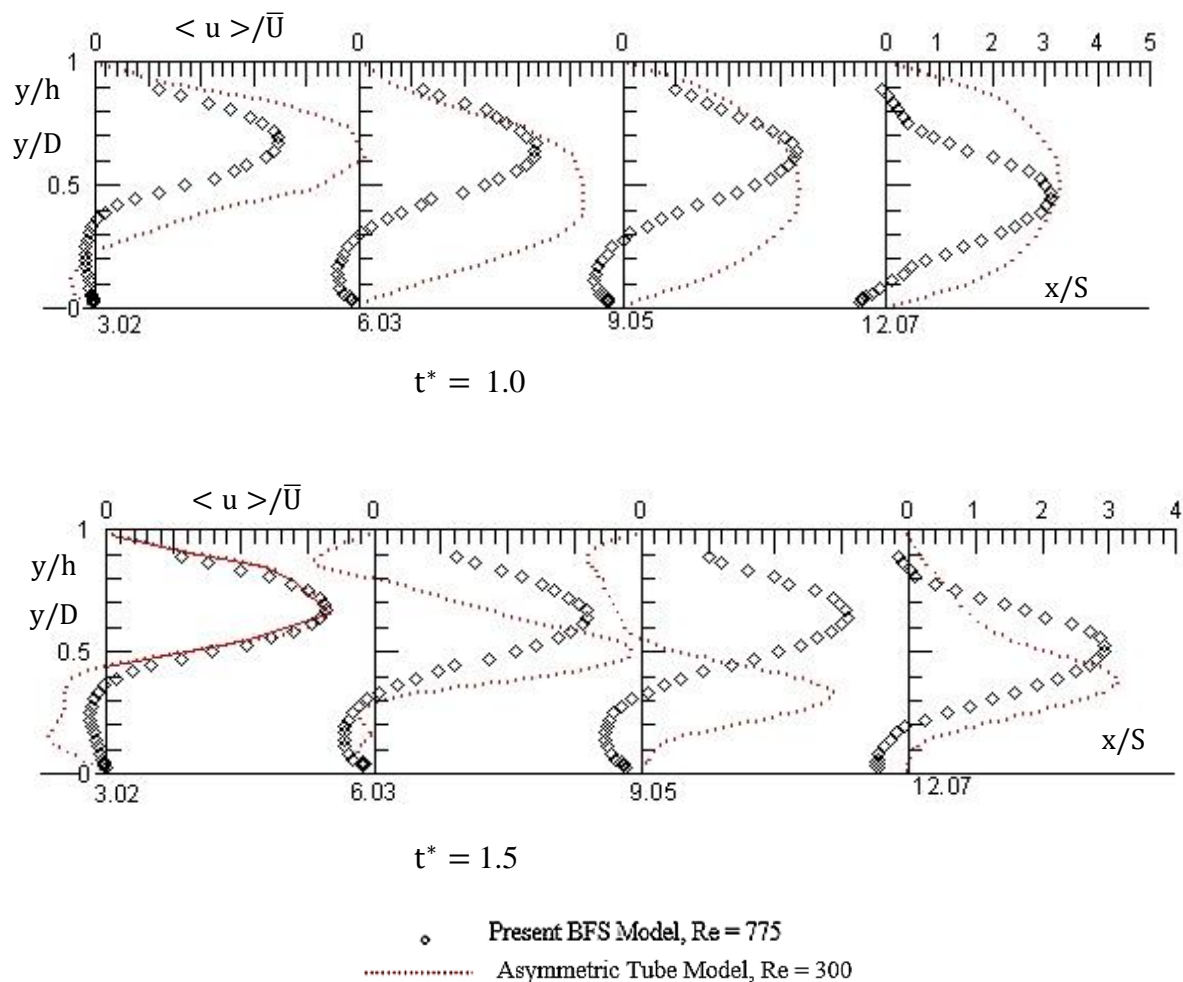


Fig. 5.17 Phase-averaged streamwise velocity profiles downstream of the blockage (comparing the present BFS model with the asymmetric tube model) at various measurement stations (x/S) and time instants (t^*). The normalized typical uncertainty at $y/h = 0.50$ (midplane in reference to the height) is $\epsilon_{\langle u \rangle} / |\langle u \rangle| = \pm 2.50\%$. The streamwise phase-averaged velocity is normalized with the mean bulk velocity (\bar{U}) upstream of the blockage.

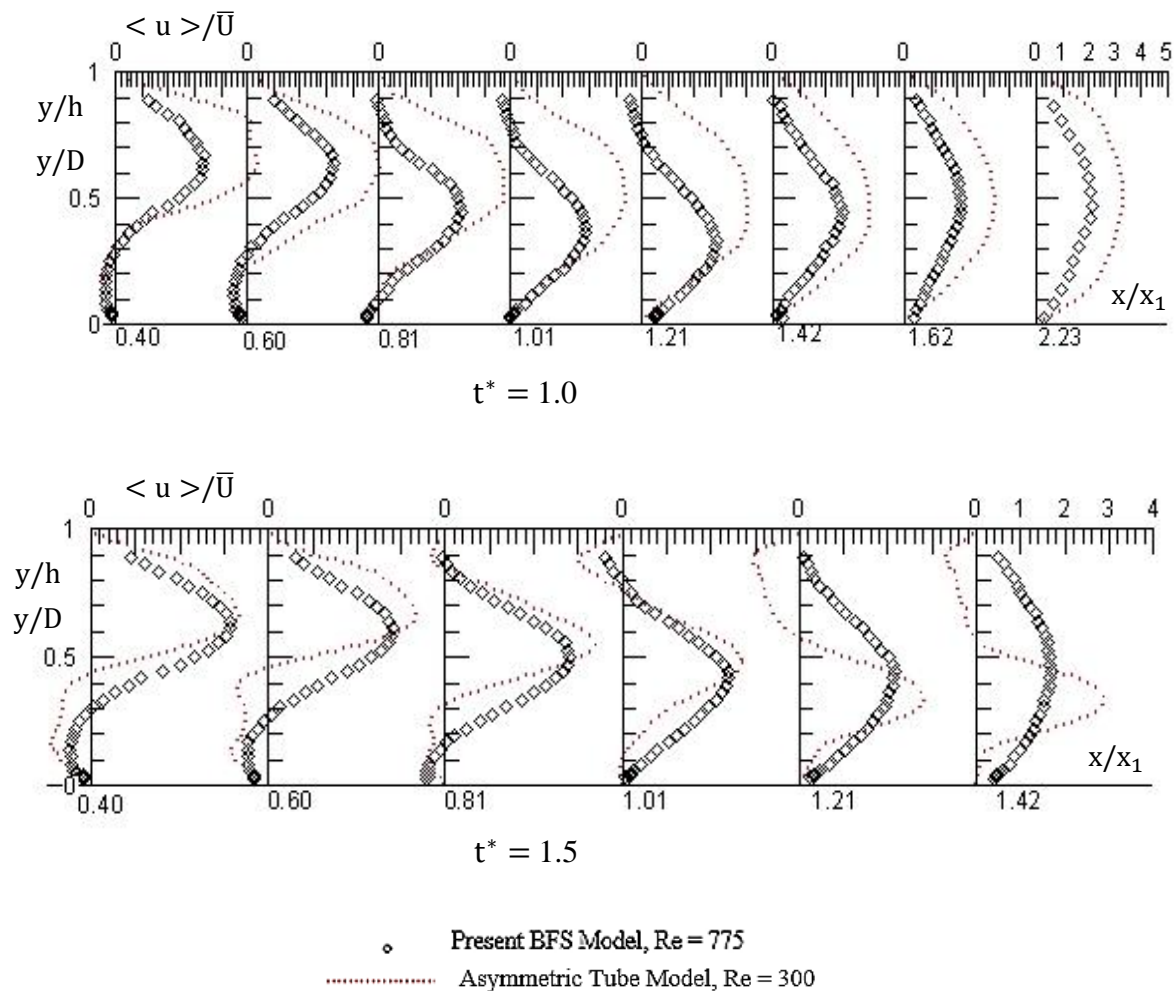


Fig. 5.18 Phase-averaged streamwise velocity profiles downstream of the blockage (comparing the present BFS model with the asymmetric tube model) at various measurement stations (x/x_1) and time instants (t^*). The normalized typical uncertainty at $y/h = 0.50$ (midplane in reference to the height) is $\epsilon_{\langle u \rangle} / |\langle u \rangle| = \pm 2.50\%$. The streamwise phase-averaged velocity is normalized with the mean bulk velocity (\bar{U}) upstream of the blockage.

with Re (for laminar regime) for obstructed PFFC/tube pulsatile flows (Valencia, 1997; Griffith, 2009). Once again, using the work of Armaly et al (1983) at $Re = 300$ (see Fig. 2.8) yields a reattachment length which is larger by the amount of $\Delta x_1^* \approx 1.64$ that of the asymmetric tube model. During deceleration of the mass flux at $t^* = 1.5$, both the present BFS and the asymmetric tube models show an increase in x_1^* by the amount of 11.1% and 23.8%, respectively. The increase in x_1^* during the decrease in the mass flux can be attributed to an increase in the adverse pressure gradient (Valencia, 1997). The relatively larger increase in x_1^* at $t^* = 1.5$ for the asymmetric tube mode is presumably as a result of a larger deceleration (i.e. $d\langle u \rangle / dt$ – refer to Fig. 5.11b).

The comparison of the $\langle u \rangle^* = \langle u \rangle / \bar{U}$ profiles between the present BFS model and the asymmetric tube model in Fig. 5.18 corresponding to $t^* = 1.0$ are in much better agreement given that the streamwise distance is scaled with the reattachment length (at that phase of the cycle). Immediately downstream of the blockage, the maximum value of $\langle u \rangle^*$ is relatively larger for the asymmetric tube model with a difference of $\Delta \langle u \rangle^* \approx 2$. The reason for this is presumably due to the larger amplitude of pulsation for the tube model (depicted in Fig. 5.11b) together with the actual blockage ratio of $b = 0.46$ for the present BFS model. Beneath the blockage (i.e. $y/h < 0.4$) to the point of flow reattachment (i.e. $x/x_1 = 1.01$), the $\langle u \rangle^*$ values between the two models are nearly identical with an average deviation of $\pm 4.7\%$. The largest discrepancy among the profiles (between the two studies) is realized between $x/x_1 = 0.81$ and 1.21, given that the present BFS model displays an upper wall recirculation region commencing at $x/x_1 \approx 0.81$. The presence of the upper wall recirculation is responsible for downward displacement of the flow which results in a difference between the $\langle u \rangle^*$ profiles for $y/h > 0.4$. The presumable reason for the asymmetric tube model not revealing an upper wall recirculation region is the relatively smaller Re value. This is because in the work of Armaly et al (1983), the second recirculation region only appears for $Re > 400$. Downstream of $x/x_1 = 1.42$, the $\langle u \rangle^*$ profiles start to redevelop and the difference in maximum value at $y/h \approx 0.5$ is $\Delta \langle u \rangle^* = 1.1$ as a result of the larger amplitude of pulsation. Furthermore, during deceleration at $t^* = 1.5$ until the point of flow reattachment the maximum values of $\langle u \rangle^*$ are in better agreement between the models, with a maximum difference of $\Delta \langle u \rangle^* = 0.4$. The reason

for the more favorable agreement is that the U/\bar{U} values at that phase of the pulse cycle give a smaller deviation (in reference to magnitude) between the two models (i.e. $\Delta U/\bar{U} \approx 0.2$). In contrast to the peak mass flow phase, during deceleration the $\langle u \rangle^*$ values are not in favorable agreement beneath the step (i.e. $y/h < 0.5$). The asymmetric tube model displays a relatively larger recirculation depth together with larger velocity magnitudes. In fact, the $\langle u \rangle^*$ profile shape seems distorted in the recirculation region for the asymmetric tube model. According to Long et al (2001), the distortion is a direct result of the recirculation region breaking down, thereby resulting in a third recirculation region further downstream of the primary reattachment point on the lower wall. This is somewhat evident at $x/x_1 = 1.21$ and 1.42 in the vicinity of the lower wall. However, it is confined to a very thin layer and, hence, extraction of the data presented difficulty for the present author. The interesting observation is that Armaly et al (1983), as well, report a third recirculation region on the lower wall throughout the laminar and transitional flow regime (considering a BFS model with single-component LDV). Considering $Re \approx 300$ (at $t^* = 1.5$ for the tube model) and comparing to the work of Armaly et al (1983) at $Re = 400$, the difference in the start location of the third recirculation region is $\Delta x/x_1 \approx 0.15$. It should be noted that the third recirculation region on the lower wall is not detected in the present work. This is in favorable agreement with the work of Lima et al (2008) which only reports the third recirculating region at $Re = 1800$ persisting until $Re = 2500$ (considering BFS flow with $b = 0.5$).

Furthermore, downstream of flow reattachment the $\langle u \rangle^*$ profiles continue to show unfavorable collapse of data between the present BFS model and the tube model. For the tube model, the flow is displaced downward as a result of the relatively larger recirculation region on the upper wall which extends for an additional $\Delta_{(x_5^* - x_4^*)/x_1^*} \approx 0.21$ in comparison to the present BFS model. The depth of the upper wall recirculation region at $x/x_1 = 1.42$ is $\Delta y/h \approx 0.45$ for the tube model whereas, for the present BFS model the largest depth occurs at flow reattachment (i.e. $x/x_1 = 1.01$) of $\Delta y/h \approx 0.23$. This discrepancy can presumably be attributed to the differences in the deceleration (i.e. $d\langle u \rangle/dt$) whereby, the tube models experiences a larger opposing pressure.

Long et al (2001) do provide dimensional wall shear data for both the peak mass flow and deceleration phases. However, the authors do not provide fluid density or dynamic viscosity (or the fluid type) and, hence, the present author uses 2nd order curve fitting on the authors $\langle u \rangle$ profiles to deduce the dynamic viscosity. In addition, the kinematic viscosity is deduced by the present author from the Re value given by Long et al (2001). The skin friction streamwise distribution (together with its spatial and temporal gradient) along the lower wall is presented for both studies in Fig. 5.19, whereby the wall shear stress is scaled with $\frac{1}{2}\rho U^2$ (dynamic pressure). The skin friction streamwise distribution is also plotted for the steady flow presented in section 5.1. It should be noted that U represents the bulk velocity corresponding to $t^* = 0.1$ (cycle start), 0.5, 1.0 and 1.5. Scaling with U as opposed to the mean bulk velocity (\bar{U}) would account for the amplitude differences between the studies. It should also be noted that in Fig. 5.19, the x-axis reflects the streamwise distance scaled with the phase-specific reattachment length (x_1).

For the present BFS model, Fig. 5.19a shows an increase in c_f (absolute maximum value) in the primary recirculation region with an increase in the phase-specific Re value. This behaviour is also reported by Kueny & Binder (1984) which present laminar steady flow over a BFS, whereby LDV is used to measure the velocity field. Pulsatile laminar flow studies also reveal an increase in the absolute maximum magnitude of the mean skin friction (in the primary recirculation region) with an increase in Re (Mittal et al. 2003). However, it should be noted that Valencia (1997) does report larger absolute magnitudes in the recirculating region during the deceleration phase (in comparison to the peak mass flow phase). This is because of the increase in the adverse pressure gradient throughout the channel resulting in a stronger backflow (despite a lower Re value during that phase). This is not observed in the present study, presumably as a result of the smaller deceleration given the damped waveform at the working section. At $t^* = 1.0$, the absolute maximum value for the skin friction in the recirculation region is $c_f = 0.08$, with a difference of $\Delta c_f = 0.02$ (larger for the present BFS model) in comparison to asymmetric tube model. This is, presumably, as a result of the larger Re value for the present study. In contrast, during the deceleration phase at $t^* = 1.5$, the asymmetric tube model shows a larger absolute maximum c_f with a difference of $\Delta c_f = 0.005$. This result is expected given the larger

deceleration in the work of Long et al (2001). It should also be noted that for the present pulsatile flow at $t^* = 1.0$, the skin friction coefficient is much larger than for the steady flow with a difference of $\Delta c_f = 0.04$. This is in agreement with the work of Valencia (1997) which reports a significantly larger skin friction coefficient on the lower channel wall (in the primary recirculation region) for the pulsatile case ($c_f = 0.28$) in comparison to steady flow ($c_f = 0.05$ at the same $Re = 100$). It should be noted that, according to Dol et al (2014) the increase in c_f for the pulsatile flow can be attributed to the modification of the momentum transfer as a result of flow pulsatility.

Downstream of flow reattachment whereby the flow starts to redevelop, the skin friction values (for all of the shear data) scale inversely proportional to the Reynolds number (i.e. $c_f = \frac{2}{Re} \frac{\partial \langle u \rangle / U}{\partial y / h}$; where $Re = Uh/\nu$ – Kueny & Binder, 1984) with a maximum value of $c_f = 0.03$ corresponding to $t^* = 0.1$ (cycle start, $Re = 620$). At both $t^* = 1.0$ and 1.5 for the present BFS model, the skin friction coefficient displays two peaks immediately downstream of flow reattachment driven by the reduced effective channel height (i.e. upper wall recirculation – Mittal et al. 2003). For the early and mid-acceleration phases (at lower Re values), the phase-averaged streamwise velocity profiles do not display an upper wall recirculation and, hence, the flow starts to redevelop immediately downstream of flow reattachment showing a gradual increase in c_f . A similar behaviour is shown for the asymmetric tube model (corresponding to the peak mass flow phase) with the flow immediately redeveloping downstream of the flow reattachment. During the deceleration phase, the asymmetric model displays a more complex c_f streamwise distribution downstream of the flow reattachment agreeing with the phase-averaged streamwise velocity profiles given in Fig. 5.18. The authors attribute this shear behaviour to the breakdown of the primary recirculation region resulting in a third recirculation region further downstream (increased adverse pressure gradient).

Furthermore, Fig. 5.19b and 5.19c give c_f' ($c_f' = \left| \frac{\partial c_f}{\partial (x/x_1)} \right|$) at $t^* = 1.0$ and 1.5 for both models, respectively. The streamwise distributions of c_f' between the present BFS model and the asymmetric model are in favorable agreement for both time instants. At $t^* = 1.0$, both models display two distinct peaks in the vicinity of flow reattachment (i.e. $x/x_1 \approx$

1.0) with a maximum value of $c_f' \approx 0.60$. Similarly, at $t^* = 1.5$ the c_f' profiles are in favorable agreement with a slightly larger maximum value for the asymmetric tube model (i.e. $\Delta c_f' \approx 0.1$). Downstream of flow reattachment, the asymmetric model shows an average $c_f' \approx 0.05$ agreeing with the more complex c_f streamwise distribution shown in Fig. 5.19a. For the present BFS model, the c_f' values are approximately zero (scatter within experimental uncertainty) reflecting a constant magnitude of c_f further downstream of flow reattachment. Given the favorable collapse of the c_f' data between the studies, it would be expected for the ECs inside the present PPFC (with a simple step model) to be subjected to spatial gradients of shear that are found in more realistic asymmetric stenosis tube models.

Given that the temporally varying wall shear stress is as equally important as the spatially varying wall shear stress in reference to the physiology of ECs (whereby White et al. 2005 report a stronger dependence of cell proliferation on the temporal gradients of WSS in comparison to spatial gradients), Fig. 5.20 gives c_f ($c_f = \tau_w / (0.5\rho\bar{U}^2)$) and c_{f_t}' ($c_{f_t}' = \left| \frac{\partial c_f}{\partial(t^*)} \right|$) at $x/x_1 = 0.75$ for both models. The spatial position ($x/x_1 = 0.75$) is specifically selected to demonstrate the effect of the waveform shape (i.e. $d\langle u \rangle / dt$) on the temporal profile of c_f (given the largest contrast between the profiles at that location). The first item to note in Fig. 5.20a is that the asymmetric tube model shows positive c_f values for $t^* < 1.0$ (acceleration phase). This is indicative of an absence of flow separation during the acceleration phase of the cycle. As noted previously, Beratlis et al (2005) also reports the same flow behaviour (during the acceleration phase) as a result of the added inertial force (i.e. $\rho \frac{\partial \langle u \rangle}{\partial t}$) that is proportional to the magnitude of the acceleration. In the present work, flow separation is evident throughout the pulse cycle and, hence, the skin friction coefficient is negative for $t^* < 1.0$. The second item to note (in reference to the asymmetric tube model) is that the skin friction temporal profile during deceleration of the systole phase (i.e. $1.0 < t^* < 1.5$) displays a rapid increase in the absolute c_f followed by a rapid decrease. For the present BFS model, the temporal profile of the absolute c_f (for the same t^* range) shows a gradual decrease due to the smaller adverse pressure gradient. Given the significant difference in the temporal profile of c_f between the models, the c_{f_t}' profiles do

not agree showing a maximum difference of $\Delta c_{f_t}' \approx 3.25$. It should be noted that c_{f_t}' is fairly consistent at all x/x_1 positions (in the recirculating region) for both models and, hence, for clarity purposes only $x/x_1 = 0.75$ is plotted. In addition to the spatial and temporal distribution of WSS, the oscillatory shear index (OSI) is another important quantity for characterizing EC response to flow (Davies, 2009). According to Davies (2009), the OSI is a measure of the shear stress experienced at a point in space which takes into account shear stresses that act in the directions that are different to that of the bulk flow. The OSI stated in terms of the skin friction coefficient can be defined as follows (Avari, 2015):

$$\text{OSI} = 0.5 \left(1.0 - \frac{\left| \int_0^T c_f dt \right|}{\int_0^T |c_f| dt} \right) \quad (5-1)$$

It should be noted that the OSI can vary between 0 and 0.5, where the former represents a unidirectional flow and the latter represents a flow whereby the shear stress direction changes during the pulse cycle. For the asymmetric tube model, at $x/x_1 = 0.75$, the OSI value is 0.44 whereas for the BFS model it is zero (no change in the shear direction during the pulse cycle). It should be noted that low WSS together with a high OSI is another contributor (in addition to spatiotemporal gradients) to EC dysfunction (Davies, 2009). From both the temporal gradient profile (given in Fig. 5.20b) and the OSI, it is abundantly clear that the present pulsatile flow (i.e. waveform shape) does not represent actual flow found in the complex regions of the arterial network (atherosclerosis prone regions).

The next section summarizes all of the findings from this Chapter with emphasis on the ability of the present BFS to model both the CA and the asymmetric stenosis tube models. A conclusion is drawn via considering both the influence of the geometry and the waveform shape on the downstream flow.

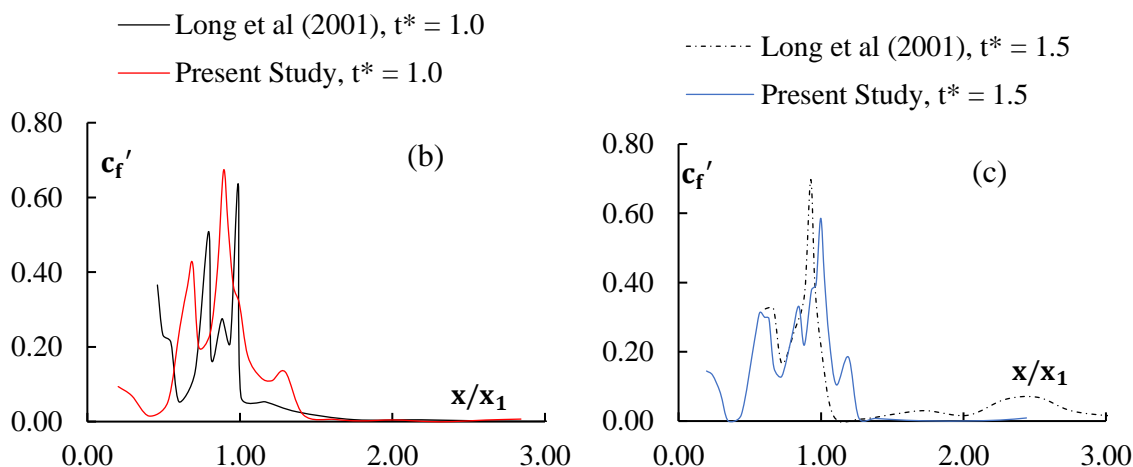
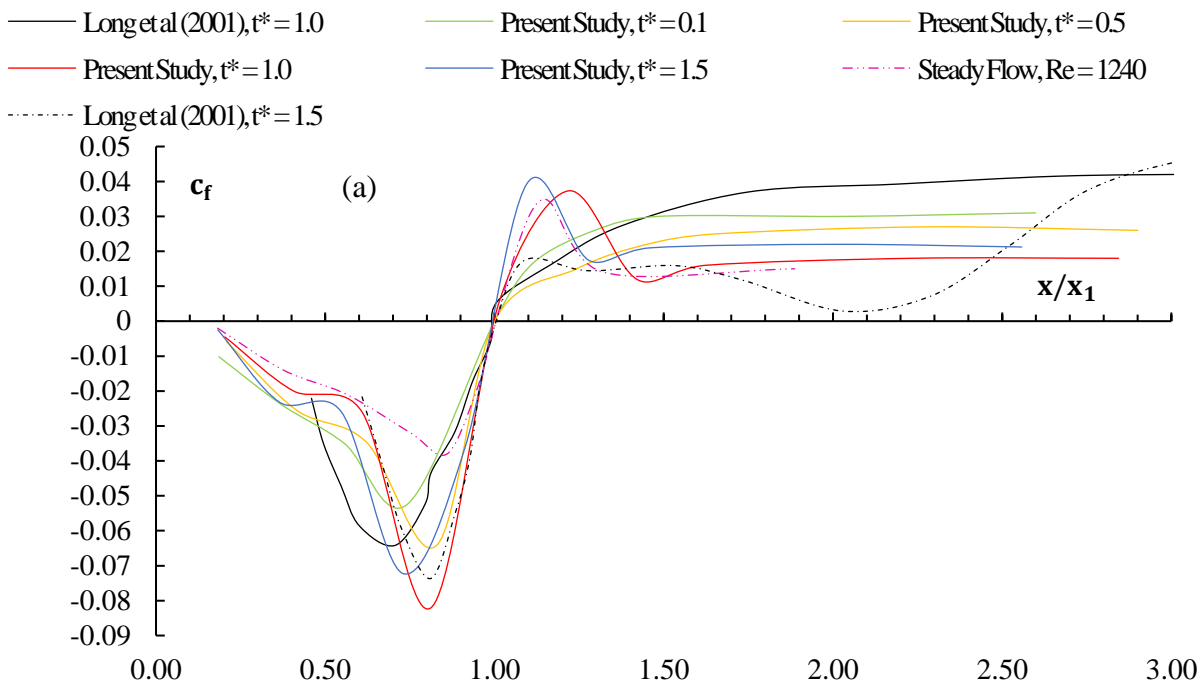


Fig. 5.19 (a) Distribution plot of the local skin friction coefficient (c_f) in the streamwise direction downstream of the blockage (i.e. $2z/w = 0$) comparing the present BFS model to the asymmetric tube model given by Long et al (2001). The average uncertainty of the skin friction is $\pm 5.2\%$. (b) streamwise distribution of the skin friction spatial gradient at $t^* = 1.0$ (peak flow), (c) streamwise distribution of the skin friction spatial gradient at $t^* = 1.5$ (deceleration phase).

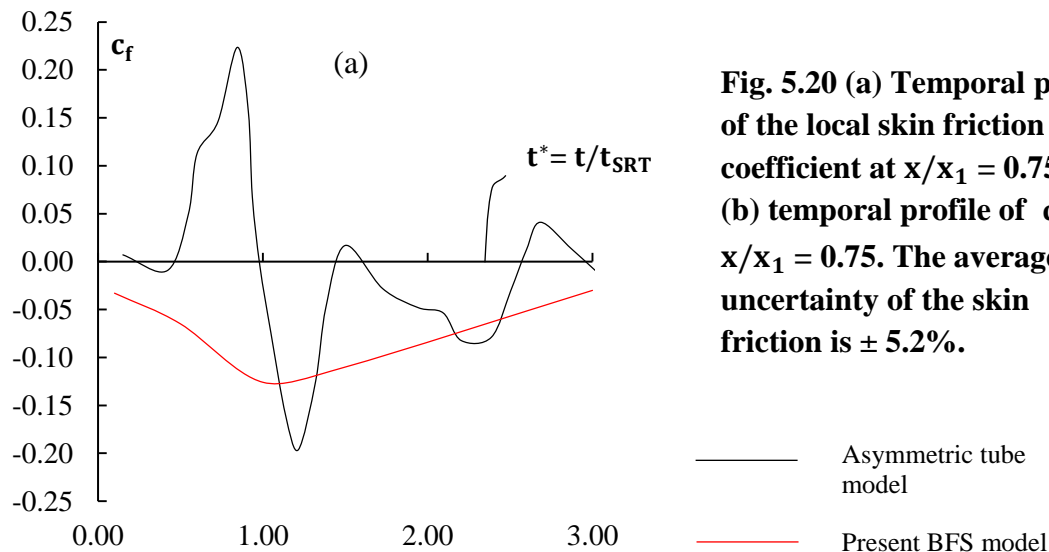
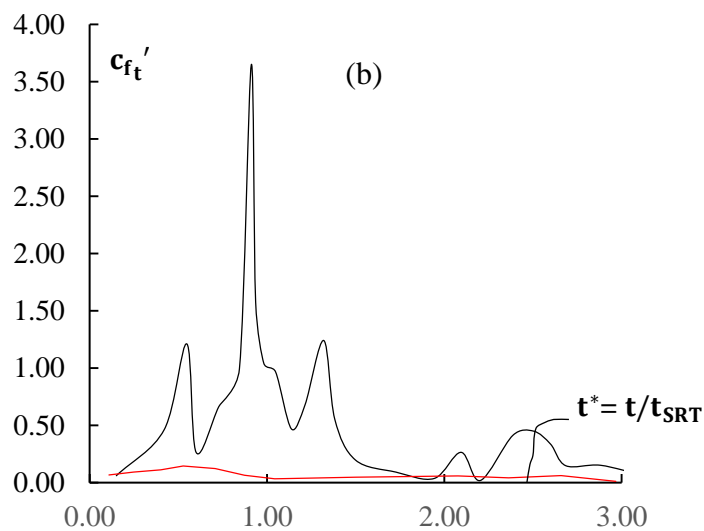


Fig. 5.20 (a) Temporal profile of the local skin friction coefficient at $x/x_1 = 0.75$ and (b) temporal profile of c_{ft}' at $x/x_1 = 0.75$. The average uncertainty of the skin friction is $\pm 5.2\%$.



5.3 Chapter Five Summary

Steady and pulsatile laminar flow was studied inside a parallel-plate flow chamber (PPFC) with a simple vertical step (inserted at the onset of the working section) to model a stenosis with 50% severity (by area). The objective of the present work was to evaluate if a simple step can emulate more realistic stenosis geometries such as those found in the human body. This evaluation was performed by quantifying the flow physics (mean flow and turbulence statistics, together with the skin friction on the lower wall) downstream of the step and by

comparing to other literature which considered more realistic models of stenosis. Various stenosis geometries were considered to gain more insight into the flow physics downstream of the stenosis with PPFC/tube type flows. However, to fulfil the objectives of this thesis work and, thereby, bring insight into whether a simple step (inside a PPFC) can model more realistic stenosis flows, both the steady and pulsatile flow cases considering the stenosed carotid artery (CA) and the asymmetric stenosis models (inside a straight section of tube) were considered paramount, respectively.

First, the steady laminar case was in excellent agreement (whereby the reattachment length was within $\pm 4.3\%$) with the experimental work of Armaly et al (1983) to the point of flow reattachment (whereby $c_f = 0$). Downstream of flow reattachment (whereby the separated flow reattached to the lower wall), favorable agreement of the streamwise velocity profiles (at the midplane) was not found, given the differences in the aspect ratio of the PPFCs. The comparison between the BFS models (inside the PPFCs – considering both experimental and 2-D numerical literature work) was considered an important comparison to better understand the influencing factors which lead to the differences of the flow physics downstream of the step. Furthermore, the semi-circle model inside a 2-D PPFC (given by Griffith, 2009) was considered an extension to the present work, whereby the semi-circle geometry resembled a more realistic stenosis. In general, closer to the lower wall (i.e. $y/h < 0.1$) the magnitudes of \bar{u}/U were in favorable agreement with an average deviation of $\pm 3.5\%$. The favorable agreement of the absolute maximum c_f value was also realized inside the primary recirculation region with a difference of $\Delta c_f = 0.005$ (within the experimental uncertainty). However, a discrepancy in c_f between the models occurred immediately downstream of flow reattachment in the range, $1.13 < x/x_1 \leq 1.70$, given the differences in the upper wall recirculation depths (i.e. reduction of the effective channel height). For the present BFS model, the difference between the measured c_f value at $x/x_1 = 1.89$ (further downstream of flow reattachment) and that of a fully-developed steady laminar flow under $Q = 7.50 \pm 0.075$ was within $\pm 2.5\%$.

The comparison continued with the axi-symmetric stenosis model inside a straight section of tube under steady laminar flow. For a more effective comparison with the axi-symmetric stenosis models (given that the flows are fundamentally different), the present author

postulated better agreement (for both steady and pulsatile flow) through considering a double backward-facing step PFFC model (whereby a step is placed on both sides of the channel). Nevertheless, the \bar{u}/U profiles (prior to flow reattachment) in the region, $0.0 < y^* < 0.1$, demonstrated favorable agreement with an average deviation of $\pm 4.3\%$. The absolute maximum value of normalized streamwise profiles (for both models) at $y^* = 0.1$ for $x/x_1 = 0.38$ and 0.57 (upstream of flow reattachment) was $\bar{u}/U \approx 0.2$. Further away from the wall in the primary recirculation region, the present BFS model displayed stronger backflow as a result of the larger Re value. The skin friction was not in favorable agreement upstream (larger for the BFS model by a factor of 1.5) and downstream of flow reattachment as a result of a larger Re value and the influence of the upper wall recirculation region for the present BFS model, respectively. Given the absence of the upper wall recirculation for the axi-symmetric model (at the plane of symmetry), the skin friction coefficient did not display a rapid increase (in the vicinity of flow reattachment) as in the case of the present BFS model.

To bring insight into how well the present BFS models a healthy and diseased (stenosed) carotid artery flow, the skin friction (c_f) and its spatial gradient (c_f') streamwise distributions were compared with *in-vitro* carotid artery models (under steady flow). The outer wall of the healthy internal carotid artery (ICA) displayed much smaller absolute values of c_f inside the primary recirculation region. This was also true for the c_f' values inside the primary recirculation region with an average difference of $\approx 133\%$ between the models. In the vicinity of flow reattachment, the healthy CA model showed c_f' values close to zero not agreeing with the present BFS model. For the stenosed CA model, the absolute maximum skin friction and the spatial gradient distribution on the inner wall of the ICA (inside the recirculation region) were in better agreement with the BFS model showing a difference of 66% and 22% (average difference), respectively. In addition, the difference in the maximum c_f' (between the models) in the vicinity of flow reattachment was $\approx 133\%$. In general, the present BFS model shear data did not demonstrate favorable agreement with both the healthy and the stenosed CA models.

The present investigation continued with studying pulsatile laminar flow (and comparing to other models of stenosis) over a BFS with the added complexity of the pulsation

amplitude, frequency and the waveform shape (i.e. dQ/dt behaviour). In comparison to the axi-symmetric stenosis model (PPFC flow), the mean flow ($\langle u \rangle^*$; for the peak mass flow phase) downstream of the blockage was not in a favorable agreement (upper half of the channel) due to the upper wall recirculation detected for the present BFS model displacing the flow downwards (negative y -direction). A more favorable agreement was found near the wall prior to flow reattachment, with an average deviation of $\pm 11.7\%$. The axi-symmetric model displayed asymmetry during the deceleration phase resulting in the jet (formed at the onset of flow expansion) attaching to the upper wall. The streamwise turbulence intensities during the peak mass flow phase were relatively larger for the axi-symmetric model, with maximum values of $\langle u' \rangle \approx 0.25$ and 0.8 (occurred at $y/h \approx 0.2$) for the present BFS and axi-symmetric models, respectively. During the acceleration phase of the pulse cycle, both studies revealed negligible turbulence production, with the $\langle u' \rangle$ data scattering around zero (within experimental uncertainty) across the channel height. The intermittent behaviour of turbulence over the pulse cycle for both studies (whereby the largest values of turbulence intensity were observed during the peak mass flow and deceleration phases of the cycle) was in good agreement with the literature which considered pulsatile laminar flow.

Lastly, the comparison of the present BFS model to the asymmetric tube model (under pulsatile flow conditions) showed excellent agreement of the streamwise velocity profiles (during the peak mass flow phase) in the primary recirculation region, whereby the $\langle u \rangle^*$ values were nearly identical with an average deviation of $\pm 2.7\%$. Notwithstanding the amplitude differences, the main discrepancy between the streamwise velocity profiles was realized between $x/x_1 = 0.81$ and 1.21 . This is because the present BFS model displayed an upper wall recirculation region commencing at $x/x_1 \approx 0.81$, displacing the flow downwards in the negative y -direction. This discrepancy was also realized in the skin friction plot, whereby the asymmetric tube model did not demonstrate a defined peak downstream of flow reattachment (associated with reduced effective channel height). During the deceleration phase of the cycle, the $\langle u \rangle^*$ profiles were not in favorable agreement inside the primary recirculation region (i.e. $y/h < 0.5$), whereby the asymmetric tube model displayed a relatively larger recirculation depth together with larger velocity

magnitudes. The difference in the profiles was attributed to the larger deceleration of flow (i.e. increase in adverse pressure gradient, $d\langle u \rangle/dt$) for the asymmetric tube model. The larger deceleration was also responsible for the unfavorable collapse of data downstream of flow reattachment as a result of flow displacement in the negative y -direction.

The c_f and c_f' spatial profiles corresponding to the peak mass flow and the deceleration time instants were generally in favorable agreement between the models in the recirculating region and in the vicinity of flow reattachment. In contrast, the temporal profile of c_f and c_{f_t}' upstream of flow reattachment (in the recirculating region) did not show any level of agreement. For the present BFS model, it is thus concluded that the waveform shape had a significant influence on the temporal profile of c_f , given that the asymmetric tube model displayed positive c_f values (no flow separation) during the early to late acceleration phase. Also, the asymmetric tube model displayed a significantly steeper slope in the temporal profile of c_f (along with a larger absolute magnitude) during the early to mid deceleration phase. In addition, the OSI value (upstream of flow reattachment) for the present BFS model reflected a non-reverse flow condition during the pulse cycle, thereby not agreeing with the asymmetric tube model.

In conclusion, it can be noted that the waveform characteristics significantly influenced the spatial and temporal profiles of wall shear stress. However, it can also be noted that the present BFS did to a certain degree emulate the asymmetric stenosis model given that the c_f' spatial profiles were in favorable agreement for the time instants considered. This is because the flow at those time instants was exempt from the large magnitude of acceleration/deceleration and, thus, behaved more as a quasi-steady flow. It can be noted that in the absence of the large added inertial force (experienced during the acceleration and early to mid deceleration phases) and, hence, considering the geometrical difference alone did demonstrate a favorable agreement in c_f and c_f' inside the recirculating region and in the vicinity of flow reattachment.

CHAPTER SIX

CONCLUSIONS AND FUTURE WORK

6.1 A Review on the Purpose of the Thesis Work

The fundamental objectives of this thesis work are to quantify the flow physics downstream of a simple step placed at the onset of the working section, assess the ability of the hemodynamic flow facility to simulate realistic waveforms (at the working section) and compare the data to other more realistic phantoms of stenoses (i.e. tube geometry with asymmetric stenosis). The present work provides insight on the fluid dynamic comparison and on how well a parallel-plate flow chamber (PPFC) with a simple step models the flow and wall shear stress (WSS) in a stenosed tube representing an artery. To the best of the author's knowledge such a quantitative comparison is not available in the literature. An additional objective is to provide measurements of u and v velocity components (via a near-wall configured LDV), thereby providing additional knowledge of stenosed cases (away from the wall in the developing shear layer) and, thus, allowing CFD modelers to validate their code and reference experimental data under steady and pulsatile flow. It should also be noted that pulsatile flow inside a two-dimensional flow channel geometry remains poorly explored both experimentally and numerically. The literature therefore benefits from the present phase-averaged data (mean flow and turbulence) downstream of the step (captured at the midplane at several measurement stations) to better understand the flow behaviour.

6.2. A Summary of the Objectives and the Corresponding Results

To accomplish the above objectives, the present thesis focuses on three main areas:

- (1) the development and validation of the hemodynamic flow facility (an *in-vitro* type facility), thereby allowing non-intrusive and simultaneous u and v measurements (using the custom near-wall configured LDV) inside a PPFC under pulsatile flow conditions;

- (2) a comprehensive analysis (with quantitative evidence) of the uncertainty and performance of the flow facility (with emphasis on the near-wall configured LDV); and,
- (3) two-component velocity measurements downstream of a backward-facing step (BFS) under a prescribed steady and pulsatile laminar flow, thereby allowing a comparison with more realistic models of stenosis reported in the literature.

The extensive work on the various design and validation phases (reported in Appendix 1) to develop a functional hemodynamic flow facility has ultimately led to the final revision PPFC and the custom LDV system used in the present work (reported in Chapter Three – Experimental Methods).

Since WSS is an important flow quantity (in reference to endothelial cell response), Appendix 2 presents steady laminar flow cases (at the working section, providing vertical profiles of the streamwise velocity $\bar{u}(y)$) inside the final revision PPFC considering two optical lenses ($F = 120$ and 261 mm) to evaluate the implications of spatial resolution (measurement volume diameter) on WSS accuracy. WSS data together with its uncertainty is presented and it is found that for all Re_m values the difference between the experimental and theoretical WSS is larger for the $F = 261$ mm lens (i.e. larger measurement volume and measurement wall offset) with the maximum error of 14.83% at $Re_m = 1240$. It is also found that the WSS is within 3.1% of the analytical solution (i.e. based on the infinitely wide plate assumption) considering the $F = 120$ mm lens, thereby supporting that the smaller measurement volume and wall offset accord better with theory. In addition, Appendix 2 also presents a low-Re turbulent flow case to test the ability of measuring u and v velocity components simultaneously and in coherence mode inside the PPFC (near and away from the wall). The validation test case shows favorable agreement with the literature for low-Re test cases ($Re_m < 3000$) in terms of the u'^+ and v'^+ profiles, thereby providing added confidence in the uv measurements.

Furthermore, the most critical findings from Chapter Four relates to damping characteristics of the normal carotid waveform across the flow circuit. It is found that the pressure waveform attenuation (presumably as a result of wave reflections) across the flow

circuit together with the effect of viscous resistance and inertance contribute to non-realistic waveform shapes at the working section. To better understand the relationship between the pressure and flow waveforms and thus the loss of amplitude in flow at the working section, a mathematical model is presented to quantify the effects of fluid resistance and inertance. The results show that reducing the hydraulic diameter of the PPFC together with eliminating several boundaries between fluid elements (i.e. valve, heater, fittings – across the flow circuit) relating to changes in the characteristic impedance would presumably reduce waveform attenuation.

Chapter Five of the thesis work presents two-component velocity measurements downstream of a simplified stenosis model (BFS model) and compares the flow physics to more realistic models of stenoses typically considered in the literature (under steady and pulsatile flow). Although various stenosis models are analyzed, the present author considers the healthy and diseased carotid artery (CA) model along with the asymmetric tube stenosis model as the most important. This is because the CA model represents actual *in-vivo* geometry (associated with the formation of plaque) and the asymmetric stenosis inside a tube is the most representative of a stenosis inside a straight segment of an artery. The quantitative comparison between the present BFS model and the latter provides insight not only on the geometry-induced flow differences but also on the effects of the waveform shape. The comparison with the asymmetric stenosis model under pulsatile laminar flow shows that the waveform shape significantly affects the mid-plane flow structure.

A comparison with the healthy *in-vitro* CA model (considering steady flow) shows poor agreement of the skin friction spatial profile (downstream of the stenosis), with much smaller absolute magnitudes in the recirculating region along with a significantly smaller spatial gradient in the vicinity of flow reattachment. In reference to the stenosed CA model, the absolute maximum skin friction and the spatial gradient streamwise profile considering the inner wall of the internal carotid artery (ICA, inside the recirculation region) show better agreement with the present BFS model, with a difference of 66% and 22% (average difference), respectively. However, in the vicinity of flow reattachment the difference in the maximum spatial gradient magnitude is 133%, thereby demonstrating poor agreement with the present BFS model.

In reference to the asymmetric stenosis model (tube flow), the skin friction data is to some extent in agreement with the BFS model; that is, both models display a recirculating flow region (a rapid increase in the absolute values of c_f) immediately downstream of the stenosis followed by a rapid decrease to the point of flow reattachment. For the peak mass flow and deceleration time instants considered in the present comparison, the difference in the absolute maximum c_f between the models is 28.5% and 7.4%, respectively. Downstream of flow reattachment, the skin friction data do not agree as well given the presence of an upper wall recirculating region (reducing the effective channel height) for the present BFS model. The c_f profiles also do not agree due to the difference in the Re values and the adverse pressure gradient magnitudes during the deceleration time instant. The spatial gradient profiles (c_f') for the two models are in favorable agreement for both of the time instants, displaying two distinct peaks in the vicinity of flow reattachment. The differences in the maximum values are 3.2% and 15.3% for the peak mass flow and deceleration time instants, respectively. Finally, the temporal profile of c_f and its temporal gradient (c_{f_t}') upstream of flow reattachment (in the recirculating region) do not show any level of agreement. It is abundantly clear that the waveform shape has a significant effect on the temporal profile of c_f , given that the asymmetric tube model displays positive c_f values (no flow separation) during the early to late acceleration phase. Also, a significantly steeper slope in c_f is realized along with larger absolute magnitudes during the early to mid-deceleration phase. Hence, given the difference in the acceleration and deceleration magnitude between the waveforms, the temporal profiles of c_f are in complete disagreement. This is also reflected in the c_{f_t}' profiles with a difference in the maximum value of 168% between the models.

From the insight gained considering the temporal profiles of shear stress, it is expected that the spatial profile of c_f and c_f' will not be in agreement with the models for most other time instants not considered in the present work (absence of data). The time instants considered for the asymmetric tube model correspond to the peak mass flow and late deceleration (significantly reduced mass flow) and, hence, are exempt from the relatively large acceleration and deceleration magnitudes. Hence, the waveform characteristics significantly influence the spatial and temporal profiles of wall shear stress and cannot be

neglected. However, it is also true that the present BFS does to a certain degree emulate the asymmetric stenosis model given that the c_f' profiles are in favorable agreement for the time instants considered. This is because the flow at the time instants considered is exempt from the large magnitude of acceleration/deceleration and, thus, behaves more as a quasi-steady flow. It can be thus noted that in the absence of the large added inertial force present during the acceleration and early-mid deceleration phases and considering the geometrical difference alone, favorable agreement in c_f and c_f' inside the recirculating region and in the vicinity of flow reattachment is demonstrated.

The present author encourages further work with a more realistic waveform shape to gain better insight into the similarities and differences between the present BFS model and other more realistic models of stenoses. This additional work will provide further clarity whether the BFS model used in the present study is a suitable substitute for more realistic stenosis models. The present author also supports a further comparison of the present results with stenosis models that have applied pulsatile waveforms from elderly people whose arteries have hardened (i.e. damped waveform). Although the results from the carotid artery model (i.e. WSS) did not agree with the present BFS model, a comparison with other *in-vivo* and *in-vitro* models representing other locations in the arterial tree is encouraged (i.e. coronary artery and/or straight segments of an artery with an asymmetric stenosis such as found farther downstream of the internal carotid artery). In parallel, the emphasis should be placed on reducing the measurement volume diameter to measure closer to the endothelial cell monolayer and, hence, obtain more realistic shear loading on the mechanosensors (i.e. glycocalyx).

6.3 Possible Future Work

Based on the research experience to date in reference to the design, validation and usage of the hemodynamic flow facility together with the technical gaps in the literature, the present author recommends the following prospective work:

(1) Re-design of the pumping unit to directly connect the piston/cylinder assembly to the PPFC via rigid tubing. The present author also recommends placing the in-line heater

between the discharge of the PPFC and the pump reservoir to reduce waveform reflections and, hence, waveform damping.

(2) Development of new methods to remove air from the pumping unit, specifically inside the cylinder during instroke/outstroke. The air bubbles significantly increase time of measurement at the working section since they interfere with the incoming laser beams. In addition, the trapped air inside the cylinder assembly affects the uncertainty of the mass flow rate throughout the flow circuit.

(3) Experimental studies of waveform damping including the carotid waveform and/or a simple sine wave programmed at the pump. An example of the latter is to measure the time-varying pressure waveform at various stations downstream from the piston/cylinder assembly. It would be advantageous to measure the flow waveform as well at those same locations to better understand the flow/pressure relationship in various regions of the flow circuitry.

(4) Experimental studies via two-component LDV measurements considering other blockage ratios (i.e. stenosis severity) including 75% (commonly reported in the literature) together with more realistic waveforms at the working section. It would also be beneficial to study the laminar, transitional and turbulent regimes (together with varying the amplitude and pulse frequency of the waveform) considering the backward-facing step to provide CFD modelers experimental data.

(5) Experimental studies via two-component LDV measurements of the spanwise profile of the streamwise velocity $\bar{u}(z)$ to better understand the effect of the side-walls on the mid-plane flow structure and, hence, two-dimensionality of the flow. Literature reports two-dimensional flow downstream of the backward-facing step (Armaly et al 1983) under a turbulent regime (i.e $Re > 6600$, turbulent separation and reattachment) and, hence, additional cell studies are recommended since the cells would be exposed to uniform flow conditions (in the spanwise direction).

(6) Experimental studies using other models of stenosis inside the PPFC at the onset of the working section, such as the asymmetric semi-circle and/or double backward-facing step, whereby the latter could compare with the axi-symmetric stenosis inside a tube. This would

allow a better comparison with the simple asymmetric backward-facing step (present study work) since these studies can have equivalent flow and geometry imposed conditions.

(7) A continuation of the work of Avari et al (2016) on further live endothelial cell testing exposed to laminar and turbulent flow conditions using the backward-facing step and results of the present study.

(8) Pulsatile flow inside two-dimensional flow channel geometry remains poorly explored both experimentally and numerically. The literature would continue to benefit from detailed phase-averaged statistics (mean flow and turbulence) downstream of the step to better understand the flow physics. The effects of pulsation amplitude, frequency, expansion ratio (ER) and aspect ratio on the pulsatile mean flow field (and turbulence statistics) could be further explored.

REFERENCES

- ABBOTT, D.E. & KLINE, S.L. 1962 Experimental Investigation Of Subsonic Turbulent Flow Over Single And Double Backward Steps. *J Basic Engng.* **84**, 317-325.
- ABE, J., HEO, K. & FUJIWARA, K. 2014 Shear Stress And Atherosclerosis. *Mol. Cells* **37**, 435-440.
- ADAMS, E.W. & JOHNSTON, J.P. 1988 Effects Of The Separating Shear Layer On The Reattachment Flow Structure, Part 1: Pressure And Turbulence Quantities. *Exp. Fluids* **6**, 400-408.
- ADRIAN, R.J. 1983 Laser Velocimetry, In Fluid Mechanics Measurements. R.J. Goldstein Ed. Hemisphere, Washington D.C.
- AGARWAL, J.K. & FINGERSON, L.M. 1979 Evaluation of Various Particles For Their Suitability As Seeds In Laser Velocimetry. In: Laser Velocimetry and Particle Sizing, Proceedings of the Third International Workshop, West Lafayette, Ind. Washington, D.C.

- AHMED, S.A & GIDDENS, D.P. 1983a Flow Disturbance Measurements Through A Constricted Tube At Moderate Reynolds Numbers. *Biomech.* **16**, 955-963.
- AHMED, S.A & GIDDENS, D.P. 1984 Pulsatile Poststenotic Flow Studies With Laser Doppler Anemometry. *Biomech.* **17**, 695-705.
- ANDERSON, E.J., FALLS, T.D., SORKIN, A.M. & KNOTHETATE, M.L. 2006 The Imperative For Controlled Mechanical Stresses In Unraveling Cellular Mechanisms Of Mechanotransduction. *Biomed. Eng. Online* **5**, 27.
- ANTONIA, R.A, KIM, M.T. & BROWNE, L.W. 1992 Low-Reynolds-Number Effects In A Fully Developed Turbulent Channel Flow. *J. Fluid Mech.* **236**, 579-605.
- ANTONY, R., NANDAGOPAL, G., SREEKOMAR, N. & SELVARAJU, N. 2014 Detection Principles And Development Of Microfluidic Sensors In The Last Decade. *Microsyst. Technol.* **20**, 1051-1061.
- APPEL, C., MANTZARAS, J., SCHAEREN, R., BOMBACH, R. & INAUEN, A. 2005 Turbulent Catalytically Stabilized Combustion Of Hydrogen/Air Mixtures In Entry Channel Flows. *Combust. Flame* **140**, 70-92.
- ARBEITER, F., GORDEEV, S., HEINZEL, V., LEICHTLE, D. & STRATMANN, E. 2007 Mini-Channel Flow Experiments And CFD Validation Analyses With The IFMIF Thermo-Hydraulic Experimental Facility (ITHEX). *Fus. Eng. Des.* **82**, 2456–2461.
- ARMALY, B.F., DURST, F., PEREIRA, J.C.F AND SCHÖNUNG. 1983 Experimental And Theoretical Investigation Of Backward-Facing Step Flow. *J. Fluid Mech.* **127**, 473-496.
- AVARI, H. 2015 Response Of Endothelial Cells To Quantified Hemodynamic Shear Stress. *Ph.D. Thesis*, Western University, London, Ontario.
- AVARI, H., SAVORY, E. & ROGERS, K.A. 2016 An In-Vitro Hemodynamic Flow System To Study The Effects Of Quantified Shear Stresses On Endothelial Cells. *Cardiovasc Eng. Tech.* **7**, 44-57.
- BACABAC, R.G., SMIT, T.H., COWIN, S.C. & VAN LOON, J.W.A., NIEUWSTADT, F.T.M., HEETHAAR, R. & KLEIN-NULEND, J. 2005 Dynamic Shear Stress In Parallel-Plate Flow Chambers. *J. of Biomech.* **38**, 159-167.
- BAEYENS, N., BANDYOPADHYAY, C., COON, B.G., YUN, S. & SCHWARTZ, M.A. 2017 Endothelial Fluid Shear Stress Sensing In Vascular Health And Disease. *J. Clin Invest.* **126**, 821-828.
- BANDRES, M.A., GUTIERREZ-VEGA & JULIO, C. 2004 Ince Gaussian beams. *Opt. Lett. OSA.* **29**, 144–146.

- BARBER, A.J., LIETH, E., KHIN, S.A., ANTONETTI, D.A., BUCHANAN, A.G. & GARDNER, T.W. 1998 Neural Apoptosis In The Retina During Experimental And Human Diabetes. Early Onset And Effect Of Insulin. *J Clin Invest.* **102**, 783-91.
- BARKLEY, D., GABRIELA, M. & GOMES, M. 2002 Three-Dimensional Instability In Flow Over A Backward-Facing Step. *J. Fluid Mech.* **473**, 167-190.
- BEER, F.P., JOHNSTON, E. R. & DEWOLF, J.T. 2006 Mechanics Of Materials. *McGraw-Hill Higher Education*, Boston.
- BELL, D.N., SPAIN, S. & GOLDSMITH, H.L. 1989 Adenosine Diphosphate-Induced Aggregation Of Human Platelets In Flow Through Tubes. I. Measurement Of Concentration And Size Of Single Platelets And Aggregates. *Biophys. J.* **56**, 817-828.
- BENDAT, J.S. & PIERSON, A.G. 1971 Random Data: Analysis And Measurement Procedures. *Wiley-Interscience*, New York.
- BENEDICT, L.H., NOBACH, H. & TROPEA, C. 2000 Estimation Of Turbulent Velocity Spectra From Laser Doppler Data. *Meas. Sci. Technol.* **11**, 1089.
- BENEDICT, L.H. & GOULD, R.D. 1996 Towards Better Uncertainty Estimates For Turbulence Statistics. *Exp. Fluids* **22**, 129-136.
- BERATLIS, N., BALARAS, B., PARVINIAN, B. & KIGER, K. 2005 A Numerical And Experimental Investigation Of Transitional Pulsatile Flow In A Stenosed Channel. *J. Biomech. Eng.* **127**, 1147-1157.
- BHARATHRAM, G. 2004 Investigation Of Turbulent Boundary Layer Structure Using Stereoscopic Particle Image Velocimetry. *Ph.D. Thesis*, University of Minnesota.
- BISWAS, G., BREUER, M. & DURST, F. 2004 Backward-Facing Step Flows For Various Expansion Ratios At Low And Moderate Reynolds Number. *J. Fluids Eng.* **126**, 362-374.
- BLACKBURN, H.M., BARKLEY, D. & SHERWIN, S.J. 2008 Convective Instability And Transient Growth In Flow Over A Backward-Facing Step. *J. Fluid Mech.* **603**, 271-304.
- BLACKBURN, H.M. & SHERWIN, S.J. 2007 Instability Modes and Transition of Pulsatile Stenotic Flow: Pulse-Period Dependence. *J. Fluid Mech.* **573**, 57-88.

- BLACKMAN, B.R., BARBEE, K. & THIBAUT, L. E. 2000 In Vitro Cell Shearing Device To Investigate The Dynamic Response Of Cells In A Controlled Hydrodynamic Environment. *Ann. Biomed. Eng.* **28**, 363-372.
- BLACKMAN, B.R., GARCÍA-CARDEÑA, G. & GIMBRONE, MA JR. 2002 A New In Vitro Model To Evaluate Differential Responses Of Endothelial Cells To Simulated Arterial Shear Stress Waveforms. *J Biomech Eng.* **124**, 397– 407.
- BOGHOSIAN, M.E. & CASSEL, K.W. 2010 Vortex-Shedding Mechanisms In Internal Flows. 48th AIAA Aerospace Sciences Meeting Including the New Horizons Forum and Aerospace Exposition.
- BUCHMANN, N.A. & JERMY, M.C. 2007 Particle Image Velocimetry Measurements Of Blood Flow In A Modeled Carotid Artery Bifurcation. in *Proceedings of the 16th Australasian Fluid Mechanics Conference*, Gold Coast, Australia.
- BUCHMANN, N.A., NGUYEN, C.V., WELLS, J.C. & JERMY, M. 2008 In-Vitro Wall Shear Stress Measurements Using Interfacial Particle Image Velocimetry (iPIV). in *14th Int. Symp. on Applications of Laser Techniques to Fluid Mechanics*, Lisbon, Portugal.
- BUSCHMANN, M.H., DIETERICH, P., ADAMS, N.A. & SCHNITTLER, H.J. 2004 Analysis Of Flow In A Cone-And-Plate Apparatus With Respect To Spatial And Temporal Effects On Endothelial Cells. *Biotechnol. Bioeng.* **89**, 493-502.
- CAMPBELL, I. C., RIES, J., DHAWAN, S. S., QUYYUMI, A. A., TAYLOR, W. R. & OSHINSKI J. N. 2012 Effect Of Inlet Velocity Profiles On Patient-Specific Computational Fluid Dynamics Simulations Of Carotid Bifurcations. *J. Biomech. Eng.* **134**, 051001-8.
- CARO, C.G., FITZ-GERALD, J.M. & SCHROTER, R.C. 1969 Arterial Wall Shear And Distribution Of Early Atheroma In Man. *Nature* **223**, 1159–60.
- CARO, C.G., FITZ-GERALD, J.M. & SCHROTER, R.C. 1971 Atheroma And Arterial Wall Shear: Observation, Correlation And Proposal Of A Shear Dependent Mass Transfer Mechanism For Atherogenesis. *Proc. R. Soc. Lond. B.* **177**, 109–59.
- CARO, C.G., PEDLEY, T.J., SCHROTER, R.C., SEED, W.A. & PARKER, K.H. 2012 The Mechanics Of The Circulation. *Cambridge University Press*, UK.
- CARPINLIOGLU, M.O. & GUNDOGDU, M.Y. 2001 A Critical Review On Pulsatile Pipe Flow Studies Directing Towards Future Research Topics. *Flow Meas. Instrum.* **12**, 163-174
- CASANOVA, R.A. & GIDDENS, D.P. 1978 Disorder Distal To Modeled Stenoses In Steady And Pulsatile Flow. *J. Biomechanics* **11**, 441–453.

- CASTREJÓN-PITA, J.R., CASTREJÓN-PITA, A.A., HUELSZ, G. & TOVAR, R. 2006 Experimental Demonstration Of The Rayleigh Acoustic Viscous Boundary Layer Theory. *Phys. Rev.* **73**, 1-5.
- CHANG, W., PU-ZHEN, G., TAN, S. & CHAO, X. 2012 Effect Of Aspect Ratio On The Laminar-To-Turbulent Transition In Rectangular Channel. *Ann. Nucl. Eng.* **46**, 90-96.
- CHIANG, T.P. & SHEU, W.H. 1998 A Numerical Revisit Of Backward-Facing Step Flow Problem. *Phys. Fluids* **11**, 862-873.
- CHIEN, S. 2007 Mechanotransduction and Endothelial Cell Homeostasis: The Wisdom Of The Cell. *Am. J. Physiol. Heart Circ. Physiol.* **292**, 1209–1224.
- CHING, C. Y., DJENIDI, L. & ANTONIA, R. A. 1995 Low-Reynolds-Number Effects In A Turbulent Boundary Layer. *Exp. Fluids* **19**, 61–68.
- CHISTIYAKOV, D.A, OREKHOV, A.N. & BOBRY SHEV 2016 Effects Of Shear Stress On Endothelial Cells: Go With The Flow. *Acta Physiologica* **219**, 382-408.
- CHIU, J.J. & CHIEN, S. 2011 Effects Of Disturbed Flow On Vascular Endothelium: Pathophysiological Basis And Clinical Perspectives. *Physiol. Rev.* **91**, 327-387.
- CHUNG, B.J., ROBERTSON, A.M. & PETERS, D.G. 2003 The Numerical Design of a Parallel Plate Flow Chamber for Investigation of Endothelial Cell Response to Shear Stress. *Comput. Struct.* **81**, 535-546.
- CHUNG, C.A., TZOU, M.R. & HO, R.W. 2005 Oscillatory Flow In A Cone-And-Plate Bioreactor. *J. Biomech Eng.* **127**, 601–610.
- CLARK, C. 1976a The Fluid Mechanics Of Aortic Stenosis – I. Theory And Steady Flow Experiments. *J. Biomech.* **9**, 521-528.
- COLEMAN, H.W. & STEELE, W.G. 2009 Experimentation, Validation, And Uncertainty Analysis For Engineers, 3rd Edition. *John Wiley & Sons*, New Jersey.
- COMPTON, D.A. & EATON, J.K. 1995 Near-Wall Measurements Of A Three-Dimensional Turbulent Boundary Layer. Thermosciences Div. Stanford University, Stanford, CA, Report MD-72
- CRAMER, D. 1997 Basic Statistics for Social Research. *Routledge*.
- DARDIK, A., CHEN, L., FRATTINI, J. & AZIZ, F. 2005 Differential Effects Of Orbital And Laminar Shear Stress On Endothelial Cells. *J. Vasc. Surg.* **41**, 869-880.
- DAVIES, P.F. 1995 Flow-Mediated Endothelial Mechanotransduction. *Physiol. Rev.* **75**, 519-560.

- DAVIES, P.F., REMUZZITT, A., GORDON, E. J., DEWEY, C. F. & GIMBRONE, M. A. 1986 Turbulent Flow Shear Stress Induces Vascular Endothelial Cell Turn Over in Vitro. *Proc. Natl. Acad. Sci.* **83**, 2114-2117.
- DAVIES, P.F. 2009 Hemodynamic Shear Stress And The Endothelium In Cardiovascular Pathophysiology. *Nat. Clin. Pract. Cardiovasc Med.* **6**, 16–26.
- DE BREDERODE, V. & BRADSHAW, P. 1972 Three-Dimensional Flow In Nominally Two-Dimensional Separation Bubbles. *Imperial College of Science and Technology*, London, Aero Report 72-19.
- DEAN, R.B. 1978 Reynolds Number Dependence of Skin Friction and Other Bulk Flow Variables in Two-Dimensional Rectangular Duct Flow. *J. Fluids Eng.* **100**, 215-223.
- DEGRAAFF, D.B. & EATON, J.K. 2001 A High-Resolution Laser Doppler Anemometer: Design, Qualification, and Uncertainty. *Experiments in Fluids* **30**, 522-530.
- DEMUREN, A.O., LELE, S. & DURBIN, P. 1994 Role of Pressure Diffusion in Non-Homogeneous Shear Flows. *Proc. CTR Summer Prog.* Center for Turbulence Research, NASA Ames/Stanford Univ.
- DEPAOLA, N., DAVIES, P.F., PRITCHARD, W.F., FLOREZ L., HARBECK N., & POLACEK D.C. 1999 Spatial And Temporal Regulation Of Gap Junction Connexin43 In Vascular Endothelial Cells Exposed To Controlled Disturbed Flows In Vitro. *Proc. Natl. Acad. Sci. USA.* **56**, 3154-3159.
- DEWEY, C.F. & BUSSOLARI, S. R 1981 The Dynamic Response Of Vascular Endothelial Cells To Fluid Shear Stress. *J. Biomech. Eng.* **103**, 177-185.
- DEWEY, C.F. & DEPAOLA, N. 1989. Exploring Flow-Cell Interactions Using Computational Fluid Dynamics. In: Woo, S.L.-Y., Seguchi, Y. (Eds.), *Tissue Engineering*, ASME, New York, **31**.
- DJENIDI, L. & ANTONIA, R.A. 1993 LDA Measurements In Low Reynolds Number Turbulent Boundary Layer. *Exp. Fluids* **14**, 280-288.
- DOANE, D.P & SEWARD, L.E. 2011 Measuring Skewness: A Forgotten Statistic?. *Journal of Statistics*. Education 19.
- DODGE, J.T., BROWN, B.G., BOLSON, E.L. & DODGE, H.T. 1992 Lumen Diameter Of Normal Human Coronary Arteries. Influence Of Age, Sex, Anatomic Variation, And Left Ventricular Hypertrophy Or Dilation. *Circulation* **86**, 232-46.
- DOL, S.S., SALEK, M.M. & MARTINUZZI, R.J. 2014 Effects Of Pulsation To The Mean Field And Vortex Development In A Backward-Facing Step Flow. *Transactions of the ASME J. of Fluids Eng.* **136**, 011001-5.

- DOL, S.S., SALEK, M.M., VIEGAS, K.D., RINKER, K.D. & MARTINUZZI, R.J. 2010 Micro-PIV and CFD Studies Show Non-Uniform Wall Shear Stress Distributions Over Endothelial Cells. Proceedings of ASME, FEDSM-ICNMM2010-30605.
- DOLAN, J.M., KOLEGA, J. & MENG, H. 2012 High Wall Shear Stress And Spatial Gradients In Vascular Pathology: A Review. *Ann. Biomed. Eng.* **41**, 1141-1427.
- DOU, H.S. & KHOO, B.C. 2010. Energy Gradient Method For Turbulent Transition With Consideration Of Effect Of Disturbance Frequency. *J. Hydrodyn.* **22**, 23-28.
- DOU, H.S. 2006. Mechanism Of Flow Instability And Transition To Turbulence. *Int. J. Non-linear Mech.* **41**, 512 -517.
- DOU, H.S., KHOO, B.C. & TSAI, H.M. 2010. Determining The Critical Condition For Turbulent Transition In A Full-Developed Annulus Flow. *J. Petrol. Sci. Eng.* **73**, 41-47.
- DRASLER, W. J., SMITH, C. M. & KELLER, K.H. 1987 Viscoelasticity Of Packed Erythrocyte Suspensions Subjected To Low Amplitude Oscillatory Deformation. *Biophys. J.* **52**, 357-365.
- DURST, F. & STEVENSON, W. H. 1976 Visual Modeling Of Laser Doppler Anemometer Signals By Moiré Fringes. *Appl. Opt.* **15**, 137-144.
- DURST, F. & WHITELOW, J. H. 1971 Integrated Optical Units For Laser Anemometry. *J. Phys. E.* **4**, 804.
- DURST, F., JOVANOVIĆ, J. & SENDER, J. 1995 LDA Measurements In The Near-Wall Region Of A Turbulent Pipe Flow. *J. Fluid Mech.* **295**, 305-335.
- DURST, F., LEKAKIS, J., JOVANOVIĆ, J. & YE Q. 1996 Wall Shear Stress Determination From Near-Wall Mean Velocity Data In Turbulent Pipe And Channel Flows. *Exp. Fluids* **20**, 417-428.
- DURST, F., MELLING, A. & WHITELOW, J. H. 1976 Principles And Practice Of Laser Doppler Anemometry. *Academic Press*, New York.
- DURST, F., MILLER, R. & JOVANOVIĆ, J. 1988 Determination Of The Measuring Position In Laser-Doppler Anemometry. *Exp. Fluids* **6**, 105- 110.
- DVINSKY, A.S. & OJHA, M. 1994 Simulation Of Three-Dimensional Pulsatile Flow Through An Asymmetric Stenosis. *Med Biol. Eng. Comput.* **32**, 138-42.
- DWARIKANATH, R. & ARINDAM, S. 2015 Analysis Of Flow Over Backward-Facing Step With Transition. *Front. Struct. Civ. Eng.* **9**, 71-81.
- EDWARDS, R.V. 1987 Report Of The Special Panel On Statistical Particle Bias Problems In Laser Anemometry. *J. Fluids Eng.* **109**, 89-92.
- EINAV, S, STOLERO, D, AVIDOR, J, ELAD, D, TALBOT, L. 1989 Wall Shear Stress Distribution Along The Cusp Of A Tri-Leaflet Prosthetic Valve. *J. Biomed. Eng.* **12**, 13-8.

- ERTURK, E. 2008 Numerical Solutions Of 2-D Steady Incompressible Flow Over A Backward-Facing Step, Part 1: High Reynolds Number Solution. *Comput. Fluids* **37**, 633-655.
- FATEMI, R.S. & RITTGERS, S.E. 1994 Derivation Of Shear Rates From Near-Wall LDA Measurements Under Steady And Pulsatile Flow Conditions. *J. Biomech. Eng.* **116**, 361-367.
- FILATOVA, O.V., SIDORENKO, A.A. & SHOROBOGATOV, Y.Y. 2014 Age And Sex Dependence Of Hemodynamic Parameters Of Human Internal Carotid Artery. *Hum. Physiol.* **40**, 93-102.
- FINGERSON, L.M., ADRIAN, R.J., MENON, R.K., KAUFMAN, S.L. & NAQWI, A. 1993 Data Analysis, Laser Doppler Velocimetry and Particle Image Velocimetry. *TSI Short Course Text*, TSI Inc., St. Paul, MN.
- FLEMING, G.A. & KUHLMAN, J.M. 1994 Experimental Investigation Of Fringe Divergence Errors In Laser Velocimetry Measurements. *AIAA Journal* **32**, 2030-2035.
- FORTIN, A., JARDAK, M., GERVAIS, J. J. & PIERRE, R. 1997 Localization Of Hopf Bifurcations In Fluid Flow Problems. *Int. J. Numer. Meth. Fluids* **24**, 1185-1210.
- FOX, J.A. & HUGH, A.F. 1966 Localization Of Atheroma: A Theory Based On Boundary Layer Separation. *Br. Heart. J.* **28**, 388-399.
- FRANGOS, J.A., ESKIN, S.G., MCINTIRE, L.V. & IVES, C.L. 1985 Flow Effects On Prostacyclin Production By Cultured Human Endothelial Cells. *Science* **227**, 1477-9.
- FRIEDMAN, M.H., HUTCHINS, G.M., BARGERON, C.B., DETERS, O.J. & MARK, F.F. 1981 Correlation Between Intimal Thickness And Fluid Shear In Human Arteries. *Atherosclerosis* **39**, 425-36.
- FRY, D.L. 1969 Certain Histological And Chemical Responses Of The Vascular Interface To Acutely Induced Mechanical Stress In The Aorta Of The Dog. *Circ. Res.* **24**, 93-108.
- FUKUSHIMA, S., NGATSU, A., KAIBARA, M., OKA, K. & TANISHITA, K. 2001 Measurement Of Surface Topography Of Endothelial Cell And Wall Shear Stress Distribution On The Cell. *JSME Int. J. C* **44**, 972-980.
- GARTLING, D. K. 1990 A Test Problem For Outflow Boundary Conditions—Flow Over A Backward-Facing Step. *Int. J. Numer. Methods Fluids* **11**, 953-967.
- GHIA, K. N., OSSWALD, G. A. & GHIA, U. 1989 Analysis Of Incompressible Massively Separated Viscous Flows Using Unsteady Navier-Stokes Equations. *Int. J. Numer. Meth. Fluids* **9**, 1025-1050.
- GIDDENS, D.P. & KU, D.N. 1987 A Note On The Relationship Between Input Flow Waveform And Wall Shear Rate In Pulsatile, Separating Flows. *J. Biomech. Eng.* **109**, 175-176.
- GIMBRONE, JR. M.A. 1999 Vascular Endothelium, Hemodynamic Forces, and Atherogenesis. *Am. J. Pathol.* **155**, 1-5.

- GIVENS, C & TZIMA, E. 2016 Endothelial Mechanosignaling: Does One Sensor Fit All?. *Antioxidants and Redox Signaling* **25**, 373-388.
- GOLDSTEIN, A.S. & DIMILLA, P.A. 1998 Comparison Of Converging And Diverging Radial Flow For Measuring Cell Adhesion. *Bioengineering, Food and Natural Products* **44**, 465-473.
- GOLDSTEIN, R. 1996 Fluid Mechanics Measurements, Second Edition. *Taylor & Francis*, Philadelphia, PA.
- GOOCH, K.J & TENNANT C.J. 1997 Mechanical Forces: Their Effects On Cells And Tissues. *Springer-Verlag Berlin Heidelberg*.
- GRIFFITH, M.D. 2009 The Stability and Behaviour of Flows in Stenotic Geometries. *Ph.D. Thesis*.
- GUNDOGDU, M.Y & CARPINLIOGLU, M.O. 1999 Present State Of Art On Pulsatile Flow Theory. Part 1. Laminar And Transitional Flow Regimes. *JSME International Journal Series B*. **42**, 384-397.
- HAGGMARK, C.P., BAKCHINOV, A.A. & ALFREDSSON, P.H. 2000 Experiments on a Two-Dimensional Laminar Separation Bubble. *Phil. Trans. R. Soc. Lond. A*, **358**, 3193-3205.
- HANSON, S. 1973 Broadening Of The Measured Frequency Spectrum In A Differential Laser Anemometer Due To Interference Plane Gradients. *J. Phys.* **6**, 164.
- HARTNETT, J.P., KOH, J.C.Y. & MCCOMAS, S.T. 1962 A Comparison Of Predicted And Measured Friction Factors For Turbulent Flow Through Rectangular Ducts. *J. Heat Transfer* **84**, 82-88.
- HASELTON, F.R. & HEIMARK, R.L. 1997 Role Of Cadherins 5 And 13 In The Aortic Endothelial Barrier. *J Cell Physiol.* **171**, 243-51.
- HE, S. & JACKSON, J.D. 2000 A Study Of Turbulence Under Conditions Of Transient Flow In A Pipe. *J. Fluid Mech.* **408**, 1-38.
- HEMLINGER, G., GEIGER, R.V., SCHRECK, S. & NEREM, R.M. 1991 Effects Of Pulsatile Flow On Cultured Vascular Endothelial Cell Morphology. *J. Biomech. Eng.* **113**, 123-131.
- HSTRONYEO, K.S., FUJIWARA, K. & ABE, J. 2014 Shear Stress And Atherosclerosis. *Mol. Cells.* **37**, 435-440.
- HEO, K.S., FUJIWARA, K. & ABE, J. 2011a Disturbed-Flow-Mediated Vascular Reactive Oxygen Species Induce Endothelial Dysfunction. *Circ. J.* **75**, 2722-2730.
- HEO, K.S., LEE, H., NIGRO, P., THOMAS, T., LE, N.T., CHANG, E., MCCLAIN, C., REINHART-KING, C.A., KING, M.R., BERK, B.C., et al. 2011b Pkc ζ Mediates Disturbed Flow-Induced Endothelial Apoptosis. *J. Cell Biol.* **193**, 867-884.
- HERRIN, J.L. & DUTTON, J.C. 1993 An Investigation Of LDV Velocity Bias Correction Technique For High-Speed Separated Flows. *Exp. Fluids* **14**, 354-363.

- HODGSON, L. & TARBELL, J.M. 2002 Solute Transport To The Endothelial Intercellular Cleft (The Effect Of Wall Shear Stress). *Ann Biomed Eng.* **30**, 936–945.
- HOESEL, W. & RODI, W. 1977 New Biasing Elimination Method For Laser Doppler Velocimetry Counter Processing. *Rev. Sci. Instr.* **48**, 910-91.
- HOLDSWORTH, D.W., RICKEY, D.W., DRANGOV, AM., MILLER, D.J.M. & FENSTER, A. 1991 Computer-Controlled Positive Displacement Pump For Physiological Flow Simulation. *Med. Biol. Eng. Comput.* **29**, 565-570.
- HOLMES D.B. & VERMEULEN J.R. 1968 Velocity Profiles In Ducts With Rectangular Cross Section. *Chem. Eng. Sci.* **23**, 717-722.
- HORIE, M. 2009 A Hemodynamic Flow Facility For Endothelial Cell Response. *MESc Thesis*, Western University, London, Ontario.
- HOSSAIN, M.A., RAHMAN, M.D.T. & RIDWAN, S. 2013 Numerical Investigation Of Fluid Flow Through A 2D Backward Facing Step Channel. *International Journal of Engineering Research & Technology* **2**.
- HUTCHINS, N. & CHOI, K. 2002 Accurate Measurements Of Local Skin Friction Coefficient Using Hot-Wire Anemometry. *Prog. Aerosp. Sci.* **38**, 421-446.
- HUTCHISON, K.J. 1991 Endothelial Cell Morphology Around Graded Stenoses Of The Dog Common Carotid Artery. *Blood Vessels* **28**, 396-406.
- IYER, V.A. & WOODMANSEE, M.A. 2005 Uncertainty Analysis Of Laser-Doppler-Velocimetry Measurements In A Swirling Flowfield. *AIAA Journal* **43**, 512-519.
- CASTREJÓN-PITA, J.R., HUELSZ, G. & TOVAR, R. 2006 Experimental Demonstration Of The Rayleigh Acoustic Viscous Boundary Layer Theory. *Phys. Rev.* **73**, 1-5.
- JOANES, D.N. & GILL, C.A. 1998 Comparing Measures Of Sample Skewness And Kurtosis. *Journal of the Royal Statistical Society Series D (The Statistician)* **47**, 183 – 189.
- JUSTE, G.L., FAJARDO, P. & GUIJARRO, A. 2016 Assessment Of Secondary Bubble Formation On A Backward-Facing Step Geometry. *Phys. Fluids* **28**.
- KAIKTSIS, L., KARNIADAKIS, G. E. & ORSZAG, S. A. 1991 Onset Of Three - Dimensionality, Equilibria, And Early Transition In Flow Over A Backward-Facing Step. *J. Fluid Mech.* **231**, 501–528.
- KAIKTSIS, L., KARNIADAKIS, G. E. & ORSZAG, S. A. 1996 Unsteadiness And Convective Instabilities In A Two-Dimensional Flow Over A Backward-Facing Step. *J. Fluid Mech.* **321**, 157–187.

- KANDLIKAR, S., GARIMELLA, S., LI, D., COLIN, S. & KING, M. 2014 Heat Transfer And Fluid Flow In Minichannels And Microchannels. *Butterworth-Heinemann*.
- KANDLIKAR, S.G. & CAMPBELL, L.A. 2002 Effect Of Entrance Condition On Frictional Losses And Transition To Turbulence. ASME International Mechanical Engineering Congress & Exposition, New Orleans, Louisiana.
- KATAOKA, N., UJITA, S. & SATO, M. 1998 Effect Of Flow Direction On The Morphological Responses Of Cultured Bovine Endothelial Cells. *Med. Biol. Eng. Comput.* **36**, 122-128.
- KEHOE, S.C. 2001 An Experimental Investigation Of The Hemodynamic Effects At Mildly Stenosed Carotid Artery Bifurcations. *Masters of Engineering Thesis*, Western University, London, Ontario.
- KHALIFA, A.M.A. & GIDDENS, D.P. 1981 Characterization And Evolution Of Post-Stenotic Disturbances. *J. Biomech.* **14**, 279-296.
- KIM, J., MOIN, P. & MOSER, R. 1987 Turbulent Statistics In Fully Developed Channel Flow At Low Reynolds Number. *J. Fluid Mech.* **177**, 133-166.
- KITOH, A., SUGAWARA, K., YOSHIKAWA, H. & OTA, T. 2007 Expansion Ratio Effects On Three-Dimensional Separated Flow And Heat Transfer Around Backward-Facing Steps. *J. Heat Transfer* **129**, 1141-1155.
- KITTEL, C. 2005 Introduction To Solid State Physics, 8th Edition, *Wiley, 2005*. Hoboken, NJ.
- KOSLOW, A.R., STROMBERG, R.R., FRIEDMAN, L.I., LUTZ, R.J., HILBERT, S.L. & SCHUSTER P. 1986 A Flow System For The Study Of Shear Forces Upon Cultured Endothelial Cells. *Transactions of ASME*, **108**.
- KU, D.N., GIDDENS, D.P., ZARINS, C.K. & GLAGOV, S. 1985 Pulsatile Flow And Atherosclerosis In The Human Carotid Bifurcation: Positive Correlation Between Plaque Location And Low Oscillating Shear Stress. *Arteriosclerosis* **5**, 293-302.
- KUENY, J.L. & BINDER, G. 1984 Viscous Flow Over Backward Facing Steps, An Experimental Investigation. *Notes On Numerical Fluid Mechanics* **9**, 32-47.
- KUNZ, R. F., D' AMICO, S. W., VASSALLO, P. & ZACCARIA, M. A. 2001 LDV Measurements Of Confined Parallel Jet Mixing. *J. Fluid Eng.* **123**, 567-573.
- KUO, S.C. & LAUFFENBURGER, D.A. 1993 Relationship Between Receptor/Ligand Binding Affinity And Adhesion Strength. *Biophys. J.* **65**, 2191-2200.
- KYSELA, B., KONFRŠT, J. & CHÁRA, Z. 2013 LDA Measurements And Turbulence Spectral Analysis In An Agitated Vessel. *EPJ Web of Conferences* **45**, 01055.
- LAI, W., SHAKAL, J. & TROOLIN, D. 2013 Accuracy, Resolution, And Repeatability Of Powersight PDPA And LDV Systems. *TSI Technical Note*, TSI Incorporated, Shoreview, MN, USA.

- LANGLOIS, W.E. & DEVILLE, M.O. 2014 Exact Solutions To The Equations Of Viscous Flow. Springer International, Switzerland.
- LAPLACA, M.C. & THIBAUT, L. E. 1997 An In Vitro Traumatic Injury Model To Examine The Response Of Neurons To A Hydodynamically-Induced Deformation Loading. *Ann. Biomed. Eng.* **25**, 655-677.
- LAWRENCE, M.B., MCINTIRE, L.V. & ESKIN, S.G. 1987 Effect Of Flow On Polymorphonuclear Leukocyte/ Endothelial Cell Adhesion. *Blood.* **70**, 1284-1290.
- LEE, T. & MATEESCU, D. 1998 Experimental And Numerical Investigation Of 2d Backward-Facing Step Flow. *J. Fluids Struct.* **12**, 703–716.
- LEVESQUE, M. J., SPRAGUE, E. A., SCHWARTZ, C. J. & NEREM, R. M. 1989 The Influence Of Shear Stress On Cultured Vascular Endothelial Cells: The Stress Response Of An Anchorage-Dependent Mammalian Cell. *Biotech. Prog.* **5**, 1-8.
- Li, H. & Olsen, M.G. 2006 Aspect Ratio Effects On Turbulent And Transitional Flow In Rectangular Microchannels As Measured With Micro-PIV. *J. Fluids Eng.* **128**, 305-315.
- LIEBER, B.B. & GIDDENS, D.P. 1990 Post-Stenotic Core Flow Behavior In Pulsatile Flow And Its Effects On Wall Shear Stress. *J. Biomech.* **23**, 597-605.
- LIGHTSTONE, N.S. 2014 Design Of A Bioreactor To Mimic Hemodynamic Shear Stresses On Endothelial Cells In Microfluidic Systems. Master's of Applied Science Thesis. University of Toronto, Toronto, Ontario.
- LIMA, R.C., ANDRADE, C.R. & ZAPAROLI, E.L. 2008 Numerical Study Of Three Recirculation Zones In The Unilateral Sudden Expansion Flow. *Int. Commun. Heat Mass Transfer* **35**, 1053-1060.
- LOGERFO, F.W., NOWAK, M.D., QUIST, W.C., CRAWSHAW, H.M. & BHARADVAJ, B.K. 1981 Flow Studies In A Model Carotid Bifurcation. *Arteriosclerosis* **1**, 235–241.
- LONG, Q., XU, X.Y., RAMNARINE, K.V. & HOSKINS, P. 2001 Numerical Investigation Of Physiologically Realistic Pulsatile Flow Through Arterial Stenosis. *J. Biomech.* **34**, 1229-1242.
- LOU, Z., YANG, W. & STEIN, P. D. 1993 Errors In The Estimation Of Arterial Wall Shear Rates That Results From Curve Fitting Of Velocity Profiles. *J. Biomech.* **26**, 183-390.
- LOUDON, C. & TORDESILLAS, A. 1998 The Use Of The Dimensionless Womersley Number To Characterize The Unsteady Nature Of Internal Flow. *J Theor. Biol.* **191**, 63-78.
- LU, P.C., GROSS, D.R. & HWANG, N.H.C. 1983 A Model Investigation Of The Velocity And Pressure Spectra In Vascular Murmurs. *J. Biomech.* **16**, 923-931.
- MÜLLER, R.T. 1992 Theoretische Und Experimentelle Untersuchungen Zur Auslegung Von Halbleiter-LDAs Für Anwendungen In Der Aerodynamik. Ph.D. Thesis, Universität Erlangen-Nürnberg.

- MALLINGER, F. & DRIKAKIS, D. 2002 Instability In Three-Dimensional, Unsteady, Stenotic Flows. *Int. J. Heat Fluid Flow* **23**, 657-663.
- MARX, D., AUREGAN, Y., BAILLIET, H. & VALIERE, J. 2010 PIV and LDV Evidence of Hydrodynamic Instability Over A Liner In A Duct With Flow. *J. Sound Vib.* **329**, 3797-3812.
- MCCANN, J.A., PETERSON, S.D., PLESNIAK, M.W., WEBSTER, T.J. & HABERSTROH, K.M. Non-Uniform Flow Behavior In A Parallel Plate Flow Chamber Alters Endothelial Cell Responses. *Ann. Biomed. Eng.* **33**, 328.
- MCDONALD, D.A. 1960 Blood Flow In Arteries. Williams & Wilkins, Baltimore.
- MCLAUGHLIN, D.K. & TIEDERMAN, W.G. 1973 Biasing Correction For Individual Realization Of Laser Anemometer Measurements In Turbulent Flow. *Phys. Fluids* **16**, 2082-2088.
- MELLING, A. 1997 Tracer Particles and Seeding For Particle Image Velocimetry. *Meas. Sci. Technol.* **8**, 1406-1416.
- MENON, R. & LAI, W.T. 1991 Key Considerations In The Selection Of Seed Particles For LDV Measurements. Fourth International Conference on Laser Anemometry, Cleveland, Ohio.
- MENON, R.K. 1987 Three-Component Velocity Measurements In The Interblade Region Of A Fan. *ASME Paper* no. 87 -GT-207, Gas Turbine Conference, Anaheim, California.
- MIAO, H., HU, Y.L., SHIU, Y.T., YUAN, S., ZHAO, Y., KAUNAS, R., WANG, Y., JIN, G., USAMI, S. & CHIEN, S. 2005 Effects Of Flow Patterns On The Localization And Expression Of VE-Cadherin At Vascular Endothelial Cell Junctions: In Vivo And In Vitro Investigations. *J Vasc Res.* **42**, 77-89.
- MITTAL, R., SIMMONS, S.P. & NAJJAR F. 2003 Numerical Study Of Pulsatile Flow In A Constricted Channel. *J. Fluid Mech.* **485**, 337-378.
- MITTAL, R., SIMMONS, S.P. & UDAYKUMAR, H.S. 2001 Application of Large-Eddy Simulation to the Study of Pulsatile Flow in a Modeled Arterial Stenosis. *J. Biomech Eng.* **123**, 325-32.
- MONTY, J.P. 2011 Developments In Smooth Wall Turbulent Duct Flows. *Ph.D. Thesis*. The University of Melbourne.
- MOTT, R.L. 2004 Machine Elements in Mechanical Design, 4th Edition. *Pearson Prentice-Hall*, New Jersey.
- MUTO, T. & NAKANE, K. 1980 Unsteady Flow In Circular Tube: Velocity Distribution Of Pulsating Flow. *Bulletin of J. ASME* **23**, 1991-1996.
- NAGEL, T., RESNICK, N., DEWEY, C.F. & GIMBRONE, M.A. JR. 1999 Vascular Endothelial Cells Respond To Spatial Gradients In Fluid Shear Stress By Enhanced Activation Of Transcription Factors. *Arterioscler Thromb Vasc Biol.* **19**, 1825-1834.

- NAGEL, T., RESNICK, N., ATKINSON, W. J., DEWEY, C. F. & GIMBRONE M. A. 1994 Shear Stress Selectively Upregulates Intercellular Adhesion Molecule-1 Expression In Cultured Human Vascular Endothelial Cells. *J. Clin. Invest.* **94**, 885– 891.
- NAQWI, A.A., REYNOLDS, W.C. & CARR, L.W. 1984 Dual Cylindrical Wave Laser-Doppler Method For Measurement of Wall Shear Stress. *Laser Anemometry in Fluid Mechanics II* **122**, 105.
- NATARAJAN, N.M. & LAKSHMANAN, S.L. 1972 Laminar Flow In Rectangular Ducts: Prediction Of Velocity Profiles And Friction Factor. *Indian J. Technol.* **10**, 435-438.
- NEREM, R. M., GIRARD, P. R., HELMLINGER, G., THOUMINE, O., WIESNER, T.F. & ZIEGLER, T. 2004 The Regulation Of Vascular Endothelial Biology By Flow. *Springer New York*.
- NIE, J.H. & ARMALY, B.F. 2002 Three-Dimensional Convective Flow Adjacent To Backward-Facing Step—Effects Of Step Height. *Int. J. Heat Mass Transfer* **45**, 2431–2438.
- NIE, J.H. & ARMALY, B.F. 2004 Reverse Flow Regions In Three-Dimensional Backward-Facing Step Flow. *Int. J. Heat Mass Transfer* **47**, 4713–472.
- OATES, C. 2001 Cardiovascular Haemodynamics And Doppler Waveforms Explained. *Cambridge University Press*, San Francisco.
- OBABKO, A.V. & CASSEL, K.W. 2002 Detachment Of The Dynamic-Stall Vortex Above A Moving Surface. *AIAA Journal* **40**, 1811-1822.
- OHASHI, T. & SATO, M. 2005 Remodeling Of Vascular Endothelial Cells Exposed To Fluid Shear Stress: Experimental And Numerical Approach. *Fluid Dyn. Res.* **37**, 40-59.
- OJHA, M., COBBOLD, R.S.C., JOHNSTON, K.W. & HUMMEL, R.L. 1989 Pulsatile Flow Through Constricted Tubes: An Experimental Investigation Using Photochromic Tracer Methods. *J. Fluid Mech.* **203**, 173-197.
- ORLU, R., FRANSSON, J.M. & ALFREDSSO, H. 2010 On Near Wall Measurements Of Wall Bounded Flows - The Necessity Of An Accurate Determination Of The Wall Position. *Prog. Aerosp. Sci.* **46**, 353–387.
- PATEL, V.C. & HEAD, M.R. 1969 Some Observations On Skin Friction And Velocity Profiles In Fully Developed Pipe And Channel Flows. *J. Fluid Mech.* **38**, 181-201.
- PATRICK, P.W. 1987 Flowfield measurements in a separated and reattached flat plate turbulent boundary layer. *NASA CR-4052*, March.
- PHELPS, J.E. & DEPAOLA, N. 2000 Spatial Variations In Endothelial Barrier Function In Disturbed Flows In Vitro. *Am. J. Physiol. Heart Circ. Physiol.* **278**, 469–476.
- PIOMELLI, U. 1999 Large-Eddy Simulation: Achievements And Challenges. *Progress Aero. Sci.* **35**, 335-362.

- POPE, S.B. 2000 Turbulent Flows. *Cambridge University Press*, Cambridge, UK.
- PURDAY, H.F.P. 1949 An Introduction To The Mechanics Of Viscous Flow . *Dover Publications*, New York.
- RADOMSKY, R.W. & THOLE, T A. 2002 Detailed Boundary Layer Measurements On A Turbine Stator Vane At Elevated Freestream Turbulence Levels. *J. Turbomach.* **124**, 104-118.
- RAGAB, A.R. & BAYOUMI, S.E. 1988 Engineering Solid Mechanics: Fundamentals And Applications. *CRC Press LLC*.
- RANI, H.P., SHEU, T.W.H. & TSAI, E.S.F. 2007 Eddy Structures In A Transitional Backward-Facing Step Flow. *J. Fluid Mech.* **588**, 43-58.
- RATHA, D. & SARKAR, A. 2015 Analysis Of Flow Over Backward Facing Step With Transition. *Frontiers of Structural and Civil Engineering* **9**, 71–81.
- REESE J.M. & THOMPSON D.S. 1998 Shear Stress In Arterial Stenoses: A Momentum Integral Model. *J. Biomech.* **31**, 1051–1057.
- REYNOLDS, W. C. & HUSSAIN, A.K.F.M. 1972 The Mechanics Of An Organized Wave In Turbulent Shear Flow; Part 3, Theoretical Models And Comparisons With Experiments. *J. Fluid Mech.* **54**, 263-268.
- RIENSTRA, S.W. & HIRSCHBERG, A. 2004 An Introduction To Acoustics. Eindhoven, Technische Universiteit Eindhoven.
- ROOD, E.P. & TELIONIS, D.P. 1991 Editorial On Experimental Uncertainty. *J. Fluids Eng.* **113**, 313-314.
- ROSENFELD, M. 1995 A Numerical Study Of Pulsating Flow Behind A Constriction. *J. Fluid Mech.* **301**, 203-223.
- RUEL, J., LEMAY, J., DUMAS, G., DOILLON, C. & CHARARA, J. 1995 Development Of A Parallel Plate Flow Chamber For Studying Cell Behavior Under Pulsatile Flow. *ASAIO J.* **41**, 876-883.
- RYVAL, J., STRAATMAN, A.G. & STEINMAN, D.A. 2004 Two-Equation Turbulence Modeling Of Pulsatile Flow In A Stenosed Tube. *J. Biomech. Eng.* **126**, 625-635.
- SALEK, M.M., JONES, S.M. & MARTINUZZI, R.J. 2009 The Influence Of Flow Cell Geometry Related Shear Stresses On The Distribution, Structure And Susceptibility Of Pseudomonas Aeruginosa O1 Biofilms. *Journal of Biofouling* **25**, 711-725.
- SATO, M., OHSHIMA, N. & NEREM, R.M. 1996. Viscoelastic Properties Of Cultured Porcine Aortic Endothelial Cells Exposed To Shear Stress. *J. of Biomech.* **29**, 461–467.
- SCHLICHTING, H. 1934 Laminar Channel Entrance Flow. *ZAMM*, **14**, 368–373.

- SCHULTZ, M.P. & FLACK, K.A. 2013 Reynolds-Number Scaling Of Turbulent Channel Flow. *Phys. Fluids* **25**, 025104-1-14.
- SCOTTI, A. & PIOMELLI, U. 2001 Numerical Simulation Of Pulsating Turbulent Channel Flow. *Phys. Fluids* **13**, 1367-1384.
- SHERWIN, S. J. & BLACKBURN, H. M. 2005 Three-Dimensional Instabilities And Transition Of Steady And Pulsatile Axisymmetric Stenotic Flows. *J. Fluid Mech.* **533**, 297-327.
- SHEN, L., QIAO, A., DING, H., MO, G., XU, G., DU, Y., LI, M., CHEN, Z. & ZENG, Y. 2006 An Apparatus For Studying The Response Of Cultured Endothelial Cells To Stresses. *Australas Phys. Eng. Sci. Med.* **29**, 196-202.
- SHIH, C. & HO, C.M. 1994 Three-Dimensional Recirculation Flow In A Backward Facing Step. *J. Fluids Eng.* **116**, 228-232.
- SHU, F., VANDENBERGHE, S. & ANTAKI, J.F. 2009 The Importance of dQ/dt on the Flow Field in a Turbodynamic Pump With Pulsatile Flow. *Artif Organs* **33**, 757-762.
- SHU, M. C. S. & HWANG, N. H. C. 1991 Haemodynamics Of Angioaccess Venous Anastomoses. *J. Biomed. Eng.* **13**, 103-112.
- SNEDECOR, G.W. & COCHRAN, W.G. 1967 Statistical Methods (6th ed.), Iowa State University Press, Ames, Iowa.
- SO, S., MORIKITA, H., TAKAGI, S. & MATSMOTU, Y. 2002 Laser Doppler Velocimetry of Turbulent Bubbly Channel Flow. *Exp. Fluids* **33**, 135-142.
- SOBEY, I.J. 1985 Observation Of Waves During Oscillatory Channel Flow. *J. Fluid Mech.* **151**, 395-426.
- SOBEY, I.J. & DRAZIN, P.G. 1986 Bifurcations Of Two-Dimensional Channel Flow. *J. Fluid. Mech.* **171**, 395-426.
- STEVENSON, W.H., THOMPSON, H.D. & ROESLER, T.C. 1982 Direct Measurement Of laser Velocimeter Bias Errors In A Turbulent Flow. *AIAA Journal* **20**, 1720-1723.
- STRAATMAN, A.G. & STEINMAN, D.A. 2002 On The Hydrodynamic Stability Of Pulsatile Flow In A Plane Channel. *Phys. Fluids* **14**, 1938-1943.
- STRONY, J., BEAUDOIN, A., BRANDS, D. & ADELMAN, B. 1993 Analysis Of Shear Stress And Hemodynamic Factors In A Model Of Coronary Artery Stenosis And Thrombosis. *Am. J. Physiol.* **265**, 1787-1796.
- STROUD, J.S., BERGER, S.A. & SALONER, D. 2002 Numerical Analysis Of Flow Through A Severely Stenotic Carotid Artery Bifurcation. *J. Biomech. Eng.* **124**, 9-19.

- TARBELL, J.M., SHI, Z.D., DUNN, J. & JO, H. 2014 Fluid Mechanics, Arterial Disease, And Gene Expression. *Annu. Rev. Fluid Mech.* **46**, 591–614.
- TAVOULARIS, S. 2005 Measurement In Fluid Mechanics, *Cambridge University Press*, New York, USA
- TEUFFL, M., TRIMIS, D., LOHMOLLER, A., TAKEDAT, Y. & DURST, F. 1992 Determination Of Velocity Profiles In Oscillating Pipe-Flows By Using Laser Doppler Velocimetry And Ultrasonic Measuring Devices. *Flow Meas. Instrum.* **3**, 95-101.
- THANGAM, S. & KNIGHT, D.D. 1989 Effect Of Step Height On The Separated Flow Past A Backward-Facing Step. *Phys. Fluids A* **1**, 604-606.
- TIHON, J., PENKAVOVA, V., HAVLICA, M. & SIMCIK, M. 2012 The Transitional Backward-Facing Step Flow In A Water Channel With Variable Expansion Geometry. *Exp. Therm Fluid Sci.* **40**, 112-125.
- TOBIN, R.J & CHANG, I.D. 1976 Wall Pressure Spectra Downstream Of Stenoses In Steady Tube Flow. *J. Biomech.* **9**, 633-640.
- TRUSKEY, G. A., YUAN, F. & KATZ, D. F. 2010 Transport Phenomena In Biological Systems. *Pearson*, New York.
- TRUSKEY, G.A. & PIRONE, J.S. 1990 The Effect Of Fluid Shear Stress Upon Cell Adhesion To Fibronectin-Treated Surfaces. *J. Biomed. Mater. Res.* **24**, 1333-1353.
- TRUSKEY, G.A., BARBER, K.M. & RINKER, K.D. 2002. Factors Influencing The Nonuniform Localization Of Monocytes In The Arterial Wall. *Biorheology* **39**, 325-329.
- TSUKAHARA, T., SEKI, Y., KAWAMURA, H. & TOCHIO, D. 2014 DNS of Turbulent Channel Flow At Very Low Reynolds Numbers. 4th Int. Symp. on Turbulence and Shear Flow Phenomena, Williamsburg, VA, USA.
- TUTTY, O.R. 1992 Pulsatile Flow In A Constricted Channel. *J. Biomech. Eng.* **114**, 50-54.
- TYLLI, N., KAIKTSIS, L. & INEICHEN, B. 2002 Sidewall Effects In Flow Over A Backward-Facing Step: Experiments And Numerical Simulations. *Phys. Fluids* **14**, 3835-3845.
- VALENCIA, A. 1997 Pulsating Flow In A Channel With A Backward-Facing Step. *Appl. Mech.* **50**, 232-236.
- VARGHESE, S.S., FRANKEL, S.H. & FISCHER, P.F. 2007a Direct Numerical Simulation Of Stenotic Flows, Part 1: Steady Flow. *J. Fluid Mech.* **582**, 253-280.
- VARGHESE, S.S., FRANKEL, S.H. & FISCHER, P.F. 2007b Direct Numerical Simulation Of Stenotic Flows, Part 2: Pulsatile Flow. *J. Fluid Mech.* **582**, 281-318.

- VERHELST, J.M. & NIEUWSTADT, F. 2004 Visco-Elastic Flow Past Circular Cylinders Mounted In A Channel: Experimental Measurements Of Velocity And Drag. *J. Nonnewton. Fluid Mech.* **116**, 301-328.
- VIEGAS, K.D., DOL, S.S., SALEK, M.M., SHEPHERD, R.D., MARTINUZZI, R.M. & RINKER, K.D. 2011 Methicillin Resistant Staphylococcus Aureus Adhesion To Human Umbilical Vein Endothelial Cells Demonstrates Wall Shear Stress Dependent Behaviour. *Biomed. Eng. Online* **22**, 10-20.
- VON TERZI, D. A. 2016 Numerical Investigation Of Transitional And Turbulent Backward-Facing Step Flows. *Ph.D. Thesis*. The University of Arizona.
- VOORHEES, A., NACKMAN, G.B. & WEI, T. 2007 Experiments Show Importance Of Flow-Induced Pressure On Endothelial Cell Shape And Alignment. *Proc. R. Soc. A.* **463**, 1409-1419.
- VOZZI, F., BIANCHI, F., AHLUWALIA, A. & DOMENICI, C. 2014 Hydrostatic Pressure And Shear Stress Affect Endothelin-1 And Nitric Oxide Release By Endothelial Cells In Bioreactors. *J. Biotechnol.* **9**, 146-154.
- WANG, L., ZHANG, Z.G. & ZHANG, R.L. 2006b Matrix Metal-Loproteinase 2 (MMP2) And MMP9 Secreted By Erythropoietin-Activated Endothelial Cells Promote Neural Progenitor Cell Mi-Gration. *J. Neurosci* **26**, 5996-6003.
- WHEELER, A.J & GANJI, A.R. 2004 Introduction To Engineering Experimentation, 2nd Edition. *Pearson Education, Inc.* New Jersey.
- WHITE, C.R., HAIDEKKER, M., BAO, X. & FRANGOS, J.A 2001 Temporal Gradients In Shear, But Not Spatial Gradients, Stimulate Endothelial Cell Proliferation. *Circulation* **103**, 2508-2513.
- WHITE, F.M. 2009 Fluid Mechanics, 6th Edition. *McGraw-Hill*, New York.
- WILLIAMS, P.T. & BAKER, A.J. 1997 Numerical Simulations Of Laminar Flow Over A 3D Backward-Facing Step. *Int. J. Numerical Methods in Fluids* **24**, 1159-1183.
- WINTER, D.C. & NEREM, R.M. 1984 Turbulence In Pulsatile Flows. *Ann. Biomed. Eng.* **12**, 357-69.
- WONG, A.J., POLLARD, T.D. & HERMAN, I.M. 1983 Actin Filament Stress Fibers In Vascular Endothelial Cells In Vivo. *Science* **219**, 867-869.
- WRIGHT, D.B. & HERRINGTON, J.A. 2011 Problematic Standard Errors And Confidence Intervals For Skewness And Kurtosis. *Behav. Res. Methods.* **43**, 8-17.
- XING, D., YAN, C., WANG, C. & SUN, L. 2013 A Theoretical Analysis About The Effect Of Aspect Ratio On Single-Phase Laminar Flow In Rectangular Ducts. *Prog. Nucl. Energy* **65**, 1-7.
- YAMAGUCHI, T., YAMAMOTO, Y., LIU, H. 2000. Computational Mechanical Model Studies On The Spontaneous Emergent Morphogenesis Of The Cultured Endothelial Cells. *J. Biomech.* **33**, 115-126.

- YOSHIKAWA T. 2009 Handbook Of Optical Metrology: Principles And Applications. *CRC Press, Taylor & Francis Group*, New York.
- ZAMIR, M. 2000 The Physics Of Pulsatile Flow. *Springer-Verlag*, New York, Inc.
- ZAMIR, M. 2005 The Physics of Coronary Blood Flow. *Springer Science + Business Media, Inc.*, New York.
- ZARINS, C.K., GIDDENS, D.P., BHARADVAJ, B.K., SOTTIURAI, V.S., MABON, R.F & GLAGOV, S. 1983 Carotid Bifurcation Atherosclerosis: Quantitative Correlation Of Plaque Localization With Flow Velocity Profiles And Wall Shear Stress. *Circ. Res.* **53**, 502–14.
- ZHANG, Z.K., EISELE, K. & HIRT, F. 1997 The Influence Of Phase-Averaging Window Size On The Determination Of Turbulent Quantities In Unsteady Turbulent Flows. *Exp. Fluids* **22**, 265–267.
- ZHOU, Z., ZHANG, Y., ZHU, C., SUI, J., WU, G., MENG, Z., HUANG, H. & CHEN, K. 2012 Cognitive Functions Of Carotid Artery Stenosis In The Aged Rat. *Neuroscience*. **219**, 137-44.
- ZHU, J.Y. 1996 Laser Doppler Velocimetry For Flow Measurements in Pulp and Paper Research. TAPPI Engineering Conference, IPST Technical Paper Series Number 618.

APPENDIX 1

TIMELINE DEVELOPMENT OF THE HEMODYNAMIC FLOW FACILITY

1A Introduction

The intent of this Appendix is to demonstrate how various design refinements of the initial hemodynamic flow facility have led to the final revision of the research facility, used to emulate pulsatile waveforms at the working section. The final hemodynamic flow facility (which is discussed in Chapter Three, experimental methods) was used to measure both an intermittently turbulent flow (under a pulsatile flow) at the working section (downstream of the backward-facing step) and to study cell response to flow (Avari et al. 2016). This Appendix presents various research challenges that were encountered in attempting to measure steady and pulsatile flow (laminar regime) inside a parallel-plate flow chamber (PPFC).

To assist the reader in the understanding of the various design revisions and testing methodologies that were undertaken, the Appendix begins with an organization chart that provides a methodical breakdown of the work outlined in this Appendix. A basic overview of the early-stage hemodynamic flow facility is provided, with emphasis on the various challenges and revisions that have led to the final design of the near-wall configured LDV system. Using the latest revision of the custom LDV, steady and pulsatile velocity (i.e. normal carotid artery) measurements were captured at the working section of both the early-stage PPFC and the subsequent revised, more compact PPFCs. A comparison was made between the two PPFCs in terms of the modeling parameters (such as the Reynolds and Womersley numbers), waveform shapes, and steady laminar wall shear stress. Analytical solutions for an infinitely wide plate (laminar flow theory) and channel flow are also presented as a comparison to the LDV measurements. Challenges arising from cell vitality inside the early-stage PPFC encountered in early work by Horie (2009) are also discussed. An overview of the LDV accuracy (based on the r.m.s. velocity) assessed inside the PPFC is also presented. Finally, a more cost-effective and modular commercial facility is presented; this facility features a new pulsatile syringe pump to simulate realistic waveforms and a commercial LDV system which was used in work by Avari et al (2016).

1A.1 Chapter Organization

The intent of this Appendix is to present the sequence of design and test iterations that ultimately led to the final design of a hemodynamic flow facility. It provides an overview of the various challenges encountered during the course of the facility development and the implications of those challenges on the final version of the flow facility.

The ultimate purpose of this facility was to simulate realistic waveforms (i.e. *in-vivo* normal carotid artery; $f \approx 1.0$ Hz) inside a rigid two-dimensional (the effects of the lateral walls to be negligible) PPFC and to allow both simultaneous LDV velocity measurements (streamwise u and wall-normal v) and real-time *in-situ* EC imaging. In addition, velocity data (u, v) were to be ideally captured extremely close ($\approx 5 \mu\text{m}$) to the cell surface (flush mounted inside the lower wall of the channel) to obtain accurate shear stresses (viscous and turbulent shear stress contributions) acting on the ECs. A hemodynamic facility existed in the laboratory at the start of this thesis research, but its characteristics had not been quantified, specifically: (1) to ensure feasibility of the facility with respect to the above noted objectives and, (2) to obtain mean flow and turbulence statistics (downstream of a backward-step which modeled arterial narrowing) under both a steady and unsteady (time-varying pulsatile flow) flow above live ECs. With respect to (1), the present author focused on developing a rigid PPFC that would allow for both optical access for LDV measurements and microscopy cell imaging. The author's focus was not to study ECs and/or to ensure correct experimental conditions for cell vitality. Work in parallel by Horie (2009) and some of the more recent work by Avari et al (2016) focused on this task. For clarity, although the author did not study EC remodeling to flow, the iterative design approach ensured such studies were able to be undertaken. To help in the understanding of the various facility refinements and various steps of validation, a research program outline is shown below in Fig. 1A-1. The subsequent sections of this Appendix reference the various revision levels shown in the diagram below.

Pilot	Research Laboratory Existed Facility
<ul style="list-style-type: none"> • Includes the LSM-designed LDV (two-component; u, v), two-dimensional PPFC and a pulsatile flow pump (purchased from Shelley Medical Imaging Technologies) 	
Revision 1	Modified LSM LDV System
<ul style="list-style-type: none"> • Includes the modified LSM LDV system, two dimensional PPFC and a pulsatile flow pump (purchased from Shelley Medical Imaging Technologies) 	
Revision 2	Modified LDV: Final system (two-component)
<ul style="list-style-type: none"> • Includes final version of the LDV system (as reported in Chapter Three), two dimensional PPFC and a pulsatile flow pump (purchased from Shelley Medical Imaging Technologies) 	
Revision 3	Modified Two-Dimensional PPFC: New PPFC design
<ul style="list-style-type: none"> • Includes final version of the LDV system, new PPFC design (i.e. smaller compact channel) and a pulsatile flow pump (purchased from Shelley Medical Imaging Technologies) 	
Commercial Facility	Entire New System: More compact and cost-effective
<ul style="list-style-type: none"> • Includes a new commercial LDV probe (small scale from TSI, USA), an innovative PPFC (small-scale PPFC), and a new pulsatile syringe pump (from Harvard Apparatus, Canada). 	
FINAL FACILITY	Used in the Present Work and in the work of Avari et al (2016)
<ul style="list-style-type: none"> • Includes the revision 3 two-component LDV system, re-designed PPFC by Avari et al (2016) and revision 3 pulsatile flow pump with additional components (in-line heater, filtration system, solenoid valve) 	

Fig. 1A-1 Development of the hemodynamic flow facility showing various revision stages that ultimately led to the final design of the facility (presented in Chapter 3: experimental methods).

1A.2 Hemodynamic Flow Facility: Pilot

The Early Concept and Its Implications on Further Development

The earliest version of the hemodynamic flow facility is based on the first concept of the PPFC (Kempston, 2006), a pulsatile flow pump (capable of flow rates range, $55 \text{ mL/s} \geq Q \geq 1 \text{ mL/s}$), and a custom LSM-designed LDV system to measure two-component (u, v) velocity inside the PPFC (at the working section). The idea behind this system was to provide a method to quantify both the surface shear stress-cell response relationship using simultaneous near-wall velocity measurements and confocal microscopy to image EC in real-time (on the order of milliseconds). This concept is shown in Fig. 1A-2 and Fig. 1A-3, respectively.

The early stage experiments were conducted with the LSM-designed LDV and the PPFC using recirculating water (driven by either a pulsatile pump or a header) concentrated with TiO_2 seeding particles. TiO_2 was reported in various studies as a suitable tracer particle (Iyer & Woodmansee, 2005), hence the reason for its selection. Findings showed an absence of and/or very low data rates resulting in no velocity measurement (u-component)

being possible. The experimental findings also demonstrated the impossibility of transmitting the green beams (wall-normal velocity component, v) into the PPFC through the optical window. The latter was attributed to a geometrical constraint of the green beam configuration. As a result of the unsuccessful trials, the author modified the existing LSM-designed LDV system, which is discussed in the next section.

It should be noted that the custom design of the LSM Tech. system involved mounting it to an existing confocal microscopy at the Anatomy & Cell Biology Department, UWO. The idea behind the system was to mount the PPFC on the microscope stage and collect the scattered light (from the measurement volume) via microscopy objective lens (bottom-top configuration), whilst measuring a 2-D (steady laminar) velocity field above the EC surface. Although the experimental findings (with the LSM-designed LDV and PPFC) as a result of the various tests performed were instrumental in further advancing the flow facility, it will not be further discussed since there were no data to report (streamwise velocity profiles and/or EC response data).

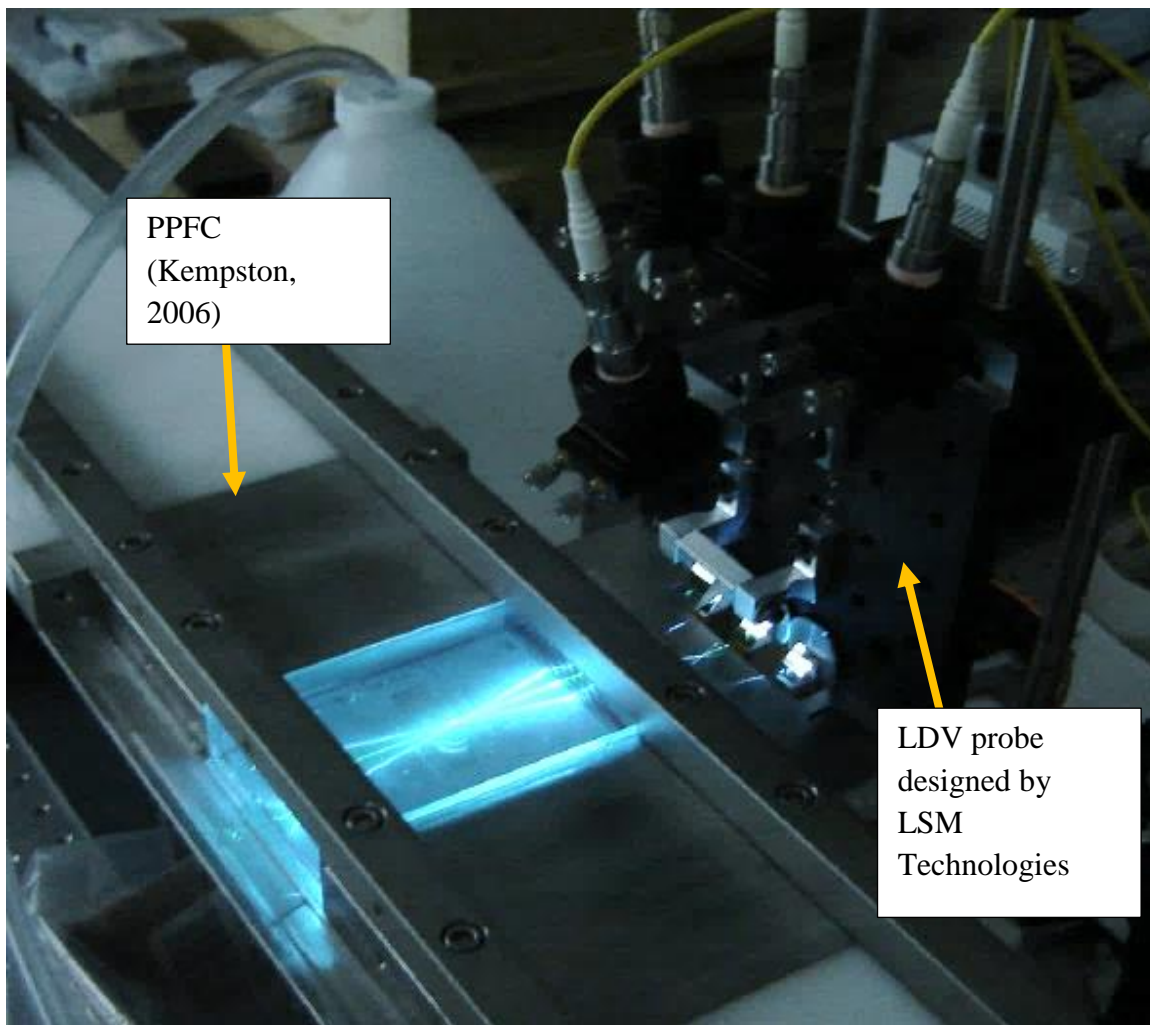


Fig. 1A-2 Custom near-wall LDV probe mounted on the side of the PPFC transmitting 4 laser beams (2 blue and 2 green) through the optical window into the working section. The working section had a rectangular cross-section ($h = 2$ mm and $w = 80$ mm). The LSM-designed LDV system consisted of an aluminum back-plate to which 4 fibers attached to from the TSI colour separator. The back-plate was mounted to a 3-axes micro-traversing platform from Thorlabs, USA. Downstream of the beams paths were 4 reflecting mirrors (at 45°) to transmit the beams inside the PPFC to one common point (measurement volume).

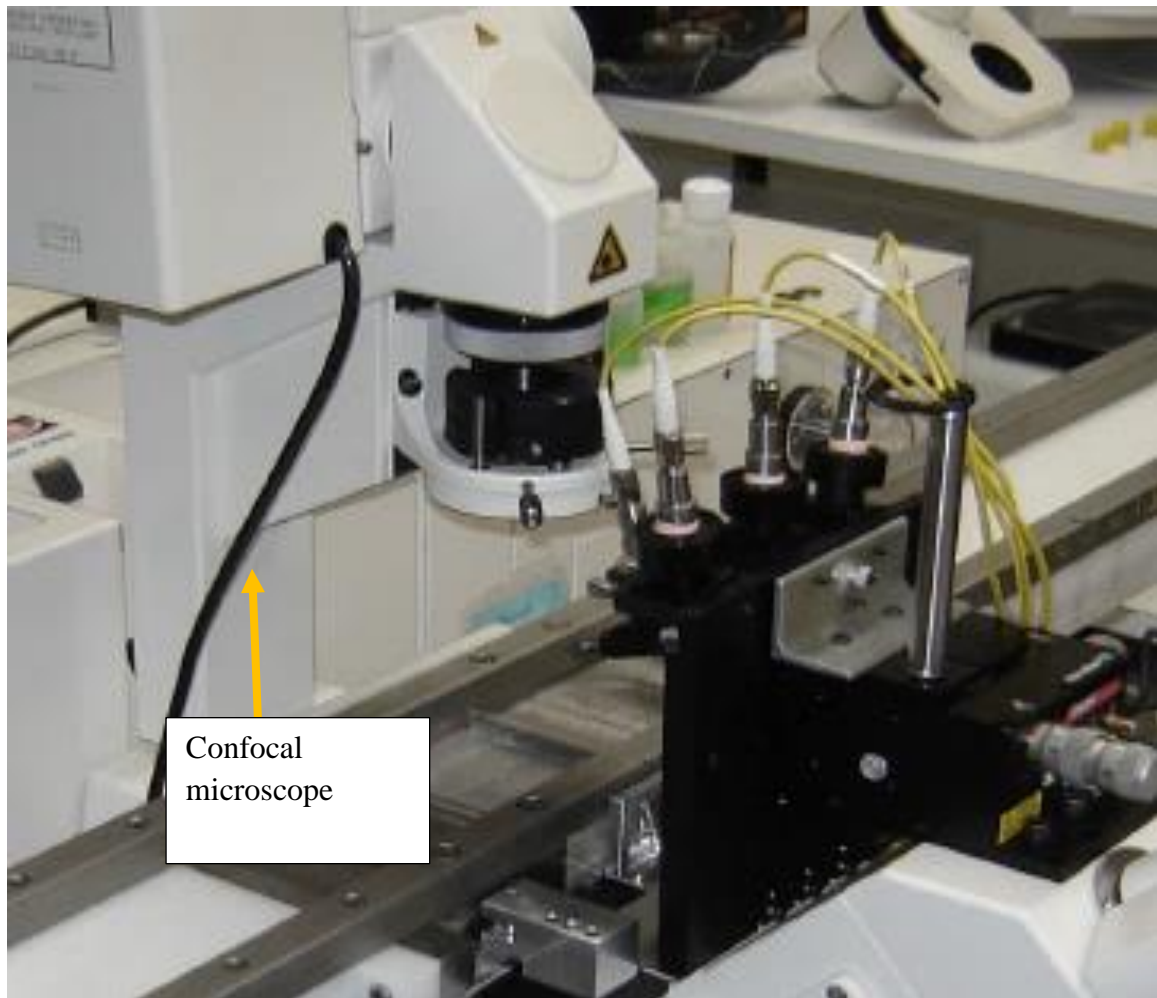


Fig. 1A-3 Custom near-wall LDV probe and the PPFC mounted on a laser scanning confocal microscope (at the Anatomy & Cell Biology Department, UWO) for simultaneous velocity measurements and EC imaging. The LSM-probe was designed to mount to an existing microscope and still allow imaging of the cells from the bottom-top configuration using an objective lens. The bottom-top collection of LDV scattered light was shown to be unsuccessful due to inability to focus onto the measurement volume. As a result, the data rate was very low.

1A.3 Re-design of the LSM-Designed LDV System: Revision 1 Extraction of the TR-360 TSI Fiber Terminations

The design of the modified LSM-designed LDV system consisted of a two-part LDV transmitter and a new custom built receiver unit to collect the scattered light from the measurement volume (see Fig. 1A-4). The focusing lens (Bi-Convex Lens, AR Coated: 350 - 700 nm) was separated from the transmitter unit and mounted on a separate fixture downstream of the transmitter back-plate. The decoupling of the focusing lens was complete since the original back-plate design from LSM Tech did not allow for additional space to mount the lens. The intent at that point of research was to ensure LDV functionality and ensure its ability to mount to the confocal microscopy stage. For this reason, other LDV configurations (designs without decoupling the focusing lens) were not contemplated or further discussed.

One of the fundamental challenges with the LSM probe lay in achieving high transmission efficiency (better than 65%) between the TSI colour separator and the laser beam fibers. The LSM-designed couplings (which mounted to the colour separator) were not optimized to provide the transmission efficiency noted above and, hence, continuous damage to the fibers was detected. The main obstacles with respect to the LSM probe were: (1) low-power (mW) of the laser beams at the measurement volume, (2) the degree of polarization and the correct polarity orientation of the laser beam pair and, (3) the size of the measurement volume diameter (larger than 100 μm as a result of long focal length of individual beam lenses, approximately 400 mm).

To overcome these challenges, the author extracted four fiber terminations (blue and green beam pairs) from a TR-360 probe (commercial TSI LDV probe). Each individual beam termination assembly consisted of a bare fiber (ferrule) and a small collimation sub-assembly that held the ferrule. The laser beam diameter (as a result of the collimation) for all 4 laser beams was 1.8 mm (reported by the manufacturer).

As per Fig. 1A-4, the four termination assemblies were mounted to individual kinematic mounts with a flat mounting surface (and kinematic dials) for controlling tip and tilt. The four laser beams were then reflected by 45° using reflecting mirrors to transmit the four

parallel beams to a downstream focusing lens. The lens was installed on a separate mount to focus and direct all four beams to a common measurement point inside the PPFC (at the working section). The advantage of the downstream lens was its proximity to the working section adjacent to the optical window. This allowed for the lens to be positioned millimetres away from the optical window of the PPFC, allowing for the use of a smaller focal length lens ($F \approx 100$ mm). The laser beam waist at the beams' crossing was approximately $35 \mu\text{m}$ (for both blue and green) and calculated based on $d_e = 4\lambda F / (\pi D_e)$, where λ is the laser beam wavelength, F is the focal length of the lens, and D_e is the upstream beam diameter (Zhu, 1996). The measurement volume diameter was calculated based on $d_m = d_e / \cos(\theta)$, where θ is the beam half-angle (Zhu, 1996). The reported measurement volume diameter for both the blue and the green beams was approximately $36 \mu\text{m}$.

The LSM-modified probe was tested by attempting to measure the streamwise velocity (u -component) inside the PPFC at the working section. To receive the scattered light from the measurement volume, a TSI TR-260 commercial probe was used in a forward-scatter mode (off-axis to avoid beam reflections). The TR-260 was used since at that time there was no available forward-scatter receiver. The microscope stage receiver designed by LSM (collection of light in a bottom-top configuration) was not used since it was not functional. Non-functionality was attributable to difficulty in focusing on the measurement volume with an objective lens, coupled with relatively lower scatter of light in that direction.

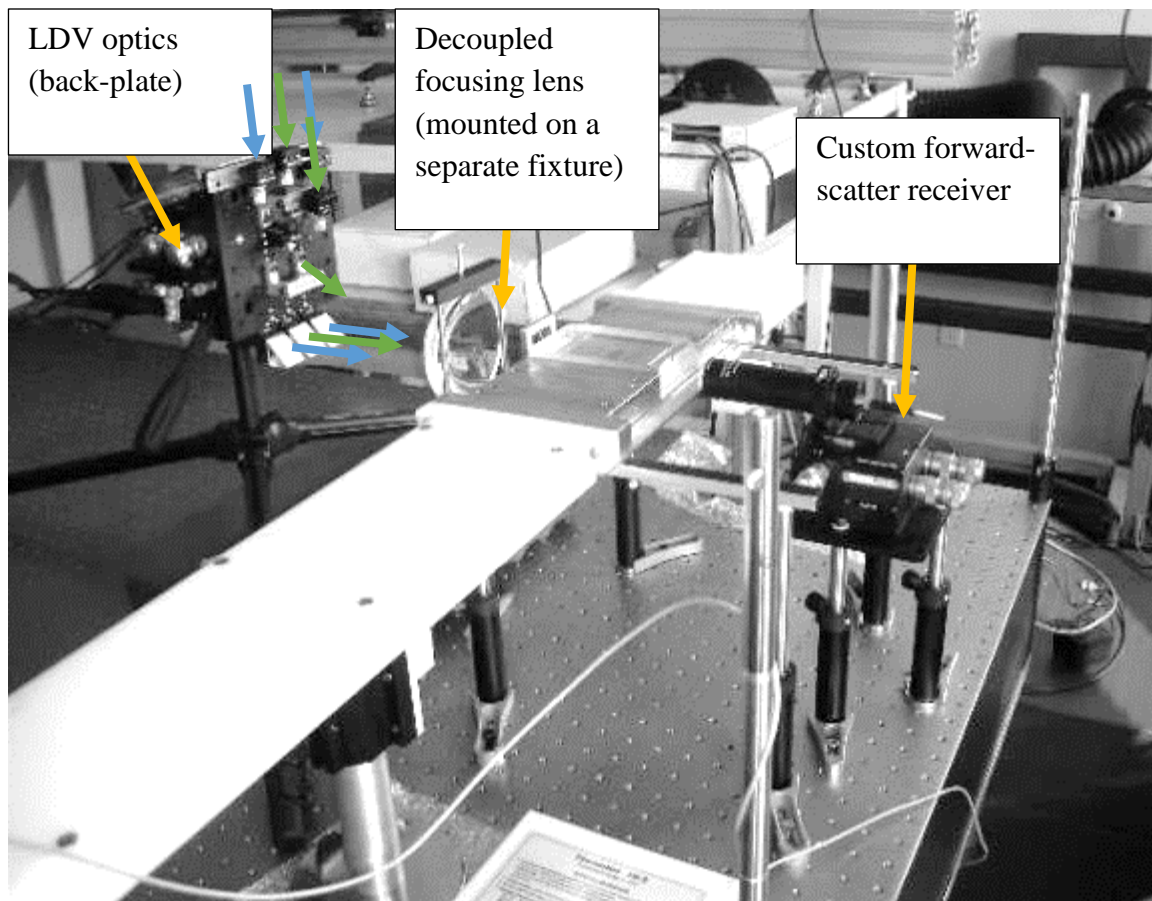


Fig. 1A-4 A modified LSM-designed LDV system consisted of a two-part LDV transmitter (the focusing lens was decoupled from the transmitter) and a new custom built receiver unit for collection of scattered light from the measurement volume. The LDV transmitting back-plate held four kinematic mounts to steer the four laser beams into the four reflecting 45° mirrors.

1A.3.1 Streamwise Velocity Measurement Findings: u-component

It was found that the u-component of the velocity vector was measurable at the working section inside the PFC with an approximate data rate range of $500 \text{ Hz} \leq \dot{N} \leq 3 \times 10^3 \text{ Hz}$, depending on the location of measurement volume. Data rates of approximately 500 Hz were observed near the wall, whereas away from the wall (approximately 200 μm) the data rates were larger. Water was supplied to the PFC using a 50-gallon header (approximate height and diameter of header was 1 m) which ensured negligible changes in the channel velocity over a 5 to 10-minute interval and, thus, a correct bandpass filter range was used (inside FlowSizer). The volumetric flow rate, Q , was approximately 5 mL/s (measured with a graduated glass beaker and a digital stopwatch) which resulted in an average channel velocity (U) and Reynolds number (Re) of approximately 0.031 m/s and 125, respectively. Flow rate through the flow circuitry was controlled by regulating a globe valve on the header tank and/or by applying back-pressure on tubing (downstream of the PFC).

It was rather difficult to position the TR-260 probe to effectively collect the scattered light since it did not have a viewport (for visualization of beams' crossing) to assist in focusing the measurement volume inside the working section to the receiving fiber ferrule. By way of general background, the TR-260 probe had a receiving fiber core size of 50 μm (reported by the manufacturer). In addition, the front lens of the probe had a focal length of approximately 260 mm and, thus, required that the probe position be much farther from the measurement volume. Both of those characteristics made it impractical to continue with this approach to receiving scattered light. Although it was possible to obtain a velocity measurement using the TR-260 as a receiver, it was extremely difficult to capture the velocity gradient ($\partial \bar{u} / \partial y$). This required $\approx 50 \mu\text{m}$ traversing in the y-direction and, thus, continuous re-positioning of the receiver (to ensure that the beams' crossing was focused on the receiving ferrule) was required. For the reasons mentioned above, a new receiving unit was designed and built with a receiving fiber core size of 150 μm . A larger core size was used to make it easier to collect the scattered light from the measurement volume. The receiver was mounted to a 3-Axis NanoMax stage (from Thorlabs: MAX313D) with a manufacturer stated resolution of 20 nm and an accuracy of $\pm 1 \mu\text{m}$. The maximum travel of the stage was 4 mm in the y-direction, which was sufficient to resolve the velocity

gradient near the cell surface. Furthermore, the receiver was designed with a visible achromatic doublet-pairs lens system (the front received light from the measurement volume and the back focused the light into the ferrule of the receiving fiber). The focal length of the front and back lens of the doublet system was approximately 120 mm, which allowed the receiver to be positioned closer to the measurement volume (inside the working section). Adjustment control and focus (x, y, z) of the receiving fiber was ensured by using a translation mount fixed to the back of the receiver body that only moved the receiving fiber and not the entire unit. This was an iterative process until the correct position of the fiber relative to the back lens (doublet-pair) was established. The receiving fiber connected to the photo-detector module (PDM) processor (TSI commercial unit) for further signal processing.

At that point of development, the u -component was measurable and given the new receiver design, it was possible to traverse with the probe in 50 μm increments and obtain velocity data near the surface. The receiver was not ideal by any means since it was still difficult to find the optimal location (with respect to the measurement volume) to effectively collect the scattered light. However, it was a good starting point to continue evaluating the LDV system and addressing other challenges such as positioning the beams' crossing close to the surface of the wall.

There remained two main challenges associated with this latest design: (1) the green beams (wall-normal velocity component) could not penetrate into the PPFC and, (2) the focusing lens of the probe required separate traversing in the y -direction each time the probe moved 50 μm . The green beam configuration on the back-plate of the initial LSM-designed probe did not provide much re-positioning flexibility, which was necessary to ensure correct geometry and transmission into the working section. Each time the back-plate of the probe was traversed 50 μm in the y -direction, the data rate dropped off as a result of partial measurement volume disconnect. This is because the lens focused and steered the beams into a common measurement point and any inaccuracies (where the incoming beams strike the lens) resulted in a disjointed measurement volume. Distinct control of the probe back-plate, the focusing lens, and the receiver was extremely difficult and, thus, a complete re-design was required to ensure no relative motion between the components. The

development and validation of a new near-wall LDV system was a major contribution of the author's intellectual work on the overall project and is explained in detail in the subsequent Appendix. However, a brief overview of the system is presented in the next section to demonstrate how the knowledge gained (with the previous LDV designs) has led to an improved LDV unit. The new LDV system made it possible to measure the u and v velocity components inside this PPFC and other PPFCs described in the subsequent sections.

1A.4 New and Final Near-Wall LDV System: Revision 2

As per Fig. 1A-1, revision 2 in the development cycle consisted of the PPFC, a pulsatile pump, and the new near-wall LDV system. The near-wall LDV system shown in Fig. 1A-5 was developed to ensure that the v -component of the velocity was measurable and to ensure a practical method of capturing the velocity gradient near the surface. The probe was designed to mount the fiber terminations (extracted from the TR-360 probe) and the focusing lens in one main assembly. This ensured that the focusing lens did not require separate movement in any of the three directions ($x - y - z$). In addition, the steering wedge optical assembly was extracted from the TR-360 probe to aid in crossing all four beams to one common point (measurement volume). The blue and the green fiber terminations were mounted on the back of the probe and transmitted to the downstream focusing lens to merge the four parallel beams to one common point. The blue beam fiber terminations were spaced approximately 50 ± 1 mm apart, whereas the green beam terminations were spaced 25 ± 1 mm apart. One of the green beams was mounted to transmit from the centre of the focusing lens to ensure transmission inside the working section of the PPFC (near-wall configuration). The focusing lens used was purchased from TSI and had a focal length of 135 mm (manufacturer reported). The measurement volume for the blue and green beams were $52 \mu\text{m}$ and $54 \mu\text{m}$, respectively. The probe was mounted on a 3-Axis NanoMax stage which allowed traversing in $1 \mu\text{m}$ increments along the x , y , and z -axis. A TSI forward-scatter receiver was purchased and also mounted on a 3-Axis NanoMax stage to coordinate with the $50 \mu\text{m}$ traverse steps of the probe. The major advantage of this commercial receiver was the optical viewport, which projected an image

of the receiving fiber core and allowed for proper positioning of the receiver in relation to the measurement volume.

The next section discusses the u-component velocity measurements for both steady and pulsatile flow under a laminar regime. The new LDV system was able to capture streamwise mean velocity profiles, $\bar{u}(y)$ and $\bar{u}(z)$, at the working section of the PPFC (where \bar{u} represents time-averaged mean of the instantaneous velocity realizations). Since the feasibility of the new LDV system was achieved (demonstrated in the next section), the research focus shifted towards evaluating the fluid dynamics inside the PPFC. At this point in the research, the following uncertainties required investigation: (1) the magnitude of the wall shear stress under a wide range of flow rates ($1 \text{ mL/s} < Q < 20 \text{ mL/s}$), (2) steady laminar and pulsatile velocity profiles and waveform shapes, respectively and, (3) precision (random error) of the new LDV system. The next section presents an investigation of the fluid mechanics under a steady and pulsatile flow (laminar regime) and a basic overview of a direct method that was used to estimate the uncertainty of the LDV measurements under a steady laminar flow. In parallel to the fluid mechanics investigation, work by Horie (2009) focused on evaluating EC vitality inside the PPFC. The outcome of the EC work inside the PPFC is discussed in the subsequent section.

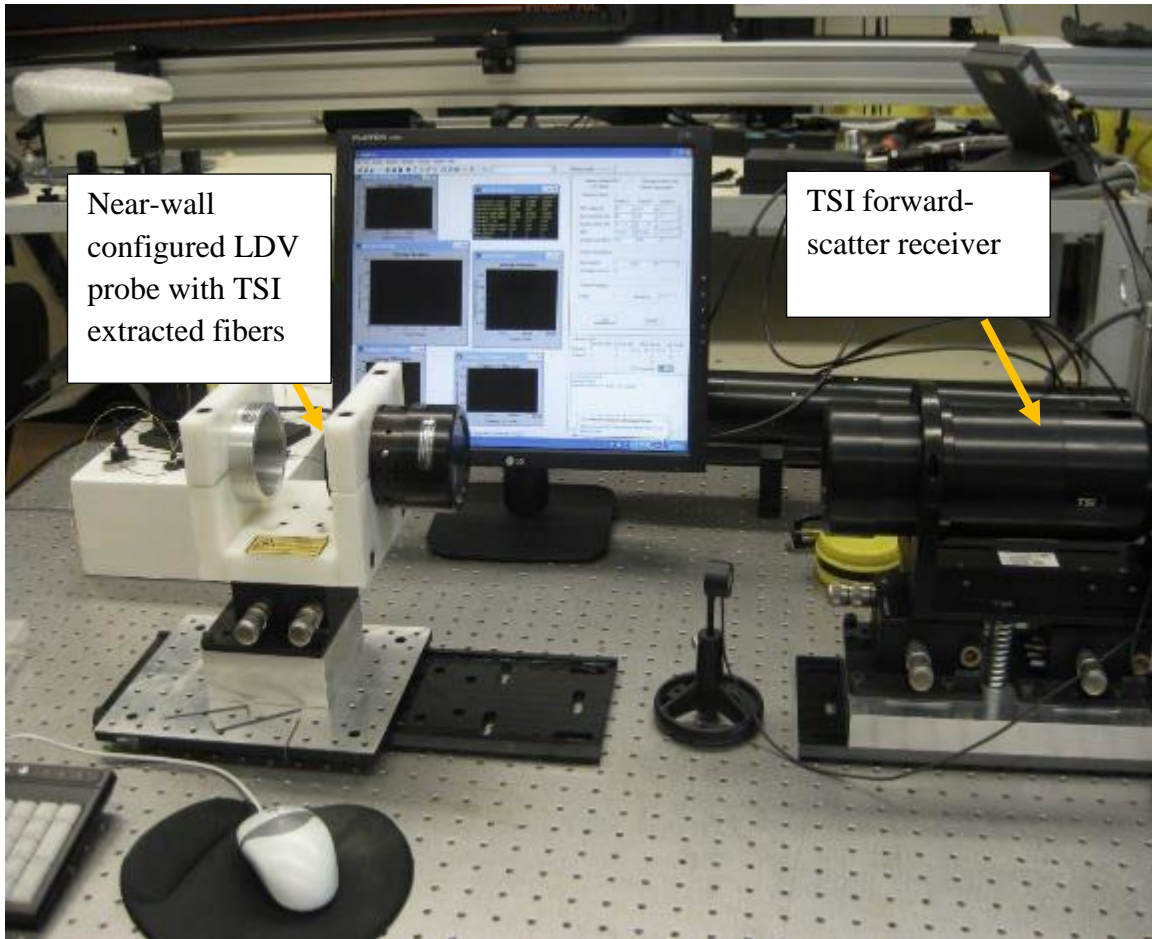


Fig. 1A-5 Final version of the LDV system showing the LDV probe and TSI forward-scatter receiver, both mounted on micro traverse systems. In addition to the 3-Axis NanoMax stages, both the probe and the receiver were mounted on precision slide tracks to allow movement in the z-direction. The probe and the receiver optical axes (centre of the front lenses) were collinear within $\pm 10 \mu\text{m}$.

1A.4.1 Early-stage PFFC Performance Assessment: Steady and Pulsatile Flow LDV Measurements of the Streamwise and Spanwise Flow Profiles

In the previous sections of this Appendix the author discussed various revisions of the near-wall LDV system and how the design and testing of these various concepts has led to the final version of the LDV system. In this section, the author discusses the application of this system and presents u-component (streamwise) velocity data as a means of demonstrating the LDV probe's ability to take velocity measurements under both steady laminar and

pulsatile flow. This section also demonstrates the challenges associated with simulating realistic waveforms at the working section of the PPFC.

Shown in Fig. 1A-6 is the initial hemodynamic flow facility (i.e. revision 2), which consisted of three major units: a pulsatile pump, the PPFC, and a near-wall LDV system designed in-house. In addition, Fig. 1A-7 shows a schematic of the closed-loop circuitry. The computer-controlled pump unit was manufactured by Shelley Medical Imaging Technologies. The pump and the PPFC were arranged in a closed-loop configuration to provide a continuous flow and to avoid disruption to the operation. The PPFC had built-in optical access to allow for direct and simultaneous velocity measurements (u and v) with the LDV system. The upstream section of the PPFC received the fluid from the pump and the downstream section returned it through flexible vinyl-braided tubing (ID = 9.5 mm). To minimize inflow and outflow disruption, the upstream and the downstream sections gradually expand and contract, respectively. The PPFC extended for 99.2 cm in length and at the working section was 80 mm wide, 70 mm long, and 2 mm high. The height of the PPFC was approximately constant along its length. The aspect ratio at the working section, $\alpha \approx 40$ (defined as $\alpha = w/h$, where w is the channel width and h is the height) helped to ensure flow uniformity at the working section and, thus, a parallel flow (Avari et al. 2016).

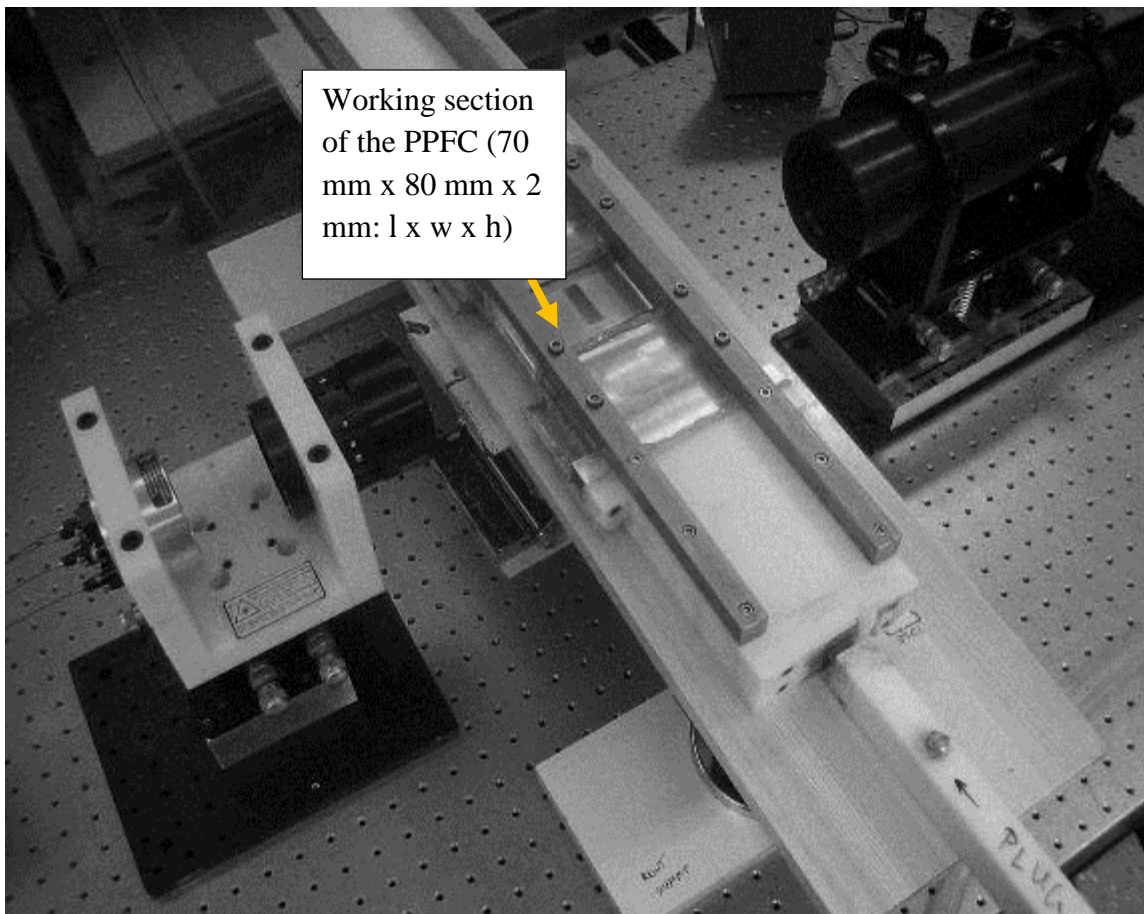


Fig. 1A-6 Initial hemodynamic flow facility showing the PPFC and the new near-wall LDV system. The LDV system shown was used in a forward-scatter configuration. A pulsatile pump from Shelley Medical Imaging Technologies was used with all experiments. The pump connected to the PPFC via flexible tubing.

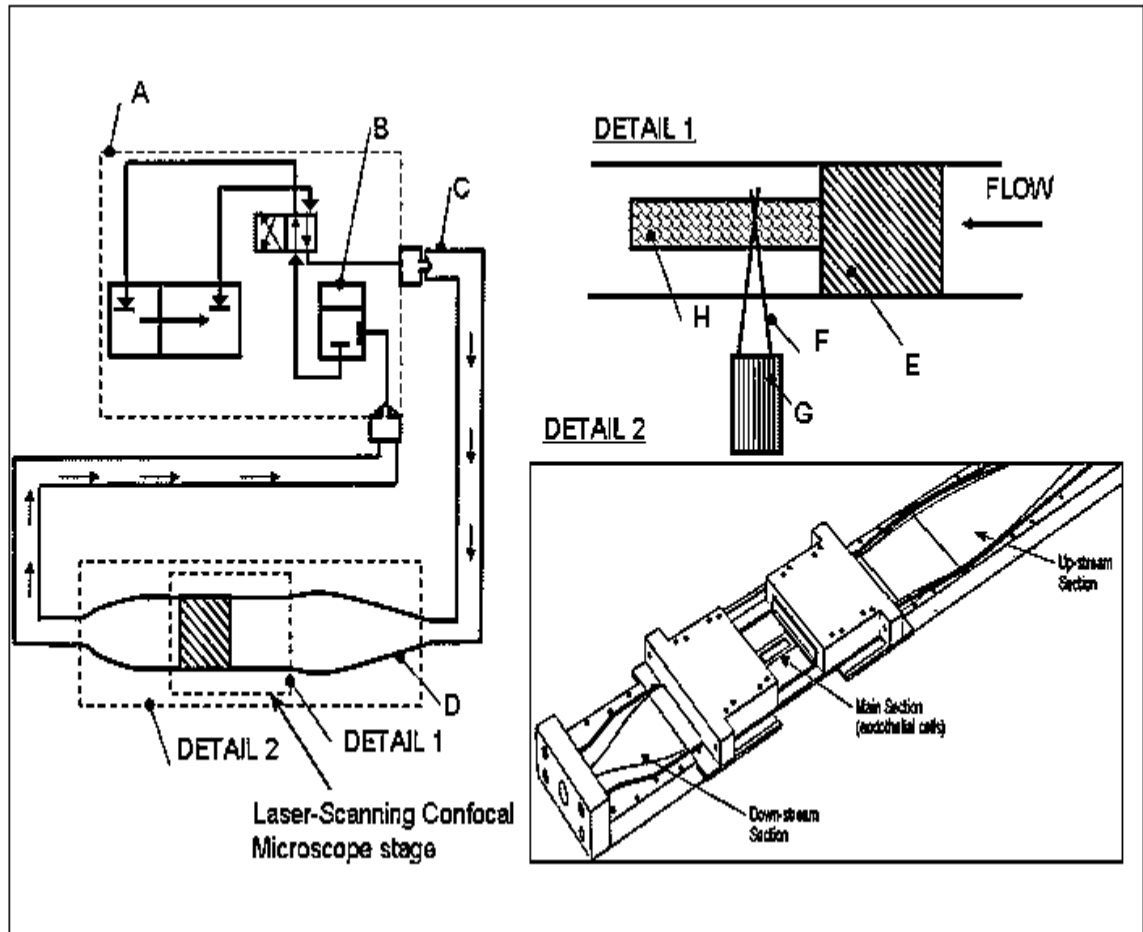


Fig. 1A-7. Technical drawing of hemodynamic flow facility and the plan view of the integrated system. (A) Pulsatile pump module with a direct 2 position solenoid valve. (B) Pump reservoir with a 4L capacity (C) Insulated Plastic tubing. (D) Contoured section. (E) Stenosis modeling flow obstruction. (F) LDV laser beams. (G) Near-wall LDV system. (H) Working section (cultured live endothelial cells on a glass cover slip).

To measure steady and pulsatile laminar flow at the working section, the near-wall LDV system was used in the forward-scatter mode. The LDV system was only used to measure the u-component of the velocity vector. This is because the green beams (the top transmitting green beam) could not penetrate into the PPFC as a result of unsuitable optical window geometry. It should be noted that the v-component was measurable at one single point inside the PPFC (very close to the wall, approximately 100 μm). However, due to the beam spacing of 25 mm (between the two green beams) and the resulting beams' half-angle, regions away from the wall could not be measured. Although this finding provided sufficient justification for the eventual re-design of the PPFC, the author continued with

the validation of the fluid mechanics to gain as much insight as possible into its suitability for this work.

Streamwise velocity, $\bar{u}(y)$ and spanwise velocity, $\bar{u}(z)$, were captured by spatially fixing the PPFC and precisely moving the LDV system in pre-determined steps. In terms of the streamwise velocity profile, $\bar{u}(y)$, the step size was chosen based on the measurement volume diameter and was set to 50 μm . For the steady and pulsatile velocity measurements reported in this section, water was used as a recirculating fluid. The temperature of the recirculating water was 21 ± 1 $^{\circ}\text{C}$ with a reported density of 998 kg/m^3 and dynamic viscosity of 1 mPa s (Oates, 2001). With all measurements, TiO_2 was used to seed the recirculating water. Details concerning TiO_2 , such as the mean particle diameter and the seeding concentration are reported in Chapter 3 of this thesis (experimental apparatus and methods) and, hence, will not further be discussed in this section. For velocity profiles, $\bar{u}(z)$, the step size was approximately 4 ± 1 mm and the first velocity measurement was captured approximately 4 mm away from the side wall (LDV probe side). The $\bar{u}(z)$ profile was only evaluated along the half-width of the PPFC (given that the steady laminar flow inside a two-dimensional channel is statistically symmetric), which yielded approximately 10 measurement points. All reported measurement locations were obtained from a dial reading on the 3-axis micron-precision traverse unit (3-Axis NanoMax Stage with Differential Adjusters) and/or an accurate steel rule. The traverse was used as a means of accurately ($\pm 1.0 \mu\text{m}$) moving the probe (and, hence, the measurement volume) along the y-axis. The steel rule was mounted to a precision slide-track, which itself attached to the probe. The track was used to move the probe (± 1 mm) along the x- and z- axes. Hence, the traverse and the track were both essential elements in spatially evaluating the flow. Fig. 1A-8 shows the geometry of the working section. The origin was placed on the centre of the microscopy slide (at $x = 0, z = 0$), and at the centre with respect to the channel height ($y = 0$). Measurements captured in all three directions were referenced from this origin.

For the steady laminar flow, the Reynolds number was defined as $\text{Re} = (QD_h)/\nu A$, where $D_h = 2h = 4$ mm (hydraulic diameter), $\nu = \mu/\rho$ is the kinematic viscosity of water, and $A = wh$ is the cross-sectional area of the working section (Koslow et al. 1986; Viegas et al. 2011). The average channel velocity (i.e. bulk velocity) $U = Q/A$ (bulk velocity) was

calculated from the velocity profiles at the centre of the working section ($x = 0, z = 0$). The flow rates, Q , under test were 5, 10, and 20 mL/s. The corresponding Re values were 125, 250 and 500 respectively. These Re numbers ensured a laminar flow since Patel & Head (1969) showed that flow is laminar for $Re < 1350$ inside a two-dimensional channel flow (with h used as a characteristic length scale in calculating Re).

Fig. 1A-9 shows the measured and normalized streamwise velocity, \bar{u}/\bar{u}_{\max} , plotted across the channel height. The y-axis was normalized against the channel half height, $2y/h$. The volumetric flow rate was $Q = 10$ mL/s. In reference to Fig. 1A-8 (working section of the PFFC), velocity profiles were captured at both $x/l \approx 0$ and $x/l \approx 0.35$. Given that the length of the working section was approximately 70 mm, $x/l \approx 0.35$ yields approximately 24 mm downstream from the origin. Two measurement locations were selected to validate that the flow was fully developed ($\partial\bar{u}/\partial x \approx 0$) at the working section. The maximum difference, $\Delta = \bar{u}_{x/l \approx 0} - \bar{u}_{x/l \approx 0.35}$, was 0.003 m/s which was within the range of the LDV spurious r.m.s. velocity (reported below). Based on this finding it was concluded that the flow was fully developed at the working section of the PFFC. The theoretical velocity profile for $Q = 10$ mL/s was also plotted in Fig. 1A-9 to compare with the measured velocity profile. The theoretical (assuming 2D flow, whereby there is no sidewall effects) streamwise mean velocity profile, $\bar{u}(y)$, was computed from the well-known laminar flow theory (White, 2009) and defined as $\bar{u}(y) = 3Q/2wh(1 - 4y^2/h^2)$. The theoretical streamwise velocity profile was also normalized against the maximum velocity, \bar{u}_{\max} . In addition, Fig. 1A-10 shows measured \bar{u}/\bar{u}_{\max} plotted against the theoretical \bar{u}/\bar{u}_{\max} for all six measured data sets; that is, at $x/l \approx 0$ and $x/l \approx 0.35$ for $Q = 5, 10, \text{ and } 20$ mL/s. For clarity, all six measured and normalized data sets were plotted on one axis against theoretical values at the corresponding y-position. The measured velocity profiles were captured in 50 μm increments (across the upper and lower channel half-height) in reference to the origin ($y = 0$) which corresponds to \bar{u}_{\max} . For reference, the \bar{u}_{\max} measured for the $Q = 5, 10, \text{ and } 20$ mL/s were approximately 0.050, 0.110, and 0.200 m/s, respectively. Fig. 1A-10 shows better agreement with the theory in the range, $0.6 < \bar{u}/\bar{u}_{\max} < 1.0$, corresponding to larger velocities. The fixed r.m.s. velocity of 0.003 m/s (reported below) was more significant near the wall, where the mean velocity (time-averaged) was smaller. Fig. 1A-9 reports a

maximum difference between the theory and measurements, $\Delta\bar{u}/\bar{u}_{\max} \approx 0.01$ in the range, $0 < 2y/h < 0.55$, whereas the maximum difference, $\Delta\bar{u}/\bar{u}_{\max} \approx 0.04$ is in the range, $0.55 < 2y/h < 1.0$. Hence, at relatively larger velocities (near the centre of the channel), the LDV measurements were in better agreement with the theory.

This section does not report experimental wall shear stress since wall datum identification (closest measurement point to the wall) was not completed. Rather, the measurement point location inside the working section (along the y –direction) was established based on detecting \bar{u}_{\max} at $2y/h \approx 0$. A detailed overview on the determination of the measuring position relative to the wall (coupled with the uncertainty of the traversing system) is discussed in Chapter Four (uncertainty Chapter). Determination of measurement point position close to the wall was completed for LDV measurements inside the final-revision PPFC (Chapter Three). Using $\tau_w = 6\mu Q/(wh^2)$ to compute wall shear stress (White, 2009), yields 0.937, 1.875, 3.750 dyne/cm² for $Q = 5, 10$ and 20 mL/s, respectively. The shear stress values computed were in the lower end of the range that is reported in the human venous system (1 to 6 dyne/cm²) and not in the range of that reported in the arteries (10 to 70 dyne/cm²; Chiu & Chien, 2011). Since the PPFC would have eventually been used to study EC response to flow, it was expected that the calculated shear stresses would have been even lower since the dynamic viscosity of the cell fluid (typically reported in the literature; Avari, 2015) is 0.737 ± 0.0012 mPa·s ($\approx 75\%$ of μ for water at $\approx 21^\circ\text{C}$).

As noted earlier, the spanwise velocity, $\bar{u}(z)$, was also evaluated along the channel half width ($w/2$) to better understand the extent of flow uniformity along the width of the PPFC at the working section. The PPFC was manufactured to 80 ± 0.2 mm (manufacturer reported) to ensure uniform shear loading across the microscopy slide. Fig. 1A-11 shows $\bar{u}(z)$ plotted against the channel half width for $Q = 5, 10$, and 20 mL/s. A theoretical prediction (see Eq. 3-4 in the experimental methods Chapter) based on work by Purday (1949) and Natarajan and Lakshmanan (1972) was also plotted to compare to the measured spanwise profiles. The experimental and theoretical data are in good agreement with the maximum error of approximately 6% at $Q = 20$ mL/s. It was found that approximately 90% of the channel half width is exposed to uniform flow ($0 < z/w < 0.45$). Given that

the microscopy slide (flush-mounted) was approximately 22 mm wide, the ECs would have been exposed to uniform shear stresses.

To evaluate the imprecision (random error) of the velocity measurements (and, hence, the LDV spurious system noise), the streamwise velocity was measured at the working section of the PPFC under a steady laminar flow. These measurements revealed sources of measured velocity fluctuations not related to turbulence. For the streamwise velocity measurements inside the PPFC (at the working section, $x/l \approx 0$, $z/w \approx 0$), the velocity was captured at various measurement locations away from the wall and at various flow rates whilst maintaining a steady laminar flow. In all cases, the r.m.s. velocity did not fall below 0.003 m/s (3 mm/s) and, thus, any value below this was considered insignificant. For example, at $Q = 5$ mL/s, the r.m.s. velocities divided by the local mean velocities of 5-7% and 9-42% were detected based on measurement points away from (near the centre region, $2y/h \approx 0$) and in proximity to the wall (within 400 μm), respectively. It should be noted that as the velocity increases the fixed r.m.s. velocity of 0.003 m/s becomes less significant. Similar studies by Kehoe (2001) and Avari (2015) reported fixed r.m.s. velocities of 0.02 m/s and 0.0025 m/s, respectively. In both of these studies LDV was used to measure the streamwise velocities near a wall. Work by Avari et al (2016) is a more applicable reference for the study reported here since the LDV measurements were captured near a wall inside a PPFC of similar height (≈ 1.8 mm). Similar measurement errors were expected since both channels had approximately equal channel heights and similar confined geometries (an increase in wall reflections generates more noise). The larger error at the wall is generally the result of both an increase in light scatter from the wall and reduced time-averaged mean velocity; the latter results in a larger ratio between the fixed r.m.s. velocity and the local mean velocity at the wall.

According to Iyer & Woodmansee (2005), the variance in the velocity mean (first moment statistics) can be defined as $\sigma_{\bar{u}} = \sigma/\sqrt{N}$, where $\sigma = \text{r. m. s. } u'$, and represents the variance in the velocity measurements as a result of the LDV system. For this study, $N \approx 5000$ (number of velocity realizations) was selected to ensure a statistically stationary mean value. Using $\text{r.m.s. } u' \approx 0.003$ m/s, the estimate of the standard deviation of the mean was approximately ± 0.00004 m/s (0.04 mm/s). The random uncertainty (precision error) in the

velocity mean is determined from $P_{\bar{u}} = \pm t\sigma_{\bar{u}}$ where $t = 2$ (confidence level of 95%, Wheeler & Ganji, 2004). Hence, for this study the random uncertainty was ± 0.00008 m/s (0.08 mm/s). In relation to the velocity measurements inside the PPFC at $Q = 5$ mL/s, the 95% confidence limit on the r.m.s. velocity (as a result of the LDV system) is $\approx 0.1\%$ \bar{u}_{\max} , where \bar{u}_{\max} was 0.105 m/s. The LDV biases (i.e. velocity, angle, gradient biases) were considered negligible in this section and discussed in detail with an in-depth uncertainty analysis in Appendix 2 and Chapter Four.

This section does not report the uncertainty of the measured mean velocities as a result of the measurement volume position uncertainty. The total variance of the mean velocity from both the precision and the measurement volume position uncertainty is discussed in the uncertainty Chapter of this thesis (Chapter Four).

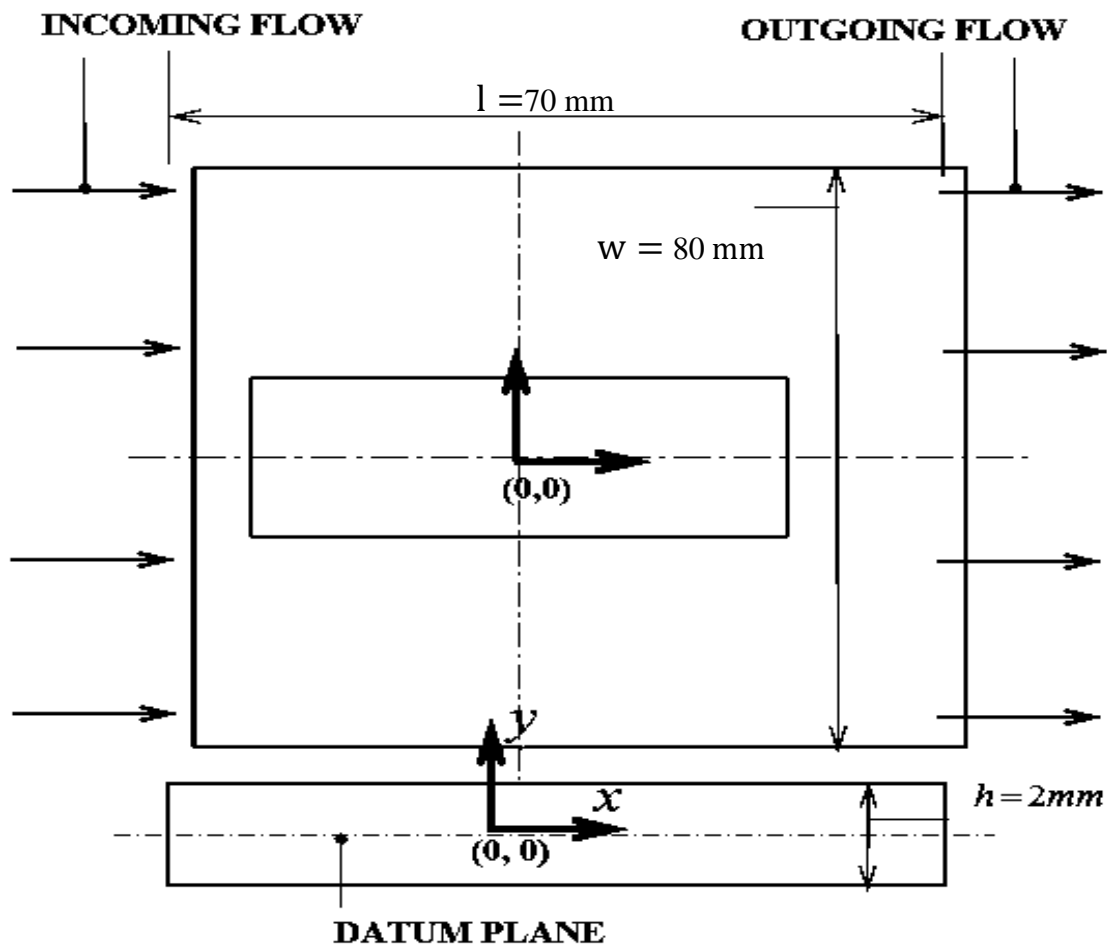


Fig. 1A-8 Working section geometry of the PFC. The working section was 70 mm long, 80 mm wide and 2 mm in height. The origin was placed at the centre of the microscopy slide.

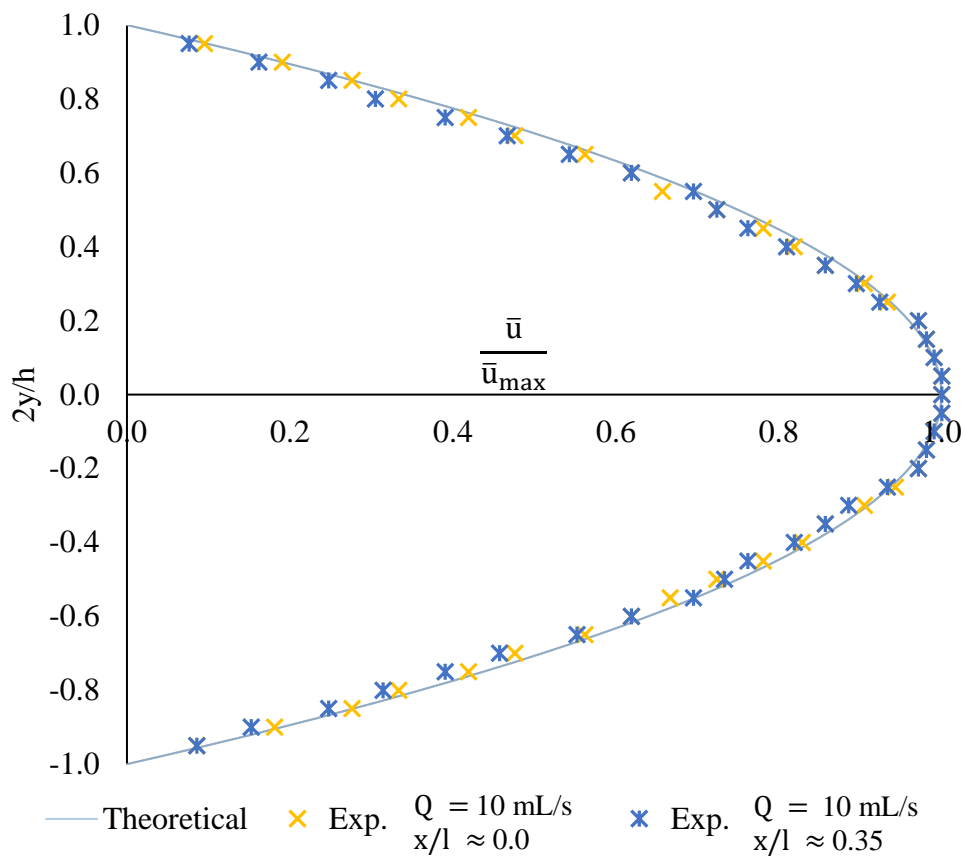


Fig. 1A-9 Theoretical vs. Experimental normalized streamwise velocity profile at the working section of the PPFC under steady laminar flow. The streamwise velocity was normalized against the maximum velocity of the profile. The volumetric flow rate at test was $Q = 10 \text{ mL/s}$. The error bars are not shown since the uncertainty is relatively small as a result of the large sample size ($N \approx 5000$) based on $\sigma_{\bar{u}} = \sigma/\sqrt{N}$. For reference, the precision uncertainty was $\pm 0.00008 \text{ m/s}$ (0.08 mm/s) based on 95% confidence interval.

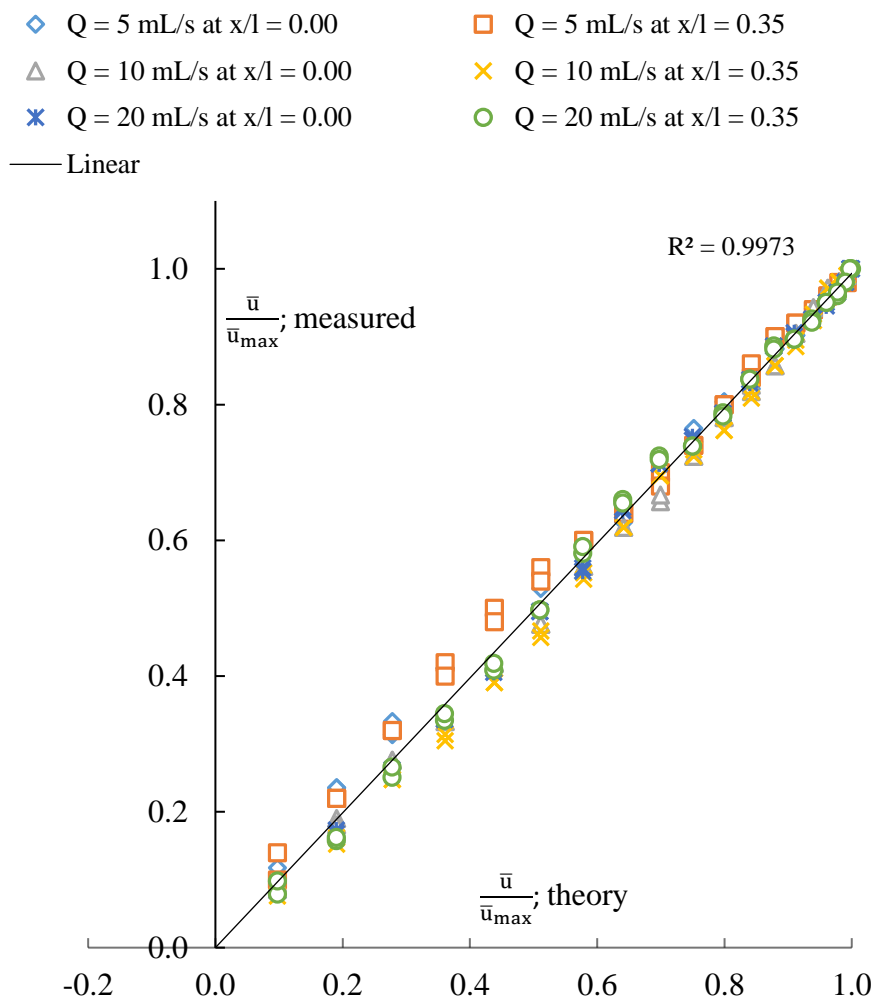


Fig. 1A-10 Theoretical vs. Measured scatter plot. The theoretical and measured streamwise velocities were normalized against the maximum velocity for each profile. The normalized data were plotted for all six measured sets on one axis against theoretical values at the corresponding y-position based on a fully developed flow profile. The theoretical velocity values were calculated at every 50 μm across the 2 mm channel. The 50 μm steps were chosen based on the step-size of the LDV system.

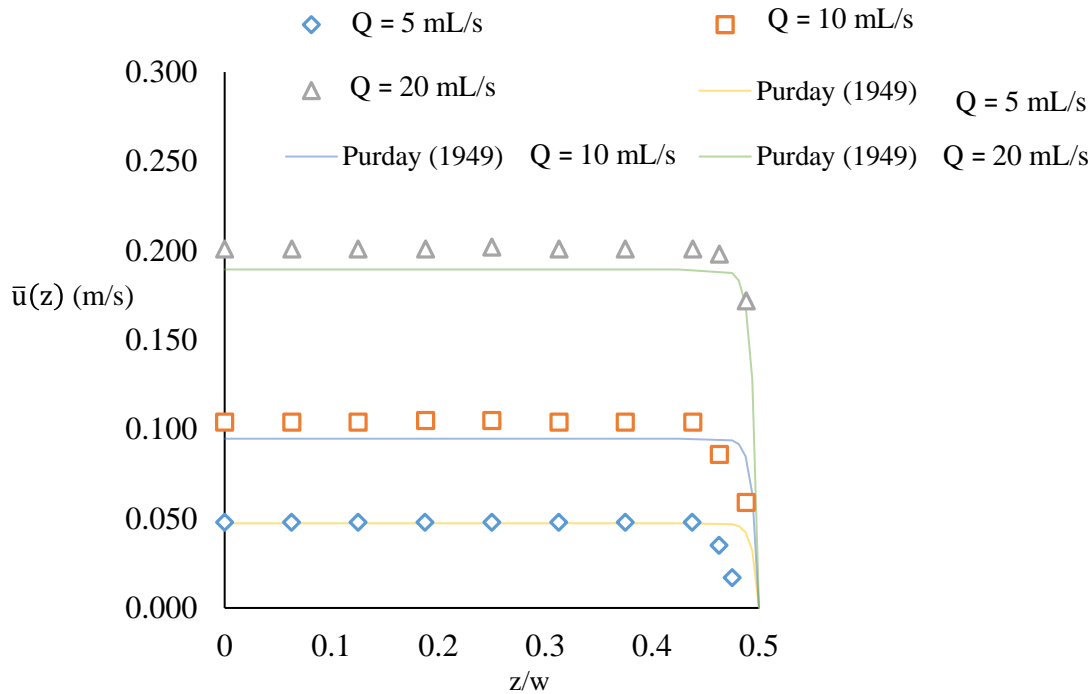


Fig. 1A-11 Theoretical vs. Measured streamwise velocity $\bar{u}(z)$. Reported data were computed/measured across the channel half width at $x/l = 0$ and $2y/h = 0$. The x -axis was normalized against the channel width of 80 mm. The aspect ratio of the channel was $\alpha = 40$. The flow rates at test were $Q = 5, 10, \text{ and } 20$ mL/s. The error bars are not shown since the uncertainty is relatively small as a result of the large sample size (N) based on $\sigma_{\bar{u}} = \sigma/\sqrt{N}$. For reference, the precision uncertainty was ± 0.00008 m/s (0.08 mm/s) based on 95% confidence interval.

To evaluate actual waveform shapes at the working section and to simulate the hemodynamic loading of realistic physiological environments, the time-varying streamwise velocity, $u(t)$, was captured at the origin over 10 pulse cycles. The bin size was determined based on the minimum number of LDV realizations (number of data points per bin) to ensure statistical accuracy. Statistical accuracy was defined by ensuring that statistical moments were independent of bin size. Each pulse cycle was separated into 46 bins (i.e. $f = 1$ Hz corresponds to bin width of 22 ms). Given the typical data rate at the centre of the channel ($2y/h \approx 0$) was $\dot{N} = 1000$ Hz, data were acquired over 10 pulse cycles at an average of approximately 220 velocity realizations per bin. In a similar study by Kehoe (2001), 10 pulse cycles were also found to be adequate, providing 80 velocity realizations per bin with an average data rate of 600 Hz. In addition, to ensure that the flow was laminar during various phases of the pulse cycle, the r.m.s. velocity was evaluated and showed to be within the experimental uncertainty (precision error).

Streamwise velocities which occurred over the same fraction of several cycles were phase-averaged (average over a large number of ensemble having the same phase) using the following instantaneous velocity decomposition method (Kehoe, 2001):

$$u = U + \tilde{u} + u' \quad \langle u \rangle = U + \tilde{u} \quad (1A-1)$$

where u is the u –component of the instantaneous velocity, U is the time-averaged bulk velocity, \tilde{u} is the periodic bin-average velocity, $\langle u \rangle$ is the phase-averaged streamwise velocity, and u' is the turbulent fluctuation of the velocity.

The normal carotid artery was studied due to its relevance in human plaque build-up and strokes (Ryval et al. 2004). Three pulse cycles were simulated with a peak flow rate (Q_{\max}) of 35 mL/s and a mean flow rate (\bar{Q}) of approximately 10.7 mL/s. The pulse frequencies, f , under tests were 0.3 Hz, 0.5 Hz, and 1 Hz corresponding to cycle periods, T , of approximately 3.3s, 2s, and 1s, respectively. The frequency of 1 Hz was specifically important since it represents the average heart rate in humans (Oates, 2001). The other frequencies were simulated to evaluate the interaction between viscous and inertial effects on the waveform shapes at the working section. At this point it was not relevant to study

spanwise waveform distortion or time-varying shear stress at the wall. Rather, it was relevant to evaluate the ability of the PPFC to simulate realistic waveforms at the working section. For a two-dimensional pulsatile channel flow, the Womersley number can be defined as $Wo = h\sqrt{\omega/\nu}$ (Oates, 2001), where $\omega = 2\pi f$ (f is the frequency in cycles) and ν is the kinematic viscosity of the fluid. According to Gundogdu & Carpinlioglu (1999), Wo is a critical modeling parameter that defines the interaction between the viscous and inertial effects and, has an important influence on the streamwise velocity profiles. As an example, Muto & Nakane (1980) performed experiments inside a pipe under a pulsatile laminar flow and found that the flow profiles varied in shape from the parabolic shape (as in steady laminar) to a plug-like shape (rectangular-like shape) as Wo increased from 0 to 5.0.

For this study, Wo was 2.7, 3.5, and 5.0 at $f = 0.3, 0.5,$ and 1 Hz, respectively. Given that the channel height of 2 mm was fixed, varying Wo was achieved by adjusting the pulse frequency of the normal carotid waveform. According to work by Campbell et al (2012) in patient-specific internal carotid arteries (ICA), Wo ranged from 3.30 to 4.69 (mean value was 4.07 ± 0.45). This is in good agreement with the reported $Wo \approx 4.2$ (resting heart rate) by Oates (2001). Hence, the modeling parameter Wo in this study was in the physiological range.

In addition, according to Truskey et al (2010), the average Re for the common carotid artery is 400. Filatova et al (2014) also noted that inside the internal carotid artery (ICA) the range, $613 \pm 134 > Re > 227 \pm 150$, is typical and depends on other factors such as age and sex. In this study and suggested by Oates (2001), Re_{PSV} (peak systole velocity calculated from the measured and phase-averaged maximum velocity during the systole phase) at the origin ($x = 0, y = 0, z = 0$) of the working section and at $f = 0.3$ Hz, $f = 0.5$ Hz, and $f = 1$ Hz was 270, 245, and 170, respectively. For a better understanding between the systolic and diastolic phases of the pulse cycle, Oates (2001) suggested dividing them into two phases. The first phase of the pulse cycle is systolic, whereby there is a large increase in flow (for normal carotid, it is followed by a sharp decrease) and the second phase is diastolic (which describes the remainder of the pulse cycle and occurs as a result of the

aortic valve closing and ventricles refilling). For the ideal normal carotid waveform shown in Fig. 1A-12, the systolic phase range is, $0.40 > t/T > 0$, whereby t is the cycle time and T is the period of the cycle (Oates, 2001). According to Oates (2001), $Re_{PSV} > 200(Wo)$ can be used to predict the initiation of a flow disturbance during the systole phase of the cycle. For example, in the normal carotid artery, $Re_{PSV} \approx 1700$ and $Wo \approx 4.2$ suggest intermittent turbulence during the systole phase of the cycle since $Re_{PSV} \approx 1700$ is larger than $200(Wo) \approx 840$. In this work, $Re_{PSV} < 200(Wo)$ at $Wo \approx 5.0$ and, hence, the flow was considered to be laminar during the entire pulse cycle.

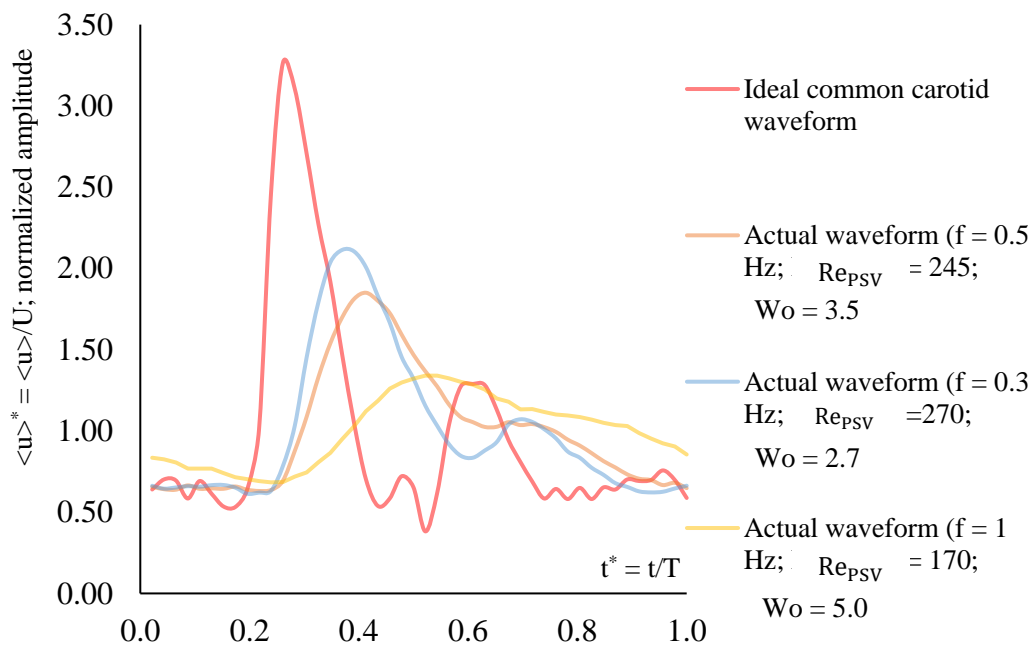


Fig. 1A-12 Ideal versus actual velocity waveforms at the working section of the PPF. The ideal common carotid waveform was provided by the pulsatile flow pump. The x-axis was normalized with the cycle period, T , whereas the y-axis was normalized with the cycle mean velocity (U).

Fig. 1A-12 shows the normalized phase-averaged streamwise velocity, $\langle u \rangle^* = \langle u \rangle / U$, for the three measured waveforms at the working section. The normalized cycle time, $t^* = t/T$, is plotted on the x-axis where T represents the cycle period. An ideal profile of the normal carotid waveform (Q data points extracted from the pump software) was also plotted in Fig. 1A-12. The volumetric flow rate data points were converted to the spatially-

averaged time-varying velocity by $u(t) = Q(t)/A$. In addition, $u(t)$ was normalized against U (cycle mean) to compare the waveform shape and amplitude against the three measured waveforms. The ideal normal carotid waveform represented the actual waveform inside the body and that which was found at the pump outlet. All three measured normal carotid waveforms demonstrated substantial damping at the working section with a peak $\langle u \rangle^*$ of approximately 2.2, 1.8, and 1.3 at $f = 0.3, 0.5,$ and 1 Hz, respectively. In addition, the second flow peak (during the diastolic phase of the cycle) which is observed with the ideal waveform (at $t^* \approx 0.60$) is not apparent in the three measured cases. There is an evident phase-shift between the ideal and the measured waveforms; that is, the maximum $\langle u \rangle^*$ occurs at $t^* \approx 0.28, 0.38, 0.42,$ and 0.52 for the ideal, $f = 0.3, f = 0.5,$ and $f = 1$ Hz waveforms, respectively. For the $f = 1$ Hz case there is a phase-lag of about $\Delta t^* \approx 0.24$ (at maximum $\langle u \rangle^*$) in comparison with the ideal waveform. There is also an amplitude difference of about $\Delta \langle u \rangle^* \approx 1.25$ between the two waveforms (peak to peak during the systolic phase of the cycle). Both the phase lag and the decrease in amplitude of the measured waveforms resulted from waveform damping. It was hypothesized that both the effect of the lateral walls (inside the PPFC) and the distance between the pump and the working section ($k/l \approx 15$, where k is the distance from the pump outlet to the working section of the rig) were contributors to waveform damping.

According to Oates (2001), the energy in a pulsatile waveform can be defined as $W = Q(t)^2 Z$, where Z is the characteristic impedance and is defined as $1/A\sqrt{\rho E t/2r}$. Note that A is the cross-sectional area of the vessel, E is the elastic modulus, t is the wall thickness and r is the vessel radius. According to Oates (2001), the characteristic impedance is a measure of the response in flow to the applied pressure and is not a function of the waveform shape but rather the properties of the vessel. Hence, the energy in a pulsatile waveform is proportional to the square root of its amplitude. Oates (2001) noted that this waveform energy is associated with the harmonic components and that the energy associated with the mean fluid flow (zero-frequency component) is described by the mean pressure and kinetic energy, $0.5\rho U^2$. Oates (2001) further observed that waveform attenuation is a function of the following: (1) viscous losses, (2) visco-elastic losses (wall compliance) and (3) inertial energy losses as a result of change in velocity direction and/or

magnitude ($\Delta E = k \frac{1}{2} \rho \Delta u^2$). It should be noted that k is a constant representing the energy loss associated with a change in velocity. Oates (2001) also noted that attenuation of a waveform increases as the frequency of the wave increases and, thus, high harmonics will experience larger attenuation. The latter is in good agreement with the work from Loudon & Tordesillas (1998) which provided an exact mathematical solution for an unsteady flow resulting from a sinusoidally-applied pressure gradient between two parallel plates. The authors derived the solutions for the velocity, volume flow rate and the velocity gradient (at the wall) and demonstrated that the analytical solution provided identical fluid behaviour to that of the flow through a cylindrical tube (for $Wo < 1$ and $Wo > 1$). Their work showed that an increase of Wo through an increase of f (at a fixed h) results in both a phase-shift and amplitude change, whereas an increase in Wo through an increase in h (at a fixed f) increases the amplitude until some critical Wo value. They have also noted that this critical Wo value depends on the channel location in the y -direction. According to Oates (2001), the decrease of amplitude at higher frequencies is a direct result of the flow not being able to follow the pressure wave; that is, the acceleration time is too short to bring the fluid to its maximum velocity before the pressure gradient changes sign.

For the reasons outlined above, it was hypothesized that the attenuation of the measured waveforms was a function of wall compliance (elasticity), viscous dissipation, and inertial energy losses. Since the walls of the PPFC were rigid (stainless steel and delrin plastic), the energy losses associated with wall compliance were negligible and not considered. However, the flexible tubing that connected the pump and the PPFC was considered as a possible source of damping and, thus, was minimized in length to reduce the damping effect. Given the overall large length of the PPFC (≈ 200 mm) it was difficult to connect the pump directly to the inlet of the rig to avoid using any flexible tubing. The viscous energy losses associated with the waveforms were a direct result of the viscosity of the fluid and the overall long upstream section (≈ 100 mm) of the PPFC. It can be seen from Fig. 1A-12 that waveforms of higher frequencies are more rounded and damped with the lower frequency components predominating the flow. This was most likely caused by the flow not being able to follow the rapid changes in pressure and, due to larger inertial energy losses as explained by Oates (2001). To quantify the degree of damping of a given

waveform, Oates (2001) suggested using the systolic rise time (SRT) parameter and the pulsatility index (PI). This is because according to Oates (2001), damped waveforms exhibit a rounded profile and relatively longer SRT. As an example, Oates (2001) noted that most normal arteries SRT is in the range of 60-90 ms whereas for damped waveforms, $SRT > 120$ ms.

In this study and at the physiological frequency of 1 Hz, PI and SRT were $\Delta \langle u \rangle^* \approx 0.65$ and $\Delta t^* \approx 0.27$, respectively. In the latter statement, $\Delta \langle u \rangle^*$ is referring to the difference between the maximum and minimum $\langle u \rangle^*$ during the pulse cycle. The systole rise time of $\Delta t^* \approx 0.27$ can be explained as the rate at which $\langle u \rangle^*$ changes (and reaches maximum velocity) during the systolic phase of the cycle. According to Oates (2001), both of these parameters provide a quantitative measurement of the waveform damping. For an ideal normal carotid waveform, the PI and SRT were $\Delta \langle u \rangle^* \approx 2.8$ and $\Delta t^* \approx 0.05$, respectively. The $\Delta t^* \approx 0.05$ corresponds to $t \approx 50$ ms (based on $T \approx 1000$ ms) which according to Oates (2001) is considered to be a normal waveform without damping characteristics.

To understand the next steps, both Wo and Re were used as modeling parameter indicators coupled with the outcome from Fig. 1A-12. According to Truskey et al (2010), both dimensional and dynamic similarity must be met between the experimental model and the original (*in-vivo* geometry and flow behaviour). For a pulsatile flow inside rectangular channels (*in-vitro*), Loudon & Tordesillas (1998) suggested that Re and Wo are acceptable parameters to evaluate the dynamic similarity of geometrically similar flows. For dimensional similarity to be met between an *in-vitro* channel flow and an *in-vivo* arterial flow, $D_h = 2h$ (hydraulic diameter) is an acceptable length (channel flow) scale proposed in the literature (Lightstone, 2014). Loudon & Tordesillas (1998) also noted that in order to make an association between unsteady fluid behaviour and the magnitude of Wo , the geometry and Re ranges need to be considered

1A.4.2 Determination of Next Steps Based on the Revision 2 Findings

In summary, there were three main factors that encouraged the author to proceed with revision 3 and re-design the PPFC. First, the wall shear stress that was calculated (using

the laminar flow theory) under a steady laminar flow was not in the physiological range ($\approx 5\text{-}20$ dyne/cm²). The latter was attributed to the relative small velocities at the working section of the PPFC. Second, the pulsatile waveform under a physiological frequency of approximately 1 Hz was not realistic in shape or amplitude and, hence, would have not exposed EC to realistic time-varying shear stress. Although $Wo \approx 5.0$ was in good agreement with the *in-vivo* normal carotid waveform value, the waveform did not have a realistic time-varying shape to expose ECs to realistic shear stress. In addition, the $Re_{PSV} \approx 170$ (at 1 Hz) was not in good agreement with physiological values for a normal carotid artery ($Re_{PSV} \approx 1700$ at 1 Hz). Third, the *v*-component of the velocity vector was not measurable inside the working section and, thus, it would not have been possible to fully characterize the flow field for a stenosed case (away from the wall in the shear layer developing from the backward-facing step). Finally, simultaneous EC work using the same PPFC (as reported with revision 1 and 2) performed by Horie (2009) demonstrated the following: (1) difficulty in maintaining a sterile environment inside the PPFC, (2) inability to maintain the pH level of the fluid inside the rig, (3) difficulty in EC forming junctions due to a relative large microscopy slide, (4) challenges associated with cell vitality (preserving life) for longer than a few hours (during the simulation) and, (5) challenges associated with assembly/disassembly of the PPFC which showed direct implications on initial cell vitality. The latter refers to preserving cell life inside the PPFC during the long assembly time (≈ 45 min). All of the reasons listed above necessitated the re-design of the early-stage PPFC, which is discussed in the subsequent section.

1A.5 Design of a New PPFC: Revision 3

To overcome the challenges listed in the previous section (1A.4.1), a revision 3 PPFC was designed and manufactured (“Revision 3”). The channel was a compact version (385 mm x 50 mm x 50 mm: l x w x h) of the original PPFC to allow for easy handling and set-up. The single-piece bottom cavity was manufactured out of stainless steel (316 SS) and the upper cavity was manufactured out of ULTEM plastic (tensile strength and density of the ULTEM plastic is 91.9-101 MPa and 1280 kg/m³, respectively). The ULTEM plastic was used due to its popularity in bioengineering research and its ability to withstand repeated autoclaving (> 100) cycles up to 170° C (Avari, 2015). The stainless steel cavity was

polished at the working section (lower wall) to provide a surface roughness of $\epsilon_s \approx 6.3 \mu\text{m}$ (reported by the manufacturer). Secondary operations such as honing and lapping were also performed to reduce surface roughness as much as possible to minimize and/or eliminate roughness effects on the flow. The surface roughness effects on the flow are discussed in Chapter Three of this thesis (experimental methods). Upon assembly of the PPFC, the upper and lower cavities formed an internal channel that was 2.5 mm in height and 12.5 mm in width (rectangular cross-section). The cross-sectional area was reduced to 31.25 mm² which was 80% less than that of the cross-sectional area (160 mm²) of the original PPFC. This was done to ensure relatively larger streamwise velocities at the working-section and thus, larger wall shear stresses. This ensured that Re and the wall shear stress were in the acceptable physiological range as reported in the literature. This is discussed further in the subsequent paragraphs. The Revision 3 PPFC also featured an optical window made of polished acrylic for both laser beam penetration of all four laser beams into the PPFC at the working section. The window also allowed for top-bottom imaging using an objective lens. An objective lens can be used to perform live cell imaging on inverted microscopes that would typically require the use of an upright microscope. The optical window wall thickness was limited to 3 mm in order to minimize laser beam distortion and refraction. There was a circular microscopy slide with a diameter of 12 ± 0.2 mm that was flush-mounted inside the bottom cavity. The thickness of the microscopy slide was $170 \pm 5 \mu\text{m}$. An adjustable (by height in the y-direction) backward-facing step was mounted upstream and adjacent to the microscopy slide to model an arterial stenosis (narrowing of the artery). The advantage of this design was that adjustments (step heights) could be made during LDV measurements without PPFC disassembly.

Furthermore, the PPFC had two pressure transducers (upstream and downstream of the working section) taps (1/4" NPT) to accommodate an industrial pressure transducer (0-25 psi from Omega). Thermocouple pin-holes were also machined to monitor the cell fluid temperature ($37 \pm 0.1^\circ\text{C}$) upstream and downstream of the working section. To seal the upper and lower cavities when assembled, an injection system was designed (as per Fig. 1A-13) which forced the sealant (Loctite 5810) into a runner system that extended across the entire length of the PPFC. The pulsatile flow pump connected to the PPFC (upstream section) with vinyl braided tubing ($\approx \text{Ø}6$ mm ID). A smooth transition loft was

incorporated into the upstream and downstream sections of the PPFC to ensure minimal flow disruption and, hence, a laminar flow at the working section. The purpose of the loft was to transition the flow from circular-to-rectangular geometry over a length of 25 mm.

The purpose of the revision 3 PPFC was: (1) to increase the streamwise velocity at the working section to that of the velocities measured in the original PPFC, (2) to ensure at least 60% of the span ($-0.6 < 2z/w < 0.6$) would be exposed to two-dimensional uniform flow ($\partial\bar{u}/\partial z \approx 0$), (3) to reduce the effects of viscous energy losses and, hence, waveform damping and, (4) to allow for easier handling and assembly/disassembly of the PPFC to ensure successful cell vitality testing. To evaluate the above design efforts, both steady and pulsatile flow measurements were carried out at the working section and are discussed in the below sections.

The image in Fig. 1A-14 shows the experimental set-up using a near-wall LDV system and the Revision 3 PPFC. The origin was placed on the centre of the microscopy slide ($2y/h = 0$, $z/w = 0$, $x/l = 0$), where x -, z -, and y - represented the streamwise, spanwise, and transverse (wall-normal) flow directions. The first set of experiments used the blue beams ($\lambda = 488$ nm) to measure the streamwise mean velocity, $\bar{u}(y)$ in order to evaluate the velocity profiles across the channel height. With all experiments, water was used and maintained at $21 \pm 1^\circ\text{C}$ with a reported density of 998 kg/m^3 and dynamic viscosity of 1 mPa s (Oates, 2001). A small amount of TiO_2 was used to seed the flow and, hence, capture velocity measurements with LDV. For each measurement point, $N \approx 5000$, which ensured a statistically stationary mean velocity. The data rate of $\dot{N} \approx 2000 \text{ Hz}$ was typical during velocity measurements for both steady and pulsatile flow cases.

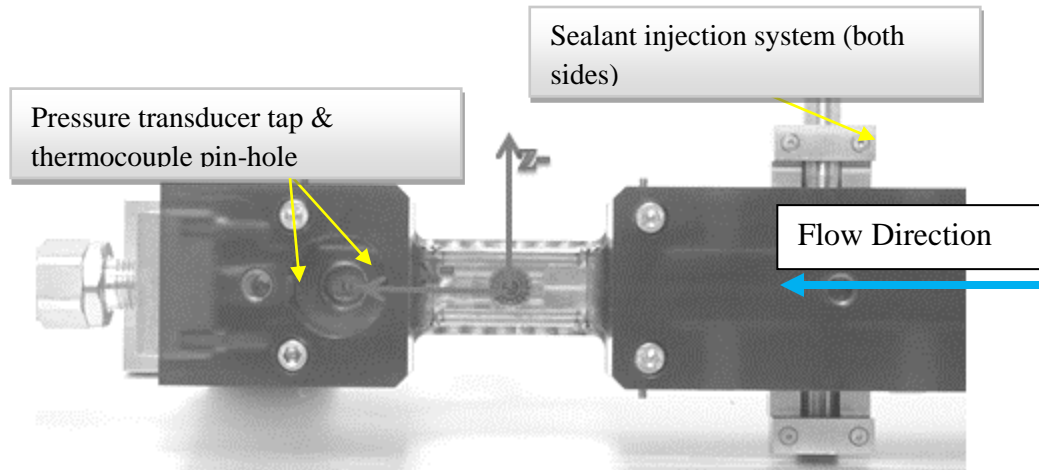


Fig. 1A-13 The newly designed and built PPFC (Revision 3). The working section was 12.5 mm in width 2.5 mm in height. The working section extended for approximately 70 mm. The envelope in terms of length, width and depth of the PPFC was 385 mm x 50 mm x 50 mm, respectively.

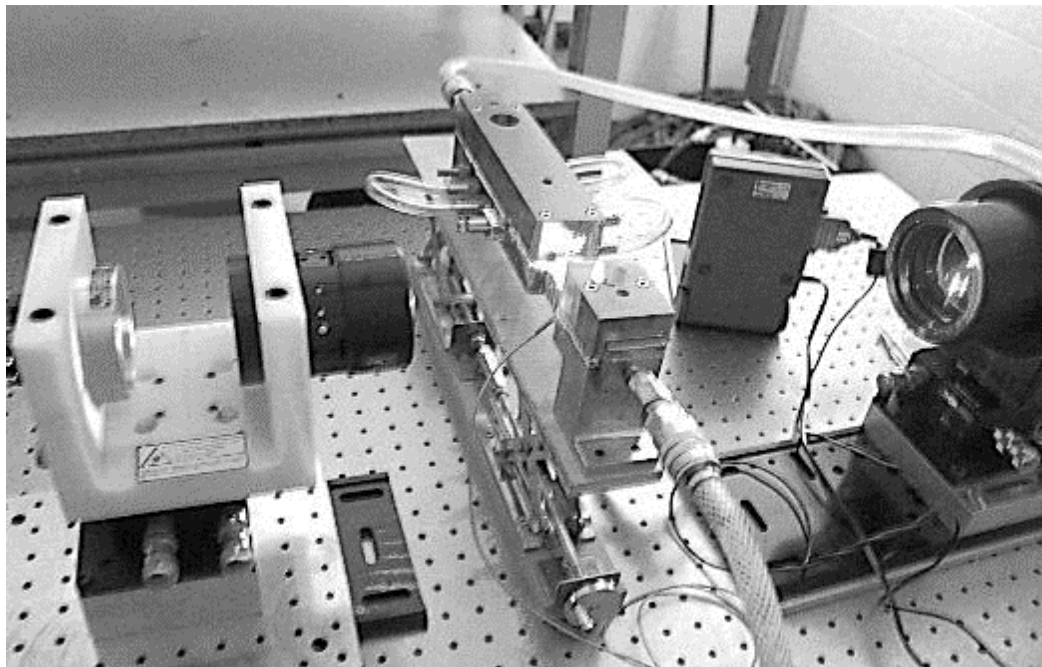


Fig. 1A-14 Velocity measurement set-up using the Revision 3 PPFC and the LDV system. The PPFC was connected in a closed-loop circuit with the Shelley Medical pulsatile pump. The PPFC was held by a mechanical jack to traverse in the y –direction until the laser beams were transmitted into the working section.

For steady laminar flow ($Q = 5 \text{ mL/s}$), Fig. 1A-15 shows the normalized streamwise mean velocity, \bar{u}/\bar{u}_{\max} , measured at the working section ($z/w \approx 0, x/l \approx 0$) which was plotted across the channel height. A velocity profile based on the channel flow approximation (see Eq. 3-4, Purday (1949)) was also plotted to compare with the LDV measurements. The approximate solution for the channel flow was computed based on $\beta \approx h/w = 0.2$. The streamwise mean velocity was normalized against the maximum velocity for both cases, the measured and the theoretical. The y-axis was normalized against the channel half-height, $2y/h$. The data points were captured every $60 \mu\text{m}$ across the channel height by keeping the PFFC stationary and traversing the LDV system as discussed in section 1A.4.1. The streamwise velocity measured at $2y/h = 0$ was $\bar{u}_{\max} \approx 0.270 \text{ m/s}$. In comparison with the velocity measurements inside the early-stage PFFC (section 3.4.1) under $Q = 5 \text{ mL/s}$, \bar{u}_{\max} was approximately 2.5 times larger. The Re value reported in this study was 1350, which was calculated based on $D_h = 2h = 5 \text{ mm}$ and the bulk velocity, U . Since $Re = 1350$, the flow was considered laminar inside the PFFC (Patel & Head, 1969). The theory for the channel flow and the measured velocities were in excellent agreement with the maximum difference of $\Delta \bar{u}/\bar{u}_{\max} \approx 0.0008$. Using the channel flow approximation to compute the wall shear stress (Eq. 3-7, Purday, 1949) yields $\tau_w \approx 4.43, 8.86$ and 15.36 dyne/cm^2 for $Q = 5, 10$ and 20 mL/s , respectively. These values correspond to the physiological range of shear stress (in the arterial vasculature) reported in the literature (Chiu & Chien, 2011). Given the relatively larger channel velocities at the working section, it was expected that there would be an increase in wall shear stress to those in the early-stage PFFC ($0.937, 1.875$ and 3.750 dyne/cm^2 for $Q = 5, 10$ and 20 mL/s , respectively). In addition, Fig. 1A-16 shows the measured and theoretical (channel flow approximation) spanwise velocity, $\bar{u}(z)$, plotted across the channel width. The z-axis was normalized against the channel half-width, $2z/w$. In terms of flow uniformity across the channel width, both the theory and LDV measurements are in good agreement since both demonstrate $\approx 50\%$ of the channel being exposed to uniform flow ($-0.5 < 2z/w < 0.5$).

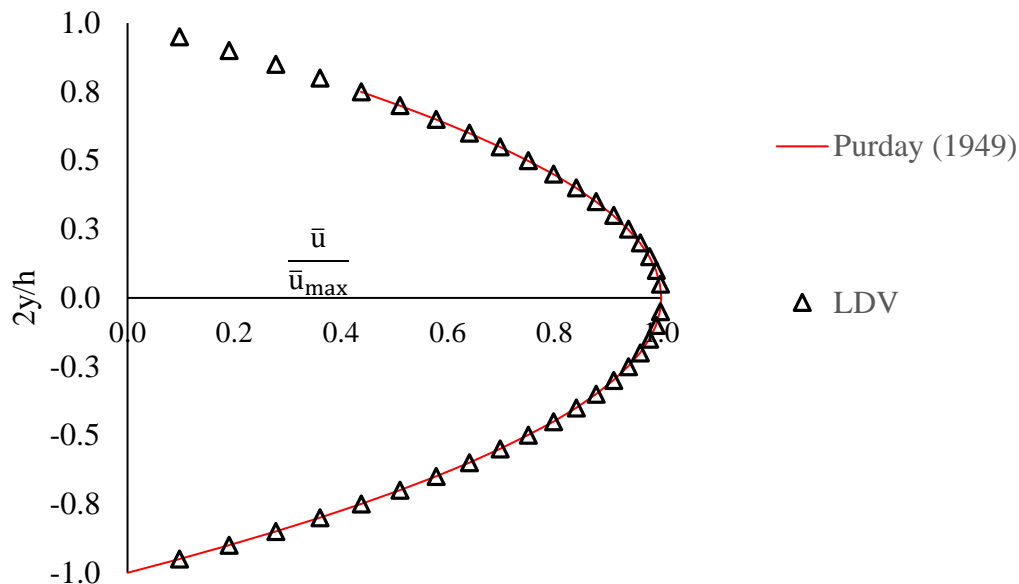


Fig. 1A-15 Normalized Streamwise velocity measurements versus normalized theoretical approximation for channel flow (Purday 1949). The velocity measurements were captured at $Q = 5$ mL/s. The y-axis was normalized against the channel half-height, $2y/h$.

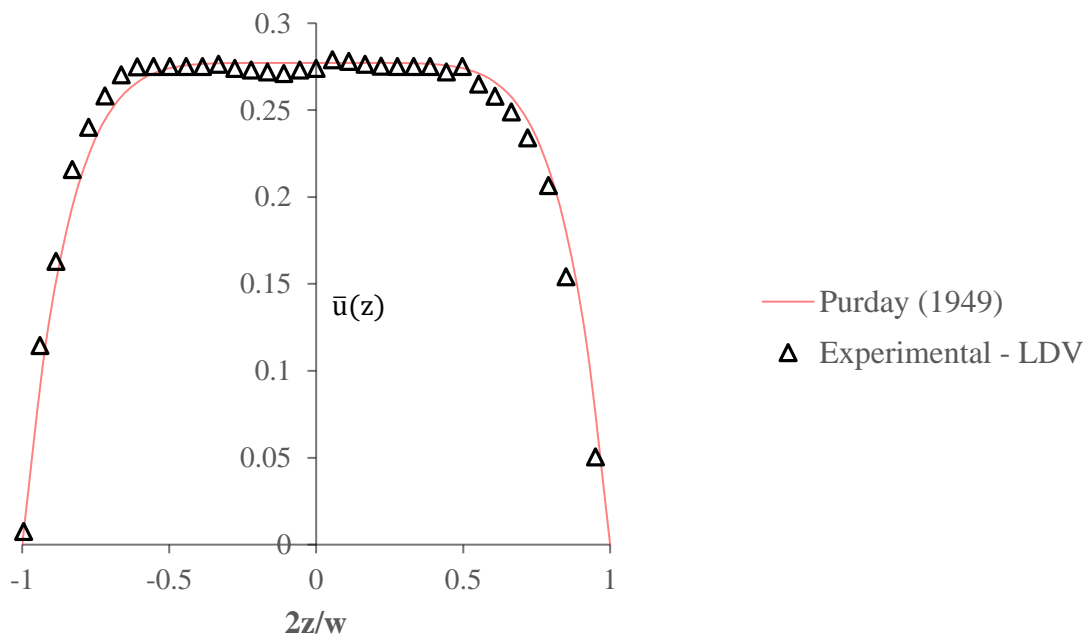


Fig. 1A-16 Spanwise velocity profiles, $\bar{u}(z)$, at $Q = 5$ mL/s: LDV measurements versus channel theory approximation (Purday, 1949).

To evaluate pulsatile laminar flow at the working section of the Revision 3 PPFC, the streamwise time-varying velocity was measured at three distinct locations near the wall. The flow rate used for this experiment was $Q = 5 \text{ mL/s}$ and the frequency of the pulse was 1 Hz. As reported in the previous section, $f = 1 \text{ Hz}$ corresponds to physiological conditions and, hence, was used to emulate *in-vivo* conditions. For information with respect to the data rate (\dot{N}), bin size selection, and the number of pulse cycles used during the velocity measurements, the reader should refer to section 1A.4.1. Since water was used with this experiment, the reported Re_{PSV} and Wo modeling parameters were 500 and 6.2, respectively. The Re_{PSV} modeling parameter was calculated based on the maximum velocity during the pulse cycle. Given that the waveforms were captured in the vicinity of the wall (within $200 \mu\text{m}$), Re_{PSV} was relatively lower than that at the centre of the channel ($2y/h \approx 0$). At the same time, $Wo = 6.2$, was slightly larger than compared to reported inside the normal carotid artery ($Wo \approx 4.2$, resting heart rate; Oates, 2001). The purpose of evaluating the waveforms at 3 distinct locations near the wall was to evaluate waveform damping effects when approaching the wall, and to assess whether the larger measurement error at the wall (r.m.s. u'/\bar{u}) affected the resolution of the waveform (shape structure). Fig. 1A-17 shows the normalized phase-averaged streamwise velocity, $\langle u \rangle/U$, for the three measured waveforms at the working section near the wall. The normalized cycle time, t/T , is plotted on the x-axis where T represents the cycle period. Also plotted in Fig. 1A-17 is the normalized phase-averaged streamwise velocity captured in the early-stage PPFC (refer to previous section 1A.4.1) at the centre ($2y/h \approx 0$). This waveform was also measured at $f = 1 \text{ Hz}$ and was plotted for comparison purposes. All three measured waveforms are in very close agreement with each other with a PI and SRT values of $\Delta\langle u \rangle/U \approx 2.25$ and $\Delta t/T \approx 0.11$, respectively. This is in much better agreement with the ideal normal carotid waveform, where the PI and SRT are $\Delta\langle u \rangle/U \approx 2.8$ and $\Delta t/T \approx 0.05$, respectively (Oates, 2001). As a review, the PI and SRT values of $\Delta\langle u \rangle/U \approx 0.65$ and $\Delta t/T \approx 0.2$, respectively were computed for the waveform measured inside the early-stage PPFC. Hence, through reduction of the cross-sectional area and the upstream length-to-working-section (Revision 3 PPFC), damping effects were significantly reduced.

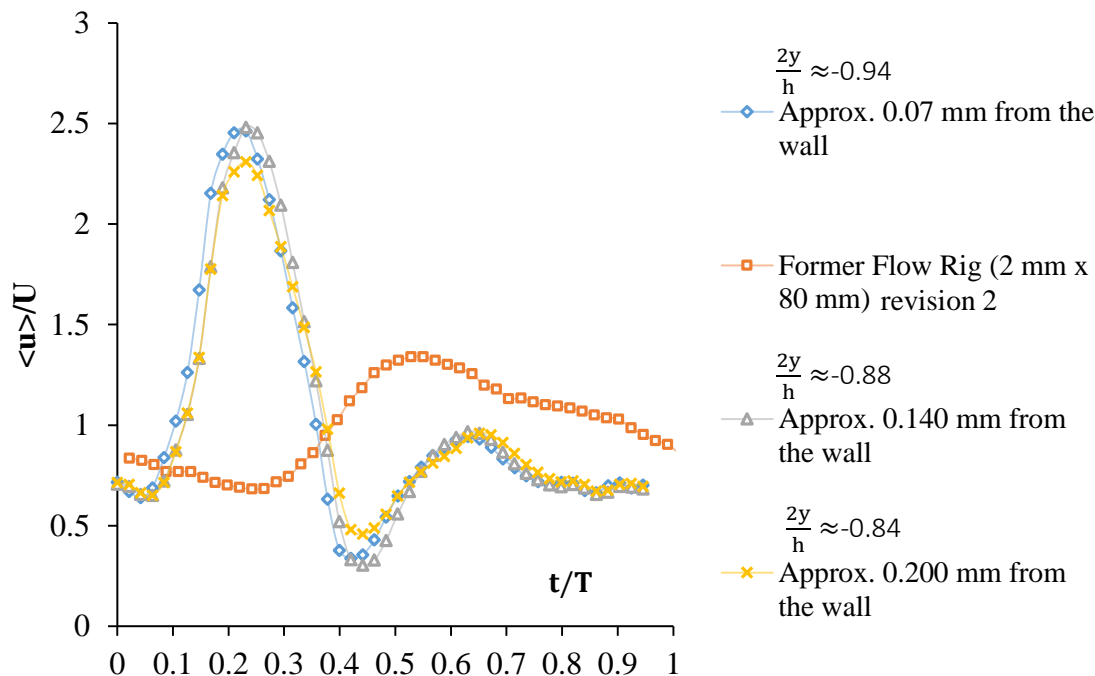


Fig. 1A-17 Normalized streamwise velocity under pulsatile laminar flow. The time-varying streamwise velocity was phase-averaged and normalized against the pulse cycle mean velocity. The time was normalized against the cycle period. Flow rate and pulse frequency under test were 5 mL/s and 1 Hz, respectively.

1A.6 Commercial Hemodynamic Flow Facility

The objective of the previous sections was to describe the purpose of this work: to develop an apparatus for university-based research aimed at understanding specific shear stress-cell response relationships and thus, the initiation and development of arterial disease. The commercial system which is discussed in this section was a revision of the research facilities described in the previous sections. The focus of this section is to provide a brief overview of the main components of the commercial facility and discuss the implications of its design on the final research-based facility, which is discussed in Chapter Three (experimental methods and apparatus). The design of the commercial PPFC was a standard from which the latest revision of the PPFC was designed (Avari et al. 2016). In addition, the commercial LDV probe (TSI) which was a part of the commercial facility (due to its small-scale size) was successfully implemented in the work by Avari et al (2016). Avari et al (2016) successfully measured both a pulsatile laminar and a Low-Re steady turbulent flow inside the final PPFC. Finally, this section will present a novel pulsatile syringe pump

(PSP) that was designed by the present author and manufactured by Harvard Apparatus (USA).

Fig. 1A-18 shows the commercial facility with focus on the three main components: (1) a PPFC, (2) a pulsatile syringe pump which was used for simulation of realistic pulsatile flow and, (3) a commercial (small-scale) two-component LDV probe. The exact model of the LDV probe was TSI's Mini-Fiber Probe Series TR 110. This probe was selected due to its relative small focal length of 110 mm and beam spacing of 15 mm. The beam spacing was ideal for measuring velocity in the confined geometry of the PPFC. The weight of the probe was approximately 200 g and, hence it was ideal for mounting to a micro-traverse platform. The disadvantage of the probe was that it was not configured for near-wall measurements (green centre beam) and, hence, tilting the probe to measure the v-component was required. According to Avari et al (2016), to avoid the lower green beam hitting the wall of the PPFC, the probe should be tilted 4.5° . Avari et al (2016) also reported that as a result of the tilting, the v-component measurements showed an approximate error of 0.3%. The measurement volume diameter of the TR110 probe was approximately 68 μm . The other disadvantage of this probe was that it could not be modified to increase the spatial resolution. The open-concept of the LDV system discussed in the previous sections allows for installing beam-expanders and/or altering the focusing lens (focal distance). Both of those key features allow for spatial resolution control (measurement volume diameter and length size). The commercial PPFC was an upgrade from the PPFC presented in section 1A.4.1. The main reason for the design alteration was to extend the width of the working section from 12 mm to 17 mm, in order to increase the uniform region along the width. The other reasons were to ensure water-tight sealing between the bottom and top cavities and to incorporate a cutout ($\approx \text{Ø}50 \text{ mm}$) inside the bottom cavity to allow for bottom-top microscopy imaging. The PPFC described in section 1A.4.1. only allowed for top-bottom imaging with an objective lens mounted to an inverted microscope. The PPFC consisted of a bottom and top cavity (both, manufactured from 316 SS) which, when assembled, formed an internal PPFC of 17 mm in width and 1.8 mm in height. A rectangular microscopy slide was flush-mounted inside the bottom cavity with a depth of $0.17 \pm 0.01 \text{ mm}$. The microscopy slide extended along the entire width of the PPFC. The length of the upstream section and the working section were approximately 190 mm and

63 mm, respectively. The upstream section of the PPFC had a transitional loft (circular-to-rectangular transition) which extended for approximately 90 mm. This ensured a smooth incoming flow and eliminated any possibility of flow disruption at the working section. At the working section, an optical window (made out of glass) was inserted to allow for both two-component LDV measurements and top-bottom microscopy imaging. The wall thickness of the optical window was 3 mm to ensure minimal distortion of the incoming laser beams. An obstacle was installed upstream of the microscopy slide to disturb the incoming flow and model arterial narrowing. The step height was adjustable with a set-screw with a 200 μm resolution.

The pulsatile syringe pump shown in Fig. 1A-18 was composed of three main components: (1) the master and slave syringe pumps, (2) a solenoid valve and (3) a cell fluid reservoir. The master and the slave consisted of two stainless steel syringes with the inside surface of the syringes coated with Teflon to minimize friction between the piston and the cylinder. Both of the syringes were manufactured out of stainless steel to withstand elevated temperatures ($\approx 125^\circ\text{C}$) inside the autoclave chamber. The pump system was programmable with LabVIEW software to deliver either a steady or a pulsatile flow to the working section of the PPFC. The pump was designed to produce a flow rate range, $1 \text{ mL/s} \leq Q \leq 20 \text{ mL/s}$. At $Q = 20 \text{ mL/s}$, the average velocity in the channel was calculated to be 0.65 m/s. Based on $D_h = 2h = 3.6 \text{ mm}$ and $U = 0.65 \text{ m/s}$, the Reynolds number was approximately 2352 (using water, $\rho \approx 998 \text{ kg/m}^3$). In terms of pulsatile flow, the pump was capable of producing waveforms with a peak flow rate of 20 mL/s and a frequency of 1 Hz (resting heart rate in humans). To ensure that the syringe plunger moved back to the original position every time during the pump's continuous operation, a limit switch was integrated into the pump system. The limit switch used was a D2MQ ultra subminiature basic switch that connected directly into a digital input channel of the DAQ card. The signal from the DAQ card was sent to LabVIEW for continuous monitoring of the plunger location. Flow rates were accurate within 0.25% and reproducibility within 0.05% (manufacturer reported). The step resolution was designed to provide 0.33 $\mu\text{m}/\text{step}$ to ensure smooth flow during the motor operation. The connections between the syringes, the reservoir and the valves were accomplished through the use of stainless steel tubing ($\approx \text{\O}3 \text{ mm}$, ID), whereas the connection to the PPFC was accomplished via flexible and bio-

compatible tubing ($\approx \text{Ø}5 \text{ mm}$, ID). The disruption time associated with the valve switching was 200 ms. This was reduced from the 400 ms, measured with the Shelley Medical pump reported in the earlier sections.

To ensure a continuous flow ($> 10 \text{ hrs.}$), additional modifications were integrated into the pumping system. The initial pump system over-heated during testing (within $\approx 1 \text{ hr.}$) which caused stalling of the plungers inside the syringes, presumably as a result of thermal expansion. To reduce the temperature of the pump motor, a miniature cooling fan was integrated into the motor assembly to provide continuous cooling. The motor temperature was monitored with a thermocouple (mounted on the motor casing surface) and the results are shown in Fig. 1A-19. With the installation of the cooling fan, the motor temperature did not exceed $\approx 33^\circ\text{C}$ and it allowed for more than 10 hours of continuous operation. Hence, this would allow for longer exposure of flow over ECs cultured at the working section of the PPFC.

In summary, there is no validation to report with the commercial hemodynamic facility (no flow measurements in the PPFC). However, it was considered as groundwork for the design of the present and the latest revision of the PPFC. In terms of the latter, the elements which fed into the final PPFC design include channel geometry and overall channel length, bottom-top microscopy imaging configuration, PPFC material (ULTEM plastic), optical canopy design for LDV measurements and integration with the TSI TR 110 probe which Avari et al (2016) reports. The commercial channel, as well, provides insight into some of the future work that would be undertaken in the lab at Western University.

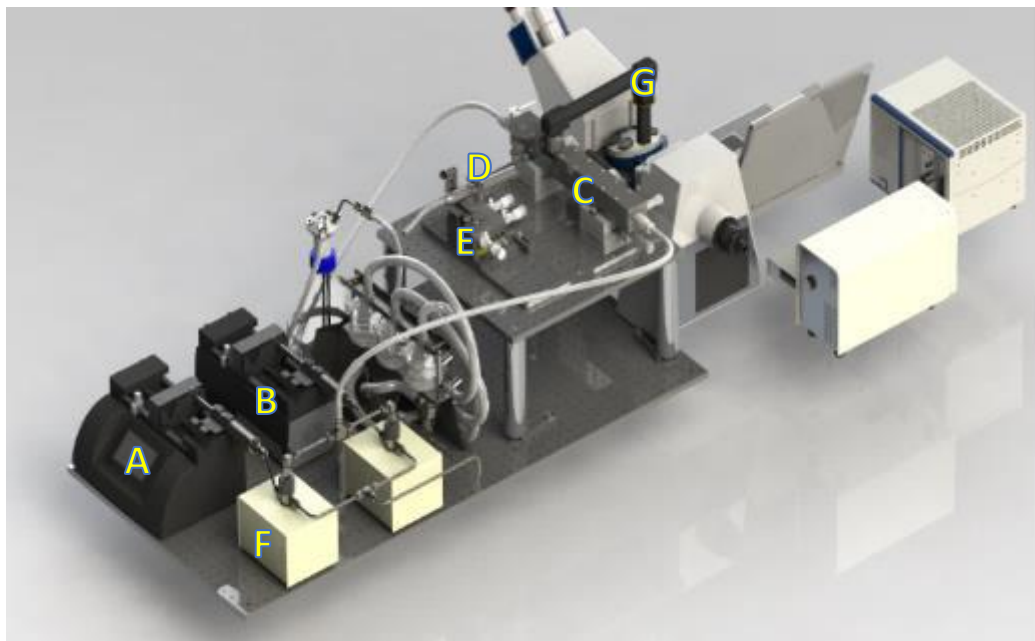


Fig. 1A-18 The commercial hemodynamic flow facility. (A) master syringe pump, (B) slave syringe pump, (C) PPFC, (D) TSI commercial LDV probe mounted on a micro-traverse system, (E) 5L cell fluid reservoir, (F) Solenoid valves, (G) objective inverter from LSM Technologies.

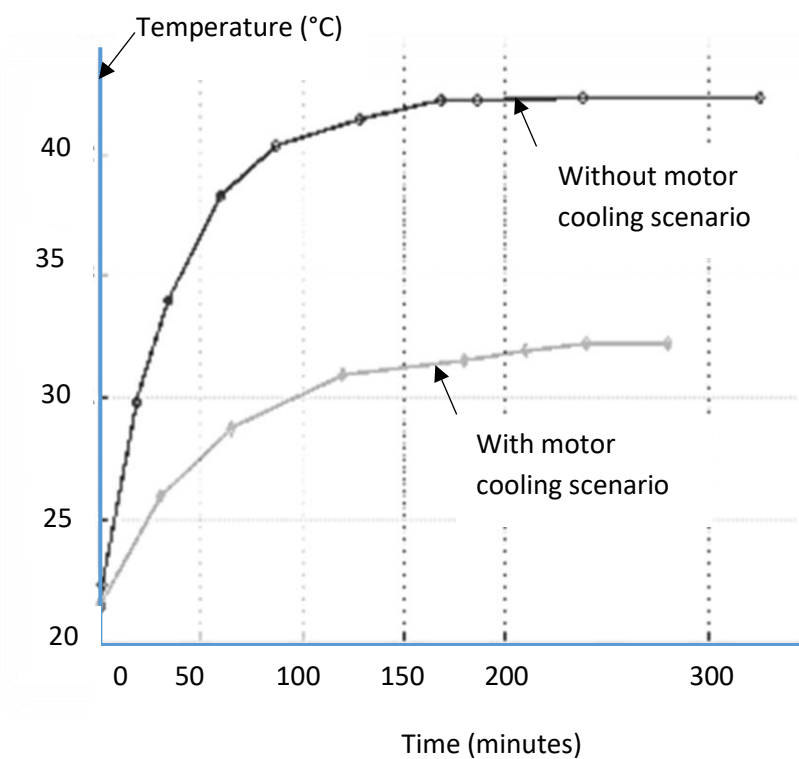


Fig. 1A-19. Motor performance temperature curve. The temperature was monitored by a thermocouple and logged using the DAQ card.

1A.7 Appendix One Summary

The early stage hemodynamic facility was discussed, which consisted of a PPFC, a commercial pulsatile flow pump (Shelley Medical Technologies), and a LSM-designed LDV system (i.e. two-component LDV). The purpose of the facility was to emulate realistic *in-vivo* conditions via simulation of physiological waveforms at the working section of the PPFC. To measure the u and v velocity components inside the working section, the final and near-wall LDV system was presented which consisted of a transmitter (LDV probe) and a commercial TSI forward-scatter receiver. The final near-wall configured LDV system was conceptualized and designed based on several iterations which were driven by the initial LSM-designed probe. The fluid dynamics inside the early-stage PPFC were evaluated by measuring the streamwise velocity (across the channel height) for both a steady and pulsatile laminar flow at the working section. Although the analytical solution (infinitely wide plate assumption) was in very good agreement with the velocity measurements, the wall shear stress values were in the lower range of physiological shear stress reported in the literature. In addition, simulation of a normal carotid waveform (under $f = 1$ Hz) at the working section showed significant damping (i.e. rounded waveforms) with PI and SRT values of $\Delta\langle u \rangle^* \approx 0.65$ and $\Delta t^* \approx 0.27$ (whereby the ideal waveform has PI and SRT values of $\Delta\langle u \rangle^* \approx 2.8$ and $\Delta t^* \approx 0.05$), respectively. It was also found through experimentation that the v component of the velocity vector was not measurable inside the early-stage PPFC as a result of a geometrical limitation.

To overcome these challenges, a new PPFC (revision 3) was developed with a working section that was 12.5 mm x 2.5 mm ($w \times h$) and with channel geometry to allow v component measurement at the working section. The reduced cross-sectional area of the working section yielded a maximum streamwise velocity that was ≈ 2.5 larger in comparison to the early-stage PPFC. Accordingly, the wall shear stress at the working section increased in magnitude and was in the physiological range (0-20 dyne/cm²). In addition, the pulsatile flow measurements at the working section under $f = 1$ Hz demonstrated waveforms that closely matched the ideal waveforms at the pump outlet, whereby the PI and SRT values were $\Delta\langle u \rangle^* \approx 2.25$ and $\Delta t^* \approx 0.11$, respectively. From a functionality point of view, the new PPFC allowed top-bottom and bottom-top imaging

of live ECs which was not possible with the early-stage PPFC. Furthermore, the challenges associated with the commercial pulsatile pump such as overheating, difficulty with sterilization of vital components and size (which affected the position of the pump relative to the channel and, hence, length of tubing required) were overcome through a design of a novel syringe pump that was more compact and cost-effective. The syringe pump was capable of continuous operation without overheating. It also featured more advanced controls (LabVIEW) and greater accuracy and reproducibility of waveforms. It should be noted that the syringe pump was not used with the two-component velocity measurements over a BFS (Chapter Five) given that it was not available to the present author at the time of the measurements.

The next Appendix provides a comprehensive overview of the design and functionality of the near-wall configured LDV system together with its performance and uncertainty. The following Appendix, as well, reports the shortfalls from this Appendix which includes: (1) quantification of wall shear stress and its accuracy (considering both the $F = 120$ mm and $F = 261$ mm lenses together with an acceptable wall datum identification method reported in the literature) under steady laminar flow considering the appropriate cell fluid (DMEM mixture), (2) transitional flow (low-Re turbulent flow) at the working section to validate the ability to measure u and v simultaneously and (3) quantification of tracer particle response time and seeding concentration requirements. It should, as well, be noted that Chapter Three (experimental apparatus and methods) discusses the final version of the flow facility in much greater depth which is used to measure steady and pulsatile flow over the BFS in Chapter Five.

APPENDIX 2

NEAR-WALL LDV SYSTEM: DESIGN, PERFORMANCE, AND UNCERTAINTY

2A Introduction

This Appendix continues the discussion surrounding the final revision near-wall configured LDV system (with added emphasis on its design, performance and uncertainty) introduced in Chapter Three. The primary lens used had a theoretical focal length and measurement volume diameter of 120 mm and 42.2 μm , respectively. A second lens was also used in the present work ($F = 261$ mm and theoretical measurement volume of 90.1 μm) for simultaneous u and v measurements and the details are provided. It should be noted that the lens reported in Appendix 1 (i.e. $F = 135$ mm) is no longer considered here onward (i.e. obsolete at TSI USA). The LDV system allowed for near-wall simultaneous velocity measurement (in coherence mode) of both, u and v velocity components inside the PPFC at the working section. The fundamental purpose for developing the present LDV system was to obtain high-accuracy velocity measurements at the working section and very close to the surface (bottom wall) downstream of the backward-facing step (i.e. idealized stenosis geometry presented in Chapter Five). Standard commercial LDV systems were not considered for this application since the typical measurement volume diameters are on the order of 150 μm and are relatively large in size, thereby not allowing mounting to micro-traversing platforms (i.e. as a result of the weight limitations). In addition, commercially available LDV systems are not configured for near-wall measurements and, thus, require tilting for such measurements. The challenge with the latter is that the upper green beam (being focused by the probe lens) would result in an even larger incidence angle that it makes with the optical window thereby limiting its transmission into relatively small channels (i.e. 1.8 mm by height).

The objective of this Appendix is to further discuss the custom LDV system which was designed and constructed for this study and used to measure the velocity field at the working section of the PPFC. The main four areas which are discussed in this Appendix are as follows: (1) an overview of the LDV technique, (2) the design and performance

(uncertainty) of the LDV system and (3) the dynamic response of tracer particles together with the seeding concentration requirements.

To further validate the probe, vertical profiles of the streamwise mean velocity $\bar{u}(y)$ under a steady laminar flow (inside the final revision PPFC) are given at the working section for $Re_m = 100, 600, 900$ and 1240 (considering the bulk velocity of the channel). Furthermore, wall shear stress (WSS) values are tabulated for both the $F = 120$ and 261 mm lenses and compared with the empirical channel flow solution to quantify the differences in WSS accuracy given the differences in the spatial resolution of the lenses.

The final section of this Appendix studies a turbulent flow (transitional regime) inside the PPFC at the working section using LDV and the results are reported together with other literature on the subject. This flow case is presented as validation to evaluate the ability to measure u and v velocity components simultaneously and in coherence mode. The results were compared with literature in which low- Re flow inside a two-dimensional channel was studied to ensure that valid measurements were taken by the LDV system at the working section of the PPFC.

2A.1 An Overview of the Two-Component LDV Technique

The method is based on two collimated and parallel beams (monochromatic, coherent, and linearly polarized), which when focused by the transmitting lens generates a measurement volume of certain size. According to Tavoularis (2005), the measurement volume which is ellipsoidal in shape is characterized by its width, height, length and volume. When the suspended discrete particles (i.e. tracer particles, T_1O_2) cross the measurement volume (across the fringe pattern) with velocity, u , they scatter light and produce a burst signal with both, high and low intensities. The Doppler frequency shift, f_D , (difference between the measured frequency and the incident light frequency) is expressed mathematically as follows (Tavoularis, 2005):

$$f_D = \frac{2\sin(\theta)}{\lambda} u \quad (2A-1)$$

where u , θ and λ are, respectively, the particle velocity vector normal to the beams' plane (or normal to the bisector of θ), the beams' half-angle and the wavelength of the laser

beams. For clarity purpose, this is demonstrated in Fig. 2A-1. In this study, the wavelengths of the blue and green beams were 488 nm and 514 nm, respectively. It should be noted that the term $[(2 \sin(\theta))/\lambda]$ in Eq. (2A-1) represents the fringe spacing, δ , and, thus, Eq. (2A-1) can as well be written in the form $f_D = u/\delta$ (Zhu, 1996). As a result of Eq. (2A-1), the particle velocity can be calculated once the Doppler frequency is measured by the LDV system. According to Zhu (1996), Eq. (2A-1) can also be expressed in the following form $1/\bar{\tau} = u/\delta$, where $\bar{\tau}$ is the transit time of the particle traveling past the measurement volume.

In the present work, the range of streamwise velocities at the working section of the PPFC was between 0.0025 to 1.000 m/s (initially calculated by the analytical technique for steady laminar flow inside a channel). The streamwise velocities under 0.0025 m/s were considered insignificant (spurious r.m.s. velocity of 0.0025 m/s). The latter is reviewed in section 2A.3.2 of this Appendix. For the $F = 120$ mm lens, the fringe spacing was, respectively, 1.196 μm and 2.483 μm for the blue and green beams'. In terms of the $F = 261$ mm lens (which was also used in the present work), the fringe spacing was 2.561 μm and 5.383 μm for the blue and green beams', respectively. The beams' half-angle, θ , was calculated based on the beam spacing which was 50 ± 0.1 mm and 25 ± 0.1 mm for the blue and green beams, respectively. Based on these beam spacing values, the beams' half-angle for the blue and the green beams ($F = 120$ mm lens) was 11.76° and 5.94° , respectively. For the $F = 261$ mm lens, the beams' half-angle for the blue and the green beams was 5.49° and 2.74° , respectively. It will be demonstrated later in this Appendix (section 2A.4) that the v-component of the velocity vector could only be measured with the $F = 261$ mm lens and inside a limited range, $0.022 \leq y/h \leq 0.6$, whereby h is the channel height at the working section. This was as a result of the small channel height (i.e. 1.8 mm) and the beams' half-angle of 2.74° . It was only possible to capture a 1-3 velocity data points near the wall ($y/h \approx 0.027$) with the $F = 120$ mm lens (given the larger beams' half-angle for the green beams).

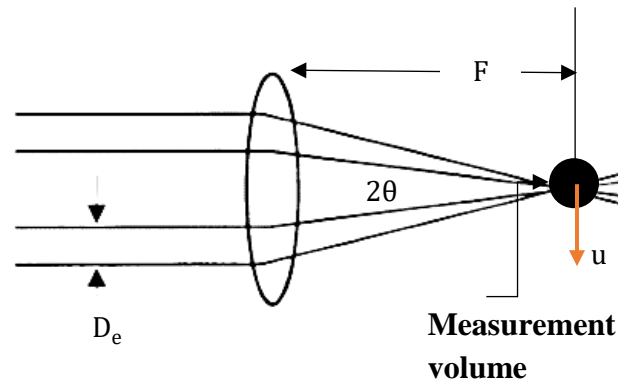


Fig. 2A-1 A schematic of two laser beams crossing. The variables F and D_e are referring to the focal length of the lens and the upstream beam diameter (prior to the beams focused by the transmitting lens), respectively. The figure was taken from Zhu (1996) and modified to show other critical variables.

Furthermore, Fig. 2A-2 plots the Doppler frequency against the expected streamwise velocity at the working section of the PPFC. The plot is rather useful for applying the correct bandpass filter (inside FlowSizer – LDV software) and, thus, optimizing the data rate. As an example, simulating a steady laminar flow at the working section with a maximum velocity of 0.500 m/s corresponds to a bandpass filter range between ≈ 0 -0.5 and 0-0.2 MHz for the $F = 120$ and $F = 261$ mm lenses, respectively. The FlowSizer software, however, has predetermined ranges which the user can select based on the expected velocity, yielding for the present study a filter range of 0.1-1 MHz (corresponding to the streamwise velocity between 0.0025-1.0000 m/s). For all the flow cases simulated in the present work (which are presented in Chapter Five), this predetermined filter range was sufficient to capture all streamwise velocities at the working section, except for relatively low velocities at the wall. Although not shown, the same analysis was conducted for the green beams (for both lenses) to ensure successful capture of all the wall-normal velocities at the working section.

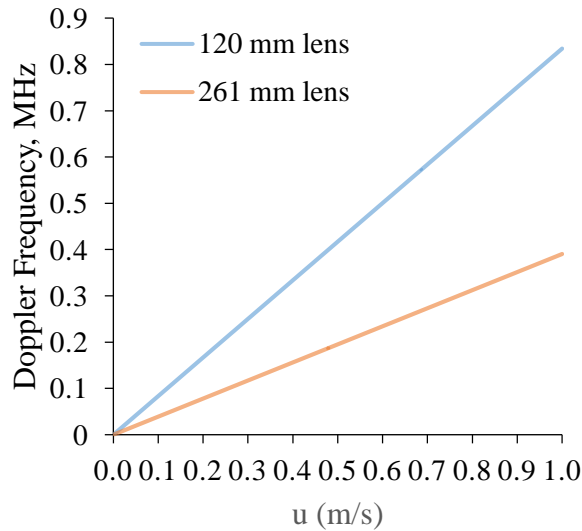


Fig. 2A-2 Calculated Doppler frequencies as a function of the streamwise velocity for $F = 120$ and 261 mm lenses used in the present work.

To capture smaller velocities found near the wall (i.e. ≈ 0.0025 - 0.100 m/s), the downmix function inside FlowSizer was used which by default is set to 40 MHz (no frequency added to the incoming signal). Adjusting this setting to 39.7 MHz adds 0.3 MHz to the Doppler frequency, thereby forcing all velocities to be detected. To better understand the concept of the down-mixing function inside Flow Sizer, a brief overview of frequency shifting is provided. According to Zhu (1996), physically the photo-detector module (PDM) will not detect negative frequencies produced by Eq. (2A-1). Hence, the fundamental objective of the frequency shift is to separate positive and negative directions of the particle motion. It is understood from fringe theory that the unmoving fringe pattern will be in motion upon frequency shifting one of the laser beams. The frequency shifting is generally done by using a Bragg cell. According to Tavoularis (2005), a single Bragg cell typically provides a 40 MHz shift to the incoming laser beam. For this study, this was accomplished inside the colour separator (Fiberlight module from TSI). A default setting of 40 MHz inside FlowSizer yields a frequency shift (f_{SHIFT}) of zero (eliminates all of the 40 MHz Bragg cell shift). Hence, downmixing to 39.5 MHz, as an example, can be mathematically explained as follows (Zhu, 1996):

$$f_D = f_{\text{SHIFT}} + u/\delta \quad (2A-2)$$

where f_{SHIFT} would correspond to 0.5 MHz. As example, using a fringe spacing of 1.196 μm and a downmix frequency of 39.5 MHz allows reverse flows to be measured up to ≈ 0.600 m/s. The latter was calculated based on $u = \lambda f_{\text{SHIFT}}/2\sin(\theta)$ (Zhu, 1996).

Furthermore, according to Zhu (1996), the diameter and length of the measurement volume can be mathematically expressed as follows:

$$L_m = d_e/\sin(\theta) \quad (2A-3a)$$

$$d_m = d_e/\cos(\theta) \quad (2A-3b)$$

where d_e is the beam waist diameter and can be expressed as follows (Zhu, 1996):

$$d_e = 4\lambda F/\pi D_e \quad (2A-4)$$

where D_e is the laser beam diameter (upstream of the focusing lens – see Fig. 2A-1), whereby the laser intensity exceeds $1/e^2$ of its maximum amplitude and F is the focal length of the transmitting lens. In the present study, the laser beam diameter (upstream of the lens) was 1.8 mm for both the blue and the green beams. There was no uncertainty reported by TSI for the latter. An alternative method to measure the beam diameter is by using an optical beam profiler through the selection of the correct wavelength range. This instrument was not available to the present researcher and, hence, uncertainty of the upstream beam diameter is not reported. Table 2A.1 summarizes the theoretical measurement volume specifications applicable to both lenses used in the present work.

Table 2A.1 Theoretical measurement volume specifications for the F = 120 mm and the F = 261 mm TSI lenses. Eq's (4-3) and (4-4) were used to calculate the measurement volume quantities.

F = 120 mm		F = 261 mm	
488 nm (Blue Beams)		488 nm (Blue Beams)	
d_m	42.2 μm	d_m	90.1 μm
L_m	203.3 μm	L_m	949.8 μm
d_e	41.4 μm	d_e	90.5 μm
514 nm (Green Beams)		514 nm (Green Beams)	
d_m	43.8 μm	d_m	95.9 μm
L_m	424.0 μm	L_m	2039.4 μm
d_e	43.6 μm	d_e	95.8 μm

According to Fingerson et al (1993), the fringe spacing reported in the preceding paragraphs is independent of the fluid medium; that is, the wavelength (λ) and the beams' half-angle (θ) terms cancel out. This was mathematically validated by Fingerson et al (1993) and it demonstrates that the LDV technique does not require calibration. According to Durst & Stevenson (1976), the beam waist (d_e) which is the smallest achievable beam diameter does not typically coincide with the beams' crossing. Durst & Stevenson (1976) noted that this absence of overlap (inadequate beam intersection) is due to the properties of the Gaussian beams (propagation characteristics) and at times should be taken into account (compensated) to accurately measure very low turbulence levels. This is because the improper intersection of the beams affects the range of the resulting Doppler signal. According to Durst & Stevenson (1976), this effect on accuracy can be neglected (usually represents a small percentage), specifically when lens aberrations (ultimately diffraction) are minimized or entirely eliminated.

According to Zhu (1996), the actual probe diameter and length should be defined based on the signal intensity as opposed to the laser beam intensity ($1/e^2$). Furthermore, DeGraaf & Eaton (2000) suggested validating the actual measurement volume diameter through timing the largest Doppler bursts (using an oscilloscope), followed by using the velocity of the particle to evaluate the actual diameter of the measurement volume. Furthermore, Durst et al (1976) determined the actual measurement volume by monitoring (using an oscilloscope) the number of fringes in a single burst and then using the mathematical relation, $N_{fr} = d_m/\delta$ to evaluate the measurement volume diameter (i.e. where N_{fr} corresponds to the number of fringes inside the measurement volume). Another technique previously used by Durst et al (1995) includes using a $2\ \mu\text{m}$ slit to scan the waist of the beam and through this method determine the accuracy of the waist of the beam (i.e. accuracy was reported as $\pm 4.5\%$). Durst et al (1995) also validated the choice of defining d_m as the measurement volume diameter (corresponding to e^{-2} light intensity) through closely matching near-wall u'/\bar{u} profiles of the measurement and the prediction (whereby the analytical prediction has a dependence on d_m).

In the present work, the measurement volume diameter was validated using the mean gate time (i.e. duration of the individual signal) and multiplying it by the streamwise mean velocity (representing the particle speed). This was verified at several measurement locations (i.e. 3 runs) at the working section of the PPFC (for blue beams) and using a glass column (for green beams) to provide various steady laminar liquid flow rates. For the blue beams, the actual measurement volume diameter (d_{ma}) together with the uncertainty (by taking the mean and the standard deviation of the three runs) was $42.0 \pm 4.5\ \mu\text{m}$ and $80.3 \pm 3.8\ \mu\text{m}$ for the $F = 120$ and $F = 261$ mm lenses, respectively. For the green beams, the values were $44.0 \pm 5.2\ \mu\text{m}$ and $86 \pm 7.2\ \mu\text{m}$ for the $F = 120$ and $F = 261$ mm lenses, respectively.

2A.2 The Near-Wall Configured LDV System: An Overview of its Design and Function

The near-wall configured LDV system is shown in Fig's 2A-3 and 2A-4. The probe body had three subunits, consisting of front optics, rear optics and the central housing. The central housing (machined out of Delrin plastic) directly mounted to a milling cross-slide table ($x - y$ table) and was secured with four machine screws. The front and the rear optics were secured on the central housing and shared a common centre axis (optical axis). The rear optics secured a precision-machined cylindrical housing (made out of aluminum 6061T6) with its centre axis coincident with the downstream focusing lens (i.e. transmitting lens). Fig. 2A-3a shows the probe cross-sectioned across the $x - z$ plane (horizontal plane) and it shows the mounting positions of the two blue collimation assemblies. In reference to the optical axis of the probe, the two blue collimation assemblies were positioned at the same radial position of 25 mm corresponding to 0° and 180° positions. For the green beam pair, one of the green beams was positioned to coincide with the optical axis of the probe (radial position of 0 mm) and, thus, this configuration allowed for a near-wall measurement (to avoid hitting the lower wall of the channel). The other green beam was positioned at a radius of 25 mm corresponding to a 90° position (see Fig. 2A-3b where the probe was cross-sectioned across the $y - z$ plane). Both of these configurations allowed for the blue and the green beams to be in the horizontal (to measure u) and vertical (to measure v) planes, respectively.

Furthermore, as per Fig. 2A-4, the green beams measured the wall-normal velocity component, v , and the blue beams measured the streamwise velocity component, u . Positive velocity directions were imposed by configuring the position of the collimation assemblies (left or right side of the probe) so that the positive direction is in the path of the unshifted to the shifted beam. The latter is because the fringe motion (as a result of the frequency shift) occurs from the shifted to the unshifted beam (i.e. a positive velocity direction opposes fringe motion, Durst et al. 1976). Since the cylindrical housing (mounted at the rear of the probe) was able to rotate (in relation to the optical axis) by 360° , the positive and negative directions could easily be reversed. In reference to Fig. 2A-4, both the measured u and v components were perpendicular to their individual beam axes.

However, the measured velocity direction for the v component did not coincide with the y -axis (wall-normal direction) of the coordinate system at the working section of the flow channel. Hence, a mathematical conversion of the measured and the non-orthogonal velocity component to the orthogonal velocity component was made. This was accomplished using a transformation matrix inside FlowSizer which resulted in a correction as such, $v_{\text{corrected}} = v = v_{\text{meas.}} \cos(\theta) + w \sin(\theta)$. The contribution of term $w \sin(\theta)$ was negligible as a result of a small angle, $\theta = 2.74^\circ$. Recently, Avari et al (2016) used a similar method to correct the measured and the non-orthogonal v -component. In terms of the latter, the author tilted the probe downwards by $\approx 4.5^\circ$ to avoid hitting the wall and found this translating to an error of $\approx 0.3\%$ in the v -component measurements.

The front optics of the probe held both the steering prism wedges and a focusing lens. Both lenses used in the present study were commercially purchased from TSI. To steer the blue and the green laser beams to a common point (the measurement volume), each beam was transmitted through its own steering prism (see Fig. 2A-3). During velocity measurements for all flow cases reported in Chapter Five, the intensity of the incident (I) blue beams was 25 ± 0.5 mW. For the green beams, the intensity of each beam was $I = 15 \pm 0.5$ mW. To achieve this beam intensity, the water-cooled laser was operated at approximately 300 mW. It was critical to ensure that each beam (in a pair) had the same intensity, since Durst & Whitelaw (1971) experimentally demonstrated the diminishing clarity of the fringes (inside the measurement volume region) as a result of unequal beam intensities. The authors also showed that the signal-to-noise ratio (SNR) which was obtained from the photomultiplier dramatically decreased due to the differences in each beam intensity. Durst et al (1976) defined fringe visibility as $\zeta \equiv 2(\sqrt{I_1 I_2}) / (I_1 + I_2)$, which for this study was $\zeta \approx 0.99$ (ideal 1.0), where I_1 and I_2 represent individual beam intensities in a monochromatic pair.

Furthermore, polarization and collimation of the laser beams were not required since both of these parameters were pre-configured at TSI (USA). The probe did allow for these parameters to be adjusted by varying the position (rotation/translation) of the fiber ferrule which itself was held inside the collimation assembly. According to Zhu (1996), collimating the incident beams (prior to striking the focusing lens) is important and if an

adequate degree of collimation is not achieved this could affect the fringe spacing and their parallelism (i.e. fringe distortion). Previously, Durst et al (1976) noted that to successfully obtain the v-component of the velocity vector, light vibrations should occur in the horizontal plane. Hence, if the blue beams are crossed in the horizontal plane, light oscillations should occur in the vertical plane for the polarization axis to be normal to the beams' plane. For this study, this was verified using an optical axis finder for both, the blue and the green beam pairs. Although the polarization was pre-conditioned at TSI, this validation was carried-out to ensure that steering of the beams did not rotate the axis of polarity. The latter statement is supported by Durst et al (1976), whereby the author noted that an incident laser beam will change polarity direction as a result of reflection, refraction and/or diffraction.

The final functional requirement of an LDV system is to ensure that the optical path distance is similar between two beams in a pair. Previously, Foreman (1967) showed that there is a reduction of the LDV signal as a result of the differences in the optical path length between two laser beams. According to Durst et al (1976), to obtain good fringe visibility, the path length difference of two beams should be smaller than that of the laser coherence length. In this study, the difference in the path length for both beam pairs (blue and green) was less than 2 mm which was smaller than the coherence length of the laser (multi-mode laser from Coherent with coherence length of ≈ 3 cm).

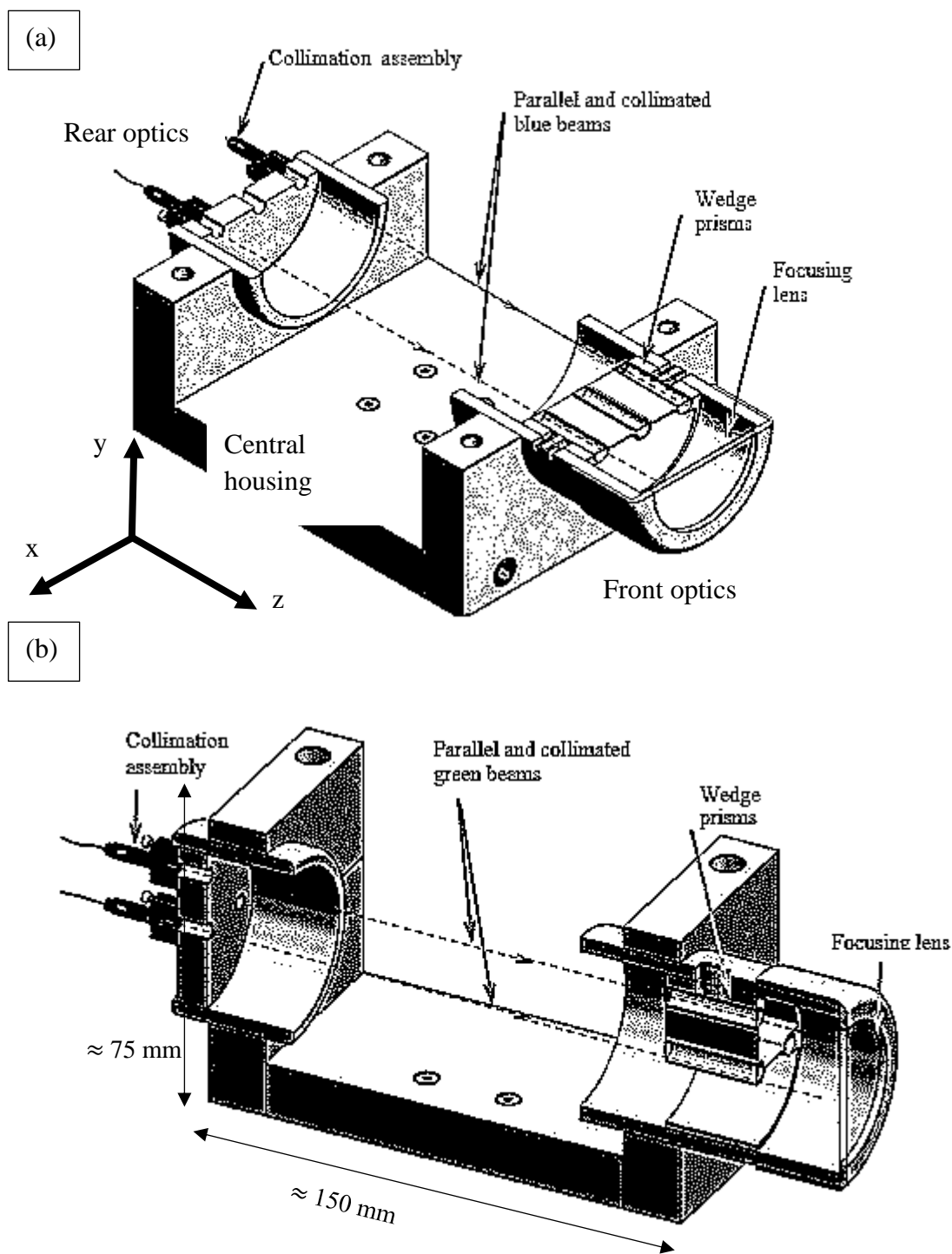


Fig. 2A-3 Near-wall LDV system. (a) blue beam configuration, (b) green beam configuration. The beam spacing was $50 \pm 0.1 \text{ mm}$ and $25 \pm 0.1 \text{ mm}$ for the blue and green beams, respectively. In terms of the coordinate system at the working section of the flow channel, the blue beams were in the $x - z$ plane and the green beams were in the $y - z$ plane.

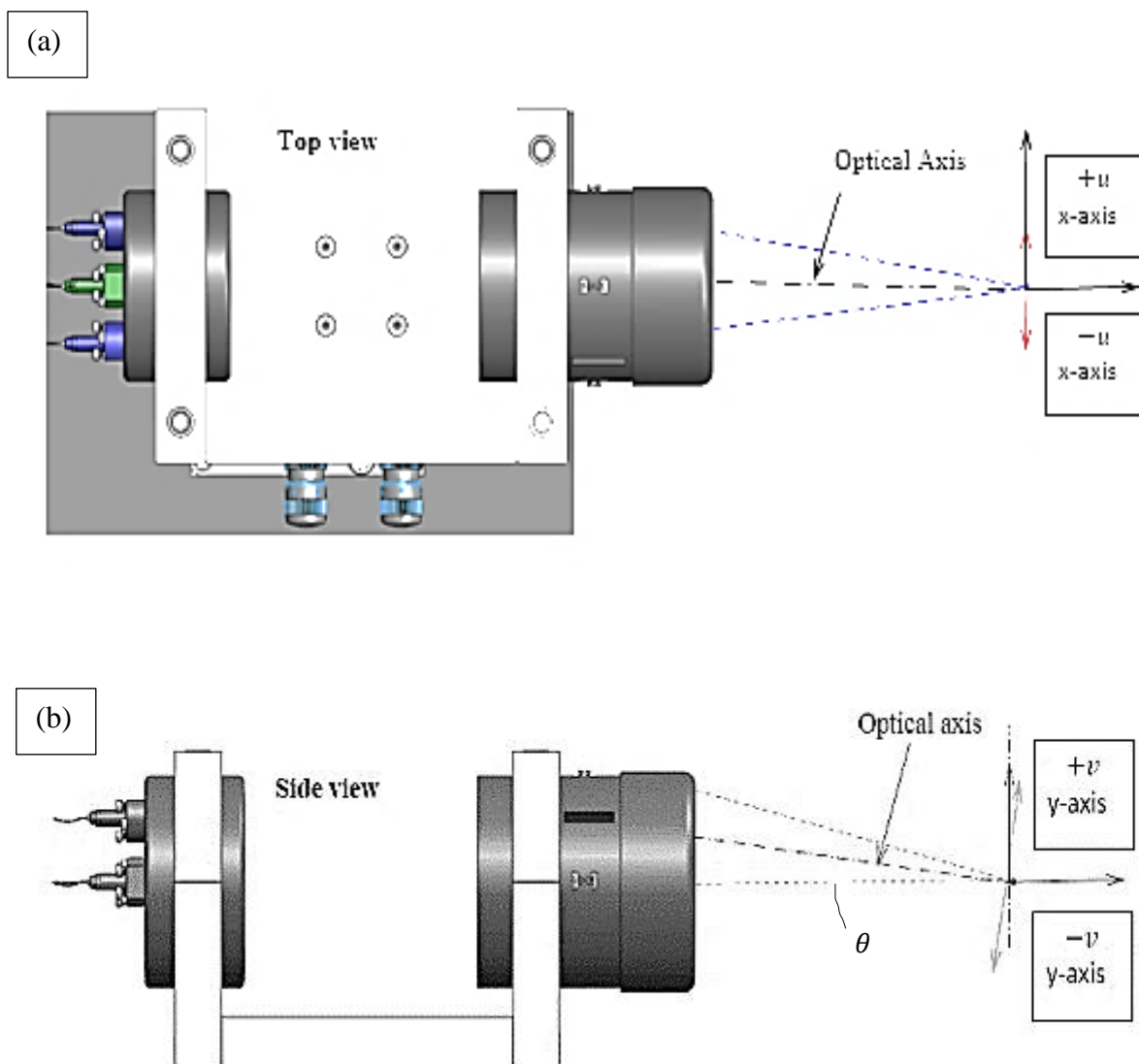


Fig. 2A-4 Near-wall LD configuration for velocity measurement at the working section of the PPFC. (a) blue beam configuration for u-component measurement, (b) green beam configuration for v-component measurement.

2A.3 LDV Measurement Uncertainty and Characterization of Noise under Steady Laminar Flow

This section provides an overview of the various sources of error attributed to the LDV technique and provides an estimate for the precision (random error) of the streamwise velocity measurements obtained using the two-component LDV system (under steady laminar flow). This study reports experimental data of the streamwise velocity inside both the PPFC (used for all flow measurements) and a long section of straight acrylic-made flow channel (whereby $l \times w \times h$: 600 x 17.5 x 1.8 mm and measurements were captured away from any entrance disturbances) to determine the accuracy and precision uncertainty of the first two velocity moments under steady laminar flow. To determine the spurious r.m.s. velocity (i.e. noise) associated with the v component of the velocity vector (r.m.s. v'), a vertical column (square cross-section whereby the length of each side was 50.8 mm) was used to simulate a quasi-steady laminar flow. For the glass flow model, the flow rate was controlled based on the elevation difference between the outlet (free jet into atmosphere) and the free surface of the fluid (in the glass column).

In terms of the precision error, the measured r.m.s. u' and v' velocities under a steady laminar flow and over a wide range of velocities (0.002-0.500 m/s) were examined to estimate the variance of statistical quantities, such as the mean and r.m.s. velocities.

It should also be noted that this Appendix only provides experimental data used to determine the LDV-induced noise and, thus, the variance of statistical quantities for steady laminar flow. The uncertainty of mean flow and turbulence quantities for steady and pulsatile flow over a backward-facing step (i.e. Chapter Five) is presented in Chapter Four (experimental uncertainty Chapter). In addition, this section does not discuss the estimation of spatial uncertainty coupled with wall datum identification (contribution of measurement volume positioning). Spatial positioning uncertainty coupled with the performance of other components, including how well the actual flow profile time history at the working section (endothelial layer) matched that specified at the pump and the repeatability of those profiles over each pulsatile cycle, is discussed in Chapter Four. The uncertainty of the experimentally measured WSS coupled with the shear rate approximation (via curve-fitting) is also discussed in Chapter Four.

According to Rood & Telionis (1991), the bias limit, B, is an estimate of the measurement accuracy and can be defined as the magnitude of the fixed, constant error. On the other hand, the precision limit, P, can be defined as an estimate of the scatter generated by random errors and unsteadiness of the signal. The precision limit generally defines the lack of repeatability of a measurement. The total measurement uncertainty is defined as follows (Rood & Telionis, 1991):

$$\epsilon_{LDV} = \sqrt{B^2 + (t_1 P)^2} \quad (2A-5)$$

According to Kunz et al (2001), a value of $t_1 = 1.96$ can be used for 95% confidence interval (sample size greater than 50). The next two sections discuss the accuracy and precision errors of the LDV technique used in this study.

2A.3.1. LDV Biases

The bias error of the mean velocity can be computed based on the following (Coleman & Steele, 2009):

$$B_U^2 = \left(\frac{\partial U}{\partial x_1}\right)^2 B_{x_1}^2 + \left(\frac{\partial U}{\partial x_2}\right)^2 B_{x_2}^2 + \dots \quad (2A-6)$$

where B_{x_i} represent the bias uncertainty related to the variable x_i . According to Edwards (1987), there are various sources of statistical bias in LDV, which include: (1) velocity bias, (2) gradient bias, (3) angle bias and (4) fringe divergence. Patrick (1987) attributes these errors to laser beam geometry, signal processing and seeding bias errors. In addition, according to Patrick (1987), the bias errors are typically much smaller in comparison to the precision errors of the LDV system and it is, thus, common for bias errors to be neglected (Kunz et al. 2001). Furthermore, according to Iyer & Woodmansee (2005), the uncertainty of the measurement volume position adds to the overall uncertainty in the mean velocity and, thus, the total uncertainty of the mean velocity will consist of both the variance associated with the LDV system (i.e. statistical sampling error) and the measurement position. The latter is further explained in Chapter Four of this thesis.

2A.3.1.1 Velocity Bias

Pioneering work by McLaughlin & Tiederman (1973) described the velocity bias error as a result of particle size distribution and particle arrival rate. As a review, it is important to understand that the mean velocity and other flow statistics are calculated from individual velocity realizations (particle velocities). McLaughlin and Tiederman (1973) explained the velocity bias by considering the velocity field as a sinusoidally varying function. Their analysis was based on assumptions that the particles are small enough to follow the mean flow accelerations and that the particles are randomly distributed with respect to the number density. The authors demonstrated that the time-averaged mean of a sinusoidally-varying velocity field (calculated from LDV-measured velocity data) is not equal (biased towards the larger velocities) to the geometrical mean of the sine-wave (plotted on a velocity-time plot). According to McLaughlin & Tiederman (1973), the bias is a result of an increase of fluid volume (per unit time) passing through the measurement volume at relative larger velocities (in contrary to period of slower velocities). The latter was explained mathematically by the authors as follows:

$$\Delta n = M\Delta V_p + |\mathbf{V}|A_pM\Delta t \quad (2A-7)$$

where Δn is the average number of velocity data points (or velocity realizations), M is the average number of seed particles per unit of volume, ΔV_p is the measurement volume, \mathbf{V} is the velocity vector magnitude and, A_p is the projected area of the measurement volume (observing from the direction from the velocity vector). Eq. (2A-7) presented by McLaughlin & Tiederman (1973) demonstrates that the number of velocity realizations (obtained in a given time interval, Δt) is proportional to the magnitude of $|\mathbf{V}|$ and, thus, will yield biased results of the mean and r.m.s. velocities. Moreover, according to Edwards (1987), additional factors that affect the velocity bias are as follows: (1) velocity gradient induced particle arrival, (2) flow turbulence induced particle arrival and, (3) seeding uniformity. McLaughlin & Tiederman (1973) proposed a correction scheme for the velocity bias which uses the inverse of the particle velocity as a weighting factor for each measured velocity, $w_i = |\mathbf{V}_i|^{-1}$. The assumptions used with this method were (1) uniform

seeding density, (2) spherical measurement volume (not ellipsoidal) and, (3) acceptance angle is 4π steradians. According to Herrin & Dutton (1993) and Hoesel & Rodi (1977) the inverse velocity magnitude method was demonstrated to be unreliable at large turbulence intensities (i.e. middle region of the shear layer) and should only be used in low-to-moderate turbulent intensity flows. Herrin & Dutton (1993) also stated that effects of compressibility would cause inaccurate results since the rate at which the particles pass the measurement volume is proportional to the mass flux and not velocity alone (volume flux). In addition, since the McLaughlin & Tiederman (1973) correction scheme uses the weighting function of $|\mathbf{V}_i|^{-1}$, the weights will approach infinity as the velocity reduces to zero and, thus, this would overcorrect the mean values (Edwards, 1987). To simplify the biasing correction method (in terms of data collection and the analysis procedure) and because not all velocity components can be available to the researcher, McLaughlin & Tiederman (1973) proposed a one-dimensional corrected distribution method (one order of magnitude estimate):

$$\frac{\overline{U_m}}{\overline{U}} \approx 1 + \frac{\overline{u^2}}{\overline{U}^2} \quad (2A-8)$$

Where $\overline{U_m}$ is the measured mean velocity, \overline{U} is the actual mean velocity, and $\overline{u^2}$ is the velocity variance. This expression shows that the bias is on the order of the square of the turbulence intensity. Stevenson et al (1982) showed that for turbulence intensities (measured with one-component LDV downstream of the step in the shear layer) less than 20% (with equal validation and sampling rates), the one-dimensional correction scheme (Eq. 2A-8) accounted for the bias error. At higher turbulence levels, the authors noted over-correction in the biased mean velocities which concurs with the premise discussed by Edwards (1987).

Various other methods have been proposed by researchers to correct for the velocity bias. The most accepted in the literature is known as the residence-time or transit-time correction (Tavoularis, 2005) and this method is applicable when the data rate (\dot{N}) is greater than $1/2\tau_\eta$ (Edwards, 1987). For further clarity, Adrian (1983) defined the data density as $\dot{N}\tau_\eta$, where τ_η is the smallest time scale in the flow (i.e. for turbulent flow it is the Kolmogorov time

scale). In general, Adrian (1983) suggested using $\dot{N}\tau_\eta > 5$ as criteria for high data density and for turbulence intensities less than 30%, the average value of \dot{N} can be used. The equations below (for the mean and r.m.s. velocities) are expressions to correct individual velocities based on the transit time of a particle across the measurement volume (Edwards, 1987):

$$\overline{u}_k = \frac{1}{T} \sum_{i=1}^N u_{k,i} \tau_i \quad (2A-9)$$

$$\sigma_k = \frac{\sqrt{\sum_{i=1}^N (u_{k,i} - \overline{u})^2 \tau_i}}{T} \quad (2A-10)$$

where $T = \sum_{i=1}^N \tau_i$ refers to the total observation time. $u_{k,i}$ is the i^{th} realization of the k -velocity component. As suggested by Edwards (1987), to evaluate whether transit-time weighting will correct for velocity bias, the $\dot{N} > \left(\frac{1}{2}\right)\tau_\eta$ criteria was evaluated for the present study. For the pulsatile flow case under the influence of a backward-facing step, the smallest time scale of the flow (based on the frequency spectra reported in Chapter Five) was $\tau_\eta \approx 0.01$ (i.e. ≈ 100 Hz) and, thus, for the smallest data rate of 100 Hz (near the wall) one obtains $\dot{N}\tau_\eta \approx 1 > 1/2$, which, according to Edwards (1987) shows that transit-time weighting would correct for the velocity bias.

For the present work and as a result of $\dot{N}\tau_\eta \approx 1 > 1/2$, a transit-time weighting technique was applied via adjusting the sampling method inside FlowSizer. There were no post-processing correction methods applied to the individual velocity realizations. Transit-time correction is very applicable to burst-analysis-type processors (Tavoularis, 2005) such as that used in the present study (FSA 3500, TSI). The FSA 3500 works on the principle of digital burst correlators with multiple 8-bit digitizers and it uses gate time weighting (transit time) to correct for the velocity bias. This ensured that each velocity data point was normalized or weighted within its own residence time. In a paper by Herrin & Dutton (1993), the authors noted that the challenge associated with using the residence time

processing technique can be the resolution and accuracy of the residence time measurement. In the present work, streamwise velocities as large as ≈ 1 m/s (for the various flow cases studied) were measured inside the measurement volume diameter of approximately $42 \mu\text{m}$ (for the $F = 120$ mm lens). Based on the latter, the particle residence time was calculated to be approximately $43 \mu\text{s}$. The FSA 3500 processor used in the present study has a minimum transit time of 100 ns (manufacturer reported) and, thus, the accuracy and the resolution was not a concern.

2A.3.1.2 Gradient Bias

Another possible source of error in LDV is the gradient bias. According to Edwards (1987), the gradient bias occurs as a result of several velocities being present inside the measurement volume at the same time. Furthermore, measurements captured closer to the wall generally increase the gradient bias as a result of heavier particles migrating away from the wall and due to the presence of a relatively greater velocity gradient (Tavoularis, 2005). To better understand the definition of the gradient bias, Naqwi et al (1984) explained this error as being due to particles with different velocities (at different y -positions) crossing the measurement volume and generating different Doppler frequencies. To correct for the velocity gradient bias, Durst et al (1995) provided the following corrections for the mean velocity and turbulence intensity:

$$\bar{U}_{\text{imeas.}} = \bar{U}_{\text{itrue}} + \frac{d_m^2}{32} \left(\frac{d^2 \bar{U}_{\text{itrue}}}{dy^2} \right) + \dots, \quad (2A-11)$$

$$\overline{u^2}_{\text{imeas.}} = \overline{u^2}_{\text{itrue.}} + \frac{d_m^2}{16} \left(\frac{d \bar{U}_{\text{itrue}}}{dy} \right)^2 + \dots, \quad (2A-12)$$

whereby the authors noted that for the mean velocity and the turbulence intensity, the corrections depend on the derivative of the variation of \bar{U}_i (with wall distance) and the mean velocity gradient, respectively. To include the correction for $\overline{v'^2}$ and $\overline{u'v'}$, Compton (1995) extended the analysis as follows:

$$\overline{v'^2}_{\text{meas}} = \overline{v'^2}_{\text{true}} + \frac{d_m^2}{32} \left(\frac{d^2 \overline{v'^2}}{dy^2} \right) + \dots, \quad (2A-13)$$

$$\overline{u'v'}_{\text{meas}} = \overline{u'v'}_{\text{true}} + \frac{d_m^2}{32} \left(\frac{d^2 \overline{u'v'}}{dy^2} \right) + \dots, \quad (2A-14)$$

Furthermore, Durst et al (1995) used LDV to carry-out near-wall measurements (streamwise velocity) inside a 50 mm diameter pipe and showed how the spatial resolution of the measurement volume (d_m) dramatically influences the turbulence intensity measurements. The author measured the turbulence intensities with a spatial resolution range, $70 \mu\text{m} < d_m < 2000 \mu\text{m}$, at several points with the outermost point at 4 mm away from the wall. The results clearly show the effect of the gradient bias since there is an increase in the r.m.s. velocity with a decrease in the spatial resolution (larger d_m). From Eq. (2A-12), Durst et al (1995) deduced the limiting behaviour of turbulence intensity as follows:

$$\left(\frac{u'}{U} \right)_{\text{meas}} = \left[\left(\frac{u'}{U} \right)_{\text{wall}}^2 + \frac{d_m^2}{16y^2} \right]^{1/2} \text{ as } y \rightarrow 0 \quad (2A-15)$$

The authors reported the measured, corrected, and predicted (Eq. 2A-15) profiles of u'/U close to the wall (in the viscous sublayer) and the findings were as follows: (1) an overestimate of the measured profile u'/U and (2) the corrected profile u'/U was in good agreement with the prediction from Eq. (2A-15). An equal observation was reported by Muller (1992), whereby the author measured (with both a custom LDV system and hot-wire anemometry) the mean velocity and turbulence intensity distributions near the wall in a boundary layer developing over a flat plate. Muller (1992) reported good agreement for the mean velocities between the two measurement techniques (and with the Blasius analytical solution), whereas the turbulence intensity profiles were much larger in magnitude in the LDV measurements. Applying the correction equations presented by Durst et al (1995), Muller (1992) was able to obtain a close match between the two techniques. Both of these research papers validate the manifestation of gradient effects in LDV (specifically for near-wall velocity measurement inside the viscous sublayer) and the implications on the measurement accuracy.

The near-wall LDV measurements by Durst et al (1995) demonstrated that the effect of the velocity gradient bias (on the streamwise turbulence intensity) is only applicable to a finite region inside the viscous sublayer (i.e. $y^+ \leq 3$). This was also noted by Benedict & Gould

(1996) whereby LDV measurements revealed high turbulence intensities (downstream of a step and just after separation) in the viscous sublayer region of $y^+ < 8$ as a result of gradient broadening. For clarity with respect to the latter, Benedict & Gould (1996) provided two-component LDV velocity data for a flow subjected to a backward-facing step under turbulent initial conditions ($Re \approx 26300$) with an ER of 1.25. For the present study (in the region $y^+ < 5$ and for the $F = 261$ mm lens), the correction equations proposed by Durst et al (1995) and Compton et al (1995) were applied and the difference between the measured and corrected values was negligible in comparison to the random errors. The latter observation was as well reported by Avari et al (2016) which used a commercial LDV to measure the streamwise velocity inside the PPFC (same channel as used in the present work) under both, a low- Re turbulent and pulsatile laminar flow.

2A.3.1.3 Angle Bias

An additional LDV bias that has been reviewed in the literature is the angle bias (also known as the fringe bias). According to Tavoularis (2005), the angle bias can cause measurement inaccuracies in highly three-dimensional flows since the particles that cross the measurement volume form small angles with the fringes and, as a result, the processor may not register all particle speeds at all angles. As example, counters typically have a predetermined criteria for the amount of fringes that the particle must come across before the velocity measurement would be considered valid (Edwards, 1987). Furthermore, according to Goldstein (1996), the effects of the angle bias on the accuracy is more evident when the particle velocities are parallel to the fringes inside the measurement volume. In addition, Goldstein (1996) suggested using frequency shifting to reduce and/or eliminate the biased velocity data since it adds cycles to the Doppler burst (as a result of the fringe motion relative to the fluid). The latter will allow particles travelling parallel to the fringes to produce an acceptable number of cycles since the fringes will move over the traveling particles (Goldstein, 1996). A similar observation was noted by Stevenson et al (1984) where mean velocity and turbulence statistics were measured downstream of backward-facing step using one-component LDV. The authors studied the effect of the angle bias on the measured mean velocities and the turbulence intensity (in a highly turbulent recirculating flow) with and without a 10 MHz frequency shift. The authors demonstrated

clear bias implications on the calculated mean velocities (resulting in higher measured velocities) and turbulence intensities for the unshifted case. In their work it was found that using a 10 MHz shift was satisfactory to eliminate the angle bias. Given that in this study frequency shifting was used (via 40 MHz Bragg cell), the angle bias was considered negligible and is not further discussed.

2A.3.1.4 Fringe Divergence

According to Zhu (1996), accurate optical alignment of the LDV system (i.e. probe) is critical to improve the SNR of a signal and to ensure measurement accuracy. According to Fleming & Kuhlman (1994), improper optical alignment of the LDV probe could lead to a diverging fringe pattern and, hence, affect the accuracy of the velocity measurements. Fringe divergence is caused by two beams crossing (in a pair) prior to or subsequent to the location of the beams waists (Fleming & Kuhlman, 1994), which results in a non-uniform fringe spacing. As a result of non-uniform fringe spacing, the conversion between frequency to velocity would be incorrect since the calculation is based on the assumption of uniform fringe spacing. In fact, theoretical predictions provided by Hanson (1973) show that accuracy errors as a result of fringe divergence are smallest when the two beams intersect relative close to the beams waists. Furthermore, Fleming & Kuhlman (1994) provided a mathematical expression that predicts maximum residual turbulence intensity (artificial increase in the measured r.m.s. velocity) caused by the fringe divergence effect. The authors defined the maximum residual turbulence intensity as $I_R = I_m/b$, where b is the confocal distance of a beam (distance over which the wave fronts are considered planar) and is defined as $b = 8\pi w_0^2/\lambda$ (where $w_0 = d_e/2$). In this study, I_R was, respectively, 0.92% and 0.91% for the $F = 120$ mm and 261 mm lenses ($\lambda = 488$ nm). These calculated values were within the precision uncertainty (isolated LDV r.m.s.. velocity under steady laminar flow) of the system (see next section, 2A.3.2) and, hence, the effect of fringe divergence was considered negligible. In addition, the noise levels from the LDV system (which is quantified in the subsequent section) was truncated (is discussed in Chapter Five) from the actual turbulence signal and, thus, the effect of fringe divergence was not considered relevant in the present work. However, the work of Fleming & Kuhlman (1994) provided a guideline to minimize the effect of fringe divergence on velocity measurements,

whereby the beams should cross at a point that is within $\pm 12.5\%$ of the confocal distance from the beams waists. In the present study, this corresponds to approximately 2.7 mm and 13 mm for the 120 mm and the 261 mm lens, respectively. To ensure this condition was met, optical alignment of the LDV probe was performed by launching the four laser beams into four pin holes (with a diameter of 1.8 ± 0.02 mm). A schematic demonstrating this alignment procedure is shown in Fig. 2A-5. The spacing between the pinholes was 50 ± 0.05 mm and 25 ± 0.05 mm corresponding to the blue and green beams, respectively (i.e. uncertainty in the spacing verified by a digital Vernier caliper). In this procedure, the focusing lens was removed to ensure that the four collimated beams were parallel with each other (i.e. to remove focusing of the beams). The first and the second block was positioned at approximately 120 mm and 300 mm away from the probe aperture, respectively. The spacing of the blocks (in relation to the probe aperture) was selected to simulate the focal length of both lenses ($F = 120$ mm and 261 mm). Steering wedges (prisms) were used to steer the four beams into the pinholes of the two blocks (see Fig. 2A-5a). This process ensured that the blue beams were parallel (in relation to each other) and in-plane ($x - z$) over a 300 mm working distance. Similarly, as a result of this procedure, the green beams were parallel and remained in-plane ($y - z$) over the 300 mm working distance. This procedure also ensured that the three incoming laser beams (excluding the green centre beam) struck the lens at equal radial positions and, thus, ensured negligible differences in the angle each beam formed with the optical (probe) axis.

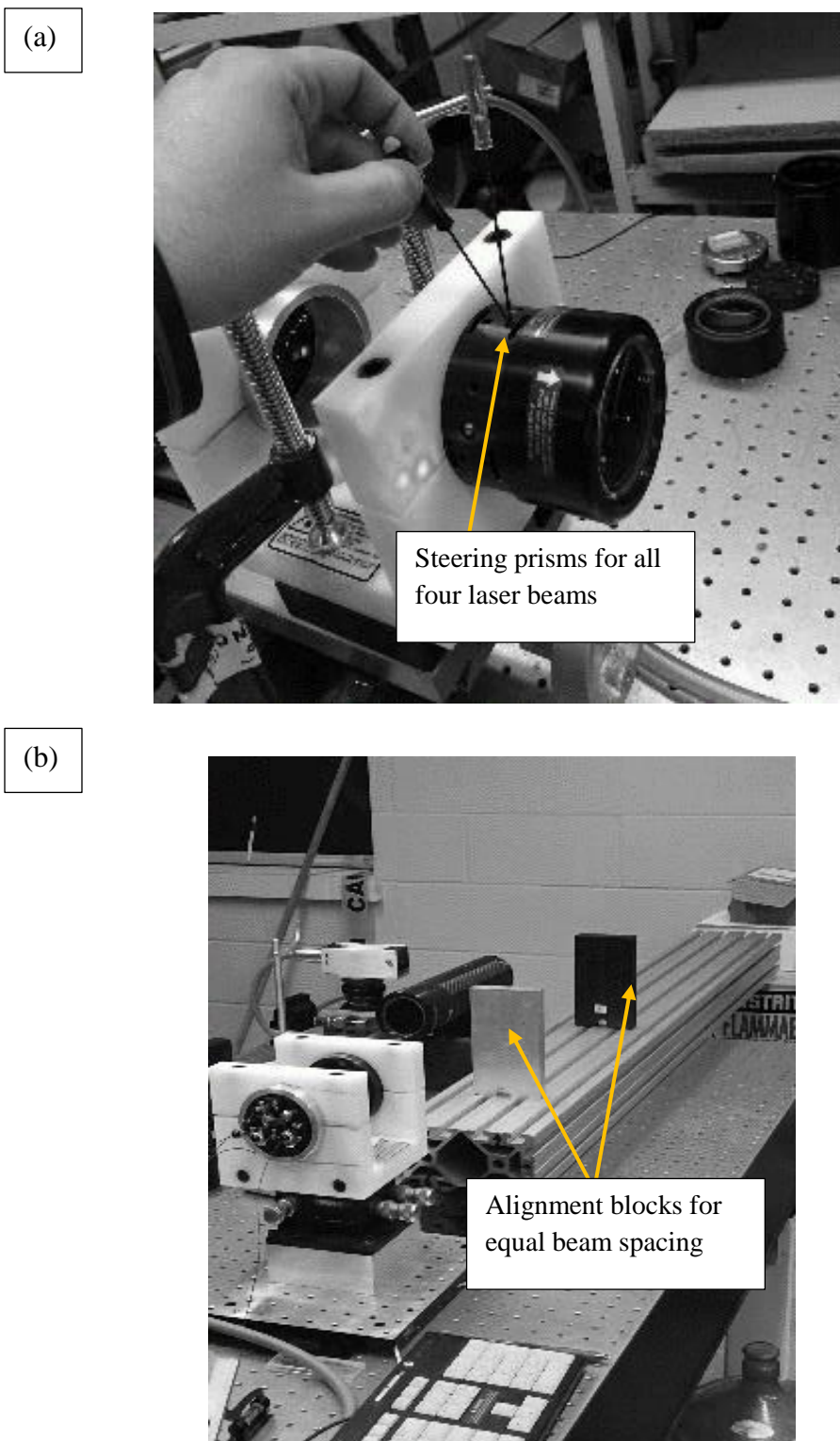


Fig. 2A-5 Procedure for optical alignment of the LDV system: (a) laser beam steering module, (b) beam spacing calibration

2A.3.2 LDV Precision Errors

In this section, a direct method is reported that was used to estimate the true precision of the LDV system. For the streamwise velocity component, this was accomplished by acquiring multiple velocity measurements across the channel height (h) at the working section. Flow rates under 10 mL/s were used to ensure steady laminar flow at the working section of the flow channel (i.e. $Re < 1350$; Patel & Head, 1969). As a result, the measured streamwise r.m.s. velocities were solely due to LDV noise (spurious r.m.s. velocity not related to turbulence). This method allowed segregation of LDV-induced noise (r. m. s. u') and, thus, quadrature subtraction (Kehoe, 2001) of the noise from the actual turbulent intensities (turbulent velocity fluctuations). Previously, Avari (2015) and Kehoe (2001) used a similar technique to segregate the LDV-induced noise by measuring a steady laminar flow and they detected spurious r.m.s. velocities (fixed) of 0.0025 m/s and 0.02 m/s, respectively. An additional study reported by Iyer & Woodmansee (2005) used an optical chopper for LDV system validation. In their study, the wheel rotated (at a specific angular velocity) relatively steady and the wheel's perforations moved across the measurement volume (fringes) to detect the streamwise and swirl velocities. The authors found that the precision of the LDV system was independent of the velocity measured (over the range, 5-35 m/s) and reported r.m.s. velocities of 1.08 m/s and 1.22 m/s (irrespective of whether the flow speed was 5 m/s or 35 m/s) for the two channels measured (u, w). According to Iyer & Woodmansee (2005), when measuring a turbulent velocity field the measured r.m.s. velocity consists of both turbulent fluctuations and LDV noise. Hence, the authors suggest subtracting the LDV noise from the measured mean square velocity fluctuations (in order to correct the r.m.s. velocity from the LDV bias).

According to Kunz et al (2001), the major contributors of precision errors in LDV measurements are data processing errors as a result of averaging a finite number of velocity realizations. In addition, Durst et al (1995) points to electronic noise as an additional contribution to precision errors, whereby the author measured non-zero turbulent intensities (inside the viscous sublayer) notwithstanding the velocity corrections due to the finite size of the measuring volume (bias errors discussed in section 2A.3.1). Durst et al (1995) found that impurities which collected on the wall (in the region of measurement)

generated a highly scattered surface contributing to the overall noise. The author also suggested reducing the frequency shift to 200 kHz and to limit the measurement distance (from the wall) to one-half of the measurement volume diameter ($0.5d_m$). In the present study, both of those considerations were implemented to reduce the noise and are discussed in Chapter Four (uncertainty Chapter).

The statistical quantities of interest in this section are the mean velocity and the root-mean-square (r.m.s.) velocity. Iyer & Woodmansee (2005) give the time-varying mean velocity of a sample of N particles as follows:

$$\bar{u} = \sum_{i=1}^N u_i / N \quad (2A-16)$$

where u_i can be defined as the instantaneous velocity measured for the i^{th} particle inside the measurement volume. In the present study (specifically for the evaluation of the LDV-induced noise), the number of velocity realizations (data points) was $N \approx 1500$ to achieve a statistically stationary velocity mean, \bar{u} . At $N > 1500$, the difference between the \bar{u} values was less than 0.2%. The sample size $N \approx 1500$ was determined by plotting \bar{u} against $N = 100, 200 \dots 20,000$ and, the cut-off value of N was selected based on a difference of 0.2% in comparison to the subsequent size of N (i.e. $N = 1600$). Essentially, there was no statistically significant differences in the mean velocity by varying the sample size from 1500 to 20000.

Furthermore, Iyer & Woodmansee (2005), as well, defined the r.m.s. velocity as follows:

$$\text{r.m.s. } u' = \left(\sum_{i=1}^N \frac{(u_i - \bar{u})^2}{N-1} \right)^{\frac{1}{2}} \quad (2A-17)$$

The r.m.s. velocity was calculated across the channel height, $h = 50, 100 \dots 1800 \mu\text{m}$, under a steady laminar flow under various flow rates for both the $F = 120 \text{ mm}$ and the 261 mm lenses. The fixed r.m.s. velocity value (no detected change) over the range of velocities examined (0.0025-0.500 m/s) was r.m.s. $u' = 0.0025 \text{ m/s}$ (2.5 mm/s). Values less than 0.0025 m/s were therefore considered insignificant. Near the centre region of the channel ($y/h \approx 0.5$), typical r.m.s. u'/\bar{u} values over the velocities examined was approximately 0.6-1% whereas, near the wall ($y/h \approx 0.95$) values as large as 100% were detected. Given

that the fixed r.m.s. velocity remained at 0.0025 m/s in the vicinity of the wall, the increase of r.m.s. u'/\bar{u} values at the wall was a result of a smaller mean velocity.

This evaluation was also performed for the green beams (v component of the velocity vector). However, the latter was not possible inside the PPFC as a result of the v -component being zero for a steady laminar flow (no data rate detected). For this reason, the present author reports the r.m.s. v' (spurious value) inside a vertical glass column under a quasi-steady flow condition. A wide-range of velocities (i.e. 0.008 to 0.038 m/s) were measured inside the column with the LDV system via controlling the downstream valve (i.e. valve openings under test were 100, 75, 50, and 25%). This experiment set-up is shown in Fig. 2A-6a. The result from this experiment showed that the spurious r.m.s. velocity (associated with the green beams) was r.m.s. $v' = 0.004$ m/s (4 mm/s), which is slightly larger than the r.m.s. $u' = 0.0025$ m/s detected inside the PPFC using the blue beams. Furthermore, the spurious r.m.s. u' was also evaluated (in addition to the PPFC used in the present work) inside a long section of straight acrylic-made flow channel (whereby $l \times w \times h$: 600 x 17.5 x 1.8 mm). The latter was investigated to compare the detected noise levels (r.m.s. u'/\bar{u}) between the two flow channels. The author had concerns in regards to the accuracy of the PPFC assembly (i.e. implications of the assembly process potentially disturbing the flow). The plexi-glass channel is also shown in Fig. 2A-6b for clarity purposes. The r.m.s. $u' = 0.0025$ m/s found inside the plexi-glass channel was the same as in the PPFC and, thus, the predetermined notion of the PPFC assembly disturbing the flow was not correct and any detected r.m.s. velocities were only a result of LDV noise (i.e. optical and processing of signal).

The final note worth mentioning is on the subject of accuracy with the LDV measurements. As pointed out in the preceding sections of this Appendix, generally the bias errors are treated as negligible in comparison to the random errors. This was verified by the theoretical model (energy equation) for the glass column in Fig. 2A-6a. The resulting error between the theory and measurement was found to be within the precision uncertainty.

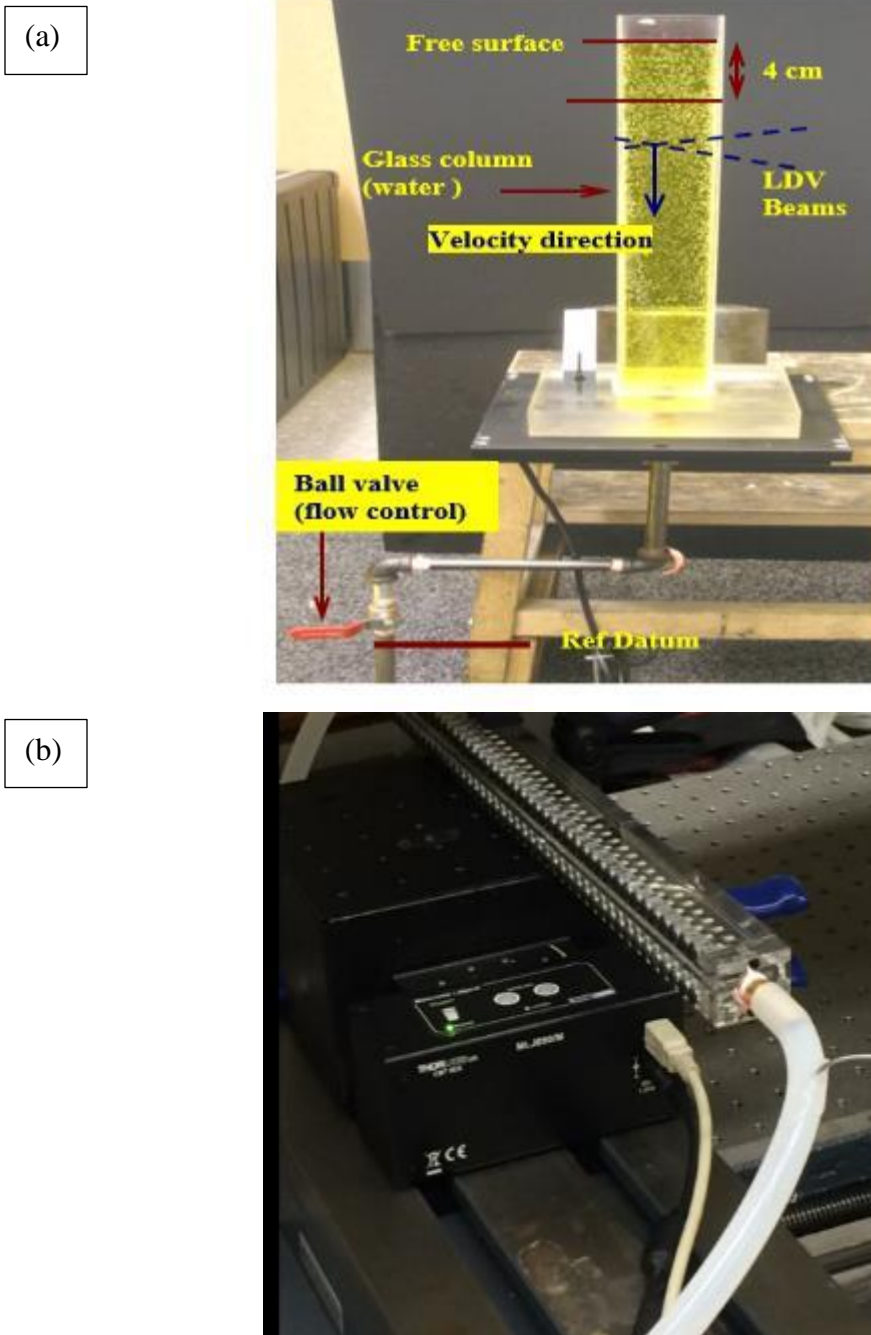


Fig. 2A- 6 Spurious r.m.s. velocity detection experiments: (a) vertical glass column, (b) plexi-glass flow channel. For the glass column experiment, the change in the flow rate over a 4 cm interval (for all tested conditions) was negligible. This allowed the flow to be considered as steady laminar over that specified range where LDV measurements were taken. This simplification was considered acceptable since the flow variability was found to be one order of magnitude larger than that of the velocity change over the 4 cm interval (i.e. verified by analytical solution: energy equation).

In the few preceding paragraphs the spurious noise level inside the PPFC was discussed and reported. This noise level which is not attributed to turbulence is removed from the r.m.s. signal and energy spectra which are reported in Chapter Five of this thesis. The noise removal from the signal allowed actual r.m.s. signals (for u and v) downstream of the backward-facing step (under steady and pulsatile flow) to be reported. In addition, the removal of the noise from the actual turbulence signal (through only considering values larger than the spurious r.m.s.) eliminates the flatness characteristic of the energy spectra and made it easier to detect the smallest time-scales of the flow together with the $-5/3$ slope (representing a fully-turbulent flow). In the present study, it was found that the position of the forward-scatter receiver significantly affected the noise levels collected by the receiver. Hence, the receiver position was fixed to an off-axis position to minimize the noise. The latter is further explained in section 2A.7 of this Appendix.

To determine the precision uncertainty interval of velocity measurements, Kunz et al (2001) provides both the precision error for the mean velocity (assuming a normal distribution) and the turbulence intensity (assuming a Chi-square distribution) as follows:

$$\frac{P_{\bar{u}}}{\bar{u}} = \pm \frac{1}{\sqrt{N}} \frac{\text{r.m.s.}u'}{\bar{u}} \quad (2A-18)$$

$$\frac{P_{\text{r.m.s.}u'}}{\text{r.m.s.}u'} = \pm \frac{1}{\sqrt{2N}} \quad (2A-19)$$

here Eq. (2A-18) represents the standard error of the mean and Eq. (2A-19) represents sample variance, r.m.s. u' . Using Eq. (2A-18) for $N = 1500$ and r.m.s. $u' = 0.0025$ m/s yields a standard error of the mean of ± 0.00006 m/s (absolute value). Hence, the precision uncertainty of the mean velocity is approximately 0.01 % of \bar{u}_{\max} , where $\bar{u}_{\max} \approx 0.500$ m/s (at $Q \approx 10$ mL/s). These values are in good agreement with those reported by Lai et al (2013) which noted that the repeatability of LDV measurements (using the FSA 3500/4000 processor) is better than 0.05% at low to moderate velocities. In the present study, the FSA 3500 processor was used and, hence, the technical note provided by Lai et al (2013) is a relevant comparison. For 95% confidence interval, using Eq. (2A-5) (i.e. $\varepsilon_{LDV} = \sqrt{B^2 + (t_1 P)^2}$; where $t_1 = 1.96$) yields a total uncertainty of $\varepsilon_{LDV} = \pm 0.00007$ m/s under steady laminar flow conditions. It should be noted that this very low uncertainty limit is

predominantly a result of the large sample size. This section only reports the uncertainty of the steady laminar flow whereas Chapter Four includes the uncertainty (as a result of the statistical sampling error) of the various mean and turbulence quantities (using Eq.'s (2A-5), (2A-18) and (2A-19)) for the different flow cases reported at various locations at the working section. In terms of the latter, given that the r.m.s. u' values are larger for cases with a highly-disturbed three-dimensional flow (i.e. backward-facing step flow cases), the reported uncertainties were larger (given a constant value of $N = 1500$). It will be demonstrated in Chapter Four that for the pulsatile flow cases (normal carotid waveform), $N = 1500$ was sufficiently large to achieve statistical convergence for the first-order, second-order, and higher order statistics (i.e. skewness and kurtosis).

2A.4 Green Beams Measurement Limitation (v-component)

The objective of the present work was to simultaneously measure both u and v velocity components at the working section (across the channel height) for several locations downstream of the backward-facing step. It was found that using the $F = 120$ mm lens the v -component could not be measured, with the exception of a few measurement points very close to the wall. For this reason, an additional lens was introduced with a focal length of $F = 261$ mm. The $F = 261$ mm lens focused the blue and green beams into the working section with a much smaller beams' half-angle (in contrast to the $F = 120$ mm lens) thereby allowing the v -component measurement over a wider range along the height of the channel. The geometrical constraints (i.e. beams' half-angle and channel height) limiting the v -component measurement is illustrated in Fig. 2A-7a. To measure the streamwise and wall-normal velocity at the midplane (i.e. $2z/w = 0$) of the channel, the probe lens (i.e. $F = 261$ mm) was positioned 250.62 mm away from the optical window (exterior surface of the window). The latter was deduced based on Snell's law (i.e. $n_1 \sin(\theta_1) = n_2 \sin(\theta_2)$); where n, θ were, respectively, the refractive index of each medium and the angle that the incident beam makes with the normal of the boundary). It should be noted that the refractive index (n) for the air, the cell fluid and the optical window were 1.00, 1.34 and 1.52, respectively (Avari, 2015). The allowable height, h_a , to traverse the green beam measurement volume in the positive y direction (across the channel height) was evaluated as $h_a = 0.81 \pm 0.070$ mm. The uncertainty was estimated based on the spot size of the

Gaussian green beam (at the optical window interface) evaluated by $s(z) = w_0 \sqrt{1 + \left(\frac{\lambda z}{\pi w_0^2}\right)^2}$ (refer to Fig. 2A-7b; where $2w_0 = d_e = 90.5 \mu\text{m}$; Bandres et al. 2004) and was approximately $s(14.75 \text{ mm}) \approx 139 \mu\text{m}$. This analysis demonstrates that starting from the closest measurement point at the wall (i.e. $\approx 40 \mu\text{m}$), the measurement volume can be traversed (in the positive y direction) only by $\approx h/2$ (i.e. 0.9 mm). This result is consistent with the actual measurements of the v -component reported in Chapter Five (i.e. measurement possible up to $y/h \approx 0.5$; whereby $y = 0$ at the lower wall).

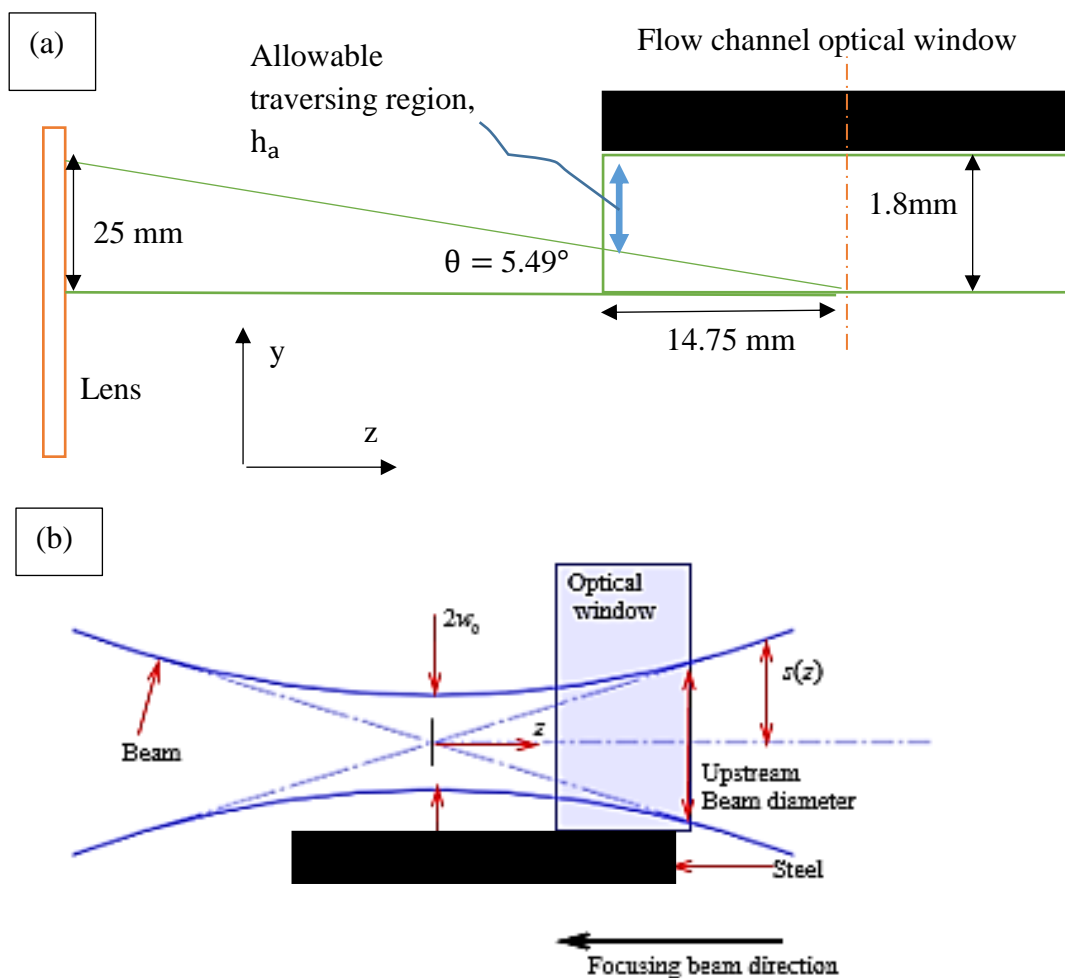


Fig. 2A-7 Green beams measurement limitation: (a) v -component ray diagram, (b) Focusing of a Gaussian beam. Diagrams are not to scale.

2A-5 Measurement Volume Alignment for Simultaneous u and v Measurements

In order to obtain accurate cross-correlated statistical quantities (i.e. $-\overline{u'v'}$), it was important to ensure that the measurement volumes from both the blue and the green beam pairs overlapped as much as possible at the working section. This is not always easy given the uncertainties associated with the geometry of the individual beams (i.e. the incident angle each beam makes with the normal of the optical window). The small channel height (1.8 mm), together with the small differences in the refraction of each beam (as they transmit into the working section), makes measurement volume overlap even more challenging. For example, Ching et al (1995) performed two-component LDV measurements inside a constant-head vertical water funnel and found that even small misalignment between the blue and the green measurement volumes results in a 35% decrease in the $-\overline{u'v'}$ values. According to the author, this error was detected since the measured velocity components were not associated with the same particle (i.e. coherence mode). In the present study, alignment between the two measurement volumes was established by transmitting the measurement volume (blue and green beams) region through an objective lens and projecting the individual beam waists onto a flat and white screen (see Fig. 2A-8). Then, steering prisms on the probe were used to correct any observable measurement volume misalignment via steering the individual beams until the correct overlap was achieved (i.e. visual observation). However, given that the four beams had to transmit through several interfaces (air, optical window and the cell fluid) to capture velocities at the working section, an additional experiment was performed to ensure accurate alignment between the two measurement volumes as a result of refraction errors. This experiment included launching the four laser beams into the working section of the PPFC (i.e. standard to any flow case investigation) and monitoring the coincidence data rate quantity inside FlowSizer. Steering prisms together with minor positioning adjustments of the PPFC (i.e. to ensure the optical axis of the probe is 90° in relation to the channel optical window) were used to maximize the coincidence data rate. This procedure was highly sensitive to the induced vibrations from the surroundings which include the operation of the pump. It was found that after installing a damping pad under the pumping unit, the vibrational effects were negligible.

For simultaneous u and v velocity measurements, coincident mode of operation (two channels obtain velocity data from the same particle) was used in order for the velocity components to be collected at the same time. For a better understanding of the reader, the coincidence window is a measure of the time in which the second channel (channel one or two in the present work) must complete the measurement once the first channel initiates the window (i.e. data-ready signal; Menon, 1987). In the present work, the coincidence data rate varied between 200-500 Hz (depending on the measurement position). The latter was influenced by the channel which had the lowest data rate which, for the present study, was the green beam channel (i.e. Ch. 1). For the present work, the setting inside FlowSizer for the coincidence interval of 50-100 μs was used which was also recommended by Menon (1987). In terms of the latter, the author suggested using a coincidence window that is at least an order of magnitude less than the inverse of the data rate (i.e. for $\dot{N} = 1000$ Hz, the coincidence window should be ≈ 100 μs). In addition, the coincidence time interval of 50 μs was much greater than the estimated arrival time of the particles (i.e. where the average time of arrival was $1/\dot{N} = 1000$ μs based on maximum $\dot{N} = 1000$ Hz) and, hence, was considered acceptable.



Fig. 2A-8 Projection of the four laser beams against a white flat background to evaluate measurement volume overlap.

2A.6 Flow Tracers and Seeding Concentration

The LDV technique functions on the presumption that the tracer particles can follow the flow and, hence, the ability of the particles to follow the rapid changes of the streamwise and wall-normal velocities downstream of the backward-facing step was evaluated. For all flow cases considered in Chapter Five, Titanium Dioxide (TiO₂) R-192 (grade number) tracer particles were used with a particle size distribution as per Fig. 2A-9 (Showa America manufacturer reported).

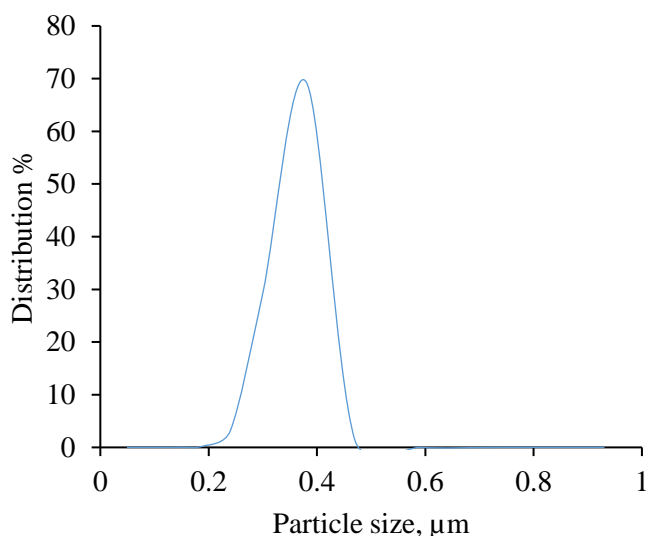


Fig. 2A-9 TiO₂ particle size distribution as reported by Showa America (supplier). The mean particle size is 0.36 μm.

According to Melling (1997), particles that are irregular in shape can be treated as spheres by defining an equivalent aerodynamic diameter. The aerodynamic diameter for the tracer particles was calculated based on work presented by Agarwal & Fingerson (1979) to be 0.72 μm based on $d_a = \sqrt{\rho_p} d_p$, where ρ_p is the density of the tracer particles (4.0 g/cm³) and d_p is the mean particle diameter (0.36 μm) of the distribution shown in Fig. 2A-9. Since the manufacturer of the seeding particles reported a spherical shape for the particles, the mean particle diameter of 0.36 μm is considered for the calculations below (not the aerodynamic diameter). The ratio between the particle and fluid densities $\gamma = \left(\frac{\rho_p}{\rho_f}\right)$ used in this study is ≈ 4.0 , since the fluid density is approximately 1.0 g/cm³ (997.96±0.12 kg/m³).

Furthermore, the dynamic response of a particle can be explained by the following differential equation (Tavoularis, 2005):

$$\vec{F}_D = m_p \frac{d\vec{u}_p}{dt} \quad (2A-20)$$

Where \vec{F}_D is the drag force acting on the particle, \vec{u}_p is the velocity of the particle moving at a constant rate, and m_p is the mass of the particle. The equation above neglects body forces and assumes that $\gamma = \left(\frac{\rho_p}{\rho_f}\right) \gg 1$. Based on the assumption that the particle is spherical in shape with a diameter, d_p , the relative Reynolds number can be expressed as follows (Tavoularis, 2005):

$$Re_p = \frac{\rho_p |\vec{u}_f - \vec{u}_p| d_p}{\mu_f} \ll 1 \quad (2A-21)$$

The above equation constitutes a Stokes flow (i.e. $Re_p \ll 1$) and for this condition the particle motion can be expressed as follows (Tavoularis, 2005):

$$\frac{\rho_p d_p^2}{18\mu_f} \frac{du_p}{dt} + u_p = u_f \quad (2A-22)$$

To calculate the response time of the tracer particle, the equation of motion of the particle is reduced to account for the acceleration terms and the Stokes drag force (Bharathram, 2004):

$$\tau_p = \frac{\rho_p d_p^2}{18\mu_f} \quad (2A-23)$$

Where d_p is the diameter of the particle and μ_f is the viscosity of the fluid (this study, $\mu = 0.748 \pm 0.001$ mPa s). Considering the mean particle diameter of $0.36 \mu\text{m}$, and a fluid density of 997.96 ± 0.12 kg/m³ yields a time response of $\tau_p \approx 0.038 \mu\text{s}$ ($f_p \approx 2.6 \times 10^7$ Hz).

As will be demonstrated in Chapter Five (for the steady and pulsatile flow over a backward-facing step), there was no energy present at frequencies greater than $f_p \approx 2.6 \times 10^7$ Hz and, thus, this demonstrates that the particles can follow the flow in its small scale motions (i.e. high-frequency fluctuations). For reference purposes, $Re_p = 0.48$ (based on the maximum velocity measured of ≈ 1 m/s), which is smaller than unity and, hence, Stoke's drag applies to the present analysis (Tavoularis, 2005).

An alternative method to determine whether the particles follow the flow (i.e. having the same velocity as the fluid with no lag) is to calculate the Stoke's number defined as follows (Avari, 2015):

$$St_\lambda = \tau_p / \tau_\lambda \quad (2A-24)$$

where τ_λ represents the turbulent integral time-scale and can be determined as follows:

$$\tau_\lambda = \frac{\Lambda}{\text{r.m.s.} u'} \quad (2A-25)$$

Where Λ is the integral length scale and r.m.s. u' is the typical turbulence intensity of the flow (in the present case for the backward-facing step flow cases). Avari (2015) further notes that the integral length scale can be defined as $0.92(h/2)$, where h is the channel height. In addition, for the unsteady pulsatile flow the Stoke's number can be defined as follows (Avari, 2015):

$$St_o = \sqrt{\omega d_p^2 / 2\nu} \quad (2A-26)$$

where $\omega = 2\pi f$ is the angular frequency of the pulsatile flow and for the present study was 6.78 rad/s.

Considering a maximum r.m.s. $u' = 0.11$ m/s (for pulsatile flow downstream of the step) and r.m.s. $u' = 0.15$ m/s (for steady flow downstream of the step), Eq's. (2A-24) and (2A-26) yield $St_o = 7.6 \times 10^{-4}$ and $St_\lambda = 6.88 \times 10^{-6}$, respectively. Given that both values are much

smaller than unity, the particles may be assumed to follow the flow at integral scale with an absence of a lag (Avari, 2015).

2A.6.1 Seeding Concentration Requirements

The amount of tracer particles inside the measurement volume (i.e. #particles/volume) influences both the data rate and the quality of the Doppler signal and, thus, the size of the particles together with the concentration should be properly selected for a given experiment (Yoshizawa, 2009). For a clean Doppler signal (i.e. normal Gaussian distribution), the ideal concentration is such that only one particle passes the measurement volume at a time (Yoshizawa, 2009). Furthermore, the coincident measurement volume (formed by the blue and green beam pairs in the present work) can be crossed by different particles at a given time instant and, for an extreme case of high seeding concentration, this can lead to incorrect cross-correlated quantities such as the Reynolds Shear Stress (Menon & Lai, 1991). In addition, if the arrival rate of the tracer particles is insufficient this can lead to problems in resolving the local velocity-time history of the flow. Given all of the reasons above, it was important to determine the ideal concentration of TiO_2 inside the 5L recirculating cell fluid mixture used with the flow experiments in the present study.

The initial concentration of TiO_2 was determined based on the theory reviewed by Durst et al (1976), whereby the minimum concentration was estimated by assuming $n \approx 0.5$ ($n = \frac{\sum \tau_k}{t_s}$, where τ_k is the transit time of the individual particles and t_s is the total sampling time).

Furthermore, the particle concentration was estimated by $\tilde{N} \approx n/V_m$, where V_m is the ellipsoidal-shaped measurement volume quantity (i.e. μm^3). For the $F = 261$ mm lens (blue beams specifically) and the control volume given by $V_m = \pi r_m^2 L_m$, the particle concentration was $\tilde{N} \approx 8.26 \times 10^{10}$ particles per m^3 . Thus, for 5L of cell fluid (i.e. $0.005 m^3$) the number of particles required was 4.13×10^8 (i.e. $\approx 322 \mu g$; considering the density and volume of the spherical particles). Furthermore, with the concentration specified above the typical data rates (for steady and pulsatile flow over the step together with LDV coherence mode) were between 200-1000 Hz (i.e. 100-200 Hz near the wall and 500-1000 Hz away from the wall). To ensure that the data rates were sufficient (and, thus, that \tilde{N} was

sufficiently large) to resolve the velocity fluctuations downstream of the backward-facing step, the following criterion was used as an estimate (Bendat & Piersol, 1971):

$$\tilde{N}\bar{u}L_m d_m \geq 2f_{\text{turb}} \quad (2A--27)$$

where \bar{u} is the time-averaged streamwise mean velocity (or phase-averaged for pulsatile flow ($\langle u \rangle$)) and f_{turb} is the frequency associated with the velocity fluctuations. It should be noted that the left term in Eq. (2A--27) represents the average rate of signals arising from the particles crossing the measurement volume.

For $\tilde{N} \approx 8.26 \times 10^{10}$ particles per m^3 and mean velocity of 0.106 m/s (found downstream of the step in the disturbed region; near the wall; $y/h = 0.022$), the left term of Eq. (2A-27) is $\tilde{N}\bar{u}L_m d_m \approx 740$ Hz. For both, the steady and pulsatile flow cases (over the backward-facing step), the criterion presented in Eq. (2A-27) is satisfied since there was no energy present at frequencies greater than 370 Hz (1/2 of $\tilde{N}\bar{u}L_m d_m$).

2A.7 Forward-Scatter Receiver Orientation for Velocity Measurements

The forward-scatter receiving imaging relay schematic (commercial TSI receiver) is shown in Fig. 2A-10. The front lens of the receiver was positioned 300 mm (focal length of lens) away from the measurement volume region and the receiver orientation (i.e. off-axis angle) was selected based on the Mie scattering theory to obtain a strong signal whilst minimizing reflections. It was not possible to position the receiver on-axis (i.e. where the probe and receiver optical axis are collinear) as a result of the green centre beam transmitting into the receiver aperture. In terms of the latter, masking the aperture (i.e. with electrical tape as suggested by the manufacturer) was not able to resolve the excess noise in the measured signal. Based on the plot presented by Menon & Lai (1991) (using the Mie scattering theory) showing the relationship between scattered light intensity and receiver orientation, a 30° off-axis orientation was selected for the present work. For receiver orientations larger than $\approx 45^\circ$, it was not possible to obtain a measurement given the confined channel geometry. Menon & Lai (1991) showed that the difference in the scattered light intensity from on-axis to off-axis 30° was rather negligible. Under a steady laminar flow inside the PPFC, the r.m.s. u' for the $\approx 45^\circ$ orientation was 0.0018 m/s whereas for the 30° case it was ≈ 0.0025 m/s. However, the signal (data rate) was not acceptable for near-wall

measurements at the 45° receiver orientation (in agreement with the significantly lowered scattered light intensity at that off-axis orientation based on Menon & Lai (1991). For this reason, the 30° orientation was used for all flow case measurements.

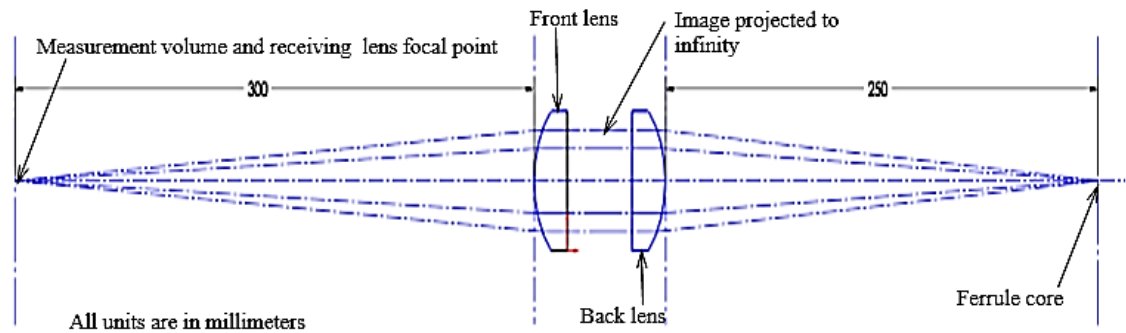


Fig. 2A-10 TSI forward-scatter receiver (receiving optics imaging relay).

2A.8 Steady Laminar Flow Investigation and Wall Shear Stress Measurements

The purpose of simulating a steady laminar flow at the working section is to: (1) measure the spurious r.m.s. values of the streamwise mean velocity at each measurement point across the channel half-height (reported in previous sections), (2) determine the closest measurement point to the wall that provides accurate mean and turbulence statistics using both the $F = 120$ and 261 mm lenses (and, hence, understand the spatial resolution implications on the WSS accuracy) and (3) obtain WSS data for $Re_m = 100, 600, 900$ and 1240 together with its uncertainty (whereby Reynolds number is calculated considering the bulk velocity and the hydraulic diameter). A final justification for prescribing steady laminar flow at the working section is to compare the vertical streamwise mean velocity profiles against the analytical solution and to the work of Avari et al (2016), which reports LDV measurements (with a commercial LDV two-component probe) using the same PPFC under steady laminar flow.

2A.8.1 Problem Definition and Scope of the Measurements

The streamwise velocity profiles were captured with the $F = 120$ mm lens with the closest measurement of $20 \pm 10 \mu\text{m}$ (i. e. $2y/h = 0.022$) in reference to the lower wall (whereby the datum identification method is explained in Chapter Four). Approximately 4 to 8 data

points (depending on the lens used) were captured in this wall region to determine WSS with sufficient accuracy (this is reviewed in Section 4.4: Curve Fitting Approximation Errors). For the $F = 261$ mm lens, the closest measurement was $40 \pm 10 \mu\text{m}$ (i. e. $2y/h = 0.044$) in reference to the lower wall. Furthermore, all velocity data were captured at the centre of the microscopy slide ($2z/w = 0$).

To determine the WSS at the working section, the following expression was used (Cierpka et al. 2014):

$$\tau_w = \mu \left. \frac{\partial \bar{u}}{\partial y} \right|_{y=0} \quad (2A-28)$$

where $\frac{\partial \bar{u}}{\partial y}$ is the velocity gradient (wall-normal direction) obtained by differentiating a 2nd order polynomial regression curve (least square model). As reviewed in Chapter Four, the 2nd order polynomial curve was extrapolated to the wall assuming the no-slip condition ($u = 0$ m/s at $y = 0$). As several authors report in the literature, this is an acceptable procedure for calculating the WSS for a steady laminar flow (Einav, 1989; Bell et al. 1989).

In addition, the spanwise profile $\bar{u}(z)$ of the streamwise mean velocity (for range, $-1 < 2z/w < 1$) is not considered in this section since results recorded by Avari et al (2016) demonstrate 65-75% of the working section is exposed to uniform flow. Avari et al (2016) described the uniformity of the streamwise mean velocity along the span at three locations along the microscopy slide (x-direction) and reported a difference of ± 2.4 , ± 2.9 and $\pm 4.4\%$ from the analytical solution for the channel flow. To assess whether the flow was fully developed at the working section (more specifically across the microscopy slide in the x-direction such that $\partial \bar{u} / \partial x \approx 0$ across that region), Avari et al (2016) measured $\bar{u}(y)$ at three locations (for $Re = 100$ and 990) and reported an average deviation from the analytical solution to be $< 6.5\%$. In the present study, the experimental data points (for $Re_m = 100, 600, 900$ and 1240) and the analytical estimation (calculated based on Eq. 3-4) were within the experimental uncertainty.

2A.8.2 Results and Discussion

The streamwise mean velocity (normalized with the bulk velocity U) plotted against the channel half-height is given in Fig. 2A-11. The normalized streamwise mean velocity profile is also shown in Fig. 2A-11, captured by means of the $F = 261$ mm lens. The normalized velocity profiles (\bar{u}/U) are only shown across the channel half-height since Avari et al (2016) reported symmetry (with respect to the channel centre-line) for steady laminar flow for $Re = 990$. For the latter, the closest measurement point to the wall reported by Avari et al (2016) was $\approx 36 \mu\text{m}$. The velocity profile measured by Avari et al (2016) is reported in Fig. 2A-11 for comparison. It should be noted that the Re definition used by Avari et al (2016) was based on the channel height (1.8 mm) and not the hydraulic diameter (3.2 mm) and, therefore, the reported Re were smaller at a fixed flow rate. To clarify, Avari et al (2016) used a programmed flow rate value of $Q = 12.8 \text{ mL/s}$ ($Re = 990$) which yielded $Re_m = 1795$ considering the hydraulic diameter as a characteristic length scale. As reviewed in Chapter Three, the subscript “m” in the Re term denotes mean velocity (i.e. bulk velocity) and is used to make effective comparisons with the literature.

An interesting observation in Fig. 2A-11 is the ratio of the streamwise mean velocity to the bulk velocity at $2y/h = 1$. For all Re_m values, \bar{u}/U is ≈ 1.6 since the bulk velocity was deduced from the centre line velocity (\bar{u}_{max}) based on $U = \bar{u}_{\text{max}}/(m + 1/m)(n + 1/n)$ and not $\bar{u}_{\text{max}} = 3/2U = 1.5U$ (Biswas et al 2004). It should be noted that the m and n are coefficients (which depend on the aspect ratio of the channel) used in the channel flow solution equation. As the channel aspect ratio approaches infinitely wide plate and increases, the two solutions yield nearly identical results. The same results for $\bar{u}/U \approx 1.6$ are reported by Avari et al (2016) for $Re = 990$. It should be noted that the bulk velocity was also calculated by $U = 1/h \int_0^h \bar{u}(y)dy$ (where \bar{u} is the time-average of the streamwise velocity sampled at various locations across the channel height), which yielded agreement within $\pm 0.2\%$ between the two methods.

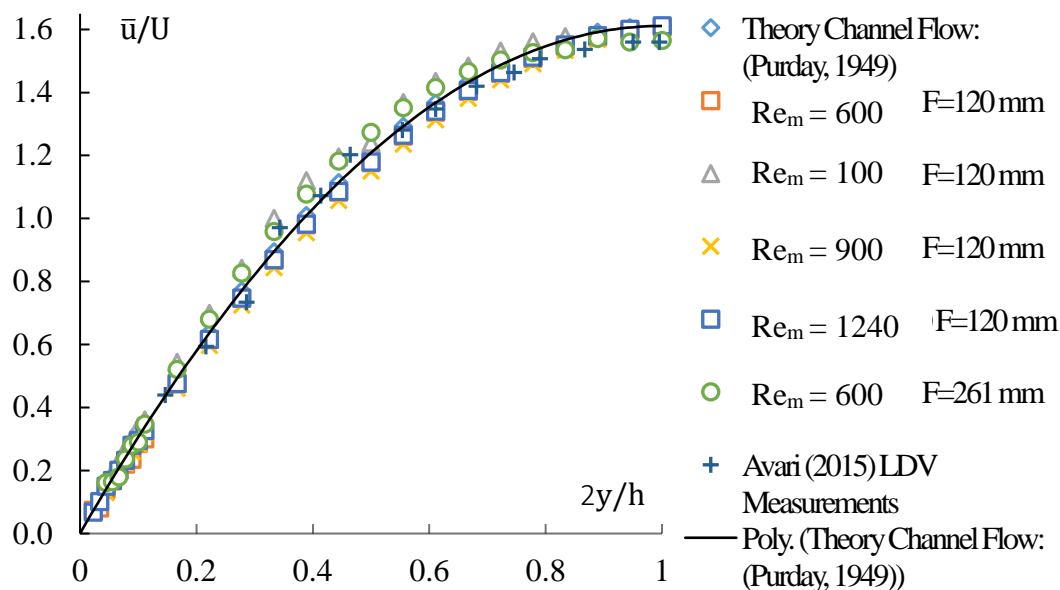


Fig. 2A-11 Streamwise mean velocity $\bar{u}(y)$ normalized with the bulk velocity U and plotted against the channel half height (Steady Laminar Flow Case). Velocity data was captured at the centre of the microscopy slide ($2z/w = 0$). For clarity, only the $Re_m = 600$ flow case is plotted for $F = 261$ mm lens (high data density at the wall). Second-order polynomial regression also shown represents theoretical data points based on Eq. 3-4. The maximum absolute error (in the wall region, $20 \mu\text{m} \leq y \leq 100 \mu\text{m}$) is ± 0.008 m/s (or 3.2% of \bar{u}_{max}).

It is evident from table 2A-2 that the difference between the experimental and theoretical WSS is larger for the $F = 261$ mm lens. The latter is a result of a larger measurement volume and thus a larger wall offset (i.e. $40 \pm 10 \mu\text{m}$). The error in the shear rate (calculated in section 4.4) is $\approx \pm 11\%$ in contrast to the error of $\approx \pm 2.3\%$ using the $F = 120$ mm lens (i.e. wall offset of $20 \pm 10 \mu\text{m}$). As expected, the error term $\left(\frac{\partial \tau_w}{\partial y}\right)^2 \epsilon_y^2$ from Eq. (4-4) is predominantly affecting the uncertainty in the τ_w value. As reviewed in Chapter Three, the WSS values in the present study are in the range of earlier *in-vitro* work (Anderson et al. 2006; Dol et al. 2010; Avari et al. 2016) which simulate shear stress in the range between 0-10 dyne/cm². The shear stress values are in the range of that found (1 to 6 dyne/cm²) inside the human venous system (Chiu & Chien, 2011).

For the $F = 120$ mm lens configuration, the present WSS values compare moderately (quantified below) with the work of Avari et al (2016), which used LDV at the working section to measure the WSS under steady laminar flow at a Reynolds number of 990 (equivalent to $Re_m = 1795$ in the present work if an equivalent definition is used). In terms of the latter, the experimental WSS reported in table 2A-2 was fitted using a straight line ($R^2 = 0.98$) and extrapolated to determine the percent difference between the present study and the work of Avari et al (2016). The WSS value at $Re_m = 1795$ yields 9.67 dyne/cm^2 which translates to a difference of 17.1% between the two studies. Using the same method for the $F = 261$ mm lens configuration, the difference in WSS between the present study and the work of Avari et al (2016) translates to 9.4%, which is within the experimental uncertainty of the present study. Hence, better agreement is found for the $F = 261$ mm lens configuration, presumably as a result of similar spatial resolution between the two studies together with the wall offset condition (i.e. $80.3 \mu\text{m}$ and $40 \pm 10 \mu\text{m}$ for the present study and $68 \mu\text{m}$ and $36 \mu\text{m}$ for the work of Avari et al 2016). It should be noted that for the present study with the $F = 120$ mm lens configuration, the WSS is within 3.1% of the value given by Avari et al (2016) based on the analytical solution (i.e infinitely wide plate). Hence, the $F = 120$ mm lens configuration seems to accord better with the theory presumably as a result of the smaller measurement volume and wall offset (i.e. $40.1 \mu\text{m}$ and $20 \pm 10 \mu\text{m}$).

Table 2A-2 Summary of τ_w deduced from experimental and analytical solutions under $Re_m = 100, 600, 900$ and 1240 . It should be noted that the analytical solution for WSS was computed using actual flow rates ($Q = 0.90 \pm 0.09, 3.90 \pm 0.039, 6.20 \pm 0.057, 7.50 \pm 0.075$ mL/s) of the pump (and not programmed, $Q = 1, 5, 8, 10$ mL/s) as reported in section 6.5. The error % in τ_w was calculated based on $|(\tau_{est} - \tau_{theory})/\tau_{theory}| \times 100\%$. The uncertainty of the experimental shear stress was deduced from Eq. (4-4).

Re_m	Experimental WSS (dyne/cm ²) $F = 120$ mm	Experimental WSS (dyne/cm ²) $F = 261$ mm	Analytical based on Eq. 3-7 (dyne/cm ²)	Error % $F = 120$ mm	Error % $F = 261$ mm
100	0.79 ± 0.03	0.83 ± 0.09	0.75	5.33	10.66
600	4.07 ± 0.12	4.47 ± 0.53	3.96	2.77	12.87
900	4.91 ± 0.13	5.33 ± 0.69	4.68	4.9	13.88
1240	6.71 ± 0.16	7.20 ± 0.80	6.27	7.1	14.83

2A.9 Turbulence Investigation: Transitional Regime Two-Dimensional Channel Flow ($\alpha = 9.72$ and $Re_m = 1430$)

It should be noted that this was the first flow case studied with the custom near-wall LDV probe/receiver which required both u and v velocity components and, given the vast amount of literature on the subject, it was considered as a reasonable approach to further validate the LDV system (to draw conclusions based on the present results in comparison to other studies) prior to measuring flow downstream of the BFS (Chapter Five). The transitional regime low-Re flow ($Re_m = 1430$; based on the bulk velocity (U) and channel height (h)) was simulated given the limitation of the pump in reference to the volumetric flow rate. It was not possible to generate a fully-developed turbulent flow at the working section.

2A.9.1 Scope of the Measurements

The velocities in the two coordinate directions (x, y) measured were $u(\bar{u}, u')$ and $v(\bar{v}, v')$ and Reynolds decomposition was applied to obtain the time-averaged components (\bar{u}, \bar{v})

and the turbulent fluctuation (u', v'), as reviewed by Pope (2000). LDV measurements of the u and v velocity components were captured simultaneously at three locations on the microscopy slide in the streamwise direction; these corresponded to $x/l = -0.13, 0$ and 0.13 (left edge, centre and right edge, respectively. It should be noted that l is the working section length). Furthermore, all velocity measurements were captured at the midplane corresponding to $2z/w = 0$.

2A.9.2 Applicable Theory and Processing Methods for the Data

For an infinitely wide plate (i.e. two-dimensional core at the centre of the channel where $w \gg h$) the Reynolds number can be defined as $Re_m = Uh/\nu$ or in terms of the maximum velocity (\bar{u}_{max}) at the centre of the channel ($2y/h = 1$) as $Re_c = \bar{u}_{max}(h/2)/\nu$ (Pope, 2000). In the present study, these Reynolds number values correspond to 1430 and 1085, respectively (corresponding to a programmed value of $Q = 25$ mL/s). Although the present author attempted to run the pump at a higher flow rate, it was not possible as a result of various challenges encountered with respect to the pump performance (i.e. volume occupied by air in the cylinder – further explained in Chapter Four). It is interesting to note as well that the actual volumetric flow rate delivered by the pump was $Q = 19.2$ mL/s, by means of considering the bulk velocity and cross-sectional area at the working section.

Furthermore, the streamwise bulk velocity is given by $U = 1/h \int_0^h \bar{u}(y)dy$ (average of the \bar{u} values across the channel height). According to Pope (2000), the flow can be considered laminar for $Re_m = Uh/\nu < 1300$ and fully turbulent for $Re_m = 1800$. In addition, Patel & Head (1969) report that transitional effects can be seen up to $Re_m = 3000$. Considering the hydraulic diameter as being a characteristic length scale gives a value of $Re_m = 2650$ for the present study. This was the approach suggested by Li & Olsen (2006), who studied turbulent channel flow for $0.97 < \alpha < 5.69$. It is important to consider the various definitions of Re presented in the literature in order to make effective comparisons with the present study and, hence, the various definitions are presented herein.

According to both Monty (2011) and Schultz & Flack (2013) turbulent channel flow remains two-dimensional for an aspect ratio larger than 7 (i.e. $w/h > 7$). In addition, Monty (2011) notes that the effect of the three-dimensional factor, $\epsilon = f(\alpha)$, on $\tau_w =$

$\epsilon h/2(\frac{dp}{dx})$ (at the midplane of the channel) is negligible for $w/h > 7$. Since, in the present study, $\alpha = 9.72$, the flow is considered to vary solely in the y -direction and $\tau_w \approx \overline{\tau_w}$ (where $\overline{\tau_w}$ is the shear stress averaged over the perimeter of the channel). It should be noted that an equivalent assumption is reported by Avari et al (2016), which reported a low-Re turbulent flow at the working section of the same PPFC.

To determine the non-dimensional mean velocity profile, u^+ , the following mathematical expression can be used (Durst et al. 1996):

$$u^+ = \frac{\bar{u}}{u_\tau}, y^+ = \frac{yu_\tau}{\nu} \quad (2A-29)$$

Durst et al (1996) notes that $u^+ = f(y^+)$ is typically represented as follows:

$$u^+ = y^+ \quad \text{for } y^+ \leq 5 \text{ (viscous sublayer)} \quad (2A-30)$$

$$u^+ = \frac{1}{k} \ln y^+ + K \quad \text{for } y^+ > 30 \text{ (logarithmic region)} \quad (2A-31)$$

where k, K, u_τ , and y^+ are, respectively, an Von Karman constant of value $k = 0.41$, an empirical constant of value $K = 5.0$, the friction velocity which can be determined by assuming a linear velocity profile close to the wall, and the non-dimensional y -axis (wall-normal distance).

In the present study, the friction velocity, $u_\tau = (\tau_w/\rho)^{0.5}$, is computed from the linear wall-slope technique (from $\partial\bar{u}/\partial y$ at the wall) suggested by both Djenidi & Antonia (1993) and Durst et al (1996). Durst et al (1996) fitted a linear line through three points (including the no-slip condition where $\bar{u} = 0$) in the viscous sub-layer (i.e. $y^+ < 5$). Similarly, in the present work a straight line (least-squares linear fit) was fitted to the near-wall data to obtain the estimate of $\partial\bar{u}/\partial y|_{y=0}$ and, hence, u_τ . An interpolation limit at $y^+ = 2$ proved the best fit, yielding a slope of 0.96 1/s which included 3 data points. A similar analysis is used by Durst et al (1995) to determine the error of the linear fitting method and the author reports that for $y^+ = 2$ as the limit (with approximately 18 data points) yields a slope of 1.0 1/s. In addition, Djenidi & Antonia (1993) were able to determine u_τ with an uncertainty of $\pm 3\%$ which was accomplished by fitting a straight line

to the measured near-wall ($y^+ < 2.5$) velocity data. The friction velocity and the WSS (averaged from the values at the three measurement locations) in the present study are 0.040 ± 0.0025 m/s and 16.31 ± 1.22 dyne/cm², respectively (uncertainty given based on the standard deviation of three measurements). The viscous length scale is $\delta_v = \nu/u_\tau = 0.018$ mm (i.e. 180 μ m) and the frictional Reynolds number, $Re_\tau = (h/2)/\delta_v \approx 50$. Both of these definitions were reviewed by Pope (2000). It should also be noted that the viscous sublayer in the present study was ≈ 0.09 mm (i.e 90 μ m) which was determined by Eq. (2A-29) by means of forcing $y^+ = 5$.

Additionally, the friction velocity can be deduced from the skin-friction coefficient, $c_f = \tau_w / (\frac{1}{2} \rho U^2) = 2(u_\tau/U)^2$ (Schultz & Flack, 2013), via equating the preceding equation to the empirical correlation equation, $c_f = 0.073(Re_m)^{-0.25}$, given by Dean (1978). For the present study, this analysis yielded $u_\tau = 0.047$ m/s (i.e. 4.7 cm/s) resulting in a difference of 14.8% in comparison to the value deduced from the linear wall-slope technique. For the present study, the skin friction deduced from the empirical correlation agrees well with the skin friction data which Tsukahara et al (2014) reports. Tsukahara et al (2014) shows that for $Re_m < 3000$, the skin friction tends to be overestimated using the empirical correlation given by Dean (1978). The skin friction data given by Tsukahara et al (2014) is congruous with the findings from Patel & Head (1969), which reported that for $Re_m < 2000$ the flow became intermittently laminar and turbulent and resulted in the deviation of the empirical c_f value.

2A.9.3 Results and Discussion

2A.9.3.1 Mean Flow

The average \bar{u}_{max}/U ratio in the present study is 1.46 ± 0.01 (based on the three measurement locations) and since the deviation of \bar{u}_{max}/U across the three points is within the experimental uncertainty the flow is considered as fully-developed. The deviation of \bar{u}_{max}/U across the three measurement points is in good agreement (i.e. same order of magnitude) with the study of Avari et al (2016), which reported $\bar{u}_{max}/U = 1.26 \pm 0.03$. Comparing the present study value of $\bar{u}_{max}/U = 1.46 \pm 0.01$ with the empirical correlation defined as $\bar{u}_{max}/U = 1.28 Re_m^{-0.0116}$ (Dean, 1978), yields a difference of 24.1%. The

empirical correlation specified above is given by Dean (1978) for a smooth, fully-developed, and two-dimensional turbulent channel flow. Table 2A-3 displays the various \bar{u}_{\max}/U values against Re_m from various literature which report studies of turbulence inside a channel. The % difference shown in the table is considered based on $|([\bar{u}_{\max}/U]_{\text{experiment}} - [\bar{u}_{\max}/U]_{\text{empirical}})/[\bar{u}_{\max}/U]_{\text{empirical}}| \times 100\%$. It can be seen from table 2A-3 that there is a relatively larger discrepancy between the experimental \bar{u}_{\max}/U and the empirical correlation equation for smaller Re_m values. Tsukahara et al (2014) attribute this discrepancy to the low-Re effect, since it is expected for \bar{u}_{\max}/U to decrease as Re_m increases (further away from the laminar prediction) since the measured velocity profiles start to resemble those of a fully-developed turbulent flow as the uniform core grows wider.

Table 2A-3. Various \bar{u}_{\max}/U values deduced from experimental methods and/or an empirical correlation for a two-dimensional turbulent flow inside a smooth channel. Results are calculated based on the empirical correlation given by Dean (1978).

Author	Present Study	Avari et al (2016)	Tsukahara et al (2014)	Kim et al (1987)	Patel & Head, (1969)
	LDV	LDV	DNS	DNS	Hot-wire
$\alpha = w/h$	9.72	9.72	11.25	Infinitely wide plate channel	48
Re_m	1430	2750	1860, 2290 and 5730	5600	1380, 1580, 1725, 6100
$(\bar{u}_{\max}/U)_{\text{experiment}}$	1.46	1.27	1.29, 1.22 and 1.17	1.16	Unreported
$(\bar{u}_{\max}/U)_{\text{empirical}}$ Dean (1978)	1.17	1.16	1.17, 1.17 and 1.15	1.16	1.17, 1.17, 1.17, 1.15
% Difference	24.1	9.4	10.2, 4.2 and 1.7	0	--

Figs 2A-12 and 2A-13 give the measured streamwise profiles in linear and semi-logarithmic co-ordinates respectively. All three LDV measurement locations (i.e. $x/l = -0.13, 0$ and 0.13) are shown in Fig. 2A-12. The maximum uncertainty in the mean value of ± 0.01 m/s (i.e. 1.1% of \bar{u}_{\max}) was calculated in the wall region (i.e. $0.11 < 2y/h < 0.04$) via $\epsilon_{\bar{u}\text{total}}^2 = \epsilon_{\bar{u}}^2 + \left(\frac{\partial \bar{u}}{\partial y}\right)^2 \epsilon_y^2$ (refer to Chapter Four in section 4.1 for further clarity). The velocity data in Fig. 2A-12 for all three measurement locations closely match the data from Patel & Head (1969) at $Re_m = 1380$, with the average deviation of $\pm 5.5\%$. As expected, the normalized velocity profile of Avari et al (2016) is more clearly distinguished (i.e. flatter shape of the profile) from the steady laminar channel flow solution as a result of a larger Re_m value ($Re_m = 2750$).

Fig. 2A-13 shows the non-dimensional u^+ profile plotted against the non-dimensional y^+ (i.e. mean velocity profiles in viscous wall units). The obtained data from Patel & Head (1969), Avari et al (2016) and Tsukahara et al (2014) are also given for an effective comparison. Reasonable agreement is shown between the present study (u^+ profile averaged for all three location measurements) and the work of Patel & Head (1969) for $Re_m = 1350$ and 1580 . The present data in Fig. 2A-13 agrees with the work of Patel & Head (1969) which reports poor data fit to the logarithmic law for $Re_m < 3000$. It is evident from Fig. 2A-13 that the mean velocity distribution measured by Avari et al (2016) does not designate a logarithmic region.

- Patel & Head (1969): $Re_m = 1380$ △ Patel & Head (1969): $Re_m = 1580$
× Patel & Head (1969): $Re_m = 1725$ × Patel & Head (1969): $Re_m = 2760$
— Parabolic (Laminar); Channel Flow ◇ Present Data: $Re_m = 1430, x/l = 0.13$
○ Present Data $Re_m = 1430, x/l = 0.00$ ■ Present Data: $Re_m = 1430, x/l = -0.13$
— Avari (2015) $Re_m = 2750$

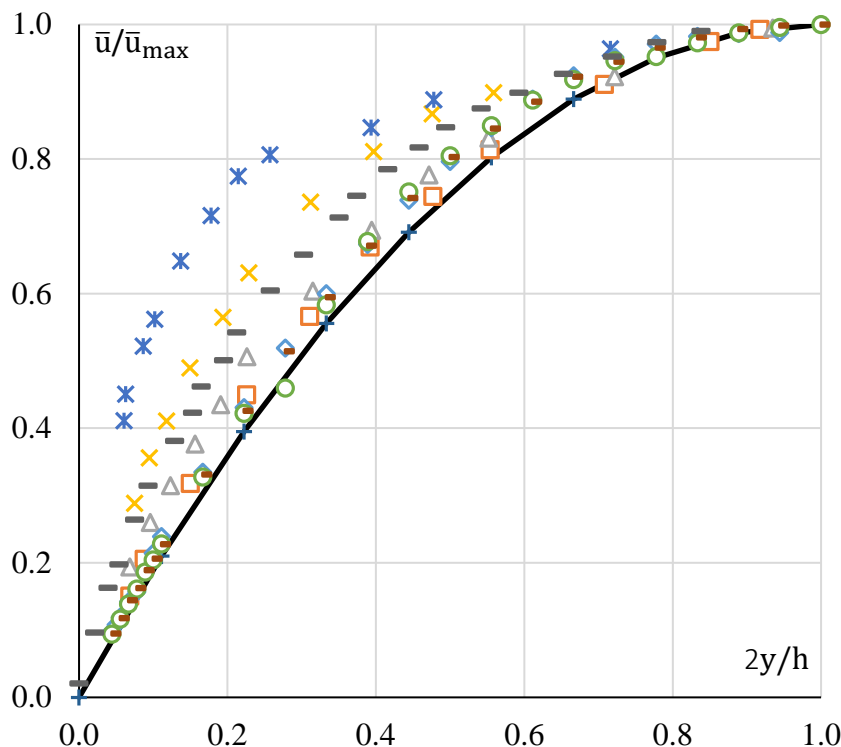


Fig. 2A-12 Normalized streamwise mean velocity plotted against the channel half-height for different Re_m values. The present results are compared with Patel & Head (1969). Present data were captured at $2z/w = 0$ and $x/l = -0.13, 0, 0.13$. The present study bulk Reynolds number (Re_m) based on the bulk velocity was 1430. In the present data, the maximum uncertainty in the mean value of ± 0.01 m/s (i.e. 1.1% of \bar{u}_{max}) was found in the wall region (i.e. $0.11 < 2y/h < 0.04$) which was calculated based on $\epsilon_{\bar{u}total}^2 = \epsilon_{\bar{u}}^2 + \left(\frac{\partial \bar{u}}{\partial y}\right)^2 \epsilon_y^2$. Error bars on the plot were not included for clarity of the figure.

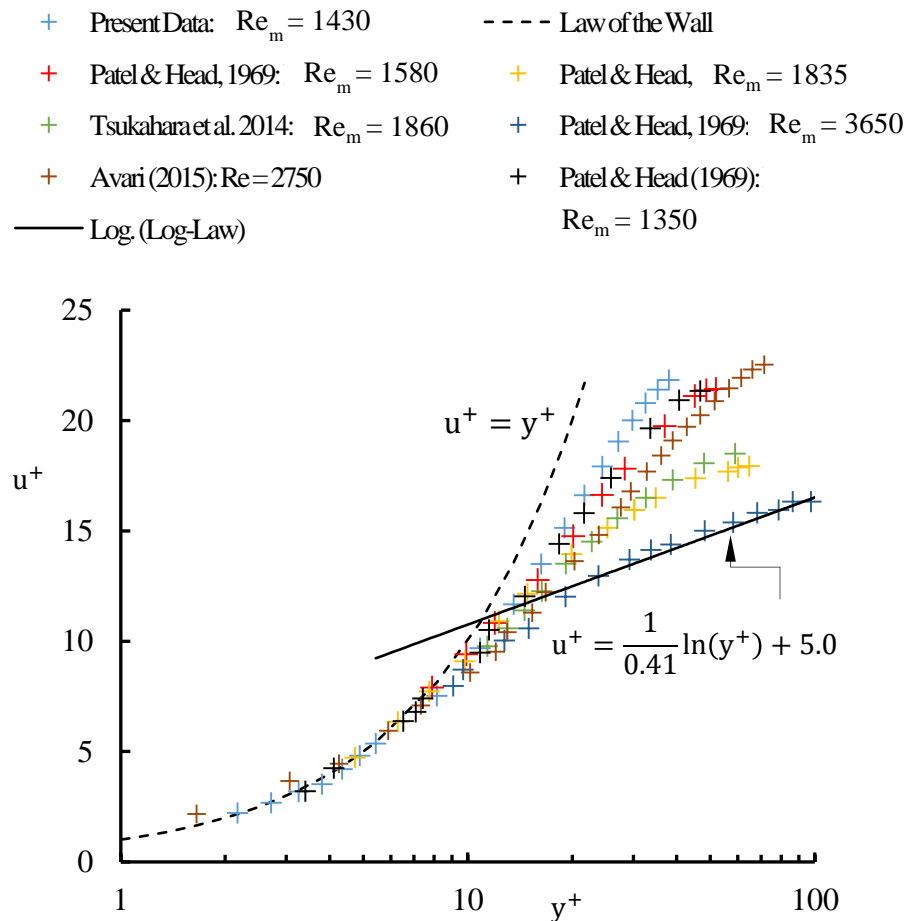


Fig. 2A-13 Mean velocity profiles for low-Re inside a two-dimensional flow channel scaled with the inner variable, u_τ . It should be noted that the data points collected from the literature have been extracted by the present author by replotting the velocity profiles. It should as well be noted that the y^+ axis was plotted on a logarithmic scale.

2A.9.3.2 Turbulence Intensity and Reynolds Shear Stress

The r.m.s. of the streamwise velocity fluctuation normalized by u_τ ($u'^+ = \sqrt{u'^2}/u_\tau$) is given in Figs. 2A-14a and 2A-14b. The normalized r.m.s. profiles were plotted against the channel half-height (i.e. $2y/h$; global coordinates) and y^+ (i.e. wall units) in Fig. 2A-14a and 2A-14b, respectively. The u'^+ profiles are given for $x/l = -0.13, 0$ and 0.13 and only across half of the channel since they are symmetrical in reference to the channel centre line

(i.e. $2y/h = 1$). The deviation of the u'^+ data (i.e. scatter of the data) across the channel half-height is within the experimental uncertainty (i.e. $\varepsilon_{r.m.s.u'}/u_\tau = \pm 0.01$). The true precision error of the LDV system which represents a source of noise not associated with the velocity fluctuations (i.e. spurious r.m.s. of ≈ 0.0025 m/s) is subtracted from the $\sqrt{u'^2}$ profile as recommended by Kehoe (2001) and Iyer & Woodmansee (2005). Also given in Figs 2A-14a and 2A-14b is the work of Tsukahara et al (2014) and Avari et al (2016) for the purposes of comparison.

It is clear from Fig 2A-14a that the maximum value of u'^+ increases with Re_m and occurs in the range, $10 < y^+ < 20$, for both the present study and the work of Tsukahara et al (2014). It should be noted that in the range, $10 < y^+ < 15$, the viscous and the Reynolds shear stress ($-\overline{uv}$) are equal and the peak production of turbulence exceeds its dissipation (Pope, 2000). The maximum value of u'^+ for the present study is 2.36 ± 0.01 (based on the standard deviation at three measurement positions reported) which occurs at $y^+ = 18$. Given the difference in the Reynolds number this is in good agreement with the work of Tsukahara et al (2014) for $Re_m = 1860$, whereby the difference in the maximum value of u'^+ is $< 10\%$. However, for the larger Re_m values, such as in the work of Avari et al (2016), the maximum u'^+ is ≈ 2.6 and occurs at $y^+ \approx 12$. The latter value is in better agreement with the literature which reports fully developed turbulent flow inside rectangular channels (Kim et al. 1987).

Moreover, in Fig. 2A-14b and considering global coordinates (i.e. $2y/h$), the maximum value of u'^+ occurs further away from the wall (i.e. $2y/h \approx 0.33$) in the present work than that of Tsukahara et al (2014) at $Re_m = 3290$, which occurred at $2y/h \approx 0.17$. Fig. 2A-14b shows that for the present work, u'^+ values for $2y/h > 0.33$ are larger than the values at higher Re_m given by Tsukahara et al (2014). This is also evident with the other u'^+ profiles reported by Tsukahara et al (2014), whereby there is an increase in u'^+ values (for lower Reynolds numbers) at any given $2y/h$ position following a maximum u'^+ . The latter is a result of the maximum u'^+ occurring further away from the wall, together with a less rapid decay of turbulence at relatively smaller Re_m values (Antonia et al 1992).

The shape of the v'^+ distributions (at all three measurement locations) given in Fig. 2A-14a is very different to that for u'^+ . However, the increase of v'^+ with Re_m is as clearly apparent when comparing the present data with the work of Tsukahara et al (2014) and Avari et al (2016). According to Antonia et al (1992), the increase of v'^+ with Re_m exhibited a plateau, whereby the author reports both DNS and experimental work inside a fully-developed duct flow ($\alpha = 18$) at four values of Re_m in the range 3300-21500.

It is clear from Fig. 2A-14a that v'^+ increases with distance from the wall, which is in good agreement with the work of Avari et al (2016). However, for the present work, the maximum v'^+ is $= 0.5$ at $y^+ = 40$ whereas Avari et al (2016) reports $v'^+ \approx 0.7$ at $y^+ \approx 30$. The results given by Avari et al (2016) are in better agreement with the literature for turbulent channel flows. This discrepancy is presumably as a result of the flow in the present work not being a fully-developed turbulent flow as a result of the relatively smaller $Re_m = 1430$. The latter statement is supported by the fact that at $Re_m = 1860$ (Tsukahara et al 2014), the maximum reported v'^+ is ≈ 0.5 at $y^+ \approx 38$.

Furthermore, Fig. 2A-15 gives the normalized Reynolds shear stress (i.e. $-\overline{(u'v')^+} = -\overline{u'v'}/u_\tau^2$) at $x/l = -0.13$ plotted across half of the channel given the v component limitation (refer to Section 2A.4 for a discussion of the green beam measurement limitation). Similarly, the data from Tsukahara et al (2014) are plotted for comparison purposes. Similar to the work of Kehoe (2001), the normalized Reynolds shear stress is only considered if one velocity component (i.e. u' and v') contains a fluctuation greater than the spurious r.m.s. velocity of 0.0025 and 0.0040 m/s for the streamwise and wall-normal fluctuations, respectively (details are outlined in Section 2A.3.2). The present author further notes that, in the present study, the $-\overline{(u'v')^+}$ profile for $Re_m = 1430$ falls below the $Re_m = 1860$ profile reasonably well (of the work of Tsukahara et al 2014), with the maximum value of $-\overline{(u'v')^+} = 0.2$ at $y^+ = 23$. These results agree well with Tsukahara et al (2014) who report a maximum value of $-\overline{(u'v')^+} = 0.72$ at $y^+ = 32$ and $-\overline{(u'v')^+} = 0.37$ at $y^+ = 26$ for $Re_m = 5730$ and 1860, respectively. The author reports a decrease in the maximum $-\overline{(u'v')^+}$ value together with a shift of the peak closer to the wall (scaled with the wall units) for a decrease in the Re_m value.

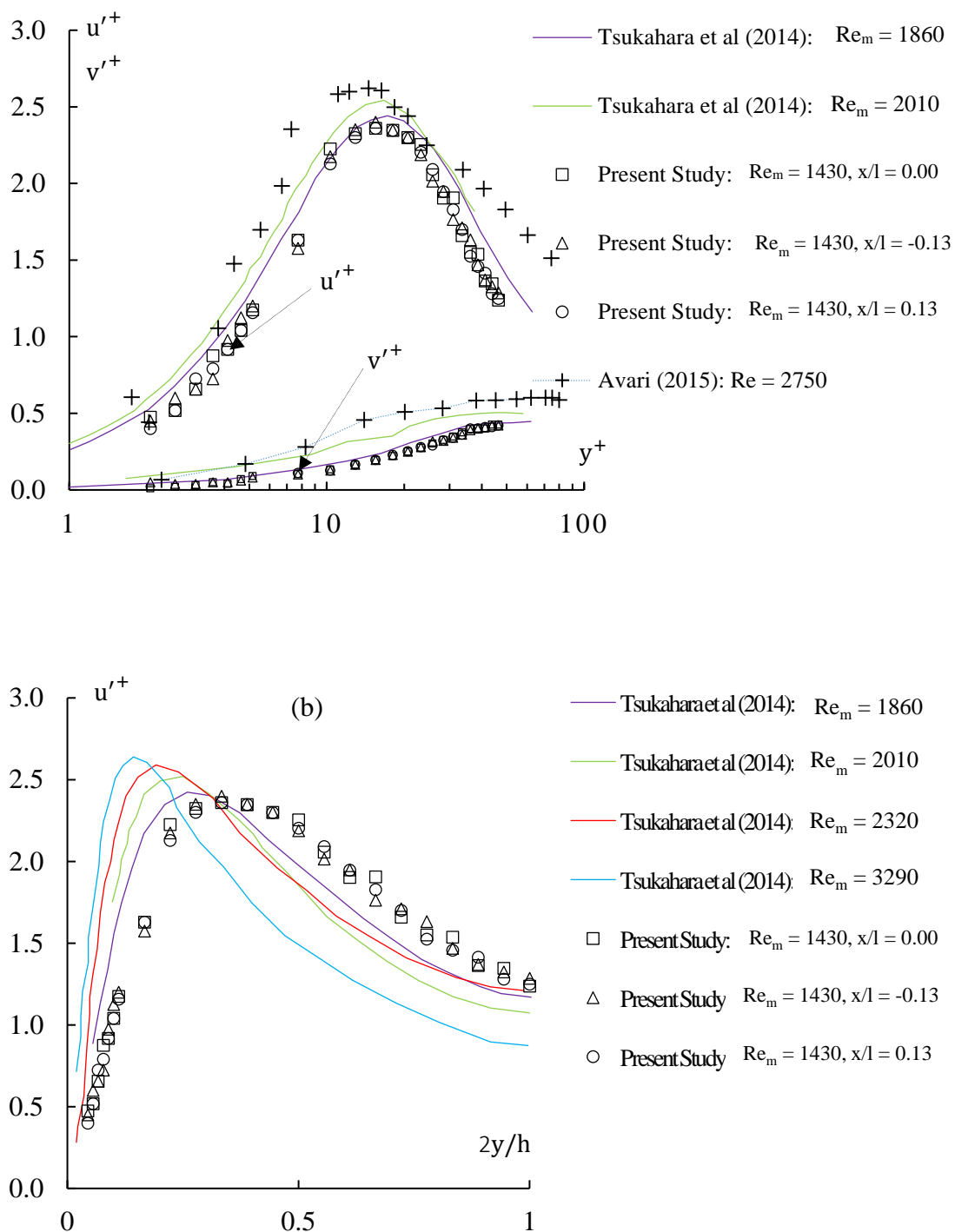


Fig. 2A-14 Normalized r.m.s. of the streamwise velocity fluctuation (denoted as u'^+) plotted against a) the y -axis normalized with the viscous length scale (denoted as y^+) and b) the channel half-height, $2y/h$. The maximum normalized error is $\epsilon_{r.m.s. u'}/u_\tau = \pm 0.01$ in the $10 < y^+ < 15$ wall region.

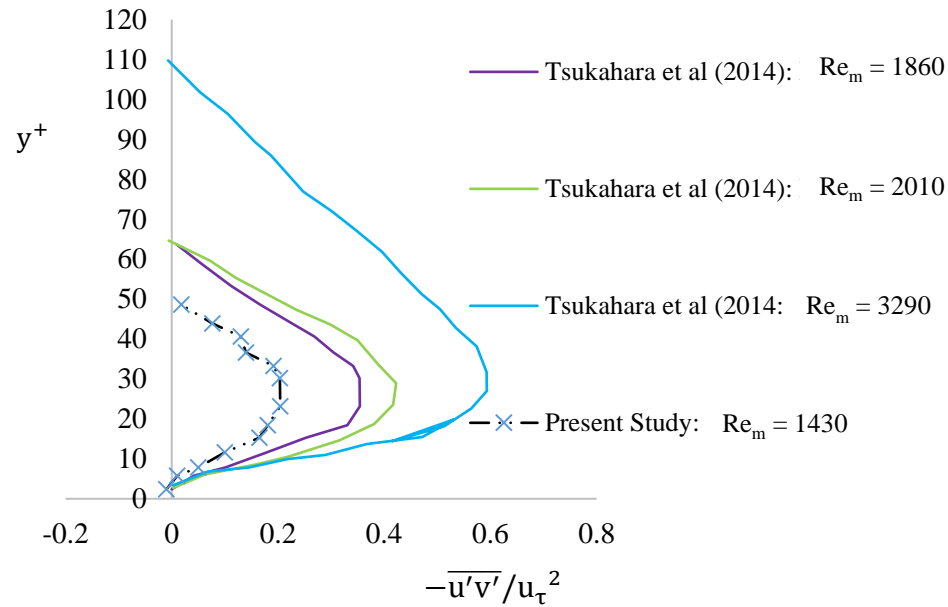


Fig. 2A-15 Reynolds shear stress normalized with the friction velocity (i.e. $-\overline{u'v'})^+ = -\overline{u'v'}/u_\tau^2$) plotted across half of the channel. The maximum normalized error is $\varepsilon_{-\overline{u'v'}/u_\tau^2} = \pm 0.015$ in the $10 < y^+ < 30$ wall region.

2A.10 Appendix 2 Summary

This Appendix provided an in-depth evaluation of the near-wall configured LDV system including its design, performance and uncertainty. It also provided two flow case studies (steady laminar and low-Re turbulent flow) to evaluate both the implications of spatial resolution (measurement volume diameter) on WSS accuracy and the ability to measure u and v velocity components simultaneously and in coherence mode inside the PPFC. Both flow cases were analyzed in the context of relevant literature for an effective comparison.

In terms of the **LDV performance**, a brief summary of the quantitative data throughout the Appendix is as follows:

- The actual measurement volume diameter (blue beams) for the $F = 120$ mm and 261 mm lens was 42.0 ± 4.5 μm and 80.3 ± 3.8 μm , respectively (validated using the mean gate time). For the green beams, the actual measurement volume diameter for the $F = 120$ mm and 261 mm lens was 44.0 ± 5.2 μm and 86 ± 7.2 μm , respectively (validated using the mean gate time).

- In terms of the precision error (i.e. random error), the measured r.m.s. u' and v' velocities under a steady laminar flow and over a wide range of velocities (0.002-0.500 m/s) were 0.0025 (2.5 mm/s) and 0.004 m/s (4 mm/s), respectively (near the centre region of the channel ($y/h \approx 0.5$), typical r.m.s. u'/\bar{u} values over the velocities examined here approximately 0.6-1% whereas, near the wall ($y/h \approx 0.95$) values as large as 100% were detected).
- Based on the smallest data rate near the wall ($\dot{N} \approx 100$ Hz; coincidence mode) and the smallest time scale (i.e. very smallest, dissipative eddies) of the flow ($t_\eta \approx 0.01$ s (100 Hz), the transit-time method was used to correct for the velocity bias based on the criterion, $\dot{N}t_\eta \approx 1 > 1/2$. Furthermore, the tracer particle residence time was 43 μ s (given 42.0 ± 4.5 μ m as the measurement volume diameter and a maximum velocity of 1 m/s). For this reason the accuracy and the resolution of the FSA 3500 processor was not a concern given its minimum transit time of 100 ns (manufacturer reported).
- The allowable height (h_a) to traverse the green beam measurement volume in the positive y direction (across the channel height) was evaluated as $h_a = 0.81 \pm 0.070$ mm. This value is consistent with the actual measurements of the v-component reported in Chapter Five (i.e. measurement possible up to $y/h \approx 0.5$; where $y = 0$ at the lower wall).
- The coincidence interval of 50-100 μ s (whereby two channels obtain velocity data from the same particle) was used with all flow case measurements. According to the literature, the coincidence window that is at least an order of magnitude less than the inverse of the data rate should be used and, hence, this condition was satisfied (i.e. for $\dot{N} = 1000$ Hz, the coincidence window should be ≈ 100 μ s).
- In terms of the flow tracers (TiO₂), the mean particle diameter was 0.36 μ m and the ratio between the particle and fluid densities was $\gamma = \left(\frac{\rho_p}{\rho_f}\right) \approx 4.0$. Furthermore, considering the mean particle diameter of 0.36 μ m, and a fluid density of 997.96 ± 0.12 kg/m³ yielded a time response of $\tau_p \approx 0.038$ μ s ($f_p \approx 2.6 \times 10^7$ Hz). There was no energy present at frequencies greater than $f_p \approx 2.6 \times 10^7$ Hz and, thus, the particles were assumed to follow the flow in its small scale motions.

- For $\tilde{N} \approx 8.26 \times 10^{10}$ particles per m^3 (estimated particle concentration) and mean velocity of 0.106 m/s (found downstream of the step in the disturbed region; near the wall; $y/h = 0.022$), the average rate of signals was $\tilde{N}\bar{u}_m d_m \approx 740$ Hz. For both, the steady and pulsatile flow cases (over the BFS) there was no energy present at frequencies (f_{turb}) greater than 370 Hz and, thus, the criterion (a sufficient \tilde{N} to resolve the velocity fluctuations) was satisfied based on $\tilde{N}\bar{u}_m d_m \geq 2f_{\text{turb}}$.

In terms of the **steady laminar flow** measurements presented in this Appendix, a brief summary of the quantitative data is as follows:

- WSS data together with its uncertainty was obtained through LDV measurements of the streamwise velocity close to the wall (the $F = 120$ mm lens yielded the closest measurement of 20 ± 10 μm and the $F = 261$ mm lens yielded a closest measurement of 40 ± 10 μm) for $Re_m = 100, 600, 900$ and 1240.
- For all Re_m values, the difference between the experimental and theoretical WSS was larger for the $F = 261$ mm lens (in comparison to the $F = 120$ mm lens) with the maximum error of 14.83% at $Re_m = 1240$.
- In comparison to the work of Avari et al (2016) which reported WSS at $Re_m = 1795$ (if equivalent definition of Re is used), a difference of 17.1% and 9.4% was found using the $F = 120$ and 261mm lens, respectively (whereby the experimental WSS data in the present study was extrapolated to determine the percent difference). Hence, better agreement was found for the $F = 261$ mm lens, presumably given the similarity in the spatial resolution and nearest measurement point (i.e. 80.3 ± 3.8 μm and 40 ± 10 μm for the present study and 68 μm and 36 μm for the work of Avari et al 2016).
- Finally, for the $F = 120$ mm lens configuration, the WSS was within 3.1% of the value given by Avari et al (2016) based on the analytical solution (i.e infinitely wide plate). Hence, the $F = 120$ mm lens configuration seemed to accord better with the theory presumably as a result of the smaller measurement volume and wall offset (i.e. 42.0 ± 4.5 μm and 20 ± 10 μm).

In terms of the **low-Re turbulent flow** (transitional regime, whereby $Re_m = 1430$ considering channel height as the characteristic length scale), a brief summary of the quantitative data is as follows:

- The velocities in the two coordinate directions (x, y) measured (captured simultaneously at three locations on the microscopy slide in the streamwise direction at the midplane of the channel) were $u(\bar{u}, u')$ and $v(\bar{v}, v')$ and Reynolds decomposition was applied to obtain the time-averaged components (\bar{u}, \bar{v}) and the turbulent fluctuation (u', v') .
- The average measured $\bar{u}_{\max}/U = 1.46 \pm 0.01$ was not in ideal agreement with the empirical correlation ($\bar{u}_{\max}/U = 1.28 Re_m^{-0.0116}$) based on a fully-developed two-dimensional turbulent channel flow, with a difference of 24.1%. in terms of the \bar{u}_{\max}/U ratio. The finding in the latter was in good agreement with the literature which credits the discrepancy to the low-Re effect since it is expected for \bar{u}_{\max}/U to decrease as Re_m increases.
- The friction velocity was deduced based on a linear wall-slope technique which yielded a difference of 14.8% in comparison to the value calculated from the empirical correlation, $c_f = 0.073(Re_m)^{-0.25}$, for channel flow. The latter was found to be in good agreement with the literature as well, whereby for $Re_m < 3000$ the skin friction tends to be overestimated using the empirical equation.
- The present data agreed with the literature for $Re_m < 3000$ whereby a poor data fit to the logarithmic law was found.
- The maximum value of u'^+ (i.e. r.m.s. u' normalized with the friction velocity) was 2.36 ± 0.01 (at $y^+ = 18$) which agreed well with the work of Tsukahara et al (2014) for $Re_m = 1860$ with a difference being $< 10\%$. In addition, the maximum v'^+ was 0.5 at $y^+ = 40$ which was as well in excellent agreement with Tsukahara et al (2014) for $Re_m = 1860$. The latter, however, did not agree well with the work of Avari et al (2016) whereby the author reported $v'^+ = 0.7$ at $y^+ = 30$ for $Re_m = 2750$ (presumably as a result of the low-Re effect).

APPENDIX 3

MATHEMATICAL DEFINITION OF SKEWNESS, KURTOSIS
AND STANDARD ERROR

The sample skewness statistic can be calculated using the following mathematical expression (Doane & Seward, 2011):

$$S = \frac{n}{(n-1)(n-2)} \sum_{i=1}^n \left(\frac{x_i - \bar{x}}{s} \right)^3 \quad (3A-1)$$

where n , s , and \bar{x} are, respectively, the sample size, standard deviation, and the sample mean. The standard error of the skewness quantity (assuming sampling distribution is approximately normal) can be calculated with 95% confidence interval as follows (Cramer, 1997):

$$SES = \pm 2.0 \sqrt{\frac{6n(n-1)}{(n-2)(n+1)(n+3)}} \quad (3A-2)$$

Furthermore, the excess sample kurtosis (i.e. kurtosis -3) can be calculated using the following mathematical expression (Joanes & Gill, 1998):

$$K = \left\{ \frac{n(n+1)}{(n-1)(n-2)(n-3)} \sum_{i=1}^n \left(\frac{x_i - \bar{x}}{s} \right)^4 \right\} - \frac{3(n-1)^2}{(n-2)(n-3)} \quad (3A-3)$$

The standard error of the kurtosis quantity (sampling distribution is approximately normal) can be calculated with 95% confidence interval as follows (Cramer, 1997):

$$SEK = \pm SES \sqrt{\frac{n^2-1}{(n-3)(n+5)}} \quad (3A-4)$$

It should be noted that for relative large sample size ($n > 1000$), the standard error of approximately $\sqrt{24/n}$ can be used (Snedecor, & Cochran, 1967). For distributions other than normal, Wright & Herrington (2011) recommend using the bootstrap standard error and confidence interval method. Since in the present work the sample size distribution was normal, the bootstrap method was not used.

APPENDIX 4

SCALING SELECTION CRITERIA FOR COMPARISON OF PPFC AND
CIRCULAR PIPE TYPE STENOSES

To the best of the present author's knowledge, there is an absence of work (specifically considering streamwise velocity profiles and analysis of reattachment length) comparing plane channel expansion (abrupt/smooth symmetric double backward-facing step or asymmetrical single step) to axi-symmetric tube expansion (i.e. stenosis). It is important to determine correct scaling of the streamwise distance (x -) to compare BFS to axi-symmetric flows to determine the main factors which contribute to the difference in the reattachment length for these types of flows (i.e. geometry, three-dimensionality, flow physics). At present, there is no clear guidance from the literature that demonstrates a scaling that is consistent between PPFC type stenoses and circular pipe stenoses.

From the state of knowledge in the literature on wake behaviour behind a circular and sufficiently long rectangular cylinder (whereby the shear layers separating at the upstream sharp corner do not interfere with the downstream corner), an analogy can be drawn to illustrate how the reattachment length scales between the backward-facing step (BFS) and the axi-symmetric tube (with a semi-circle blockage) models. A similar analogy is used by Griffith (2009) considering wake behaviour behind a circular cylinder to compare the normalized reattachment lengths for different blockage ratios (considering an axi-symmetric stenosis). According to Griffith (2009), this analogy loses applicability for blockage ratios larger than $b = 0.75$ (where $b = 1 - d^2/D^2$) and for relatively larger Reynolds numbers (at the onset of vortex shedding). A similar analogy is used in the present study considering steady laminar flow (developed boundary layer) past both a circular and rectangular cylinder to determine a consistent scaling for the present analysis to understand reattachment length differences. According to Taneda (1956), the reattachment length (x_1) for steady laminar flow (i.e. developed boundary layer) past a circular cylinder can be expressed as $x_1 = C (r_b) Re_{cyl}$ (where $Re_{cyl} = U_\infty r_b / \nu$, U_∞ is the freestream velocity, r_b is the radius of the circular cylinder and C is a proportionality constant), which demonstrates proportionality to the blockage height (i.e. radius of the cylinder) and the Reynolds number. Furthermore, using the analogy $U_\infty = U/(1 - b)$

(which represents the bulk velocity inside the tube constriction), the expression can be rewritten (to be applicable for an axi-symmetric stenosis flow) as $x_1 = C \left(\frac{r_b^2}{D} \right) \left(\frac{1}{1-b} \right) \text{Re}$ (where D is the diameter of the upstream unblocked tube and $\text{Re} = \text{UD}/\nu$). Expressing in non-dimensional form gives, $\frac{x_1}{D} = C \left(\frac{r_b}{D} \right)^2 \left(\frac{1}{1-b} \right) \text{Re}$. A similar analogy can be drawn for the BFS model by considering steady laminar flow over a sufficiently long rectangular cylinder (whereby the streamwise length of cylinder is much larger than the wall-normal direction length). For the BFS flow, the equation can be written by scaling (the reattachment length) with the hydraulic diameter as $\frac{x_1}{D_h} = C \left(\frac{S}{D_h} \right)^2 \left(\frac{1}{1-b} \right) \text{Re}$ (where $\text{Re} = \text{UD}_h/\nu$ and S is the step height). It should be noted that non-dimensionalization of x_1 with the blockage height (S, r_b) eliminates the square term in both expressions for the two models (for the BFS model and considering an infinitely wide plate assumption, the expression can be given as $\frac{x_1}{S} = C \left(\frac{b}{2} \right) \left(\frac{1}{1-b} \right) \text{Re}$). To plot the functions, the normalized reattachment length (x_1^*) is divided by the multiplier (C) to give a new scaled reattachment length (x_1^*/C). Fig. 4A-1 gives x_1^*/C (for both BFS and axi-symmetric models) as a function of Re at $b = 0.5$ (blockage ratio of 50% by area) whereby the reattachment lengths are scaled with the upstream of blockage diameter (D, D_h), $2D$ half-section of the pipe ($D/2, D_h$) and blockage height (r_b, S). The scaling of the reattachment length considering $D/2$ is generally used when comparing a double BFS (i.e. symmetric expansion) to a single BFS (i.e. asymmetric expansion, Abbott & Kline, 1962).

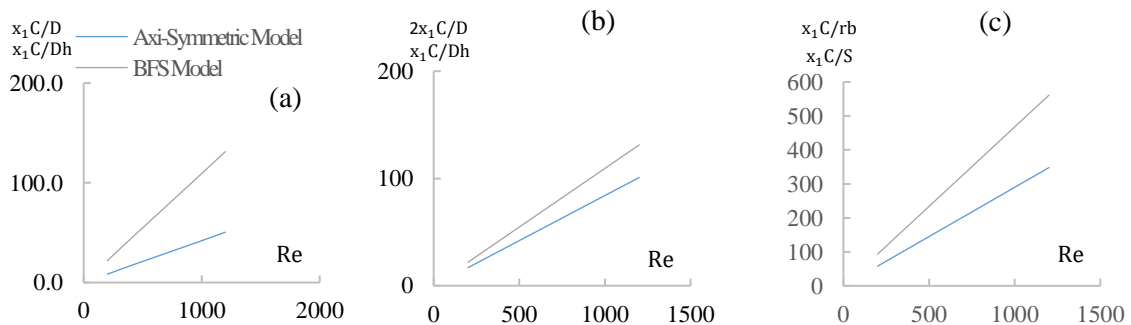
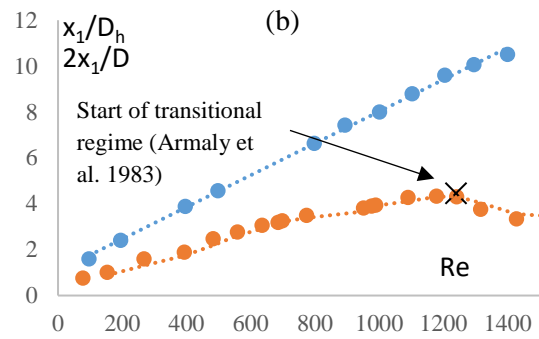
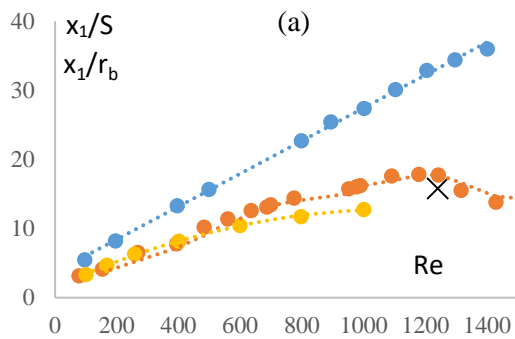
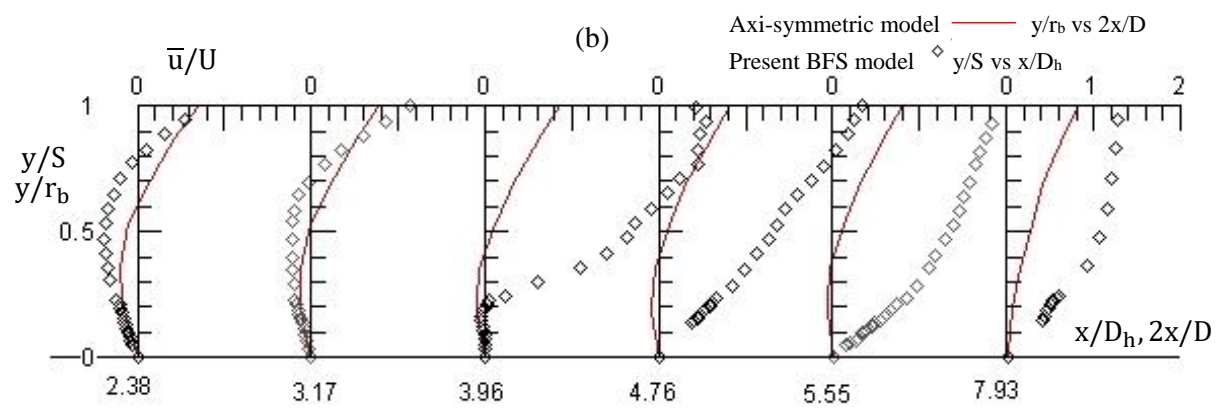
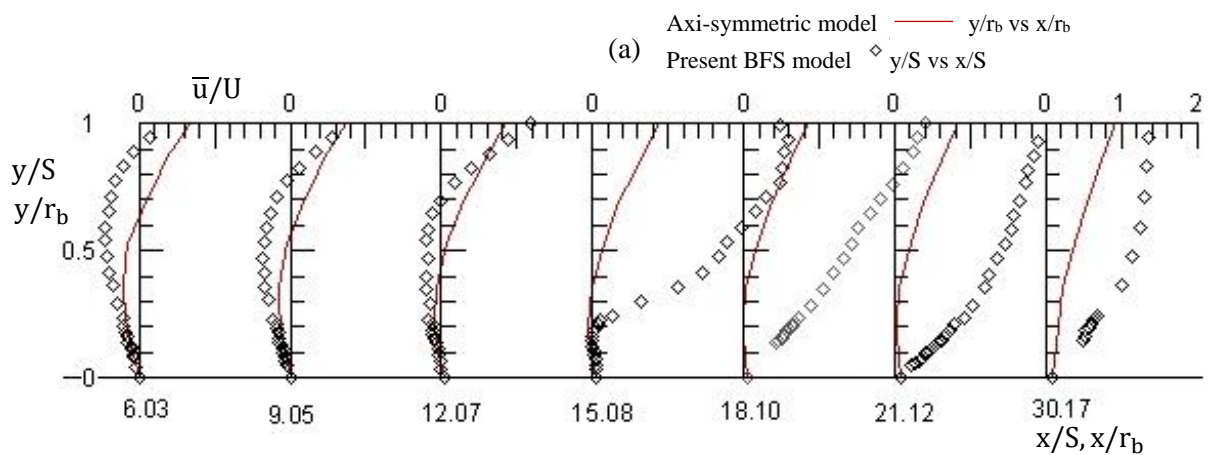


Fig. 4A-1 Normalized reattachment length as a function of Re at $b = 0.5$ comparing the axi-symmetric and BFS models: (a) scaled with D, D_h , (b) scaled with $D/2, D_h$ and (c) scaled with r_b, S .



- Axi-symmetrical model (Griffith, 2009)
- BFS model (Armaly et al. 1983)
- × BFS model: Present
- Semi-circle channel model (Griffith, 2009)
- Linear (Axi-symmetrical model (Griffith, 2009))
- 2per.Mov. Avg. (BFS model (Armaly et al. 1983))
- Poly. (Semi-circle channel model (Griffith, 2009))

Fig. 4A-2 Measured normalized reattachment lengths: (a) scaled with S , r_b and (b) scaled with D_h , $D/2$.



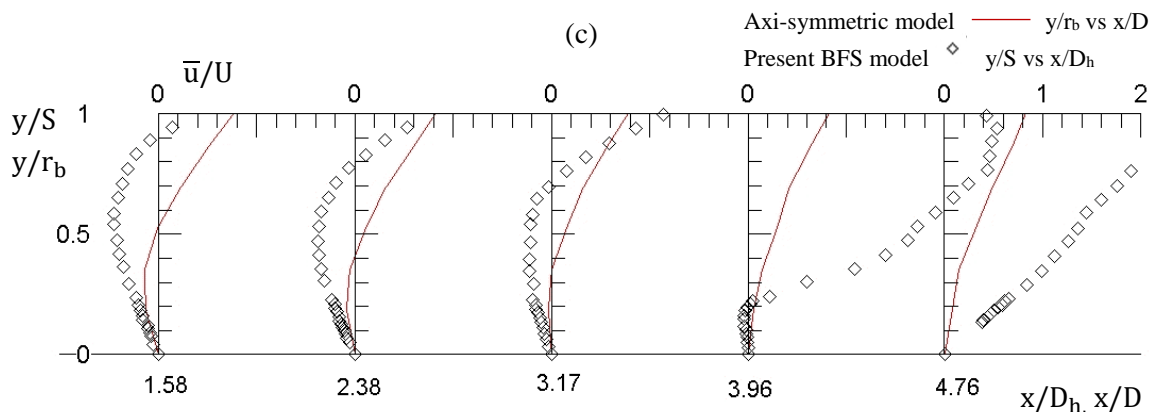


Fig. 4A-3 Normalized streamwise velocity profiles downstream of the blockage comparing the present BFS model to the axi-symmetric stenosis model given by Griffith (2009): (a) streamwise distance scaled with S, r_b (b) streamwise distance scaled with $D_h, D/2$ and (c) streamwise distance scaled with D_h, D .

Fig. 4A-1b demonstrates best scaling of the streamwise distance using the $x/D_h, 2x/D$ length scales (i.e. considering 2D half-section of the pipe) for the BFS and the axi-symmetric models, respectively. The percent difference at $Re = 1000$ is 25.7%. It should be noted that Fig. 4A-1 only reflects geometrical factors which contribute to the differences in the reattachment length between the present BFS model and the axi-symmetric model (other factors would be reflected in the C value). These include the effect of aspect ratio (i.e. side-wall effects), streamwise turbulence intensity (at the blockage), boundary layer thickness to blockage height ratio (Rajasekaran, 2011). This is further substantiated in Fig. 4A-2, whereby the measured normalized reattachment length is plotted (as a function of Re at $b \approx 0.5$) based on the work of Armaly et al (1983) and Griffith (2009) for the BFS model and the axi-symmetric model, respectively. It can be seen from Fig. 4A-2a that the reattachment length (normalized with the blockage height) is relatively larger for the axi-symmetric model than for the BFS model (in contrast to Fig. 4A-1). This is, presumably, as a result of the upper wall recirculation region (present for the BFS model) which subjects the main flow to destabilizing concave curvature (Barkley et al. 2002). The even larger discrepancy between the two models is recognized at $Re \approx 1200$ which Armaly et al (1983) characterizes as the transitional regime and shows rapid decrease of the reattachment length as a result of Reynolds stresses (turbulent reattachment). In Fig. 4A-2, the present BFS

model data point are also plotted for comparison purposes which shows to nicely coincide with the transitional regime referenced by Armaly et al (1983).

In addition, Fig. 4A-3 shows the normalized streamwise velocity profiles (for $y/S \leq 1$ and downstream of the BFS at $Re = 1240$ and the axi-symmetric tube blockage at $Re = 797$), whereby the streamwise distance is scaled with the different length scales noted in the preceding paragraphs. It can be seen from Fig. 4A-3a,b (whereby the streamwise distance is scaled with the blockage height and considering half-section of the pipe) that there is a better collapse of streamwise velocity data (between the two models and given the differences in the Re value in comparison to Fig. 4A-3c) prior to the appearance of the upper wall recirculation region for the BFS model (i.e. at $x/S = 15.08$ whereby the maximum value of the \bar{u}/U profile is shifted downward in reference to the y-axis).

Hence, in Chapter Five (two-dimensional velocity measurements) when comparing the reattachment distance downstream of the blockage, the streamwise distance (x -) is scaled with x/D_h and $2x/D$ for the BFS and axi-symmetric models, respectively.

CURRICULUM VITAE

Name: Marin Vratonjic

Place of Birth: Rijeka Croatia (Canadian Citizen)

Post-Secondary Education and Degrees:

Doctor of Philosophy (Mechanical)
Western University
London, Ontario
2017

Masters of Engineering (Mechanical)
University of Toronto
Toronto, Canada
2007

Bachelor of Engineering (Mechanical)
McMaster University
Hamilton, Ontario
2005

Diploma, Mechanical Engineering
Sheridan College
Brampton, Ontario
2003

Professional Associations:

Professional Engineers of Ontario
P.Eng Status, 2009.

Certified Engineering Technologist (OACETT)
C.E.T. Status, 2009.

Related Work Experience:

VP Operation and Engineering
Electrical Contacts Limited
Hanover, Ontario
2013-2017

President/Mech. Engineer
MV & Associates Corp
London, Ontario
2009-2013

Mechanical Engineer (Part Time)
Universal Mould and Die
Stoney Creek, Ontario
1999-2007

Conferences: VRATONJIC, M., SAVORY, E., GHOLAMREZA-KASHI, S., KEMPSTON, J., HORIE, M. & ROGERS, K. 2008 Experimental Investigation Of Flow-Induced Shear Stress On Endothelial Integrity. Canadian Society for Mechanical Engineering Forum, Ottawa, Canada.